

MICROHYDRODYNAMICS OF VESICLES IN CHANNEL FLOW

A DISSERTATION
SUBMITTED TO THE DEPARTMENT OF CHEMICAL ENGINEERING
AND THE COMMITTEE ON GRADUATE STUDIES
OF STANFORD UNIVERSITY
IN PARTIAL FULFILLMENT OF THE REQUIREMENTS
FOR THE DEGREE OF
DOCTOR OF PHILOSOPHY

Joseph Michael Barakat

June 2018

© 2018 by Joseph Michael Barakat. All Rights Reserved.
Re-distributed by Stanford University under license with the author.

This dissertation is online at: <http://purl.stanford.edu/jx327sv2755>

I certify that I have read this dissertation and that, in my opinion, it is fully adequate in scope and quality as a dissertation for the degree of Doctor of Philosophy.

Eric Shaqfeh, Primary Adviser

I certify that I have read this dissertation and that, in my opinion, it is fully adequate in scope and quality as a dissertation for the degree of Doctor of Philosophy.

Gerald Fuller

I certify that I have read this dissertation and that, in my opinion, it is fully adequate in scope and quality as a dissertation for the degree of Doctor of Philosophy.

Andrew Spakowitz

I certify that I have read this dissertation and that, in my opinion, it is fully adequate in scope and quality as a dissertation for the degree of Doctor of Philosophy.

Roseanna Zia

Approved for the Stanford University Committee on Graduate Studies.

Patricia J. Gumpert, Vice Provost for Graduate Education

This signature page was generated electronically upon submission of this dissertation in electronic format. An original signed hard copy of the signature page is on file in University Archives.

Abstract

The hydrodynamic resistance of fluid vesicles suspended in channel flow is studied theoretically as a model system for single-cell microfluidic measurements. When freely suspended in fluid flow, particles (e.g., rigid and soft particles, droplets, vesicles, and biological cells) act as “resistors” in a fluidic circuit. The relationship between the hydrodynamic resistance generated by even a single particle is complicated when the particle can deform, due to the nonlinear coupling between fluid flow and shape deformation. This coupling is markedly more complex for vesicles than for droplets, due to the diverse shape space promoted by the constraint that the surface of a vesicle remains incompressible. In this thesis, we tackle the challenging problem of determining the motion of vesicles – both single vesicles and vesicle trains – in channel flow using a variety of tools, drawing from perturbation techniques, coarse-grained theory, and direct numerical simulations.

The problem investigated in this thesis can be defined by three regimes of vesicle confinement. Under high confinement, the vesicle is lubricated by a very thin film and the flow is well described by lubrication theory. We investigate this regime for circular Poiseuille flow by means of narrow-gap analysis, wherein the clearance is defined as a small parameter and a formal perturbation series is constructed. We find that the vesicle length plays a crucial role in determining the scaling of the hydrodynamic figures of merit – namely, the relative velocity of the vesicle compared to the mean flow and the extra pressure drop required to push it through the channel – with respect to the clearance. Membrane bending elasticity is included as a parameter in the theoretical result, and is shown to break the linear dependence of the vesicle velocity and extra pressure drop on the applied mean flow.

Under moderate confinement, the lack of a separation of length scales precludes the use of narrow-gap analysis. One must resort to direct numerical calculations, which have proven to be challenging despite the rapid evolution of modern computers. We tackle this challenging regime for both circular tubes and square channels using a combination of boundary element simulations and lubrication theory. Our numerical results were verified using the aforementioned narrow-gap analysis. It is shown that relaxing the confinement greatly expands the variety of accessible vesicle shape configurations. Significantly, as the vesicle aspect ratio increases, the centerline shape becomes unstable and breaks symmetry. At high confinement, this effect is damped. Bending elasticity

qualitatively changes both the vesicle shape configurations and hydrodynamical integral quantities, with increasing sensitivity as the vesicle becomes less confined. For square channels, an interesting new phenomenon is observed wherein the vesicle can move slower than the mean fluid velocity. This observation is validated by microfluidic experiments, in collaboration with our colleagues at Texas Tech University.

Finally, under low confinement the disturbance produced by a vesicle is relatively weak. It is challenging to apply direct numerical calculations to this regime due to the high degree of resolution needed to compute the extra pressure drop. Numerically, this arises as a limitation in discretization of the channel wall, because the extra pressure drop is determined from an integral of the wall surface tractions. If these tractions are weak, then a high density of surface elements is required in order to accurately compute the force integral. An alternative approach, which has become popular in the literature, is to assume that the vesicle is in an unbounded flow to leading order. It is then possible to determine the theoretical limit of the relative velocity and extra pressure drop at low confinement, by use of the reciprocal theorem. We tackle this problem for a restricted subset of vesicle shapes (small, quasi-spherical vesicles) and show how the extra pressure drop couples to the shape deformation in this regime. In doing so, we also generalize previous theories of vesicle motion, which have hitherto focused on specific flow types, to an arbitrary, quadratic flow field.

Acknowledgments

There are many people to whom I owe a great deal of gratitude. First and foremost, I would like to thank my thesis advisor, Prof. Eric Shaqfeh, for creating a space for me to develop as an independent researcher and for being a constant source of support, mentorship, and friendship during my graduate studies. When I first entered Eric’s group, I was hungry to make sense of physical phenomena through mathematics. Eric understood this immediately and reinforced my curiosity. He taught me exactly how to take a fundamental engineering question and pose a mathematical problem that could be solved. He encouraged me to tackle problems rigorously, to not take shortcuts, to be unflinching in the face of great complexity and nonlinearity. He enabled me to contribute presentations at nine conferences throughout my graduate studies, through which I have built my own network of scientists and engineers. Most of all, I admire the attention Eric gives to his students and the value he places in advising and teaching. His course in complex fluids was nothing short of a mind-expanding experience. Eric is my biggest supporter, and I am certain that he will remain a role model for me as I pursue my own scientific career.

I am indebted to Prof. Gerry Fuller, with whom I worked for one year as a graduate student before being seduced by theoretical science. It is not hyperbolic to say that my current trajectory was set into motion in large part due to Gerry’s influence. Virtually everything I know about experimental fluid mechanics can be traced to my time working in Gerry’s lab. He sparked my interest in interfacial flows, which ultimately motivated the topic for my thesis. As a mentor, Gerry showed me incredible patience and generosity, despite my stubbornness and naïveté. He has always been supportive of me, even when I eventually decided to leave his group for more theoretical endeavors. Since that time, he has consistently taken an interest in my current work and we have collaborated on other projects. My relationship with Gerry is quite precious to me, something I will continue to nurture in the years to come.

I would like to thank the other members of my reading committee, Profs. Andy Spakowitz and Roseanna Zia. I have had the good fortune during my years at Stanford to learn from Andy through his courses and our conversations. Andy’s expertise in biopolymers and biomembranes was crucial during my early years in Eric’s group, as I strived to understand the interplay among membrane tension, bending elasticity, and fluid flow. Andy has also given me some very good career advice –

do not be afraid of who you are, be secure in your identity as a researcher, and make no apologies for your chosen path. For someone like me, who constantly questions his own choices, Andy's advice has given me a sorely needed sense of calm and confidence.

I was delighted when Roseanna joined our department in my last year of graduate study, and did not hesitate to ask her to serve as a fourth reader in my thesis committee. What a fantastic decision that was, for it opened up conversations with Roseanna about my work and afforded me a glimpse into her expertise on hydrodynamic interactions of many-body suspensions. In our individual meetings, Roseanna frequently challenged me to think critically about my work and how I chose to present it, and my thesis presentation came out all the better as a result of her input. I have loved every single one of our interactions and look forward to many more in the years to come.

In my first three years of doctoral study, I was supported by the National Science Foundation (NSF) through the Graduate Research Fellowship Program. In my later years, I was funded through the Stanford School of Engineering. The research conducted in this thesis would not have been possible without the financial support of these institutions, and for that I am truly grateful.

There are several other professors at Stanford who have played an important role in my graduate studies. In my very first year, Prof. Alex Dunn sat down with me and gave me detailed feedback as I was writing graduate fellowship proposals; I am certain that I would not have won the NSF Graduate Research Fellowship without his crucial input, and for that I owe him a debt. Prof. Curt Frank advised me for a quarter during that first year as a rotation student, and I am grateful for his advice and patience. Prof. Jian Qin has always been a warm and friendly face; I have appreciated our many conversations, his scientific input, and his great sense of humor.

During my last year at Stanford, I have had the good fortune to spend some time with my “grand-advisor” and living legend, Prof. Andy Acrivos. Andy and I have sat down on a number of occasions to discuss my projects. He came to each of these meetings having read my papers in detail, with specific questions and comments to be addressed. All of our discussions forced me to reevaluate my work and put it in a wider context. The fruit of those discussions can be found in the second section of Chapter 3, which was written largely in response to Andy’s questions. During our last meeting, Andy generously took me out to lunch with his wife, Jennie, at the Faculty Club, which incited a delightful cascade of spirited conversations. I am humbled and grateful to have gotten to know Andy a bit during this last year. It has been a singular privilege, and I look forward to keeping in touch with him after I leave Stanford.

Stanford has been a fertile environment for my graduate studies, in no small part due to the wonderful research group carefully assembled by Eric. The Shaqfeh Group is like the “X-Men School” for complex fluid theoreticians, each member equipped with his or her own set of powers derived from an exciting diversity of research problems. This diversity has exposed me to different topics in complex fluids beyond my own thesis project, including the dynamics polymer solutions, Brownian

motion of colloidal suspensions, and fluid flow in the lungs and in blood. Each Shaqfeh Group member – Travis Walker, Sean Fitzgibbon, Vivek Narsimhan, Andrew Spann, Eleanor Lin, Jorge Bernate, Preyas Shah, Sreenath Krishnan, Mengfei Yang, Maggie Qi, Will Murch, Taylor Geisler, Chris Guido, Tiras Lin, Sourav Padhy, Jonas Einarsson, Amir Saadat, Xingyi Shi, Jeremy Binagia, Anika Jain, and Anni Zhang – has touched my life in some way. I’d like to give specific thanks to Travis and Sean, for their continued friendship, loyalty, and honesty; to Maggie and Mengfei, for being my “partners in crime” in our journey through graduate school together; to Vivek, for giving me an early education on vesicles and analytical tools; to Andrew, for teaching me about the boundary element method and working with me on the implementation of 3D simulations of vesicles in channel flows; to Jorge, who gave me an early primer on low-level programming languages; to Preyas and Sreenath, for their vast knowledge of mathematics and willingness to lend help whenever asked; to Chris, for taking me to Yosemite for the first time and for indulging me on my academic endeavors to learn diagrammatic methods; to Tiras, for being my officemate and enduring my endless barrage of jokes and exclamations; to Taylor and Will, for making me feel young again; to Amir, for teaching me about large-scale computing and Ewald summation; to Jonas, for being a fantastic collaborator (Chapter 6) and giving me a proper education symbolic programming and Fourier transforms; to Anika, for kindness and curiosity, and for always being a friendly face in the office; to Xingyi, for being a thoughtful research collaborator and student.

Members of the Fuller Group, past and present, also deserve recognition. I’d like to thank Emily Hollenbeck, Gigi Lin, and Vinay Surya, for being wonderful officemates during my brief time in the Fuller Group; Saad Bhamla, for being one of my earliest mentors and teaching me the ropes of interferometry; Dan Walls, for the Philadelphia connection (Superbowl LII Champions!) and for being my Bridge partner; John Frostad, for his thoughtful advice, for initiating a research collaboration between me and the Fuller Group, and for teaching me how to play Bridge; Mariana Rodríguez Hakim, for being my first rotation student and since becoming a wonderful research collaborator.

The research conducted in this thesis would not have been possible without the support of the Stanford staff. I’d like to acknowledge Minh Lan Nguyen, the Administrative Assistant for the Shaqfeh Group; Andrea Blake Hubbard, the Administrative Assistant for the Fuller Group; Kumiko Jacobs, the Department Executive Assistant; Stella Minaev, the Chemical Engineering Department Manager; Ash Snowden, the Student Services Manager; Pat Carlson, the Building Manager for the Shriram Center. Former members of the staff also deserve my gratitude: Jeanne Cosby, previously the Student Services Manager and my first point of contact at Stanford; Eric Nguyen, previously the Departmental & Industrial Affiliates Administrative Associate; Annie Jensen, previously the Administrative Assistant for the Shaqfeh Group.

The numerical calculations performed in Chapters 4 and 5 were performed on the Certainty

computing cluster at Stanford. I'd like to thank Steve Jones, the Director of the High Performance Computing Center at Stanford, for maintaining this cluster and for answering my frequent inquiries with amazing, bordering on terrifying, efficiency.

I would be remiss if I did not mention several key people outside the Stanford community who have influenced my thesis work. Prof. Siva Vanapalli, who I met at a Gordon Research Conference in 2015, has given me some terrific advice over the years and has been a fantastic research collaborator. He and his student, Shamim Ahmmmed, contributed the experimental measurements described in Chapter 5. Prof. Bud Homsy, who I met during his sabbatical at Stanford, originally inspired the asymptotic work presented in Chapter 3 through his work with Harish Dixit on the so-called "elastic Landau-Levich problem." Prof. Susan Muller (and her student, Kari Storslett) introduced me to electroformation methods for manufacturing vesicles in the laboratory.

At this point, I would like to acknowledge several professors from my alma mater. First and foremost, I want to thank Prof. V. Faye McNeill, who was my undergraduate research advisor. Without Faye's guidance, I surely would not have landed where I am today. She inspired me to pursue research as a career and quickly became a role model for me. I am thankful for her continued mentorship and friendship since my graduation from Columbia. Thanks also to the McNeill Group alumni: Allison Schwier, Neha Sareen, Joe Woo, Dhruv Mitroo, Giuliana Viglione, and Nikki Lugo. Two other professors at Columbia have had a great influence on me. Prof. Chris Durning's course in transport phenomena was undoubtedly the seed that planted in me a great love for the subject; I have found out since then that we are now, ironically, academic "cousins." Prof. Sanat Kumar was and remains another person to whom I frequently turn for advice; I'd like to thank him for keeping in touch with me throughout my graduate studies.

I have an amazing group of friends both within and outside the Stanford community. I'd like to acknowledge some of the members of my Stanford Ph.D. class: Jeremy Feaster, Josh Willis, Alex Diaz de Arce, Axel Palmstrom, David Bergsman, Jeff Lopez, Tommy Hellstern, Emma Chory, Matt Ostrowski, and Eva Huang. Also a special shout-out to Tom Dusseault (who left us for industry), Tom Lampo (our honorary classmate), and Leanna Owen. I'd also like to thank my amazing roommates, Eric Hall and Nicholas Hall, with whom I've lived for three years, and my friend Eric Chipin, my former neighbor, fellow Philadelphia Eagles fan, and good friend. My friends from Columbia with whom I've remained in contact over the years (too many to name, but I'll try): Javier Rivera, Spencer Almen, Anthony Battaglia, Samantha Roberts, Daniel Vecchiolla, Jane Zellar, Alba Luengo, Matt Kalish, Madeleine Jensen, Rhonda Shafei, Caroline Corley, Kat Chan, Lisa Mack, Jordan Hollarsmith, Danielle Rubin, Mary Ye, Courtney Giannini, Leandra Gerena, Andy Surinach, Christine Currie, Tom Morell, Kendra Joseph, Monica Landrove, Lauren Alpert, Kristina Bebedzakova, Lina Gebremariam, Bianca Rahill-Marier, Nida Vidutis, Zach Sims, Mike Enciso, Hefei Li, Matt Star, and Victoria Steffes. Thanks for all of the good times.

Of course, I would not be here without my wonderful family. My mother and father, Nadia and Joseph Barakat, deserve all of my love and gratitude for raising me to be the man I am today. Nearly a decade after I've left home, I take with me all of their values and life lessons. I am happy to share this moment with both of them. I am grateful to have an amazing sister, Katie, who always makes me laugh. I am also fortunate to have an enormous extended family: my uncles (Fred, John, Dave, Cary); my aunts (Mary Ann, Linda, Nancy, Rachel, Tracy, Elsie); my cousins (D.J., Kristi, Brian, Jennifer, Andrew, Alex, Alexa, Julia, Dave, Mike, Nicole, Jackie, Jake, Jarrod); and my grandmother (Adele). It is thanks to them that I will never feel truly alone, afraid, or unloved. My family will forever be my foundation.

Finally, I would like to thank my girlfriend, Kate Meier, for giving me love, support, and strength every single day. I am immeasurably happier with her in my life, and I'm looking forward to what the future holds in store for us.

Contents

Abstract	iv
Acknowledgments	vi
1 Introduction	1
1.1 Vesicles in fluid flow	1
1.2 Properties of lipid-bilayer membranes	5
1.3 Flow of particles through conduits	7
1.3.1 Rigid particles	10
1.3.2 Red blood cells	11
1.3.3 Vesicles	15
1.4 Objectives and scope of this thesis	18
2 Theoretical formulation	20
2.1 Equations of fluid mechanics	20
2.2 Equations of membrane mechanics	22
2.3 Initial-boundary value problem	24
2.4 Vesicle velocity and extra pressure drop	26
2.5 Scalings and dimensionless groups	27
2.5.1 Typical values of the dimensionless parameters	28
2.5.2 Other dimensionless groups	29
2.6 Summary	30
3 Vesicles in narrow tubes	31
3.1 Narrow-gap assumption	31
3.2 Previous theories	34
3.3 Exchange of parameters	37
3.4 Narrow-gap equations	39
3.4.1 Outer equations	40

3.4.2	Inner equations	42
3.4.3	Matching conditions	43
3.5	Small- ϵ expansion	44
3.5.1	Transfer of boundary conditions	45
3.5.2	Outer region	46
3.5.3	Inner region	48
3.5.4	Higher-order corrections	50
3.6	Asymptotic solutions for $\bar{\beta} = 0$	55
3.6.1	Long, spherocylindrical vesicles ($\bar{\ell} \gg 1$)	55
3.6.2	Short, spherical vesicles ($\bar{\ell} \ll 1$)	58
3.7	Effect of bending elasticity ($\bar{\beta} \neq 0$)	62
3.8	Elimination of ϵ and ℓ as parameters	64
3.9	Discussion of results	68
3.9.1	Vesicle shapes	68
3.9.2	Relative velocity and extra pressure drop	68
3.9.3	Comparison to direct numerical simulations	71
3.9.4	Comparison to experiments and previous theories	73
3.10	Review of assumptions	75
3.11	Concluding remarks	77
4	Vesicles in wider tubes	78
4.1	Direct numerical calculations	78
4.2	Boundary element method (BEM)	82
4.3	Axisymmetric lubrication theory	88
4.4	Discussion of results	92
4.4.1	Flow fields	92
4.4.2	Symmetry breaking and time-dependent states	95
4.4.3	Effect of confinement and reduced volume	99
4.4.4	Effect of membrane bending elasticity	104
4.5	Concluding remarks	107
5	Vesicles in square channels	110
5.1	Non-circular conduits	110
5.2	BEM for non-circular conduits	112
5.3	Non-axisymmetric lubrication theory	113
5.3.1	Formulation	116
5.3.2	Error analysis	122

5.4	Experimental	124
5.5	Discussion of results	128
5.5.1	Vesicle flow through a contraction	128
5.5.2	Steady vesicle shapes, surface tractions, and surface velocities	130
5.5.3	Critical geometry	135
5.5.4	Vesicle velocity and extra pressure drop	140
5.6	Concluding remarks	141
6	Small, quasi-spherical vesicles	143
6.1	Quasi-spherical assumption	143
6.2	Previous theories	145
6.3	Undisturbed flow	148
6.4	Disturbance fields	151
6.5	Fundamental harmonics	152
6.6	Lamb's general solution	154
6.7	Vesicle geometry	156
6.8	Small- Δ expansion	157
6.8.1	Transfer of boundary conditions	158
6.8.2	Leading-order solution	159
6.8.3	Higher-order corrections	169
6.9	Concluding remarks	172
7	Conclusions and directions for future work	174
7.1	Conclusions	174
7.2	Future prospects	178
7.3	Further reading	179
Appendices		181
Appendix A	Differential geometry of surfaces in space	182
A.1	Review of vector and tensor analysis	182
A.2	Dual bases for a surface	185
A.3	Surface components of vectors and tensors	187
A.4	Surface gradient	188
A.5	Surface curvature	189
A.6	Surface divergence theorem	191
A.7	Surface geometry in various coordinate systems	192

A.7.1	Cartesian coordinates, $z = z_s(x, y)$	192
A.7.2	Cylindrical coordinates, $\rho = \rho_s(\phi, z)$	194
A.7.3	Cylindrical coordinates, $z = z_s(\rho, \phi)$	196
A.7.4	Spherical coordinates, $r = r_s(\theta, \phi)$	199
A.7.5	Two-dimensional Cartesian coordinates, $z = z_s(x)$	201
A.7.6	Axisymmetric cylindrical coordinates, $\rho = \rho_s(z)$	203
A.7.7	Axisymmetric cylindrical coordinates, $z = z_s(\rho)$	205
Appendix B	Ordered perturbation equations in the narrow-gap limit	208
B.1	Outer equations	208
B.2	Inner equations	213
B.3	Matching conditions	217
Appendix C	Short, spherical vesicles in the narrow-gap limit	218
C.1	Zeroth-order solution in $\epsilon^{\frac{1}{2}}$	218
C.1.1	Outer equations	218
C.1.2	Inner equations	219
C.1.3	Matching conditions	220
C.1.4	Solution	221
C.2	First-order solution in $\epsilon^{\frac{1}{2}}$	224
C.2.1	Outer equations	224
C.2.2	Inner equations	225
C.2.3	Matching conditions	226
C.2.4	Solution	227
Appendix D	Periodic fundamental solutions of creeping flow	230
D.1	Periodic boundary-value problem for the Green's functions	230
D.1.1	Fourier transform of the creeping flow equations	231
D.1.2	Solution for the velocity and pressure gradient in the reciprocal space	233
D.1.3	Inverting the Fourier transforms	235
D.1.4	Green's functions for the velocity, pressure, and stress	236
D.2	Ewald summation formula for the Green's functions	237
D.3	Numerical evaluation of the Green's functions	240
Appendix E	Boundary integral equations for vesicles in channel flow	242
E.1	Reciprocal identity	242
E.2	Volume integral of the reciprocal identity	244
E.2.1	Case 1: the source point lies outside the volume	245

E.2.2	Case 2: the source point lies inside the volume	245
E.2.3	Case 3: the source point lies on the boundary	246
E.3	Representation theorem	248
E.4	Boundary integral equations	248
E.4.1	Interior points	249
E.4.2	Points on the wall boundary	251
E.4.3	Points on the vesicle boundary	252
E.4.4	Summary of the boundary integral equations	253
E.5	Numerical solution of the linear system	254
Appendix F	Numerical methods for lubrication calculations	255
F.1	Multiple shooting method	255
F.1.1	Shooting from one end	259
F.1.2	Shooting from both ends to a fitting point	263
F.2	Nonlinear finite difference method	266
F.2.1	Linearization	269
F.2.2	Discretization	274
Appendix G	Ordered perturbation equations in the quasi-spherical limit	286
Bibliography		291

Nomenclature

a	the radius ratio based on the particle volumetric radius ($= r_0/R$)
A^*	the apparent lubrication contact area
A_0	the particle surface area
A_x	the channel cross sectional surface area
β	the bending parameter based on the channel radius [$= E_B/(\mu V R^2)$]
\mathbf{b}	the body force density vector
\mathbf{c}	the principal-value (second-order) tensor
χ	the bending parameter based on the particle volumetric radius [$= E_B/(\mu V r_0^2)$]
Ca	the capillary number
c	the suspension concentration (volume fraction)
δ	the unit tensor
$\boldsymbol{\delta}_s$	the surface unit tensor
∇	the gradient operator
∇_s	the surface gradient operator
\mathbf{d}	the (far-field) irreducible vector of the velocity curvature
δ	the separation parameter
D/Dt	the material time derivative
$\partial/\partial t$	the spatial time derivative
Δp	the channel pressure drop
Δp^+	the extra pressure drop

Δp°	the particle-free pressure drop
Δ	the particle excess surface area
D	the deviatoric curvature of a surface
$[\eta]$	the relative intrinsic viscosity
ϵ	the permutation tensor
η	the (far-field, third-order) irreducible tensor of the velocity curvature
ϵ	the clearance parameter
$\hat{\mathbf{e}}_\rho, \hat{\mathbf{e}}_\phi, \hat{\mathbf{e}}_z$	the unit basis vectors of a cylindrical coordinate system
$\hat{\mathbf{e}}_r, \hat{\mathbf{e}}_\theta, \hat{\mathbf{e}}_\phi$	the unit basis vectors of a spherical coordinate system
$\hat{\mathbf{e}}_x, \hat{\mathbf{e}}_y, \hat{\mathbf{e}}_z$	the unit basis vectors of a Cartesian coordinate system
$\hat{\mathbf{e}}_{(1)}, \hat{\mathbf{e}}_{(2)}, \hat{\mathbf{e}}_{(3)}$	the unit basis vectors of an orthonormal coordinate system
E_B	the membrane bending modulus
E_D	the membrane dilatational modulus
E_S	the membrane shear modulus
\mathbf{f}	the surface traction vector
\mathbf{f}_s	the membrane surface traction vector
$\mathbf{f}_s^{\text{bending}}$	the membrane bending force density vector
$\mathbf{f}_s^{\text{tension}}$	the membrane tension force density vector
\mathbf{f}_w	the wall surface traction
\mathcal{G}	the periodic fundamental (second-order) tensor for the velocity
$\dot{\gamma}$	the (far-field) rate-of-strain tensor
γ	the surface tension
G	the mean pressure gradient
G_s	the surface metric
$\overset{(n)}{\mathbf{H}}^+$	the growing harmonic of order n

$\overset{(n)}{\boldsymbol{H}}^-$	the decaying harmonic of order n
H	the mean curvature of a surface
κ_s	the surface curvature tensor
\boldsymbol{k}	the wavevector
κ	the viscosity contrast
κ_1, κ_2	the principal curvatures of a surface
K	the Gaussian curvature of a surface
k	the (spherical) radial wavenumber
K_{hyd}	the channel hydraulic resistivity
ℓ	the particle reduced length
λ	the radius ratio based on the particle areal radius ($= R_0/R$)
λ^*	the critical radius ratio
L	the particle length
L^*	the particle length at maximum confinement
L_c	the channel length
L_x, L_y, L_z	the Cartesian dimensions of a periodic cell
μ	the fluid shear viscosity
μ_{eff}	the effective shear viscosity
$\hat{\mathbf{n}}$	the unit normal vector of a surface
N	the number of edges in a polygonal cross section
$\boldsymbol{\omega}$	the (far-field) vorticity tensor
$\boldsymbol{\Omega}$	the particle rotational velocity vector
Ω	the solid angle
Ω_0	the particle volume
\mathcal{P}	the periodic fundamental vector for the pressure

ϕ	the azimuthal angle
ψ	an arbitrary scalar
φ	the level set function of a surface
p	the fluid pressure
P_x	the channel wetted perimeter
\mathbf{q}	the leakback flux vector
Q	the channel flow rate
q	the leakback flux per unit circumference
\mathbf{r}	the separation vector
ρ	the (cylindrical) radial distance
Re	the Reynolds number
ϱ	the fluid density
ϱ_s	the surface mass density
R	the channel hydraulic radius
r	the (spherical) radial distance
R_0	the particle areal radius
r_0	the particle volumetric radius
r_p	the sphere radius
$\boldsymbol{\sigma}$	the Cauchy stress tensor
\mathcal{S}	a set of contiguous positions on a surface
\mathcal{S}_s	the set of points on the membrane surface
\mathcal{S}_w	the set of points on the wall surface
s	the arc length
\mathcal{T}	the periodic fundamental (third-order) tensor for the stress
τ	an arbitrary second-order tensor

θ	the (far-field, second-order) irreducible tensor of the velocity curvature
$\mathbf{t}^{(1)}, \mathbf{t}^{(2)}$	the contravariant tangential vectors of a surface
$\mathbf{t}_{(1)}, \mathbf{t}_{(2)}$	the covariant tangential vectors of a surface
τ	the membrane tension
θ	the polar angle
ϑ	the tilt angle
t	the time
$\bar{\mathbf{u}}_s$	the membrane slip velocity vector
\mathbf{U}	the particle translational velocity vector
\mathbf{u}	the fluid velocity vector
\mathbf{u}_s	the membrane surface velocity vector
v	the particle reduced volume
U	the axial component of the particle translational velocity
\mathbf{v}	an arbitrary vector
\mathcal{V}	a set of contiguous positions in a volume
V	the mean channel velocity
\mathbf{w}	the (far-field) vorticity vector
W	the membrane work functional
\mathbf{x}	the spatial position vector
\mathbf{x}_s	the surface position vector
$\hat{\mathbf{x}}$	the unit vector in the radial direction
ξ, η	an arbitrary pair of surface coordinates
x	the axial distance
$\overset{(n)}{\mathbf{Y}}$	the surface harmonic of order n
y_p	the sphere-center displacement from the centerline in tube flow

List of Tables

1.1	Elastic properties of (unilamellar) lipid-bilayer vesicles, as measured experimentally. Tabulated are the dilatational modulus E_D , the bending modulus E_B , and the lysis tension τ^* . The tabulated values are the mean \pm s.d. except for the value of τ^* reported by [120] for sarcolemmal muscle, which is the median \pm 95% confidence interval. Also tabulated is the temperature T at which each measurement was taken, if reported (r.t. = room temperature, taken to be in the range 20-25 °C).	5
1.2	Cross sectional surface area A_\times , wetted perimeter P_\times , and hydraulic resistivity K_{hyd} for straight channels with circular or polygonal cross sections.	8
3.1	Numerical results for long, spherocylindrical vesicles ($\bar{\ell} \gg 1$) with negligible bending stiffness ($\bar{\beta} = 0$).	57
3.2	Analytical results for short, spherical vesicles ($\bar{\ell} \ll 1$) with negligible bending stiffness ($\bar{\beta} = 0$).	60
3.3	Numerical results for the membrane tension $\bar{\tau}_0$ and characteristic ratio $(6/\bar{\tau}_0)^{\frac{2}{3}}(\bar{\beta}/\bar{\tau}_0)$ for long, spherocylindrical vesicles ($\bar{\ell} \gg 1$) and several values of $\bar{\beta}$. The transition between the tension- and bending-dominant eigenmodes occurs at a critical bending parameter $\bar{\beta}^*$, where $(6/\bar{\tau}_0)^{\frac{2}{3}}(\bar{\beta}^*/\bar{\tau}_0) \simeq 0.3257$	63
3.4	Relative velocity U/V and dimensionless extra pressure drop $\Delta p^+ R/(\mu V)$ for different values of the reduced volume v , confinement ratio λ/λ^* (or radius ratio λ , also shown), and bending parameter β . The clearance parameter is in the range $0 < \epsilon < 0.3$	70
3.5	Asymptotic behavior of the relative velocity U/V and dimensionless extra pressure drop $\Delta p^+ R/(\mu V)$ as $\lambda \rightarrow \lambda^*$ for spherocylindrical and spherical vesicles. The two limiting cases are nicely interpolated by (3.9.1).	71
4.1	Parameters a_n , b_n , c_n , and d_n used in the rational fraction approximants (4.4.2) (plotted as dotted curves in Figures 4.11-4.12), as determined by nonlinear least-squares regression. Also tabulated are the critical radius ratios λ^* for each reduced volume.	104

List of Figures

1.1	Vesicles at equilibrium, as determined via experiment and theory (reproduced from [10]). (<i>Left</i>) Symmetric-asymmetric transition (temperatures from bottom to top are $T = 30.7, 32.6, 40.0$, and 44.4°C). (<i>Center</i>) Budding transition ($T = 31.4, 35.5, 35.6$, and 35.8°C ; an air bubble enters the measurement chamber in the second and third panes). (<i>Right</i>) Discocyte-stomatocyte transition ($T = 43.8, 43.9, 44.0$, and 44.1°C). The theoretical curves were computed by minimization of the curvature free energy of the bilayer [equation (1.2.1)].	2
1.2	Vesicles in linear flow, as observed via experiment. All experiments were performed at room temperature. (<i>Top</i>) A vesicle undergoing a steady tank-treading motion in shear flow (reproduced from [84]). (<i>Bottom</i>) A vesicle undergoing an asymmetric-dumbbell transition in elongational flow (reproduced from [152]).	3
1.3	Vesicles in quadratic flow, as observed via experiment (reproduced from [169]). Each of the four panes corresponds to a different set of experimental conditions, all at room temperature. The height of each pane is about $50\ \mu\text{m}$	3
1.4	Schematic of a freely suspended particle in channel flow.	9
1.5	Microhydrodynamics of concentric rigid spheres in circular-tube flow. (<i>a</i>) The relative velocity U/V plotted against the radius ratio r_p/R . (<i>b</i>) The dimensionless extra pressure drop $\Delta p^+ R / (\mu V)$ plotted against the radius ratio r_p/R	12
1.6	Microhydrodynamics of red blood cells in capillary flow. (<i>a</i>) The relative velocity U/V plotted against the radius ratio R_0/R . (<i>b</i>) The dimensionless extra pressure drop $\Delta p^+ R / (\mu V)$ plotted against the radius ratio R_0/R . The vertical scatter in the data is due to the distribution of channel velocities and suspension concentrations. .	14

1.7 Microfluidic platform for making measurements of the particle velocity U and extra pressure drop Δp^+ in square microchannels (reproduced from [90]). (a) Two co-flowing streams in a microfluidic “manometer” are driven at a fixed inlet pressure. A Jurkat leukemia cell (colored red) flows through test channel; the reference channel contains a clear fluid (darkened for visualization). When the particle squeezes through a constriction, the fluid-fluid interface located downstream (in the “comparator region”) deflects. A balance of normal stresses on the fluid-fluid interface enables measurement of Δp^+ . (b) Time series of the particle positions. Taking the ratio of the relative particle position Δx and the elapsed time Δt enables measurement of U . (c) Time series of the extra pressure drop Δp^+ corresponding to the images in (b). The error bars correspond to uncertainty (about 10%) in image-analyzing the displacement of the diffuse interface. (d) Time series of the vesicle velocity U for the same experiment. The error bar reflects the width of the distribution of the instantaneous particle velocities.	17
3.1 Schematic of a closely fitting vesicle translating in a circular tube due to pressure-driven flow. The system is rotationally symmetric about the x -axis. In a reference frame moving with the vesicle, the walls translate with velocity $-U\hat{e}_x$	32
3.2 Critical radius ratio λ^* plotted against the reduced volume v , as given by (3.1.10). Membrane rupture occurs for $\lambda > \lambda^*$, which is indicated by the shaded region.	34
3.3 The domain is divided into three regions: a “rear outer region” (I), an “inner region” (II), and a “front outer region” (III). The inner coordinates \bar{x} and \bar{x}^* are related by a shift of origin, $\bar{x}^* = \bar{x} - 2\bar{\ell}$	40
3.4 Gap height \bar{h} plotted against the shifted axial coordinate $\bar{x} + \bar{\ell}$ for negligible bending stiffness ($\bar{\beta} = 0$). The left column is the leading-order solution \bar{h}_0 determined by integrating (3.5.29)-(3.5.33). The right column is the first correction \bar{h}_1 determined by integrating (3.5.49)-(3.5.53). The solid lines are the full numerical solutions. (a) Long, spherocylindrical vesicle ($\bar{\ell} = 10$), including the large- $\bar{\ell}$ approximation derived in §3.6.1. (b) Intermediate-length vesicle ($\bar{\ell} = 1$). (c) Short, spherical vesicle ($\bar{\ell} = 0.01$), including the small- $\bar{\ell}$ approximation derived in §3.6.2 [cf. (3.6.18) and (3.6.26) truncated after the $O(1)$ term].	50
3.5 Caption on the following page.	51
3.5 (a) Leakback flux \bar{q} , (b) membrane tension $\bar{\tau}$, (c) front intercept b , (d) rear intercept b^* , and (e) extra pressure drop $\Delta\bar{p}^+$ plotted against the reduced length $\bar{\ell}$ for negligible bending stiffness ($\bar{\beta} = 0$). The left column is the leading-order solution; the right column is the first correction.	52

3.6	Separation of the front and rear parts of the inner region for a long, spherocylindrical vesicle ($\bar{\ell} \gg 1$). The dashed curves are the linearized solutions near $\bar{h} = 1$	56
3.7	Coordinate system for a short, spherical vesicle ($\bar{\ell} \ll 1$). The “outer region” is located inside the dashed box. The “inner region” is located outside the dashed box within an $O(\bar{\ell}^{-\frac{1}{2}})$ boundary layer.	59
3.8	Gap height \bar{h}_0 plotted against the shifted axial coordinate $\bar{x} + \bar{\ell}$ for several values of $\bar{\beta}$. (a) Long, spherocylindrical vesicle ($\bar{\ell} = 10$). (b) Intermediate-length vesicle ($\bar{\ell} = 1$). (c) Short, spherical vesicle ($\bar{\ell} = 0.01$).	62
3.9	Leading-order solution for (a) the leakback flux \bar{q}_0 , (b) the membrane tension $\bar{\tau}_0$, (c) the front intercept b_0 , (d) the rear intercept b_0^* , and (e) the extra pressure drop $\Delta\bar{p}_0^+$ plotted against the reduced length $\bar{\ell}$ for several values of $\bar{\beta}$. <i>Inset:</i> curvature contribution to the extra pressure drop $\Delta\bar{p}_0^+ - 4\bar{\ell}$ plotted against the reduced length $\bar{\ell}$	65
3.10	Vesicle shapes (the ordinate is ρ_s/R) for (a) $v = 0.99$, (b) $v = 0.95$, (c) $v = 0.90$, (d) $v = 0.85$, (e) $v = 0.80$, (f) $v = 0.75$, (g) $v = 0.70$, (h) $v = 0.65$, and (e) $v = 0.60$. The ratio λ/λ^* is indicated for each shape. Left column: $\beta = 0$. Right column: $\beta = 10$	69
3.11	Comparison of the present theoretical predictions for the membrane shape ρ_s and traction components f_{sx} and f_{sp} to the boundary element simulations of [163] (viscosity ratio $\kappa = 1$). Results are shown for (a) $v = 0.84$, $\lambda = 1.2$, $\beta = 0.01$ ($\epsilon = 0.22$, $\bar{\ell} = 1.6$, $\bar{\beta} = 0.006$) and (b) $v = 0.61$, $\lambda = 2.1$, $\beta = 0.03$ ($\epsilon = 0.057$, $\bar{\ell} = 16$, $\bar{\beta} = 0.008$).	72
3.12	(a) Relative velocity U/V and (b) dimensionless extra pressure drop $\Delta p^+ R / (\mu V)$ plotted against the radius ratio λ for $\beta = 0$ and several reduced volumes v . Also shown are the experimental measurements of [169], [3] (for vesicles), [4], and [128] (for red blood cells), as well as previous theories due to [139] and [71] (for red blood cells).	74
4.1	Schematic of a periodic train of identical vesicles in a circular tube. Only the $z = 0$ plane is shown. The system is rotationally symmetric about the x -axis at $t = 0$	80
4.2	Schematic of the unit cell used in the 3D BEM simulations. The unit cell is periodically replicated in the x , y , and z directions.	82
4.3	Unstructured meshes. (a) Tube wall surface \mathcal{S}_w of length $L_x = 4R$ discretized into $N_w = 5,796$ triangular elements. (b) Vesicle surface \mathcal{S}_s discretized into $N_s = 162$ (<i>left</i>) and 642 (<i>right</i>) triangular elements by successively subdividing an icosahedron four and eight times, respectively. This type of mesh is appropriate if the reduced volume v is close to unity. (c) Vesicle surface \mathcal{S}_s discretized into $N_s = 5,376$ triangular elements by first Loop subdividing a cylindrical surface (<i>left</i>) and subsequently relaxing the mesh in a Stokes-flow BEM simulation with $\langle \mathbf{u} \rangle = \mathbf{0}$ (<i>right</i>). This type of mesh is appropriate if the reduced volume v is far from unity.	84

4.4	Comparison of the present 3D BEM simulations with the axisymmetric BEM simulations of [163], Figure 15a ($v = 0.84$, $\lambda = 1.2$, $\beta = 0.01$, $\kappa = 1$, $\delta = 10$). (a) Membrane radius ρ_s . (b) Axial component of the membrane surface traction f_{sx} . (b) Radial component of the membrane surface traction f_{sp} .	86
4.5	Comparison of the present 3D BEM simulations with the axisymmetric BEM simulations of [163], Figure 15b ($v = 0.61$, $\lambda = 2.1$, $\beta = 0.03$, $\kappa = 1$, $\delta = 10$). (a) Membrane radius ρ_s . (b) Axial component of the membrane surface traction f_{sx} . (b) Radial component of the membrane surface traction f_{sp} .	87
4.6	Velocity field from 3D BEM simulations. Results are shown for $v = 0.99$, $\lambda = 0.7$, $\beta = 0$, $\kappa = 1$, (a) $\delta = 1.5$, (b) $\delta = 2$, (c) $\delta = 4$, and (d) $\delta = 10$.	93
4.7	Velocity field from 3D BEM simulations. Results are shown for $v = 0.80$, $\lambda = 1$, $\beta = 0$, $\kappa = 1$, (a) $\delta = 3$, (b) $\delta = 4$, (c) $\delta = 6$, and (d) $\delta = 10$.	94
4.8	Time sequence of the vesicle shape evolved from an initially equilibrium configuration. Results were computed via 3D BEM for $v = 0.8$, $\kappa = 1$, $\beta = 0.02$, $\delta = 10$, $\lambda =$ (a) 0.4, (b) 0.6, (c) 0.7, (d) 0.8, (e) 0.9, (f) 1, and (g) 1.2. At this reduced volume, $\lambda^* = 1.64$. Vesicles for which $\lambda < 0.9$ transition to an asymmetric secondary shape at longer times.	96
4.9	Caption on the following page.	97
4.9	Time series of the relative velocity U/V and dimensionless extra pressure drop $\Delta p^+ R / (\mu V)$ for the 3D BEM simulations shown in Figure 4.8.	98
4.10	Vesicle shapes computed by 3D BEM simulation (solid lines) and axisymmetric lubrication theory (dashed lines) for $\kappa = 1$, $\beta = 0.02$, and $\delta = 10$. (a) $v = 0.99$, BEM: $\lambda = 0.9, 0.8, 0.7$; LT: $\lambda = 1, 0.9, 0.8$. (b) $v = 0.9$, BEM: $\lambda = 1.2, 1, 0.8$; LT: $\lambda = 1.3, 1.2, 1$. (c) $v = 0.8$, BEM: $\lambda = 1.4, 1.2, 1$; LT: $\lambda = 1.6, 1.4, 1.2$. (d) $v = 0.7$, BEM: $\lambda = 1.6, 1.4$; LT: $\lambda = 1.8, 1.6, 1.4$.	100
4.11	Relative velocity U/V plotted against the radius ratio λ for a range of reduced volumes v ($\kappa = 1$, $\beta = 0.02$, $\delta = 10$). Shown are the experimental measurements of [169], calculations via 3D BEM simulation and axisymmetric lubrication theory, the asymptotic correlation (3.9.1a), and the rational fraction approximant (4.4.2a) (dotted curves). Where appropriate, error bars are used to quantify the maximum change observed after start-up in the BEM simulations.	102
4.12	Dimensionless extra pressure drop $\Delta p^+ R / (\mu V)$ plotted against the radius ratio λ for a range of reduced volumes v ($\kappa = 1$, $\beta = 0.02$, $\delta = 10$). Shown are calculations from 3D BEM simulations, the axisymmetric lubrication theory, the asymptotic correlation (3.9.1b) (dashed curves), and the rational fraction approximant (4.4.2b) (dotted curves). Where appropriate, error bars are used to quantify the maximum change observed after start-up in the BEM simulations.	103

4.13 Vesicle shapes computed by 3D BEM simulation (solid lines) and axisymmetric lubrication theory (dashed lines) for $v = 0.90$, $\lambda = 1.22$, $\kappa = 1$, and $\delta = 10$. (a) $\beta = 0.02$. (b) $\beta = 2$. (c) $\beta = 200$	105
4.14 Vesicle shapes computed by 3D BEM simulation (solid lines) and axisymmetric lubrication theory (dashed lines) for $v = 0.70$, $\lambda = 1.58$, $\kappa = 1$, and $\delta = 10$. (a) $\beta = 0.02$. (b) $\beta = 2$. (c) $\beta = 200$	106
4.15 Relative velocity U/V and dimensionless extra pressure drop $\Delta p^+ R / (\mu V)$ plotted against the bending parameter β for several values of v and λ . All results shown were computed via axisymmetric lubrication theory. (a) $\lambda/\lambda^* = 0.8$. (b) $\lambda/\lambda^* = 0.9$. (c) $\lambda/\lambda^* = 0.99$	108
 5.1 Schematic of a vesicle flowing through a square duct, as viewed from the xz and yz planes.	111
5.2 Unstructured surface meshes. (a) Vesicle surface \mathcal{S}_v for a sphere-like vesicle, generated by subdividing an icosahedron. (b) Wall surface \mathcal{S}_w for a straight conduit with a square cross section. (b) Wall surface \mathcal{S}_w for a contraction-expansion channel; the inlet and outlet are connected by a straight conduit with a square cross section.	113
5.3 Relative velocity U/V plotted against the radius ratio λ for $v = 0.99$ and (a) $N = 4$ (square), (b) $N = 6$ (hexagon), (c) $N = 12$ (dodecagon), and (d) $N \rightarrow \infty$ (circle). The symbols are the BEM simulations, while the solid lines are the predictions from lubrication theory.	122
5.4 Dimensionless extra pressure drop $\Delta p^+ R / (\mu V)$ plotted against the radius ratio λ for $v = 0.99$ and (a) $N = 4$ (square), (b) $N = 6$ (hexagon), (c) $N = 12$ (dodecagon), and (d) $N \rightarrow \infty$ (circle). The symbols are the BEM simulations, while the solid lines are the predictions from lubrication theory.	123
5.5 Working principle of the microfluidic manometer. Equal driving pressures are applied to a test channel (containing a single vesicle) and a reference channel (containing a clear fluid). The co-flowing fluids meet at a downstream comparator, forming a fluid-fluid interface. In the absence of a vesicle, the interface is flat (parallel to the streamwise direction). In the presence of a vesicle, a measurable displacement ΔY is observed due to the excess flow resistance in the test channel.	125
5.6 (a) Time-stamped images showing vesicle motion in the test channel and the concomitant interface deflection. The test channel is about 12.6 μm wide and 330 μm long. (b) Time evolution of the relative velocity U/V and dimensionless extra pressure drop $\Delta p^+ R / (\mu V)$ for a vesicle of reduced volume v near unity ($\lambda = 1.65$).	127

5.7 (a) Time sequence of a vesicle (reduced volume $v = 0.99$) passing through a square constriction channel, as computed via BEM simulation. The left and right columns correspond to $\lambda = 0.6$ and 0.8 , respectively. (b) Relative velocity U/V and dimensionless extra pressure drop $\Delta p^+ R / (\mu V)$ plotted against the dimensionless time tV/R for $v = 0.99$ and $\lambda = 0.6, 0.8$. The dashed, horizontal lines correspond to the steady-state results for an infinitely long, square conduit.	129
5.8 Vesicles ($v = 0.99$) in square ducts as determined by 3D BEM simulation, viewed from yz (left) and xy (right) planes. The colors indicate the normal component of the membrane surface traction jump $f_{sn} = \hat{\mathbf{n}} \cdot \mathbf{f}_s$. Shown are results for $\lambda = (a) 0.6, (b) 0.7, (c) 0.8$, and $(d) 0.9$	131
5.9 Vesicles ($v = 0.99$) in square ducts as determined by lubrication theory, viewed from yz (left) and xy (right) planes. The colors have the same meaning as in Figure 5.8. Shown are results for $\lambda = (a) 0.9, (b) 1.0, (c) 1.1$, and $(d) 1.12$	132
5.10 Vesicles ($v = 0.90$) in square ducts as determined by 3D BEM simulation, viewed from yz (left) and xy (right) planes. The colors indicate the normal component of the membrane surface traction jump $f_{sn} = \hat{\mathbf{n}} \cdot \mathbf{f}_s$. Shown are results for $\lambda = (a) 0.7, (b) 0.8, (c) 0.9, (d) 1.0$, and $(e) 1.1$	133
5.11 Vesicles ($v = 0.90$) in square ducts as determined by lubrication theory, viewed from yz (left) and xy (right) planes. The colors have the same meaning as in Figure 5.10. Shown are results for $\lambda = (a) 1.1, (b) 1.2, (c) 1.3, (d) 1.4$, and $(e) 1.43$	134
5.12 Normalized membrane surface velocity vectors $\mathbf{u}_s / \ \mathbf{u}_s\ $ (in a reference frame moving with the vesicle), as computed by lubrication theory. (a) $v = 0.99, \lambda = 0.9$ (left) and 1.12 (right). (a) $v = 0.90, \lambda = 1.1$ (left) and 1.43 (right). The corresponding surface traction distributions are shown in Figures 5.9a,d and 5.11a,e.	136
5.13 Estimates of (a) the critical radius ratio λ^* , (b) the dimensionless contact area A^*/R^2 , and (c) the aspect ratio $L^*/(2R)$ plotted against the reduced volume v , as determined via lubrication theory. Results for both square and circular cross sections are shown.	137
5.14 Aspect ratio $L/(2R)$ plotted against the radius ratio λ . In the experimental measurements, the aspect ratio $L/(2R)$ is measured and the reduced volume v is estimated based on the correlation (5.5.2) from the lubrication theory; the diamond markers are colored accordingly.	139
5.15 Relative velocity U/V plotted against the radius ratio λ	140
5.16 Dimensionless extra pressure drop $\Delta p^+ R / (\mu V)$ plotted against the radius ratio λ	141
6.1 A quasi-spherical vesicle in a channel, as viewed from (a) the xy plane and (b) the yz plane. The particularly geometry shown is a circular tube of constant radius $R_{\bar{\phi}} = R$	145

Chapter 1

Introduction

1.1 Vesicles in fluid flow

The transport of viscous fluids encapsulated by lipid-bilayer membranes is ubiquitous in biological and biomimetic processes. In many situations, these processes involve the passage of biofluidic materials through conduits of sub-millimeter dimensions. In the human body, red blood cells flowing through the circulatory system take up oxygen in the lungs and deliver it to body tissues while squeezing through microcapillaries [63]. In the laboratory, microfluidic devices have become an efficient, low-cost workhorse for conducting cell-based assays [61], cell trapping and separation [11, 89], and single-cell sequencing [110, 188]. Liposomes (artificial vesicles) and living cells are naturally biocompatible and useful for drug delivery applications [64, 65, 66]. Recent work with mammalian cells, for instance, has shown that mechanically induced poration by squeezing a cell through a narrow constriction can enhance the permeability of the biomembrane, enabling the uptake of macromolecules for targeted delivery [143]. As biomedical technologies continue to develop and become increasingly miniaturized, we can expect a concomitant improvement in our ability to manipulate soft, biological materials via fluid flow.

Vesicles are liquid droplets enclosed by a lipid-bilayer membrane. They represent an attractive model system for understanding the behavior of biomembranes in quiescent and flowing fluids, due to the simplicity in their mechanics as well as the ease with which they may be manufactured in a laboratory. Populations of (giant, unilamellar) vesicles prepared by electroformation can have dimensions in the range of 1-100 μm [5, 124]. The shape configuration space of vesicles, even at equilibrium, is quite vast (Figure 1.1). Unlike droplets, which prefer to take on a spherical shape at equilibrium in order to minimize their *surface energy*, vesicles can adopt a variety of shapes that minimizes the *curvature energy* of their membranes [see equation (1.2.1), below] [141, 140]. The lipid-bilayer membranes of vesicles share many of the characteristics of those found in real cells –

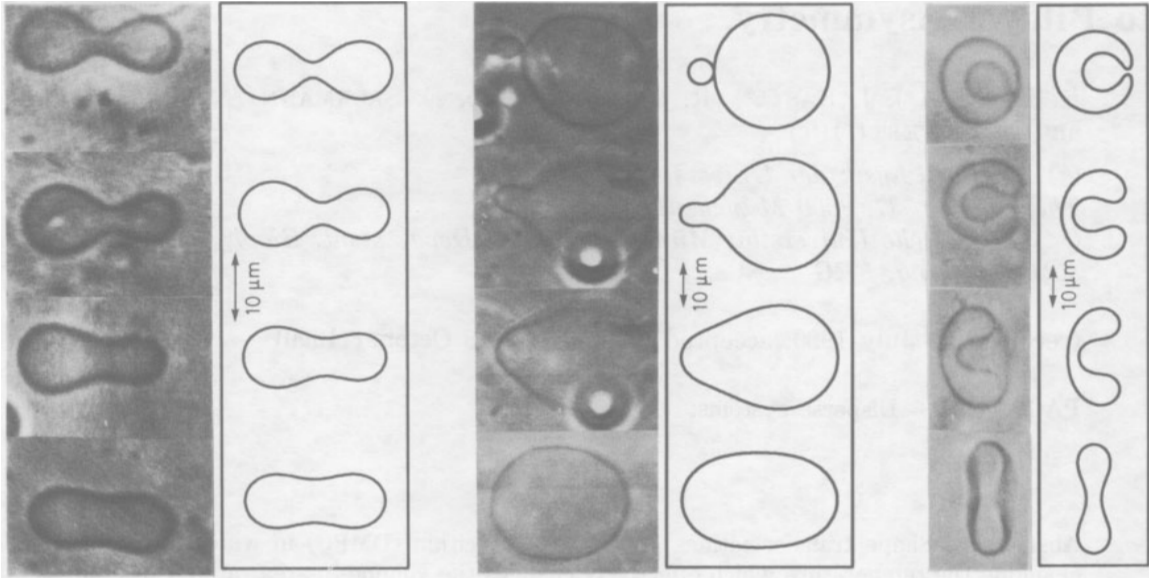


Figure 1.1: Vesicles at equilibrium, as determined via experiment and theory (reproduced from [10]). (*Left*) Symmetric-asymmetric transition (temperatures from bottom to top are $T = 30.7, 32.6, 40.0$, and 44.4°C). (*Center*) Budding transition ($T = 31.4, 35.5, 35.6$, and 35.8°C ; an air bubble enters the measurement chamber in the second and third panes). (*Right*) Discocyte-stomatocyte transition ($T = 43.8, 43.9, 44.0$, and 44.1°C). The theoretical curves were computed by minimization of the curvature free energy of the bilayer [equation (1.2.1)].

namely, a lamellar bilayer structure [109], internal fluidity [56], and elasticity [74]. In contrast to the cell membrane, which is a veritable “fluid mosaic” of integral membrane proteins, cholesterol, and other components [147], membranes of artificial vesicles prepared using a controlled lipid formulation can be homogeneous down to molecular dimensions. This property makes vesicles an ideal candidate for scientific study as “toy models” for real biological cells, despite the obvious dissimilarities.

Predicting the flow of vesicles requires a detailed understanding of their *microhydrodynamics* – that is, how the stresses induced by fluid motion couple to the kinematics and dynamics of the lipid-bilayer membrane. From a theoretical point of view, modeling the microhydrodynamics of vesicles is challenging due to the coupling between fluid flow and membrane deformation, which results in a *free-boundary problem* [132]. The equations governing the motion of the lipid-bilayer membrane are inherently nonlinear and difficult to solve due to kinematic constraints posed by strong resistance to membrane surface dilatation. One of the earliest studies of vesicles in fluid flow applied a numerical method to integrate the discrete form of the equations of motion in the absence of fluid inertia [94]. Subsequent numerical investigations have yielded insight into experimentally observed vesicle dynamics in various canonical flow types (Figure 1.2), including shear flows [181, 185, 182] and elongational flows [183]. Analytical progress towards solving the equations of motion has been made by use of asymptotic methods [77, 166], usually in the limit of small deformations from a reference shape (e.g., a sphere). Small-deformation theories for vesicles in unbounded shear flows

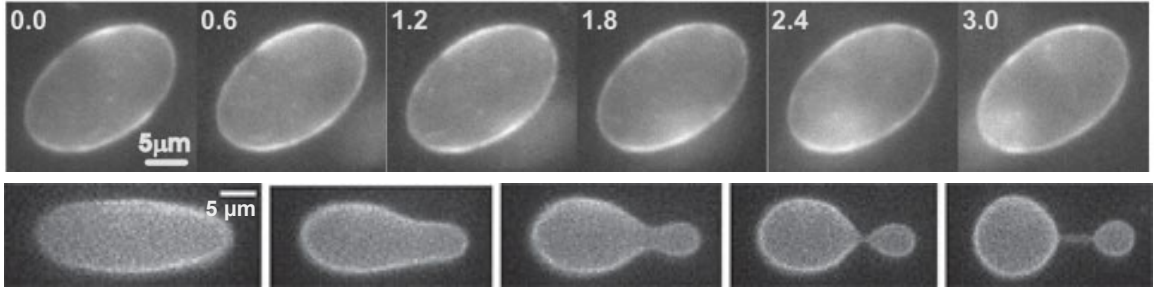


Figure 1.2: Vesicles in linear flow, as observed via experiment. All experiments were performed at room temperature. (*Top*) A vesicle undergoing a steady tank-treading motion in shear flow (reproduced from [84]). (*Bottom*) A vesicle undergoing an asymmetric-dumbbell transition in elongational flow (reproduced from [152]).

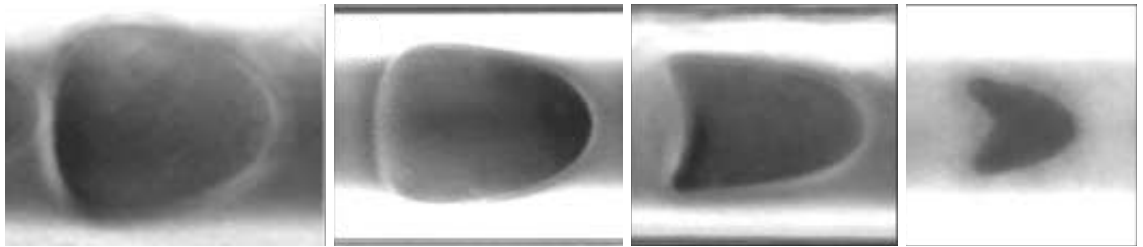


Figure 1.3: Vesicles in quadratic flow, as observed via experiment (reproduced from [169]). Each of the four panes corresponds to a different set of experimental conditions, all at room temperature. The height of each pane is about 50 μm .

have yielded useful analytical formulas which have since been used to validate numerical results [112, 31, 30, 170, 102].

The motion of vesicles in quadratic flows (e.g., flow through conduits) has received considerably less attention than linear flows (e.g., shear and elongational flows). One reason for this is that the local flow field around a vesicle in a general flow type can often be approximated as a linear flow, to leading order in a Taylor series about the vesicle's center of mass. Quadratic flows exhibit a spatial gradient in the local shear rate, resulting in cross-streamline vesicle migration (oftentimes towards the region of zero shear) [28]. In flow through conduits, the shear rate vanishes at the flow centerline and the local flow field there cannot be approximated as a linear flow. To date, the only experimental observation of vesicles in channel flow is due to Vitkova and coworkers [169]; they observed left-right asymmetric shapes at the flow centerline (Figure 1.3). Recently [163] performed numerical calculations and reproduced several of the vesicle shapes observed in the experiments of [169].

The primary reason for the dearth of theoretical studies of vesicles in channel flows is the difficulty in resolving hydrodynamic interactions between vesicles and the enclosing wall boundaries. These interactions frequently result in infinite series or integrals with slow convergence properties,

which are computationally expensive to evaluate. Consequently, many of the existing numerical studies of vesicles in channel flows have focused on two-dimensional (2D) analogs of the physically realistic three-dimensional (3D) geometry [88, 157, 7, 6]. The reduction in dimensionality affords a reduced computational cost, and many of the qualitative features of the 3D geometry (e.g., dynamical transitions and shape configurations of vesicles) are also seen in the 2D analogy. Of course, achieving quantitative predictions is virtually impossible using the 2D framework. At present, most numerical investigations (with the exception of the study performed by [163], mentioned above) have focused on unbounded channel flows, in which the typical dimension of the vesicle is presumed small compared to that of the channel cross section and the vesicle-wall interaction is neglected [52]. Analytical developments by means of small-deformation theory have also invoked this assumption [32]. If the characteristic vesicle dimension is small relative to the inverse of the curvature of the velocity profile (the so-called “point-particle approximation”), then the *instantaneous* vesicle motion is given by the velocity of the local fluid streamline. In the absence of wall effects, cross-streamline migration takes place only when there is a non-negligible gradient in the local shear rate across the vesicle.

Vesicle-wall interactions are central to predicting the microhydrodynamics of finite-sized vesicles in channel flows. A freely suspended vesicle produces a velocity disturbance that enhances the drag on the conduit wall, which in turn creates extra resistance to flow. The strength of this disturbance is enhanced as the vesicle increases in size, and is expected to depend strongly on membrane flow and deformation. Consequently, the instantaneous vesicle motion will be different from the velocity of the local fluid streamline when the vesicle is not very small. Moreover, the extra drag on the channel wall due to the disturbance produced by vesicles results in an “apparent fluid viscosity” that is different from that of the suspending fluid. Although these effects have been exhaustively studied for the flow of rigid particles [62, 103, 79, 14, 16, 173, 25] and red blood cells [4, 128, 139, 129, 126, 159, 158, 180, 135], they remain virtually unexplored (both theoretically and experimentally) for vesicles. To date, the number of theoretical studies which have attempted to incorporate wall effects into the vesicle motion and apparent fluid viscosity are few [18, 121] and, for reasons that will be explained further in §1.3.3, relatively incomplete.

In this thesis, we will develop a theory for the transport of vesicles through channels and focus on predicting the vesicle motion and apparent fluid viscosity due to finite-size effects. We will have the occasion to draw upon various mathematical methods – both analytical and numerical – in order to solve the equations of motion for the vesicle membrane. Before discussing these methods and outlining the organization of the thesis, some further background on the properties of lipid bilayers (§1.2) and the fluid mechanics of channel flow with freely suspended particles (§1.3) are in order.

lipid	$T, ^\circ\text{C}$	$E_D, \text{dyn/cm}$	$E_B \times 10^{12}, \text{dyn} \cdot \text{cm}$	$\tau^*, \text{dyn/cm}$	source(s)
DMPC	29	145 ± 10	0.56 ± 0.06	2-3	[42, 117, 43]
	8	855 ± 140	—	>15	[42, 117]
	—	—	1.1	—	[38]
	—	—	—	—	[42]
SOPC	15	200 ± 13	—	6	[43]
	18	190 ± 10	0.90 ± 0.06	—	[186]
	14	178-182	0.6-1.15	—	[118]
	—	193 ± 20	—	5.7 ± 0.2	[150]
DAPC	18	135 ± 20	0.44 ± 0.05	—	[43]
DGDG	23	160 ± 7	0.44 ± 0.03	—	[43]
DOPC	21	265 ± 18	0.85 ± 0.10	—	[131]
DEEDMAC	r.t.	99 ± 14	0.31 ± 0.04	2.5 ± 1.0	[142]
egg lecithin	r.t.	140	—	3-4	[97]
—	—	—	1-2	—	[136]
RBC lipids	—	420 ± 36	—	9.7 ± 0.8	[118]
sarcolemmal muscle	r.t.	490 ± 88	—	12.4 ± 0.2	[120]

Table 1.1: Elastic properties of (unilamellar) lipid-bilayer vesicles, as measured experimentally. Tabulated are the dilatational modulus E_D , the bending modulus E_B , and the lysis tension τ^* . The tabulated values are the mean \pm s.d. except for the value of τ^* reported by [120] for sarcolemmal muscle, which is the median \pm 95% confidence interval. Also tabulated is the temperature T at which each measurement was taken, if reported (r.t. = room temperature, taken to be in the range 20-25 °C).

1.2 Properties of lipid-bilayer membranes

The basic structure of vesicle membranes is the lipid bilayer, which can be thought of as a 2D fluid sheet that admits an elastic response when subjected to an external stress [80]. Some of their elastic properties have been measured and are reported in Table 1.1 for different lipid types.¹ There are three important features of the lipid-bilayer membrane of vesicles that are worth committing to memory:

1. Vesicle membranes are internally fluid and do not admit resistance to in-plane shearing.
2. Vesicle membranes admit very strong resistance to in-plane dilatation.
3. Vesicle membranes admit resistance to out-of-plane bending.

Supporting evidence for each of these statements is given in the remainder of this section.

1. Vesicle membranes are internally fluid and do not admit resistance to in-plane shearing.

Most bilayers at room temperature are internally fluid, as verified by fluorescent imaging

¹The mechanical properties of vesicle membranes can be altered by the addition of foreign constituents to the lipid bilayer [42]. These so-called “defects” create regions of local heterogeneity that can disrupt or enhance intramolecular interactions. Several authors have shown that the addition of cholesterol can substantially increase cohesion among lipid molecules, thus increasing the elastic moduli and tensile strength of the bilayer [41, 42, 119, 26]. Conversely, the addition of peptide has been shown to decrease bilayer rigidity [41, 42]. Electrostatic effects in charged lipid bilayers have also been shown to reduce the elastic moduli [144, 142].

studies of mammalian cells [56]. Early X-ray scattering measurements of lipid-water systems verified that lipid molecules can form lamellar liquid crystals [109]. Membranes of biological cells include integral proteins embedded in the bilayer structure (e.g., ion channels, receptors, and signaling molecules). Eukaryotic cell membranes are additionally reinforced by a cortical cytoskeleton that is bound to the interior of the bilayer via protein-mediated interactions [21]. This “protein backbone” comprises a spectrin-actin network that imbues the membrane with a shear elasticity. The shear-elastic modulus is denoted by E_S and is about 4×10^{-3} dyn/cm for red blood cells [148, 46, 139].

Artificial vesicles (so-called “liposomes”) lack the spectrin-actin cortex of real cells, and therefore do not admit a shear-elastic response [74]. Hence, no measurements of E_S appear in Table 1.1. The surface shear viscosity of lipid-bilayer membranes is very small, estimated to be in the range 10^{-6} - 10^{-5} dyn · s/cm from surface diffusivity measurements of fluorescent membrane probes [33, 133, 60]. This weak viscous response is usually neglected in fluid-mechanical analyses with an imposed flow field, since momentum dissipation in the bulk viscous fluid often outweighs dissipation in the membrane.

2. Vesicle membranes admit very strong resistance to in-plane dilatation. Lateral interactions between lipid molecules result in an elastic-like response to local area changes. The areal dilatational modulus E_D , which gauges the relative increase in membrane tension for a fractional increase in membrane surface area, has been measured (e.g., by micropipette aspiration) to be in the range 10^2 - 10^3 dyn/cm for most lipid systems (a selection of such measurements are reported in the third column of Table 1.1). Physically, the explanation for such large values of E_D is the high density of a fixed number of lipids in the bilayer [80]. Although lipid molecules are free to diffuse within a single lamellar sheet, it is energetically unfavorable for them to deviate from the bilayer configuration. Based on this reasoning, it is not so surprising that lipid-bilayer membranes can only sustain about 2-3% of areal strain before rupturing. The so-called “lysis tension” τ^* associated with this type of mechanical failure is about 10 dyn/cm (the fifth column in Table 1.1).

Due to their strong resistance to areal dilatation, bilayer membranes are often simplified as 2D incompressible fluids in fluid-mechanical analyses.² Since the surface density of lipid molecules is fixed, this assumption forbids the local creation or destruction of surface area in the membrane. The assignment of a dilatational-elastic modulus E_D is inappropriate in such circumstances, since we have essentially assumed this quantity to be infinitely large relative to the membrane tractions induced by fluid motion. Thus, the *surface-incompressibility assumption* eliminates the need to know the precise value of E_D , reducing the number of controlled parameters by one. The isotropic membrane tension τ gains the interpretation as a Lagrange function that preserves surface area locally.

²Exceptions arise, for instance, in vesicle swelling, where the dilatational response of the bilayer is expected be dominant. Such situations will not be considered in this thesis.

3. Vesicle membranes admit resistance to out-of-plane bending. Additional resistance to out-of-plane deformations results from the transverse distribution of lateral lipid-lipid interactions. The finite thickness of bilayers (about 5 nm) results in a nontrivial moment of the transverse tension distribution that opposes lateral torques. This material response is elastic in character and is typically quantified by a bending modulus E_B (the fourth column in Table 1.1). Various methods exist for measuring the bending modulus of bilayer membranes, e.g., micropipette aspiration [42], two-pipette suction [186], shape fluctuation analysis [38], and tether formation [150]. Measurements of E_B are typically about 10^{-12} dyn · cm.

In 1973, Helfrich correctly identified bending as the “easiest” deformation mode for lipid-bilayer membranes [74]. Using this guiding principle, he posited the following work functional W for the curvature energy for symmetric lipid bilayers:³

$$W = E_B \int_{\mathcal{S}} 2H^2 dS, \quad (1.2.1)$$

where H is the mean curvature and \mathcal{S} denotes a surface of integration. By applying the principle of virtual work to (1.2.1), one obtains the bending-elastic surface force density directed normal to the membrane [82, 187]. The surface force density induced by the membrane tension τ has both normal and tangential components. Under the auspices of surface incompressibility, these tensile forces are obtained by requiring that a virtual displacement preserves surface area locally when applying the principle of virtual work. We shall make use of (1.2.1) in Chapter 2, when we formulate the theoretical mechanics of the vesicle membrane.

1.3 Flow of particles through conduits

Channel flows are canonical in the subject of fluid mechanics [12]. In this section, we introduce some of the important nomenclature that will be used throughout this thesis. The geometry of a channel cross section is characterized by its surface area A_x and wetted perimeter P_x . The *channel hydraulic radius* R is defined by the ratio of these quantities,

$$R = \frac{2A_x}{P_x}. \quad (1.3.1)$$

³A generalization of (1.2.1) commonly seen in the literature is,

$$W = E_B \int_{\mathcal{S}} 2(H - H_0)^2 dS + E_K \int_{\mathcal{S}} K dS,$$

where K is the Gaussian curvature, E_K is the Gaussian-curvature modulus, and H_0 is the spontaneous mean curvature. The second term on the right-hand side is the free energy contribution from the integrated Gaussian curvature, which, according to the Gauss-Bonnet theorem, is a constant for topologically equivalent surfaces. The vesicles considered in this thesis have the same topology as the sphere, and so the Gaussian-curvature term may be omitted without loss of generality. The spontaneous mean curvature H_0 accounts for possible asymmetries in the lipid bilayer, which are not considered in the present work.

cross section	A_{\times}/R^2	P_{\times}/R	$K_{\text{hyd}}R^4/\mu$
circle	$\pi \simeq 3.14$	$2\pi \simeq 6.28$	$8/\pi \simeq 2.55$
triangle	$3\sqrt{3} \simeq 5.20$	$6\sqrt{3} \simeq 10.4$	$20/(9\sqrt{3}) \simeq 1.28$
square	4	8	1.78
hexagon	$2\sqrt{3} \simeq 3.46$	$4\sqrt{3} \simeq 6.93$	2.18
dodecagon	$12/(2 + \sqrt{3}) \simeq 3.22$	$12/(2 + \sqrt{3}) \simeq 6.43$	2.45

Table 1.2: Cross sectional surface area A_{\times} , wetted perimeter P_{\times} , and hydraulic resistivity K_{hyd} for straight channels with circular or polygonal cross sections.

The concept of a hydraulic radius arises from a force balance on a control volume bounded externally by the channel walls, an upstream cross section, and a downstream cross section [174]. Supposing that the inlet pressure at the upstream cross section is p_1 , the outlet pressure downstream is $p_0 = p_1 - \Delta p^\circ$, and the length of the channel is L_c , then the resultant of wall shear stresses per unit circumference is $\frac{1}{2}R\Delta p^\circ$.

The fluid flow rate through the channel is denoted by $Q = A_{\times}V$, where V is the average fluid velocity in a given cross section. For a clear fluid, Poiseuille's law relates the flow rate Q to the (particle-free) pressure drop $\Delta p^\circ = p_1 - p_0$ [156]:

$$\frac{\Delta p^\circ}{L_c} = K_{\text{hyd}}Q = K_{\text{hyd}}A_{\times}V, \quad (1.3.2)$$

where K_{hyd} is a hydraulic resistance coefficient (or resistivity). Equation (1.3.2) is the analog of Ohm's law for electrical circuits – it relates the pressure gradient $\Delta p^\circ/L_c$ (akin to an electrical voltage) to the flow rate Q (electrical current) by means of a proportionality constant K_{hyd} (electrical resistance). For *Newtonian fluids* (homogeneous, isotropic small-molecule fluids with constant density), K_{hyd} depends only on the shear viscosity μ of the fluid and the geometry of the channel. Values of A_{\times} , P_{\times} , and K_{hyd} for various straight-channel geometries are given in Table 1.2.

When microscopic particles (e.g., rigid and soft particles, droplets, vesicles, or cells) are introduced to the fluid, the pressure drop required to flow the suspension at the same flow rate Q is higher than that which would be necessary in the absence of particles [13] (Figure 1.4). As before, we let $\Delta p^\circ = p_1 - p_0$ denote the particle-free pressure drop across a fluid-filled channel of length L_c . The total pressure drop required to flow a suspension of particles is distinct from Δp° and is denoted by Δp . The *extra pressure drop* is thus defined as,

$$\Delta p^+ = \lim_{L_c \rightarrow \infty} (\Delta p - \Delta p^\circ) = \lim_{L_c \rightarrow \infty} (\Delta p - L_c A_{\times} K_{\text{hyd}} V). \quad (1.3.3)$$

This formula was first given by Brenner [13]. Physically, one can think of a flowing particulate suspension as a continuous medium with effective viscosity μ_{eff} . If the suspension concentration

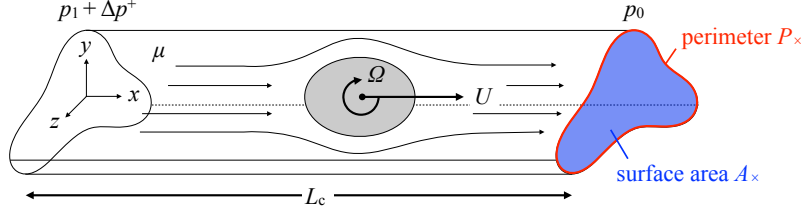


Figure 1.4: Schematic of a freely suspended particle in channel flow.

(volume fraction) is denoted by c , then μ_{eff} is related to the fluid shear viscosity μ by,

$$\mu_{\text{eff}} = \mu(1 + c[\eta]), \quad (1.3.4)$$

where

$$[\eta] = \frac{\Delta p^+}{c \Delta p^\circ} \quad (1.3.5)$$

is known as the *relative intrinsic viscosity* of the suspension. Thus, the relative intrinsic viscosity $[\eta]$ and extra pressure drop Δp^+ contain the same information! Both quantities give a measure of the dissipation produced by a flowing particulate suspension above and beyond that which would be generated by the clear fluid alone. The equivalent “resistance law,” which is given by (1.3.2) for clear fluids, is obtained by replacing μ by μ_{eff} in the definition of K_{hyd} . In subsequent chapters, we shall only speak of the extra pressure drop Δp^+ , with the understanding that this quantity may be related to μ_{eff} through (1.3.4)-(1.3.5).

In channel flow of a suspension of force-free particles, one typically seeks answers to the following questions:

1. Will the particles fit inside the channel?
2. What is the particle translational velocity \mathbf{U} (and, in some cases, the particle rotational velocity $\boldsymbol{\Omega}$)?
3. What is the extra pressure drop Δp^+ ?

Answers to these questions will become our main objectives in our study of the motion of vesicles in channel flow. In order to gain some insight as to how these quantities depend on the available degrees of freedom in a flow system, it behooves us to review some of the important theoretical results derived for suspensions of rigid particles (§1.3.1) and red blood cells (§1.3.2). We then turn our attention to previous studies of vesicles in channel flow in §1.3.3, including open questions and problem areas.

1.3.1 Rigid particles

Much of what we know about bounded fluid flow of particulate matter is due to early studies of rigid particles in channel flows. Aside from the suspension concentration c , which gauges the strength of particle-particle hydrodynamic interactions, the available degrees of freedom are those which specify the instantaneous configuration of the flowing suspension. The number of distinguishable configurations depends on the specific geometry of the particle and the channel. As before, we denote the channel hydraulic radius by R , the mean channel velocity by V , and the suspending fluid viscosity by μ .

In the absence of fluid inertia, rigid particles do not migrate across fluid streamlines [78]. This is a key distinction between rigid and deformable particles. In fact, inertialess flows (also known as *creeping flows* or *Stokes flows*) enjoy a number of useful mathematical properties, including symmetry, linearity, reciprocity, and time-reversibility [72, 92]. These properties allowed Brenner to derive general results for rigid particles of arbitrary shape in flows through conduits of arbitrary cross section [14].

We focus our attention in the remainder of this subsection to some of the key results for dilute, monodisperse suspensions of rigid spheres in inertialess, circular-tube flow. Of all studies on rigid-particle suspensions, this subject has received by far the most attention in the literature [62, 103, 79, 14, 16, 173, 25]. Non-spherical particles [172, 14, 25] and channels of non-circular cross sections [14, 164] have also been explored by several authors, but we shall not recapitulate all of the results from these studies here. For a dilute suspension of spheres, $c \ll 1$ and hydrodynamic interactions may be neglected.

As a model problem for a dilute suspension, consider a single sphere (radius r_p) placed in the xy plane of a circular tube (radius R) containing a fluid of viscosity μ , with a mean flow V in the x direction. By Stokes symmetry, the sphere translational velocity is $\mathbf{U} = U\hat{\mathbf{e}}_x$ and the rotational velocity is $\boldsymbol{\Omega} = \Omega\hat{\mathbf{e}}_z$. Stokes linearity further requires that U , Ω scale in proportion to V , and Δp^+ in proportion to μV . The sphere configurations are entirely specified by the sphere radius r_p , the sphere-center displacement from the tube centerline y_p , and the tube radius R . Obviously, a rigid sphere can only fit inside a circular tube if $r_p < R$. Bungay and Brenner derived asymptotic formulas for the dimensionless quantities U/V , $\Omega R/V$, and $\Delta p^+ R/(\mu V)$ in the limit as $r_p/R \rightarrow 1$, which physically corresponds to a closely fitting sphere in a fluid-filled tube [20]. For the special case in which the spheres are positioned concentrically inside the tube ($y_p = 0$), these formulas read,

$$\frac{U}{V} = 1 + \frac{4}{3} \left(1 - \frac{r_p}{R}\right) + O\left[\left(1 - \frac{r_p}{R}\right)^2\right], \quad (1.3.6a)$$

$$\frac{\Omega R}{V} = 0, \quad (1.3.6b)$$

$$\frac{\Delta p^+ R}{\mu V} = 4\sqrt{2}\pi \left(1 - \frac{r_p}{R}\right)^{-\frac{1}{2}} + O(1). \quad (1.3.6c)$$

For $y_p \neq 0$, the formulas (1.3.6) depend on the eccentricity $y_p/(R - r_p)$ in a complicated manner (see [20] for the more general expressions). Significantly, the rotational velocity Ω is nonzero only if $y_p \neq 0$. The translational velocity of the sphere U is higher than the mean fluid velocity V because the sphere surface only samples the fastest moving streamlines clustered near the center of the tube. The dimensionless extra pressure drop $\Delta p^+ R / (\mu V)$ is a (weakly) singular function of $(1 - r_p/R)$ when r_p/R is close to unity. The weak singularity arises from the contact area for hydrodynamic lubrication, which is isolated to a circumferential contour around the sphere. As a point of comparison, the singular contribution for a rigid cylinder is $O[(1 - r_p/R)^{-1}]$ instead of $O[(1 - r_p/R)^{-\frac{1}{2}}]$ due to the increased contact area. Hochmuth and Sutera suggested that the $O(1)$ term in (1.3.6c) is approximately -31 (a negative correction to the extra pressure drop) (see Appendix B of [79]). This result neglects details about flow outside the lubrication region, but gives quantitative agreement with available experiments and numerical results.

In the opposite limit as $r_p/R \rightarrow 0$ (a point-sphere in a fluid-filled tube), asymptotic expansions were derived by Brenner [14]. They are presented below for arbitrary values of y_p/R :

$$\frac{U}{V} = 2 \left[1 - \left(\frac{y_p}{R} \right)^2 \right] - \frac{4}{3} \left(\frac{r_p}{R} \right)^2 + O \left[\left(\frac{r_p}{R} \right)^3 \right], \quad (1.3.7a)$$

$$\frac{\Omega R}{V} = \frac{2y_p}{R}, \quad (1.3.7b)$$

$$\frac{\Delta p^+ R}{\mu V} = \frac{160\pi}{3} \left(\frac{y_p}{R} \right)^2 \left(\frac{r_p}{R} \right)^3 + 16 \left(\frac{r_p}{R} \right)^5 + O \left[\left(\frac{r_p}{R} \right)^6 \right]. \quad (1.3.7c)$$

Clearly, U is maximized and $\Omega = 0$ when the sphere is in the concentric position ($y_p = 0$). The leading-order contribution on the right-hand side of (1.3.7c) is due to the finite shear rate away from the tube centerline; the second term is due to the curvature of the velocity distribution. For concentrically positioned spheres, Hochmuth and Sutera developed a series expansion for $\Delta p^+ R / (\mu V)$ based on the series solution of Haberman and Sayre [70] (see Appendix A of [79]). However, for the concentric-sphere case the error in (1.3.7c) drops from $O[(r_p/R)^6]$ to $O[(r_p/R)^{10}]$, so the series solution is not significantly more accurate than the asymptotic prediction.

The asymptotic results (1.3.6)-(1.3.7) for concentric rigid spheres are plotted in Figure 1.5. Comparison to numerical results via series expansions [173] and experimental measurements [79] are also plotted, and it is clear that these results agree with the asymptotic predictions. The approximate $O(1)$ correction to (1.3.6c) proposed by [79] greatly improves the agreement with the experimental and numerical results when r_p/R is close to unity.

1.3.2 Red blood cells

The wealth of scientific publications that emerged in the 1960s and ‘70s on the motion of rigid particles in circular tubes was largely motivated by the study of blood flow [63]. Blood is a suspension

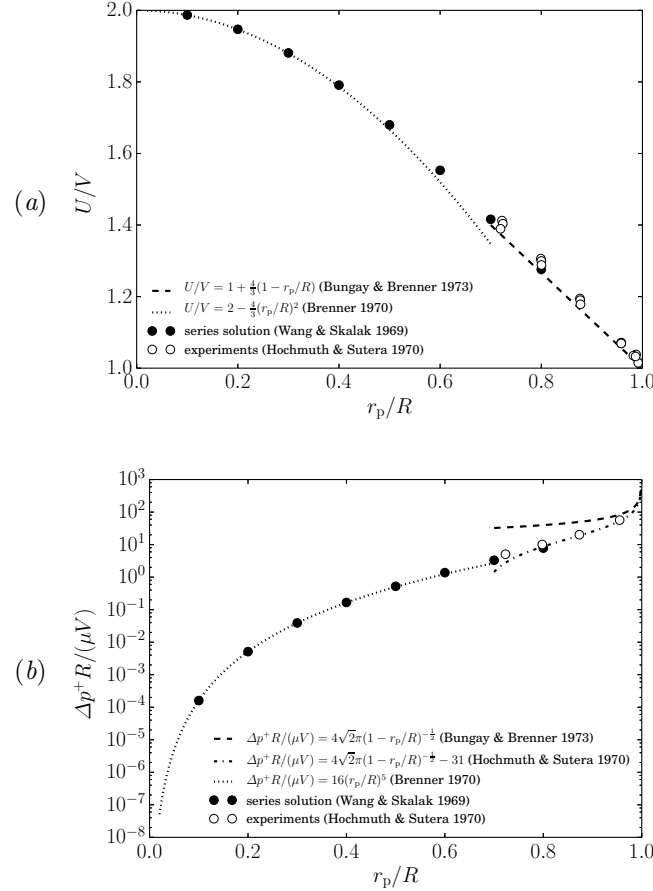


Figure 1.5: Microhydrodynamics of concentric rigid spheres in circular-tube flow. (a) The relative velocity U/V plotted against the radius ratio r_p/R . (b) The dimensionless extra pressure drop $\Delta p^+ R / (\mu V)$ plotted against the radius ratio r_p/R .

primarily comprised of red blood cells – biconcave discs about $8 \mu\text{m}$ in diameter. By the 1980s, fluid mechanicians had begun to incorporate the constitutive properties of the red-blood-cell membrane into fluid flow calculations. Similar to the membranes of vesicles, red-blood-cell membranes admit very strong resistance to dilatation and modest resistance to bending. However, red blood cells are additionally fortified by a spectrin-actin cortex, which imbues their membranes with a shear elasticity. Another key distinctive feature of red-blood-cell suspensions is a very narrow distribution of shapes and sizes, with a surface area of about $A_0 \simeq 135 \mu\text{m}^2$ and volume of $\Omega_0 \simeq 90 \mu\text{m}^3$ [22].

The deformability of red-blood-cell membranes breaks many of the useful symmetry and linearity properties of Stokes flow. As such, red blood cells in the microcirculation tend to migrate towards the centerline of blood capillaries (the so-called “Fåhræus-Lindqvist effect”). The geometry of a flowing suspension of red blood cells is much more complex than that of a rigid-particle suspension, for every position on the red-blood-cell membrane is kinematically coupled to the local flow field.

That is to say, the red-blood-cell membrane is a free boundary that must be determined as part of the solution to a fluid-flow problem. Recall from our discussion in §1.1 that free-boundary problems are governed by nonlinear equations of motion, which usually precludes analytical solutions except under special circumstances. Consequently, most theoretical studies of red-blood-cell motion have relied on numerical methods in order to simultaneously determine the cell shape and flow field [139, 129, 126, 180]. The nonlinear coupling between membrane mechanics and hydrodynamics has been generically classified as *elastohydrodynamics* [149].

In our previous discussion of rigid-sphere suspensions in §1.3.1, the sphere radius r_p was the natural choice of characteristic length scale for the particle. For red blood cells, we must form a length scale based on either its surface area A_0 or enclosed volume Ω_0 , both of which are fixed quantities due to surface-area-incompressibility of the membrane and volume-incompressibility of the enclosed fluid. We define the *areal radius* of a particle R_0 as the radius of a sphere of equal surface area A_0 :

$$R_0 = \sqrt{\frac{A_0}{4\pi}}. \quad (1.3.8)$$

Using R_0 as a characteristic length scale, we can form a dimensionless group from the volume Ω_0 as follows:

$$v = \frac{\Omega_0}{\frac{4}{3}\pi R_0^3}, \quad (1.3.9)$$

where v is known as the *reduced volume* and is a measure of the degree of sphericity of a particle. It lies in the range $0 \leq v \leq 1$, with a value of unity corresponding to a perfect sphere. Red blood cells typically have a reduced volume of about $v \simeq 0.61$. Halpern and Secomb noted that red blood cells can have a distribution of reduced volumes [71], although the width of this distribution is not that large. Osmotically pre-swelling red blood cells can increase their reduced volume [45, 135], thus making them more “sphere-like.” Vesicles can have a wide distribution of reduced volumes, and in fact we shall see that v is a crucial parameter governing the microhydrodynamics of vesicles in channel flows.

As an alternative to R_0 , we could define the *volumetric radius* of a particle r_0 as the radius of a sphere of equal volume Ω_0 :

$$r_0 = \left(\frac{\Omega_0}{\frac{4}{3}\pi} \right)^{\frac{1}{3}}. \quad (1.3.10)$$

Forming a dimensionless group from A_0 and r_0 leads to the definition of the *excess surface area*,

$$\Delta = \frac{A_0}{r_0^2} - 4\pi. \quad (1.3.11)$$

Like v , the excess surface area Δ is a measure of particle sphericity, with $\Delta = 0$ corresponding to a perfect sphere. Red blood cells have an excess surface area of about $\Delta \simeq 4.9$. The choice of R_0 or r_0 as a characteristic scale for the particle is usually a matter of preference. In most of the work

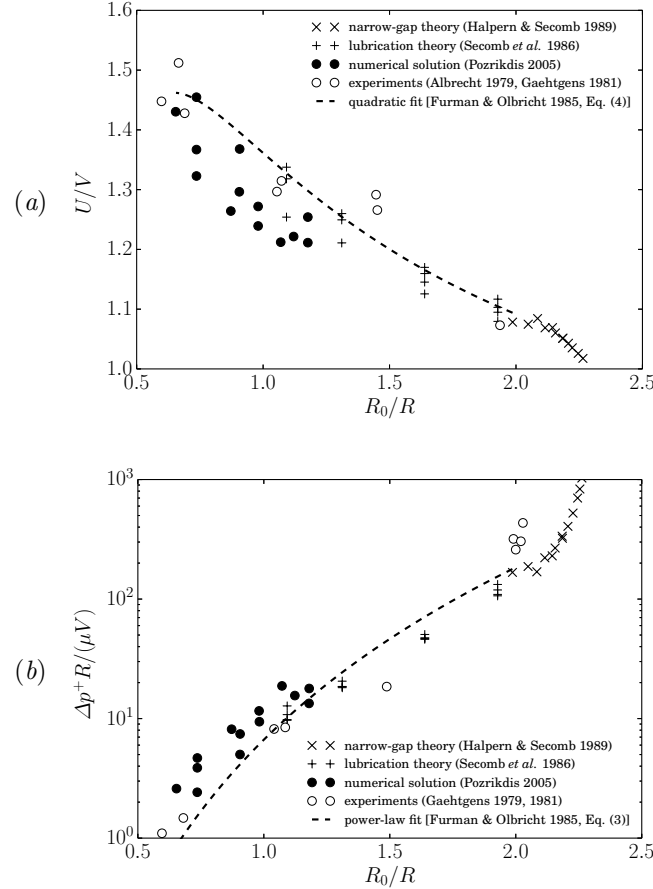


Figure 1.6: Microhydrodynamics of red blood cells in capillary flow. (a) The relative velocity U/V plotted against the radius ratio R_0/R . (b) The dimensionless extra pressure drop $\Delta p^+ R / (\mu V)$ plotted against the radius ratio R_0/R . The vertical scatter in the data is due to the distribution of channel velocities and suspension concentrations.

presented in this thesis (Chapters 3–5), we shall use R_0 as a characteristic particle length scale and therefore measure the sphericity of a particle by v . In Chapter 6, we shall switch to using r_0 as a length scale for reasons that will be made clear in that chapter, making Δ the natural measure of particle sphericity.

Some of the key results – the relative velocity U/V and dimensionless extra pressure drop $\Delta p^+ R / (\mu V)$ – from fluid-mechanical studies of blood flow in microcapillaries (circular tubes) are

summarized in Figure 1.6.⁴ The cell translational velocity U is that measured in the axial direction. The cell rotational velocity Ω is of secondary concern and is rarely reported. In all of the data shown in Figure 1.6, the red-blood-cell radius is estimated to be about $R_0 \simeq 3.3 \mu\text{m}$. Experimental measurements were performed by Albrecht, Gaehtgens, Pries, and coworkers [4, 58, 59]. Secomb and coworkers pioneered the use of lubrication theory to numerically model microcapillary blood flow for large radius ratios R_0/R [139, 71]. (For more background on lubrication theory, refer to [9].) Numerical calculations have been performed by several authors for smaller radius ratios R_0/R [129, 126, 180]. Also plotted are empirical correlations developed by [57] from fitting the experimental data, which help to guide the eye.

The nonlinear deformation of the red-blood-cell membrane breaks the linear dependence of U and Δp^+ on the channel velocity V . Consequently, the microhydrodynamics of blood flow is parametrized by a dimensionless shear-elastic modulus $E_S/(\mu V)$, which weights membrane resistance to in-plane shear deformation against the strength of flow. The vertical scatter in the data shown in Figure 1.6 is due to variations in the suspension concentration c (in the experiments, c varies from 10–30%) and the dimensionless shear modulus $E_S/(\mu V)$ (typically in the range 0.1–10). Clearly, these variations are small compared to those induced by changes in the radius ratio R_0/R .

Another important feature to note in Figure 1.6 is that the minimum cell velocity and maximum pressure drop occur at a critical radius ratio of about $R_0/R \simeq 2.3$ (or a tube radius of $R = 1.4 \mu\text{m}$), according to the asymptotic theory of [71]. Above this value of R_0/R , the red blood cell cannot pass through the capillary cleanly without rupturing. The critical tube radius can be predicted by assuming the red blood cell adopts the shape of a spherocylinder whose radius is equal to the tube radius and whose surface area and volume are $A_0 \simeq 135 \mu\text{m}^2$ and $\Omega_0 \simeq 90 \mu\text{m}^3$, respectively [22]. These assumptions directly lead to a prediction of $R = 1.4 \mu\text{m}$ for the critical tube radius.

1.3.3 Vesicles

Vesicles and red blood cells share similar features: both are fluidic, deformable, and enclosed by an inextensible lipid-bilayer membrane. Artificial vesicles are a somewhat simpler system to study than red blood cells, since they lack a cortical cytoskeleton and hence a membrane shear modulus. More to the point is the number of shape configurations that can be adopted by artificial vesicles, which results in a wide distribution of reduced volumes. To date, even those studies which have examined swollen red blood cells in capillary flow either theoretically [71] or experimentally [135] have not systematically investigated a large range of reduced volumes. In order to properly explore

⁴In the hemodynamics literature, it is common to see the ratio of the tube hematocrit H_T to the discharge hematocrit H_D reported. The hematocrit ratio H_T/H_D is related to the relative velocity U/V by [155, 139],

$$\frac{H_T}{H_D} = \frac{V}{U}.$$

It is also common to see the relative intrinsic viscosity $[\eta]$ reported instead of the extra pressure drop Δp^+ [cf. (1.3.5)]. The symbol K_T is often used instead of $[\eta]$ to denote the relative intrinsic viscosity.

this phase space, we must depart from red blood cells and turn our attention back to vesicles.

As was first mentioned in §1.1, Vitkova and coworkers published the first study of vesicle motion in capillary flow [169]. Some of their micrographs are reproduced in Figure 1.3. Using optical microscopy, these authors measured the relative velocity U/V of small vesicles at high reduced volumes v , and found that their data was adequately fit by the asymptotic prediction (1.3.7a) for small, rigid spheres. The good agreement with the rigid-sphere result can be attributed to the symmetry of the circular geometry, wherein the membrane flow must be uniform in order to preserve surface area locally (this statement is given mathematical foundation at the beginning of Chapter 3). Thus, a concentric vesicle behaves something like a rigid particle, with a shape determined by solving the membrane equations of motion. Unfortunately, measurements of the dimensionless extra pressure pressure drop $\Delta p^+ R/(\mu V)$ have not been made. Moreover, the sensitivity of the reduced volume v on the microhydrodynamics remains unexplored in the study by [169].

Theoretical developments on the motion of finite-sized vesicles in channel flow have been similarly sparse [18, 121, 163]. Bruinsma developed an asymptotic theory to predict the velocity and extra pressure drop of closely fitting vesicles in capillary tubes [18], much in the same spirit as the work of [71] for red-blood-cell flow. His theory produced some key insights, namely the interplay between bending and tension in the membrane and its consequences on the vesicle shape. However, his study is also fraught with faulty assumptions associated with how the membrane tension τ is computed. One consequence of these incorrect assumptions is an apparently anomalous scaling for the extra pressure drop [equation (4.4) in [18]], which renders many of his results essentially unusable. We shall discuss the specific problems with Bruinsma’s theory in §3.2 of Chapter 3, after the theoretical problem is formulated in Chapter 2. A revised theory in the regime of very narrow gaps is one of the main objectives of Chapter 3.

By far the best theoretical study of finite-sized vesicles in capillary flow is due to Trozzo *et al.*, who performed high-fidelity numerical simulations [163]. However, this study focuses primarily on computation of the vesicle shape and membrane surface tractions, without computing either the relative velocity U/V or dimensionless extra pressure drop $\Delta p^+ R/(\mu V)$. Noguchi and Gompper performed mesoscopic simulations of vesicles in capillary flow for a limited set of conditions, [121]. The membranes in their study were approximated by a triangulated mesh of springs with potentials assigned to each edge. Such mesoscopic approaches are typically overdetermined systems and cannot recapitulate the continuum-mechanical membrane properties [e.g., the bending-elastic modulus E_B appearing in the expression for the Helfrich Hamiltonian, equation (1.2.1)]. However, these methods offer the benefit of reduced computational cost, owing to the coarse-grained representation of a continuum surface as a network of beads and springs. Three reduced volumes ($v = 0.59, 0.78$, and 0.9) were investigated in the study by [121], and it is claimed by the authors that their simulations “qualitatively reproduce the observed deformations,” referring to the measurements made by [169].

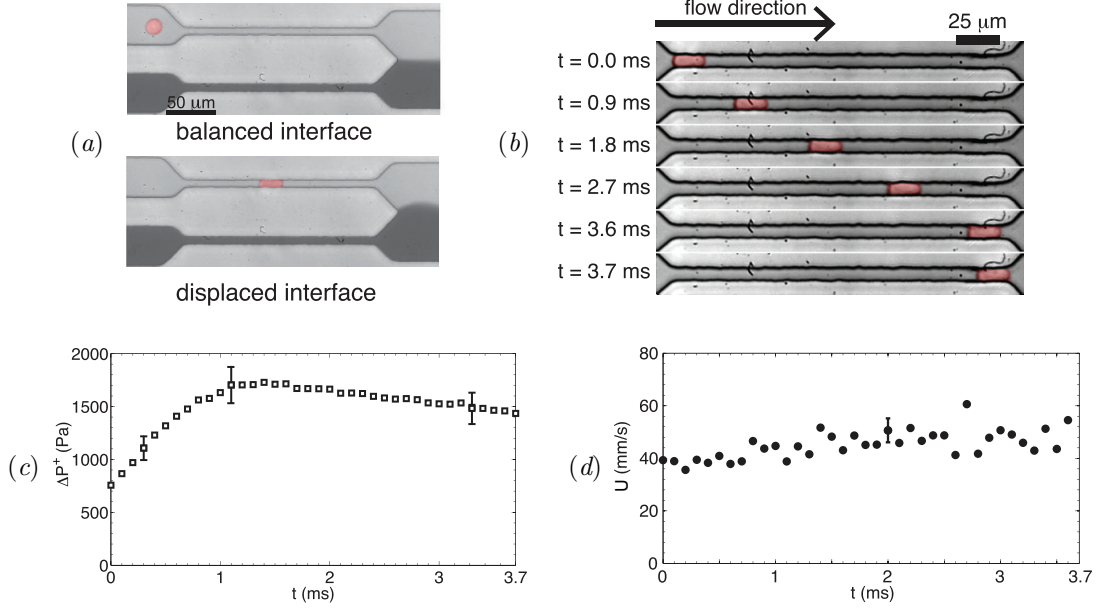


Figure 1.7: Microfluidic platform for making measurements of the particle velocity U and extra pressure drop Δp^+ in square microchannels (reproduced from [90]). (a) Two co-flowing streams in a microfluidic “manometer” are driven at a fixed inlet pressure. A Jurkat leukemia cell (colored red) flows through test channel; the reference channel contains a clear fluid (darkened for visualization). When the particle squeezes through a constriction, the fluid-fluid interface located downstream (in the “comparator region”) deflects. A balance of normal stresses on the fluid-fluid interface enables measurement of Δp^+ . (b) Time series of the particle positions. Taking the ratio of the relative particle position Δx and the elapsed time Δt enables measurement of U . (c) Time series of the extra pressure drop Δp^+ corresponding to the images in (b). The error bars correspond to uncertainty (about 10%) in image-analyzing the displacement of the diffuse interface. (d) Time series of the vesicle velocity U for the same experiment. The error bar reflects the width of the distribution of the instantaneous particle velocities.

It is unclear what is meant here by qualitative agreement, other than the obvious fore-aft symmetry breaking in quadratic flow (see Figure 1.3). Moreover, it is clear from Figure 6 in [121] that the mesoscopic simulation approach can only yield approximate predictions, given the large uncertainty in the predicted quantities U/V and $\Delta p^+ R / (\mu V)$ at moderate flow rates. An alternative simulation method, rooted in continuum mechanics, would be highly preferable; this is the main objective of Chapter 4.

In recent years, advanced microfluidic techniques have been applied to vesicle-flow experiments. Researchers at Harvard University developed a new method of fabricating vesicles via double-emulsion templating in coaxial microcapillary devices [165, 108, 145]. This method offers advantages over the other vesicle fabrication methods (e.g., electroformation [5]) by producing a monodisperse vesicle suspension. A microfluidic “manometer” for measuring the relative velocity U/V and dimensionless extra pressure drop $\Delta p^+ R / (\mu V)$ was developed by Abkarian and coworkers for the study of

red blood cells [2, 1]. This platform, which is illustrated in Figure 1.7, was later adopted by the Vanapalli Group for the study of droplets [167], cancer cells [91, 90], and, more recently, vesicles (personal communication). Recent measurements from this group have quantified the relative velocity U/V of vesicles in square microchannels at various reduced volumes and radius ratios [3], reporting larger mobilities than those reported by [169] for vesicles in circular tubes. It is hypothesized that the observed differences between the two studies can be attributed to bypass flow through the corners of the square channel. Interestingly, recent measurements using the microfluidic manometer (unpublished) show qualitatively different trends in U/V and $\Delta p^+ R / (\mu V)$ as a function of the radius ratio R_0/R when the vesicle is highly confined. Unfortunately, there is no existing theory for vesicles or red-blood-cells in conduits of non-circular cross section. Such a theory is becoming more desirable as microfluidic technologies continue to advance. We address the problem of non-circular conduits in Chapter 5.

Finally, we reiterate that the theoretical investigations of vesicles in 3D quadratic flow discussed in §1.1 have, for the most part, neglected wall effects due to computational limitations, and therefore may be associated with the “unbounded-flow regime.” However, this regime obviously has practical value, as Brenner has shown through his derivation of (1.3.7) that predictions for the particle velocity and extra pressure drop can be obtained by use of integral theorems. Furthermore, these predictions apply (to within a reasonable tolerance) over a large range of radius ratios. Unfortunately, no such predictions exist for vesicles, despite a number of continuum-mechanical studies performed for vesicles in unbounded Poiseuille flows [32, 52]. Rather, these studies have focused on the vesicle migration phenomena. It is our objective in Chapter 6 to derive predictions for U/V and $\Delta p^+ R / (\mu V)$ for vesicles under very weak confinement, focusing on the case of quasi-spherical vesicles (which admits analytical solutions to the membrane equations of motion).

1.4 Objectives and scope of this thesis

From our discussion in the last section, we have identified several theoretical challenges that remain unresolved in the study of vesicles in channel flow:

1. Most studies on vesicles have been intrinsically linked to studies of red blood cells. This restriction limits the phase space to a very narrow distribution of vesicle shapes (i.e., reduced volumes).
2. Lubrication theory, which has been used to great effect by [139, 71] to model microcapillary blood flow, has been applied to the motion of vesicles in capillary flow with some incorrect assumptions [18]. This is a significant issue because it is challenging to apply direct numerical calculations towards lubricated motion at reasonable computational cost.

3. The most extensive microhydrodynamical study of vesicles in channel flow makes use of a mesoscopic simulation approach [121], which, despite offering certain qualitative insight, is fundamentally inconsistent with continuum-mechanical theory.
4. State-of-the art continuum-mechanical theories (using either small-deformation analysis [32] or direct numerical methods [52]) typically omit wall effects due to computational limitations.
5. In continuum-mechanical models where wall effects are included [163], the vesicle velocity and extra pressure drop are not reported.
6. Non-circular conduits, which are prevalent in microfluidic devices, have not been investigated.

In this thesis, we shall address each of these issues under the auspices of rigorous continuum-mechanical theory, employing both asymptotic and numerical methods towards the solution of the membrane equations of motion. Our primary objectives will be to compute the vesicle shape deformation, relative velocity, and extra pressure drop in channel flow over a range of parameters hitherto unexplored.

The remainder of this thesis is organized as follows. In Chapter 2, we set up the basic equations that govern the fluid flow in and around the vesicle as well as the membrane kinematics. The resulting initial-boundary-value problem is solved in subsequent chapters using a plethora of mathematical techniques. We tackle this problem first via a perturbative approach (Chapter 3), wherein we assume *a priori* that a single vesicle occludes the cross section of a circular-tube flow. This theory is asymptotically valid in the regime wherein the gap separating the vesicle membrane and the tube wall is very small. In Chapter 4, numerical calculations of moderately sized vesicles in tube flow are presented without making the so-called “narrow-gap assumption.” These calculations rely on both direct numerical simulations (the boundary element method) as well as a coarse-grained approach in which the lateral velocity gradients are neglected (the lubrication approximation). In Chapter 5, we extend these methods to study the motion of vesicles in square microchannels, where there exists experimental measurements thanks to the popularity of microfluidics. We then pursue the “opposite limit” in which the the vesicle is small relative to the hydraulic diameter of the conduit (Chapter 6). A small-deformation theory, valid for vesicles that are nearly spherical, is developed in this chapter by use of spherical harmonic expansions. Conclusions and directions for future work are given in Chapter 7.

Chapter 2

Theoretical formulation

In this chapter, the basic equations relevant to the motion of vesicles in channel flow are presented. These are partial differential equations governing field quantities that vary continuously with spatial position \mathbf{x} and time t . Theoretical analysis of microscopic fluid flow phenomena hinges on the *continuum hypothesis*, wherein any point in space is assumed to comprise a large enough parcel of fluid molecules whose average properties have vanishingly small statistical fluctuations. Within the continuum framework, we present the basic equations of fluid mechanics (§2.1) and membrane mechanics (§2.2), including some of the key assumptions made in the theoretical development. Significantly, the inertia of the fluids and the vesicle membrane will be neglected, reducing the governing equations of fluid flow to a set of *linear* equations that are complicated by the nonlinear interaction between the vesicle membrane and the flowing fluid. We then state the initial-boundary-value problem in §2.3, which will form the basis for our theoretical calculations. The remainder of the thesis will be devoted to the solution of these equations, using a variety of (both analytical and numerical) methods.

2.1 Equations of fluid mechanics

We begin with a brief review of the most elementary principles of fluid dynamics (or *hydrodynamics*, when applied to liquids), which concerns the relationship between *kinematical* quantities (e.g., velocities and velocity-gradients) and *(hydro)dynamical* quantities (e.g., stresses) [9, 72, 92]. In the continuum limit, the local fluid velocity \mathbf{u} is related to position \mathbf{x} in the Lagrangian sense,

$$\frac{D\mathbf{x}}{Dt} = \mathbf{u}, \quad (2.1.1)$$

where

$$\frac{D}{Dt} = \frac{\partial}{\partial t} + \mathbf{u} \cdot \nabla$$

is the *material time derivative* and ∇ is the gradient operator. Physically, the material time derivative can be thought of as the time rate of change of a quantity that moves with the fluid element. The *spatial time derivative* $\partial/\partial t$ represents the time rate of change of a quantity in a fixed (laboratory) reference frame.

The stress tensor $\boldsymbol{\sigma}$ must be related to gradients of the velocity in a fluid. In this thesis, we shall only be concerned with fluids of the “Newtonian” variety – viscous, small-molecule fluids that are *homogeneous*, *isotropic*, and *incompressible*. Water is an example of a Newtonian fluid at modest shear rates. *Newton’s law of viscosity* relates the components of the stress tensor $\boldsymbol{\sigma}$ to the symmetric part of the velocity-gradient tensor $\nabla\mathbf{u}$:

$$\boldsymbol{\sigma} = \boldsymbol{\sigma}^\dagger = -p\boldsymbol{\delta} + \mu [\nabla\mathbf{u} + (\nabla\mathbf{u})^\dagger], \quad (2.1.2)$$

where p is the fluid pressure, μ is the fluid shear viscosity, and $\boldsymbol{\delta}$ is the unit tensor. The isotropic contribution to the stress is given by $-p/3$. The deviatoric contribution is given by the second term on the right-hand side of (2.1.2). It is clear from (2.1.2) that the stress tensor is symmetric with six independent scalar components. This is required by conservation of angular momentum:

$$\boldsymbol{\epsilon} : \boldsymbol{\sigma} = \mathbf{0}, \quad (2.1.3)$$

where $\boldsymbol{\epsilon}$ is the (third-order) permutation tensor.

For Newtonian fluids subject to an external force density \mathbf{b} , the fluid velocity \mathbf{u} and stress $\boldsymbol{\sigma}$ are governed by the *Navier-Stokes equations*,

$$\nabla \cdot \mathbf{u} = 0, \quad (2.1.4a)$$

$$\varrho \left(\frac{\partial \mathbf{u}}{\partial t} + \mathbf{u} \cdot \nabla \mathbf{u} \right) = -\nabla p + \mu \nabla^2 \mathbf{u} + \mathbf{b}, \quad (2.1.4b)$$

where ϱ is the fluid density. Equations (2.1.4a) and (2.1.4b) *locally* conserve mass and (linear) momentum in the fluid, respectively. They form the basis for the vast majority of calculations in fluid mechanics. Here, the pressure p acts as a Lagrange function so that the volume-incompressibility condition (2.1.4a) is satisfied.

The terms on the left-hand side of (2.1.4b), which are attributed to fluid inertia, are frequently neglected in viscous flow calculations. There are two main reasons to do so. One reason is that the flow streamlines are *steady* and *parallel* (or very nearly so), in which case the terms within the parentheses on the left-hand side are vanishingly small. Another reason to neglect these terms arises in cases where inertial forces are small compared to viscous forces. If R , R/V , V , and $\mu V/R$ denote the characteristic scales for position \mathbf{x} , time t , velocity \mathbf{u} , and pressure p , respectively, then the

latter condition is met if the *Reynolds number*,

$$\text{Re} = \frac{\varrho V R}{\mu}, \quad (2.1.5)$$

is small compared to unity. For microscale flows, typical length and velocity scales are $R = 10 \mu\text{m}$ and $V = 10 \text{ mm/s}$, respectively. Taking water as a typical working fluid (viscosity $\mu = 1 \text{ cP}$ and density $\varrho = 1 \text{ g/cm}^3$), one obtains Reynolds numbers as large as $\text{Re} = 0.1$.¹

If one neglects the left-hand side of (2.1.4b), for any one of the reasons given above, then we are left with *Stokes' equations*:

$$\nabla \cdot \mathbf{u} = 0, \quad (2.1.6a)$$

$$\nabla \cdot \boldsymbol{\sigma} = -\nabla p + \mu \nabla^2 \mathbf{u} = \mathbf{0}. \quad (2.1.6b)$$

Here, we have absorbed the body force density into the definition of the pressure, replacing $p - \mathbf{b} \cdot \mathbf{x}$ by p in (2.1.6b). The pressure p appearing in (2.1.6b) is interpreted as a *dynamic pressure*, whereas in (2.1.4b) it is the *total pressure*.

Equations (2.1.6) will supply the basis of our fluid flow calculations. The main advantage of (2.1.6) over (2.1.4) is that the governing equations are now *linear* in the velocity and stress fields. Additional advantages – linearity, reciprocity, symmetry, and time-reversibility – are gained through the use of Stokes' equations [92].

2.2 Equations of membrane mechanics

The vesicle membrane is treated as a free surface with unknown surface position vector \mathbf{x}_s . This vector is a field that varies in both time and space. As was described in §1.2, the membrane is fluidic and hence can be studied in an Eulerian reference frame. By the kinematic condition (2.1.1), the motion of the vesicle membrane is given by,

$$\frac{D\mathbf{x}_s}{Dt} = \frac{\partial \mathbf{x}_s}{\partial t} + \mathbf{u}_s \cdot \nabla \mathbf{x}_s = \mathbf{u}_s, \quad (2.2.1)$$

where $\mathbf{u}_s = \mathbf{u}|_{\mathbf{x}=\mathbf{x}_s}$ is the membrane surface velocity. Equation (2.2.1) is a transport equation for the position of the membrane surface.

The surface position \mathbf{x}_s can be given either an Eulerian or Lagrangian representation. In the first case, a fixed coordinate system is chosen and the surface position vector \mathbf{x}_s is defined with respect to the spatial coordinates as well as time. The instantaneous value of \mathbf{x}_s is then time-advanced

¹It is important to be mindful when neglecting inertial forces. Frequently, this limit is a singular one in unbounded flows, where the characteristic length of the system is actually not small. In bounded flows, like the ones considered in the present work, this issue rarely arises.

(in the Eulerian reference frame) using the spatial time derivative $\partial/\partial t$. On many occasions, we shall use an Eulerian representation for the vesicle surface in a convenient coordinate system – e.g., by definition of a level set function $\varphi(\mathbf{x}, t) = 0$ on the surface – which facilitates analytical calculations. On the other hand, a Lagrangian representation of the surface position requires no choice of a fixed coordinate system, and the evolution of \mathbf{x}_s (in the Lagrangian reference frame) is governed by the material time derivative D/Dt . We use the latter type of representation in our boundary element calculations (Chapters 4 and 5), wherein the vesicle surface is represented by an unstructured, triangulated mesh in three dimensions.

Due to the close packing of lipid molecules in the bilayer configuration, the membrane behaves as an incompressible material in the plane of the surface (refer back to §1.2 for further description). Hence, the surface velocity \mathbf{u}_s must be solenoidal in the plane,

$$\nabla_s \cdot \mathbf{u}_s = 0, \quad (2.2.2)$$

where $\nabla_s = \nabla - \hat{\mathbf{n}}(\hat{\mathbf{n}} \cdot \nabla)$ is the surface gradient operator (see Appendix A.4) and $\hat{\mathbf{n}}$ is the unit normal vector. Equation (2.2.2) implicitly states that the surface mass density ϱ_s is constant on the vesicle surface.

The unit normal $\hat{\mathbf{n}}$ can be related to \mathbf{x}_s via standard relations from differential geometry [95]. Some of the more important results from differential geometry are presented in Appendix A, including the relationship between $\hat{\mathbf{n}}$ and \mathbf{x}_s [refer to equations (A.2.3) and (A.2.6)]. In equation (A.5.5), the mean curvature H and Gaussian curvature K are shown to be the principal scalar invariants of the (symmetric) curvature tensor $-\nabla_s \hat{\mathbf{n}}$:

$$2H = -\nabla_s \cdot \hat{\mathbf{n}}, \quad 2K = (\nabla_s \cdot \hat{\mathbf{n}})^2 - \nabla_s \hat{\mathbf{n}} : \nabla_s \hat{\mathbf{n}}. \quad (2.2.3)$$

The square of the deviatoric curvature of the surface is denoted by $D^2 = H^2 - K$ [defined in Appendix A, equation (A.5.8)]. This quantity vanishes for a spherical surface.

As we have approximated the vesicle membrane as a mathematical surface, the internal stresses in the bilayer are averaged over the transverse thickness, resulting in lateral tensions and transverse-shear tensions due to bending moments [44]. The bending stresses exerted by the membrane on its surroundings may be computed by applying the principle of virtual work to the Helfrich Hamiltonian introduced in §1.2:

$$W = E_B \int_{\mathcal{S}} 2H^2 dS. \quad (1.2.1)$$

When the principle of virtual work is applied to (1.2.1), we derive the following bending force density per unit area [82, 187]:

$$\mathbf{f}_s^{\text{bending}} = 2E_B [\nabla_s^2 H + 2(H^2 - K)H] \hat{\mathbf{n}}. \quad (2.2.4)$$

Note that the right-hand side of (2.2.4) vanishes for a perfect sphere. Thus, the bending force density $\mathbf{f}_s^{\text{bending}}$ is induced by variations in surface curvature relative to a spherical surface.²

A Lagrange field τ (i.e., the membrane tension) is introduced to enforce the surface-incompressibility condition (2.2.2). Equivalently, we require that all virtual displacements preserve the local surface metric G_s [defined by equation (A.2.10)]. The force density due to membrane tension is found to be [82],

$$\mathbf{f}_s^{\text{tension}} = -2H\tau\hat{\mathbf{n}} - \nabla_s\tau, \quad (2.2.5)$$

which has components normal and tangential to the vesicle surface. Equations (2.2.4)-(2.2.5) will be used in the stress jump condition (2.3.6), below.

2.3 Initial-boundary value problem

In subsequent chapters, we will consider the generic problem of a monodisperse vesicle suspension at concentration c flowing through a conduit with hydraulic radius R . In the creeping flow regime, the fluid velocity \mathbf{u} and stress $\boldsymbol{\sigma}$ satisfy Stokes' equations,

$$\left. \begin{aligned} \nabla \cdot \mathbf{u} &= 0, \\ \nabla \cdot \boldsymbol{\sigma} &= -\nabla p + \mu \nabla^2 \mathbf{u} = 0, \end{aligned} \right\} \quad \text{in the suspending fluid,} \quad (2.3.1a)$$

$$\left. \begin{aligned} \nabla \cdot \mathbf{u} &= 0, \\ \nabla \cdot \boldsymbol{\sigma} &= -\nabla p + \check{\mu} \nabla^2 \mathbf{u} = 0, \end{aligned} \right\} \quad \text{inside the vesicles,} \quad (2.3.1b)$$

where μ is the exterior fluid viscosity, $\check{\mu}$ is the interior fluid viscosity. The pressure p is made “dynamic” by absorbing the “static pressure” $-\mathbf{b} \cdot \mathbf{x}$ as described at the end of §2.1. It is implicitly assumed here that this density is the same for the exterior and interior fluids (e.g., if the fluids have the same density ϱ , then the gravitational body force density $\mathbf{b} = \varrho \mathbf{g}$ is the same for both fluids).

The vesicle suspension is forced into motion by a mean velocity V , where

$$VA_{\times}\hat{\mathbf{e}}_x = \int_{\mathcal{S}_{\times}} \mathbf{u} dS \quad \text{as } x \rightarrow \pm\infty. \quad (2.3.2)$$

Here, \mathcal{S}_{\times} denotes a cross-sectional surface in the channel with surface area A_{\times} . In this and in forthcoming chapters, the mean flow is always taken to be in the x direction. On the channel wall, the velocity \mathbf{u} is subject to the “no-slip condition,”

$$\mathbf{u} = \mathbf{u}_w = \mathbf{0} \quad \text{on the channel wall.} \quad (2.3.3)$$

²In the original formulation by Helfrich [74], a spontaneous curvature H_0 is introduced to allow for the possibility of asymmetries in the lipid bilayer. When this term is nonzero, the equivalent “reference surface” is not a sphere.

Kinematic continuity requires that the velocity \mathbf{u} be continuous across the membrane surface,

$$[\![\mathbf{u}]\!] = \mathbf{0} \quad \text{on the vesicle membrane,} \quad (2.3.4)$$

where $[\![\cdot]]$ is the jump operator. The membrane surface velocity,

$$\mathbf{u} = \mathbf{u}_s \quad \text{on the vesicle membrane,} \quad (2.3.5)$$

is unknown *a priori* and must be determined as part of the solution for the flow field. Additionally, we stipulate the kinematic condition (2.2.1) and surface-incompressibility condition (2.2.2) for all points on the membrane.

Whereas the velocity is continuous across the membrane, the stress has a discontinuity. Letting $\mathbf{f} = \boldsymbol{\sigma} \cdot \hat{\mathbf{n}}$ denote the traction on the membrane due to the bulk fluid, mechanical equilibrium dictates that the jump in traction across an arbitrary patch of membrane balance the work done by the membrane [cf. (2.2.4)-(2.2.5)]:

$$\begin{aligned} [\![\mathbf{f}]\!] &= \mathbf{f}_s = \mathbf{f}_s^{\text{bending}} + \mathbf{f}_s^{\text{tension}} \\ &= \{2E_B [\nabla_s^2 H + 2(H^2 - K)H] - 2H\tau\} \hat{\mathbf{n}} - \nabla_s \tau \quad \text{on the vesicle membrane.} \end{aligned} \quad (2.3.6)$$

Here, $\mathbf{f}_s = [\![\mathbf{f}]\!]|_{\mathbf{x}=\mathbf{x}_s} = [\![\boldsymbol{\sigma} \cdot \hat{\mathbf{n}}]\!]|_{\mathbf{x}=\mathbf{x}_s}$ is the jump in surface traction across the membrane. Since the body force density \mathbf{b} is presumed to be the same in both fluids, there is no net traction on the membrane exerted by fluid body forces.

Although Stokes' equations are steady, the boundary-value problem is time dependent through the kinematic condition (2.2.1). Thus, in principle one must evolve the configuration from some initial condition. At the initial time point, we specify the total volume and surface area of any single vesicle in the suspension:

$$\text{at } t = 0 : \quad \int_{\mathcal{V}_0} d^3 \mathbf{x} = \Omega_0, \quad \int_{\partial \mathcal{V}_0} dS = A_0. \quad (2.3.7)$$

where \mathcal{V}_0 denotes a region occupied by a single vesicle. Thus, the vesicle volume Ω_0 and surface area A_0 take the role of parameters in the initial-boundary-value problem. Surface-area and volume incompressibility require that Ω_0 and A_0 be time-invariant in the Lagrangian sense,

$$\frac{D\Omega_0}{Dt} = 0, \quad \frac{DA_0}{Dt} = 0. \quad (2.3.8)$$

In practice, it is a challenging task to exactly control the distributions of vesicle volumes Ω_0 and surface areas A_0 for a vesicle population prepared by, say, electroformation methods [5]. Typically,

statistical information on the size and shape distribution of the population can be obtained via phase-contrast microscopy or fluorescent microscopy (in the latter method, the vesicles must be prepared with trace amount of fluorescently tagged lipid in the formulation). In the last decade, advancements in microfluidics have led to more sophisticated vesicle preparation techniques by means of double emulsions [108, 145], which allows for more precise control of Ω_0 and A_0 .

2.4 Vesicle velocity and extra pressure drop

The *translational velocity* \mathbf{U} of any single vesicle in the suspension is defined as a volume average of the internal velocity,

$$\begin{aligned}\mathbf{U} &= \frac{1}{\Omega_0} \int_{\mathcal{V}_0} \mathbf{u} d^3x \\ &= \frac{1}{\Omega_0} \int_{\partial\mathcal{V}_0} \mathbf{x}(\mathbf{u}_s \cdot \hat{\mathbf{n}}) dS,\end{aligned}\tag{2.4.1}$$

where to obtain the second line we have applied the divergence theorem and used the fact that the velocity is solenoidal. If the flow system has reached a steady state, then $\mathbf{u}_s \cdot \hat{\mathbf{n}} = \mathbf{U} \cdot \hat{\mathbf{n}}$ everywhere on $\partial\mathcal{V}_0$ and (2.4.1) is identically satisfied.³ Though not of principal concern to the present work, we may also define the *rotational velocity* $\boldsymbol{\Omega}$ of the vesicle,

$$\begin{aligned}\boldsymbol{\Omega} &= \frac{1}{\Omega_0} \int_{\mathcal{V}_0} \frac{1}{2}(\nabla \times \mathbf{u}) d^3x \\ &= \frac{1}{\Omega_0} \int_{\partial\mathcal{V}_0} \frac{1}{2}(\hat{\mathbf{n}} \times \mathbf{u}_s) dS,\end{aligned}\tag{2.4.2}$$

where to obtain the second line we have applied the divergence theorem.

The extra pressure drop Δp^+ is obtained by requiring the vesicle suspension to be force-free. We apply a force balance to a control volume containing the suspending fluid, bounded internally by the vesicle surfaces and externally by the channel walls and two cross sectional surfaces separated by a distance L_c . Requiring that the vesicles be force-free, we obtain the relation,

$$\Delta p A_x \hat{\mathbf{e}}_x = - \int_{\mathcal{S}_w} \mathbf{f}_w dS,\tag{2.4.3}$$

where \mathcal{S}_w is the wall surface spanning an axial distance L_c , Δp is the drop in pressure across a distance L_c , and \mathbf{f}_w is the wall surface traction. Taking the formal limit as $L_c \rightarrow \infty$ results in a diverging pressure drop. A bounded quantity may be obtained by first subtracting out the Poiseuille-flow contribution and taking the limit thereafter. The result is equation (1.3.3), reproduced below

³This result can be shown by use of the identity $\int_{\partial\mathcal{V}_0} \mathbf{x} \hat{\mathbf{n}} dS = \Omega_0 \boldsymbol{\delta}$ (provable via the divergence theorem) for any closed body of volume $\Omega_0 = \int_{\mathcal{V}_0} d^3x$.

for convenience:

$$\Delta p^+ = \lim_{L_c \rightarrow \infty} (\Delta p - \Delta p^\circ) = \lim_{L_c \rightarrow \infty} (\Delta p - L_c A_\times K_{\text{hyd}} V). \quad (1.3.3)$$

Recall from §1.3 that K_{hyd} is the specific hydraulic resistivity of the channel. The extra pressure drop Δp^+ is bounded and can be directly related to the intrinsic viscosity of the vesicle suspension by (1.3.5).

Equations (2.3.2) and (2.4.3) prescribe the mean channel velocity V and channel pressure drop Δp , respectively, for an *infinitely long channel* ($L_c \rightarrow \infty$). This formulation is appropriate for dilute suspension calculations, in which hydrodynamic interactions among vesicles are neglected. In Chapter 4, we introduce a numerical method based on a periodic formulation of the boundary-value problem, which includes hydrodynamic interactions among periodic images. In the periodic formulation, the channel wall spans the axial distance of a finite cell volume, and so one cannot apply boundary conditions at a fictitious surface in the far field. The appropriate periodic boundary conditions, which supplant the far-field conditions (1.3.3) and (2.3.2), are specified at the beginning of Chapter 4.

2.5 Scalings and dimensionless groups

The basic equations may be put into dimensionless form upon selection of characteristic scales for the base units. Here, it is natural to use R as a measure for distance, R/V for time, and $\mu V/R$ for stress. Using these scales, the variables are rendered dimensionless as follows:

$$x, y, z \quad \text{are scaled by } R, \quad (2.5.1a)$$

$$u_x, u_y, u_z \quad \text{are scaled by } V, \quad (2.5.1b)$$

$$p \quad \text{is scaled by } \mu V/R, \quad (2.5.1c)$$

$$\tau \quad \text{is scaled by } \mu V. \quad (2.5.1d)$$

Buckingham's Pi theorem then stipulates that the solution of the governing equations be parameterized by five dimensionless groups [19]:

$$\kappa = \frac{\check{\mu}}{\mu} \quad \text{(the viscosity ratio)}, \quad (2.5.2)$$

$$\beta = \frac{E_B}{\mu V R^2} \quad \text{(the bending parameter)}, \quad (2.5.3)$$

$$\lambda = \frac{R_0}{R} \quad \text{(the radius ratio)}, \quad (2.5.4)$$

$$v = \frac{\Omega_0}{\frac{4}{3}\pi R_0^3} \quad \text{(the reduced volume)}, \quad (2.5.5)$$

$$c \quad \text{(the suspension concentration)}. \quad (2.5.6)$$

Here, $R_0 = \sqrt{A_0/(4\pi)}$ is the effective vesicle radius based on its surface area [cf. (1.3.8)].

The physical significance of these dimensionless groups is easily interpreted. The viscosity ratio κ is a measure of the relative dissipation between the interior and exterior fluids. The bending parameter β gauges the relative importance of membrane bending stiffness and viscous traction in the balance of normal stress on the membrane.⁴ The reduced volume v varies between 0 and 1 and gauges the “vesicle sphericity” (a reduced volume of unity corresponds to a perfectly spherical vesicle). The radius ratio λ measures the size of the vesicle relative to the size of the tube, and thus is a measure for flow confinement. The suspension concentration c gauges the strength of vesicle-vesicle hydrodynamic interactions.

2.5.1 Typical values of the dimensionless parameters

Under typical experimental conditions (using water as the working fluid, with some combination of dissolved electrolytes), $\mu = \check{\mu} = 1$ cP, which gives $\kappa = 1$. The microchannels of interest in this work have dimensions of $R \simeq 10$ μm . Giant, unilamellar vesicles span a distribution of length scales with radii R_0 ranging from 1-100 μm . Thus, the radius ratio λ can take on a range of values. When prepared using electroformation, vesicles are typically spherical or nearly spherical, meaning that their reduced volume v is close to unity. Changes in reduced volume can be induced by changing the lipid formulation or by introducing a gentle osmotic shock, giving a distribution typically in the range $v = 0.6\text{-}1$ (red blood cells have an average reduced volume of about $v = 0.61$).

From Table 1.1, we can estimate the bending moduli of unilamellar, bilayer vesicles to be $E_B \simeq 10^{-12}$ dyn · cm, although higher moduli can be obtained by addition of cholesterol or some other additive to the lipid formulation [41, 42, 119, 26]. If we estimate the mean fluid velocity to be in the range $V = 0.1\text{-}10$ mm/s, we obtain a viscous energy scale of $\mu V R^2 = 10^{-10}\text{-}10^{-8}$ dyn·cm. (One could make the argument that the vesicle radius R_0 is the proper length scale to use here. However, the channel hydraulic radius R typically bounds the membrane radius of curvature, making it the more suitable choice of length scale for larger vesicles.) From this estimate, we obtain $\beta = 10^{-4}\text{-}10^{-2}$ for a typical microfluidic experiment. Higher values of β are concomitant with “weak-flow” conditions, wherein the imposed fluid velocity is very small and the vesicle tends to approach its equilibrium shape. As shown in Figure 1.1, the equilibrium shape is not necessarily a sphere and in fact is controlled by the reduced volume v [141]. It is expected that bending elasticity plays a more significant role when the reduced volume v is low, for regions of high curvature induced by flow can result in cusps in the absence of bending resistance (put another way, the *local* bending parameter can be large, even if β is small, when weighted by the local surface curvature). Thus, setting $\beta = 0$

⁴The reciprocal of β is sometimes called the “capillary number” in connection with vesicles. This terminology is avoided here because the capillary number is usually defined as the ratio of viscous stresses to surface-tension stresses, the latter of which act to resist changes in *surface area*. Bending stresses act to resist changes in *surface curvature*, which is a fundamentally different effect.

can be a singular limit if the local curvature diverges. Mathematically, this can be seen from the fact that E_B in (2.3.6) multiplies the highest derivative (fourth-order in space) of the surface position vector \mathbf{x}_s . For sphere-like vesicles ($v \simeq 1$), the term multiplying E_B in (2.3.6) is vanishingly small, and bending elasticity can typically be neglected even in very weak flows.

2.5.2 Other dimensionless groups

The dimensionless parameters (2.5.2)-(2.5.6) completely specify solutions of the initial-boundary-value problem. It is possible, however, to form other dimensionless parameters using different combinations of the “dimensional” parameters (e.g., μ , R , and so on). Depending on the particular regime in the phase space under consideration, it may be convenient to use a different set of dimensionless groups in order to parametrize the solutions. We shall introduce some of these alternatives below.

In Chapter 3, we shall assume the vesicle is highly confined and lubricated by a very thin film of characteristic thickness h° . The length of the vesicle is denoted by L . The mathematical analysis in Chapter 3 is made simpler by replacing the radius ratio λ and reduced volume v with the following dimensionless groups:

$$\epsilon = \frac{h^\circ}{R} \quad (\text{the clearance parameter}), \quad (2.5.7)$$

$$\ell = \frac{L}{R} \quad (\text{the reduced length}). \quad (2.5.8)$$

The reasoning behind this exchange of parameters is explained in §3.3 of the next chapter.

In Chapter 4, we shall dispense with the “axially unbounded” flow configuration and instead assume a periodic vesicle suspension. This formulation enables us to consider hydrodynamic interactions among periodic images in a model suspension configuration. Denoting by L_x the axial length of one basic cell, the separation between neighboring images is quantified by the dimensionless group,

$$\delta = \frac{L_x}{R} \quad (\text{the separation parameter}). \quad (2.5.9)$$

This quantity supplants the suspension concentration c as a gauge for hydrodynamic interactions.

In Chapter 6, we shall assume that the vesicle is very small and quasi-spherical. Instead of the areal radius R_0 , the volumetric radius r_0 [cf. (1.3.10)] becomes a natural choice of length scale for the vesicle. In this chapter, we replace the bending parameter β , radius ratio λ , and reduced volume v by the following dimensionless groups:

$$\chi = \frac{E_B}{\mu V r_0^2} \quad (\text{the bending parameter}), \quad (2.5.10)$$

$$a = \frac{r_0}{R} \quad (\text{the radius ratio}), \quad (2.5.11)$$

$$\Delta = \frac{A_0}{r_0^2} - 4\pi \quad (\text{the excess surface area}). \quad (2.5.12)$$

Note that, although we have used the same names for some of the dimensionless groups, the definitions (2.5.10)-(2.5.11) are distinct from (2.5.3)-(2.5.4).

2.6 Summary

Taken together, the preceding equations form an initial-boundary-value problem for the velocity \mathbf{u} , pressure p , membrane tension τ , and membrane surface position \mathbf{x}_s , parametrized by five dimensionless groups. The main quantities of interest are the vesicle velocity \mathbf{U} and extra pressure drop Δp^+ .

Of the five dimensionless groups, we shall focus much of our attention on the radius ratio λ , reduced volume v , and bending parameter β . Taken together, the first and second parameters specify the geometry of the system; the third reflects the dynamic interplay between membrane bending elasticity and stresses induced by fluid flow. The viscosity contrast κ is typically $O(1)$ in many physical systems. We shall not be too concerned with the effect of a viscosity mismatch, although this is a key parameter in controlling vesicle shape dynamics [112, 31]. Hydrodynamic interactions, measured by the suspension concentration c , plays a small role when the radius ratio λ is large. Although we shall briefly consider the effect of hydrodynamic interactions in Chapter 4, for the most part we shall assume c is sufficiently small such that hydrodynamic interactions among vesicles can be neglected.

In subsequent chapters, we attack this problem using various theoretical approaches that are best suited to particular regimes of the parameter space. We begin in the next chapter with a perturbative solution of the governing equations, for vesicles swollen to near-critical confinement.

Chapter 3

Vesicles in narrow tubes

3.1 Narrow-gap assumption

The initial-boundary-value problem described in Chapter 2 is highly nonlinear due to the coupling between membrane deformation and fluid flow. To gain insight into the structure of the solutions, we first pursue an asymptotic solution in the limit of vanishingly small separation distances between the membrane surface and the conduit wall. We pursue this analysis only for a circular-tube geometry using cylindrical coordinates (ρ, ϕ, x) . Here, the axial coordinate is denoted by x , adopting the convention that gravity points in the $-z$ direction. Thus, $\rho = \sqrt{y^2 + z^2}$ is the radial coordinate and $\phi = \arctan(z/y)$ is the azimuthal angle.

To be explicit, in this chapter we shall make the following assumptions:

1. The vesicles are sufficiently well separated such that vesicle-vesicle hydrodynamic interactions are irrelevant (i.e., the suspension concentration c is small compared to unity). Thus, we may consider the flow field in and around a single vesicle.
2. The system has reached some steady configuration, implying that all derivatives of fields with respect to t vanish and $\hat{\mathbf{n}} \cdot \mathbf{u} = \hat{\mathbf{n}} \cdot \mathbf{U}$ on the vesicle membrane.
3. The system remains circularly symmetric about the x -axis, implying that $u_\phi = 0$ and derivatives of fields with respect to ϕ vanish. A useful consequence of this and the previous assumptions is that the velocity on the vesicle membrane is uniform with vanishing components in the ρ and ϕ directions:

$$\mathbf{u} = \mathbf{u}_s = \mathbf{U} = U \hat{\mathbf{e}}_x \quad \text{on the membrane.} \quad (3.1.1)$$

To obtain this result, one need only write down the steady form of the surface-area incompressibility condition (2.2.2) in axisymmetric cylindrical coordinates [using equation (A.7.89b)

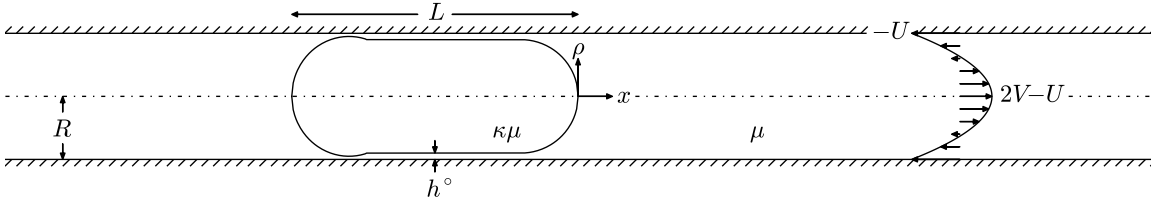


Figure 3.1: Schematic of a closely fitting vesicle translating in a circular tube due to pressure-driven flow. The system is rotationally symmetric about the x -axis. In a reference frame moving with the vesicle, the walls translate with velocity $-U\hat{e}_x$.

with x replacing z], set $\partial u_\phi / \partial \phi = 0$, and integrate the result with respect to x . The requirement that \mathbf{u} be regular at the poles leads directly to (3.1.1). This condition implies that an axisymmetric vesicle in tube flow resembles a rigid particle, since the membrane velocity is uniform. However, the shape of the vesicle is unknown *a priori* and must be determined as part of the solution to the flow problem.

Since the velocity on the membrane is uniform, it is convenient to adopt a reference frame that moves with the vesicle. In the new reference frame,

$$\mathbf{u} = \mathbf{u}_s = \mathbf{0} \quad \text{on the membrane,} \quad (3.1.2)$$

$$\mathbf{u} = \mathbf{u}_w = -U\hat{e}_x \quad \text{on the tube wall.} \quad (3.1.3)$$

4. The viscosity contrast κ is $O(1)$.

A schematic of the model geometry is shown in Figure 3.1. The origin of the cylindrical coordinate system is placed at the front (or downstream) tip of the vesicle, so that the geometry is defined in a reference frame moving with the vesicle. The length of the vesicle is denoted by L , so the rearmost end of the vesicle is located at $x = -L$. The gap thickness at the midplane $x = -L/2$ is denoted by h° . In steady, axisymmetric cylindrical coordinates, the vesicle surface position \mathbf{x}_s is given by the Eulerian representation,

$$\mathbf{x}_s(\phi, x) = x\hat{e}_x + \rho_s(x) \cos \phi \hat{e}_y + \rho_s(x) \sin \phi \hat{e}_z, \quad (3.1.4)$$

where $\rho_s(x)$ is the azimuthal radius of curvature of the vesicle. Thus, the vesicle surface is defined by the scalar equation,

$$\rho = \rho_s(x) = R - h(x), \quad (3.1.5)$$

where we have defined the gap height $h(x)$ separating the vesicle membrane from the tube wall. The differential geometry associated with the representation (3.1.5) is given in Appendix A.7.6.

In axisymmetric cylindrical coordinates, the velocity vector \mathbf{u} and stress tensor $\boldsymbol{\sigma}$ have the following decomposition:

$$\mathbf{u} = u_x \hat{\mathbf{e}}_x + u_\rho \hat{\mathbf{e}}_\rho, \quad (3.1.6)$$

$$\boldsymbol{\sigma} = \left(-p + 2\mu \frac{\partial u_x}{\partial x} \right) \hat{\mathbf{e}}_x \hat{\mathbf{e}}_x + \left(-p + 2\mu \frac{\partial u_\rho}{\partial \rho} \right) \hat{\mathbf{e}}_\rho \hat{\mathbf{e}}_\rho + \left(-p + \frac{2\mu u_\rho}{\rho} \right) \hat{\mathbf{e}}_\phi \hat{\mathbf{e}}_\phi + \mu \left(\frac{\partial u_x}{\partial \rho} + \frac{\partial u_\rho}{\partial x} \right) (\hat{\mathbf{e}}_x \hat{\mathbf{e}}_\rho + \hat{\mathbf{e}}_\rho \hat{\mathbf{e}}_x). \quad (3.1.7)$$

Since the system is assumed to have reached steady state, the fluid leakback flux per unit circumference q must be constant everywhere in the gap:

$$-2\pi q = Q - \pi R^2 U = \pi R^2 (V - U) = 2\pi \int_r^R u_x \rho d\rho = \text{constant}. \quad (3.1.8)$$

(Here, the axial component of velocity u_x is written in a reference frame that translates with the vesicle.) Thus, the leakback flux q uniquely specifies the relative velocity U/V . For a circular tube of “infinite” length, the extra pressure drop Δp^+ across the vesicle is given by,

$$\Delta p^+ = - \int_{-\infty}^{\infty} \left[\frac{2\mu}{R} \left(\frac{\partial u_x}{\partial \rho} + \frac{\partial u_\rho}{\partial x} \right) \Big|_{\rho=R} + \frac{8\mu V}{R^2} \right] dx = \text{constant}. \quad (3.1.9)$$

Assumptions 1-4 above are justifiable if the vesicle is highly confined. In such a state, the membrane surface conforms to the (axisymmetric) wall surface and translates with a velocity nearly equal to the (steady) mean channel velocity. To state this last condition mathematically, we add an additional assumption to the above list:

5. The radius ratio λ is close to a maximum λ^* , implying that the vesicle is swollen to a size so large that it fits snugly inside the tube. For an axisymmetric system, simple geometric arguments suggest that the vesicle shape be something like a spherocylinder, for which the reduced volume v and critical radius ratio λ^* are simply related by the cubic equation,

$$2v\lambda^{*3} - 3\lambda^{*2} + 1 = 0. \quad (3.1.10a)$$

To derive (3.1.10a), one need only write down the volume Ω_0 and surface area A_0 of a spherocylindrical vesicle of length L , assuming that it fills a tube of radius R . By eliminating L and recasting the resulting equation in dimensionless form, one obtains (3.1.10a). An exact solution of (3.1.10a) exists and is given by,

$$\lambda^* = \frac{1}{2v} \left[1 + \left(1 - 2v^2 + 2v\sqrt{v^2 - 1} \right)^{-\frac{1}{3}} + \left(1 - 2v^2 + 2v\sqrt{v^2 - 1} \right)^{\frac{1}{3}} \right], \quad (3.1.10b)$$

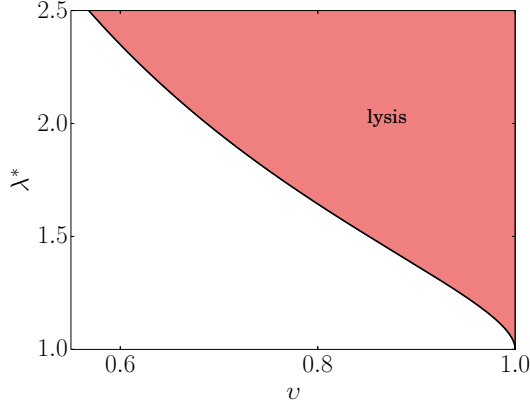


Figure 3.2: Critical radius ratio λ^* plotted against the reduced volume v , as given by (3.1.10). Membrane rupture occurs for $\lambda > \lambda^*$, which is indicated by the shaded region.

which yields real values for $0 \leq v \leq 1$. A plot of λ^* against v is shown in Figure 3.2. The ratio λ/λ^* is properly normalized so that a value of unity denotes the maximum vesicle size for a given tube radius. If $\lambda > \lambda^*$, the vesicle cannot pass through the tube without rupturing. Experiments with swollen red blood cells (reduced volume $v \simeq 0.9$) indicate that lysis occurs above $\lambda^* \simeq 1.5$ [135], which is in excellent agreement with the theoretical prediction of 1.4 from (3.1.10). In this chapter, we shall seek asymptotic solutions for which,

$$\left(1 - \frac{\lambda}{\lambda^*}\right) \ll 1, \quad (3.1.11)$$

noting that λ^* is a function of v .

The last assumption above is the so-called *narrow-gap assumption*. Invoking the condition (3.1.11) is equivalent to stating that the gap separating the membrane from the tube wall is very small. One can then pursue a perturbative solution in terms of the small parameter $(1 - \lambda/\lambda^*)$.

3.2 Previous theories

The landmark work motivating the set of assumptions just delineated is due to Bretherton, who famously developed a prediction for the relative velocity and dimensionless extra pressure drop for large bubbles of fixed volume in circular tubes [17]. In his theory, the “small parameter” controlling the size of the gap distance is the capillary number, $\text{Ca} = \mu V / \gamma$, which reflects the ratio of viscous stresses to the Laplace pressure across the bubble surface (here, γ is a material property known as the *surface tension*). The basic reason for this dependence is that a bubble’s surface is free to dilate its surface area without bound; thus, a sufficiently large bubble will wet the tube wall unless

suspended by a viscous pressure created by fluid flow. By contrast, a vesicle's surface area is tightly controlled due to the fixed lipid content in the bilayer. The membrane tension τ is thus distinct from the surface tension γ in that the former is not a material property of the membrane. Rather, τ is a *field* that adjusts itself in order to preserve surface area locally. The fixed surface area A_0 of a vesicle implies that the “proper” narrow-gap assumption – given by (3.1.11) – is a *purely geometric criterion*, independent of the flow conditions. This is not to say that narrow gaps between the vesicle membrane and the wall of a tube cannot develop when (3.1.11) is not satisfied. Such solutions of the flow problem may indeed exist in the phase space under certain conditions, for the vesicle geometry can become remarkably complex under flow. The condition (3.1.11) restricts our attention to the subset of these solutions wherein the vesicle can no longer increase in size without rupturing inside the tube.

A similar set of assumptions was adopted by Halpern and Secomb (following up on the work of [139]) in analyzing the lubricated motion of red blood cells through narrow capillaries [71]. In their theory, they examine swollen red blood cells with volumes Ω_0 in excess of the physiological value of $90 \mu\text{m}^3$ (such volumes are practically achievable by osmotically pre-swelling the red blood cells [45, 135]). They found that the dimensionless extra pressure drop scales linearly with the length L of the red blood cell, $\Delta p^+ R / (\mu V) \simeq 2L/R$, whereas the relative velocity (called the “relative hematocrit” in their work) is approximately unity with a small correction, $U/V \simeq 1$.

Due to the similarities between vesicles and red blood cells, it is instructive to point out the regime in which the theoretical predictions of Halpern and Secomb applies and how it differs from the one laid out in this chapter. In their theory, an implicit assumption is made wherein the length L of the red blood cell is presumed long enough such that the “front nose” or downstream section of the red blood cell is hydrodynamically isolated from the “rear tail” or upstream section. An important consequence of this assumption is that the middle section of the red blood cell is cylindrical, lubricated by a film of uniform thickness $h^\circ = O(1 - \lambda/\lambda^*)$ and length $L - 2R + O(1 - \lambda/\lambda^*)$. Mathematically, this assumption amounts to the following restriction on the cell length:

$$L \gg 2R \left[1 + \left(\frac{h^\circ}{R} \right)^{\frac{1}{2}} \right]. \quad (3.2.1a)$$

Stated in terms of the dimensionless groups (2.5.2)-(2.5.6) [with λ^* being exchanged for v by use of (3.1.10)], this condition translates to,

$$\lambda^{*2} \gg 2 + \left(1 - \frac{\lambda^*}{\lambda} \right)^{\frac{1}{2}}. \quad (3.2.1b)$$

Clearly, however, this assumption breaks down as the length L approaches the channel diameter $2R$ (equivalently, as reduced volume v approaches unity), which physically corresponds to a spherical

cell. One expects that predictions for the relative velocity and dimensionless extra pressure drop would change qualitatively for spherical cells relative to spherocylindrical cells, an observation noted in the appendix of [135]. It turns out that the condition (3.2.1) is singular when the cell is “sphere-like,” as will be shown later in this chapter. For vesicles, whose populations frequently include spherical or nearly spherical shapes, this turns out to be quite a crucial oversight. Alternatively, the condition (3.2.1) can also break down if the gap thickness h° is not sufficiently small. In this instance, the front nose and rear tail are not hydrodynamically isolated but in fact are coupled through the narrow-gap region. These points motivate a revised theory wherein the *long-length assumption* (3.2.1) is not invoked outright.

An additional difference between the work of [71] and our present problem is the extent to which the effect of bending elasticity is investigated. In the study by [71], bending elasticity is considered as a minor correction to the effects of isotropic tension and shear elasticity. Moreover, the effects of shear elasticity and bending elasticity are never decoupled, which obfuscates interpretation of some of their results. Vesicles lack the spectrin-actin cortex of red blood cells, so we will not consider the effects of shear elasticity in this work. The effect of bending elasticity is investigated extensively in this chapter, above and beyond the regime considered by [71]. This portion of our work is somewhat an academic exercise, since (as was pointed out at the end of §2.5) the bending parameter β is usually small in microfluidic experiments. Nevertheless, the regime of the phase space where β is not small is inherently interesting due to the nonlinear coupling between bending elasticity and membrane tension. Such couplings can be found in many other “membrane problems” in engineering physics [105, 24]. Thus, from a purely intellectual standpoint, the high- β regime merits consideration.

Finally, we must acknowledge the work of Bruinsma [18], who developed a theory for vesicles in the same spirit as those of [17] (for bubbles) and [71] (for red blood cells). By invoking the lubrication approximation, Bruinsma supplied predictions for the vesicle shape and dimensionless extra pressure drop $\Delta p^+ R / (\mu V)$. One of the more important contributions from his study is an eigenvalue analysis of the fifth-order “membrane equation” governing the shape of the vesicle in the region of lubrication. Bruinsma showed that the structure of the solutions change qualitatively at some critical ratio between the bending parameter β and the membrane tension τ . However, his prediction for the dimensionless extra pressure drop for high vesicle velocities $\Delta p^+ R / (\mu V) \simeq 0.233(\mu V/R)(L/R)^3$ {equation (4.4) in [18]} is dubious, due to misguided steps in his analysis of the membrane tension field. Rather than enforce surface-area conservation, Bruinsma makes the claim that there is an osmotic pressure across the vesicle membrane (due to the difference in osmolarity of the interior and exterior fluid) that must balance the hydrodynamic pressure. In doing so, he acknowledges that lipid bilayers are semi-permeable to water with finite permeability (although the rate of permeation is very slow, in reality) and then claims that the net volume current across the membrane must vanish for the vesicle to maintain constant volume. This leads to a direct expression for the pressure

jump across the membrane at the front and rear ends of the vesicle (where viscous stresses are weak) in terms of the osmotic pressure. The membrane tension at the front and rear ends then follows from the normal component of the stress condition (2.3.6) – essentially, he has fixed the membrane tension at the two ends of the vesicle, which then serve as boundary conditions for the membrane tension. The governing field equation for the membrane tension is the tangential component of the stress condition (2.3.6), which can be integrated explicitly with respect to the axial coordinate in axisymmetric domains. Applying the aforementioned “osmotic balance condition” at one of the poles closes the problem. Finally, he claims that when the pressure drop gets high enough, the membrane tension will vanish at the rear end (based on the argument that a negative tension is impossible since the membrane would become unstable), and this leads to an anomalous cubic scaling with the vesicle length L , $\Delta p^+ R / (\mu V) \sim (L/R)^3$. By contrast, the linear scaling $\Delta p^+ R / (\mu V) \sim (L/R)$ of [71] is much more reasonable. Moreover, Bruinsma's assumption that the membrane tension is specified independently of the vesicle's surface area leads directly to the conclusion that bending stiffness would have no effect on the hydrodynamics, which is quite clearly wrong.

Bruinsma's theory reflects a fundamental misunderstanding of the function of the membrane tension τ in the Helfrich model for lipid bilayers (1.2.1). It is the nature of vesicles to preserve their surface area to within at most a couple percent areal strain. The tension in the membrane must act to preserve surface area locally, and therefore is a field to be determined for a given flow configuration. That is to say, if one imposes a stronger flow and hence impose a larger traction on the membrane, then the membrane tension must increase in order to prevent local dilatation. If we accept that the membrane tension must conserve surface area locally, then the correct closure for the tangential stress balance on the membrane is to treat the total surface area A_0 of the vesicle as a fixed quantity. This choice directly leads to the narrow-gap condition (3.1.11) and supplies a different closure for the membrane tension field than the one used in [18]. Consideration of the difference in osmolarity between the interior and exterior fluids is, therefore, unnecessary to close the hydrodynamic problem.

3.3 Exchange of parameters

It is shown in this chapter that conserving surface area globally leads to a prediction for $\Delta p^+ R / (\mu V)$ that agrees with that of [71] and invalidates the prediction of [18]. In the spirit of the work of [123], who modernized Bretherton's theory by use of the method of matched asymptotic expansions, we shall develop our solution as a formal perturbation series in terms of a small parameter.

From the narrow-gap condition (3.1.11), an obvious choice for the perturbation parameter would seem to be $(1 - \lambda/\lambda^*)$. Setting $\lambda = \lambda^*$ collapses the vesicle shape onto a spherocylinder – a cylinder of length $L - 2R$ capped by two hemispheres of radius R . For small (but non-vanishing)

values of $(1 - \lambda/\lambda^*)$, a lubrication layer (the “inner region”) of length $L - 2R$ develops around the vesicle midsection. Within this lubrication layer, viscous shear stresses are amplified and drive large pressures. Outside this layer (the “outer region”), viscous stresses play a comparatively weaker role and the shape of the membrane is dictated by hydrostatics. This regional segregation of “dominant” physical forces suggests that the limit $\lambda \rightarrow \lambda^*$ is a singular one and, therefore, a perturbative solution “for small $(1 - \lambda/\lambda^*)$ ” must be constructed by the method of matched asymptotic expansions.

Unfortunately, the choice of $(1 - \lambda/\lambda^*)$ as a perturbation parameter is not convenient for mathematical analysis. The dimensionless parameters v and λ appear in integral conditions for the membrane shape, which conserve volume and surface area globally and thus depend on both the outer and inner solutions. Furthermore, the critical radius ratio λ^* is nonlinearly related to the reduced volume v through (3.1.10). A more convenient choice of perturbation parameter would be the dimensionless gap thickness,

$$\epsilon = \frac{h^\circ}{R} \quad (\text{the clearance parameter}), \quad (2.5.7)$$

where h° is defined at the middle plane $x = -L/2$ (as shown in Figure 3.1). A natural complement would be the dimensionless vesicle length,

$$\ell = \frac{L}{R} \quad (\text{the reduced length}). \quad (2.5.8)$$

When performing experiments, one cannot directly control the values of ϵ and ℓ . These parameters depend on the local flow conditions and therefore must be measured. By contrast, the reduced volume v and radius ratio λ depend only on the geometric properties of the system, independent of the local flow conditions. From a mathematical viewpoint, a tremendous amount of simplicity is gained if one assumes that ϵ and ℓ are held fixed, whence v and λ must be determined incidentally as part of the calculation. This choice seems rather *ad hoc*, at first, but reveals itself naturally upon setting up the boundary-value problem.

Fortunately, it turns out that there exists a one-to-one mapping between solutions of fixed (ϵ, ℓ) to those of fixed (v, λ) so long as the condition (3.1.11) is met. This mapping is nonlinear, but in view of the narrow-gap assumption can be expressed formally as a perturbation series. Thus, it would seem permissible to choose the clearance parameter ϵ as the perturbation parameter, presume ϵ and ℓ to be fixed, and determine v and λ *a posteriori*. We shall adopt this strategy here.

The remainder of this chapter is organized in the following way. In §3.4, the dimensionless equations are expanded in terms of ϵ , yielding a singular perturbation problem. The perturbative solution is derived in §3.5, including higher-order corrections. Two particular asymptotic limits, neglecting the effect of membrane bending elasticity, are considered in §3.6: one in which the vesicle is long and spherocylindrical, the other in which it is short and spherical. The effect of membrane bending

elasticity is then examined in §3.7. In §3.8, the gap thickness and vesicle length are eliminated as parameters, leading to an alternative (and useful) parametrization of the theoretical results. A discussion of the results is presented in §3.9. Concluding remarks are given in §3.11.

The analytical development is greatly simplified by use of dimensionless variables. In the forthcoming sections (§3.4-3.8), it is implicitly assumed that all variables with units of distance are scaled by R , velocity by V , pressure by $\mu V/R$, and tension by μV (see also §2.5 of the previous chapter). As an example, ρ denotes the radial distance in units of R , so $\rho = 1$ demarcates the position of the tube wall. In §3.9, we dispense with these implied scalings and present the main theoretical results in terms of “dimensional variables.”

3.4 Narrow-gap equations

The domain is separated into three regions, as shown in Figure 3.3. Regions I and III demarcate the “outer region” while Region II denotes the “inner region.” O’Neill and Stewartson, in their study of spheres translating in the vicinity of planar boundaries, showed that the lateral and transverse length scales in the inner region must be stretched by $\epsilon^{\frac{1}{2}}$ and ϵ , respectively, in order for the particle surface to have contiguous curvature [122]. Using the same arguments, the “inner coordinates” in this work are defined as

$$(\bar{x}, \bar{x}^*, \bar{y}) = \left(\frac{x+1}{\epsilon^{\frac{1}{2}}}, \frac{x+\ell-1}{\epsilon^{\frac{1}{2}}}, \frac{1-\rho}{\epsilon} \right), \quad (3.4.1)$$

where an “overbar” is used to denote a rescaling with respect to $\epsilon^{\frac{1}{2}}$ and an “asterisk” is used to denote a shift of origin in the inner region. It is taken as an ansatz that $x = -1$ and $x = -\ell+1$ demarcate the “matching points” separating the inner region from the outer regions. A more general formulation would leave the locations of the matching points as extra degrees of freedom to be determined as part of the solution [123].

In the forthcoming equations, we denote variables associated with the interior fluid with an lopsided overhat, $(\check{\cdot})$. Thus, p and \check{p} denote the pressure in the exterior and interior fluids, respectively. By stretching the coordinates according to (3.4.1) and requiring that the dependent variables balance in the governing equations, one deduces the following “stretched variables”:¹

$$(\bar{u}_{\bar{x}}, \bar{u}_{\bar{y}}, \check{u}_{\bar{x}}, \check{u}_{\rho}, \bar{p}, \check{p}, \bar{\tau}, \check{\tau}, \bar{h}, \check{q}, \Delta p^+) = \left(u_x, -\frac{u_\rho}{\epsilon^{\frac{1}{2}}}, \check{u}_x, \epsilon^{\frac{1}{2}} \check{u}_\rho, \epsilon^{\frac{3}{2}} p, \epsilon^{\frac{3}{2}} \check{p}, \epsilon^{\frac{3}{2}} \tau, \frac{h}{\epsilon}, \frac{q}{\epsilon}, \epsilon^{\frac{1}{2}} \Delta p^+ \right). \quad (3.4.2)$$

The scalings for the transverse velocities $\bar{u}_{\bar{y}}$ and \check{u}_ρ are different because there is no need to rescale the transverse coordinate ρ in the interior fluid.

Finally, it is necessary to rescale the bending parameter β and reduced length ℓ such that they

¹The term “inner variable” is avoided here, because in practice the variables may be stretched in either the outer or inner regions. The stretched pressures \bar{p} and \check{p} , for instance, are $O(1)$ in both regions.

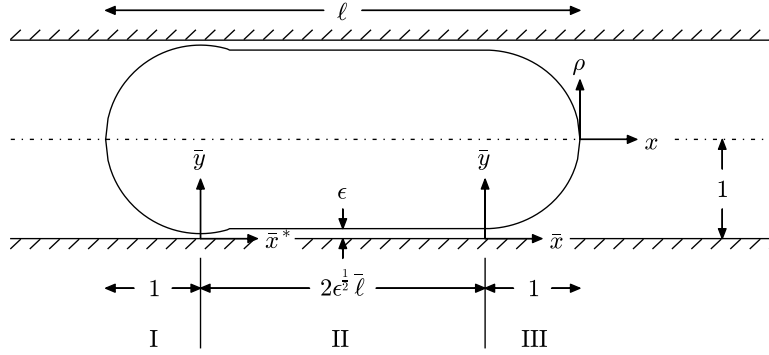


Figure 3.3: The domain is divided into three regions: a “rear outer region” (I), an “inner region” (II), and a “front outer region” (III). The inner coordinates \bar{x} and \bar{x}^* are related by a shift of origin, $\bar{x}^* = \bar{x} - 2\bar{\ell}$.

are retained at leading order in the narrow-gap equations:

$$(\bar{\beta}, \bar{\ell}) = \left(\epsilon^{\frac{1}{2}} \beta, \frac{\frac{1}{2}\ell - 1}{\epsilon^{\frac{1}{2}}} \right). \quad (3.4.3)$$

The viscosity ratio κ need not be rescaled. The rescaled bending parameter $\bar{\beta}$ represents the correct balance of bending and viscous stresses in the narrow-gap limit. The rescaled length $2\bar{\ell}$ is the axial distance (in inner coordinates) spanned by the lubricating film. In the following development, it is tacitly assumed that

$$\kappa = o(\epsilon^{-\frac{1}{2}}) \quad \text{and} \quad \bar{\beta} = o(\epsilon^{-\frac{1}{2}}),$$

so that the subsequent expansions are “uniformly asymptotic.”

In the next few subsections, the basic equations are rescaled and equations appropriate to the outer and inner regions are derived in light of the new scalings. Matching conditions at $x = -1$ and $x = -\ell + 1$ will be presented thereafter.

3.4.1 Outer equations

In the outer region, the coordinates are not stretched and the velocity components need not be rescaled. The pressures $p(\rho, x)$ and $\check{p}(\rho, x)$ and membrane tension $\tau(x)$ must be stretched according to (3.4.2) in order to match consistently with the inner solution. The radius of curvature $\rho_s(x)$, which spans the tube cross section, is a suitable shape function for describing the membrane shape in the outer region.

The governing equations and boundary conditions for the outer region are as follows:

$$\frac{\partial u_x}{\partial x} + \left(\frac{\partial}{\partial \rho} + \frac{1}{\rho} \right) u_\rho = 0, \quad (3.4.4a)$$

$$\frac{\partial \bar{p}}{\partial x} - \epsilon^{\frac{3}{2}} \left(\frac{\partial^2}{\partial x^2} + \frac{\partial^2}{\partial \rho^2} + \frac{1}{\rho} \frac{\partial}{\partial \rho} \right) u_x = 0, \quad (3.4.4b)$$

$$\frac{\partial \bar{p}}{\partial \rho} - \epsilon^{\frac{3}{2}} \left(\frac{\partial^2}{\partial x^2} + \frac{\partial^2}{\partial \rho^2} + \frac{1}{\rho} \frac{\partial}{\partial \rho} - \frac{1}{\rho^2} \right) u_\rho = 0, \quad (3.4.4c)$$

$$\frac{\partial \check{u}_x}{\partial x} + \left(\frac{\partial}{\partial \rho} + \frac{1}{\rho} \right) \check{u}_\rho = 0, \quad (3.4.5a)$$

$$\frac{\partial \check{p}}{\partial x} - \epsilon^{\frac{3}{2}} \kappa \left(\frac{\partial^2}{\partial x^2} + \frac{\partial^2}{\partial \rho^2} + \frac{1}{\rho} \frac{\partial}{\partial \rho} \right) \check{u}_x = 0, \quad (3.4.5b)$$

$$\frac{\partial \check{p}}{\partial \rho} - \epsilon^{\frac{3}{2}} \kappa \left(\frac{\partial^2}{\partial x^2} + \frac{\partial^2}{\partial \rho^2} + \frac{1}{\rho} \frac{\partial}{\partial \rho} - \frac{1}{\rho^2} \right) \check{u}_\rho = 0, \quad (3.4.5c)$$

$$\text{as } x \rightarrow \pm\infty : \quad u_x \rightarrow 2(1 - \rho^2) - 1 - 2q, \quad u_\rho = 0, \quad (3.4.6)$$

$$\text{at } \rho = 1 : \quad u_x = -1 - 2q, \quad u_\rho = 0, \quad (3.4.7)$$

$$\text{at } \rho = \rho_s(x) : \quad u_x = 0, \quad u_\rho = 0, \quad (3.4.8)$$

$$\text{at } \rho = 0 : \quad \frac{\partial \check{u}_x}{\partial \rho} = 0, \quad \check{u}_\rho = 0, \quad (3.4.9)$$

$$\text{at } \rho = \rho_s(x) : \quad \check{u}_x = 0, \quad \check{u}_\rho = 0, \quad (3.4.10)$$

$$\text{at } \rho = \rho_s(x) :$$

$$\begin{aligned} & - (\bar{p} - \check{p}) + \frac{2\epsilon^{\frac{3}{2}}}{1 + (d\rho_s/dx)^2} \left[\left(\frac{\partial}{\partial \rho} - \frac{d\rho_s}{dx} \frac{\partial}{\partial x} \right) (u_\rho - \kappa \check{u}_\rho) - \frac{d\rho_s}{dx} \left(\frac{\partial}{\partial \rho} - \frac{d\rho_s}{dx} \frac{\partial}{\partial x} \right) (u_x - \kappa \check{u}_x) \right] \\ &= \bar{\tau} \left(\frac{1}{\rho_s \sqrt{1 + (d\rho_s/dx)^2}} - \frac{d^2 \rho_s / dx^2}{\sqrt{1 + (d\rho_s/dx)^2}^3} \right) \\ &+ \epsilon \bar{\beta} \left\{ \frac{1}{2} \left(\frac{1}{\rho_s \sqrt{1 + (d\rho_s/dx)^2}} + \frac{d^2 \rho_s / dx^2}{\sqrt{1 + (d\rho_s/dx)^2}^3} \right)^2 + \frac{1}{1 + (d\rho_s/dx)^2} \frac{d^2}{dx^2} \right. \\ &\quad \left. - \frac{1}{\sqrt{1 + (d\rho_s/dx)^2}} \frac{d\rho_s}{dx} \left(- \frac{1}{\rho_s \sqrt{1 + (d\rho_s/dx)^2}} + \frac{d^2 \rho_s / dx^2}{\sqrt{1 + (d\rho_s/dx)^2}^3} \right) \frac{d}{dx} \right\} \\ &\quad \times \left(- \frac{1}{\rho_s \sqrt{1 + (d\rho_s/dx)^2}} + \frac{d^2 \rho_s / dx^2}{\sqrt{1 + (d\rho_s/dx)^2}^3} \right), \end{aligned} \quad (3.4.11)$$

at $\rho = \rho_s(x)$:

$$\frac{1}{\sqrt{1 + (\mathrm{d}\rho_s/\mathrm{d}x)^2}} \frac{\mathrm{d}\bar{\tau}}{\mathrm{d}x} + \frac{2\epsilon^{\frac{3}{2}}}{1 + (\mathrm{d}\rho_s/\mathrm{d}x)^2} \left(\left\{ \frac{\mathrm{d}\rho_s}{\mathrm{d}x} \frac{\partial}{\partial \rho} + \left[1 - \left(\frac{\mathrm{d}\rho_s}{\mathrm{d}x} \right)^2 \right] \frac{\partial}{\partial x} \right\} (u_\rho - \kappa \check{u}_\rho) - \left\{ \frac{\mathrm{d}\rho_s}{\mathrm{d}x} \frac{\partial}{\partial x} - \left[1 - \left(\frac{\mathrm{d}\rho_s}{\mathrm{d}x} \right)^2 \right] \frac{\partial}{\partial \rho} \right\} (u_x - \kappa \check{u}_x) \right) = 0, \quad (3.4.12)$$

at $x = 0$:

$$\rho_s = 0, \quad \frac{1}{\sqrt{1 + (\mathrm{d}\rho_s/\mathrm{d}x)^2}} \frac{\mathrm{d}\rho_s}{\mathrm{d}x} = -1, \quad (3.4.13)$$

at $x = -\ell$:

$$\rho_s = 0, \quad \frac{1}{\sqrt{1 + (\mathrm{d}\rho_s/\mathrm{d}x)^2}} \frac{\mathrm{d}\rho_s}{\mathrm{d}x} = +1. \quad (3.4.14)$$

Equations (3.1.8) and (3.1.9) are not presented for the outer problem. The leakback flux q and extra pressure drop Δp^+ may be uniquely determined from the inner equations, which are presented in the next subsection.

3.4.2 Inner equations

The variables in the inner region are stretched according to the definitions in (3.4.1)-(3.4.3). The radius of curvature $\rho_s(x)$ is replaced by the scaled gap thickness $\bar{h}(\bar{x})$, which is a more suitable choice of shape function in the inner region. Since the governing equations are autonomous, it is understood that derivatives with respect to \bar{x} may equivalently be written with respect to \bar{x}^* . In the development of the inner equations, only terms up to $O(\epsilon, \epsilon\kappa, \epsilon\bar{\beta})$ are retained.

The governing equations and boundary conditions for the inner region are as follows:

$$\frac{\partial \bar{u}_{\bar{x}}}{\partial \bar{x}} + \left(\frac{\partial}{\partial \bar{y}} - \epsilon \right) \bar{u}_{\bar{y}} = O(\epsilon^2), \quad (3.4.15a)$$

$$\frac{\partial \bar{p}}{\partial \bar{x}} - \left[\frac{\partial^2}{\partial \bar{y}^2} + \epsilon \left(\frac{\partial^2}{\partial \bar{x}^2} - \frac{\partial}{\partial \bar{y}} \right) \right] \bar{u}_{\bar{x}} = O(\epsilon^2), \quad (3.4.15b)$$

$$\frac{\partial \bar{p}}{\partial \bar{y}} - \epsilon \frac{\partial^2 \bar{u}_{\bar{y}}}{\partial \bar{y}^2} = O(\epsilon^2), \quad (3.4.15c)$$

$$\frac{\partial \check{u}_{\bar{x}}}{\partial \bar{x}} + \left(\frac{\partial}{\partial \rho} + \frac{1}{\rho} \right) \check{u}_\rho = 0, \quad (3.4.16a)$$

$$\frac{\partial \check{p}}{\partial \bar{x}} - \epsilon \kappa \frac{\partial^2 \check{u}_{\bar{x}}}{\partial \bar{x}^2} = O(\epsilon^2 \kappa), \quad (3.4.16b)$$

$$\frac{\partial \check{p}}{\partial \rho} - \kappa \left[\frac{\partial^2}{\partial \bar{x}^2} + \epsilon \left(\frac{\partial^2}{\partial \rho^2} + \frac{1}{\rho} \frac{\partial}{\partial \rho} - \frac{1}{\rho^2} \right) \right] \check{u}_\rho = O(\epsilon^2 \kappa), \quad (3.4.16c)$$

$$\text{at } \bar{y} = 0 : \quad \bar{u}_{\bar{x}} = -1 - 2\epsilon\bar{q}, \quad \bar{u}_{\bar{y}} = 0, \quad (3.4.17)$$

$$\text{at } \bar{y} = \bar{h}(\bar{x}) : \quad \bar{u}_{\bar{x}} = 0, \quad \bar{u}_{\bar{y}} = 0, \quad (3.4.18)$$

$$\text{at } \rho = 0 : \quad \frac{\partial \check{u}_{\bar{x}}}{\partial \rho} = 0, \quad \check{u}_{\rho} = 0, \quad (3.4.19)$$

$$\text{at } \rho = 1 - \epsilon\bar{h}(\bar{x}) : \quad \check{u}_{\bar{x}} = 0, \quad \check{u}_{\rho} = 0, \quad (3.4.20)$$

at $\bar{y} = \bar{h}(\bar{x})$, $\rho = 1 - \epsilon\bar{h}(\bar{x})$:

$$\begin{aligned} & -(\bar{p} - \check{p}) + 2\epsilon \left[\frac{\partial \bar{u}_{\bar{y}}}{\partial \bar{y}} - \frac{d\bar{h}}{d\bar{x}} \frac{\partial \bar{u}_{\bar{x}}}{\partial \bar{y}} - \kappa \left(\frac{\partial}{\partial \rho} + \frac{d\bar{h}}{d\bar{x}} \frac{\partial}{\partial \bar{x}} \right) \check{u}_{\rho} \right] \\ &= \bar{\tau} \left\{ \left(1 + \frac{d^2\bar{h}}{d\bar{x}^2} \right) + \epsilon \left[\bar{h} - \frac{1}{2} \left(\frac{d\bar{h}}{d\bar{x}} \right)^2 \left(1 + 3 \frac{d^2\bar{h}}{d\bar{x}^2} \right) \right] \right\} \\ & - \bar{\beta} \left\{ \frac{d^4\bar{h}}{d\bar{x}^4} + \epsilon \left[\frac{1}{2} \left(1 + \frac{d^2\bar{h}}{d\bar{x}^2} \right) - \frac{3}{2} \left(\frac{d^2\bar{h}}{d\bar{x}^2} \right)^2 - 2 \frac{d\bar{h}}{d\bar{x}} \frac{d^3\bar{h}}{d\bar{x}^3} - \frac{5}{2} \left(\frac{d^2\bar{h}}{d\bar{x}^2} \right)^3 \right. \right. \\ & \left. \left. - 10 \frac{d\bar{h}}{d\bar{x}} \frac{d^2\bar{h}}{d\bar{x}^2} \frac{d^3\bar{h}}{d\bar{x}^3} - \frac{5}{2} \left(\frac{d\bar{h}}{d\bar{x}} \right)^2 \frac{d^4\bar{h}}{d\bar{x}^4} \right] \right\} + O(\epsilon^2 \bar{\beta}, \epsilon^2, \epsilon^2 \kappa), \end{aligned} \quad (3.4.21)$$

$$\text{at } \bar{y} = \bar{h}(\bar{x}), \rho = 1 - \epsilon\bar{h}(\bar{x}) : \quad \frac{d\bar{\tau}}{d\bar{x}} - \epsilon \frac{\partial \bar{u}_{\bar{x}}}{\partial \bar{y}} - \epsilon \kappa \frac{\partial \check{u}_{\rho}}{\partial \bar{x}} = O(\epsilon^2, \epsilon^2 \kappa), \quad (3.4.22)$$

$$\text{at } \bar{x} = -\bar{\ell}, \bar{x}^* = \bar{\ell} : \quad \bar{h} = 1, \quad (3.4.23)$$

$$\bar{q} = - \int_0^{\bar{h}(\bar{x})} \bar{u}_{\bar{x}} (1 - \epsilon\bar{y}) d\bar{y} = \text{constant}, \quad (3.4.24)$$

$$\frac{1}{2} \Delta \bar{p}^+ = \int_{-\infty}^{\bar{\ell}} \frac{\partial \bar{u}_{\bar{x}}}{\partial \bar{y}} \Big|_{\bar{y}=0} d\bar{x}^* + \int_{-\bar{\ell}}^{\infty} \frac{\partial \bar{u}_{\bar{x}}}{\partial \bar{y}} \Big|_{\bar{y}=0} d\bar{x} + O(\epsilon^{1/2}) = \text{constant}. \quad (3.4.25)$$

To leading order, the leakback flux \bar{q} and extra pressure drop $\Delta \bar{p}^+$ are determined entirely from the inner solution. The error term omitted in (3.4.25) contains higher-order contributions from the inner region as well as the leading-order contribution from the outer region.

3.4.3 Matching conditions

The foregoing equations are valid in the outer and inner regions separately. In order to unify the solutions, matching conditions must be developed at the matching points $x = -1$ and $-\ell + 1$. Of

particular importance are the matching conditions for the membrane shape:

$$\lim_{x \rightarrow -1} 1 - \rho_s(x) = \lim_{\bar{x} \rightarrow \infty} \epsilon \bar{h}(\bar{x}) \quad (3.4.26a)$$

at the front nose and

$$\lim_{x \rightarrow -\ell+1} 1 - \rho_s(x) = \lim_{\bar{x}^* \rightarrow -\infty} \epsilon \bar{h}(\bar{x}) \quad (3.4.26b)$$

at the rear tail. The limits are interpreted in the spirit of the matching principle of van Dyke [166].

With the inclusion of these matching conditions, the boundary-value problem is well posed.

3.5 Small- ϵ expansion

Rather than solve for the unknown variables using methods for partial differential equations, we expand the dependent variables in power series with respect to $\epsilon^{1/2}$, viz.,

$$\psi(x, \rho) = \psi_0(x, \rho) + \epsilon^{1/2} \psi_1(x, \rho) + \epsilon \psi_2(x, \rho) + \dots \quad (3.5.1)$$

for the generic “unstretched” variable ψ and

$$\bar{\psi}(\bar{x}, \bar{y}) = \bar{\psi}_0(\bar{x}, \bar{y}) + \epsilon^{1/2} \bar{\psi}_1(\bar{x}, \bar{y}) + \epsilon \bar{\psi}_2(\bar{x}, \bar{y}) + \dots \quad (3.5.2)$$

for the generic “stretched” variable $\bar{\psi}$. By expanding the dependent variables in powers of $\epsilon^{1/2}$ and collecting terms of like order in $\epsilon^{1/2}$ from the equations presented in §3.4, an ordered set of perturbation equations is obtained. As these equations are rather lengthy, the reader is referred to Appendix B for a complete list of equations at each order in $\epsilon^{1/2}$. The perturbation equations are to be solved sequentially, beginning by setting $\epsilon = 0$ so as to derive the so-called “leading-order solution.” Corrections to this solution are subsequently obtained by expanding the perturbation equations to higher order in $\epsilon^{1/2}$.

Before attempting a solution, instruction on the procedure for transferring boundary conditions (for both outer and inner variables) is given in §3.5.1. The solution procedure then begins with consideration of the outer region (§3.5.2), in which viscous stresses are relatively unimportant and the shape of the membrane is controlled by hydrostatics. In the inner region (§3.5.3), the fluid flow is governed by the equations of lubrication theory. The outer solution forces the inner solution through the matching conditions, which are applied as needed during the course of constructing the solutions. Higher-order corrections are evaluated in §3.5.4.

3.5.1 Transfer of boundary conditions

Since the boundary $\rho = \rho_s(x)$ is perturbed as part of the expansion procedure, it is necessary to transfer boundary conditions to the “unperturbed boundary” at $\rho = \rho_{s0}$. For a generic “outer variable” ψ , this task may be accomplished by expanding the field in a power series according to (3.5.1), Taylor-expanding the series about $\rho = \rho_{s0}$, and evaluating the result at $\rho = \rho_s$:

$$\psi|_{\rho=\rho_s} = \left\{ \psi_0 + \epsilon^{\frac{1}{2}} \left(\psi_1 + \rho_{s1} \frac{\partial \psi_0}{\partial \rho} \right) + \epsilon \left[\psi_2 + \rho_{s1} \frac{\partial \psi_1}{\partial \rho} + \left(\rho_{s2} + \frac{\rho_{s1}^2}{2} \frac{\partial}{\partial \rho} \right) \frac{\partial \psi_0}{\partial \rho} \right] + O(\epsilon^{\frac{3}{2}}) \right\} \Big|_{\rho=\rho_{s0}}. \quad (3.5.3)$$

For definite integrals of ψ over the range $\rho_s \leq \rho \leq 1$, the lower limit of integration must also be transferred to the new boundary $\rho = \rho_{s0}$. This task may be accomplished by separating the integral into two parts, applying a Taylor series about $\rho = \rho_{s0}$, and integrating the resulting moments:

$$\begin{aligned} \int_{\rho_s}^1 \psi \, d\rho &= \int_{\rho_{s0}}^1 \psi \, d\rho + \int_{\rho_s}^{\rho_{s0}} \psi \, d\rho \\ &= \int_{\rho_{s0}}^1 \psi \, d\rho + \int_{\rho}^{\rho_{s0}} \left(\psi|_{\rho=\rho_{s0}} + (\rho - \rho_{s0}) \frac{\partial \psi}{\partial \rho} \Big|_{\rho=\rho_{s0}} + \frac{(\rho - \rho_{s0})^2}{2} \frac{\partial^2 \psi}{\partial \rho^2} \Big|_{\rho=\rho_{s0}} + \dots \right) d\rho \\ &= \int_{\rho_{s0}}^1 \psi \, d\rho - (\rho - \rho_{s0}) \psi|_{\rho=\rho_{s0}} - \frac{(\rho - \rho_{s0})^2}{2} \frac{\partial \psi}{\partial \rho} \Big|_{\rho=\rho_{s0}} - \frac{(\rho - \rho_{s0})^3}{6} \frac{\partial^2 \psi}{\partial \rho^2} \Big|_{\rho=\rho_{s0}} + \dots \\ &= \left\{ \int_{\rho_{s0}}^1 \psi_0 \, d\rho + \epsilon^{\frac{1}{2}} \left(\int_{\rho_{s0}}^1 \psi_1 \, d\rho - \rho_{s1} \psi_0 \right) + \epsilon \left[\int_{\rho_{s0}}^1 \psi_2 \, d\rho - \rho_{s1} \psi_1 - \left(\rho_{s2} + \frac{\rho_{s1}^2}{2} \frac{\partial}{\partial \rho} \right) \psi_0 \right] \right. \\ &\quad \left. + O(\epsilon^{\frac{3}{2}}) \right\} \Big|_{\rho=\rho_{s0}}. \end{aligned} \quad (3.5.4)$$

The same procedure must be applied to the generic “inner variable” $\bar{\psi}$, which is expanded in a power series according to (3.5.2). Boundary values evaluated at $\bar{y} = \bar{h}(\bar{x})$ must be transferred to the new boundary $\bar{y} = \bar{h}_0(\bar{x})$. This task may be accomplished by Taylor-expanding the power series about $\bar{y} = \bar{h}_0$ and evaluating the result at $\bar{y} = \bar{h}$:

$$\bar{\psi}|_{\bar{y}=\bar{h}} = \left\{ \bar{\psi}_0 + \epsilon^{\frac{1}{2}} \left(\bar{\psi}_1 + \bar{h}_1 \frac{\partial \bar{\psi}_0}{\partial \bar{y}} \right) + \epsilon \left[\bar{\psi}_2 + \bar{h}_1 \frac{\partial \bar{\psi}_1}{\partial \bar{y}} + \left(\bar{h}_2 + \frac{\bar{h}_1^2}{2} \frac{\partial}{\partial \bar{y}} \right) \frac{\partial \bar{\psi}_0}{\partial \bar{y}} \right] + O(\epsilon^{\frac{3}{2}}) \right\} \Big|_{\bar{y}=\bar{h}_0}. \quad (3.5.5)$$

For integrals over the range $0 \leq \bar{y} \leq \bar{h}$, the upper limit of integration is perturbed and must be transferred. Following the same procedure as before, we first separate the integral into two parts, apply a Taylor series about $\bar{y} = \bar{h}_0$, and integrate the resulting moments:

$$\begin{aligned} \int_0^{\bar{h}} \bar{\psi} \, d\bar{y} &= \int_0^{\bar{h}_0} \bar{\psi} \, d\bar{y} + \int_{\bar{h}_0}^{\bar{h}} \bar{\psi} \, d\bar{y} \\ &= \int_0^{\bar{h}_0} \bar{\psi} \, d\bar{y} + \int_{\bar{h}_0}^{\bar{h}} \left(\bar{\psi}|_{\bar{y}=\bar{h}_0} + (\bar{y} - \bar{h}_0) \frac{\partial \bar{\psi}}{\partial \bar{y}} \Big|_{\bar{y}=\bar{h}_0} + \frac{(\bar{y} - \bar{h}_0)^2}{2} \frac{\partial^2 \bar{\psi}}{\partial \bar{y}^2} \Big|_{\bar{y}=\bar{h}_0} + \dots \right) d\bar{y} \end{aligned}$$

$$\begin{aligned}
&= \int_0^{\bar{h}_0} \bar{\psi} d\bar{y} + (\bar{h} - \bar{h}_0)\bar{\psi}|_{\bar{y}=\bar{h}_0} + \frac{(\bar{h} - \bar{h}_0)^2}{2} \frac{\partial \bar{\psi}}{\partial \bar{y}} \Big|_{\bar{y}=\bar{h}_0} + \frac{(\bar{h} - \bar{h}_0)^3}{6} \frac{\partial^2 \bar{\psi}}{\partial \bar{y}^2} \Big|_{\bar{y}=\bar{h}_0} + \dots \\
&= \left\{ \int_0^{\bar{h}_0} \bar{\psi}_0 d\bar{y} + \epsilon^{\frac{1}{2}} \left(\int_0^{\bar{h}_0} \bar{\psi}_1 d\bar{y} + \bar{h}_1 \bar{\psi}_0 \right) + \epsilon \left[\int_0^{\bar{h}_0} \bar{\psi}_2(\bar{y}) d\bar{y} + \bar{h}_1 \bar{\psi}_1 + \left(\bar{h}_2 + \frac{\bar{h}_1^2}{2} \frac{\partial}{\partial \bar{y}} \right) \bar{\psi}_0 \right] \right. \\
&\quad \left. + O(\epsilon^{\frac{3}{2}}) \right\} \Big|_{\bar{y}=\bar{h}_0}.
\end{aligned} \tag{3.5.6}$$

Matching conditions between the outer and inner regions must also be developed at each order in $\epsilon^{\frac{1}{2}}$. This task may be accomplished by first Taylor expanding the generic outer variable ψ about the matching point, say at $x = -1$, and rewriting the resulting series in terms of the inner coordinate:

$$\begin{aligned}
\psi &= \psi|_{x=-1} + \frac{\partial \psi}{\partial x} \Big|_{x=-1} (x+1) + \frac{1}{2} \frac{\partial^2 \psi}{\partial x^2} \Big|_{x=-1} (x+1)^2 + \dots \\
&= \left[\psi_0 + \epsilon^{\frac{1}{2}} \left(\psi_1 + \bar{x} \frac{\partial \psi_0}{\partial x} \right) + \epsilon \left(\psi_2 + \bar{x} \frac{\partial \psi_1}{\partial x} + \frac{\bar{x}^2}{2} \frac{\partial^2 \psi_0}{\partial x^2} \right) + O(\epsilon^{\frac{3}{2}}) \right] \Big|_{x=-1}.
\end{aligned} \tag{3.5.7}$$

Each term in this expression is to be equated to the like-ordered term corresponding to the limit of the inner variable as $\bar{x} \rightarrow \infty$, as prescribed by van Dyke's matching rule [166]. A similar expression may be written for the outer variable evaluated at $x = -\ell + 1$, with the inner limit taken as $\bar{x}^* \rightarrow -\infty$.

3.5.2 Outer region

The ordered perturbation equations for the outer region are given in Appendix B.1. By expanding (3.4.4), (3.4.5), and (3.4.12) with respect to $\epsilon^{\frac{1}{2}}$ and setting $\epsilon = 0$, one immediately deduces that \bar{p}_0 , \check{p}_0 , and $\bar{\tau}_0$ are independent of spatial position. Thus, viscous stresses play no appreciable role in the outer region at this order. The leading-order problem reduces to the solution of the normal stress condition for the shape function $\rho_{s0}(x)$ [cf. (3.4.11)],

$$\bar{p}_0 - \check{p}_0 = -\bar{\tau}_0 \left(\frac{1}{\rho_{s0} \sqrt{1 + (\partial \rho_{s0}/\partial x)^2}} - \frac{\partial^2 \rho_{s0}/\partial x^2}{\sqrt{1 + (\partial \rho_{s0}/\partial x)^2}^3} \right), \tag{3.5.8}$$

with the boundary conditions [cf. (3.4.13)-(3.4.14) and (3.4.26)],

$$\text{at } x = 0 : \quad \rho_{s0} = 0, \quad \frac{1}{\sqrt{1 + (\partial \rho_{s0}/\partial x)^2}} \frac{\partial \rho_{s0}}{\partial x} = -1, \tag{3.5.9}$$

$$\text{at } x = -\ell : \quad \rho_{s0} = 0, \quad \frac{1}{\sqrt{1 + (\partial \rho_{s0}/\partial x)^2}} \frac{\partial \rho_{s0}}{\partial x} = +1, \tag{3.5.10}$$

$$\text{at } x = -1, -\ell + 1 : \quad \rho_{s0} = 1. \tag{3.5.11}$$

Although the fluid pressures and membrane tension do not vary in the outer region, there exists the possibility of a mismatch between their “front” and “rear” values as a result of variations through the inner region. Thus, it is in general necessary to determine the outer solutions at the front nose

and rear tail independently of each other and unify them through the inner solution.

The solution of (3.5.8)-(3.5.11) is

$$\rho_{s0} = \sqrt{1 - \xi^2}, \quad \bar{p}_0 - \check{p}_0 = -2\bar{\tau}_0, \quad (3.5.12)$$

where $\xi = \begin{cases} x + 1, & \text{for } x \in [-1, 0], \\ x + \ell - 1, & \text{for } x \in [-\ell, -\ell + 1], \\ 0, & \text{otherwise.} \end{cases}$

Thus, the leading-order vesicle shape is a spherocylinder (a cylinder capped by two hemispheres). The membrane tension $\bar{\tau}_0$ remains unknown and must be determined from matching to the inner solution.

It happens that the $O(\epsilon^{1/2})$ correction to the shape function, $\rho_{s1}(x)$, may be determined without knowledge of the inner solution. The corrections \bar{p}_1 , \check{p}_1 , and $\bar{\tau}_1$ are spatially invariant, whence the $O(\epsilon^{1/2})$ term in (3.4.11) simplifies to

$$\bar{p}_1 - \check{p}_1 = -2\bar{\tau}_1 + \bar{\tau}_0 \left(\frac{\rho_{s1}}{\rho_{s0}} - 4\rho_{s0} \sqrt{1 - \rho_{s0}^2} \frac{d\rho_{s1}}{dx} + \rho_{s0}^3 \frac{d^2\rho_{s1}}{dx^2} \right). \quad (3.5.13)$$

With some rearrangement and introduction of the modified variables,

$$f_1 = \rho_{s0}\rho_{s1}, \quad a_1 = \frac{\bar{\tau}_1}{\bar{\tau}_0} - \frac{\bar{p}_1 - \check{p}_1}{\bar{p}_0 - \check{p}_0} = \text{constant},$$

equation (3.5.13) may be recast as an inhomogeneous Legendre equation of order one,

$$(1 - \xi^2) \frac{d^2 f_1}{d\xi^2} - 2\xi \frac{df_1}{d\xi} + 2f_1 = 2a_1. \quad (3.5.14)$$

Here, the shifted coordinate ξ is defined as before. The rear tail spans the region $\xi \in [-1, 0]$, while the front nose spans $\xi \in [0, 1]$. The boundary conditions for $f_1(\xi)$ are

at $\xi = 0$: $f_1 = 0, \quad (3.5.15)$

at $\xi = \pm 1$: $f_1 = 0. \quad (3.5.16)$

The only solution of (3.5.14) which satisfies (3.5.15)-(3.5.16) is the trivial solution,

$$f_1 = 0, \quad a_1 = 0. \quad (3.5.17)$$

Therefore,

$$\rho_{s1} = 0, \quad \bar{p}_1 - \check{p}_1 = -2\bar{\tau}_1, \quad (3.5.18)$$

i.e., the $O(\epsilon^{\frac{1}{2}})$ solution admits no correction to the shape. The membrane tension $\bar{\tau}_1$ remains unknown and must be determined from matching to the inner solution.

3.5.3 Inner region

The ordered perturbation equations for the inner region are given in Appendix B.2. In contrast to the “static” outer region, viscous stresses play a significant role in the inner region. The governing equations and boundary conditions are

$$\frac{\partial \bar{u}_{\bar{x}0}}{\partial \bar{x}} + \frac{\partial \bar{u}_{\bar{y}0}}{\partial \bar{y}} = 0, \quad \frac{\partial \bar{p}_0}{\partial \bar{x}} - \frac{\partial^2 \bar{u}_{\bar{x}0}}{\partial \bar{y}^2} = 0, \quad \frac{\partial \bar{p}_0}{\partial \bar{y}} = 0, \quad (3.5.19)$$

$$\frac{\partial \check{u}_{\bar{x}0}}{\partial \bar{x}} + \left(\frac{\partial}{\partial \rho} + \frac{1}{\rho} \right) \check{u}_{\rho 0} = 0, \quad \frac{\partial \check{p}_0}{\partial \bar{x}} = 0, \quad \frac{\partial \check{p}_0}{\partial \rho} - \kappa \frac{\partial^2 \check{u}_{\rho 0}}{\partial \bar{x}^2} = 0, \quad (3.5.20)$$

$$\text{at } \bar{y} = 0 : \quad \bar{u}_{\bar{x}0} = -1, \quad \bar{u}_{\bar{y}0} = 0, \quad (3.5.21)$$

$$\text{at } \bar{y} = \bar{h}_0(\bar{x}) : \quad \bar{u}_{\bar{x}0} = 0, \quad \bar{u}_{\bar{y}0} = 0, \quad (3.5.22)$$

$$\text{at } \rho = 0 : \quad \frac{\partial \check{u}_{\bar{x}0}}{\partial \rho} = 0, \quad \check{u}_{\rho 0} = 0, \quad (3.5.23)$$

$$\text{at } \rho = 1 : \quad \check{u}_{\bar{x}0} = 0, \quad \check{u}_{\rho 0} = 0, \quad (3.5.24)$$

$$\text{at } \bar{y} = \bar{h}_0(\bar{x}) : \quad \bar{p}_0 - \check{p}_0 = -\bar{\tau}_0 \left(1 + \frac{d^2 \bar{h}_0}{d \bar{x}^2} \right) + \bar{\beta} \frac{d^4 \bar{h}_0}{d \bar{x}^4}, \quad \bar{\tau}_0 = \text{constant}, \quad (3.5.25)$$

$$\bar{q}_0 = - \int_0^{\bar{h}_0(\bar{x})} \bar{u}_{\bar{x}0} d\bar{y} = \text{constant}, \quad (3.5.26)$$

$$\frac{1}{2} \Delta \bar{p}_0^+ = \int_{-\infty}^{\bar{\ell}} \frac{\partial \bar{u}_{\bar{x}0}}{\partial \bar{y}} \Big|_{\bar{y}=0} d\bar{x}^* + \int_{-\bar{\ell}}^{\infty} \frac{\partial \bar{u}_{\bar{x}0}}{\partial \bar{y}} \Big|_{\bar{y}=0} d\bar{x} = \text{constant}. \quad (3.5.27)$$

Equations (3.5.19)-(3.5.24) and (3.5.26)-(3.5.27) are the equations of lubrication theory. Following [103], they may be used to derive the so-called “Reynolds equation” for the pressure gradient,

$$\frac{d\bar{p}_0}{d\bar{x}} = \frac{d(\bar{p}_0 - \check{p}_0)}{d\bar{x}} = -\frac{6}{\bar{h}_0^2} \left(1 - \frac{2\bar{q}_0}{\bar{h}_0} \right), \quad (3.5.28)$$

as well as an expression for the extra pressure drop,

$$\Delta p_0^+ = \int_{-\infty}^{\bar{\ell}} \frac{4}{\bar{h}_0} \left(2 - \frac{3\bar{q}_0}{\bar{h}_0} \right) d\bar{x}^* + \int_{-\bar{\ell}}^{\infty} \frac{4}{\bar{h}_0} \left(2 - \frac{3\bar{q}_0}{\bar{h}_0} \right) d\bar{x}. \quad (3.5.29)$$

The gap height $\bar{h}_0(\bar{x})$ remains to be determined. Combining the Reynolds equation (3.5.28) with the stress condition (3.5.25) leads to a differential equation for $\bar{h}_0(\bar{x})$ that bears some resemblance to the one originally considered by [99] (with the addition of the bending term):

$$\bar{\beta} \frac{d^5 \bar{h}_0}{d\bar{x}^5} - \bar{\tau}_0 \frac{d^3 \bar{h}_0}{d\bar{x}^3} + \frac{6}{\bar{h}_0^2} \left(1 - \frac{2\bar{q}_0}{\bar{h}_0} \right) = 0. \quad (3.5.30)$$

Equation (3.5.30) is the so-called *elastic Landau-Levich equation*. This name is due to Dixit and Homsy, who derived a similar expression to (3.5.30) for a stress-free interface in their study of particle-laden, dip-coating flow [36, 35]. The boundary conditions associated with (3.5.30) are as follows [cf. (3.4.23) and (3.4.26)]:

$$\text{at } \bar{x} = -\bar{\ell}, \bar{x}^* = \bar{\ell} : \quad \bar{h}_0 = 1, \quad (3.5.31)$$

$$\text{as } \bar{x} \rightarrow \infty : \quad \bar{h}_0 \rightarrow b_0 + \frac{1}{2}\bar{x}^2, \quad (3.5.32)$$

$$\text{as } \bar{x}^* \rightarrow -\infty : \quad \bar{h}_0 \rightarrow b_0^* + \frac{1}{2}\bar{x}^{*2}, \quad (3.5.33)$$

where

$$b_0 = -\rho_{s2}(-1), \quad b_0^* = -\rho_{s2}(-\ell + 1)$$

are constants of integration. Since (3.5.30) is autonomous, it may be rewritten with $\bar{x}^* = \bar{x} - 2\bar{\ell}$ substituted for \bar{x} as the independent variable. Thus, matching with the “front” and “rear” outer solutions is facilitated by a simple shift of origin.

Equations (3.5.29)-(3.5.33) must be integrated numerically for specific values of the reduced length $\bar{\ell}$ and bending parameter $\bar{\beta}$. The constants \bar{q}_0 , $\bar{\tau}_0$, b_0 , b_0^* , and Δp_0^+ are determined simultaneously with $\bar{h}_0(\bar{x})$ during the integration procedure. Since the boundary-value problem is ill-conditioned for many values of the parameters, the multiple shooting method is employed for the numerical integration [113]. A good description of the method is given in [154]. In brief, the domain is first divided into two subdomains $\bar{x} \in [-\bar{\ell}, \bar{X}]$ and $\bar{x}^* \in [-\bar{X}^*, \bar{\ell}]$. The boundary conditions are applied at $\bar{x} = \bar{X}$, $\bar{x} = -\bar{\ell}$, $\bar{x}^* = \bar{X}^*$, and $\bar{x}^* = \bar{\ell}$. Care is taken to subtract off the error incurred by applying the far-field conditions (3.5.32)-(3.5.33) at finite boundaries $\bar{x} = \bar{X}$ and $\bar{x} = \bar{X}^*$. Each subdomain is further divided into $O(10-100)$ segments separated by “shooting points” at which continuity conditions are applied. Integration is carried out over each segment using a fourth-order Runge-Kutta scheme. Newton iteration with line search and backtracking is used to enforce the boundary and continuity conditions at the shooting points. The iteration is truncated when the

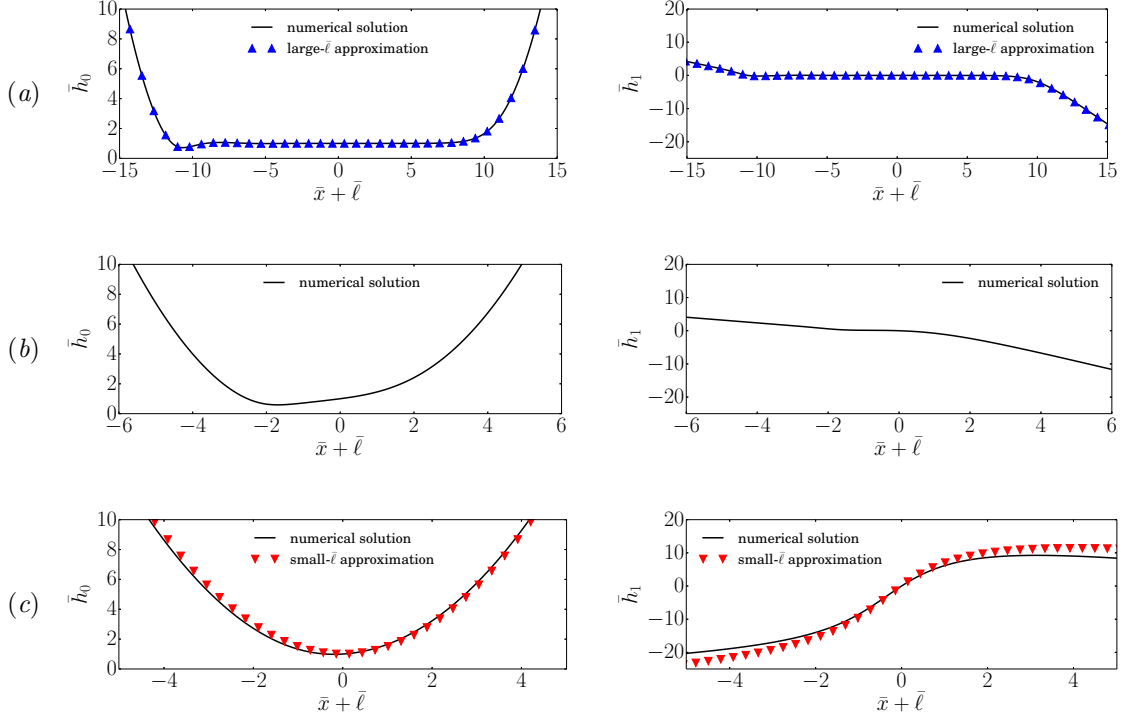


Figure 3.4: Gap height \bar{h} plotted against the shifted axial coordinate $\bar{x} + \bar{\ell}$ for negligible bending stiffness ($\bar{\beta} = 0$). The left column is the leading-order solution \bar{h}_0 determined by integrating (3.5.29)-(3.5.33). The right column is the first correction \bar{h}_1 determined by integrating (3.5.49)-(3.5.53). The solid lines are the full numerical solutions. (a) Long, spherocylindrical vesicle ($\bar{\ell} = 10$), including the large- $\bar{\ell}$ approximation derived in §3.6.1. (b) Intermediate-length vesicle ($\bar{\ell} = 1$). (c) Short, spherical vesicle ($\bar{\ell} = 0.01$), including the small- $\bar{\ell}$ approximation derived in §3.6.2 [cf. (3.6.18) and (3.6.26) truncated after the $O(1)$ term].

norm of the subsequent Newton step or the norm of the function to be zeroed falls below 10^{-12} . In order to avoid numerical errors associated with the behavior of the solution near the boundaries, integration always proceeds away from the boundary points towards a “fitting point” located at the center of the subdomain. Once a solution for particular values of $\bar{\ell}$ and $\bar{\beta}$ is known, additional solutions may be generated using the continuation method.

Representative profiles of $\bar{h}_0(\bar{x})$ are plotted in Figure 3.4 for $\bar{\beta} = 0$ and three different values of $\bar{\ell}$. The constants \bar{q}_0 , $\bar{\tau}_0$, b_0 , b_0^* , and $\Delta\bar{p}_0^+$ are plotted against $\bar{\ell}$ for $\bar{\beta} = 0$ in Figure 3.5. Results for finite values of $\bar{\beta}$ are delayed until §3.7.

3.5.4 Higher-order corrections

Corrections to the leading-order solution may be derived by expanding the narrow-gap equations to higher order in $\epsilon^{1/2}$. In the outer region, we derive an expression similar to (3.5.14) for the $O(\epsilon)$

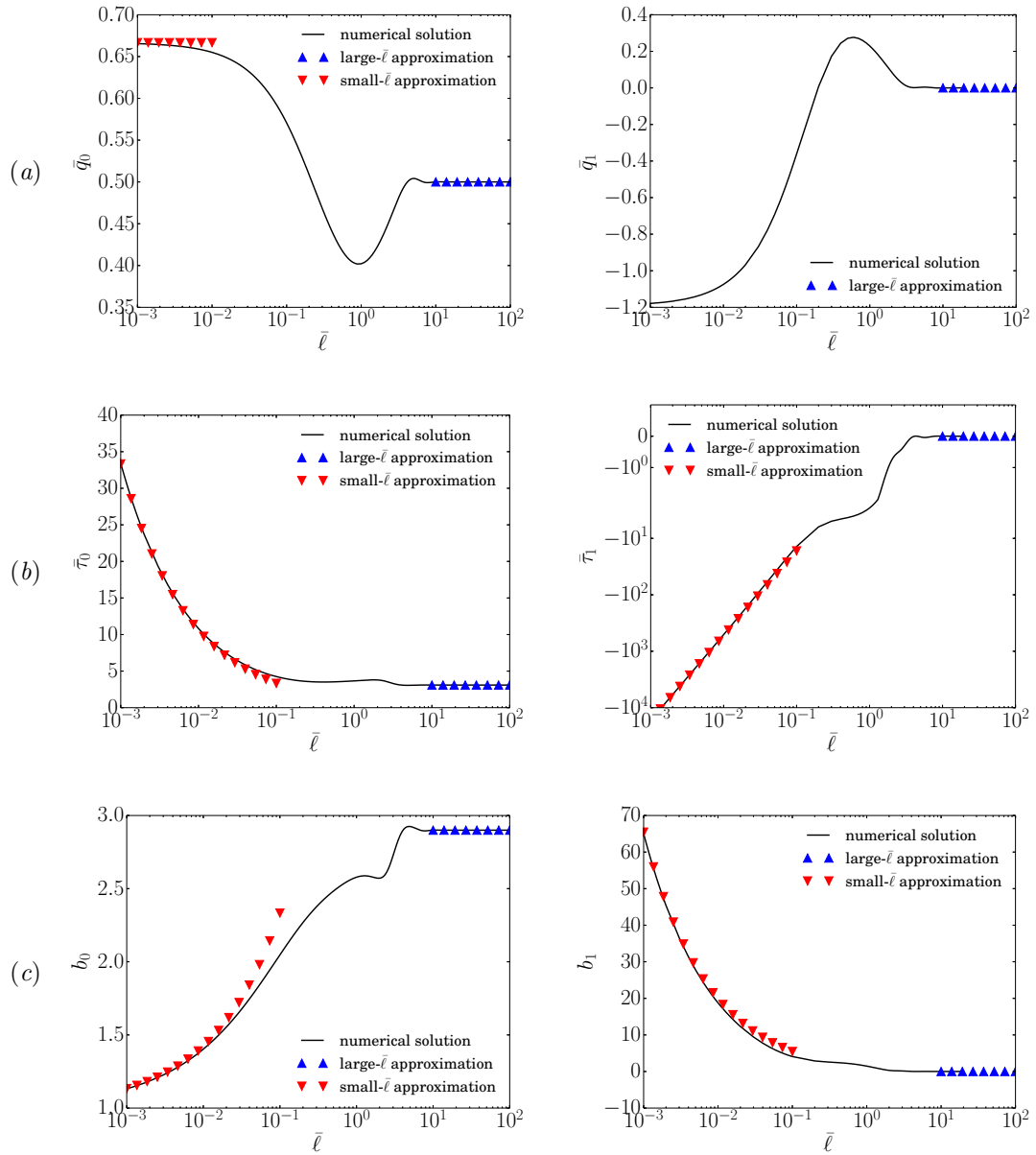


Figure 3.5: Caption on the following page.

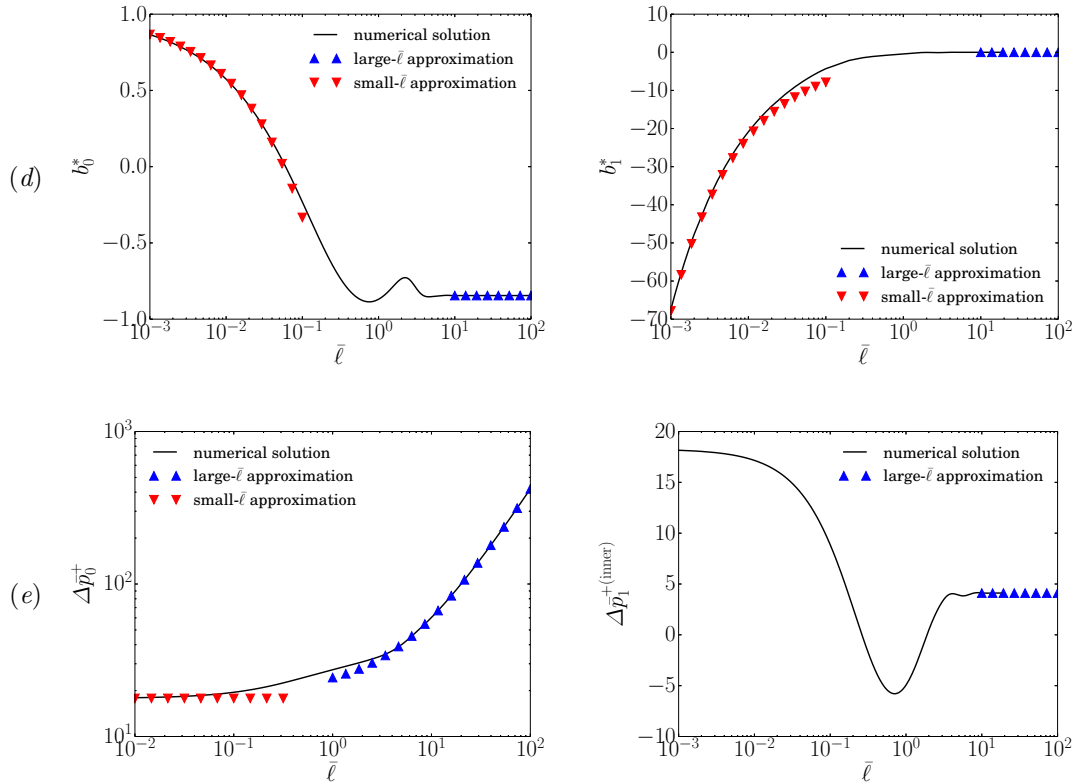


Figure 3.5: (a) Leakback flux \bar{q} , (b) membrane tension $\bar{\tau}$, (c) front intercept b , (d) rear intercept b^* , and (e) extra pressure drop $\Delta\bar{p}_1^+$ plotted against the reduced length $\bar{\ell}$ for negligible bending stiffness ($\bar{\beta} = 0$). The left column is the leading-order solution; the right column is the first correction.

shape correction:

$$(1 - \xi^2) \frac{d^2 f_2}{d\xi^2} - 2\xi \frac{df_2}{d\xi} + 2f_2 = 2a_2, \quad (3.5.34)$$

where $f_2 = \rho_{s0}\rho_{s2}$, $a_2 = \frac{\bar{\tau}_2}{\bar{\tau}_0} - \frac{\bar{p}_2 - \check{p}_2}{\bar{p}_0 - \check{p}_0} = \text{constant.}$

In deriving (3.5.34), equations (3.5.12) and (3.5.18) were used to eliminate ρ_{s0} and ρ_{s1} . The boundary conditions for $f_2(\xi)$ are

$$\text{as } \xi \rightarrow 0^+ : \quad f_2 = -b_0, \quad (3.5.35)$$

$$\text{as } \xi \rightarrow 0^- : \quad f_2 = -b_0^*, \quad (3.5.36)$$

$$\text{at } \xi = \pm 1 : \quad f_2 = 0, \quad (3.5.37)$$

where a superscript “plus” or “minus” indicates that the boundary $\xi = 0$ is approached in a limiting sense from positive or negative numbers, respectively. The constants b_0 and b_0^* are known from the solution of the leading-order, inner problem. The only solution of (3.5.34) which satisfies (3.5.35)-(3.5.37) is

$$\rho_{s2} = \frac{f_2}{\sqrt{1 - \xi^2}} = \begin{cases} -\frac{b_0(1 - \xi)}{\sqrt{1 - \xi^2}} & \text{for } \xi \in (0, 1], \\ -\frac{b_0^*(1 + \xi)}{\sqrt{1 - \xi^2}} & \text{for } \xi \in [-1, 0), \end{cases} \quad (3.5.38a)$$

$$\bar{p}_2 - \check{p}_2 = \begin{cases} -2\bar{\tau}_2 - 2b_0\bar{\tau}_0 & \text{for } \xi \in (0, 1], \\ -2\bar{\tau}_2 - 2b_0^*\bar{\tau}_0 & \text{for } \xi \in [-1, 0). \end{cases} \quad (3.5.38b)$$

While $\bar{\tau}_0$ is known from the leading-order problem, $\bar{\tau}_2$ remains unknown. The discontinuity in the solution at $\xi = 0$ is resolved through construction of the inner solution.

In the inner region, the $O(\epsilon^{1/2})$ correction fields are governed by the following equations and boundary conditions:

$$\frac{\partial \bar{u}_{\bar{x}1}}{\partial \bar{x}} + \frac{\partial \bar{u}_{\bar{y}1}}{\partial \bar{y}} = 0, \quad \frac{\partial \bar{p}_1}{\partial \bar{x}} - \frac{\partial^2 \bar{u}_{\bar{x}1}}{\partial \bar{y}^2} = 0, \quad \frac{\partial \bar{p}_1}{\partial \bar{y}} = 0, \quad (3.5.39)$$

$$\frac{\partial \check{u}_{\bar{x}1}}{\partial \bar{x}} + \left(\frac{\partial}{\partial \rho} + \frac{1}{\rho} \right) \check{u}_{\rho 1} = 0, \quad \frac{\partial \check{p}_1}{\partial \bar{x}} = 0, \quad \frac{\partial \check{p}_1}{\partial \rho} - \kappa \frac{\partial^2 \check{u}_{\rho 1}}{\partial \bar{x}^2} = 0, \quad (3.5.40)$$

at $\bar{y} = 0$: $\bar{u}_{\bar{x}1} = 0, \quad \bar{u}_{\bar{y}1} = 0,$ $(3.5.41)$

$$\text{at } \bar{y} = \bar{h}_0(\bar{x}) : \quad \bar{u}_{\bar{x}1} = -\bar{h}_1 \frac{\partial \bar{u}_{\bar{x}0}}{\partial \bar{y}}, \quad \bar{u}_{\bar{y}1} = -\bar{h}_1 \frac{\partial \bar{u}_{\bar{y}0}}{\partial \bar{y}}, \quad (3.5.42)$$

$$\text{at } \rho = 0 : \quad \frac{\partial \check{u}_{\bar{x}1}}{\partial \rho} = 0, \quad \check{u}_{\rho 1} = 0, \quad (3.5.43)$$

$$\text{at } \rho = 1 : \quad \check{u}_{\bar{x}1} = 0, \quad \check{u}_{\rho 1} = 0, \quad (3.5.44)$$

$$\text{at } \bar{y} = \bar{h}_0(\bar{x}) : \quad \bar{p}_1 - \check{p}_1 = -\bar{\tau}_1 \left(1 + \frac{d^2 \bar{h}_0}{d\bar{x}^2} \right) - \bar{\tau}_0 \frac{d^2 \bar{h}_1}{d\bar{x}^2} + \bar{\beta} \frac{d^4 \bar{h}_1}{d\bar{x}^4}, \quad \bar{\tau}_1 = \text{constant}, \quad (3.5.45)$$

$$\bar{q}_1 = - \int_0^{\bar{h}_0(\bar{x})} \bar{u}_{\bar{x}1} d\bar{y} + \bar{h}_1 \bar{u}_0|_{\bar{y}=\bar{h}_0(\bar{x})} = \text{constant}, \quad (3.5.46)$$

$$\frac{1}{2} \Delta \bar{p}_1^+ = \int_{-\infty}^{\bar{\ell}} \frac{\partial \bar{u}_{\bar{x}1}}{\partial \bar{y}} \Big|_{\bar{y}=0} d\bar{x}^* + \int_{-\bar{\ell}}^{\infty} \frac{\partial \bar{u}_{\bar{x}1}}{\partial \bar{y}} \Big|_{\bar{y}=0} d\bar{x} + O(1) = \text{constant}, \quad (3.5.47)$$

The terms multiplied by \bar{h}_1 on the right-hand side of (3.5.42) and (3.5.46) appear as a result of transferring the boundary from $\bar{y} = \bar{h}(\bar{x})$ to $\bar{y} = \bar{h}_0(\bar{x})$ [20]. Following the same procedure as in §3.5.3, the first correction to the pressure gradient and extra pressure drop are derived:

$$\frac{d\bar{p}_1}{d\bar{x}} = \frac{d(\bar{p}_1 - \check{p}_1)}{d\bar{x}} = \frac{12}{\bar{h}_0^2} \left[\frac{\bar{h}_1}{\bar{h}_0} \left(1 - \frac{3\bar{q}_0}{\bar{h}_0} \right) + \frac{\bar{q}_1}{\bar{h}_0} \right], \quad (3.5.48)$$

$$\Delta \bar{p}_1^{+(\text{inner})} = - \int_{-\infty}^{\bar{\ell}} \left[\frac{8\bar{h}_1}{\bar{h}_0^2} \left(1 - \frac{3\bar{q}_0}{\bar{h}_0} \right) + \frac{12\bar{q}_1}{\bar{h}_0^2} \right] d\bar{x}^* - \int_{-\bar{\ell}}^{\infty} \left[\frac{8\bar{h}_1}{\bar{h}_0^2} \left(1 - \frac{3\bar{q}_0}{\bar{h}_0} \right) + \frac{12\bar{q}_1}{\bar{h}_0^2} \right] d\bar{x}, \quad (3.5.49)$$

where the superscript “(inner)” is ascribed to indicate that additional contributions from the outer region may contribute at this order.

It remains to calculate $\bar{h}_1(\bar{x})$, the first correction to the gap height. Combining (3.5.48) with (3.5.45) yields an inhomogeneous differential equation for $\bar{h}_1(\bar{x})$:

$$\bar{\beta} \frac{d^5 \bar{h}_1}{d\bar{x}^5} - \bar{\tau}_0 \frac{d^3 \bar{h}_1}{d\bar{x}^3} - \frac{12\bar{h}_1}{\bar{h}_0^3} \left(1 - \frac{3\bar{q}_0}{\bar{h}_0} \right) = \bar{\tau}_1 \frac{d^3 \bar{h}_0}{d\bar{x}^3} + \frac{12\bar{q}_1}{\bar{h}_0^3}. \quad (3.5.50)$$

As before, the independent variable \bar{x} may be exchanged for \bar{x}^* by a simple shift of origin. The boundary conditions associated with (3.5.50) are

$$\text{at } \bar{x} = -\bar{\ell}, \bar{x}^* = \bar{\ell} : \quad \bar{h}_1 = 0, \quad (3.5.51)$$

$$\text{as } \bar{x} \rightarrow \infty : \quad \bar{h}_1 \rightarrow b_1 - b_0 \bar{x}, \quad (3.5.52)$$

$$\text{as } \bar{x}^* \rightarrow -\infty : \quad \bar{h}_1 \rightarrow b_1^* + b_0^* \bar{x}^*, \quad (3.5.53)$$

where

$$b_1 = -\rho_{s3}(-1), \quad b_1^* = -\rho_{s3}(-\ell + 1)$$

are constants of integration.

Equations (3.5.49)-(3.5.53) must be integrated numerically for specific values of the reduced length $\bar{\ell}$ and bending parameter $\bar{\beta}$. As with all perturbation theories, the correction fields are forced by source terms that depend on the leading-order fields. Thus, any numerical solution requires accurate tabulation of \bar{h}_0 at discrete points in \bar{x} . Above $\bar{\ell} \simeq 20$, the system becomes numerically stiff and roundoff errors accumulate. Numerical results for $\bar{\beta} = 0$ are shown in Figure 3.4 and 3.5 alongside the leading-order solutions. Results for finite values of $\bar{\beta}$ are delayed until §3.7.

At the next order in ϵ , the outer correction to the shape ρ_{s3} forces a condition on the slope of \bar{h}_2 in the far field. The key result from the $O(\epsilon)$ inner problem is a non-constant correction to the membrane tension $\bar{\tau}_2$ that increases monotonically from the rear tail to the front nose. The pressure jump $\bar{p}_2 - \check{p}_2$, in turn, decreases along the axial coordinate, resulting in a pressure drop of $O(\epsilon)$. Calculation of ρ_{s3} requires consideration of the outer flow field and is beyond the scope of the present work. Thus, further corrections are not pursued here.

3.6 Asymptotic solutions for $\bar{\beta} = 0$

Asymptotic solutions of (3.5.29)-(3.5.33) and (3.5.49)-(3.5.53) may be determined when the reduced length $\bar{\ell}$ is either very large or very small, the former being a regular limit and the latter being a singular one. The asymptotic solution “for large $\bar{\ell}$ ” is the subject of the next subsection. Solutions “for small $\bar{\ell}$ ” are discussed in §3.6.2. In this section, the bending terms in the shape equations are neglected by setting $\bar{\beta} = 0$. This limit might raise concerns, since $\bar{\beta}$ is multiplying the highest derivative in (3.5.30) and (3.5.50). However, it turns out that the limit $\bar{\beta} \rightarrow 0$ is a regular one, so setting $\bar{\beta} = 0$ does not preclude satisfaction of the boundary conditions. Results for finite values of $\bar{\beta}$ are discussed in §3.7.

3.6.1 Long, spherocylindrical vesicles ($\bar{\ell} \gg 1$)

As $\bar{\ell} \rightarrow \infty$, the midsection of the vesicle adopts a cylindrical shape and the supporting film becomes asymptotically uniform with thickness $\bar{h} = 1$ and flux $\bar{q} = \frac{1}{2} + O(\epsilon)$. A numerical solution for \bar{h}_0 and \bar{h}_1 may be derived using the procedure originally outlined by [17]. In brief, the domain is separated into a “front” and “rear” part separated by a long, middle section where $\bar{h} = 1$, as shown in Figure 3.6. Linearizing (3.5.30) (with $\bar{\beta} = 0$) about the fixed point $(\bar{h}_0, \bar{q}_0) = (1, \frac{1}{2})$ yields

$$\bar{\tau}_0 \frac{d^3 \bar{h}_0}{d\bar{x}^3} - 6(\bar{h}_0 - 1) = 0. \quad (3.6.1)$$

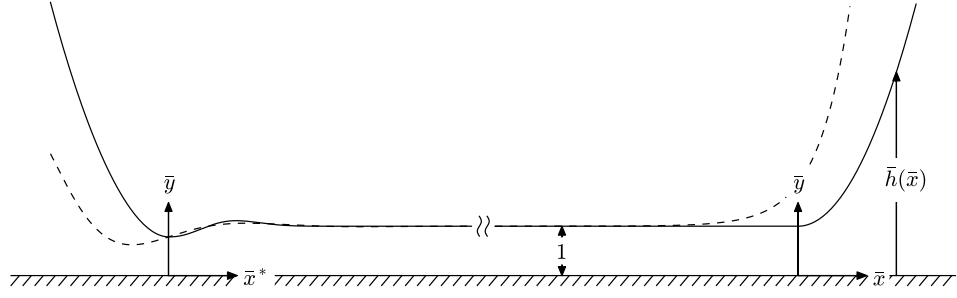


Figure 3.6: Separation of the front and rear parts of the inner region for a long, spherocylindrical vesicle ($\ell \gg 1$). The dashed curves are the linearized solutions near $\bar{h} = 1$.

Starting from the front end of the vesicle, the dominant trajectory approaching the uniform film is an exponential profile,

$$\text{as } \bar{x} \rightarrow -\infty : \quad \bar{h}_0 - 1 \rightarrow c_0 e^{\eta_0 \bar{x}}, \quad (3.6.2)$$

where c_0 is a constant of integration and $\eta_0 = (6/\bar{\tau}_0)^{1/3}$. From the rear end, the trajectory towards the uniform film oscillates in space,

$$\text{as } \bar{x}^* \rightarrow \infty : \quad \bar{h}_0 - 1 \rightarrow e^{-\eta_0 \bar{x}^*/2} \left[c_0^* \cos(\sqrt{3}\eta_0 \bar{x}^*/2) + d_0^* \sin(\sqrt{3}\eta_0 \bar{x}^*/2) \right], \quad (3.6.3)$$

where c_0^* and d_0^* are constants of integration. Equations (3.6.2)-(3.6.3) are meant to supplant (3.5.31) in the double limit $(\bar{\beta}, \bar{\ell}) \rightarrow (0, \infty)$. The front part of the shape is determined first and forced to match to (3.6.2), which then specifies a unique rear profile that matches to (3.6.3).

A similar analysis may be applied to $\bar{h}_1(\bar{x})$. Linearizing (3.5.50) (with $\bar{\beta} = 0$) near the fixed point $(\bar{h}_1, \bar{q}_1) = (0, 0)$ yields

$$\bar{\tau}_0 \frac{d^3 \bar{h}_1}{d \bar{x}^3} - 6 \bar{h}_1 = -\frac{6 \bar{\tau}_1}{\bar{\tau}_0} (\bar{h}_0 - 1). \quad (3.6.4)$$

Equation (3.6.4) admits the linearized trajectories,

$$\text{as } \bar{x} \rightarrow -\infty : \quad \bar{h}_1 \rightarrow c_1 e^{\eta_0 \bar{x}} - \frac{1}{3} c_0 (\bar{\tau}_1 / \bar{\tau}_0) \eta_0 \bar{x} e^{\eta_0 \bar{x}}, \quad (3.6.5)$$

starting from the front end and

$$\text{as } \bar{x}^* \rightarrow \infty : \quad \bar{h}_1 \rightarrow e^{-\eta_0 \bar{x}^*/2} \left[c_1^* \cos(\sqrt{3}\eta_0 \bar{x}^*/2) + d_1^* \sin(\sqrt{3}\eta_0 \bar{x}^*/2) \right], \quad (3.6.6)$$

from the rear end. Here, c_1 , c_1^* , and d_1^* are constants of integration. Equations (3.6.5)-(3.6.6)

\bar{q}_0	=	$\frac{1}{2}$	\bar{q}_1	=	0
$\bar{\tau}_0$	=	3.0939	$\bar{\tau}_1$	=	0
b_0	=	2.8996	b_1	=	0
b_0^*	=	-0.8453	b_1^*	=	0
c_0	=	0.8616	c_1	=	-3.1155
c_0^*	=	-0.2162	c_1^*	=	-0.2167
d_0^*	=	0.1125	d_1^*	=	-0.1381
$\Delta\bar{p}_0^+$	=	$4\bar{\ell} + 20.3442$	$\Delta\bar{p}_1^{+(inner)}$	=	$4.1086 = 2(b_0 + b_0^*)$

Table 3.1: Numerical results for long, spherocylindrical vesicles ($\bar{\ell} \gg 1$) with negligible bending stiffness ($\bar{\beta} = 0$).

supplant (3.5.51) in the double limit $(\bar{\beta}, \bar{\ell}) \rightarrow (0, \infty)$. The second term on the right-hand side of (3.6.5) is the particular solution forced by the $\bar{\tau}_1(d^3\bar{h}_0/d\bar{x}^3)$ term in (3.5.50). Carrying out the numerical integration at the front end reveals that $\bar{\tau}_1 = 0$, which is why no such term appears in (3.6.6).

Numerical solutions for \bar{h}_0 and \bar{h}_1 in the limit $\bar{\ell} \rightarrow \infty$ are plotted in Figure 3.4a atop the numerical solutions for finite $\bar{\ell}$. Numerical results for the constants \bar{q} , $\bar{\tau}$, b , b^* , c , c^* , d^* , and $\Delta\bar{p}^+$ are tabulated in Table 3.1 and plotted in Figure 3.5 for large $\bar{\ell}$. Of particular interest is the extra pressure drop,

$$\Delta\bar{p}^+ = 2(\bar{\ell} - 2)\epsilon^{-\frac{1}{2}} + 20.3442 + 4.1086\epsilon^{\frac{1}{2}} + O(\epsilon^{\frac{1}{2}}), \quad (3.6.7)$$

where $(\frac{1}{2}\bar{\ell} - 1)/\epsilon^{\frac{1}{2}}$ has been exchanged for $\bar{\ell}$ since $\bar{\ell} \gg 1$. The first term on the right-hand side of (3.6.7) is dominant for small ϵ and arises from the dissipation in the uniform-film region. This term scales *linearly* with the length of the midsection $L - 2R$, in agreement with the prediction made by [71] and invalidating the fallacious cubic scaling suggested by [18]. The second and third terms in (3.6.7) are corrections due to dissipation through the “transitions regions,” in which \bar{h}_0 deviates from unity in order to match with the outer solution. These corrections are independent of the vesicle length. Finally, the $O(\epsilon^{\frac{1}{2}})$ error term is meant to account for additional “outer contributions,” which were not computed here.

An expression similar to (3.6.7) was derived by Cantat for the extra pressure drop across “no-slip bubble” whose surface is loaded with a high concentration of insoluble surfactant [23]. She computed a numerical value of 19.9 for the second term (when expressed in the present nomenclature). The claim here is that the discrepancy between her result and (3.6.7) is due to the difference in the computed values of b_0 and b_0^* . Cantat reported $b_0 = 2.88$ and $b_0^* = -0.82$, which may be compared to the values $b_0 = 2.8996$ and $b_0^* = -0.8453$ reported in Table 3.1 and even Bretherton’s original calculations of $b_0 = 2.79$ and $b_0^* = -0.73$. The latter values have been cited as inaccurate by [177], among others. The constants b_0 and b_0^* are determined through application of the far-field conditions (3.5.32)-(3.5.33) at finite domain boundaries \bar{X} and $-\bar{X}^*$. Since \bar{h}_0 grows like \bar{x}^2 in the far field, the error in \bar{h}_0 incurred by truncating the domain decays like $1/\bar{X}$ [cf. (3.5.30)], which is a *slow*,

algebraic decay. In computing the coefficients in Table 3.1, we found it necessary to subtract off the error in successive powers of $1/\bar{X}$ until the computed values of b_0 and b_0^* became independent of domain size. The values reported in Table 3.1 were determined to an accuracy of four (or more) decimal places by following this procedure.

To conclude this section, it is worth quoting Bretherton's result for the extra pressure drop across a long bubble in a tube, which when expressed in the present notation² is given by

$$\Delta\bar{p}^+ = 11.586 + O(\epsilon^{1/2}). \quad (3.6.8)$$

Two important differences between (3.6.8) and (3.6.7) are worth mentioning. Firstly, it is apparent that (3.6.8) does not depend on the bubble length. This result is somewhat intuitive: since the bubble surface is shear-free, the long, cylindrical portion of the bubble does not drag fluid and so, in principle, would not contribute to the extra pressure drop. Later studies, however, have indicated a dependence on bubble length when ϵ is not vanishingly small [137]. The second important difference can be seen in the $O(1)$ term in (3.6.8), which is nearly half that of (3.6.7). Again, the difference can be traced to the fact that a bubble surface is a "shear-free surface," whereas the vesicle membrane is treated here as a "no-slip surface." The latter admits higher dissipation in the transition regions between the uniform-film and end-cap regions.

3.6.2 Short, spherical vesicles ($\bar{\ell} \ll 1$)

As $\bar{\ell} \rightarrow 0$, the front nose and rear tail interact through a very short distance. The vesicle is forced into a nearly spherical shape and, consequently, the ability of the surface curvature to change in response to large lubrication pressures is dampened. In response, the membrane tension diverges to balance normal stresses on the membrane. Since the membrane is immobile, the flow field, leakback flux \bar{q} , and extra pressure drop $\Delta\bar{p}^+$ are adequately described by the theory for closely fitting, rigid spheres that are freely suspended in a fluid-filled tube [79, 20].

The shape deformation \bar{h} and resulting membrane tension $\bar{\tau}$ for small but *finite* values of $\bar{\ell}$ are not immediately obvious. In fact, their solution in the limit of vanishing $\bar{\ell}$ requires a singular perturbation theory in terms of a second small parameter $\bar{\ell}^{1/2} \ll 1$. In the limit $\bar{\ell} \rightarrow 0$, it is convenient to shift the origin to the midplane of the vesicle,

$$\bar{\xi} = \bar{x} + \bar{\ell} = \bar{x}^* - \bar{\ell}, \quad (3.6.9)$$

²Equation (3.6.8) (in terms of outer variables) is typically expressed as $\Delta p^+ = 10.02 \text{Ca}^{-1/3} + O(1)$, where $\text{Ca} = \mu V / \gamma$ is the capillary number and γ is the bubble surface tension. The capillary number has been eliminated using the well-known result for the clearance, $\epsilon = 1.337 \text{Ca}^{2/3} + O(\text{Ca})$.

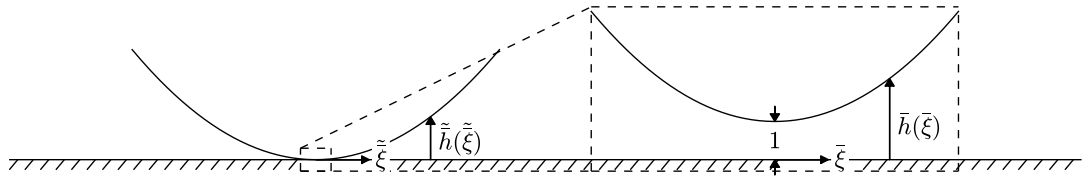


Figure 3.7: Coordinate system for a short, spherical vesicle ($\bar{\ell} \ll 1$). The “outer region” is located inside the dashed box. The “inner region” is located outside the dashed box within an $O(\bar{\ell}^{-\frac{1}{2}})$ boundary layer.

which represents the “outer coordinate” for small $\bar{\ell}$. The associated “inner coordinate” is given by

$$\tilde{\xi} = \bar{\ell}^{\frac{1}{2}} \bar{\xi}, \quad (3.6.10)$$

where an “overtilde” is used to denote a rescaling with respect to $\bar{\ell}^{\frac{1}{2}}$. A schematic of the new coordinate system is shown in Figure 3.7. The “inner region” for small $\bar{\ell}$ is located in the far field ($\bar{\xi} \rightarrow \pm\infty$), where \bar{h} is very large. The width of this region is of $O(\bar{\ell}^{-\frac{1}{2}})$. The inner solution must be matched to an outer solution near $\tilde{\xi} = 0$, where $\bar{h} = O(1)$.

It is instructive at this point to derive the perturbative solution to (3.5.30)-(3.5.33) for the gap height $\bar{h}_0(\bar{\xi})$ in the limit $\bar{\ell} \rightarrow 0$, setting $\bar{\beta} = 0$. Rescaling the dependent variables gives

$$(\tilde{\bar{h}}_0, \tilde{\bar{q}}_0, \tilde{\bar{\tau}}_0, \tilde{\bar{b}}_0, \tilde{\bar{b}}_0^*, \Delta\bar{p}_0^+) = (\bar{\ell}\bar{h}_0, \bar{q}_0, \bar{\ell}^{\frac{1}{2}}\bar{\tau}_0, b_0, b_0^*, \Delta\bar{p}_0^+). \quad (3.6.11)$$

These scalings are necessary in order to satisfy all of the boundary conditions. The outer equations, which govern the unstretched gap height $\bar{h}_0(\bar{\xi})$, are given by

$$\tilde{\bar{\tau}}_0 \frac{d^3 \bar{h}_0}{d\bar{\xi}^3} = \frac{6\bar{\ell}^{\frac{1}{2}}}{\bar{h}_0^2} \left(1 - \frac{2\bar{q}_0}{\bar{h}_0} \right), \quad (3.6.12)$$

at $\bar{\xi} = 0$:

$$\bar{h}_0 = 1. \quad (3.6.13)$$

The corresponding inner equations for the stretched gap height $\tilde{\bar{h}}_0(\tilde{\xi})$ are

$$\tilde{\bar{\tau}}_0 \frac{d^3 \tilde{\bar{h}}_0}{d\tilde{\xi}^3} = \frac{6\bar{\ell}^2}{\tilde{\bar{h}}_0^2} - \frac{12\bar{\ell}^3 \tilde{\bar{q}}_0}{\tilde{\bar{h}}_0^3}, \quad (3.6.14)$$

as $\tilde{\xi} \rightarrow \infty$:

$$\tilde{\bar{h}}_0 \rightarrow \frac{1}{2}\tilde{\xi}^2 + \bar{\ell}\tilde{b}_0 - \bar{\ell}^{\frac{3}{2}}\tilde{\xi} + \frac{1}{2}\bar{\ell}^3, \quad (3.6.15)$$

$$\begin{array}{lll}
\bar{q}_0 & = & \frac{2}{3} + O(\bar{\ell}) \\
\bar{\tau}_0 & = & [\pi/(2\sqrt{2}\bar{\ell})]^{\frac{1}{2}} + O(\bar{\ell}^{\frac{1}{2}}) \\
b_0 & = & 1 + (4\sqrt{2}\pi\bar{\ell})^{\frac{1}{2}} + O(\bar{\ell}) \\
b_0^* & = & 1 - (4\sqrt{2}\pi\bar{\ell})^{\frac{1}{2}} + O(\bar{\ell}) \\
\Delta\bar{p}_0^+ & = & 4\sqrt{2}\pi + O(\bar{\ell})
\end{array}
\quad
\begin{array}{lll}
\bar{q}_1 & = & - \\
\bar{\tau}_1 & = & -[\pi/(8\sqrt{2}\bar{\ell}^3)]^{\frac{1}{2}} + O(\bar{\ell}^{-\frac{1}{2}}) \\
b_1 & = & (\sqrt{2}\pi/\bar{\ell})^{\frac{1}{2}} - \frac{8}{3}(\sqrt{2}/\pi) + O(\bar{\ell}^{\frac{1}{2}}) \\
b_1^* & = & -(\sqrt{2}\pi/\bar{\ell})^{\frac{1}{2}} - \frac{8}{3}(\sqrt{2}/\pi) + O(\bar{\ell}^{\frac{1}{2}}) \\
\Delta\bar{p}_1^{+(inner)} & = & -
\end{array}$$

Table 3.2: Analytical results for short, spherical vesicles ($\bar{\ell} \ll 1$) with negligible bending stiffness ($\beta = 0$).

$$\text{as } \tilde{\xi} \rightarrow -\infty : \quad \tilde{h}_0 \rightarrow \frac{1}{2}\tilde{\xi}^2 + \bar{\ell}b_0^* + \bar{\ell}^{\frac{3}{2}}\tilde{\xi} + \frac{1}{2}\bar{\ell}^3. \quad (3.6.16)$$

The outer and inner solutions are then matched according to the matching conditions,

$$\lim_{\tilde{\xi} \rightarrow 0^+} \tilde{h}_0 = \lim_{\tilde{\xi} \rightarrow \infty} \bar{h}_0, \quad (3.6.17a)$$

$$\lim_{\tilde{\xi} \rightarrow 0^-} \tilde{h}_0 = \lim_{\tilde{\xi}^* \rightarrow -\infty} \bar{h}_0. \quad (3.6.17b)$$

A perturbative solution to (3.6.12)-(3.6.17) may be derived by expanding the outer and inner variables in powers of $\bar{\ell}^{\frac{1}{2}}$, inserting the expansions into the governing equations and auxiliary conditions, and solving the resulting ordered perturbation equations in sequence. Since $\bar{\beta}$ has been set equal to zero, the composite expansion for $\bar{h}_0(\tilde{\xi})$ may be derived analytically, viz.,

$$\begin{aligned}
\bar{h}_0 = & 1 + \frac{1}{2}\tilde{\xi}^2 + \left(\frac{\sqrt{2}\bar{\ell}}{\pi}\right)^{\frac{1}{2}} 4 \arctan\left(\frac{\tilde{\xi}}{\sqrt{2}}\right) + \left(\frac{\sqrt{2}\bar{\ell}}{\pi}\right) \left[-\frac{3\pi^2\tilde{\xi}^2}{2} + \frac{11}{3} \left(\frac{\tilde{\xi}^2}{1 + \frac{1}{2}\tilde{\xi}^2}\right) \right. \\
& \left. + \left(22 - \frac{8}{1 + \frac{1}{2}\tilde{\xi}^2}\right) \frac{\tilde{\xi}}{\sqrt{2}} \arctan\left(\frac{\tilde{\xi}}{\sqrt{2}}\right) + 6\tilde{\xi}^2 \arctan^2\left(\frac{\tilde{\xi}}{\sqrt{2}}\right) \right] + O\left[\left(\frac{\sqrt{2}\bar{\ell}}{\pi}\right)^{\frac{3}{2}}\right]. \quad (3.6.18)
\end{aligned}$$

The algebra leading to (3.6.18) [as well as (3.6.26), below] is presented in Appendix C.

A similar procedure may be applied to the solution of (3.5.50)-(3.5.53) for $\bar{h}_1(\tilde{\xi})$ after setting $\bar{\beta} = 0$. The rescaled dependent variables are

$$(\tilde{\bar{h}}_1, \tilde{\bar{q}}_1, \tilde{\bar{\tau}}_1, \tilde{\bar{b}}_1, \tilde{\bar{b}}_1^*, \Delta\tilde{\bar{p}}_1^+) = (\bar{\ell}^{\frac{1}{2}}\bar{h}_1, \bar{q}_1, \bar{\ell}^{\frac{3}{2}}\bar{\tau}_1, \bar{\ell}^{\frac{1}{2}}\bar{b}_1, \bar{\ell}^{\frac{1}{2}}\bar{b}_1^*, \Delta\bar{p}_1^+). \quad (3.6.19)$$

As it turns out, it is necessary to stretch \bar{h}_1 to $\tilde{\bar{h}}_1$ in both regions of the domain in order to formulate a consistent expansion. Using the above definitions, it is straightforward to derive the outer equations,

$$\tilde{\bar{\tau}}_0 \frac{d^3\tilde{\bar{h}}_1}{d\tilde{\xi}^3} = -\frac{6\tilde{\bar{\tau}}_1}{\bar{h}_0^2\tilde{\bar{\tau}}_0} \left(1 - \frac{2\bar{q}_0}{\bar{h}_0}\right) - \frac{12\bar{\ell}^{\frac{1}{2}}\tilde{\bar{h}}_1}{\bar{h}_0^3} \left(1 - \frac{3\bar{q}_0}{\bar{h}_0}\right) - \frac{12\bar{\ell}\bar{q}_1}{\bar{h}_0^3}, \quad (3.6.20)$$

$$\text{at } \tilde{\xi} = 0 : \quad \tilde{\bar{h}}_1 = 0, \quad (3.6.21)$$

the inner equations,

$$\tilde{\tau}_0 \frac{d^3 \tilde{h}_1}{d\tilde{\xi}^3} = -\frac{6\bar{\ell}^{\frac{1}{2}}\tilde{\tau}_1}{\tilde{h}_0^2\tilde{\tau}_0} + \frac{12\bar{\ell}^{\frac{3}{2}}\tilde{q}_0\tilde{\tau}_1}{\tilde{h}_0^3\tilde{\tau}_0} - \frac{12\bar{\ell}^2\tilde{h}_1}{\tilde{h}_0^3} - \frac{12\bar{\ell}^{\frac{5}{2}}\tilde{q}_1}{\tilde{h}_0^3} + \frac{36\bar{\ell}^3\tilde{h}_1\tilde{q}_0}{\tilde{h}_0^4}, \quad (3.6.22)$$

$$\text{as } \tilde{\xi} \rightarrow \infty : \quad \tilde{h}_1 \rightarrow \tilde{b}_1 - \tilde{b}_0 \tilde{\xi} + \bar{\ell}^{\frac{3}{2}} \tilde{b}_0, \quad (3.6.23)$$

$$\text{as } \tilde{\xi} \rightarrow -\infty : \quad \tilde{h}_1 \rightarrow \tilde{b}_1^* + \tilde{b}_0^* \tilde{\xi} + \bar{\ell}^{\frac{3}{2}} \tilde{b}_0^*, \quad (3.6.24)$$

and the matching conditions,

$$\lim_{\tilde{\xi} \rightarrow 0^+} \tilde{h}_1 = \lim_{\tilde{\xi} \rightarrow \infty} \tilde{h}_1, \quad (3.6.25a)$$

$$\lim_{\tilde{\xi} \rightarrow 0^-} \tilde{h}_1 = \lim_{\tilde{\xi}^* \rightarrow -\infty} \tilde{h}_1. \quad (3.6.25b)$$

Equations (3.6.20)-(3.6.25) may be solved by the method of matched asymptotic expansions after inserting (3.6.18) for \bar{h}_0 . The composite expansion for $\bar{h}_1(\bar{\xi})$ is

$$\begin{aligned} \bar{h}_1 = & \left(\frac{\sqrt{2}}{\pi \bar{\ell}} \right)^{\frac{1}{2}} \left\{ 2 \arctan \left(\frac{\bar{\xi}}{\sqrt{2}} \right) + \left(\frac{\sqrt{2}\bar{\ell}}{\pi} \right)^{\frac{1}{2}} \left[-\frac{3\pi^2 \bar{\xi}^2}{2} + \frac{11}{3} \left(\frac{\bar{\xi}^2}{1 + \frac{1}{2}\bar{\xi}^2} \right) \right. \right. \\ & \left. \left. + \left(22 - \frac{8}{1 + \frac{1}{2}\bar{\xi}^2} \right) \frac{\bar{\xi}}{\sqrt{2}} \arctan \left(\frac{\bar{\xi}}{\sqrt{2}} \right) + 6\bar{\xi}^2 \arctan^2 \left(\frac{\bar{\xi}}{\sqrt{2}} \right) \right] + O\left(\frac{\sqrt{2}\bar{\ell}}{\pi} \right) \right\}. \end{aligned} \quad (3.6.26)$$

The algebra leading to this result is presented in Appendix C.

Equations (3.6.18) and (3.6.26), truncated after the $O(1)$ term, are plotted in Figure 3.4c atop the full numerical solutions for finite $\bar{\ell}$. Analytical results for the constants \bar{q} , $\bar{\tau}$, b , b^* , and $\Delta\bar{p}^+$ are tabulated in Table 3.2 and plotted in Figure 3.5 for small $\bar{\ell}$. The corrections \bar{q}_1 and $\Delta\bar{p}_1^{+(\text{inner})}$ were not computed. One of the more important consequences is the divergence of the membrane tension as $\bar{\ell} \rightarrow 0$. This result implies that spherical vesicles support the *largest membrane tensions* and may be most susceptible to rupture.

The extra pressure drop, to leading order, is given by

$$\begin{aligned} \Delta\bar{p}^+ &= 4\sqrt{2}\pi + O(\epsilon^{\frac{1}{2}}) \\ &\simeq 17.7715 + O(\epsilon^{\frac{1}{2}}), \end{aligned} \quad (3.6.27)$$

which is simply the result for a rigid sphere that is freely suspended in a Poiseuille flow [79, 20]. It is noteworthy that the $O(1)$ term in (3.6.27) is smaller than the like-ordered term in (3.6.7). This reduction in drag arises because the outer solution is forced to match to an inner solution with finite curvature rather than to a uniform film.

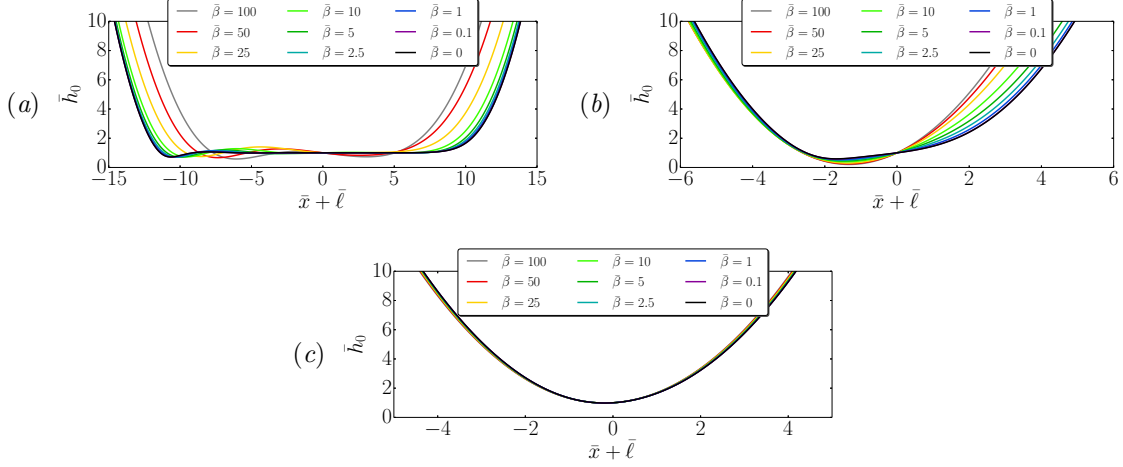


Figure 3.8: Gap height \bar{h}_0 plotted against the shifted axial coordinate $\bar{x} + \bar{\ell}$ for several values of $\bar{\beta}$. (a) Long, spherocylindrical vesicle ($\bar{\ell} = 10$). (b) Intermediate-length vesicle ($\bar{\ell} = 1$). (c) Short, spherical vesicle ($\bar{\ell} = 0.01$).

3.7 Effect of bending elasticity ($\bar{\beta} \neq 0$)

The results presented thus far have not taken into account the effect of bending elasticity. In this section, results for non-vanishing values of $\bar{\beta}$ are presented for the leading-order, inner problem [cf. (3.5.29)-(3.5.33)]. Care must be taken when numerically integrating (3.5.30) for $\bar{\beta} \neq 0$. The general solution of the fifth-order differential equation for $\bar{h}_0(\bar{x})$ can grow exponentially in the far field, which is forbidden by the matching conditions (3.5.32)-(3.5.33). The growth rate of the dominant exponential contribution scales with either $\bar{\beta}^{\frac{1}{2}}$ or $\bar{\beta}^{-\frac{1}{2}}$, depending on the magnitude of $\bar{\beta}$. Consequently, the boundary-value problem becomes numerically stiff when $\bar{\beta}$ is not $O(1)$. In order to circumvent this difficulty, a solution of (3.5.29)-(3.5.33) was obtained first for $\bar{\beta} = 1$, which minimizes the growth rate of the exponentials. Solutions for other values of $\bar{\beta}$ were then obtained by incrementally “marching” up or down in $\bar{\beta}$ using the continuation method.

Figure 3.8 shows the effect of bending elasticity on \bar{h}_0 . Clearly, this effect is marginalized when $\bar{\ell}$ is small (Figure 3.8c). As the vesicle is forced into a spherical shape, it becomes insensitive to changes in curvature. By contrast, bending elasticity has noticeable impact on the vesicle shape when $\bar{\ell}$ is large (Figure 3.8a). The shape exhibits increasingly oscillatory behavior in the thin-film region as $\bar{\beta}$ is increased. These oscillations may be understood by considering the linearized form of (3.5.30) near the fixed point $(\bar{h}_0, \bar{q}_0) = (1, \frac{1}{2})$:

$$\bar{\beta} \frac{d^5 \bar{h}_0}{d\bar{x}^5} - \bar{\tau}_0 \frac{d^3 \bar{h}_0}{d\bar{x}^3} + 6(\bar{h}_0 - 1) = 0, \quad (3.7.1)$$

which is the analog of (3.6.1) for $\bar{\beta} \neq 0$. The exponential solution $\bar{h}_0 = 1 + e^{\eta \bar{x}}$ admits a characteristic

$\bar{\beta}$	$\bar{\tau}_0$	$(6/\bar{\tau}_0)^{\frac{2}{3}}(\bar{\beta}/\bar{\tau}_0)$
100	2.0665	98.4885
50	2.2735	41.9992
25	2.4710	18.2779
10	2.6989	6.3113
5	2.8348	2.9076
2.5	2.9350	1.3720
1	3.0181	0.5239
0.1	3.0851	0.0505
0	3.0939	0

Table 3.3: Numerical results for the membrane tension $\bar{\tau}_0$ and characteristic ratio $(6/\bar{\tau}_0)^{\frac{2}{3}}(\bar{\beta}/\bar{\tau}_0)$ for long, spherocylindrical vesicles ($\bar{\ell} \gg 1$) and several values of $\bar{\beta}$. The transition between the tension- and bending-dominant eigenmodes occurs at a critical bending parameter $\bar{\beta}^*$, where $(6/\bar{\tau}_0)^{\frac{2}{3}}(\bar{\beta}^*/\bar{\tau}_0) \simeq 0.3257$.

quintic for the eigenvalues η :

$$\bar{\beta}\eta^5 - \bar{\tau}_0\eta^3 + 6 = 0. \quad (3.7.2)$$

[18] showed that the roots of (3.7.2) depend on the magnitude of the characteristic ratio $(6/\bar{\tau}_0)^{\frac{2}{3}}(\bar{\beta}/\bar{\tau}_0)$, which gauges the relative importance of bending and tension in the membrane. Values of this quantity corresponding to the profiles shown in Figure 3.8a are tabulated in Table 3.3. The asymptotic solutions for the eigenvalues η are

$$\text{as } (6/\bar{\tau}_0)^{\frac{2}{3}}(\bar{\beta}/\bar{\tau}_0) \rightarrow 0 : \quad \eta = (6/\bar{\tau}_0)^{\frac{1}{3}} \left\{ 1, \pm[(6/\bar{\tau}_0)^{\frac{2}{3}}(\bar{\beta}/\bar{\tau}_0)]^{-\frac{1}{2}}, e^{\pm 2\pi i/3} \right\} \quad (\text{tension-dominant}), \quad (3.7.3a)$$

$$\text{as } (6/\bar{\tau}_0)^{\frac{2}{3}}(\bar{\beta}/\bar{\tau}_0) \rightarrow \infty : \quad \eta = (6/\bar{\beta})^{\frac{1}{5}} \left\{ -1, e^{\pm \pi i/5}, e^{\pm 3\pi i/5} \right\} \quad (\text{bending-dominant}), \quad (3.7.3b)$$

and the transition between the two regimes occurs at a critical bending parameter $\bar{\beta}^*$, where

$$\left(\frac{6}{\bar{\tau}_0} \right)^{\frac{2}{3}} \left(\frac{\bar{\beta}^*}{\bar{\tau}_0} \right) = \left[\left(\frac{3}{5} \right)^{\frac{3}{2}} - \left(\frac{3}{5} \right)^{\frac{5}{2}} \right]^{\frac{2}{3}} \simeq 0.3257. \quad (3.7.4)$$

Shape oscillations are the result of complex eigenvalues η . When $\bar{\beta} < \bar{\beta}^*$ (the tension-dominated regime), the eigenvalues scale like $(6/\bar{\tau}_0)^{\frac{1}{3}}$ and are independent of $\bar{\beta}$.³ Two of the eigenvalues are a complex-conjugate pair and are associated with the approach to the uniform film from the rear tail [cf. (3.6.3)]. When $\bar{\beta} > \bar{\beta}^*$ (the bending-dominated regime), the linearized shape equation gains complex eigenmodes at both ends of the uniform film. The eigenvalues in this regime scale like $(6/\bar{\beta})^{\frac{1}{5}}$ and are independent of $\bar{\tau}_0$. As $(6/\bar{\tau}_0)^{\frac{2}{3}}(\bar{\beta}/\bar{\tau}_0) \rightarrow \infty$, the term multiplied by $\bar{\tau}_0$ in (3.7.1) asymptotically decays, resulting in a differential balance between bending elasticity and viscous

³Two of the real roots diverge as $(6/\bar{\tau}_0)^{\frac{2}{3}}(\bar{\beta}/\bar{\tau}_0) \rightarrow 0$ and hence are unphysical.

traction over a stretched increment $d\bar{x} = O(\bar{\beta}^{\frac{1}{5}})$. For fixed $\bar{\ell}$, this results in “apparent shortening” of the thin-film region with increasing $\bar{\beta}$, as seen in Figure 3.8a.

Figure 3.9 extends the leading-order results of Figure 3.5 to non-vanishing values of $\bar{\beta}$. Although the effect of bending elasticity is non-monotonic over the range of $\bar{\ell}$ considered, some general trends may be deduced. The addition of bending resistance typically reduces the membrane tension $\bar{\tau}_0$. This is an expected effect, since bending moments can also exert an in-plane tension [138]. The shape coefficients b_0 and b_0^* also change with $\bar{\beta}$, and in §3.8 it is shown that this change has a direct consequence on the available vesicle surface area and enclosed volume. When $\bar{\ell} = O(1)$, increasing $\bar{\beta}$ tends to reduce the leakback flux \bar{q}_0 and increase the extra pressure drop $\Delta\bar{p}_0^+$. This trend implies that undulations in \bar{h}_0 result in local occlusion of flow in the thin-gap region, which hinders vesicle mobility and enhances wall resistance. As $\bar{\ell}$ increases, “stiffer vesicles” (larger $\bar{\beta}$) are forced into a shape that occludes most of the tube cross section. This effect manifests in enhanced sensitivity of the constants \bar{q}_0 , $\bar{\tau}_0$, b_0 , b_0^* , and $\Delta\bar{p}_0^+$ to changes in $\bar{\ell}$, as indicated by the sharp gradients between $\bar{\ell} = 1$ and 10 in Figure 3.9. Since the governing equations are numerically stiff in this region of the parameter space, smaller “steps” in $\bar{\beta}$ and $\bar{\ell}$ were required during the continuation procedure in order to ensure convergence and accuracy within the desired tolerance. When $\bar{\ell}$ becomes very large, \bar{q}_0 , $\bar{\tau}_0$, b_0 , and b_0^* plateau to a value that depends on $\bar{\beta}$ but not $\bar{\ell}$. Changes in $\Delta\bar{p}_0^+$ are masked by a “cylinder contribution” of size $4\bar{\ell}$ [cf. Table 3.1]. The $4\bar{\ell}$ contribution is subtracted out in the inset of Figure 3.9e so as to isolate the “curvature contribution” to $\Delta\bar{p}_0^+$. It is seen that bending elasticity can *reduce* the wall drag when $\bar{\ell}$ is large. This result contrasts with Bruinsma’s prediction that the pressure drop across a long vesicle should be independent of membrane bending elasticity [18].

3.8 Elimination of ϵ and ℓ as parameters

The theory put forth has been parametrized in terms of four dimensionless groups, three of which (ϵ, ℓ, β) depend on the local flow conditions. In order to put the results of §3.5-3.7 into a more useable form, it is necessary to recast the results in terms of (v, λ, β) , where v (the reduced volume) and λ (the radius ratio) were defined at the end of the previous chapter [cf. (2.5.4)-(2.5.5)]. These parameters are more commonly found in the existing literature [169, 163]. An entirely equivalent parametrization is $(\lambda^*, \lambda, \beta)$, where λ^* is related to v by (3.1.10).

The clearance parameter ϵ and reduced length ℓ , which were the appropriate parameters for constructing the narrow-gap perturbation theory, may now be eliminated in favor of the geometric parameters λ and λ^* by applying integral constraints for the vesicle surface area A_0 and enclosed volume Ω_0 . Supposing that A_0 is made dimensionless by R^2 , we may decompose the surface-area

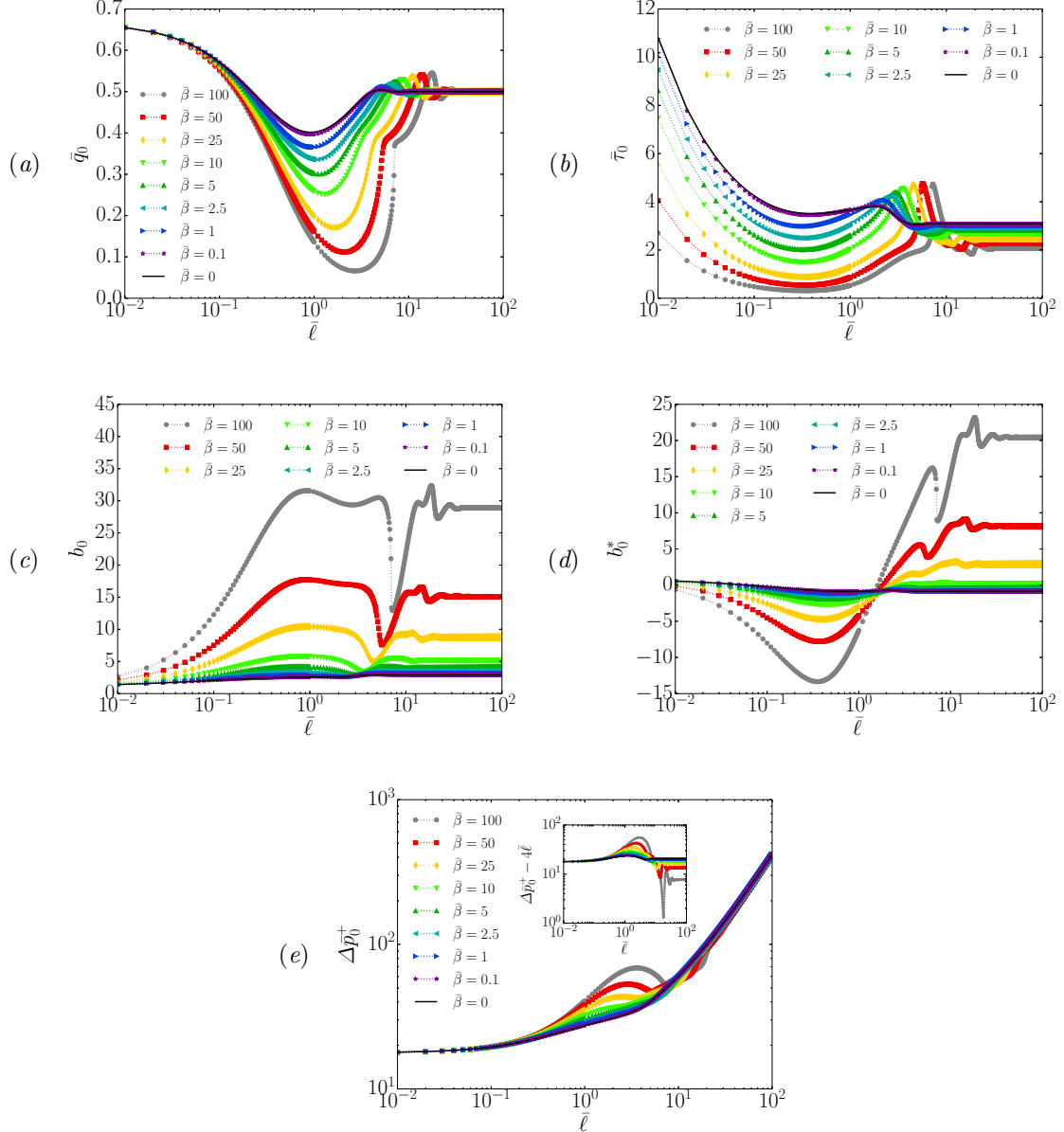


Figure 3.9: Leading-order solution for (a) the leakback flux \bar{q}_0 , (b) the membrane tension $\bar{\tau}_0$, (c) the front intercept b_0 , (d) the rear intercept b_0^* , and (e) the extra pressure drop $\Delta \bar{p}_0^+$ plotted against the reduced length $\bar{\ell}$ for several values of $\bar{\beta}$. Inset: curvature contribution to the extra pressure drop $\Delta \bar{p}_0^+ - 4\bar{\ell}$ plotted against the reduced length $\bar{\ell}$.

constraint as follows:

$$\frac{A_0}{2\pi} = \int_{-\ell}^0 \rho_s \sqrt{1 + \left(\frac{d\rho_s}{dx}\right)^2} dx \quad (3.8.1a)$$

$$\begin{aligned} &= \int_{-\ell}^{-\ell+1-X^*} \rho_s \sqrt{1 + \left(\frac{d\rho_s}{dx}\right)^2} dx + \int_{-X^*/\epsilon^{1/2}}^{\bar{\ell}} \left\{ 1 + \epsilon \left[\frac{1}{2} \left(\frac{d\bar{h}}{d\bar{x}} \right)^2 - \bar{h} \right] + O(\epsilon^2) \right\} \epsilon^{1/2} d\bar{x}^* \\ &\quad + \int_{-\bar{\ell}}^{X/\epsilon^{1/2}} \left\{ 1 + \epsilon \left[\frac{1}{2} \left(\frac{d\bar{h}}{d\bar{x}} \right)^2 - \bar{h} \right] + O(\epsilon^2) \right\} \epsilon^{1/2} d\bar{x} + \int_{-1+X}^0 \rho_s \sqrt{1 + \left(\frac{d\rho_s}{dx}\right)^2} dx. \end{aligned} \quad (3.8.1b)$$

where X and X^* are “intermediate variables” of order less than ϵ and greater than $\epsilon^{1/2}$. The right-hand side of (3.8.1b) contains four integrals, each corresponding to a contribution from the front or rear part of the outer or inner region. Making use of (3.5.12), (3.5.18), and (3.5.38), the “rear-outer contribution” becomes

$$\int_{-\ell}^{-\ell+1-X^*} \rho_s \sqrt{1 + \left(\frac{d\rho_s}{dx}\right)^2} dx = 1 - X^* - \epsilon b_0^*(1 - X^*) + O(\epsilon^{3/2}).$$

Likewise, the “front-outer contribution” gives

$$\int_{-1+X}^0 \rho_s \sqrt{1 + \left(\frac{d\rho_s}{dx}\right)^2} dx = 1 - X - \epsilon b_0(1 - X) + O(\epsilon^{3/2}).$$

Making use of the numerical solution for \bar{h}_0 and \bar{h}_1 , the “rear-inner contribution” becomes

$$\begin{aligned} &\int_{-X^*/\epsilon^{1/2}}^{\bar{\ell}} \left\{ 1 + \epsilon \left[\frac{1}{2} \left(\frac{d\bar{h}}{d\bar{x}} \right)^2 - \bar{h} \right] + O(\epsilon^2) \right\} \epsilon^{1/2} d\bar{x}^* \\ &= X^* + \epsilon^{1/2} \bar{\ell} - \epsilon b_0^* X^* - \epsilon^{3/2} \bar{\ell} + O(\epsilon^{3/2}, \epsilon^2 \bar{\ell}). \end{aligned}$$

Likewise, the “front-inner contribution” gives

$$\begin{aligned} &\int_{-\bar{\ell}}^{X/\epsilon^{1/2}} \left\{ 1 + \epsilon \left[\frac{1}{2} \left(\frac{d\bar{h}}{d\bar{x}} \right)^2 - \bar{h} \right] + O(\epsilon^2) \right\} \epsilon^{1/2} d\bar{x} \\ &= X + \epsilon^{1/2} \bar{\ell} - \epsilon b_0 X - \epsilon^{3/2} \bar{\ell} + O(\epsilon^{3/2}, \epsilon^2 \bar{\ell}). \end{aligned}$$

Inserting the last four results into (3.8.1b) gives

$$\frac{A_0}{4\pi} = 1 + \epsilon^{1/2} \bar{\ell} - \frac{1}{2} \epsilon (b_0 + b_0^*) - \epsilon^{3/2} \bar{\ell} + O(\epsilon^{3/2}, \epsilon^2 \bar{\ell}), \quad (3.8.2)$$

where X and X^* have properly cancelled.

The enclosed volume Ω_0 may be evaluated in a similar fashion. Supposing that Ω_0 is made

dimensionless by R^3 , the volume constraint may be decomposed as follows:

$$\frac{\Omega_0}{\pi} = \int_{-\ell}^0 \rho_s^2 dx \quad (3.8.3a)$$

$$\begin{aligned} &= \int_{-\ell}^{-\ell+1-X^*} \rho_s^2 dx + \int_{-X^*/\epsilon^{1/2}}^{\bar{\ell}} [1 - 2\epsilon\bar{h} + O(\epsilon^2)] \epsilon^{1/2} d\bar{x}^* \\ &\quad + \int_{-\bar{\ell}}^{X/\epsilon^{1/2}} [1 - 2\epsilon\bar{h} + O(\epsilon^2)] \epsilon^{1/2} d\bar{x} + \int_{-1+X}^0 \rho_s^2 dx. \end{aligned} \quad (3.8.3b)$$

Again, (3.8.3b) contains four contributions, including the “rear-outer contribution,”

$$\int_{-\ell}^{-\ell+1-X^*} \rho_s^2 dx = \frac{2}{3} - X^*(1 - \frac{1}{3}X^{*2}) - \epsilon b_0^*(1 - X^*)^2 + O(\epsilon^{3/2});$$

the “front-outer contribution,”

$$\int_{-1+X}^0 \rho_s^2 dx = \frac{2}{3} - X(1 - \frac{1}{3}X^2) - \epsilon b_0(1 - X)^2 + O(\epsilon^{3/2});$$

the “rear-inner contribution,”

$$\begin{aligned} &\int_{-X^*/\epsilon^{1/2}}^{\bar{\ell}} [1 - 2\epsilon\bar{h} + O(\epsilon^2)] \epsilon^{1/2} d\bar{x}^* \\ &= X^*(1 - \frac{1}{3}X^{*2}) + \epsilon^{1/2}\bar{\ell} - \epsilon b_0^* X^*(2 - X^*) - 2\epsilon^{3/2}\bar{\ell} + O(\epsilon^{3/2}, \epsilon^2\bar{\ell}); \end{aligned}$$

and, finally, the “front-inner contribution,”

$$\begin{aligned} &\int_{-\bar{\ell}}^{X^*/\epsilon^{1/2}} [1 - 2\epsilon\bar{h} + O(\epsilon^2)] \epsilon^{1/2} d\bar{x} \\ &= X(1 - \frac{1}{3}X^2) + \epsilon^{1/2}\bar{\ell} - \epsilon b_0 X(2 - X) - 2\epsilon^{3/2}\bar{\ell} + O(\epsilon^{3/2}, \epsilon^2\bar{\ell}). \end{aligned}$$

Inserting the last four results into (3.8.3b) gives

$$\frac{\Omega_0}{2\pi} = \frac{2}{3} + \epsilon^{1/2}\bar{\ell} - \frac{1}{2}\epsilon(b_0 + b_0^*) - 2\epsilon^{3/2}\bar{\ell} + O(\epsilon^{3/2}, \epsilon^2\bar{\ell}), \quad (3.8.4)$$

where again the intermediate variables X and X^* have properly cancelled.

After substituting $\ell = 2(1 + \epsilon^{1/2}\bar{\ell})$ and

$$\frac{A_0}{4\pi} = \lambda^2, \quad \frac{\Omega_0}{2\pi} = \frac{2}{3}\nu\lambda^3 = \left(\frac{\lambda^{*2} - \frac{1}{3}}{\lambda^{*3}}\right)\lambda^3,$$

equations (3.8.2) and (3.8.4) may be inverted to give the desired expansions:

$$\epsilon = 1 - \frac{\lambda}{\lambda^*} + O\left[\left(1 - \frac{\lambda}{\lambda^*}\right)^2\right], \quad (3.8.5)$$

$$\frac{1}{2}\ell = \lambda^{*2} - \left[1 + \lambda^{*2} - \frac{1}{2}(b_0 + b_0^*)\right]\left(1 - \frac{\lambda}{\lambda^*}\right) + O\left[\left(1 - \frac{\lambda}{\lambda^*}\right)^2\right]. \quad (3.8.6)$$

The coefficients b_0 and b_0^* depend upon the stretched parameters $\bar{\ell}$ and $\bar{\beta}$ (shown in Figure 3.9c,d) and hence vary with both geometry *and* flow conditions. The error terms neglected in (3.8.5)-(3.8.6) can also depend on the flow conditions. By using (3.8.5)-(3.8.6), it is possible to eliminate ϵ and ℓ from the theory entirely and parametrize the results of the previous sections in terms of the reduced volume v , radius ratio λ , and (unstretched) bending parameter β . The utility of this alternative parametrization is that v and λ are *purely geometric quantities*, with all of the dynamical information contained in β . The limit $\epsilon \rightarrow 0$ is directly mapped to $\lambda \rightarrow \lambda^*$.

3.9 Discussion of results

Having presented the main theoretical content, we now discuss the main results. Herein, we do away with implied scalings and present the dimensionless groups explicitly (e.g., instead of ρ_s , we write ρ_s/R).

3.9.1 Vesicle shapes

Vesicle shapes for fixed v , λ , and β are shown in Figure 3.10. The shapes were generated by additive composition of the outer and inner expansions for $\rho_s(x) = R - h(x)$ [166]. The shape change between $\beta = 0$ and 10 is nearly indiscernible – except when v and λ/λ^* are small – because confinement suppresses bending elasticity. As λ/λ^* is increased (for fixed v), the narrow gap widens and the vesicle elongates. Vesicles of lower reduced volume v (for fixed λ/λ^*) tend to be longer.

3.9.2 Relative velocity and extra pressure drop

The most important *hydrodynamical* quantities of interest are the relative velocity $U/V = 1 + 2q/(R^2V)$ and extra pressure drop $\Delta p^+R/(\mu V)$. These quantities were calculated from composite expansions and the numerical results are tabulated in Table 3.4 for fixed v , λ , and β . The relative velocity U/V is relatively unchanged across reduced volumes v so long as the confinement ratio λ/λ^* is kept constant. This is because the effective cross-sectional area occluded by the vesicle is independent of the vesicle length. On the other hand, the extra pressure drop $\Delta p^+R/(\mu V)$ is highly sensitive to v because the drag scales linearly with the vesicle length. As shown in Table 3.4, the value of λ/λ^* for which $\Delta p^+R/(\mu V) \approx 80$ decreases as v is decreased.

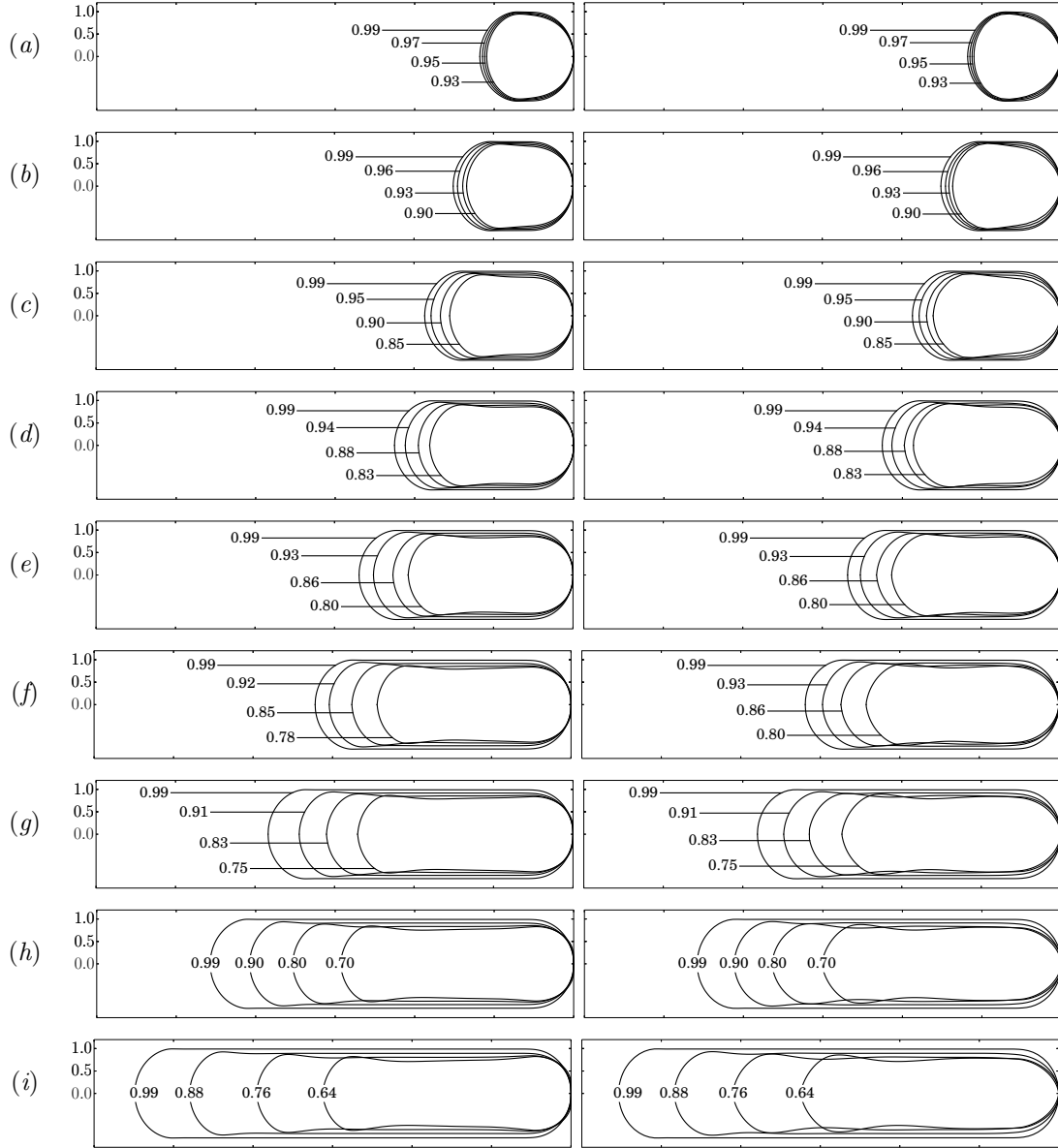


Figure 3.10: Vesicle shapes (the ordinate is ρ_s/R) for (a) $v = 0.99$, (b) $v = 0.95$, (c) $v = 0.90$, (d) $v = 0.85$, (e) $v = 0.80$, (f) $v = 0.75$, (g) $v = 0.70$, (h) $v = 0.65$, and (i) $v = 0.60$. The ratio λ/λ^* is indicated for each shape. Left column: $\beta = 0$. Right column: $\beta = 10$.

v	λ/λ^*	λ	U/V				$\Delta p^+ R/(\mu V) \times 10^{-2}$			
			$\beta = 0$	$\beta = 0.1$	$\beta = 1$	$\beta = 10$	$\beta = 0$	$\beta = 0.1$	$\beta = 1$	$\beta = 10$
0.99	1	1.0903	1	1	1	1	∞	∞	∞	∞
	0.99	1.08	1.01	1.01	1.01	1.01	3.0	3.0	3.0	3.1
	0.97	1.06	1.03	1.03	1.03	1.02	1.5	1.5	1.5	1.6
	0.95	1.04	1.05	1.05	1.05	1.04	1.0	1.0	1.0	1.1
	0.93	1.01	1.07	1.07	1.07	1.06	0.8	0.8	0.8	0.9
0.95	1	1.2324	1	1	1	1	∞	∞	∞	∞
	0.99	1.22	1.01	1.01	1.01	1.01	4.1	4.1	4.1	4.1
	0.96	1.18	1.04	1.04	1.04	1.03	1.6	1.6	1.6	1.7
	0.93	1.14	1.06	1.06	1.06	1.05	1.1	1.1	1.1	1.2
	0.90	1.11	1.09	1.09	1.09	1.07	0.9	0.9	0.9	1.0
0.90	1	1.3712	1	1	1	1	∞	∞	∞	∞
	0.99	1.36	1.01	1.01	1.01	1.01	5.6	5.6	5.6	5.6
	0.95	1.30	1.05	1.05	1.05	1.04	1.65	1.65	1.65	1.7
	0.90	1.23	1.09	1.09	1.08	1.07	1.1	1.1	1.1	1.2
	0.86	1.17	1.13	1.13	1.12	1.10	0.8	0.8	0.8	0.9
0.85	1	1.5050	1	1	1	1	∞	∞	∞	∞
	0.99	1.49	1.01	1.01	1.01	1.01	7.2	7.2	7.2	7.2
	0.94	1.41	1.06	1.06	1.06	1.05	1.7	1.7	1.7	1.7
	0.88	1.32	1.10	1.10	1.10	1.09	1.0	1.0	1.1	1.1
	0.83	1.25	1.14	1.14	1.14	1.11	0.8	0.8	0.8	0.9
0.80	1	1.6437	1	1	1	1	∞	∞	∞	∞
	0.99	1.63	1.01	1.01	1.01	1.01	9.0	9.0	9.0	8.9
	0.93	1.53	1.07	1.07	1.07	1.07	1.8	1.8	1.7	1.7
	0.86	1.41	1.12	1.12	1.12	1.11	1.0	1.0	1.1	1.1
	0.80	1.31	1.16	1.16	1.16	1.14	0.8	0.8	0.8	0.9
0.75	1	1.7925	1	1	1	1	∞	∞	∞	∞
	0.99	1.77	1.01	1.01	1.01	1.01	11.3	11.3	11.3	11.0
	0.92	1.67	1.07	1.07	1.07	1.07	1.8	1.8	1.8	1.8
	0.85	1.54	1.13	1.13	1.13	1.12	1.1	1.1	1.1	1.2
	0.78	1.40	1.18	1.18	1.18	1.15	0.8	0.8	0.8	0.9
0.70	1	1.9562	1	1	1	1	∞	∞	∞	∞
	0.99	1.94	1.01	1.01	1.01	1.01	13.9	13.9	13.9	13.7
	0.91	1.78	1.08	1.08	1.08	1.08	1.9	1.9	1.9	2.0
	0.83	1.62	1.15	1.15	1.15	1.14	1.1	1.1	1.1	1.2
	0.75	1.47	1.20	1.20	1.20	1.18	0.8	0.8	0.8	0.9
0.65	1	2.1397	1	1	1	1	∞	∞	∞	∞
	0.99	2.12	1.01	1.01	1.01	1.01	16.8	16.8	16.8	17.0
	0.90	1.93	1.09	1.09	1.09	1.09	2.1	2.1	2.1	2.1
	0.80	1.71	1.17	1.17	1.17	1.17	1.1	1.1	1.1	1.2
	0.70	1.50	1.23	1.23	1.23	1.21	0.8	0.8	0.8	0.9
0.60	1	2.3490	1	1	1	1	∞	∞	∞	∞
	0.99	2.33	1.01	1.01	1.01	1.01	20.4	20.5	20.5	20.9
	0.88	2.07	1.11	1.11	1.11	1.11	2.1	2.1	2.1	2.1
	0.76	1.79	1.20	1.20	1.20	1.20	1.1	1.1	1.1	1.1
	0.64	1.50	1.27	1.27	1.27	1.23	0.8	0.8	0.8	0.8

Table 3.4: Relative velocity U/V and dimensionless extra pressure drop $\Delta p^+ R/(\mu V)$ for different values of the reduced volume v , confinement ratio λ/λ^* (or radius ratio λ , also shown), and bending parameter β . The clearance parameter is in the range $0 < \epsilon < 0.3$.

	spherocylinder ($\lambda^* > 1$)	sphere ($\lambda^* \simeq 1$)
$\frac{U}{V}$	$1 + \left(1 - \frac{\lambda}{\lambda^*}\right)$	$1 + \frac{4}{3} \left(1 - \frac{\lambda}{\lambda^*}\right)$
$\frac{\Delta p^+ R}{\mu V}$	$4(\lambda^{*2} - 1) \left(1 - \frac{\lambda}{\lambda^*}\right)^{-1}$	$4\sqrt{2}\pi \left(1 - \frac{\lambda}{\lambda^*}\right)^{-\frac{1}{2}}$

Table 3.5: Asymptotic behavior of the relative velocity U/V and dimensionless extra pressure drop $\Delta p^+ R/(\mu V)$ as $\lambda \rightarrow \lambda^*$ for spherocylindrical and spherical vesicles. The two limiting cases are nicely interpolated by (3.9.1).

The asymptotic behavior of U/V and $\Delta p^+ R/(\mu V)$ as $\lambda \rightarrow \lambda^*$ (maximum confinement) depends on the vesicle shape. Two limiting cases for $\beta = 0$ were considered in §3.6, which correspond to either long, spherocylindrical vesicles ($v < 1$, $\lambda^* > 1$) or short, spherical vesicles ($v \simeq 1$, $\lambda^* \simeq 1$). After using (3.8.5)-(3.8.6) to eliminate ϵ and ℓ , the asymptotes may be written in terms of the geometric parameters. These results summarized in Table 3.5. [135] showed that separate results for spherocylindrical and spherical red blood cells may be unified by interpolating over the reduced length $\ell = 2\lambda^{*2} + O(1 - \lambda/\lambda^*)$. In this spirit, the following *approximate* expressions nicely interpolate the results presented in Table 3.5 for *all* reduced volumes as $\lambda \rightarrow \lambda^*$:

$$\frac{U}{V} = 1 + \frac{4}{3} \left(\frac{3\lambda^{*2} - 2}{4\lambda^{*2} - 3} \right) \left(1 - \frac{\lambda}{\lambda^*}\right) + O\left[\left(1 - \frac{\lambda}{\lambda^*}\right)^2\right], \quad (3.9.1a)$$

$$\frac{\Delta p^+ R}{\mu V} = 4(\lambda^{*2} - 1) \left(1 - \frac{\lambda}{\lambda^*}\right)^{-1} + \left(\frac{4\sqrt{2}\pi}{4\lambda^{*2} - 3} \right) \left(1 - \frac{\lambda}{\lambda^*}\right)^{-\frac{1}{2}} + O(1). \quad (3.9.1b)$$

Equation (3.9.1) is the most practical result of this chapter. Since bending elasticity has a negligible effect for most reasonable values of β , it is expected that these expressions be insensitive to the flow conditions. Thus, the predictions for U/V and $\Delta p^+ R/(\mu V)$ under high confinement are set entirely by the *geometry* of the system.

3.9.3 Comparison to direct numerical simulations

In the next chapter, we shall introduce a numerical method to solve Stokes' equations without having to make the narrow-gap assumption. For the time being, it behooves us to compare our present asymptotic predictions against the axisymmetric simulations performed by Trozzo and coworkers [163]. A comparison of the present theory to their results for the radius of curvature $\rho_s = R - h$ and membrane traction jump $\mathbf{f}_s = (\boldsymbol{\sigma} - \check{\boldsymbol{\sigma}}) \cdot \hat{\mathbf{n}}$ (with components f_{sx} and $f_{s\rho}$) is shown in Figure 3.11 for two sets of the parameters v , λ , and β . Also reported are the associated parameters ϵ , $\bar{\ell}$, and $\bar{\beta}$ used in the perturbation theory.

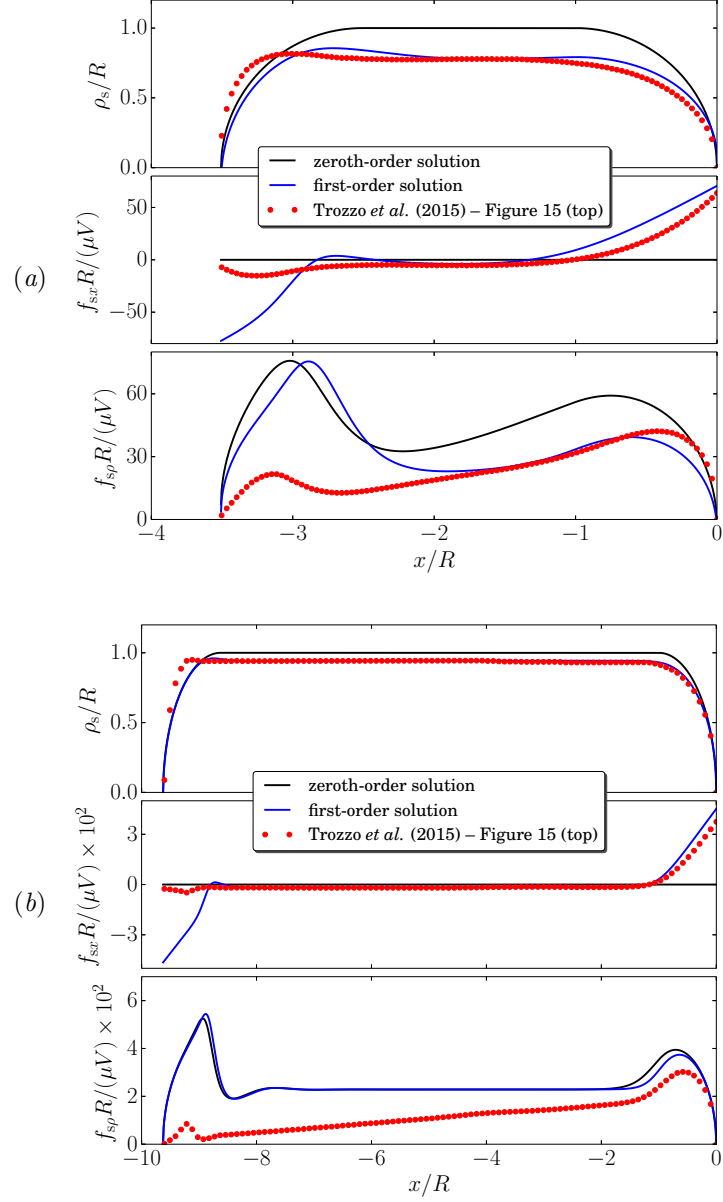


Figure 3.11: Comparison of the present theoretical predictions for the membrane shape ρ_s and traction components f_{sx} and f_{sp} to the boundary element simulations of [163] (viscosity ratio $\kappa = 1$). Results are shown for (a) $v = 0.84$, $\lambda = 1.2$, $\beta = 0.01$ ($\epsilon = 0.22$, $\bar{\ell} = 1.6$, $\bar{\beta} = 0.006$) and (b) $v = 0.61$, $\lambda = 2.1$, $\beta = 0.03$ ($\epsilon = 0.057$, $\bar{\ell} = 16$, $\bar{\beta} = 0.008$).

The agreement between the theory and the simulations improves with decreasing ϵ , as expected. The theoretical prediction for the radial component of the membrane traction $f_{s\rho}$ exhibits the largest discrepancy with the simulation result. Whereas the simulation reports a linearly increasing profile over the majority of the thin-film region, the perturbative result is mostly flat. This discrepancy is due to the neglect of higher-order perturbative corrections that scale linearly with $\bar{\ell}$. The radial traction $f_{s\rho}$ is approximately given by the radial projection of the pressure jump vector $-(p - \check{p})|_{\rho=\rho_s(x)} \hat{n}$, which is expanded up to first order in $\epsilon^{\frac{1}{2}}$ in this work:

$$(p - \check{p})|_{\rho=\rho_s(x)} = \epsilon^{-\frac{3}{2}} [\bar{p}_0 - \check{p}_0 + \epsilon^{\frac{1}{2}} (\bar{p}_1 - \check{p}_1) + O(\epsilon, \epsilon \bar{\ell})].$$

Since $\Delta \bar{p}_0^+ \sim 4\bar{\ell}$, according to (3.6.7), the coefficient $\bar{p}_2 - \check{p}_2$ of the next term in the asymptotic series must be a function that decreases by an amount $4\bar{\ell}$ through the thin-film region. This inner correction forces an outer correction to the rear pressure that is $O(\epsilon \bar{\ell})$.

By contrast, both the vesicle radius ρ_s and the axial component of the membrane traction f_{sx} are well approximated by the perturbation theory within the front-nose and thin-film regions. Significant errors in these functions are only observed at the rear tail – again, due to the neglect of $O(\epsilon \bar{\ell})$ terms in the perturbative solution. In the thin-film region, the dominant contribution to f_{sx} is the membrane shear stress $(\partial u / \partial \rho)|_{\rho=\rho_s(x)}$:

$$\frac{\partial u}{\partial \rho} \Big|_{\rho=\rho_s(x)} = -\epsilon^{-1} \left(\frac{\partial \bar{u}_0}{\partial \bar{y}} \Big|_{\bar{y}=\bar{h}_0(\bar{x})} + \epsilon^{\frac{1}{2}} \frac{\partial \bar{u}_1}{\partial \bar{y}} \Big|_{\bar{y}=\bar{h}_0(\bar{x})} + O(\epsilon, \epsilon \bar{\ell}) \right). \quad (3.9.2)$$

The agreement with the perturbation theory is therefore expected, since the small- ϵ assumption resolves parallel flow (and, therefore, shear stresses) within the narrow gap. The fact that shear stresses are more well resolved by the perturbation theory than normal stresses is important for calculating the dimensionless extra pressure drop $\Delta p^+ R / (\mu V)$, which is given by the resultant of shear stresses on the tube wall.

3.9.4 Comparison to experiments and previous theories

In Figure 3.12, predictions for the relative velocity U/V and dimensionless extra pressure drop $\Delta p^+ R / (\mu V)$ are compared to available experimental measurements for vesicles and red blood cells in capillary flow. Both the composite expansions (solid lines) as well as the asymptotic interpolants (3.9.1) (dashed lines) are plotted.

Measurements of U/V for vesicles in circular capillaries ($v = 0.924-0.999$) and square channels ($v = 0.80-1$) were collected by [169] and [3], respectively. Unfortunately, experimental measurements of $\Delta p^+ R / (\mu V)$ for vesicles in channel flow are currently unavailable. The experimental data compiled from [4] and [128] are for suspensions of red blood cells flowing in capillary tubes at various volume

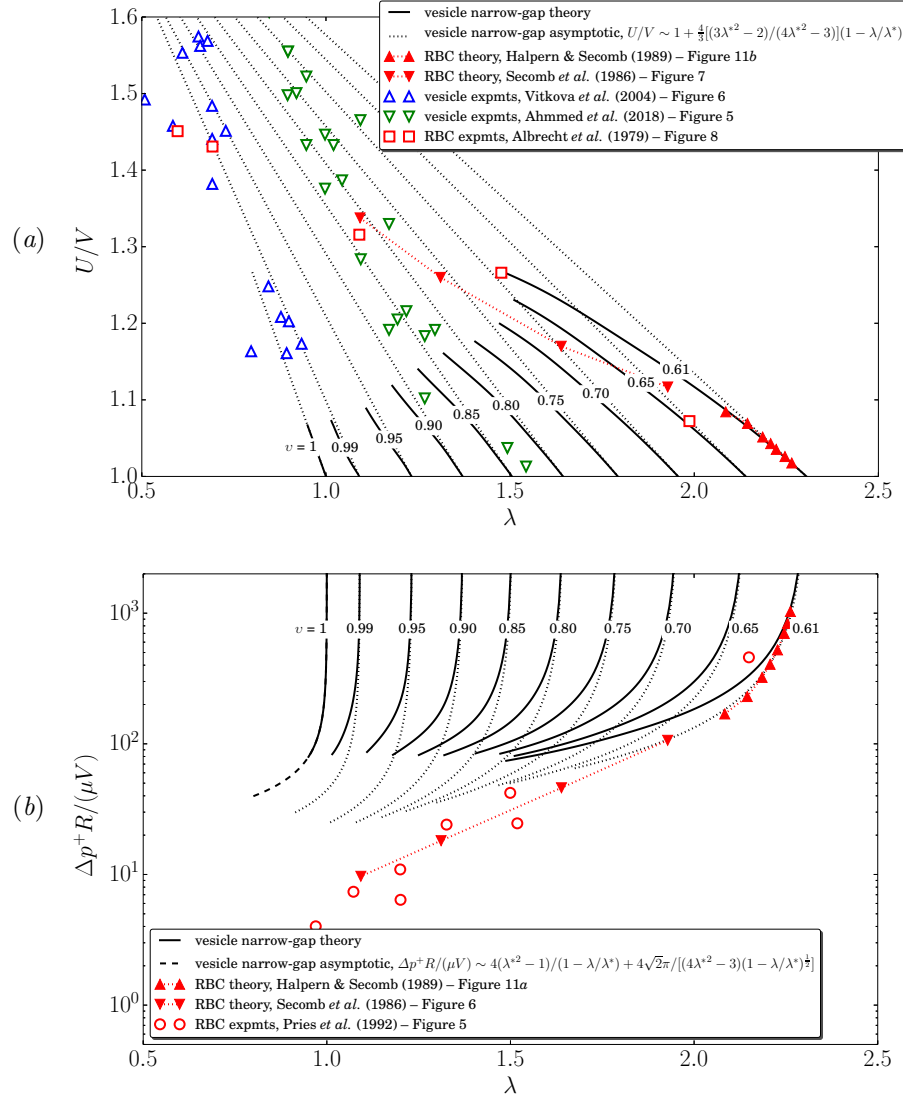


Figure 3.12: (a) Relative velocity U/V and (b) dimensionless extra pressure drop $\Delta p^+ R / (\mu V)$ plotted against the radius ratio λ for $\beta = 0$ and several reduced volumes v . Also shown are the experimental measurements of [169], [3] (for vesicles), [4], and [128] (for red blood cells), as well as previous theories due to [139] and [71] (for red blood cells).

concentrations (or “hematocrits”). Other reported measurements [e.g., those of [159]] were rejected on the basis that the red blood cells were not highly confined. Also shown are the theories of [139] and [71] for red blood cells with vanishing shear and bending elasticity. The predictions of [18], which are not of the correct scale, are omitted for the sake of clarity.

It is clear that U/V and $\Delta p^+ R/(\mu V)$ are highly sensitive to v and λ . Figure 3.12a shows that a 5% change in the reduced volume v can lead to as much as a 10% change in the predicted relative velocity U/V . As illustrated by the vesicle shapes in Figure 3.10, decreasing v tends to “streamline” the body of the vesicle, which enhances its mobility in the tube. Variation in the measured values of v and λ can explain the scatter in the experimental measurements of [169] and [3]. It is important to keep in mind that the measurements of [3] were conducted in square conduits rather than circular capillaries, which would enhance the vesicle mobility for a given hydraulic channel radius.

The present theory, which is valid for all reduced volumes, complements and extends previous results for red blood cells, which are typically restricted to a narrow window of reduced volumes centered about $v \simeq 0.61$ [22]. Since shear and bending elasticity play only a secondary role relative to the isotropic membrane tension under high confinement, one expects the results for red blood cells and vesicles to be comparable. The present theory converges to the results of [71] as $\lambda \rightarrow \lambda^* = 2.3047$ for $v = 0.61$. Relatively good agreement with the data reported by [4] and [128] is observed, although the present theory overpredicts the data of [128] for smaller values of λ due to the neglect of higher-order perturbative corrections. In this regime, the parallel-flow theory of [139], in which the transverse component of the velocity is neglected in lieu of invoking the narrow-gap assumption, more accurately captures the experimental data.

3.10 Review of assumptions

The narrow-gap theory presented in this chapter was developed after making several assumptions other than the obvious restriction $\epsilon \ll 1$. These include *axisymmetry* and *steadiness*. It is instructive at this point to review these assumptions and highlight conditions under which they would be expected to break down. In the next chapter, we will relax these conditions and show that indeed there are instances of symmetry breaking and unsteadiness (§4.4.2).

The condition of *axisymmetry* implies that all variations with respect to the azimuthal angle ϕ are vanishingly small. Only axisymmetric vesicle shapes are reported in this chapter, raising the question as to whether non-axisymmetric solutions exist. Since the azimuthal angle ϕ is not stretched in the small- ϵ expansion,

$$\frac{|\partial^2 h / \partial \phi^2|}{|\partial^2 h / \partial x^2|} = \epsilon \left(\frac{|\partial^2 \bar{h} / \partial \phi^2|}{|\partial^2 \bar{h} / \partial \bar{x}^2|} \right) = O(\epsilon), \quad (3.10.1)$$

which implies that the change in the azimuthal curvature due to variations of h along ϕ is small

relative to the meridional curvature. Thus, non-axisymmetric solutions do not enter into the leading-order theory if $\epsilon \ll 1$. As ϵ increases in magnitude, however, it would be expected that gradients of h with respect to x and ϕ would be on “equal footing,” and in such cases there is no reason to believe that the stable state is axisymmetric.

The condition of *steadiness* implies that all variations with respect to time t are vanishingly small. The steady-state form of the kinematic condition, $dq/dx = 0$, was used in the development of the narrow-gap theory. The unsteady form is,

$$\frac{\partial h}{\partial t} + \frac{\partial q}{\partial x} = 0, \quad (3.10.2)$$

where t is scaled by R/V . Rescaling $\bar{t} = t/\epsilon$ and eliminating q from the expression, one obtains at leading order,

$$\frac{\partial \bar{h}_0}{\partial \bar{t}} - \frac{\partial}{\partial \bar{x}} \left[\frac{\bar{h}_0}{2} + \frac{\bar{h}_0^3}{12} \left(\bar{\beta} \frac{\partial^5 \bar{h}_0}{\partial \bar{x}^5} - \bar{\tau}_0 \frac{\partial^3 \bar{h}_0}{\partial \bar{x}^3} \right) \right] = 0. \quad (3.10.3)$$

Equation (3.10.3) is the unsteady analog of (3.5.30). The linear stability of $\bar{h}_0(\bar{x}, \bar{t})$ near the fixed point $\bar{h}_0 = 1$ is analyzed by introducing a Fourier perturbation $\bar{h}_0(\bar{x}, \bar{t}) = 1 + H e^{\omega \bar{t} + i k \bar{x}}$, where H is the amplitude, ω is the frequency, and k is the wavenumber. After neglecting $O(H^2)$ terms, the dispersion relationship between ω and k is found to be

$$\omega = -\frac{1}{12} (\bar{\beta} k^6 + \bar{\tau}_0 k^4) + \frac{1}{2} i k. \quad (3.10.4)$$

Equation (3.10.4) indicates that the Fourier perturbations are traveling waves with phase speed $k/2$. The waves decay in time so long as $\bar{\tau}_0 + \bar{\beta} k^2 > 0$. Thus, the membrane is stable to small-amplitude perturbations when under tension ($\bar{\tau}_0 > 0$). It is not possible, under the auspices of the theory, for the vesicle to be put under compression ($\bar{\tau}_0 < 0$), as can occur when the vesicle is freely suspended in a quiescent fluid. Since it was previously stipulated that $\bar{\beta} = o(\epsilon^{-\frac{1}{2}})$, the viscous stress term in (3.5.30) remains dominant for any choice of the parameters. As $\bar{\beta}$ increases, the membrane tension $\bar{\tau}_0$ decreases in magnitude (but remains positively valued), resulting in a balance between curvature elasticity and viscous stress in (3.5.30).

The crucial criteria for shape stability were $\epsilon \ll 1$ and $\bar{\beta} = o(\epsilon^{-\frac{1}{2}})$. For larger values of ϵ , it is possible for the membrane tension to balance (even locally) the curvature-elastic term in (3.5.30). When this balance occurs, the membrane tension can become negatively valued and locally flat sections of membrane become linearly unstable to large-wavenumber perturbations. [137] also showed that variations in the azimuthal curvature can become non-negligible and destabilizing when ϵ is not small.

3.11 Concluding remarks

A theory for the steady motion of a vesicle (of arbitrary reduced length ℓ) in a tube has been developed for small clearances $\epsilon \ll 1$. Two apparent shortcomings in the theory of [18] are resolved. Firstly, membrane bending elasticity was shown to affect (albeit modestly) the vesicle shape, vesicle mobility, and wall resistance, and this effect is enhanced when the ratio $(\frac{1}{2}\ell - 1)/\epsilon^{\frac{1}{2}} = O(1)$. Secondly, it was rigorously proven that $\Delta p^+ R/(\mu V)$ is of $O(\ell/\epsilon)$ [and not $O(\ell^3)$, as is claimed by Bruinsma] when $\frac{1}{2}\ell \gg 1$, in agreement with previous results for red blood cells [71] and surfactant-laden bubbles [23].

The results of the theory show that the relative velocity U/V and dimensionless extra pressure drop $\Delta p^+ R/(\mu V)$ strongly depend on the geometry of the flow system, but are only weakly affected by the strength of flow relative to membrane bending stiffness if $\beta = o(\epsilon^{-1})$. The viscosity contrast κ plays no appreciable role so long as $\kappa = o(\epsilon^{-\frac{1}{2}})$. By recasting the results in terms of *measurable* quantities v , λ , and β , it was possible to show that the relative velocity U/V and dimensionless extra pressure drop $\Delta p^+ R/(\mu V)$ are, to a good approximation, entirely specified by the confinement ratio λ/λ^* and the reduced volume v (or critical radius ratio λ^*) when $(1 - \lambda/\lambda^*) \ll 1$. The approximate interpolating formulas (3.9.1) supply the correct asymptotic behavior of U/V and $\Delta p^+ R/(\mu V)$ as $\lambda \rightarrow \lambda^*$. Comparison with experimental measurements and previous theories show good agreement, although the dearth of available experimental data for the extra pressure drop is unfortunate.

Comparison of the present asymptotic model to direct numerical simulations show that errors in model amplify as the clearance parameter ϵ or reduced length ℓ become large. These errors are associated with the failure of the narrow-gap assumption at the rear tail of the vesicle. Higher-order perturbative corrections (beyond the first correction, which was computed) are difficult to obtain, as these require knowledge of the flow field in the outer region. A more direct approach to obtain more accurate prediction is to turn to direct numerical methods (rather than asymptotic methods) in order to solve the Stokes-flow problem. We apply such techniques in the next chapter for vesicles in circular-tube flow.

Chapter 4

Vesicles in wider tubes

4.1 Direct numerical calculations

In the previous chapter, we developed a rigorous theory using the method of matched asymptotic expansions for the motion of a vesicle in a circular Poiseuille flow in the limit where the ratio of the vesicle radius to the tube radius $\lambda = R_0/R$ approaches a critical value λ^* (recall that $R_0 = \sqrt{A_0/(4\pi)}$ is defined with respect to the vesicle surface area A_0). The critical radius ratio λ^* is related to the vesicle reduced volume $v = \Omega_0 / (\frac{4}{3}\pi R_0^3)$ (Ω_0 being the vesicle volume) by the equation for a spherocylinder,

$$2v\lambda^{*3} - 3\lambda^{*2} + 1 = 0. \quad (3.1.10a)$$

For $\lambda > \lambda^*$, the vesicle cannot pass through the tube cleanly without rupturing. In the limit as $\lambda \rightarrow \lambda^*$, the thin film separating the vesicle membrane from the tube wall becomes vanishingly small compared to the tube radius. The asymptotic theory of the previous chapter produced the following predictions for the relative velocity U/V and dimensionless extra pressure drop $\Delta p^+R/(\mu V)$ as $\lambda \rightarrow \lambda^*$:

$$\frac{U}{V} = 1 + \frac{4}{3} \left(\frac{3\lambda^{*2} - 2}{4\lambda^{*2} - 3} \right) \left(1 - \frac{\lambda}{\lambda^*} \right) + O \left[\left(1 - \frac{\lambda}{\lambda^*} \right)^2 \right], \quad (3.9.1a)$$

$$\frac{\Delta p^+R}{\mu V} = 4(\lambda^{*2} - 1) \left(1 - \frac{\lambda}{\lambda^*} \right)^{-1} + \left(\frac{4\sqrt{2}\pi}{4\lambda^{*2} - 3} \right) \left(1 - \frac{\lambda}{\lambda^*} \right)^{-\frac{1}{2}} + O(1). \quad (3.9.1b)$$

These equations were obtained by approximating results for a wide range of values of λ^* , spanning “sphere-like” vesicles ($\lambda^* = 1$) to “spherocylinder-like” vesicles ($\lambda^* > 1$). The effect of bending elasticity, which can become relevant at low flow rates, is neglected in (3.9.1). Although the theory of the previous chapter is asymptotic in the limit $\lambda/\lambda^* \rightarrow 1$, the radius of convergence of the asymptotic series is extremely small due to the singular nature of the perturbation problem. As

such, this theory cannot yield quantitative results when the ratio λ/λ^* is sufficiently less than unity. Although some analytical progress is possible in the opposite limit ($\lambda/\lambda^* \rightarrow 0$) via small-deformation theory [32, 50], the resulting predictions are limited to nearly spherical vesicles and cannot be used to study a large shape configuration space. Therefore, direct numerical methods are vital to supply accurate predictions when $\lambda/\lambda^* = O(1)$.

From a computational point of view, predicting the motion of vesicles in conduit flow has remained a challenging task, mainly for two reasons. Firstly, vesicles that are suspended in a viscous flow are prone to shape transitions [85, 34, 181, 51] and shape instabilities [83, 183, 115, 116] due to nonlinearities associated with vesicle membrane incompressibility. These phenomena are further convoluted by the various numerical instabilities that can arise in a hydrodynamical computation, which are sometimes difficult to differentiate from actual “physical instabilities.” Secondly, bounded fluid-flow calculations typically require highly refined grids in order to resolve the hydrodynamic interaction between the vesicle surface and the wall boundary. As a result, these calculations can become computationally expensive. The latter issue is a general facet of all bounded suspension calculations. For example, [81] reported that the collective motion of droplets and rigid particles between two parallel plates could take up to months to resolve (very long residence times) using the boundary element method (BEM). Particle motion in conduit flow represents an even more challenging task due to enhanced particle-wall interactions, which result in an exponential decay of the velocity disturbance as a function of distance from the source. By contrast, the disturbance field in a parallel-plate geometry decays *algebraically*, as shown by [104].

Due to the aforementioned challenges, previous numerical studies on bounded vesicle suspensions have mainly focused on two-dimensional (2D) or axisymmetric geometries, specifically examining morphological (i.e., shape) changes due to confinement. As pointed out in an appendix by [157], the velocity disturbance produced in a 2D Poiseuille flow decays exponentially and, therefore, is somewhat analogous to the particle-wall interaction of a particle suspended in 3D circular Poiseuille flow. [88] reported a theoretical phase diagram of shapes for 2D vesicles in bounded channel flow. Although these authors reported some results for 3D vesicles (including evidence for asymmetric shapes), they concluded that the equivalent 3D calculations were “too time consuming” for systematic study. [6] examined the hydrodynamic interaction for a pair of vesicles, also focusing on a 2D geometry. [163] reported axisymmetric Stokes-flow simulations of vesicles in circular tubes, reproducing several of the shapes observed experimentally by [169]. Their method relies on the axisymmetric Green’s function of [161] and thus does not require discretization of the channel wall. However, in light of the asymmetric shapes reported by [88] and others, it is unclear that the axisymmetric geometry is an accurate reflection of the actual 3D motion of vesicles in wider tubes – that is, for motion less confined. Moreover, the relative velocity U/V and dimensionless extra pressure drop $\Delta p^+ R/(\mu V)$ was not reported in the study by [163].

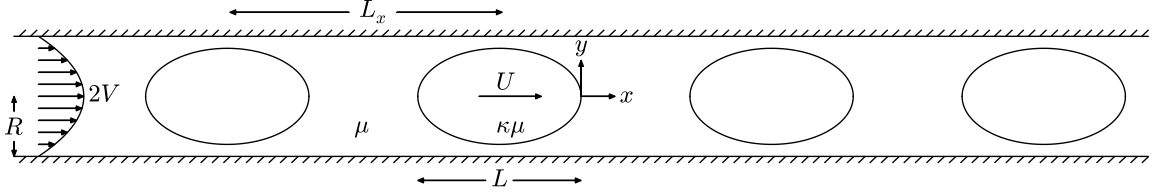


Figure 4.1: Schematic of a periodic train of identical vesicles in a circular tube. Only the $z = 0$ plane is shown. The system is rotationally symmetric about the x -axis at $t = 0$.

In the present chapter, the initial-boundary-value problem described in Chapter 2 is solved numerically using the BEM (§4.2). We focus our attention on the circular-tube geometry sketched in Figure 4.1, delaying consideration of non-circular conduits until Chapter 5. As shown in Figure 4.1, a periodic train of identical vesicles with uniform spacing in the axial direction is placed along the axis of a circular tube of radius R . The origin is placed at the tip of the front nose of a vesicle. The vesicles are oriented so that their initial configuration at time $t = 0$ is symmetric about the x -axis with spacing L_x between their centroids. Here, the vesicle-vesicle separation distance L_x supplants the suspension concentration c as an independent parameter, due to the assumed periodic configuration. The vesicle-vesicle separation is thus characterized by the dimensionless group,

$$\delta = \frac{L_x}{R} \quad (\text{the separation parameter}). \quad (2.5.9)$$

Periodic boundary conditions must replace the far-field boundary conditions (1.3.3) and (2.3.2), which specify, respectively, the extra pressure drop Δp^+ and mean channel velocity V for a channel of infinite length. Let \mathcal{S}_x denote a channel cross sectional surface excluding the interior (vesicle) fluid phase and \mathcal{S}_w the wall surface spanning a length L_x of the periodic domain. If the axial length of the vesicle is L , then the mean channel velocity is defined as,

$$VA_x \hat{\mathbf{e}}_x = \int_{\mathcal{S}_x} \mathbf{u} dS \quad \text{at } x + \frac{L}{2} = \pm \frac{L_x}{2}. \quad (4.1.2)$$

Equation (4.1.2) supplants (2.3.2) as the definition of V for periodic domains. The pressure drop across one periodic cell is defined as,

$$\Delta p A_x \hat{\mathbf{e}}_x = - \int_{\mathcal{S}_w} \mathbf{f}_w dS \quad \text{for } \mathcal{S}_w \text{ spanning } -\frac{L_x}{2} \leq x + \frac{L}{2} \leq +\frac{L_x}{2}, \quad (4.1.3)$$

which supplants (2.4.3). The “extra” contribution to the pressure drop induced by the vesicle suspension is

$$\Delta p^+ = \Delta p - L_x A_x K_{\text{hyd}} V, \quad (4.1.4)$$

which supplants (1.3.3). Equation (4.1.4) includes contributions from vesicle-vesicle hydrodynamic interactions. Since the velocity disturbance decays exponentially in circular-tube flow, these contributions will be dominated by pair interactions between neighboring vesicles in the periodic train.

The periodic configuration is an idealization of vesicle suspension flow through a conduit. In reality, the suspension configuration will depend on both the concentration and polydispersity of the suspension. Such effects are not the focus of the present chapter, nor is the stability of the assumed arrangement with respect to fluctuations in concentration. The justification for the periodic arrangement is that configurational changes in the suspension microstructure are expected to play a minor role in the hydrodynamics, as compared to the vesicle geometry and membrane mechanics.

The principal goal of this chapter is to examine the influence of the relevant dimensionless parameters on vesicle shape deformation and hydrodynamics in the confined geometry. Under moderate confinement, the numerical simulation technique accurately and efficiently solves the Stokes-flow problem for a wide variety of conditions. As confinement increases, regions of the fluid film become thin, demanding the use of sufficiently refined meshes to accurately capture the lubrication interaction. 3D numerical simulation techniques become impractical in this regime due to the high computational cost, even with the speedup gained by using a fast, matrix-free iterative solver. It is for this reason that a lubrication theory is also developed in this chapter (§4.3) in order to predict the vesicle motion under high confinement. The assumptions going into this theory are distinct from those made in the previous chapter, and it is shown that this theory accurately predicts the (most confined) BEM calculations and achieves the correct asymptotic behavior reported previously.

Although the focus of the present chapter is on the steady-state motion, it is demonstrated herein that the nonlinear evolution of the vesicle shape introduces temporal dynamics and symmetry breaking. These temporal variations in vesicle shape morphology typically result in only minor changes to the relative velocity U/V and dimensionless extra pressure drop $\Delta p^+ R / (\mu V)$. Consequently, while it is a rather laborious task to systematically map out the long-time dynamics of vesicle shape *morphology* in conduit flow, it is comparatively easier (and useful) to quantify the *hydrodynamics* over a wide parameter space with acceptable accuracy. Furthermore, it is shown that when vesicles are highly confined, their motion is steady and well described by lubrication theory.

The remainder of this chapter is organized as follows. The numerical method using the boundary integral formulation is discussed in §4.2. A lubrication theory is developed in §4.3 for concentric vesicles in circular tubes. A discussion of the numerical results is presented in §4.4. Concluding remarks are given in §4.5.

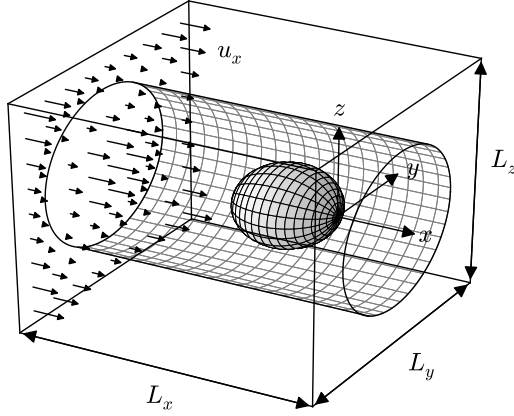


Figure 4.2: Schematic of the unit cell used in the 3D BEM simulations. The unit cell is periodically replicated in the x , y , and z directions.

4.2 Boundary element method (BEM)

The Stokes-flow problem described in Chapter 2 is solved using a previously reported boundary integral equation method [184, 182]. A summary of the method is outlined below. First, by use of Green's theorem, the fluid velocity inside a test volume \mathcal{V} can be represented by a convolution of point forces and point force dipoles distributed over the bounding surface $\partial\mathcal{V}$ [125]:

$$\begin{aligned} & -\frac{1}{8\pi\mu} \int_{\partial\mathcal{V}} \mathbf{f}(\mathbf{x}) \cdot \mathbf{G}(\mathbf{x}, \mathbf{x}_0) dS(\mathbf{x}) + \frac{1}{8\pi} \int_{\partial\mathcal{V}} \mathbf{u}(\mathbf{x}) \cdot \mathbf{T}(\mathbf{x}, \mathbf{x}_0) \cdot \hat{\mathbf{n}}(\mathbf{x}) dS(\mathbf{x}) \\ &= \begin{cases} 0 & \text{for } \mathbf{x}_0 \notin \mathcal{V}, \\ \mathbf{u}(\mathbf{x}_0) & \text{for } \mathbf{x}_0 \in \mathcal{V} \setminus \partial\mathcal{V}, \\ \frac{1}{2} \mathbf{C}(\mathbf{x}_0) \cdot \mathbf{u}(\mathbf{x}_0) & \text{for } \mathbf{x}_0 \in \partial\mathcal{V}, \end{cases} \quad (4.2.1) \end{aligned}$$

where $\mathbf{f} = \boldsymbol{\sigma} \cdot \hat{\mathbf{n}}$ is the surface traction, \mathbf{G} is the periodic fundamental (second-order) tensor for the velocity, \mathbf{T} is the periodic fundamental (third-order) tensor for the stress, and \mathbf{C} is the (second-order) principal-value tensor. (If the field point \mathbf{x}_0 lies on a Lyapunov smooth surface, then $\mathbf{C} = \boldsymbol{\delta}$.) The fundamental tensors (Green's functions) \mathbf{G} and \mathbf{T} are originally due to [73]. They are periodic in the x , y , and z directions with the lattice vector (L_x, L_y, L_z) , as shown in Figure 4.2. Expressions for these tensors are derived in Appendix D, which includes a practical discussion of their implementation in the boundary element context.

Since the channel wall is a no-slip surface, the addition of periodic boundary conditions in the y and z directions is inconsequential to the flow field inside the tube so long as $L_y > R$ and $L_z > R$.

(Verification tests were performed to ensure that the numerical results were insensitive to the box dimensions in the y and z directions.) Numerically, there is an advantage to using fully periodic boundary conditions in that the Green's functions may be rapidly computed by use of the Smooth Particle Mesh Ewald (SPME) algorithm [40, 134, 180].

Let \mathcal{S}_s and \mathcal{S}_w denote the membrane and wall surfaces, respectively. By taking the limit as the field point \mathbf{x}_0 approaches the boundary positions $\mathbf{x}_s \in \mathcal{S}_s$ and $\mathbf{x}_w \in \mathcal{S}_w$, we derive from (4.2.1) a system of boundary integral equations for the membrane surface velocity \mathbf{u}_s and wall surface traction \mathbf{f}_w . The result, expressed in matrix-vector form, is

$$\begin{bmatrix} \int_{\mathcal{S}_s} \mathcal{K}_{ss}(\mathbf{x}, \mathbf{x}_s) & \int_{\mathcal{S}_w} \mathcal{K}_{sw}(\mathbf{x}, \mathbf{x}_s) \\ \int_{\mathcal{S}_s} \mathcal{K}_{ws}(\mathbf{x}, \mathbf{x}_w) & \int_{\mathcal{S}_w} \mathcal{K}_{ww}(\mathbf{x}, \mathbf{x}_w) \end{bmatrix} \cdot \begin{bmatrix} \mathbf{u}_s(\mathbf{x}) \\ \mathbf{f}_w(\mathbf{x}) \end{bmatrix} dS(\mathbf{x}) = \begin{bmatrix} \mathbf{s}(\mathbf{x}_s) \\ \mathbf{s}(\mathbf{x}_w) \end{bmatrix}, \quad (4.2.2)$$

where

$$\begin{aligned} \mathcal{K}_{ss}(\mathbf{x}, \mathbf{x}_0) &= \frac{1+\kappa}{2} \delta(\mathbf{x} - \mathbf{x}_0) \mathcal{C}(\mathbf{x}) - \frac{1-\kappa}{8\pi} [\mathcal{T}(\mathbf{x}, \mathbf{x}_0) \cdot \hat{\mathbf{n}}(\mathbf{x})]^\dagger, \\ \mathcal{K}_{ws}(\mathbf{x}, \mathbf{x}_0) &= \frac{1}{8\pi\mu} \mathcal{G}(\mathbf{x}, \mathbf{x}_0), \\ \mathcal{K}_{sw}(\mathbf{x}, \mathbf{x}_0) &= -\frac{1-\kappa}{8\pi} [\mathcal{T}(\mathbf{x}, \mathbf{x}_0) \cdot \hat{\mathbf{n}}(\mathbf{x})]^\dagger, \\ \mathcal{K}_{ww}(\mathbf{x}, \mathbf{x}_0) &= \frac{1}{8\pi\mu} \mathcal{G}(\mathbf{x}, \mathbf{x}_0) \end{aligned}$$

are the kernels and

$$\mathbf{s}(\mathbf{x}_0) = -\frac{1}{8\pi\mu} \int_{\mathcal{S}_s} \mathbf{f}_s(\mathbf{x}) \cdot \mathcal{G}(\mathbf{x}, \mathbf{x}_0) dS(\mathbf{x}) + \langle \mathbf{u} \rangle$$

is the source. A subscripted “s” or “w” indicates that the quantity is evaluated on the surfaces \mathcal{S}_s or \mathcal{S}_w , respectively (the traction vectors \mathbf{f}_s and \mathbf{f}_w actually represent a *jump* in the surface traction across the membrane and wall, respectively). The volume-averaged velocity $\langle \mathbf{u} \rangle$ naturally appears in the source as a direct consequence of applying the divergence theorem to the surface integrals over the bounding surface of the periodic cell. A derivation of (4.2.1)-(4.2.2) is given in Appendix E.

The boundary integral equations (4.2.2) are solved for the membrane surface velocity \mathbf{u}_s and wall surface traction \mathbf{f}_w via the collocation method [179, 125]. Collocation points are placed at the vertices of unstructured, triangulated meshes approximating the surfaces \mathcal{S}_s and \mathcal{S}_w . Some of the unstructured meshes used in the presently reported simulations are shown in Figure 4.3. The wall mesh is discretized into N_w equally sized triangles (Figure 4.3a). The vesicle mesh is discretized into N_s triangles either by successive subdivision of an icosahedron (Figure 4.3b, appropriate for nearly spherical vesicles, for which the reduced volume v is close to unity) or by Loop subdivision

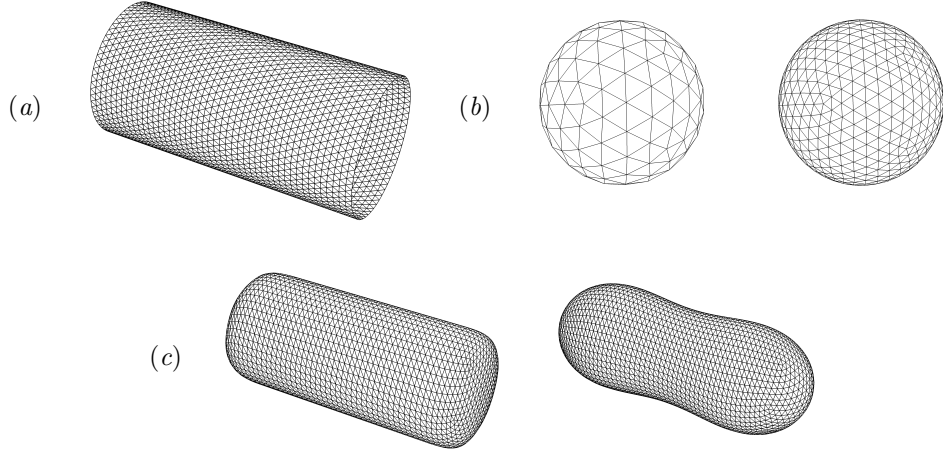


Figure 4.3: Unstructured meshes. (a) Tube wall surface \mathcal{S}_w of length $L_x = 4R$ discretized into $N_w = 5,796$ triangular elements. (b) Vesicle surface \mathcal{S}_s discretized into $N_s = 162$ (left) and 642 (right) triangular elements by successively subdividing an icosahedron four and eight times, respectively. This type of mesh is appropriate if the reduced volume v is close to unity. (c) Vesicle surface \mathcal{S}_s discretized into $N_s = 5,376$ triangular elements by first Loop subdividing a cylindrical surface (left) and subsequently relaxing the mesh in a Stokes-flow BEM simulation with $\langle \mathbf{u} \rangle = \mathbf{0}$ (right). This type of mesh is appropriate if the reduced volume v is far from unity.

of a cylindrical surface and subsequent mesh relaxation in a Stokes-flow simulation (Figure 4.3c, for “deflated” vesicles of reduced volume $v < 1$). The smooth subdivision method of [107] allows for high-fidelity calculation of membrane curvature for vesicles that are highly aspherical, which is necessary in order to accurately compute the membrane surface traction \mathbf{f}_s [151]. The latter is evaluated by a virtual work principle – i.e., by discretely evaluating the variational derivative of (1.2.1) with respect to a virtual displacement – as described in the appendix of [185].

The unknown density fields \mathbf{u}_s and \mathbf{f}_w are approximated by piecewise linear interpolants on the discretized surfaces \mathcal{S}_s and \mathcal{S}_w , respectively. The Green’s functions \mathcal{G} and \mathcal{T} are evaluated by the SPME method using a commercially available fast Fourier transform package. Numerical integration was carried out using a standard three-point quadrature (for regular kernels) or Duffy quadrature (for singular kernels) [37]. The discrete form of (4.2.2) (evaluated at the mesh vertices) is then solved using a matrix-free generalized minimal residual (GMRES) solver on distributed memory parallel computer architectures.

The membrane tension τ is determined by discretely satisfying (2.2.2), which requires that the area of a local surface patch on \mathcal{S}_s remain time invariant in the Lagrangian sense. Owing to numerical errors, the instantaneous membrane surface area A_0^* will evolve over time and is in general not exactly equal to the target value A_0 [183]. The error in the total surface area is controlled by adding a source

term $\dot{\epsilon}_{\text{area}} = (A_0/A_0^* - 1)/t_{\text{relax}}$ to the right-hand side of (2.2.2),

$$\nabla_s \cdot \mathbf{u}_s = \dot{\epsilon}_{\text{area}}, \quad (4.2.3)$$

where t_{relax} is a relaxation time chosen to control the relative change in surface area. If $A_0^* = A_0$, then $\dot{\epsilon}_{\text{area}} = 0$ and the membrane surface velocity \mathbf{u}_s is divergence-free (in the two dimensional sense) on \mathcal{S}_s . A predictor-corrector method is used to update the membrane velocity \mathbf{u}_s and tension τ such that (4.2.2) and (4.2.3) are both satisfied [185, 182]. The bending contribution to the membrane surface traction \mathbf{f}_s is computed implicitly via finite differences during the prediction step in order to preserve numerical stability [93]. In all of the simulations reported herein, the relative error $|A_0/A_0^* - 1|$ was constrained to within 10^{-4} by using $t_{\text{relax}}V/R = 1$.

Once a converged solution of (4.2.2)-(4.2.3) is obtained, the Lagrangian surface mesh is evolved in time using the discrete form of the kinematic condition (2.2.1). To formulate the right-hand side of (2.2.1), the vesicle translational velocity \mathbf{U} is first subtracted from the membrane velocity \mathbf{u}_s and the difference is subsequently projected into the local normal and tangent of each vertex. Following [106], the tangential components of \mathbf{u}_s are adjusted by a mesh relaxation velocity $\delta_s \cdot \mathbf{u}_s^* = \mathbf{u}_s - \hat{\mathbf{n}}(\hat{\mathbf{n}} \cdot \mathbf{u}_s^*)$ in order to correct local distortion of the mesh elements due to in-plane shear ($\delta_s = \delta - \hat{\mathbf{n}}\hat{\mathbf{n}}$ being the surface unit tensor). This adjustment is necessary to keep a close-to-uniform distribution of vertices in the surface mesh. Thus, (2.2.1) is modified to read,

$$\frac{D\mathbf{x}_s}{Dt} = \mathbf{U} + \hat{\mathbf{n}}[\hat{\mathbf{n}} \cdot (\mathbf{u}_s - \mathbf{U})] + \delta_s \cdot (\mathbf{u}_s - \mathbf{U} + \mathbf{u}_s^*). \quad (4.2.4)$$

The surface positions \mathbf{x}_s are advected using forward Euler timestepping. After the surface is advanced in time, the mesh points are adjusted so that the instantaneous vesicle volume Ω_0^* does not change by more than 1%. In practice, the relative error $|\Omega_0/\Omega_0^* - 1|$ is negligibly small.

Additional mesh control procedures, such as re-meshing or edge-swapping, were found to be unnecessary to preserve a high-quality mesh for the results shown herein. Numerical instabilities can develop in regions of high curvature (as is common for “weakly confined” vesicles at low reduced volumes $v \lesssim 0.85$) if the bending parameter β is small. In such cases, it is necessary to maintain a sufficient number of mesh points in regions of high curvature in order to stabilize high-wavenumber shape fluctuations.

The extra pressure drop is computed as $\Delta p^+ = -\langle \partial p / \partial x \rangle / (L_y L_z) - 8\mu V L_x / R^2$, where the mean pressure gradient $\langle \partial p / \partial x \rangle = -G$ is computed as a volume average over the periodic cell. The (axial component of the) vesicle translational velocity U is obtained by numerically integrating $\mathbf{x}(\hat{\mathbf{n}} \cdot \mathbf{u}_s)/\Omega_0$ over the discretized vesicle surface \mathcal{S}_s [cf. (2.4.1)]. In the simulation, the volume-averaged velocity $\langle \mathbf{u} \rangle$ is prescribed and the mean channel velocity V is obtained by assigning “probes” over a channel cross sectional surface of constant x and subsequently performing an areal average of $\hat{\mathbf{e}}_x \cdot \mathbf{u}_s$ over

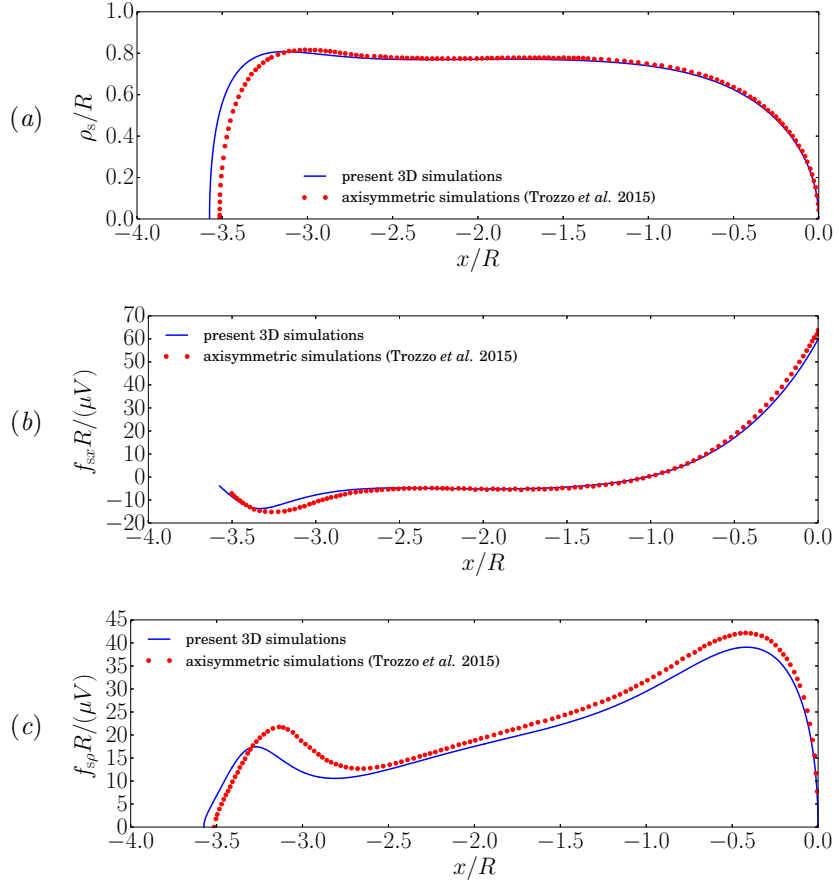


Figure 4.4: Comparison of the present 3D BEM simulations with the axisymmetric BEM simulations of [163], Figure 15a ($v = 0.84$, $\lambda = 1.2$, $\beta = 0.01$, $\kappa = 1$, $\delta = 10$). (a) Membrane radius ρ_s . (b) Axial component of the membrane surface traction f_{sx} . (c) Radial component of the membrane surface traction f_{sp} .

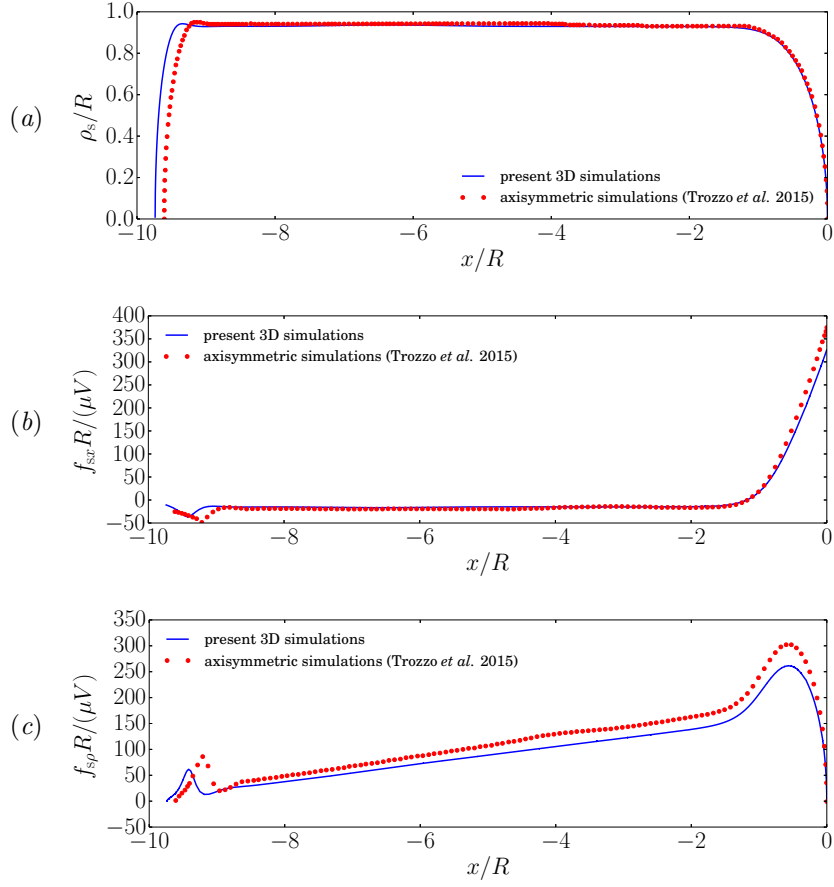


Figure 4.5: Comparison of the present 3D BEM simulations with the axisymmetric BEM simulations of [163], Figure 15b ($v = 0.61$, $\lambda = 2.1$, $\beta = 0.03$, $\kappa = 1$, $\delta = 10$). (a) Membrane radius ρ_s . (b) Axial component of the membrane surface traction f_{sx} . (b) Radial component of the membrane surface traction f_{sp} .

that surface [cf. (2.3.2)]. Since the simulation is time dependent, there is some cause for concern in prescribing a volume-averaged velocity $\langle \mathbf{u} \rangle$ instead of the channel velocity V – the system geometry can change in time, so the channel velocity V is not necessarily steady in the simulation! This issue may be circumvented by adjusting $\langle \mathbf{u} \rangle$ at each timestep such that V remains steady.

The present 3D BEM simulations were compared to the axisymmetric simulations of [163] in order to verify that the vesicle shape and membrane surface traction \mathbf{f}_s are accurately resolved. The comparisons in Figure 4.4-4.5 show excellent agreement – a significant improvement over the narrow-gap theory presented in the previous chapter (see Figure 3.11). The slight discrepancy between the two simulations is due to aforementioned numerical errors in discretely satisfying surface-area incompressibility at each timestep. Additional numerical experiments (not shown) were conducted in order to ensure that the relative velocity U/V and dimensionless extra pressure drop $\Delta p^+ R / (\mu V)$ were accurately computed using previously reported results for trains of rigid spheres in circular tubes [173].

4.3 Axisymmetric lubrication theory

The boundary integral equations (4.2.2) become numerically stiff when the gap thickness separating the vesicle membrane and the tube wall becomes small. The high number of mesh elements N_s and N_w required to accurately resolve the fluid flow in the thin gap renders the full simulation method computationally expensive due to the density of the BEM matrix. In the previous chapter, we developed a narrow-gap perturbation theory for the motion of a single vesicle in a circular tube for $(1 - \lambda/\lambda^*) \ll 1$, in view of the computational difficulties encountered in this regime. Unfortunately, the radius of convergence of the perturbative solution (in particular, the solution for the extra pressure drop) is very small, owing to the singular nature of the limit $\lambda/\lambda^* \rightarrow 1$.

An alternative approach, which was used by [139] to study red blood cells in capillary flow, is to assume that the fluid flow near the vesicle surface is *steady, axisymmetric, and nearly parallel*, the latter of which implies that all velocity components transverse to the flow axis can be neglected (and in turn all velocity gradients along the flow axis are vanishingly small). This approximation is appropriate if the gap thickness is small relative to the vesicle length L (but not necessarily small relative to the channel radius R). Under conditions of axisymmetry, the surface position vector \mathbf{x}_s has the Eulerian representation,

$$\mathbf{x}_s(\phi, x) = x\hat{\mathbf{e}}_x + \rho_s(x) \cos \phi \hat{\mathbf{e}}_y + \rho_s(x) \sin \phi \hat{\mathbf{e}}_z, \quad (4.3.1)$$

where $\rho = \sqrt{y^2 + z^2}$ is the radius of a cylinder, $\phi = \arctan(z/y)$ is the azimuthal angle, and $\rho = \rho_s(x)$ defines the location of the vesicle membrane in space. The curvature invariants H and K

can be written entirely in terms of $\rho_s(x)$ and its derivatives:

$$2H = \frac{\rho_s^3}{G_s^3} \frac{d^2\rho_s}{dx^2} - \frac{1}{G_s}, \quad K = -\frac{\rho_s^3}{G_s^4} \frac{d^2\rho_s}{dx^2}. \quad (4.3.2)$$

where $G_s = \rho_s \sqrt{1 + (d\rho_s/dx)^2}$ is the surface metric (see also Appendix A.7.6).

Due to the assumed symmetry, the only admissible solution of (2.2.2) is a uniform velocity on the membrane. Hence, the vesicle behaves like a rigid body with velocity U whose shape must be determined from the membrane stress conditions. In the lubrication approximation, the axial velocity field u_x is governed by the boundary-value problem,

$$\frac{1}{\rho} \frac{\partial}{\partial \rho} \left(\rho \frac{\partial u_x}{\partial \rho} \right) = \frac{1}{\mu} \frac{dp}{dx}, \quad (4.3.3)$$

$$u_x = 0 \quad \text{at } \rho = R, \quad (4.3.4a)$$

$$u_x = U \quad \text{at } \rho = \rho_s(x), \quad (4.3.4b)$$

$$\int_{\rho_s(x)}^R 2\pi\rho(u_x - U) d\rho = \pi R^2(V - U). \quad (4.3.5)$$

Here, the axial velocity u_x depends parametrically on x only through variations in the membrane shape $\rho_s(x)$. Variations in p with respect to ρ are also neglected. Equations (4.3.3)-(4.3.5) may be directly solved to yield the Reynolds lubrication equation [79],

$$\frac{dp}{dx} = -\frac{8\mu}{R^2 - \rho_s^2} \left[R^2 V + \left(\frac{R^2 - \rho_s^2}{2 \log(\rho_s/R)} \right) U \right] \left[R^2 + \rho_s^2 + \frac{R^2 - \rho_s^2}{\log(\rho_s/R)} \right]^{-1}. \quad (4.3.6)$$

This expression governs the pressure gradient in the gap separating the membrane from the tube wall. The pressure inside the vesicle is of no consequence, and one may equivalently define p with respect to this pressure. Approximating the normal traction on the membrane by $-p$ and the shear traction by $\mu(\partial u_x/\partial \rho)$ (due to flow in the suspending fluid), the stress conditions at $\rho = \rho_s(x)$ reduce to a coupled system of *ordinary* differential equations with respect to the axial coordinate x :

$$2E_B \left[\frac{1}{G_s} \frac{d}{dx} \left(\frac{\rho_s^2}{G_s} \frac{dH}{dx} \right) + 2(H^2 - K)H \right] = 2H\tau - p, \quad (4.3.7)$$

$$\frac{\rho_s}{G_s} \frac{d\tau}{dx} = \frac{1}{4} \frac{dp}{dx} \left(2\rho_s + \frac{R^2 - \rho_s^2}{\rho_s \log(\rho_s/R)} \right) - \frac{\mu U}{\rho_s \log(\rho_s/R)}, \quad (4.3.8)$$

where $H(x)$ and $K(x)$ are related to $\rho_s(x)$ according to (4.3.2) and dp/dx is given by (4.3.6). It is worth noting that the normal stress condition (4.3.7) has been modified from the analogous expression in [139] by (i) correcting the bending stress term, as described by [138, 71], and (ii)

neglecting membrane shear elasticity, which is negligible for vesicles. The boundary conditions are the usual symmetry conditions at the poles:

$$\text{at } x = 0 : \quad \rho_s = 0, \quad \frac{\rho_s}{G_s} \frac{d\rho_s}{dx} = -1, \quad \frac{\rho_s}{G_s} \frac{dH}{dx} = 0, \quad (4.3.9a)$$

$$\text{at } x = -L : \quad \rho_s = 0, \quad \frac{\rho_s}{G_s} \frac{d\rho_s}{dx} = +1, \quad \frac{\rho_s}{G_s} \frac{dH}{dx} = 0, \quad (4.3.9b)$$

where L is the axial length of the vesicle (a free boundary). To close the problem, the enclosed volume and surface area are prescribed as integral constraints on $\rho_s(x)$:

$$\Omega_0 = \int_{-L}^0 \pi \rho_s^2 dx, \quad A_0 = \int_{-L}^0 2\pi G_s dx. \quad (4.3.10)$$

Equations (4.3.6)-(4.3.10) form a boundary-value problem for the pressure $p(x)$, membrane tension $\tau(x)$, and membrane radius $\rho_s(x)$. The vesicle velocity U and axial length L are uniquely determined for specified values of μ , R , V , E_B , Ω_0 , and A_0 (equivalently, we may specify the dimensionless groups λ , v , and β and set μ , R , and V equal to unity). The extra pressure drop Δp^+ is approximated as the extra pressure difference across the length of the vesicle, $\Delta p^+ \approx p|_{x=-L} - p|_{x=0} - 8\mu VL/R^2$.

Solutions of (4.3.6)-(4.3.10) can be multivalued functions of x when the rear tail of the vesicle develops concave curvature. Such situations are not uncommon for vesicles of low reduced volume. Multivalued solutions can be avoided by re-parametrizing the boundary-value problem in terms of the meridional arc length s [130, 139], which is related to x by the differential relation,

$$\rho_s ds = G_s dx. \quad (4.3.11)$$

Using s instead of x as the independent variable has the added benefit of regularizing the slope singularity at the poles $x = 0, -L$. One may additionally define the so-called “tilt angle” ϑ by the differential relations,

$$dx = \cos \vartheta ds, \quad d\rho_s = -\sin \vartheta ds, \quad (4.3.12)$$

whence (4.3.6)-(4.3.10) may be transformed into a system of first-order differential equations with respect to the meridional arc length s [130, 139]. For more details on this transformation, the reader is referred to Appendix F.1.

The axisymmetric lubrication equations (4.3.6)-(4.3.10) are expected to be good approximations if the membrane slope $|d\rho_s/dx|$ is sufficiently small. However, since the suspending fluid pressure p is typically large, these equations may be extended outside the “lubrication zone” without incurring much error [25]. The utility of this approximation is that the flow around the vesicle is completely specified in the lubrication approximation; the flow inside the vesicle is approximated as a rigid-body motion. Since the membrane traction is dominated by the relatively large lubrication stresses,

the hydrodynamic interaction between vesicles in a periodic train is negligible. Thus, the originally formulated periodic problem reduces to the consideration of a single vesicle.

Equations (4.3.6)-(4.3.10) are recast in dimensionless form and integrated numerically using the multiple shooting method [113, 154], which was introduced in §3.5.3. Details of the numerical method are given in Appendix F.1. In brief, the domain $-L \leq x \leq 0$ is divided into $O(10-100)$ segments separated by “shooting points” at which continuity conditions are applied. At the poles $x = 0$ and $-L$, the surface is approximated by a spherical section in order to avoid polar coordinate singularities. Numerical integration is carried out over each segment using a fourth-order Runge-Kutta scheme. Newton iteration with line search and backtracking is used to enforce the boundary and continuity conditions at the shooting points. The iteration is truncated when the norm of the subsequent Newton step or the norm of the function to be zeroed falls below 10^{-12} . Since the integral conditions (4.3.10) are enforced during the Newton iteration procedure, the vesicle volume Ω_0 and surface area A_0 always converge to the target values. In order to avoid numerical errors associated with the behavior of the solution near the boundaries, integration always proceeds away from the boundary points towards a “fitting point” located at the center of the domain. The solution is parametrized by the reduced volume v , radius ratio λ , and bending parameter β . The special case $\beta = 0$ (a regular limit) reduces the order of the system by two. The viscosity ratio κ and separation parameter δ do not appear in the lubrication approximation. Once a solution for a particular triplet (v, λ, β) is known, other solutions may be determined using the continuation method.

It is important to note the difference between the approach delineated in this section and that adopted in the previous chapter. In Chapter 3, we developed a formal perturbation theory in terms of a small parameter (the ratio of a characteristic gap thickness to the tube radius) in order to obtain asymptotic scalings for the vesicle shape, relative velocity, and extra pressure drop in the singular limit $\lambda \rightarrow \lambda^*$. This procedure invoked the method of matched asymptotic expansions in order to unify an “outer solution” in the bulk region, where viscous stresses are weak compared to membrane tension, to an “inner solution” in the boundary-layer region, where lubrication theory accurately approximates the flow field. While this method gives the correct asymptotic behavior, quantitative predictions are challenging due to the slow convergence of the perturbation series. Furthermore, higher-order corrections to the asymptotic theory (recall that we computed only the first correction) are difficult to compute due to the emergence of viscous stresses in the bulk region. In essence, the next-order correction to the outer solution requires knowledge of an axisymmetric Stokes flow with a singular line forcing at the matching point. This problem is compounded by the laborious matching procedure required at each order of the perturbation theory.

By contrast, in the present formulation one need only approximate the velocity as a unidirectional field *everywhere* in the flow domain in order to develop a solution. This approximation effectively

simplifies the Stokes-flow problem while leaving the full curvature terms in the normal stress condition for the eventual vesicle shape calculation. The axisymmetric lubrication theory has several advantages: (i) it resolves “all orders” in the narrow-gap parameter, which in turn regularizes the perturbation series; (ii) it exhibits the same asymptotic behavior as the narrow-gap theory in the limit $\lambda \rightarrow \lambda^*$ and, therefore, should approach our asymptotic prediction in that limit; and (iii) the vesicle shape is more accurately resolved due to the inclusion of all curvature terms in the normal stress condition (4.3.7), which is important for ratios λ/λ^* far from unity. Further discussion of the advantages of this method, as well as examples pertaining to rigid particles, red blood cells, and bubbles, can be found in earlier works [25, 139, 130].

4.4 Discussion of results

In the forthcoming discussion, the results of the 3D BEM simulations and axisymmetric lubrication theory are presented to give a cohesive picture of the effects of the dimensionless parameters on the flow fields, vesicle deformation, relative velocity, and extra pressure drop. Due to the large parameter space, it is instructive to focus on a specific regime. Particular attention is given here to cases where $\lambda/\lambda^* = O(1)$, such that wall effects are significant to the vesicle deformation. For sufficiently large λ , the vesicle train attains an axisymmetric steady-state configuration at long times. Local surface-area incompressibility thus requires a uniform membrane velocity, so the vesicle train behaves as a line of rigid particles. This result implies that the viscosity contrast κ will have no observable effect on the configuration if it is very nearly axisymmetric. For this reason, all results presented below are for $\kappa = 1$.

4.4.1 Flow fields

Representative flow fields are depicted in Figure 4.6 for trains of “sphere-like” vesicles under moderate confinement and various inter-vesicle spacings ($v = 0.99$, $\lambda = 0.7$, $\lambda/\lambda^* = 0.64$, $\delta = 1.5\text{-}10$). Flow fields for more elongated vesicles at roughly the same confinement ($v = 0.8$, $\lambda = 1$, $\lambda/\lambda^* = 0.61$, $\delta = 3\text{-}10$) are shown in Figure 4.7. In these simulations, $\beta = 0$ and $\kappa = 1$. The velocity vectors are drawn in a reference frame moving with the vesicle train at steady velocity U . As indicated previously, the interior fluid velocity is stagnant in the moving reference frame. Thus, the vesicle train resembles a line of rigid particles. The flow in the gap separating the vesicle membrane and the tube wall is a simple shear flow with a velocity gradient equal to the train velocity U divided by the gap thickness. As the separation parameter δ decreases to the point at which neighboring vesicles are closely spaced, the interstitial fluid between vesicles moves with the train velocity U .

Previous studies of periodic trains of rigid particles in bounded Poiseuille flow have shown that the relative velocity U/V is relatively insensitive to the value of the separation parameter δ [173, 25].

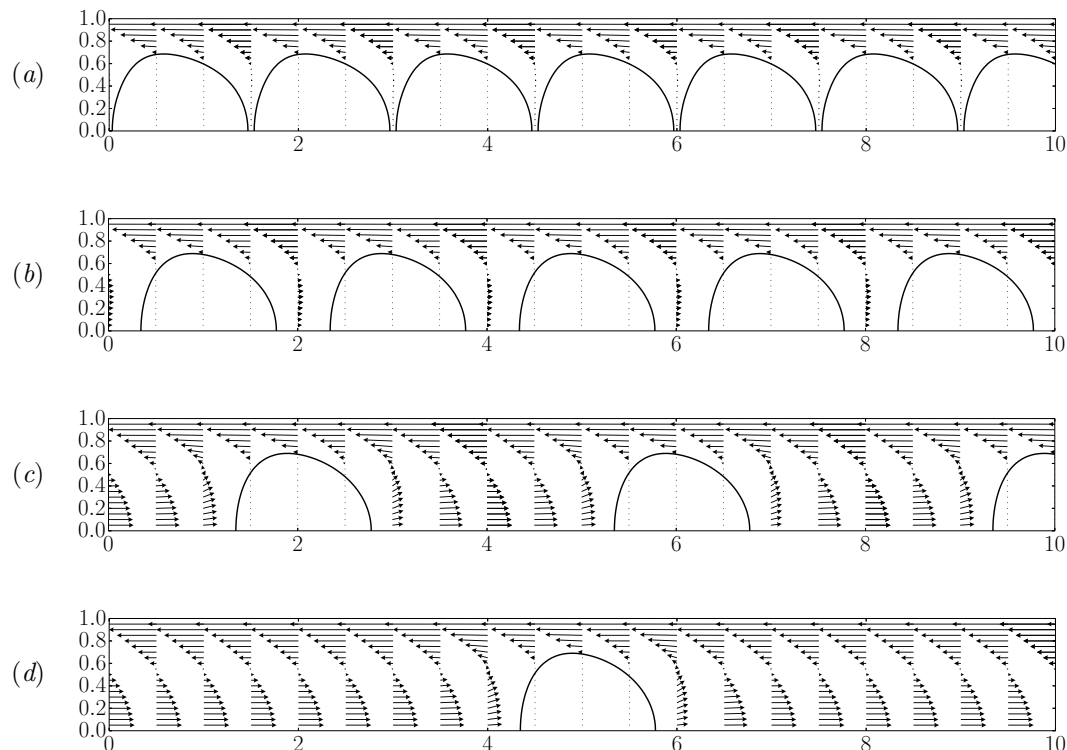


Figure 4.6: Velocity field from 3D BEM simulations. Results are shown for $v = 0.99$, $\lambda = 0.7$, $\beta = 0$, $\kappa = 1$, (a) $\delta = 1.5$, (b) $\delta = 2$, (c) $\delta = 4$, and (d) $\delta = 10$.

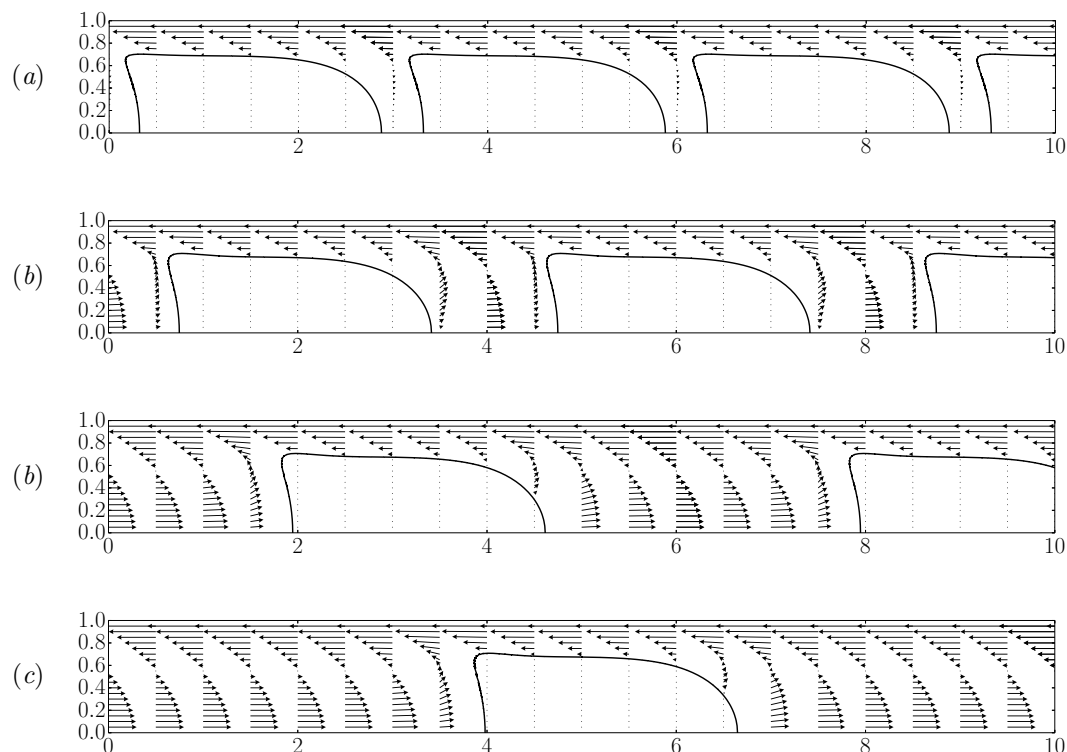


Figure 4.7: Velocity field from 3D BEM simulations. Results are shown for $v = 0.80$, $\lambda = 1$, $\beta = 0$, $\kappa = 1$, (a) $\delta = 3$, (b) $\delta = 4$, (c) $\delta = 6$, and (d) $\delta = 10$.

The present simulations verify this trend: vesicle trains in which the vesicles are either nearly touching ($\delta R \simeq L$, where L is the vesicle length) or well separated ($\delta R \gg L$) exhibit as large as a 2% difference in U/V . The corresponding change to the dimensionless pressure drop $\Delta p^+ R / (\mu V)$ is $O(1)$, which is negligible compared to the relative change with confinement. The insensitivity of these parameters to changes in δ is attributable to the exponentially decaying velocity disturbance in conduit flow, which limits the hydrodynamic interactions to pairwise interactions between nearest neighbors. Since the effect of δ on trains of rigid particles has already been studied extensively by other authors [173, 25], it will not be discussed further in this work. The remainder of this chapter is devoted to the parameter space that is unique to vesicles – namely, the interplay of confinement, reduced volume, and bending elasticity. Unless otherwise indicated, all simulations reported below are for $\delta = 10$ (all vesicle lengths L computed are smaller than $10R$). In these cases, vesicle-vesicle interactions may be safely neglected and one need only consider a single vesicle.

4.4.2 Symmetry breaking and time-dependent states

In this section, some attention is given to the emergence of (rotationally) asymmetric and time-dependent states in the 3D BEM simulations. Such phenomena cannot be predicted using the lubrication approximation of §4.3, as steadiness and axisymmetry are assumed *a priori* in that theory. These assumptions are justified by the fact that, when the ratio λ/λ^* is sufficiently close to unity, cylindrical confinement suppresses the formation of asymmetric shape modes. However, when the reduced volume v and radius ratio λ are small enough (criteria to be made more precise in due course), an initially axisymmetric vesicle may in fact break symmetry even though the imposed flow field is axisymmetric.

Before proceeding any further, it is instructive to review previously published studies of vesicle shape dynamics in Poiseuille flows. [32] published the first small-deformation theory for vesicles in quadratic flow fields, focusing on the migration phenomenon when the vesicle is displaced from the flow centerline. In this situation, the flow field is dominated by the shear contribution and the quadratic part supplies only a weak correction. [50] later reported a phase diagram for vesicle shapes parametrized by the bending parameter β (defined in their paper as the reciprocal of a “bending capillary number”), again using small-deformation theory. They reported only axisymmetric shapes when the vesicle is on the centerline and asymmetric shapes when off the centerline. The former results were later confirmed by experiments of [27]. Later, [52] conducted 3D BEM simulations and reported symmetry-breaking vesicle shapes – including the so-called “croissant” and “slipper” shapes – at the centerline of unbounded, circular Poiseuille flow when the bending parameter β is sufficiently large. As β was decreased, the axisymmetric state was recovered in their simulations.

All of the aforementioned studies focused on vesicles of reduced volumes v near unity. [88] and later [7] employed the 2D boundary integral method to map out the vesicle shape configuration

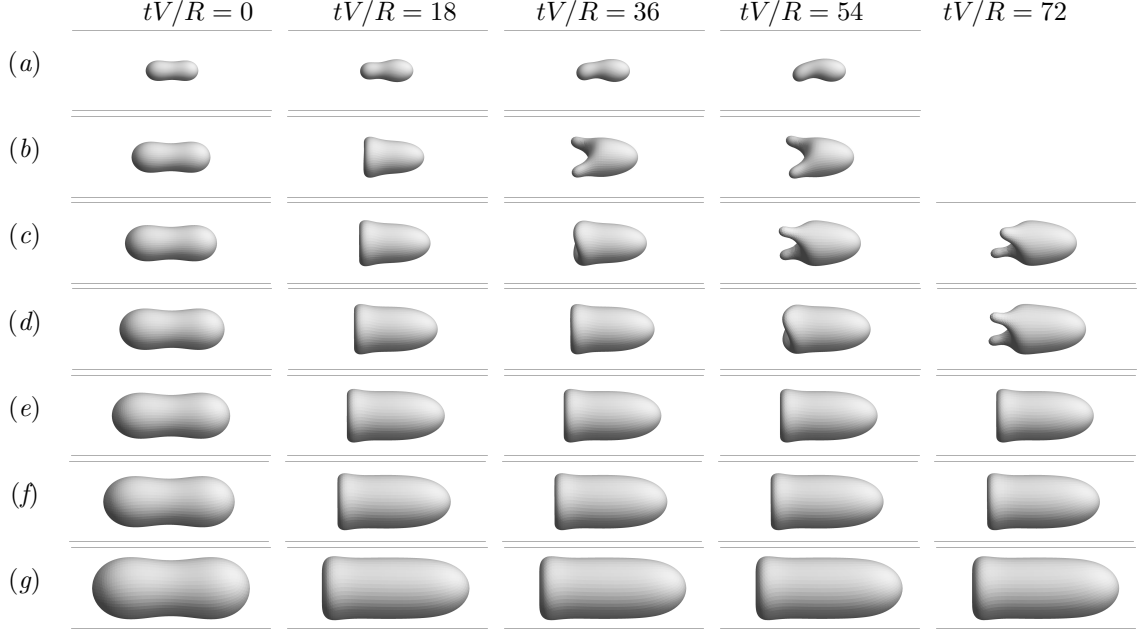


Figure 4.8: Time sequence of the vesicle shape evolved from an initially equilibrium configuration. Results were computed via 3D BEM for $v = 0.8$, $\kappa = 1$, $\beta = 0.02$, $\delta = 10$, $\lambda = (a) 0.4$, $(b) 0.6$, $(c) 0.7$, $(d) 0.8$, $(e) 0.9$, $(f) 1$, and $(g) 1.2$. At this reduced volume, $\lambda^* = 1.64$. Vesicles for which $\lambda < 0.9$ transition to an asymmetric secondary shape at longer times.

space for a wide range of the parameters v , λ , and β in the 2D geometry. These authors uncovered a rich phase space containing a variety of vesicle shape morphologies. Among these, 2D asymmetric shapes were observed for concentrically positioned vesicles of low reduced volume, including the slipper shape. [88] also reported some preliminary 3D calculations for *planar* Poiseuille flow, but provided only a sparse discussion of their results.

As pointed out by [88], determination of the phase diagram for 3D vesicle shape morphologies in *circular* Poiseuille flow remains a computationally intensive task. 3D computations take significantly longer to complete than the analogous 2D computations. Moreover, circular Poiseuille flow is a more intensive calculation than planar Poiseuille flow due to the enhanced vesicle-wall interactions. Compounding this increase in computational time are three issues. Firstly, the phase space for the nonlinear dynamical problem is vast, spanning all possible values of v , λ , and β (in addition to κ and δ). Secondly, the nonlinear shape evolution may be slow, requiring a prohibitively long time to reach steady-state. Lastly, it is not clear *a priori* whether a steady state exists or if the vesicle shape will become unstable. This latter concern is supported by the vast literature documenting the onset of shape instabilities in the presence of a straining field [83, 183, 115, 116].

As it is not the objective of this chapter to map out the entire phase diagram for the 3D geometry, only some of the salient features of the shape dynamics in 3D are presented here. These include long-time shape transitions from axisymmetric to asymmetric states when $v \lesssim 0.85$. A representative

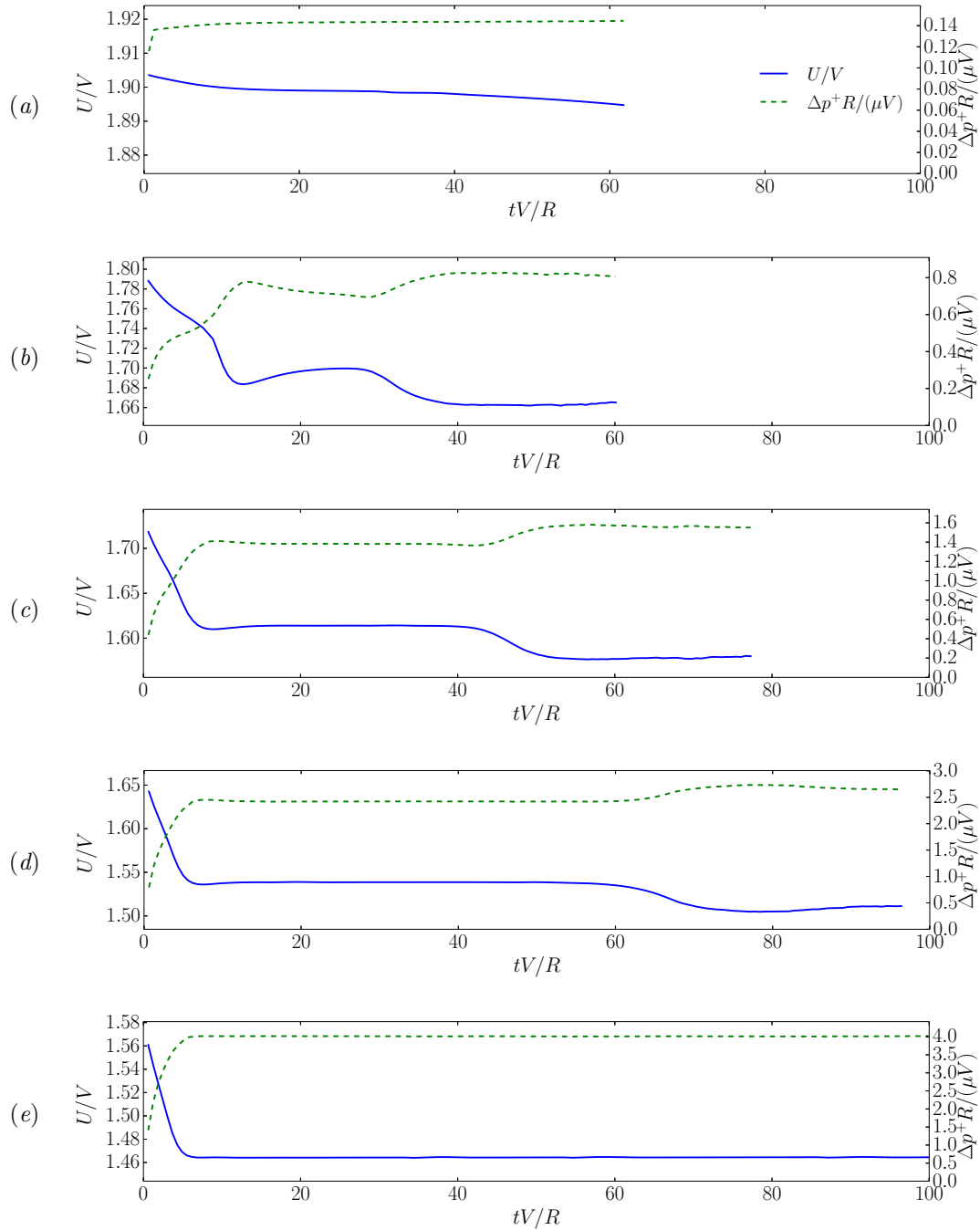


Figure 4.9: Caption on the following page.

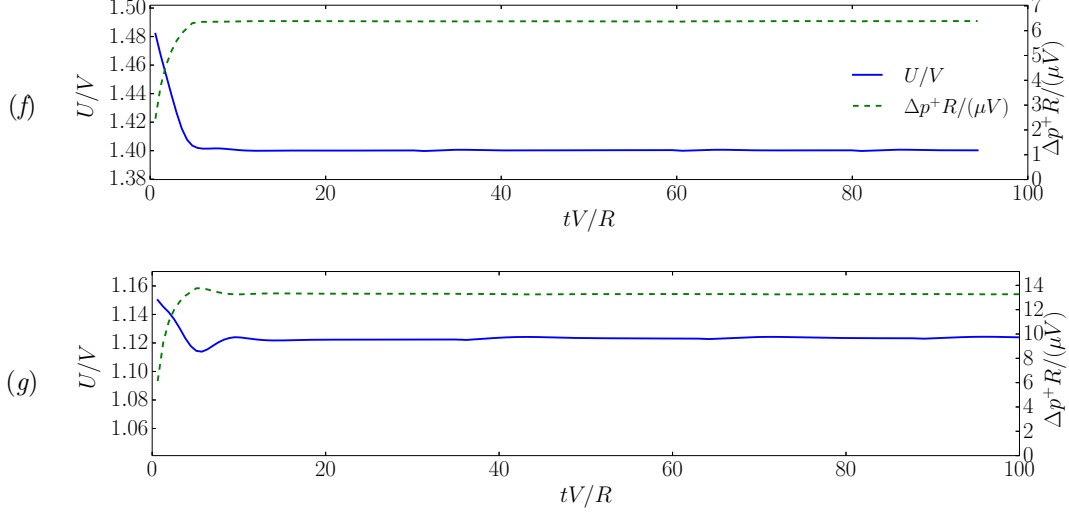


Figure 4.9: Time series of the relative velocity U/V and dimensionless extra pressure drop $\Delta p^+ R / (\mu V)$ for the 3D BEM simulations shown in Figure 4.8.

example is shown in Figure 4.8 for $v = 0.8$, $\beta = 0.02$, and various values of λ . At this reduced volume, the vesicle remains in a steady, axisymmetric configuration (up to $tV/R = 100$) for $\lambda > 0.9$ (the so-called ‘‘parachute’’ shape, shown in Figure 4.8e-g). However, once less confined the vesicle spontaneously breaks symmetry at later times, resulting in an asymmetric shape with two rear lobes that align along the local rate of extension (Figure 4.8b-d). The time at which this shape transition occurs depends on the degree of confinement. As can be seen from comparing Figure 4.8b, 4.8c, and 4.8d, increasing λ delays the onset of the transition. The existence of two ‘‘long-lived’’ states for this particular parameter set lends evidence for multiple fixed points of the (nonlinear) evolution equation for the surface position $\mathbf{x}_s(\mathbf{x}, t)$. Smaller vesicles (i.e., lower values of λ) exhibit different shape morphologies, including the slipper shape shown in Figure 4.8a. Similar observations were reported by [7] in 2D.

It is not clear whether or not the latter-stage states shown in Figure 4.8 for $\lambda < 0.9$ are steady. Literature precedent suggests that the rear lobes shown in Figure 4.8b-d will feel a local extensional field and therefore should elongate over time. Membrane curvature gradients drive this elongation (akin to the Rayleigh-Plateau instability), whereas finite bending resistance will confer a stabilizing effect [115]. As the local extensional field is relatively weak, the evolution of the secondary shape is slow (note, for instance, the small difference between time points $tV/R = 54$ and 72 in Figure 4.8c). The evolution of the slipper shape shown in Figure 4.8a is similarly slow (i.e., noticeable shape change occurs over 10-100 tV/R). In their 2D calculations, [7] reported that the slipper shape moves like a spermatozoon and exhibits period-doubling dynamics. It is expected that the simulations reported in Figure 4.8 would have to be continued for hundreds of dimensionless time

points tV/R in order to ascertain whether the system is steady or unstable (equivalent to weeks or months of computer time on a massively parallel supercomputer). In view of these possibilities, the term “long-lived state” is preferred over “steady state” to describe the latter-stage vesicle shapes in Figure 4.8*a-d*.

Time-dependent states and symmetry breaking are also observed at lower reduced volumes. For $v = 0.7$ and $\beta = 0.02$, a slight asymmetry in the membrane velocity profile induces tank-treading in the direction perpendicular to the flow axis when $\lambda \lesssim 1.2$. This in turn creates an “asymmetric parachute” shape akin to those predicted by [180] for red blood cells. The two-lobed shape is also observed at lower reduced volume, with the transition occurring around $\lambda \simeq 1.1$ for $v = 0.7$ (as compared to $\lambda \simeq 0.8$ for $v = 0.8$, shown in Figure 4.8*d*). Further discussion of these cases, as well as an exhaustive parametric study of the dynamics of vesicles in 3D bounded Poiseuille flows, is beyond the scope of the present work.

In order to gauge how the shape transitions reported in Figure 4.8 affect the Stokes disturbance field, the relative velocity U/V and dimensionless extra pressure drop $\Delta p^+ R/(\mu V)$ are plotted over time in Figure 4.9. The time-dependent shape transitions induce a 2-3% relative change in U/V and up to a 70% relative change in $\Delta p^+ R/(\mu V)$. However, it is worth emphasizing that these deviations are small compared to those incurred by increasing vesicle confinement. This is easily deduced by examining the scale of the ordinate in Figure 4.9*a-g*. The relative velocity U/V decreases in proportion to λ at an $O(1)$ rate, while the dimensionless extra pressure drop $\Delta p^+ R/(\mu V)$ increases precipitously (i.e., exponentially) with increasing λ .

From these observations, one may arrive at a rather intuitive conclusion: the detailed vesicle *shape* is less significant than its *size* in determining hydrodynamical figures of merit. Deviations in vesicle shape morphology induced by unsteadiness contribute relatively small corrections to U/V and $\Delta p^+ R/(\mu V)$ once the influence of the other dimensionless parameters are taken into account. Among these, the *geometric* parameters (v and λ) are expected to have the greatest impact. A comprehensive discussion of the effects of these parameters is presented in the next section. The influence of the bending parameter β is later examined in §4.4.4.

4.4.3 Effect of confinement and reduced volume

Figure 4.10 shows steady, axisymmetric vesicle shapes in bounded tube flow as computed via 3D BEM simulation and axisymmetric lubrication theory. For the range of reduced volumes v and radius ratios λ shown, no indications of unsteady behavior are observed within the timeframe of the simulation (up to $tV/R = 100$). The bending parameter is set to a small value $\beta = 0.02$ to minimize the effect of bending elasticity while also avoiding numerical instabilities associated with high-wavenumber shape fluctuations. Reduced volumes near unity are “sphere-like” and deform very little due to flow. As the reduced volume decreases at fixed confinement λ/λ^* , the vesicle

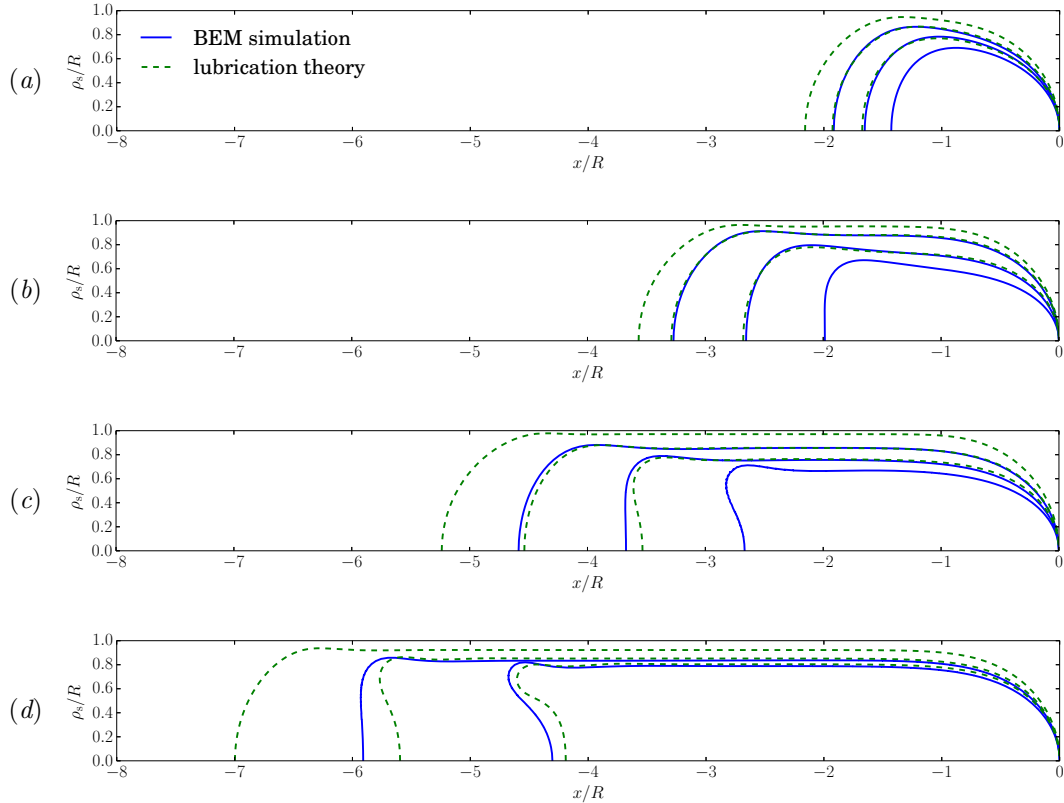


Figure 4.10: Vesicle shapes computed by 3D BEM simulation (solid lines) and axisymmetric lubrication theory (dashed lines) for $\kappa = 1$, $\beta = 0.02$, and $\delta = 10$. (a) $v = 0.99$, BEM: $\lambda = 0.9, 0.8, 0.7$; LT: $\lambda = 1, 0.9, 0.8$. (b) $v = 0.9$, BEM: $\lambda = 1.2, 1, 0.8$; LT: $\lambda = 1.3, 1.2, 1$. (c) $v = 0.8$, BEM: $\lambda = 1.4, 1.2, 1$; LT: $\lambda = 1.6, 1.4, 1.2$. (d) $v = 0.7$, BEM: $\lambda = 1.6, 1.4$; LT: $\lambda = 1.8, 1.6, 1.4$.

elongates and the rear tail of the vesicle can develop concave curvature. The lubrication theory does a remarkable job of reproducing the vesicle shape from the fully 3D BEM simulations. The error in the calculated shape increases as the reduced volume is decreased, with the maximum local error at the rear tail (as large as 5% for $v = 0.70$). There are two sources of error that can explain the discrepancy. The first is the relative change in surface area during shape evolution in the BEM simulations, which can result in global changes to the vesicle shape for a target surface area A_0 . Second, the Stokes velocity field at the rear end of the vesicle is approximated by a quasi-parallel flow in the lubrication approximation, which is not strictly valid. As shown in Figures 4.6-4.7, the flow near the front and rear ends is not exactly unidirectional. Non-parallel velocity components contribute additional normal and shear tractions [neglected in (4.3.7)-(4.3.8)], which in turn affect the membrane tension τ , pressure p , and vesicle shape. The error in neglecting these membrane tractions become increasingly significant as the rear tail develops concave curvature (typically, this occurs when $v \lesssim 0.85$ and $\lambda/\lambda^* \lesssim 0.85$).

The relative velocity U/V is plotted against λ for several values of v in Figure 4.11. In addition to the simulations that reached steady-state, unsteady results are plotted if the vesicle attains a “long-lived state” (i.e., marginal shape change occurs over $\sim 50 tV/R$). In these latter cases, error bars are used to indicate the maximum change in the relative velocity over time after the initial start-up period. The bending parameter is again kept small ($\beta = 0.02$) so that bending elasticity has a negligible effect on the Stokes flow. The experimental measurements of [169] are plotted for comparison and show excellent agreement with the simulation results for $v = 0.90-0.99$. Near $\lambda = \lambda^*$, the enormous number of mesh elements required in order to resolve the lubrication interaction renders the BEM simulation computationally infeasible. Fortunately, the axisymmetric lubrication theory nicely interpolates the simulation data with the asymptotic correlation (3.9.1a). Of particular note is the data for $v = 0.70$, wherein the lubrication theory accurately captures the transition from a “spherocylinder” shape to a “parachute” shape around $\lambda = 1.7$ (also shown in Figure 4.10d). This transition is accompanied by a sharp decrease in vesicle length and a comparably smaller change in the separation gap distance, which in turn decreases the rate of change of U/V with respect to λ . The asymptotic theory developed in Chapter 3, which assumes weak perturbations from the spherocylinder shape, cannot capture this shape transition.

The dimensionless extra pressure drop $\Delta p^+ R / (\mu V)$ is plotted against λ in Figure 4.12 for the same set of conditions reported in Figure 4.11. Again, error bars are used to quantify the maximum deviation after start-up when long-lived unsteadiness is observed in the BEM simulations. Unfortunately, no experimental results are available for this flow geometry. Again, the lubrication theory nicely interpolates the BEM simulation data with the asymptotic prediction (3.9.1b). This is a crucial improvement, because the drag is singular in the limit as $\lambda \rightarrow \lambda^*$. Consequently, the perturbative approximation (3.9.1b) with respect to the small parameter $(1 - \lambda/\lambda^*)$ overestimates

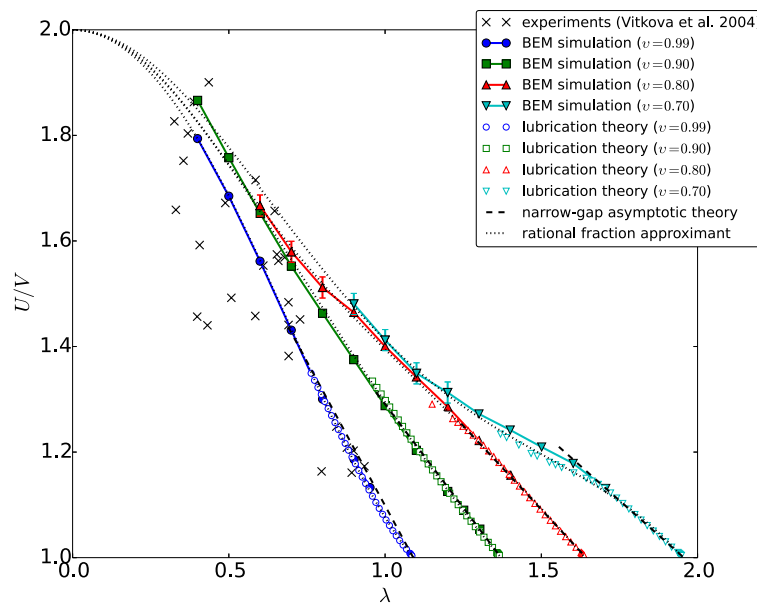


Figure 4.11: Relative velocity U/V plotted against the radius ratio λ for a range of reduced volumes v ($\kappa = 1$, $\beta = 0.02$, $\delta = 10$). Shown are the experimental measurements of [169], calculations via 3D BEM simulation and axisymmetric lubrication theory, the asymptotic correlation (3.9.1a), and the rational fraction approximant (4.4.2a) (dotted curves). Where appropriate, error bars are used to quantify the maximum change observed after start-up in the BEM simulations.

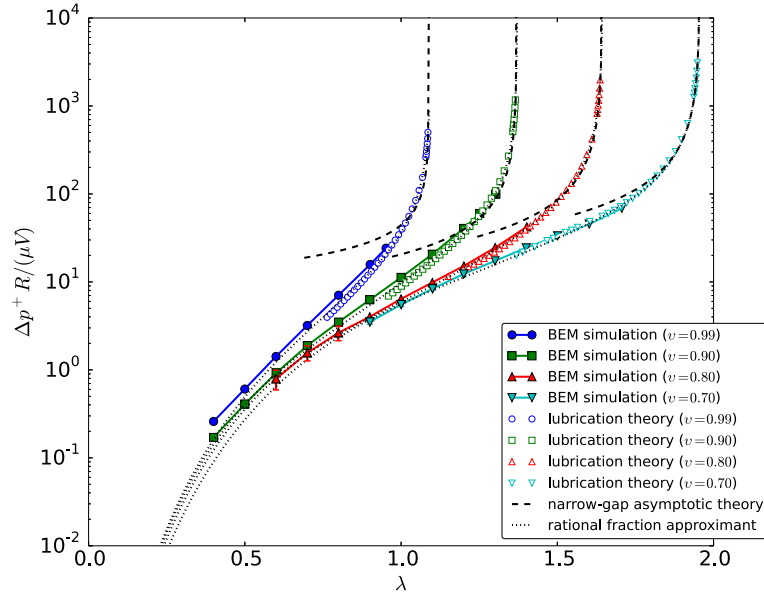


Figure 4.12: Dimensionless extra pressure drop $\Delta p^+ R / (\mu V)$ plotted against the radius ratio λ for a range of reduced volumes v ($\kappa = 1$, $\beta = 0.02$, $\delta = 10$). Shown are calculations from 3D BEM simulations, the axisymmetric lubrication theory, the asymptotic correlation (3.9.1b) (dashed curves), and the rational fraction approximant (4.4.2b) (dotted curves). Where appropriate, error bars are used to quantify the maximum change observed after start-up in the BEM simulations.

$\Delta p^+ R / (\mu V)$ when λ is not close to λ^* . The present lubrication theory, which makes no assumptions about the smallness of $(1 - \lambda/\lambda^*)$, introduces a negative correction.

Despite the wealth of numerical data presented in Figures 4.11-4.12, it is desirable to unify these results by means of interpolation formulas. “Admissible” interpolants are those which (i) follow the asymptotic predictions (3.9.1) as $\lambda/\lambda^* \rightarrow 1$; (ii) interpolate the numerical results from the 3D BEM simulations and axisymmetric lubrication theory; and (iii) exhibit the correct asymptotic behavior as $\lambda \rightarrow 0$. The latter asymptote represents the physical situation of a freely suspended vesicle in a tube wherein the vesicle radius is small compared to the tube radius. [32] studied this regime by means of small-deformation theory, but did not compute corrections to the relative velocity U/V or dimensionless extra pressure drop $\Delta p^+ R / (\mu V)$ as a result of deformation. As these corrections are expected to be relatively weak, as a first approximation one may replace the vesicle with a rigid sphere of the same diameter. Asymptotic approximations (in the limit $\lambda \rightarrow 0$) for rigid spheres in circular tubes are canonical [172, 16, 14]; the most relevant results are

$$\frac{U}{V} = 2 - \frac{4}{3} \left(v^{\frac{1}{3}} \lambda \right)^2 + O \left[\left(v^{\frac{1}{3}} \lambda \right)^3 \right], \quad (4.4.1a)$$

$$\frac{\Delta p^+ R}{\mu V} = 16 \left(v^{\frac{1}{3}} \lambda \right)^5 + O \left[\left(v^{\frac{1}{3}} \lambda \right)^{10} \right]. \quad (4.4.1b)$$

v	λ^*	a_1	a_2	b_1	b_2	c_1	c_2	c_3	d_1	d_2	d_3
0.99	1.090	2.11	0.45	2.05	-0.58	3.98	2.60	-0.62	2.46	2.47	-2.83
0.90	1.371	1.01	-0.10	0.13	-0.04	6.59	7.31	-8.94	2.95	3.46	-3.11
0.80	1.644	2.33	4.96	2.51	0.86	-0.93	8.40	-4.80	0.94	0.35	-0.27
0.70	1.956	-0.48	-0.01	-0.21	0.03	2.31	1.76	-1.51	1.96	-0.95	0.07

Table 4.1: Parameters a_n , b_n , c_n , and d_n used in the rational fraction approximants (4.4.2) (plotted as dotted curves in Figures 4.11-4.12), as determined by nonlinear least-squares regression. Also tabulated are the critical radius ratios λ^* for each reduced volume.

(Note that $v = 1$ for spheres.) In (4.4.1), the small parameter λ has been “stretched” by $v^{\frac{1}{3}}$ so that the dimensionless group $v^{\frac{1}{3}}\lambda = r_0/R$ represents the ratio of the vesicle’s *volumetric* radius $r_0 = [\Omega_0/(\frac{4}{3})]^{\frac{1}{2}}$ to the tube radius R . The volumetric radius r_0 is defined here as the radius of a sphere with the same volume as the vesicle.

Taking (4.4.1) as the leading-order approximation for small λ , utilize the BEM simulations, lubrication theory, and asymptotic formulas (3.9.1) in order to construct approximate correlations for the whole range of λ . There are many ways in which one may construct such correlations – e.g., rational fraction (Padé) approximants are quite popular [55]. The data shown in Figures 4.11-4.12 are nicely interpolated by rational fractions of the form,

$$\frac{U}{V} = 2 - \frac{4}{3} \left(v^{\frac{1}{3}} \lambda \right)^2 \left[\frac{1 + b_1 \lambda^2 + b_2 \lambda^4 + \dots}{1 + a_1 \lambda^2 + a_2 \lambda^4 + \dots} \right], \quad (4.4.2a)$$

$$\frac{\Delta p^+ R}{\mu V} = 16 \left(v^{\frac{1}{3}} \lambda \right)^5 \left[\frac{1 + d_1 \lambda^5 + d_2 \lambda^6 + \dots}{1 + c_1 \lambda^5 + c_2 \lambda^6 + \dots} \right], \quad (4.4.2b)$$

where the coefficients a_n , b_n , c_n , and d_n are chosen to give the best fit to the numerical data using nonlinear least-squares regression. These correlations are plotted as dotted curves in Figures 4.11-4.12 using the parameters shown in Table 4.1. The agreement with the numerical data is surprisingly good. It should be emphasized that the extrapolated predictions for small values of λ are only approximate; more detailed information about the lower asymptote is required to improve the predictions in this range.

4.4.4 Effect of membrane bending elasticity

In the previous chapter, we noted that membrane bending elasticity – measured by the bending parameter β – plays a minor role in disturbing the Stokes flow when λ/λ^* is close to unity. The reason for this relative insensitivity to β is that the available shape configuration space is restricted when the vesicle is near critical confinement. As λ decreases, it is expected that changing β will have a more pronounced effect on the disturbance field produced by the vesicle, which in turn will affect the relative velocity and dimensionless extra pressure drop.

The numerical challenges associated with computing the membrane bending stresses in (2.3.6)

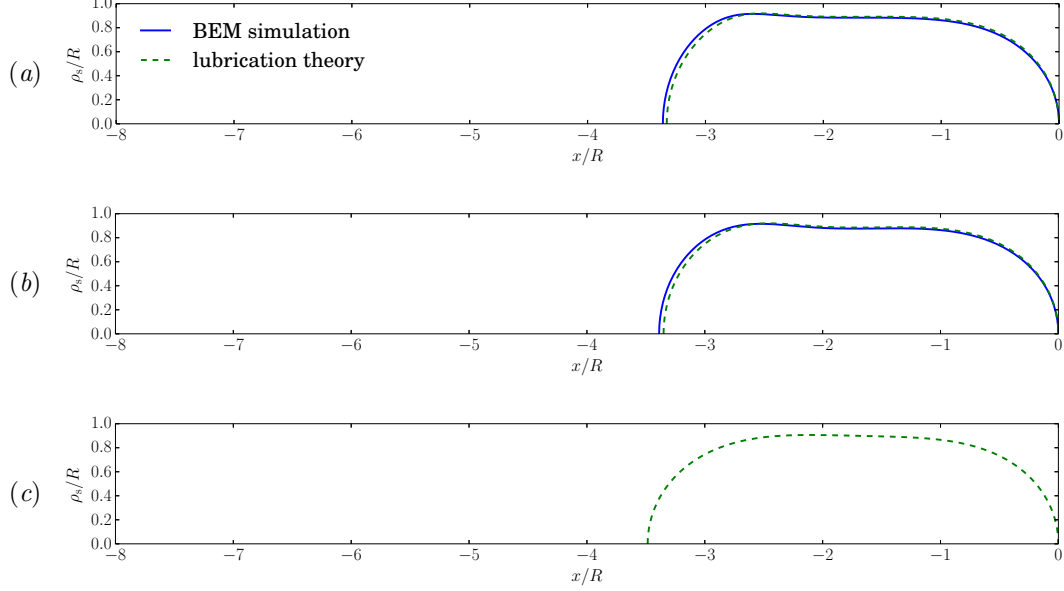


Figure 4.13: Vesicle shapes computed by 3D BEM simulation (solid lines) and axisymmetric lubrication theory (dashed lines) for $v = 0.90$, $\lambda = 1.22$, $\kappa = 1$, and $\delta = 10$. (a) $\beta = 0.02$. (b) $\beta = 2$. (c) $\beta = 200$.

are well documented [69]. These challenges originate from the need to numerically compute high-order derivatives of the surface position $\mathbf{x}_s(\mathbf{x}, t)$ in 3D. The scheme used in the present 3D BEM implementation relies on discretely evaluating the first variation of the Helfrich energy functional (1.2.1) using a smooth surrogate surface constructed by Loop subdivision [107, 185], with an error that scales linearly with mesh size [182]. It is possible to obtain accurate numerical simulations for $\beta = O(1)$ using this implementation. However, for large values of β (the “weak-flow regime”), the numerical fidelity of the method breaks down as the system becomes dominated by membrane bending stresses. Large values of β are therefore not accessible via 3D BEM. However, this latter regime is easily accessed using the aforementioned axisymmetric lubrication theory because the Laplace-Beltrami operator for the surface only requires computation of one-dimensional derivatives along the meridional contour. Since the full (axisymmetric) curvature operators are retained in (4.3.7), it is possible to resolve vesicle shapes very close to equilibrium. The limitation of this approach is that the accessible shape configuration space is now restricted to axisymmetric geometries. However, as shown previously, it is expected that the vesicle shape retains symmetry when it is highly confined. As this regime is of practical interest, the subsequent discussion will focus on confinement ratios λ/λ^* near unity.

Figures 4.13 and 4.14 show the effect of membrane bending elasticity on the vesicle shape for two different reduced volumes ($v = 0.90$ and 0.70) at high confinement. As the bending parameter β increases, the vesicle is forced towards its “equilibrium” configuration, which is both axisymmetric

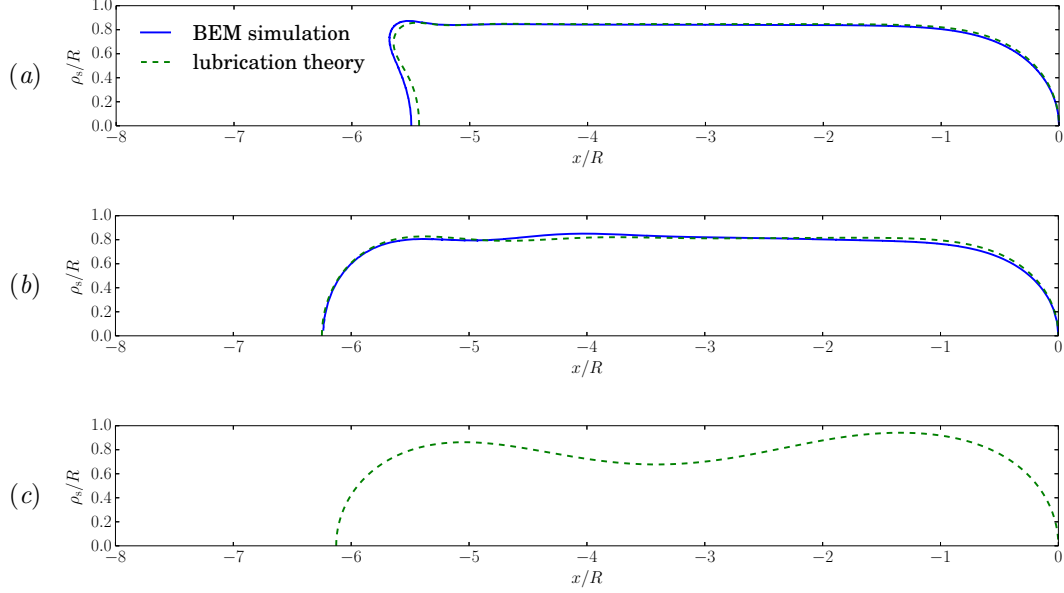


Figure 4.14: Vesicle shapes computed by 3D BEM simulation (solid lines) and axisymmetric lubrication theory (dashed lines) for $v = 0.70$, $\lambda = 1.58$, $\kappa = 1$, and $\delta = 10$. (a) $\beta = 0.02$. (b) $\beta = 2$. (c) $\beta = 200$.

and mirror-plane symmetric. A full catalog of equilibrium vesicle shapes has been documented by many authors, most notably by [141]. As was previously shown in §4.4.3, the accessible shape configuration space expands as the reduced volume v is decreased. Consequently, the shape change with increasing β illustrated in Figure 4.14 is far more dramatic than in Figure 4.13. Interestingly, the weak flow in Figure 4.14c results in lobe swelling at the downstream end of the vesicle. This phenomenon is akin to the “slider block effect,” wherein a negative pressure created by flow into a wedge creates suction between two surfaces [9].

It is expected that the shape transformations described above have a marked effect on the disturbance field. In Figure 4.15, the relative velocity U/V and dimensionless extra pressure drop $\Delta p^+ R / (\mu V)$ are plotted against the bending parameter β for three different confinement ratios λ/λ^* . All of the calculations presented in Figure 4.15 are via axisymmetric lubrication theory, through which large data sets spanning many decades in β can be obtained expeditiously. Clearly, the dependence of the hydrodynamic figures of merit on β is highly complex, especially at low reduced volume. This complexity stems from the large family of shape configurations that the vesicle is able to access at low reduced volume. In the remainder of this section, special attention given to each of the cases shown in Figure 4.15, with the aim of elucidating the competition between bending elasticity and viscous flow when vesicles are confined.

At low to moderate confinement (Figure 4.15a,b), the vesicle shape undergoes a transition at some intermediate value of β . The nature of this transition depends on the reduced volume v . At

high reduced volume ($v = 0.99$ and 0.90), the transition is characterized by a modest enhancement of vesicle mobility [i.e., an increase in U/V and decrease in $\Delta p^+ R/(\mu V)$]. On examining Figure 4.13, it becomes apparent that the vesicle shape near equilibrium (i.e., under weak flow) is more streamlined than the “pear” shape that develops under stronger flow conditions. In the latter situation, the rear end of the vesicle occludes a greater portion of the tube cross section, which in turn reduces its mobility.

At lower reduced volume ($v = 0.80$ and 0.70), the transitions are much more complex due to the larger family of shapes that are accessible (as shown in Figure 4.14). Still focusing for the time being on Figure 4.15*a,b*, it is apparent that increasing β can result in either a reduction *or* an enhancement of vesicle mobility when v is small. Typically, the “dumbbell” shape characteristic of low-reduced-volume vesicles at equilibrium ($\beta \rightarrow \infty$) is less streamlined than the “parachute” shape that forms under strong flow conditions ($\beta \rightarrow 0$). However, at some intermediate value of β the vesicle can be forced into a shape that occludes nearly the entire tube cross section, resulting in a local minimum value of U/V and maximum value of $\Delta p^+ R/(\mu V)$. For a given reduced volume v , the location of this extremum along the β -axis is shifted to higher values with increasing confinement ratio λ/λ^* .

At near-critical confinement (Figure 4.15*c*), the shape configuration space becomes highly restricted. Increasing β in this regime forces the vesicle into a shape that is geometrically prohibited by the tube boundary, resulting in very narrow separation distances. That is to say, the “equilibrium shape” that the vesicle would likely adopt in an unbounded, weak flow (as $\beta \rightarrow \infty$) cannot be accessed. Thus, a local extremum with respect to β is not observed for near-critical confinement. Rather, the vesicle mobility continues to drop with increasing β , in accordance with predictions made in the previous chapter.

4.5 Concluding remarks

The motion of vesicles in circular tubes has been studied using a combination of 3D BEM simulations and lubrication theory. The relative velocity U/V and dimensionless extra pressure drop $\Delta p^+ R/(\mu V)$ were computed as functions of reduced volume, confinement, and membrane bending stiffness. It was shown that the reduced volume v and radius ratio λ had the most pronounced impact on vesicle hydrodynamics. Decreasing v tends to “streamline” the vesicle body and hence increase U/V . Increasing the vesicle size tends to enhance the wall friction force and hence $\Delta p^+ R/(\mu V)$. Rational fraction approximants for U/V and $\Delta p^+ R/(\mu V)$ were developed [cf. (4.4.2)] and extend the correlations (3.9.1) derived in Chapter 3, which are asymptotically valid in the limit as the confinement ratio $\lambda/\lambda^* \rightarrow 1$. The latter correlation is appropriate when the vesicle shape is highly confined.

At lower values of v and λ , asymmetric vesicle shapes were observed. Some of these have no

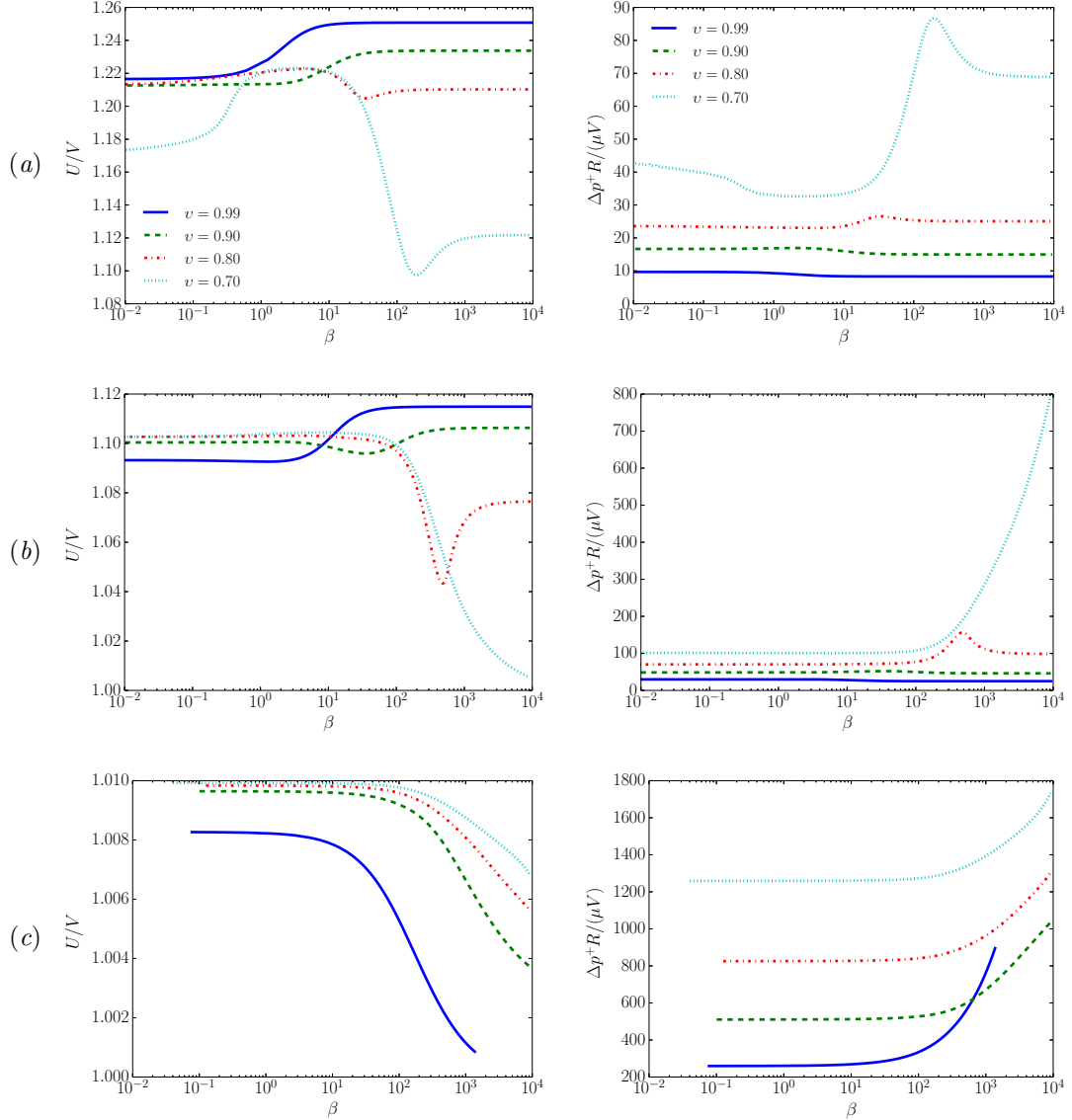


Figure 4.15: Relative velocity U/V and dimensionless extra pressure drop $\Delta p^+ R / (\mu V)$ plotted against the bending parameter β for several values of v and λ . All results shown were computed via axisymmetric lubrication theory. (a) $\lambda/\lambda^* = 0.8$. (b) $\lambda/\lambda^* = 0.9$. (c) $\lambda/\lambda^* = 0.99$.

analog in 2D and, to the best of the authors' knowledge, have not been reported elsewhere. It was shown that asymmetric modes can be excited after the start-up period, with a time delay (ranging from $\Delta t V/R = 1\text{-}10$) that depends on the degree of confinement. Various shape morphologies were observed, including the "slipper" shape and "two-lobed" shape, and continue to evolve in time. Despite this unsteadiness, the relative changes to the vesicle velocity and extra pressure drop were small compared to geometrically induced changes (i.e., changing the confinement or reduced volume). Further study into vesicle symmetry breaking in quadratic flows remains an open and interesting area, though it is beyond the scope of the present work.

Changing the separation parameter δ (equivalently, the suspension concentration c) had little effect on the morphology and hydrodynamics of the periodic train. By contrast, the bending parameter β has a marked impact – by increasing β , the vesicle tends to return to its "equilibrium shape" and significantly alters the geometry. The effect of bending stiffness is highly nonlinear and qualitatively dependent on the other dimensionless groups, as the reduced volume v and radius ratio λ effectively restricts the accessible shape configuration space. At high confinement (large λ), increasing β tends to increase the dissipation in the thin fluid layer, thus enhancing the wall drag and decreasing vesicle mobility.

The results of this study can be used in capillary-flow experiments to correlate hydrodynamical figures of merit – U/V and $\Delta p^+ R/(\mu V)$ – to vesicle shape deformation. Specifically, the strong dependence of these quantities on the reduced volume v and radius ratio λ suggests a means for accurately predicting v and λ by simultaneously measuring U/V and $\Delta p^+ R/(\mu V)$. Such measurements do not require advanced microscopy techniques and can be used in tandem with the results of this work – in particular, the correlations (4.4.2) – to extract important geometric information on a confined vesicle system. Uncertainties associated with shape asymmetries, unsteadiness, and membrane bending stiffness are also quantified in this chapter.

Chapter 5

Vesicles in square channels

5.1 Non-circular conduits

Up until this point, we have focused exclusively on circular tubes and have examined the effects of reduced volume, confinement, membrane bending elasticity, and hydrodynamic interactions on vesicle motion. In this chapter, we turn our attention to square ducts, a relevant geometry for microfluidics. Modern microfluidic devices have revolutionized experimental study of the transport and fluid dynamics of biological cells [110]. Virtually all microfluidic channels fabricated using soft photolithography have a rectangular cross section [178]. The main attraction of these devices is the relative ease with which they may be fabricated and the small volume of fluid sample required for experimentation. Consequently, many experiments may be conducted simultaneously at relatively low cost. Moreover, at length scales on the order of 10-100 μm , inertial forces are often negligible and hence microfluidic fluid flow typically is in the Stokes regime [153].

Unfortunately, theoretical studies of particulate flow through non-circular conduits are relatively sparse in the literature [176, 177, 164]. (The closely analogous “plane-Poiseuille flow” is not included in this group, since the areal cross section is not well defined and thus the quantities U/V and $\Delta p^+ R/(\mu V)$ cease to have meaning.) Theoretical analysis of particulate flow through non-circular channels is challenging due to the lack of geometric symmetries. In the circular-tube geometry, we found a region of the parameter space where the vesicle shape remained rotationally symmetric about the channel axis. Thus, solutions of the initial-boundary-value problem could be obtained by considering only an azimuthal plane. One consequence of this reduction in dimensionality, as was pointed out in the beginning Chapter 3, is that the membrane flow field must be uniform in order to satisfy the surface-area-incompressibility constraint. Thus, a vesicle flowing through a circular tube behaves much like a rigid particle if sufficiently confined, with a shape that is determined through application of the normal-stress and kinematic conditions.

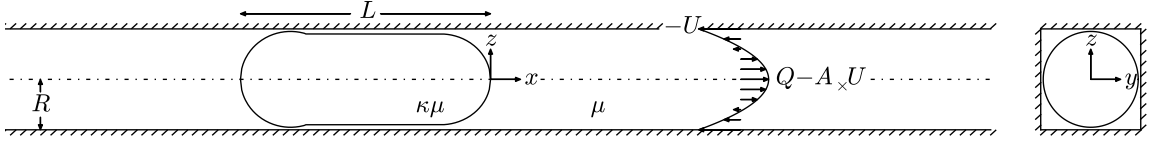


Figure 5.1: Schematic of a vesicle flowing through a square duct, as viewed from the xz and yz planes.

In non-circular conduits, the situation is qualitatively different. We can no longer reduce the geometry to an azimuthal plane; the initial-boundary-value problem must be solved in the fully 3D space. Moreover, the absence of rotational symmetry allows for the possibility of non-uniform membrane flow, breaking the connection to rigid-particle models. Two of our experimental collaborators have previously compared the relative velocity U/V of wax particles, vesicles, and cancer cells traveling through square ducts [3]. It was shown that the relative velocity of cancer cells is higher than that of solid particles but lower than that of vesicles for fixed radius ratio $\lambda = R_0/R$, presumably due to differences in surface mobility. The marked differences observed between these three systems, in addition to qualitative deviations from the circular-tube geometry, motivates additional experimentation as well as a theoretical complement.

We shall pursue the square-duct problem for a single vesicle (Figure 5.1), using the BEM as described in the previous chapter. Some remarks on the parameter space to be studied are in order. Unlike in previous chapters, bending elasticity will be neglected so that the only characteristic feature of the vesicles is that they have incompressible surfaces. We shall also assume that the interior and exterior fluids are the same. That is, we formally assume that,

$$\kappa = 1, \quad \beta = 0. \quad (5.1.1)$$

To avoid curvature singularities associated with cusps, we focus in this chapter on high reduced volumes: $0.85 \leq v \leq 1$.

Our theoretical methods are applicable to channels of arbitrary cross section; we focus here on ducts of polygonal cross section, with special attention paid to the square geometry. Table 1.2 lists the hydraulic resistivity and geometric parameters for various polygonal ducts. In addition to the BEM, which results in a numerical solution of Stokes' equations, we shall develop a new lubrication theory for the polygonal-duct geometry in order to obtain solutions at high flow confinement. We shall show that the pressure-driven motion of a vesicle in a square duct is qualitatively different from that in a circular tube. It turns out that the lubrication approximation introduces significant errors

at low confinement not previously observed for the circular-tube problem, due to the importance of velocity gradients along the azimuth neglected in the approximation. However, the lubrication theory is *essential* in order to perform calculations at high confinement, in which the “narrow-gap limit” is approached and the lubrication approximation is justified. BEM simulations are prohibitively expensive in this regime due to the high degree of resolution required for the surface meshes.

We shall compare our theoretical predictions to experimental measurements performed by the Ahmmmed, Vanapalli, and coworkers at Texas Tech University, using the “microfluidic manometer” (shown in Figure 1.7). This experimental apparatus has been previously used to study droplets, wax particles, and cancer cells [167, 91, 90]. The extra-pressure-drop measurements are most readily performed at high confinement, for this regime results in the largest pressure drops and hence the best “signal-to-noise ratio.” We show that the lubrication approximation yields excellent agreement between theory and experiment.

This chapter is organized as follows. In §5.2, we review the BEM and apply it to the Stokes flow of vesicles in square ducts. A non-axisymmetric lubrication theory is developed in §5.3 for a polygonal=duct geometry. The experimental protocol used for comparison (performed by our collaborators at Texas Tech University) is presented in §5.4. A discussion of the results, including comparison between theory and experiment, is presented in §5.5. Concluding remarks are given in §5.6.

5.2 BEM for non-circular conduits

The BEM was originally introduced in §4.2, with the derivation of the relevant equations given in Appendices D and E. For the sake of brevity, we shall not reiterate the equations here. Suffice it to say, the method is completely general for arbitrary geometries, and here we apply the method to the study of polygonal ducts with N sides. Some of the unstructured meshes used in this chapter are shown in Figure 5.2 for $N = 4$ (square ducts). The vesicle surface mesh is obtained by subdividing an icosahedron (Figure 5.2a); for lower reduced volumes, we map this surface onto a prolate spheroid. For the wall mesh, we employ both a straight-channel geometry (Figure 5.2b) as well as a contraction-expansion geometry (Figure 5.2c). The latter type of geometry is a realistic model for the microfluidic device used in the complementary experiments. We use the contraction-expansion geometry in order to determine the time to reach a fully developed state, which can then be compared to results obtained for infinitely long channels.

Since bending elasticity has been neglected and the viscosity ratio κ has been set equal to unity, the family of solutions is parametrized by the reduced volume v and radius ratio λ . Experimental measurements of the dimensionless extra pressure drop $\Delta p^+ R / (\mu V)$ typically require very small membrane-wall separation distances in order to achieve a good signal-to-noise ratio. As will later be

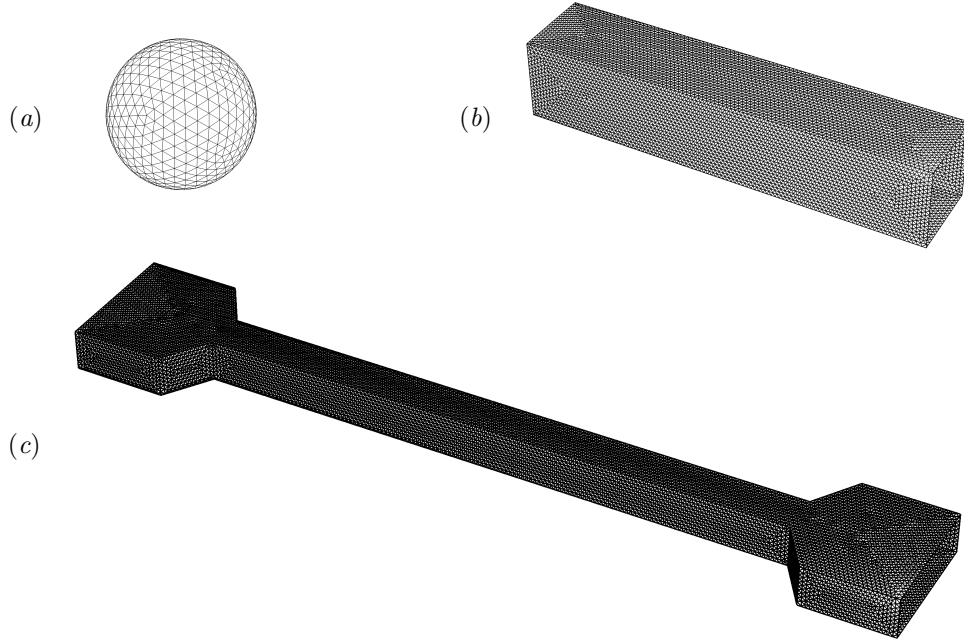


Figure 5.2: Unstructured surface meshes. (a) Vesicle surface \mathcal{I}_s for a sphere-like vesicle, generated by subdividing an icosahedron. (b) Wall surface \mathcal{I}_w for a straight conduit with a square cross section. (b) Wall surface \mathcal{I}_w for a contraction-expansion channel; the inlet and outlet are connected by a straight conduit with a square cross section.

shown in §5.4, the vesicles studied experimentally are highly confined, at radius ratios λ much higher than what is easily accessed via 3D BEM simulation. Lubrication layers result in ill-conditioning of the collocation matrix, and the hydrodynamic interaction between the membrane and channel wall becomes difficult to resolve with acceptable accuracy. This restriction suggests the use of an alternative approach in order to predict the motion of vesicles at high confinement, which is the subject of the next section.

5.3 Non-axisymmetric lubrication theory

Lubrication theory is a powerful means of regularizing the stress singularity that emerges when the distance between two boundaries separated by a viscous, flowing fluid becomes small compared to the lateral distance traveled by the fluid [9]. We applied lubrication theory to great effect in §4.3 for the circular-tube geometry, which allowed us to access a regime in confinement not accessible by BEM simulations. In the circular-tube problem, we showed that the maximum radius ratio λ^* is related to the reduced volume v by the geometric constraint,

$$2v\lambda^{*3} - 3\lambda^{*2} + 1 = 0 \quad (\text{circular tubes}). \quad (3.1.10a)$$

Equation (3.1.10a) is a simple cubic equation for λ^* that can be derived by first assuming the vesicle is a spherocylinder (the shape that conforms to the tube boundary), and then requiring that the radius of the spherocylinder be equal to the channel hydraulic radius R . By computing the surface area and volume of this shape, it is only a matter of algebra to arrive at (3.1.10a). The narrow-gap approximation considered in Chapter 3 for closely fitting vesicles in circular tubes is expected to be valid when the quantity $(1 - \lambda/\lambda^*)$ is small compared to unity.

For the square-duct geometry, the problem of determining the maximum vesicle size to fit inside the duct is not so simple because a spherocylindrical vesicle shape no longer conforms to the wall boundary. Nevertheless, one expects that there is indeed a critical radius ratio λ^* – for fixed reduced volume v – above which the radius ratio λ cannot exceed if the vesicle is to fit inside the duct. Furthermore, one expects that this critical value λ^* exceeds the analogous value for the circular tube geometry, because of the larger available cross-sectional area A_x . It is not the objective of the present study to calculate λ^* exactly for square ducts at any reduced volume, nor is it the objective to develop a rigorous perturbation theory for $(1 - \lambda/\lambda^*) \ll 1$ (as was done in Chapter 3 for the circular-tube geometry). Without performing such rigorous calculations, some of the salient features of a maximally sized vesicle in a square conduit can be deduced from physical intuition:

1. At the point of critical confinement $\lambda = \lambda^*$, portions of the vesicle membrane make “apparent contact” with the duct boundary. Other portions of the membrane are “free.”
2. The area of contact A^* between the membrane and the duct wall at $\lambda = \lambda^*$ depends on the reduced volume v . For example, at $v = 1$ (a spherical vesicle), it is obvious that the critical radius ratio is $\lambda^* = 1$ and membrane-wall contact is concentrated at four points. As v decreases from unity, these points of contact grow into surfaces.
3. At some reduced volume v below unity, the vesicle would presumably fill the entire space and occlude flow through the duct. Complete occlusion is clearly forbidden since the membrane would have infinite curvature at the corners of the duct. Wong, Radke, and Morris showed that, for bubbles in polygonal capillaries, there is a cutoff length scale α^{-1} that sets the surface curvature in the corner regions [175, 176, 177]. A similar length scale most likely exists for vesicles of low reduced volume, although this is beyond the scope of the present study.

A conclusion that can be drawn from item 2 above is that the applicability of the lubrication approximation strongly depends on the reduced volume v and radius ratio λ , because these parameters affect the available contact area A^* . Significantly, when v is close to unity, then the vesicle is quasi-spherical and the region of lubrication is concentrated at points. Since the study of [122] on the motion of rigid spheres translating parallel to plane walls, it has been well known that lubrication theory provides an accurate description of the *local* flow in the region of lubrication. However, the theory provides an inaccurate measure of *global* figures of merit (e.g., forces and force moments on a

particle) when the region of lubrication is concentrated at a point and not a surface. The failure of lubrication theory can be attributed to the strength of the surface force density (measured in units of $\mu V/R$) in comparison with the surface area (measured in units of R^2). In the region of lubrication, the contact area A^* is small, say $O(\epsilon)$ with $\epsilon \approx 1 - \lambda/\lambda^* \ll 1$, whereas the surface traction diverges, say with strength $O(\epsilon^{-1})$. The overall force moment is then $O(1)$. In the bulk region (outside the lubrication zone), the traction is $O(1)$ and the particle surface area is also $O(1)$, which results in an $O(1)$ contribution to the force moment. Since the lubrication and bulk regions are on “equal footing,” both are significant to the calculation of integral quantities of hydrodynamics. In relation to the present study, this means that lubrication theory is expected to supply a poor approximation of the dimensionless extra pressure drop $\Delta p^+ R / (\mu V)$ – which is computed from a force integral over the wall surface – when the reduced volume v is very close to unity. The situation qualitatively changes when the duct cross section is not a regular polygon but rather is circle. In the latter case, the region of lubrication between a large spherical particle and the duct boundary is concentrated at a contour (not a point) spanning the circumference of the cross section. Thus, a sphere translating through a circular tube has $O(\epsilon^{1/2})$ contact area with the wall and the resulting force moment [hence, the dimensionless extra pressure drop $\Delta p^+ R / (\mu V)$] is $O(\epsilon^{-1/2})$, a singular contribution for $\epsilon \ll 1$.

However, the situation again *qualitatively* changes when the reduced volume v is not very close to unity. For sufficiently large λ (close enough to the maximum value λ^*), the apparent contact area A^* at reduced volumes $v < 1$ is $O(1)$, giving an integral contribution to a force moment that is $O(\epsilon^{-1})$. We proved this result rigorously in Chapter 3 for vesicles in circular tubes – the dimensionless extra pressure drop $\Delta p^+ R / (\mu V)$ was shown to diverge like $\epsilon^{-1/2}$ for “sphere-like” vesicles and like ϵ^{-1} for “spherocylinder-like” vesicles at conditions of maximal confinement. In both of these cases, the “excess” relative velocity $U/V - 1$ is $O(\epsilon)$ and *always positive*, with a coefficient that depends on the vesicle shape at steady-state. For vesicles in the square-duct geometry considered presently, it is expected that lubrication theory provide the leading-order approximation, with errors that diminish as the apparent contact area A^* increases (i.e., the reduced volume v decreases). However, we also expect the membrane surface flow to be non-uniform, unlike in the circular-tube geometry. This effect can have two significant consequences. For one, the presence of non-uniform surface flow changes the shear stresses in the gap and hence the dimensionless extra pressure drop $\Delta p^+ R / (\mu V)$. The ability for flow to bypass the vesicle through the corner regions suggests that the pressure drop will be weaker in the square-duct geometry as compared to circular tubes. Second, the backflow in the region of lubrication indicates the possibility of the excess relative velocity $U/V - 1$ being *negative*. That is to say, a sufficiently large vesicle could travel at a velocity U slower than that of the mean flow V in a square duct.

The above discussion motivates the development of a new lubrication theory, in the same spirit

as the one developed in §4.3. In the previous chapter, we exploited the axisymmetry of the geometry in order to derive a system of ordinary differential equations (a one-dimensional boundary-value problem) for the membrane shape, pressure jump, and tension. These equations could be solved numerically using standard methods for ordinary differential equations (e.g., the multiple shooting method, described in Appendix F.1). However, in the square-duct problem the lubrication approximation yields a two-dimensional boundary-value problem governed by elliptic partial differential equations. Such equations cannot be integrated using shooting methods, so we apply the nonlinear finite difference method below to obtain a numerical solution (described in Appendix F.2). A derivation of the basic lubrication equations is presented in the next section.

5.3.1 Formulation

As in §4.3, cylindrical coordinates (ρ, ϕ, x) are conveniently adopted here. Recall that $\rho = \sqrt{y^2 + z^2}$ is the radial distance, $\phi = \arctan(z/y)$ the azimuthal angle, and x the axial distance. The lubrication theory will be generally formulated for a polygonal duct with N sides at steady state, assuming that the system has N -fold symmetry (i.e., the geometry possess reflectional symmetry at the planes $\phi = j\pi/N$, $j = 1, 2, \dots, 2N$). Unlike in the BEM, where the vesicle is given a Lagrangian representation, in the forthcoming development the surface position vector \mathbf{x}_s will be given the Eulerian representation,

$$\mathbf{x}_s(\phi, x) = x\hat{\mathbf{e}}_x + \rho_s(\phi, x) \cos \phi \hat{\mathbf{e}}_y + \rho_s(\phi, x) \sin \phi \hat{\mathbf{e}}_z, \quad (5.3.1)$$

where $\rho = \rho_s(\phi, x)$ defines the location of the vesicle membrane in space. The basic assumption of lubrication theory is to neglect velocity gradients in the ϕ and x directions and pressure gradients in the ρ direction. This assumption implies that spatial variations in the velocity field are most rapid in the transverse (ρ) direction as compared to the lateral (ϕ, x) directions. In this approximation, the relevant velocity components u_ϕ and u_x are governed by the simplified equations of motion,

$$\frac{\partial p}{\partial \rho} = 0, \quad (5.3.2a)$$

$$\frac{\partial p}{\partial \phi} = \mu \rho \frac{\partial}{\partial \rho} \left(\frac{1}{\rho} \frac{\partial}{\partial \rho} (\rho u_\phi) \right), \quad (5.3.2b)$$

$$\frac{\partial p}{\partial x} = \mu \frac{\partial}{\partial \rho} \left(\rho \frac{\partial u_x}{\partial \rho} \right), \quad (5.3.2c)$$

with boundary conditions (the no-slip condition on the wall and tangential stress balance condition on the membrane),

$$u_x = u_\phi = 0 \quad \text{at } \rho = R_\phi(\phi), \quad (5.3.3a)$$

$$\mu \rho \frac{\partial}{\partial \rho} \left(\frac{u_\phi}{\rho} \right) = - \frac{\partial \tau}{\partial s_\phi} \quad \text{at } \rho = \rho_s(\phi, x), \quad (5.3.3b)$$

$$\mu \frac{\partial u_x}{\partial \rho} = - \frac{\partial \tau}{\partial s_x} \quad \text{at } \rho = \rho_s(\phi, x). \quad (5.3.3c)$$

Here, $ds_\phi = \sqrt{\rho_s^2 + (\partial \rho_s / \partial \phi)^2} d\phi$ and $ds_x = \sqrt{1 + (\partial \rho_s / \partial x)^2} dx$ are the differential arc lengths along the azimuth and channel axis, respectively. The local duct radius $R_\phi(\phi)$ is given by,

$$R_\phi(\phi) = R \sec \phi, \quad 0 \leq \phi \leq \frac{\pi}{N}, \quad (5.3.4)$$

where $N = 4$ for a square duct. Due to symmetry, one need only consider the section of the domain bounded by $\phi = 0$ and $\phi = \pi/N$. It is expected that these equations supply a good approximation of the local flow conditions provided that $|\partial \rho_s / \partial x|$ and $|\partial \rho_s / \partial \phi|$ are not very large.

The pressure p must be determined by conserving volume in the suspending fluid. (Consideration of the fluid inside the vesicle is immaterial, since the shear rates in the suspending fluid are presumably much larger than those in the interior fluid for sufficiently narrow gaps.) Depth-averaging the equation of continuity and applying the kinematic condition for a *steady* vesicle shape ($\hat{n} \cdot \mathbf{u}_s = 0$) yields a local mass balance condition,

$$\frac{\partial}{\partial \phi} \left(\frac{q_\phi}{R} \right) + \frac{\partial q_x}{\partial x} = 0, \quad (5.3.5)$$

where

$$q_\phi = \int_{\rho_s(\phi, x)}^{R_\phi(\phi)} R u_\phi d\rho, \quad q_x = \int_{\rho_s(\phi, x)}^{R_\phi(\phi)} \rho (u_x - U) d\rho \quad (5.3.6)$$

are the leakback fluxes (here, the factor of R is introduced arbitrarily so that q_ϕ and q_x have the same dimensions). Multiplying (5.3.5) by $d\phi$, integrating from $\phi = 0$ to 2π , and applying periodicity conditions yields a macroscopic mass balance,

$$\int_0^{2\pi} q_x d\phi = \int_0^{\pi/N} 2N q_x d\phi = Q - A_\times U = A_\times (V - U), \quad (5.3.7)$$

where

$$A_\times = \int_0^{\pi/N} N R_\phi^2 d\phi \quad (5.3.8)$$

is the cross-sectional surface area. Equation (5.3.7) holds for all $-L \leq x \leq 0$, where L is the length of the vesicle (a free boundary). Obviously, the velocities U and V cannot be specified independently. Rather, by specifying one, the other must be determined as part of the solution to the boundary-value problem. In an experiment, the mean fluid velocity V is imposed and the vesicle velocity U is measured. Here, it is more convenient to specify U *a priori* and determine V *a posteriori*.

The membrane tension τ must also be determined, by conserving surface area locally on the membrane. This requirement is enforced by (2.2.2), which when written in cylindrical coordinates

(with $\hat{\mathbf{n}} \cdot \mathbf{u}_s = 0$) becomes,

$$\frac{1}{G_s} \frac{\partial}{\partial \phi} \left(\frac{G_s \bar{u}_{s\phi}}{\rho_s} \right) + \frac{1}{G_s} \frac{\partial}{\partial x} (G_s \bar{u}_{sx}) = 0, \quad (5.3.9)$$

where $G_s = \sqrt{\rho_s^2[1 + (\partial \rho_s / \partial x)^2] + (\partial \rho_s / \partial \phi)^2}$ is the surface metric and

$$\bar{u}_{s\phi} = u_\phi|_{\rho=\rho_s(\phi,x)}, \quad \bar{u}_{sx} = (u_x - U)|_{\rho=\rho_s(\phi,x)} \quad (5.3.10)$$

are the membrane slip velocities. (For more details on the differential geometry of surfaces in cylindrical coordinates, see Appendix A.7.2 with “z” replaced by “x.”) Multiplying (5.3.9) by $G_s d\phi$, integrating from $\phi = 0$ to 2π , and applying periodicity conditions gives,

$$\int_0^{2\pi} G_s \bar{u}_{sx} d\phi = \int_0^{\pi/N} 2NG_s \bar{u}_{sx} d\phi = 0. \quad (5.3.11)$$

The right-hand side of (5.3.11) has been set equal to zero by the requirement that the vesicle remain stationary in the moving reference frame. This condition holds for all $-L \leq x \leq 0$.

Equations (5.3.9)-(5.3.11) are exact at steady state, but require as input the local flow field \mathbf{u} . The lubrication approximation allows one to analytically compute the flow field by considering only the dominant shear stresses in the $x\rho$ and $\phi\rho$ planes. Thus, expressions for the components of the leakback flux vector \mathbf{q} and membrane slip velocity vector $\bar{\mathbf{u}}_s$ can be obtained directly by integrating (5.3.2)-(5.3.3) with respect to ρ :

$$\frac{q_\phi}{R} = \frac{m_\phi^{(qp)}}{\rho_s} \frac{\partial p}{\partial \phi} + m_\phi^{(q\tau)} \frac{\partial \tau}{\partial s_\phi}, \quad q_x = m_x^{(qp)} \frac{\partial p}{\partial x} + m_x^{(q\tau)} \frac{\partial \tau}{\partial s_x} - \frac{1}{2} U(R_\phi^2 - \rho_s^2), \quad (5.3.12a)$$

$$\frac{\bar{u}_{s\phi}}{\rho_s} = \frac{m_\phi^{(up)}}{\rho_s} \frac{\partial p}{\partial \phi} + m_\phi^{(u\tau)} \frac{\partial \tau}{\partial s_\phi}, \quad \bar{u}_{sx} = m_x^{(up)} \frac{\partial p}{\partial x} + m_x^{(u\tau)} \frac{\partial \tau}{\partial s_x} - U, \quad (5.3.12b)$$

where

$$m_\phi^{(qp)} = -\frac{R_\phi^3}{8\mu} \left[\frac{\rho_s}{R_\phi} - \frac{\rho_s^5}{R_\phi^5} + \frac{4\rho_s^3}{R_\phi^3} \log \left(\frac{\rho_s}{R_\phi} \right) \right], \quad (5.3.13a)$$

$$m_\phi^{(q\tau)} = -\frac{R_\phi^2}{4\mu} \left[\frac{\rho_s^2}{R_\phi^2} - \frac{\rho_s^4}{R_\phi^4} + \frac{2\rho_s^2}{R_\phi^2} \log \left(\frac{\rho_s}{R_\phi} \right) \right], \quad (5.3.13b)$$

$$m_x^{(qp)} = -\frac{R_\phi^4}{16\mu} \left[\left(1 - \frac{3\rho_s^2}{R_\phi^2} \right) \left(1 - \frac{\rho_s^2}{R_\phi^2} \right) - \frac{4\rho_s^4}{R_\phi^4} \log \left(\frac{\rho_s}{R_\phi} \right) \right], \quad (5.3.13c)$$

$$m_x^{(q\tau)} = \frac{R_\phi^3}{4\mu} \left[\frac{\rho_s}{R_\phi} - \frac{\rho_s^3}{R_\phi^3} + \frac{2\rho_s^3}{R_\phi^3} \log \left(\frac{\rho_s}{R_\phi} \right) \right], \quad (5.3.13d)$$

$$m_\phi^{(up)} = \frac{R_\phi}{4\mu} \left[\frac{\rho_s}{R_\phi} - \frac{\rho_s^3}{R_\phi^3} + \frac{2\rho_s}{R_\phi} \log \left(\frac{\rho_s}{R_\phi} \right) \right], \quad (5.3.13e)$$

$$m_{\phi}^{(u\tau)} = \frac{1}{2\mu} \left(1 - \frac{\rho_s^2}{R_{\phi}^2} \right) \quad (5.3.13f)$$

$$m_x^{(up)} = -\frac{R_{\phi}^2}{4\mu} \left[1 - \frac{\rho_s^2}{R_{\phi}^2} + \frac{2\rho_s^2}{R_{\phi}^2} \log \left(\frac{\rho_s}{R_{\phi}} \right) \right], \quad (5.3.13g)$$

$$m_x^{(u\tau)} = -\frac{\rho_s}{\mu} \log \left(\frac{\rho_s}{R_{\phi}} \right) \quad (5.3.13h)$$

are the mobility functions. Clearly, these functions depend only on μ , ρ_s , and R_{ϕ} . Inserting (5.3.12) into (5.3.5) and (5.3.9) yields two second-order PDEs for the unknown fields p and τ :

$$\begin{aligned} & \frac{\partial}{\partial \phi} \left(\frac{m_{\phi}^{(qp)}}{\rho_s} \frac{\partial p}{\partial \phi} \right) + \frac{\partial}{\partial x} \left(m_x^{(qp)} \frac{\partial p}{\partial x} \right) \\ & + \frac{\partial}{\partial \phi} \left(m_{\phi}^{(q\tau)} \frac{\partial \tau}{\partial s_{\phi}} \right) + \frac{\partial}{\partial x} \left(m_x^{(q\tau)} \frac{\partial \tau}{\partial s_x} \right) = \frac{\partial}{\partial x} [\frac{1}{2} U (R_{\phi}^2 - \rho_s^2)], \end{aligned} \quad (5.3.14)$$

$$\begin{aligned} & \frac{\partial}{\partial \phi} \left(\frac{G_s m_{\phi}^{(up)}}{\rho_s} \frac{\partial p}{\partial \phi} \right) + \frac{\partial}{\partial x} \left(G_s m_x^{(up)} \frac{\partial p}{\partial x} \right) \\ & + \frac{\partial}{\partial \phi} \left(G_s m_{\phi}^{(u\tau)} \frac{\partial \tau}{\partial s_{\phi}} \right) + \frac{\partial}{\partial x} \left(G_s m_x^{(u\tau)} \frac{\partial \tau}{\partial s_x} \right) = \frac{\partial}{\partial x} (G_s U). \end{aligned} \quad (5.3.15)$$

Although these equations are linear in p and τ , the boundary-value problem is nonlinear because the membrane radius ρ_s must also be determined as part of the solution. The governing PDE for ρ_s is the normal stress balance condition on the membrane:

$$\begin{aligned} & \frac{1}{G_s^3} \left\{ \rho_s \frac{\partial^2 \rho_s}{\partial x^2} \left[\rho_s^2 + \left(\frac{\partial \rho_s}{\partial \phi} \right)^2 \right] + \rho_s \frac{\partial^2 \rho_s}{\partial \phi^2} \left[1 + \left(\frac{\partial \rho_s}{\partial x} \right)^2 \right] - 2\rho_s \frac{\partial \rho_s}{\partial x} \frac{\partial \rho_s}{\partial \phi} \frac{\partial^2 \rho_s}{\partial x \partial \phi} \right. \\ & \left. - \left(\frac{\partial \rho_s}{\partial \phi} \right)^2 \right\} - \frac{1}{G_s} = \frac{p}{\tau}. \end{aligned} \quad (5.3.16)$$

The left-hand side of (5.3.16) is twice the mean curvature $2H$ expressed in cylindrical coordinates. The reference pressure is chosen to be the interior vesicle pressure (assumed spatially homogeneous), so that the pressure p the right-hand side of (5.3.16) approximates the jump in the normal component of the membrane surface traction.

Although, strictly speaking, the lubrication equations (5.3.14)-(5.3.16) are only valid in regions where the bounding surfaces are nearly parallel, we have previously found success in extending these equations outside the lubrication region under axisymmetric conditions (§4.3). The rationale behind this approach is to avoid the laborious matching procedure carried out in Chapter 3 between an “outer region” (where viscous flow is negligible) and an “inner region” (where the flow is well approximated by lubrication theory). Instead, by integrating equations (5.3.14)-(5.3.16) over the whole domain $-L \leq x \leq 0$ and $0 \leq \phi \leq \pi/N$, we both resolve the viscous flow in the inner region as well as the full membrane curvature in the outer region, with the matching occurring internally [130]. The basic justification for applying (5.3.14)-(5.3.16) outside the regions of lubrication hinges

on the assumption that errors made in approximating the flow field outside the lubrication zone are of little consequence to the shape deformation and force moment integrals. This assumption breaks down when the region of closest separation between the vesicle membrane and the duct wall degenerates to points, as was discussed at the beginning of this section. However, the applicability of lubrication theory in this case is altogether questionable, so this restriction is not a major concern.

Equations (5.3.14)-(5.3.16) are nonlinear, elliptic PDEs for the fields p , τ , and ρ_s . In applying these equations to the whole domain, boundary conditions are required at the planes $x = 0$, $x = -L$, $\phi = 0$, and $\phi = \pi/N$. Simple geometric considerations yield the following conditions:

$$\text{at } \phi = 0 : \quad \frac{\partial \rho_s}{\partial \phi} = 0, \quad \frac{\partial p}{\partial \phi} = 0, \quad \frac{\partial \tau}{\partial \phi} = 0, \quad (5.3.17a)$$

$$\text{at } \phi = \frac{\pi}{N} : \quad \frac{\partial \rho_s}{\partial \phi} = 0, \quad \frac{\partial p}{\partial \phi} = 0, \quad \frac{\partial \tau}{\partial \phi} = 0, \quad (5.3.17b)$$

$$\text{at } x = 0 : \quad \rho_s = 0, \quad \frac{\rho_s}{G_s} \frac{\partial \rho_s}{\partial x} = -1, \quad \frac{\partial}{\partial \phi} \left(\frac{p}{\tau} \right) = 0, \quad (5.3.17c)$$

$$\text{at } x = -L : \quad \rho_s = 0, \quad \frac{\rho_s}{G_s} \frac{\partial \rho_s}{\partial x} = +1, \quad \frac{\partial}{\partial \phi} \left(\frac{p}{\tau} \right) = 0. \quad (5.3.17d)$$

The integral conditions (5.3.7) and (5.3.11) are applied at some value of x (say, $x = -L/2$) in order to conserve the total rate of flow of volume and surface area. The vesicle volume Ω_0 and surface area A_0 are related to ρ_s by the integral equations,

$$\Omega_0 = \int_0^{\pi/N} \int_{-L}^0 N \rho_s^2 dx d\phi, \quad (5.3.18)$$

$$A_0 = \int_0^{\pi/N} \int_{-L}^0 2NG_s dx d\phi, \quad (5.3.19)$$

which must be satisfied simultaneously with (5.3.7), (5.3.11), and (5.3.14)-(5.3.17). The boundary-value problem is now closed. Once a solution for the fields p , τ , and ρ_s is obtained, the extra pressure drop Δp^+ is approximated by the difference in total pressure at the planes tangent to the front and rear ends of the vesicle:

$$\Delta p^+ \simeq \frac{1}{A_x} \int_0^{\pi/N} NR_\phi^2(p|_{x=-L} - p|_{x=0}) d\phi - LK_{hyd} A_x V. \quad (5.3.20)$$

Recall that $K_{hyd} = 1.78$ for a square duct ($N = 4$). Values of K_{hyd} for $N = 3, 4, 6$, and 12 can be found in Table 1.2. It is noteworthy that, although the derivation above was performed for a conduit whose cross section is a polygon with N sides, in principle this derivation could be applied to *any* cross section. The applicability of the lubrication solution, however, is inherently dependent on the validity of neglecting additional viscous stresses in (5.3.2)-(5.3.3).

As is common for problems in cylindrical coordinates, polar singularities occur at $x = 0$ and $-L$, resulting in a divergence of the membrane slope $|\partial \rho_s / \partial x| \sim |x|^{-\frac{1}{2}}$ near these points. Following [175],

a coordinate transformation removes the polar singularity:

$$x = -\frac{L}{2} (1 - \cos \xi), \quad \xi = \arccos \left(1 + \frac{2x}{L} \right), \quad (5.3.21)$$

where $0 \leq \xi \leq \pi$. The coordinate transformation (5.3.21) has the additional benefit of clustering grid points near $x = 0$ and $x = -L$, which in turn enables resolution of sharp gradients near the poles. Conversion between x - and ξ -operations (i.e., derivatives and integrals) is easily achieved via the chain rule. In the transformed domain, the polar singularity is removed by application of L'Hôpital's rule at $\xi = 0$ and π [175]. However, two additional concerns remain. Firstly, removing the polar singularity does nothing to alleviate the membrane shear stress singularity that results from the failure of the lubrication approximation at the poles. Although this latter kind of singularity cannot be removed, it is of little consequence to the solution of the boundary-value problem. The stresses computed via lubrication theory diverge within a very small region near the front nose and rear tail of the vesicle, and hence their overall contribution to the shape deformation and force moment integrals is negligible. Secondly, the one-to-one mapping between x and ξ excludes the possibility of multivalued solutions to the boundary value problem. Such solutions can occur, for instance, when the vesicle develops concave curvature in the rear end (the so-called “parachute shape”). This restriction is somewhat mild, however, as the vesicles considered in the present work have reduced volumes in the range $0.85 \leq v \leq 1$. Such vesicles are “sphere-like” and do not typically develop concave curvature under flow.

Equations (5.3.7), (5.3.11), and (5.3.14)-(5.3.19) were solved using the finite difference method (details of the numerical method are given in Appendix F.2). The poles $\xi = 0$ and π were excluded from the domain in order to avoid the stress singularity at these points. The membrane shape at the poles was approximated by a spherical section with constant curvature. The 2D domain was discretized into a uniform grid and second-order accurate spatial difference operators were used to approximate derivatives and integrals with respect to ϕ and ξ . Applying the difference analogy to the governing equations (5.3.7), (5.3.11), and (5.3.14)-(5.3.19) results in a system of nonlinear algebraic equations, which was subsequently solved iteratively using a Newton-Raphson procedure. For each Newton step, the Jacobian matrix was pre-computed analytically and subsequently discretized using finite differences (see Appendices F.2.1 for the linearization and F.2.1 for the discretization). Iteration proceeded until the merit function to be zeroed fell below 10^{-6} or the Newton step in the descent direction fell below 10^{-6} . Starting from some initial guess (e.g., solutions of the analogous axisymmetric problem, considered in the previous chapter), convergence was typically achieved in under 10 iterations. A family of solutions parametrized by v and λ were obtained using the continuation method. Typically, higher spatial resolution was necessary in order to achieve convergence for large values of λ .

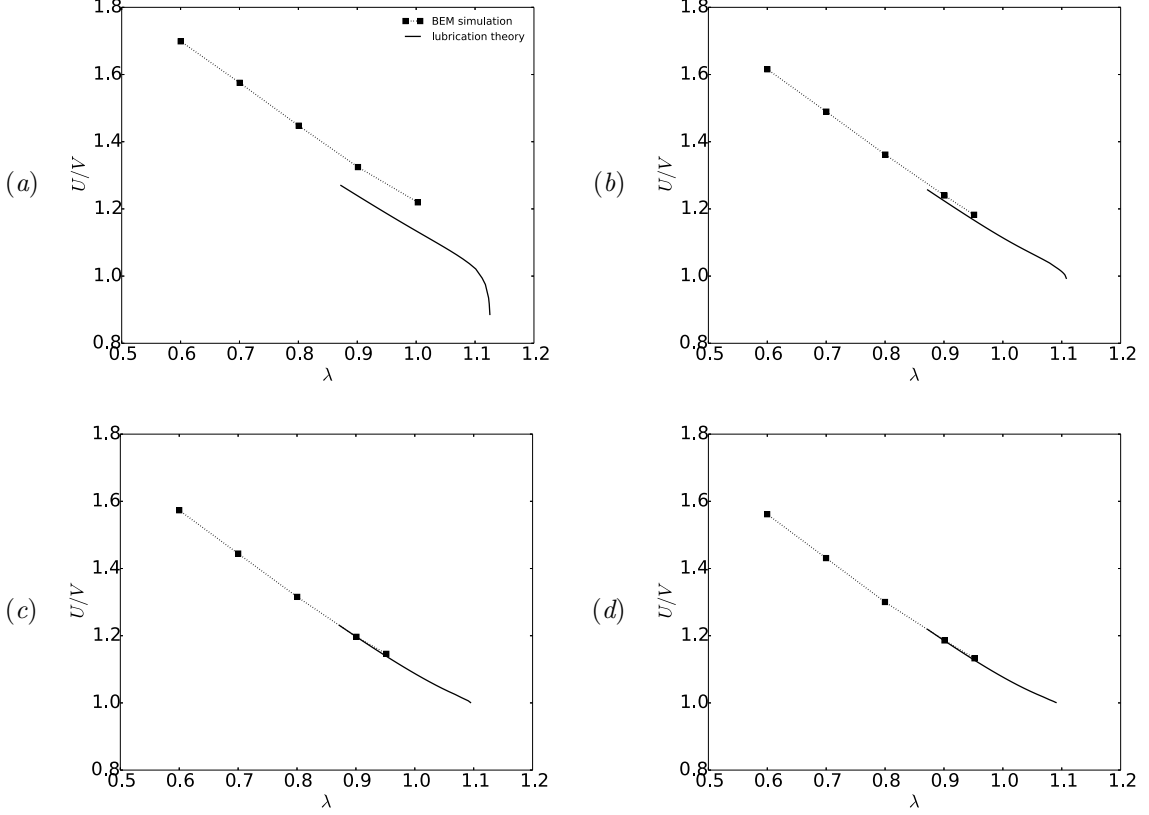


Figure 5.3: Relative velocity U/V plotted against the radius ratio λ for $v = 0.99$ and (a) $N = 4$ (square), (b) $N = 6$ (hexagon), (c) $N = 12$ (dodecagon), and (d) $N \rightarrow \infty$ (circle). The symbols are the BEM simulations, while the solid lines are the predictions from lubrication theory.

5.3.2 Error analysis

The lubrication approximation is not an exact solution of Stokes' equations of motion. Viscous stresses induced by velocity gradients neglected in the approximation can contribute to the momentum flux in the x and ϕ directions. These stresses are not expected to contribute significantly when the flow is axisymmetric. For the non-axisymmetric flow in square ducts, these stresses are expected to play a more significant role. There are large portions of the domain (e.g., the corners and the ends of the vesicle) where the gap separating the membrane and the duct wall is not narrow, nor is it slowly varying in the axial or circumferential directions. Consequently, while we expect the local flow field in the narrow-gap region to be well approximated by the lubrication theory, the macroscopic mass and momentum balance may incur substantial errors due to neglected viscous stresses, particularly for motion tangential to the wall (less so for normal motion, which is not considered here) [122]. These errors are expected to decrease if the flow becomes axisymmetric, the narrow gap thins, or the apparent contact area A^* increases.

The macroscopic mass and momentum balances lead directly to the integral figures of merit: the

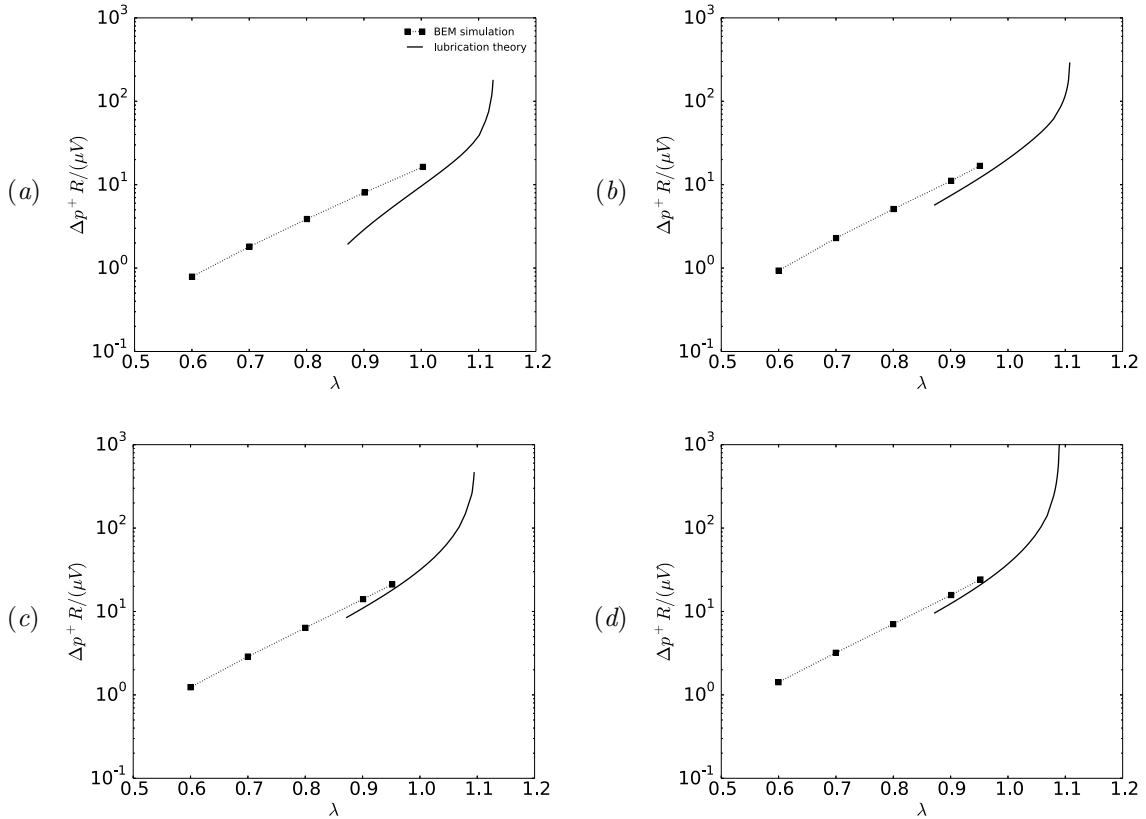


Figure 5.4: Dimensionless extra pressure drop $\Delta p^+ R / (\mu V)$ plotted against the radius ratio λ for $v = 0.99$ and (a) $N = 4$ (square), (b) $N = 6$ (hexagon), (c) $N = 12$ (dodecagon), and (d) $N \rightarrow \infty$ (circle). The symbols are the BEM simulations, while the solid lines are the predictions from lubrication theory.

relative velocity U/V and dimensionless extra pressure drop $\Delta p^+ R/(\mu V)$. In order to estimate the errors made in the lubrication approximation, we compute these quantities at different values of N (polygonal ducts with varying number of edges in a cross section) and compare to the analogous BEM simulations. Results for the relative velocity U/V and dimensionless extra pressure drop $\Delta p^+ R/(\mu V)$ are shown in Figures 5.3 and 5.4, respectively, for $N = 4$ (square cross section), 6 (hexagonal), 12 (dodecagonal) and ∞ (circular). These geometries are presented in order of increasing rotational symmetry. From comparing the two methods, it is clear that the lubrication theory underpredicts both the relative velocity and extra pressure drop. The error is most significant for the square cross section, and decreases as the symmetry of the system increases. For the circular-tube case, the error in the relative velocity nearly vanishes, whereas there remains a very small error in the extra pressure drop. This error is likely due to the approximation (5.3.20), which neglects wall stresses upstream and downstream of the ends of the vesicle.

From Figures 5.3 and 5.4, we may reasonably conclude that the errors in the lubrication approximation arise from the neglect of velocity gradients in the azimuthal direction (e.g., $\partial u_x/\partial\phi$ and $\partial u_\phi/\partial\phi$) in the equations of motion and stress conditions. These terms are not necessarily small and should play a significant role when the duct is not axisymmetric. However, we expect that these terms become less important as the vesicle becomes more confined. As the radius ratio λ increases, the vesicle fills the entire cross section and the gap separating the membrane from the duct wall becomes very small in certain regions. Velocity gradients with respect to the radial distance (e.g., $\partial u_x/\partial\rho$ and $\partial u_\phi/\partial\rho$) are dominant in this case, and lubrication theory is expected to predict the singular contribution to integral force moments.

Unfortunately, it is not possible to compare the lubrication theory to the BEM simulations at very high confinement, since the BEM calculations become prohibitively expensive in this regime. Instead, we compare our lubrication theory to experimental measurements at similarly high confinement (delayed until §5.5). Details of the experimental methods are given in the next section.

5.4 Experimental

Experiments were carried out by Ahmmmed, Vanapalli and coworkers at Texas Tech University to complement our theoretical predictions. A description of their experimental method is provided below.

A microfluidic manometer method, previously used to study the extra pressure drop across single droplets [167] and cells [2, 91, 90] was adopted to simultaneously measure the relative velocity U/V and dimensionless extra pressure drop $\Delta p^+ R/(\mu V)$. The manometer principle (illustrated in Figure 5.5) involves applying a constant pressure at the inlets of the so-called reference and test channels, and recording the fluid-fluid interface deflection in the comparator region downstream as

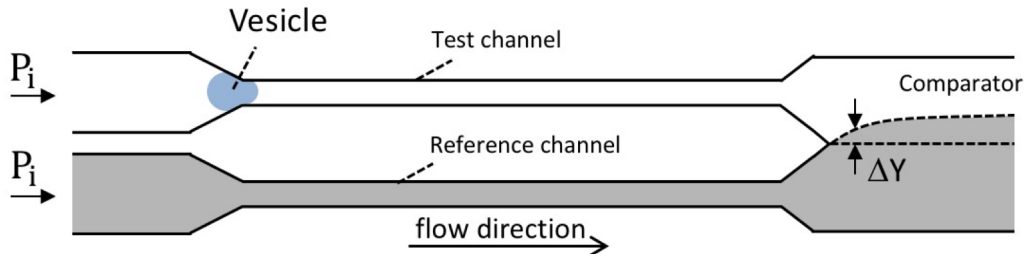


Figure 5.5: Working principle of the microfluidic manometer. Equal driving pressures are applied to a test channel (containing a single vesicle) and a reference channel (containing a clear fluid). The co-flowing fluids meet at a downstream comparator, forming a fluid-fluid interface. In the absence of a vesicle, the interface is flat (parallel to the streamwise direction). In the presence of a vesicle, a measurable displacement ΔY is observed due to the excess flow resistance in the test channel.

the vesicle passes through the test channel [68, 168]. From applying the Young-Laplace equation (i.e., the normal stress balance in the absence of normal viscous traction) to the fluid-fluid interface, the pressure difference between the co-flowing fluids can be directly measured. Hence, the extra pressure drop Δp^+ due to the presence of the vesicle in the test channel is obtained directly from the interface displacement ΔY .

Vesicles were synthesized using standard electroformation methods [5, 3]. The formulation consisted of 1-stearoyl-2-oleoyl-sn-glycero-3-phospho-choline (SOPC) and cholesterol at 1:1 molar ratio, or SOPC:Cl. The internal and suspending phase of the vesicles was 0.11 M sucrose and 0.12 M glucose solution, respectively, with viscosities ≈ 1 mPa·s. Literature precedent suggests a distribution of reduced volumes with a mean value of $v = 0.98$ for SOPC:Cl vesicles prepared by electroformation [124] (the standard deviation was not reported). It is expected that, without the addition of electrolytes to induce a gentle osmotic shock, the vesicles prepared will have reduced volumes in the range $0.85 \leq v \leq 1$. The possibility of multilamellarity was not considered.

The microfluidic manometer devices were fabricated using standard soft lithography techniques [178]. The manometer design consisted of two square channels of width \times height \times length = $(12.6 \pm 0.6) \times (12.8 \pm 0.7) \times 330$ μm , which meet downstream to form a comparator region of width 110 μm (see Figure 5.5). Vesicles were introduced into the test channel; in the reference channel, a 0.12 M glucose solution with a trace amount of black food dye was used to facilitate visualization of the deflected interface downstream. The pressure gradients in the channels were controlled using an electronic pressure controller system (MFCS, Fluigent Inc.). Imaging was conducted on an inverted microscope (IX 71, Olympus Inc.) in the phase contrast mode and images were acquired with a CMOS camera (Phantom v310, Vision Research) at an exposure time of 50 μs and a frame rate of 2000 fps. The effective pixel size for this optical setup is 0.97 μm .

Prior to the vesicle experiments, a calibration curve was generated to relate the extra pressure

drop Δp^+ to the interface displacement ΔY , by varying the test channel driving pressure and capturing the corresponding interface displacement while keeping the reference channel driving pressure fixed. The interface displacement was obtained from the captured images by fitting an error function to the intensity values of a vertical row of pixels 10 μm away from the tip, where the two fluids first meet in the comparator. The true interface position was deemed to be the midpoint between the lowest and highest gray scale regions of the fitted curve. When a vesicle occludes the test channel, the flow rate in it is reduced and therefore the interface is displaced in the comparator region. The calibration curve enables one to directly map ΔY to Δp^+ . One limitation of this method, as was mentioned at the end of §5.2, is that the pressure drop must be sufficiently high in order to achieve a significant enough deflection. As such, measurements of Δp^+ could only be obtained for sufficiently large radius ratios λ (typically greater than unity).

The vesicle translational velocity U was measured manually using ImageJ software (v.1.6.0-24, NIH). For each experiment, the time taken for a vesicle to travel the channel length (330 μm) was recorded, provided that the vesicle's motion was steady. Using this transit time and travel distance, the vesicle velocity was computed (maximum error < 3%, based on image resolution).

Independent experiments were performed in order to determine the mean fluid velocity V during the vesicle transport through the test channel. In the absence of vesicles, a flow rate Q was imposed using a syringe pump (PHD 2000, Harvard Apparatus) in the test channel, with a constant pressure imposed at the inlet of the reference channel. The interface displacements were recorded as a function of the pump flow rate. Therefore, using the two curves Δp^+ vs. ΔY and Q vs. ΔY , a one-to-one mapping between Δp^+ and Q was obtained. Using this relationship, the mean fluid velocity V in the presence of the vesicle was determined. The errors incurred due to the fact that the vesicle-free fluid has a smaller effective viscosity are expected to be small, since the additional viscosity imparted by the vesicle to the fluid is an $O(c)$ contribution ($c \ll 1$ being the volume fraction occupied by the vesicle in the fluid system). In all of the reported experiments, the applied pressure drop in the manometer was such that mean fluid velocities and shear rates ($\sim V/H$) were 11.5-21.2 mm/s and 750-1700 s^{-1} , respectively.

To calculate the radius ratio λ , the size of each vesicle was measured prior to entering the constriction (where a vesicle has a “pancake” shape due to the converging duct cross section). Specifically, the projected area of the vesicle was measured using ImageJ and fit to a circle (measurement error < 3% due to image resolution); the volume and surface area were estimated by assuming the vesicle to be a body of revolution, as described by Vuong and Anna [171]. The equivalent vesicle radius R_0 was then computed and normalized by the channel hydraulic radius R in order to obtain the radius ratio λ .

Due to optical limitations, the reduced volume v could not be accurately measured during the microfluidic experiments. Computing v based on the “pancake” model described above typically

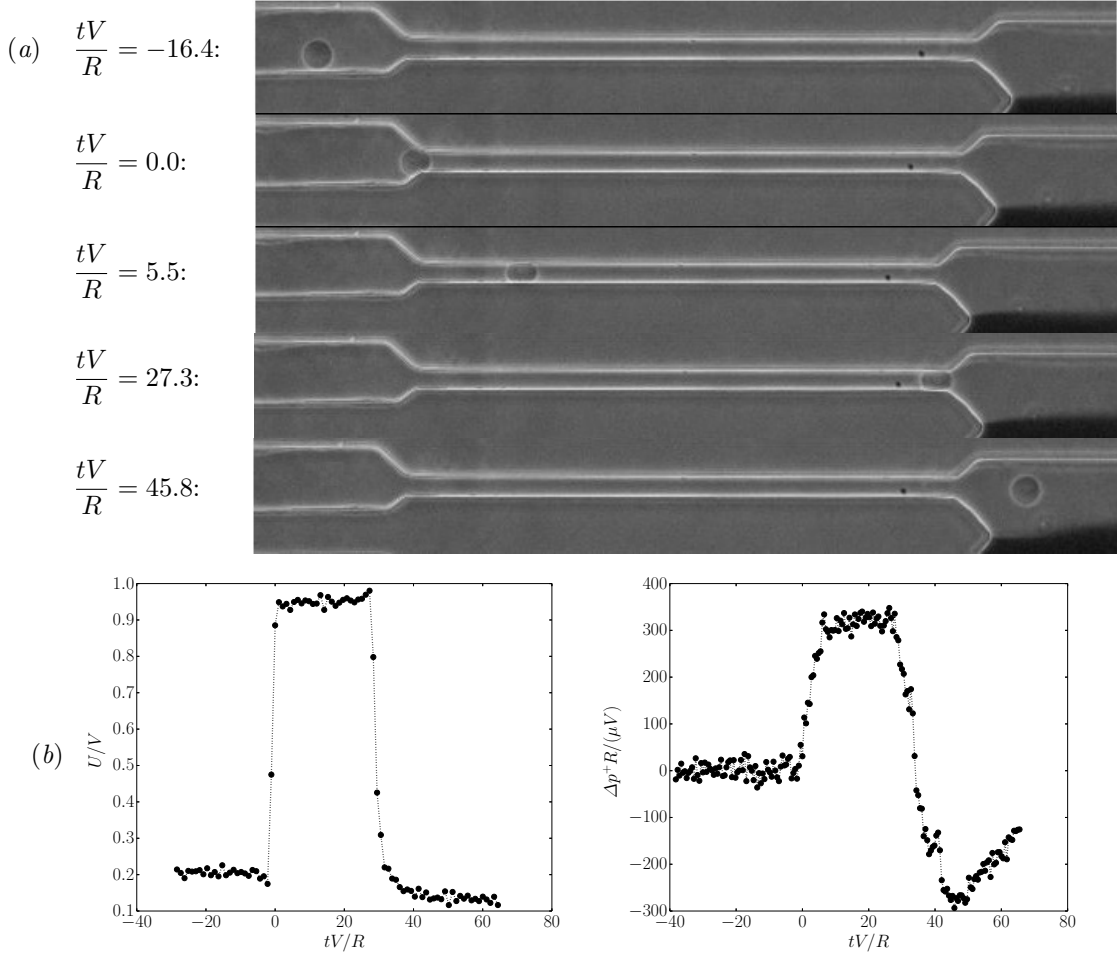


Figure 5.6: (a) Time-stamped images showing vesicle motion in the test channel and the concomitant interface deflection. The test channel is about $12.6 \mu\text{m}$ wide and $330 \mu\text{m}$ long. (b) Time evolution of the relative velocity U/V and dimensionless extra pressure drop $\Delta p^+ R / (\mu V)$ for a vesicle of reduced volume v near unity ($\lambda = 1.65$).

results in an overestimation (reduced volumes very close to unity). When the vesicle enters the narrow channel, the aspect ratio $L/(2R)$ is typically larger than unity, indicating that the vesicle is aspherical under confinement.¹ We approximate the reduced volume by measuring the aspect ratio $L/(2R)$ and using the lubrication solutions of the vesicle shape at near-critical confinement in order to relate $L/(2R)$ to v (discussed further in §5.5.3, below).

A representative experiment is shown in Figure 5.6. Figure 5.6a shows time-stamped images of a SOPC:Cl vesicle translating through the test channel and the induced interface deflection. From observation, the vesicle deforms at the constriction entrance but does not slow down as it penetrates into the channel. Figure 5.6b shows the associated time evolution of the relative velocity U/V and dimensionless extra pressure drop $\Delta p^+ R / (\mu V)$ as the vesicle translates through the channel. As

¹Note that the aspect ratio $L/(2R)$ is one-half of the reduced length $\ell = L/R$, which was defined in Chapter 3.

expected, the extra pressure drop is nearly zero prior to the vesicle reaching the constriction entrance. Then, there is a sharp rise in extra pressure drop, which reaches a maximum at a few channel diameters away from the constriction entrance. This maximum in the extra pressure drop signal is maintained, producing a plateau region until the vesicle reaches the channel exit. Thereafter, the extra pressure drop decreases and actually appears to be negative, since the presence of vesicle in the comparator region perturbs the interface location. For the purposes of comparing the measurements to our theoretical predictions, the mean value of the extra pressure drop in the plateau region was evaluated. The fluctuations in the plateau region is < 5% for a large vesicle ($\lambda \geq 1.3$) and 5 -10% for smaller vesicles ($1 < \lambda < 1.3$). The relative velocity U/V time course mirrors that of the extra pressure drop except that the rise in velocity occurs slightly earlier than the extra pressure drop. This delay is likely due to the response time of the manometer.

5.5 Discussion of results

In this section, we present our main results using a combination of BEM simulations, lubrication theory, and microfluidic experiments to investigate the motion of vesicles in square conduits. We found success in the previous chapter by using the “two-pronged approach” of direct numerical simulations and coarse-grained theory, in that we were able to develop predictions spanning a large range of radius ratios λ . In §5.3.2, we showed that the lubrication approximation yields more significant errors in the square-duct geometry than in the circular-tube geometry, due to the importance of azimuthal stresses neglected in the approximation (these errors essentially disappear as the symmetry of the duct increases, i.e., as $N \rightarrow \infty$). However, we expect that this approximation yields the correct *singular* contribution to the relative velocity U/V and dimensionless extra pressure drop $\Delta p^+ R / (\mu V)$ as λ approaches a maximum. This information will be crucial when comparing to the experimental results.

5.5.1 Vesicle flow through a contraction

We begin by comparing our BEM simulations for straight channels with square cross section to our contraction-expansion simulations. Our goal here is to correlate the *instantaneous* vesicle confinement, relative velocity U/V , and dimensionless extra pressure drop $\Delta p^+ R / (\mu V)$. We are also interested in the time to reach steady state.

Figure 5.7 shows BEM simulation results for a vesicle (reduced volume $v = 0.99$) entering a constriction, at two different radius ratios ($\lambda = 0.6$ and 0.8). The mesh geometry (shown in Figure 5.2c) has the same dimensions as the “test channel” of the microfluidic manometer (Figures 5.5 and 5.6). The straight-channel portion of the geometry is sufficiently long such that the expansion flow downstream does not affect the vesicle motion. In the experiment shown in Figure 5.6, the radius

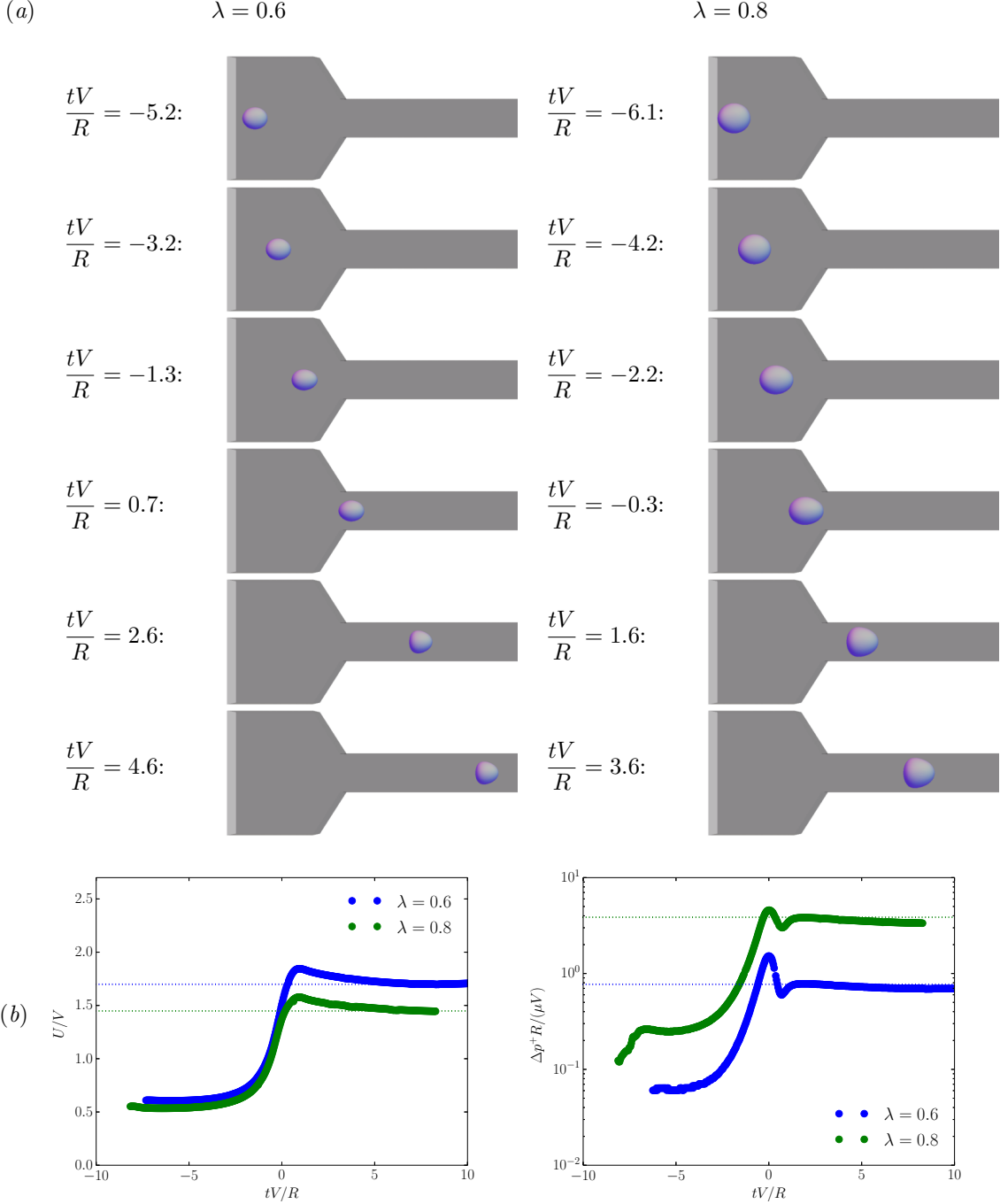


Figure 5.7: (a) Time sequence of a vesicle (reduced volume $v = 0.99$) passing through a square constriction channel, as computed via BEM simulation. The left and right columns correspond to $\lambda = 0.6$ and 0.8 , respectively. (b) Relative velocity U/V and dimensionless extra pressure drop $\Delta p^+ R / (\mu V)$ plotted against the dimensionless time tV/R for $v = 0.99$ and $\lambda = 0.6, 0.8$. The dashed, horizontal lines correspond to the steady-state results for an infinitely long, square conduit.

ratio λ is higher than the simulations shown in Figure 5.7. High-confinement simulations require an exorbitant number of mesh elements and are prohibitively costly with the current implementation. As such, one should not directly compare Figure 5.7 to Figure 5.6. Nevertheless, the simulations can give insight into the transient effects at the entrance of the manometer, at lower confinement.

The vesicle shape (Figure 5.7a) is tracked together with the relative velocity U/V and dimensionless extra pressure drop $\Delta p^+ R / (\mu V)$ (Figure 5.7b). As the vesicle approaches the entrance of the narrow channel, it accelerates due to the converging flow field; the extra pressure drop rises simultaneously. At $tV/R = 0$, the vesicle enters the square duct and the pressure drop fluctuates; these fluctuations are damped as confinement increases. Steady state is achieved after the vesicle travels several channel radii (roughly $tV/R \simeq 3$), which is consistent with the experiment shown in Figure 5.6 (physically, this distance is about 40 μm). Increasing the flow confinement (λ) results in a slight reduction in the relative velocity U/V and a dramatic increase in the dimensionless extra pressure drop $\Delta p^+ R / (\mu V)$. Similar trends are observed for lower reduced volumes (not shown here).

Quéguiner and Barthès-Biesel performed BEM simulations of a capsule (a model for a red blood cell) entering an axisymmetric contraction-expansion geometry [129]. These authors modeled the capsule membrane as either a neo-Hookean solid or as an incompressible sheet; the latter is equivalent to the membrane model used in this chapter. They tracked the pressure drop as a function of distance travelled and showed that a steady state was achieved after several channel radii, as is shown here. To the best of our knowledge, the present simulations are the first to model a vesicle flowing through *rectangular* contraction-expansion geometry, which is fully 3D and hence cannot be investigated using the axisymmetric boundary integral equations.

5.5.2 Steady vesicle shapes, surface tractions, and surface velocities

In Figures 5.8-5.11, we show our theoretical predictions for the vesicle shape in square conduits at two different reduced volumes ($v = 0.99$ and 0.90) and a range of radius ratios λ . The images are ordered (top-to-bottom) with increasing radius ratio λ ; thus, vesicle confinement increases down the page. The colors indicate the normal component of the membrane surface traction jump (i.e., the “total pressure”), $f_{sn} = \hat{\mathbf{n}} \cdot \mathbf{f}_s$. Larger values of f_{sn} (towards positively valued numbers) indicates higher pressures in the suspending fluid phase. The results shown in Figures 5.8 and 5.10 were obtained using BEM simulations; those shown in Figures 5.9 and 5.11 were obtained using lubrication theory. In order to compare results from the BEM and lubrication theory, one may juxtapose Figures 5.8d and 5.9a (for $v = 0.99$, $\lambda = 0.9$), as well as Figures 5.10e and 5.11a (for $v = 0.90$, $\lambda = 1.1$). Clearly, the two methods produce qualitatively similar shapes and pressure distributions. Quantitative differences in the computed pressures are also observed.

Figures 5.8a, 5.10a show that the pressure distribution in the vicinity of the vesicle surface is nearly axisymmetric at low flow confinement. Were the vesicle to shrink to a point, local analysis

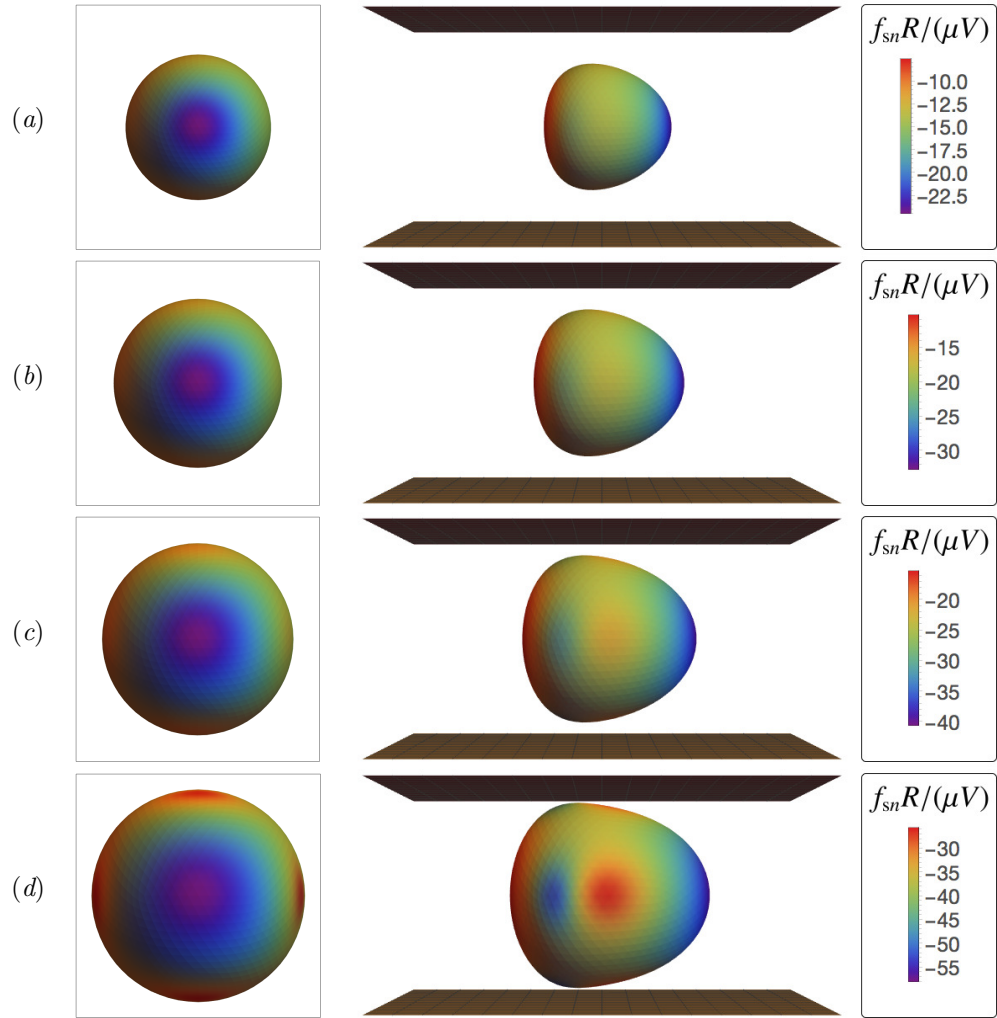


Figure 5.8: Vesicles ($v = 0.99$) in square ducts as determined by 3D BEM simulation, viewed from yz (left) and xy (right) planes. The colors indicate the normal component of the membrane surface traction jump $f_{sn} = \hat{\mathbf{n}} \cdot \mathbf{f}_s$. Shown are results for $\lambda = (a) 0.6$, $(b) 0.7$, $(c) 0.8$, and $(d) 0.9$.

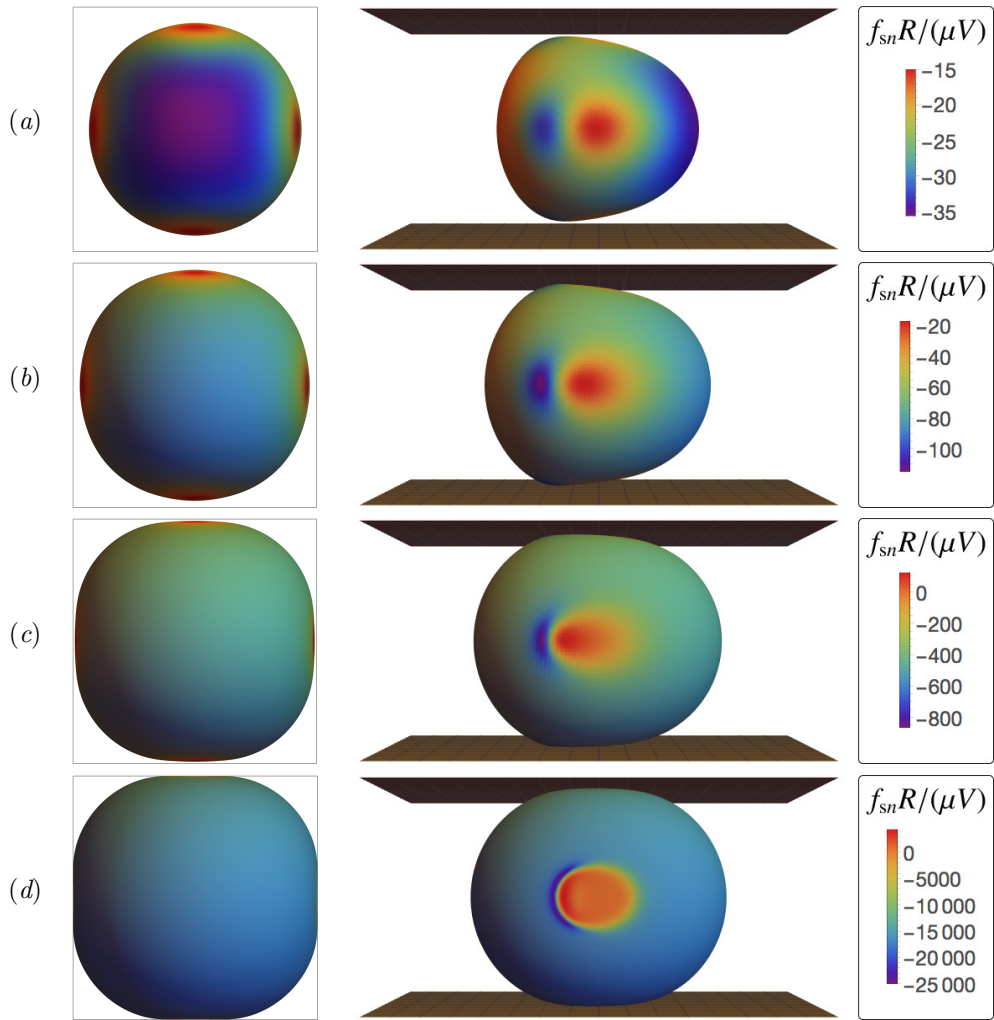


Figure 5.9: Vesicles ($v = 0.99$) in square ducts as determined by lubrication theory, viewed from yz (left) and xy (right) planes. The colors have the same meaning as in Figure 5.8. Shown are results for $\lambda = (a) 0.9, (b) 1.0, (c) 1.1$, and (d) 1.12.

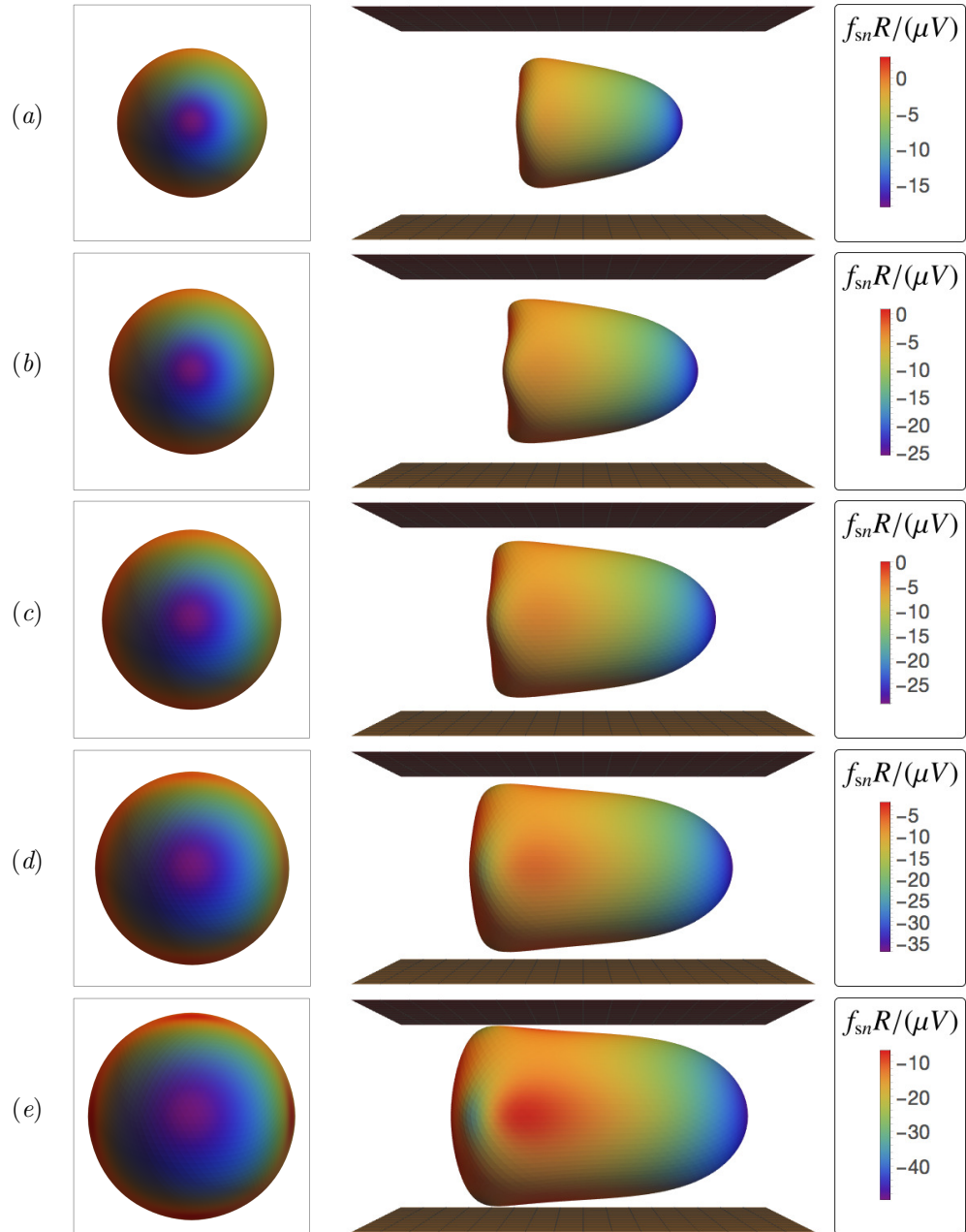


Figure 5.10: Vesicles ($v = 0.90$) in square ducts as determined by 3D BEM simulation, viewed from yz (left) and xy (right) planes. The colors indicate the normal component of the membrane surface traction $f_{sn} = \hat{\mathbf{n}} \cdot \mathbf{f}_s$. Shown are results for $\lambda = (a) 0.7, (b) 0.8, (c) 0.9, (d) 1.0$, and (e) 1.1.

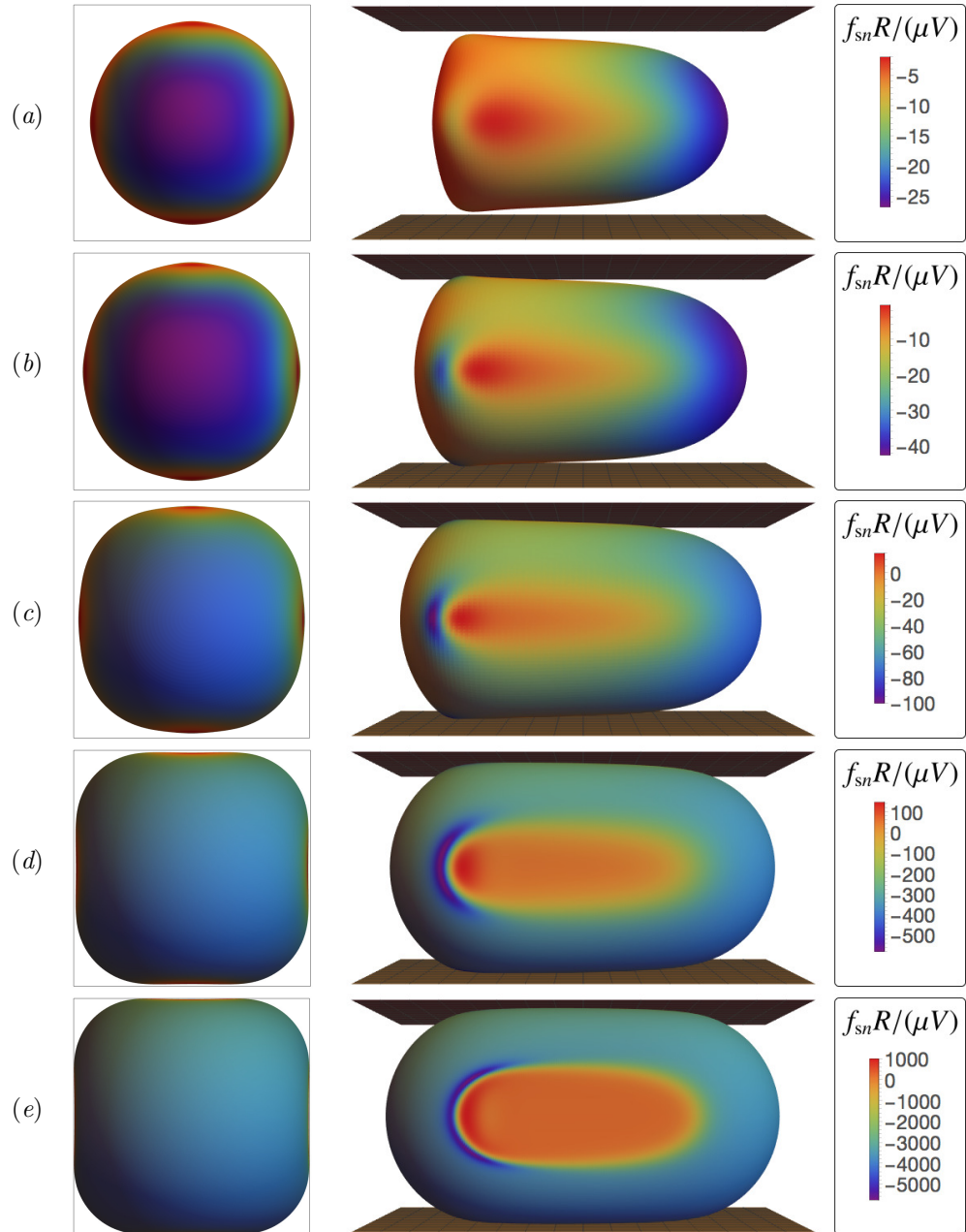


Figure 5.11: Vesicles ($v = 0.90$) in square ducts as determined by lubrication theory, viewed from yz (left) and xy (right) planes. The colors have the same meaning as in Figure 5.10. Shown are results for $\lambda = (a) 1.1, (b) 1.2, (c) 1.3, (d) 1.4, \text{ and } (e) 1.43$.

of the flow field in a square duct yields an axisymmetric flow field at the channel centerline. Finite-sized vesicles sample a non-axisymmetric flow field. Figures 5.10*a,b* show a four-fold symmetric “parachute shape” for $v = 0.90$, with four lobes appearing at the rear end. This is not observed in circular tubes, wherein a vesicle of this reduced volume would develop an axisymmetric parachute shape.

As the confinement is increased, the pressure distribution becomes increasingly asymmetric with “hot spots” (regions of high pressure) localized at four discrete areas where the gap widths are narrow. These hot spots become less localized at lower reduced volume (comparing $v = 0.99$ to 0.90), indicating that there is a smaller variation in the local distance between the vesicle membrane and the duct wall. Moreover, the magnitude of the pressure is significantly lessened as the reduced volume is decreased (at fixed radius ratio); this result is expected, since lower-reduced-volume vesicles can form more streamlined bodies in pressured-driven flow. The non-axisymmetric pressure distribution confirms that the velocity field will exhibit a strong dependence on the azimuthal angle ϕ . This dependence is neglected in the lubrication approximation, and so quantitative discrepancies between the lubrication theory and the BEM simulations are expected at low confinement.

At very high confinement, the lubrication solutions indicate that the vesicle conforms to the duct boundary and makes “apparent contact,” from a macroscopic point of view (Figures 5.9*d*, 5.11*e*). The apparent contact area A^* widens as the reduced volume v is decreased. Microscopically, a thin layer of suspending fluid separates the membrane from the wall. The color contours indicate very large pressures in this region. The distribution of pressure is also interesting: the highest pressures are located downstream and distributed uniformly over a wide area (the “orange ellipse” in Figures 5.9*d*, 5.11*e*), while a thin “suction” layer (the “blue croissant”) develops upstream.

The pressure distributions described above allude to a backflow (opposite in direction to the mean flow) in the region of apparent contact. In Figure 5.12, the membrane surface velocity \mathbf{u}_s is plotted for the parameter sets shown in Figures 5.9*a,d* and 5.11*a,e* (computed via lubrication theory). The vectors are normalized so that only the direction of flow is indicated. The velocity vectors indeed indicate a backflow in the apparent contact region. In the “corner regions,” the membrane flows in the direction of the mean flow; the local speed (not shown) is also high in the corner regions, relative to the contact regions. Thus, the wall “drags” fluid backward, with forward flow supplied in the corner regions, and the vesicle “tank-treads” through the duct. This motion is markedly unlike that of rigid particles, and is permitted by the spatial asymmetry of the duct cross section.

5.5.3 Critical geometry

The lubrication theory can be used to estimate the vesicle geometry at maximum confinement (minimal clearance between the membrane and the wall). We say “estimate” here, because it is numerically impossible to set the gap distance to zero in our calculations. However, we can

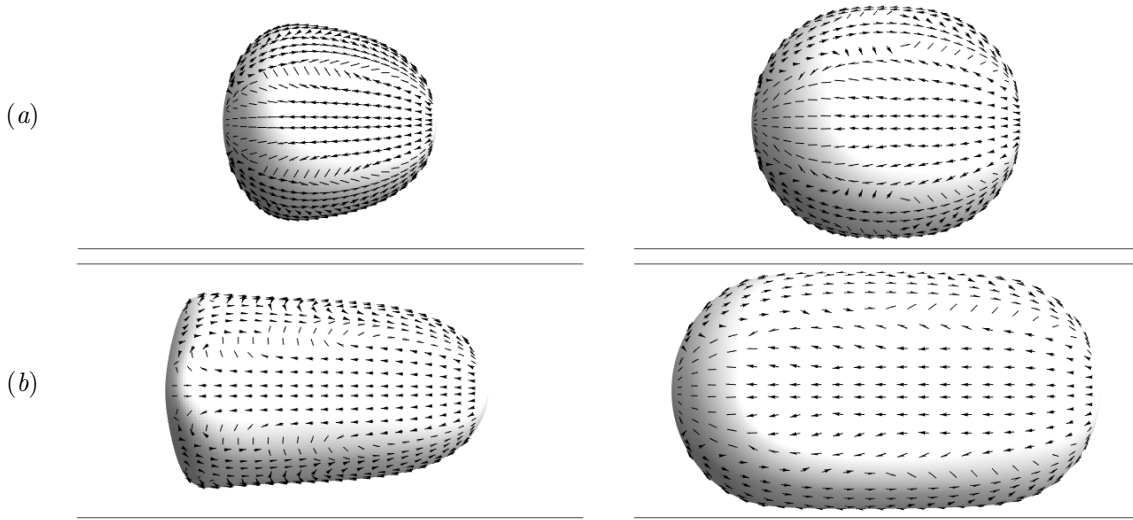


Figure 5.12: Normalized membrane surface velocity vectors $\mathbf{u}_s/\|\mathbf{u}_s\|$ (in a reference frame moving with the vesicle), as computed by lubrication theory. (a) $v = 0.99$, $\lambda = 0.9$ (left) and 1.12 (right). (a) $v = 0.90$, $\lambda = 1.1$ (left) and 1.43 (right). The corresponding surface traction distributions are shown in Figures 5.9a,d and 5.11a,e.

incrementally ‘‘march up’’ in λ (at fixed v) using the continuation method, decreasing the gap distance until some acceptable threshold. Here, we choose the minimum gap distance to be $0.001R$, at which point we truncate the continuation procedure and denote the value of λ as the ‘‘apparent critical radius ratio’’ λ^* . To reiterate, the *exact value* of λ^* is theoretically achieved by continuing until the film thickness drops to zero. Examples of the near-critical geometry are shown in Figures 5.9d and 5.11e for $v = 0.99$ and 0.90 , respectively.

From the numerical solutions at near-critical confinement, we can extract three important geometric parameters: the critical radius ratio λ^* , the lubrication contact area A^* , and the critical vesicle length L^* . The apparent contact area A^* can be estimated by computing the total area of the region in which the pressure $f_{sn} \approx -p$ exceeds a predetermined threshold (say, $100\mu V/R$); we denote this region as the ‘‘contact region,’’ since the vesicle makes apparent contact with the wall from a macroscopic viewpoint. Figure 5.13 shows plots of our estimates for λ^* , A^* , and L^* against the reduced volume v , with the analogous circular-tube results shown for comparison.

At fixed reduced volume, the critical radius ratio λ^* is higher in the square-duct geometry than in the circular-tube geometry (Figure 5.13a). Physically, this implies that vesicles will have an easier time squeezing through a square duct than a circular tube, due to the larger available cross sectional area (relative to the square of the hydraulic radius R^2). The contact area A^* in the square-duct geometry is much smaller than in the circular tube (Figure 5.13b), due to a larger fraction of ‘‘free’’ surface in the corner regions. As v approaches unity, the contact area A^* approaches zero in the square-duct geometry, indicating that the surfaces of contact degenerate to points. As was

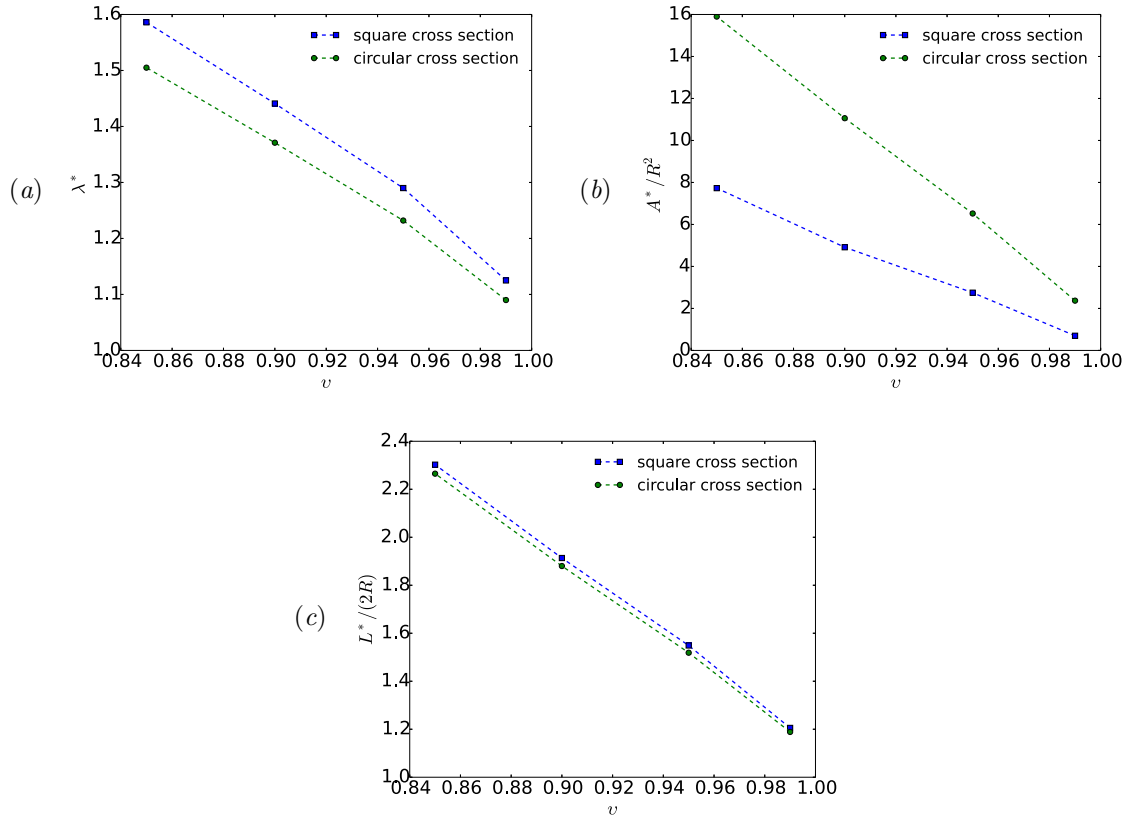


Figure 5.13: Estimates of (a) the critical radius ratio λ^* , (b) the dimensionless contact area A^*/R^2 , and (c) the aspect ratio $L^*/(2R)$ plotted against the reduced volume v , as determined via lubrication theory. Results for both square and circular cross sections are shown.

mentioned near the beginning of §5.3, the applicability of lubrication theory when $A^* = 0$ is dubious in the evaluation of integral force moments. For $v = 0.99$, the apparent contact area A^* is small, but finite.

The critical vesicle length L^* does not differ significantly between the square and circular cross sections (Figure 5.13c), indicating that the vesicle shape is very nearly a spherocylinder at maximal confinement. For vesicles in circular tubes, there are exact equations relating the reduced volume v and critical radius ratio λ^* to the aspect ratio $L^*/(2R)$:

$$v = \frac{3[L^*/(2R)] - 1}{2[L^*/(2R)]^{\frac{3}{2}}}, \quad \lambda^* = \sqrt{\frac{L^*}{2R}} \quad (\text{circular tubes}). \quad (5.5.1)$$

For the square-duct geometry, we can fit a polynomial to the numerical data in order to relate v and λ^* to $L^*/(2R)$ over the range $0.85 \leq v \leq 1$:

$$\left. \begin{aligned} v &= 0.0594 \left(\frac{L^*}{2R} \right)^3 - 0.3221 \left(\frac{L^*}{2R} \right)^2 + 0.4372 \left(\frac{L^*}{2R} \right) + 0.8259 \\ \lambda^* &= 0.0747 \left(\frac{L^*}{2R} \right)^3 - 0.4697 \left(\frac{L^*}{2R} \right)^2 + 1.3582 \left(\frac{L^*}{2R} \right) + 0.0376 \end{aligned} \right\} \quad (\text{square ducts}). \quad (5.5.2)$$

The maximum relative difference in the reduced volume v between (5.5.1) and (5.5.2) (within the range of interpolation) is only 1%; the maximum relative difference in λ^* is 5%.

In equations (5.5.1)-(5.5.2), we have chosen to express v and λ^* in terms of L^* as though L^* were the independent variable (in reality, v is the control variable since the vesicle volume and surface area are presumed to be constant). The reason for this choice is motivated by the experimental measurements, in that it is relatively easy to measure the vesicle length L using optical microscopy. By contrast, the vesicle reduced volume v is less accurately measured. This quantity requires measurement of *both* the vesicle volume and surface area, which are difficult to obtain with high accuracy from 2D micrographs. A large set of micrographs is required in order to improve the statistical certainty of a reduced-volume measurement [29]. However, in the presently considered flow geometry, only a single image of the vesicle can be taken within a given time interval.

In order to estimate the reduced volume from the experiments, we have to make an assumption about the vesicle shape. We assume here that the vesicle conforms to the duct walls and is given by the “critical geometry” predicted via lubrication theory. The analogous assumption for vesicle flow in circular tubes is that the vesicle is a spherocylinder, which is the wall-conformal shape for that geometry. Thus, in the experiments we assume that

$$L \approx L^*. \quad (5.5.3)$$

By measuring the aspect ratio $L/(2R)$ in the experiments, we obtain the reduced volume v from

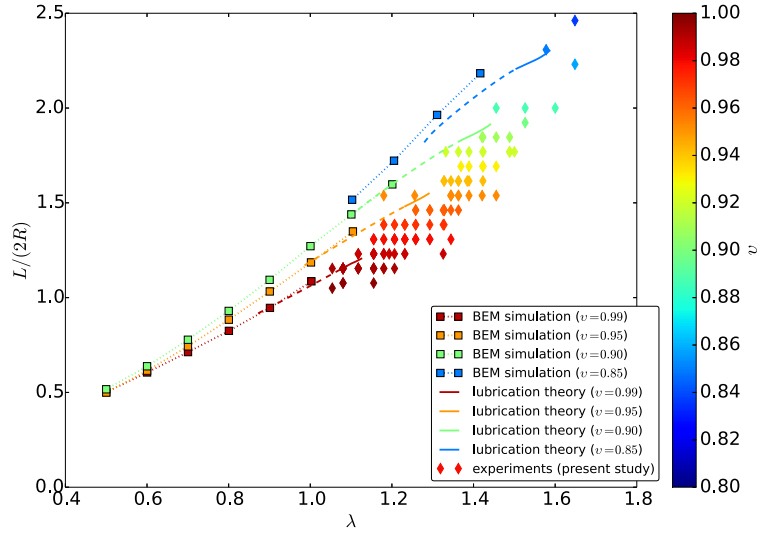


Figure 5.14: Aspect ratio $L/(2R)$ plotted against the radius ratio λ . In the experimental measurements, the aspect ratio $L/(2R)$ is measured and the reduced volume v is estimated based on the correlation (5.5.2) from the lubrication theory; the diamond markers are colored accordingly.

the correlation (5.5.2) [the analogous correlation for circular tubes is (5.5.1)]. We show results from this procedure in Figure 5.14, where we have plotted the aspect ratio $L/(2R)$ (determined by BEM, lubrication theory, and experiments) against the radius ratio λ . The solid lines indicate the lubrication solution above the critical limit for a circular tube, while the dashed lines indicate solutions below this limit. We have colored the experimental data by reduced volume using the correlation (5.5.2) for the assumed critical geometry. The general trend shown is that as the vesicle lengthens, the reduced volume decreases.

There are obvious uncertainties with the assumption made above. Essentially, we have approximated the reduced volume by assuming that the vesicle is critically confined, even though the radius ratio is varied in the experiments. The main justification for this assumption is that we select only those experiments that give a *measurable* extra pressure drop, which must be sufficiently large in order to produce an observable deflection in the comparator (see Figure 5.6). Since the measured pressure drops are very large, it is reasonable to assume that the vesicle fills a large portion of the cross section. The slight geometric variations between the actual shape and the shape assumed here are, therefore, probably small. Thus, we expect that the above approximation will give us a good sense of the distribution of reduced volumes in the vesicle populations studied experimentally. This will be important when quantifying the relative velocity U/V and dimensionless extra pressure drop $\Delta p^+ R/(\mu V)$ (presented below), which depend strongly on the reduced volume.

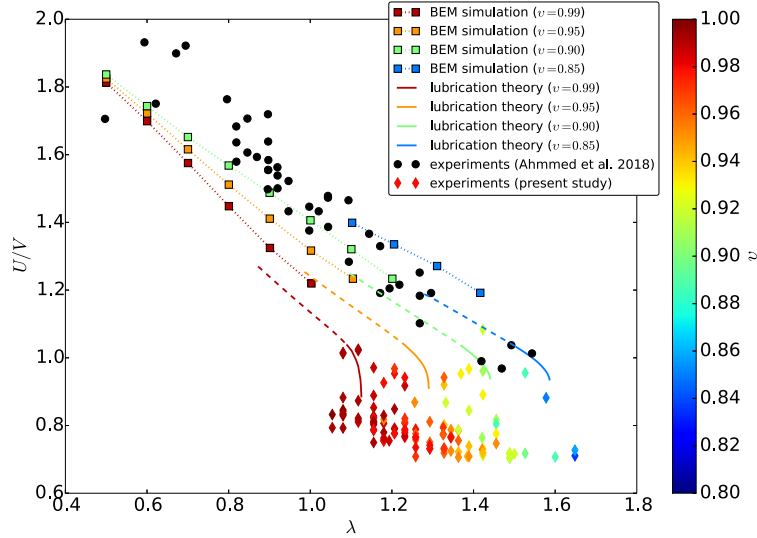


Figure 5.15: Relative velocity U/V plotted against the radius ratio λ .

5.5.4 Vesicle velocity and extra pressure drop

Figure 5.15 shows the relative velocity U/V plotted against the radius ratio λ as determined by 3D BEM simulations, lubrication theory, and experiments. The solid lines indicate the lubrication solution above the critical limit for a circular tube, while the dashed lines indicate solutions below this limit. Also shown are the experimental measurements of [3] for smaller vesicles translating through square ducts, in order to illustrate the dependence of U/V on λ . Accounting for the distribution of reduced volumes in the experiments, the agreement between the lubrication theory and the experiments of the present work is remarkable. Significantly, the theory correctly predicts subunit relative velocities ($U/V < 1$) at high confinement. At lower confinement (λ), the BEM simulations agree qualitatively with previous experimental measurements reported by [3]. The apparent discrepancy between the BEM and the lubrication theory at intermediate λ is attributed to the neglect of velocity gradients along the azimuth in the lubrication theory, as discussed previously. These errors were quantified in §5.3.2 as a function of duct symmetry. Unfortunately, it is not feasible at present to perform BEM simulations at much higher values of λ to within a reasonable degree of accuracy.

Figure 5.16 shows the dimensionless extra pressure drop $\Delta p^+ R / (\mu V)$ plotted against λ , again comparing the simulations, theory, and experiments. As expected, it is shown that the distribution of the pressure-drop measurements can be attributed to variations in the reduced volume v and the radius ratio λ . All of the experimental measurements fall within the predictions of the lubrication theory. The BEM predictions for $\Delta p^+ R / (\mu V)$ lie in a regime outside the range accessible by the experiment, since at lower confinement the extra pressure drop is relatively small (a “weak signal”).

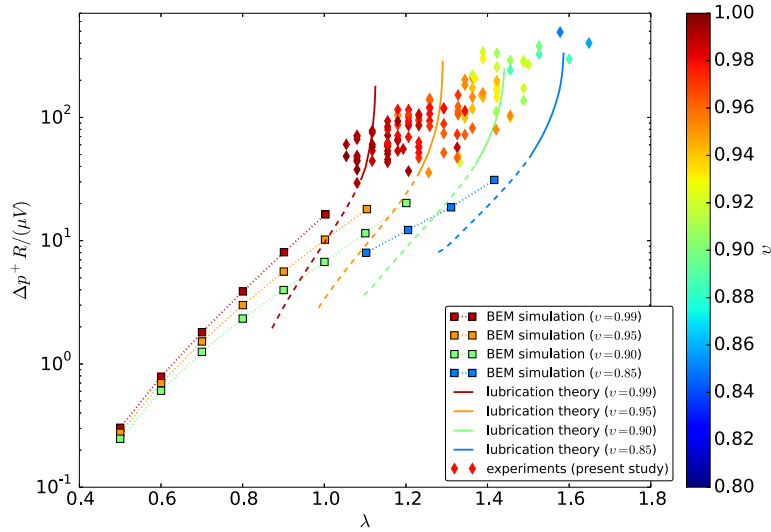


Figure 5.16: Dimensionless extra pressure drop $\Delta p^+ R / (\mu V)$ plotted against the radius ratio λ .

The origin of the discrepancy between the BEM simulations and the lubrication theory in Figure 5.16 has already been described in detail.

5.6 Concluding remarks

The hydrodynamics of a vesicle translating through a square duct has been investigated theoretically and compared against experimental measurements in microfluidic channels. This study focused on vesicles of reduced volumes in the range $0.85 \leq v \leq 1$ with unit viscosity contrast κ . The effect of the radius ratio λ was explored, highlighting the impact of confinement. Bending elasticity is expected to be negligible under the flow conditions considered in this study; thus, we set $\beta = 0$ in all of the calculations reported.

The 3D BEM simulations are capable of simulating complex geometries and represents an “exact solution” (within numerical error) of Stokes’ equations of motion. However, the BEM simulations cannot access the regime of high confinement (large radius ratios λ) due to the prohibitive number of mesh elements required to resolve the fluid flow in regions of lubrication. For this reason, a non-axisymmetric lubrication theory was developed to predict the hydrodynamics of single vesicles at high confinement. This theory falls into the regime accessible by microfluidic manometer measurements, also presented in this chapter for single vesicles. The theoretical calculations and experimental measurements show excellent agreement. Discrepancies between the BEM calculations and the lubrication theory are attributed to neglected viscous stresses (specifically, those associated with velocity gradients in the azimuthal direction) in the lubrication approximation.

Several key insights were obtained from studying the transport of vesicles through square conduits. Firstly, spatial inhomogeneities in surface flow on the vesicle membrane creates a mechanism by which the vesicle can tank tread along the duct at a velocity U that is smaller than the mean fluid velocity V . This result was seen in both the lubrication calculations and in the microfluidic experiments. By contrast, in circular tubes the surface flow is uniform and so a vesicle in transit behaves much like a rigid particle. Secondly, the area of contact A^* is greatly reduced (whereas the maximum radius ratio λ^* is increased) in the square-duct geometry as compared to the circular-tube geometry. This difference has a qualitative effect on the extra pressure drop Δp^+ , which increases with increasing A^* . As the reduced volume v approaches unity, surfaces of contact reduce to points of contact ($A^* \rightarrow 0$), which invalidates the use of lubrication theory to accurately predict the extra pressure drop.

One of the more significant consequences of the work presented herein is that the basic ingredient for predicting the vesicle's motion is the surface incompressibility of the membrane. All of the intrinsic membrane mechanics – e.g., bending elasticity – were neglected. Bending elasticity is expected to play a role when the reduced volume v is smaller than the range under consideration here. Surface incompressibility seems to be the key characteristic that separates vesicles from, say, droplets and rigid particles flowing through polygonal conduits. As such, it is expected that the results of this work be applicable to other systems. For instance, Pickering droplets contain particle-laden fluid-fluid interfaces, which are essentially incompressible. Hydrogel beads, which are important in various fluidic applications, may also be characterized as fluid particles with incompressible surfaces. Surfactant-laden droplets and bubbles at high surface pressures (high Gibbs elasticity) represent yet another system connected to the present work.

Chapter 6

Small, quasi-spherical vesicles

6.1 Quasi-spherical assumption

In this chapter, we shall develop an analytical theory for the motion of small, quasi-spherical vesicles in a channel of arbitrary cross section. This regime is difficult to attack by direct numerical methods due to the degree of resolution required in computing the wall surface tractions. Moreover, it represents the opposite limit to that considered in Chapter 3, wherein the vesicles were assumed to fill the entire channel cross section. It was shown in that chapter (and later validated Chapter 4 by direct numerical calculations) that the details of the vesicle shape has a pronounced effect on the extra pressure drop Δp^+ . We also showed in Chapters 4 and 5 that as the channel widens ($\lambda = R_0/R$ decreases), the relative velocity U/V and dimensionless extra pressure drop $\Delta p^+ R/(\mu V)$ depend only weakly on the reduced volume v . One may reasonably conclude that the vesicle's motion is rather insensitive to shape variations when the vesicle is small compared to the channel radius.

The study of *quasi-spherical vesicles* has many obvious merits. From a practical point of view, they are by far the most commonly observed shapes in the laboratory and *in vivo*. From a physical point of view, the occurrence of various shape transitions and shape instabilities is suppressed when v is close to unity. These latter phenomena, which highlight a rich phase space of nonlinear dynamics, are clearly interesting in their own right. We showed in Chapter 4, for instance, that vesicles of low reduced volume are able to access a diverse array of shape configurations, some of which break symmetry and evolve over time. However, these phenomena can become a nuisance when performing hydrodynamical calculations, since the relevant figures of merit [U/V and $\Delta p^+ R/(\mu V)$] must now be defined in a statistical sense and can depend on many degrees of freedom. Quasi-spherical vesicles are also easy to define mathematically using spherical coordinates (r, θ, ϕ) , with r being the radial coordinate, θ the polar angle, and ϕ the azimuthal angle.

In the first section of Chapter 4, we stated the relevant assumptions underlying a formal perturbation theory for large, closely fitting vesicles in channel flow. In this chapter, we shall develop a new perturbation theory for small, quasi-spherical vesicles based on the following assumptions:

1. Hydrodynamic interactions between vesicles are irrelevant (i.e., the suspension concentration c is small compared to unity). Thus, we may consider the flow field in and around a single vesicle, just as we did in Chapter 3. Vesicle-wall interactions are expected to play a role.
2. The system unsteady in general, meaning that the position of the vesicle surface is a function of both space and time, $\mathbf{x}_s = \mathbf{x}_s(\mathbf{x}, t)$.
3. The system is three-dimensional in general, with no obvious symmetries. This statement implies that the vesicle's center of mass may be displaced from the channel axis.
4. The viscosity contrast κ is $O(1)$.
5. The characteristic vesicle dimension is small compared to the channel hydraulic radius R . In previous chapters, we defined the effective vesicle radius $R_0 = \sqrt{A_0/(4\pi)}$ as the radius of a sphere with the same surface area A_0 . In this chapter, it is more convenient to define a volumetric radius $r_0 = [\Omega_0/(\frac{4}{3}\pi)]^{\frac{1}{3}}$ based on a sphere with the same volume Ω_0 . The ratio of this length scale to the channel radius is denoted by a , where

$$a = \frac{r_0}{R} \quad (\text{the radius ratio}). \quad (2.5.11)$$

In this chapter, we assume that $a \ll 1$.

6. The vesicle surface adopts a shape that is very nearly spherical. In terms of the reduced volume v , this assumption implies that $(1 - v) \ll 1$. Thus, deviation from sphericity is measured by how far v is from unity. In this chapter, it is more convenient to characterize the vesicle by its *excess surface area*:

$$\Delta = \frac{A_0}{r_0^2} - 4\pi \quad (\text{the excess surface area}), \quad (2.5.12)$$

where r_0 was defined previously. The *quasi-spherical assumption* implies that $\Delta \ll 1$.

A schematic of the geometry is shown in Figure 6.1. Spherical coordinates (r, θ, ϕ) are defined with origin P placed at the vesicle center. A channel of arbitrary cross section with radius $R_{\bar{\phi}}(\bar{\phi})$ is defined using cylindrical coordinates $(\bar{\rho}, \bar{\phi}, x)$, with the origin O placed at the channel axis. An “overbar” is used here to distinguish curvilinear coordinates defined with respect to the origin O from those referenced to P .

The formalism just developed has a decade-long history, with contributions by several authors in the field. Thus, before proceeding any further, it behoves us to examine previous theoretical

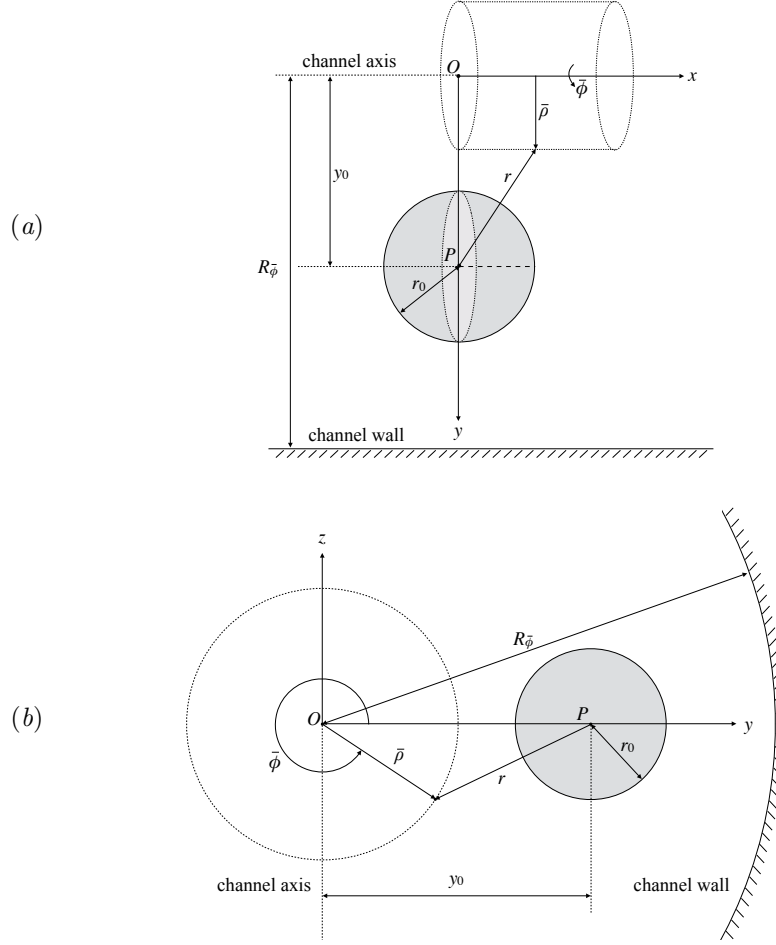


Figure 6.1: A quasi-spherical vesicle in a channel, as viewed from (a) the xy plane and (b) the yz plane. The particular geometry shown is a circular tube of constant radius $R_{\bar{\phi}} = R$.

developments in the study of quasi-spherical vesicles in Stokes flows (the subject of the next section). In doing so, we shall make evident where our contribution fits in, and how we distinguish our theory from prior work.

6.2 Previous theories

Misbah developed the first theoretical prediction of the relative intrinsic viscosity of quasi-spherical vesicles in shear flow by means of spherical harmonic expansions [112]. He determined that the intrinsic viscosity of vesicles depends strongly on the viscosity ratio κ and the vesicle inclination angle when Δ is small. The viscosity ratio also demarcates transitions between various dynamical states in shear flow, including “tank-treading,” “tumbling,” and “trembling” [102]. Several authors later extended Misbah’s result to *arbitrary* linear flows, determined corrections to higher order in

the perturbation parameter Δ , computed normal stress differences, and determined the effect of membrane bending elasticity on vesicle shear rheology [31, 30, 170, 102]. The main complication in developing higher-order corrections for small Δ is that the leading-order theory is nonlinear through the surface-incompressibility constraint, which precludes the guarantee of a unique solution [112, 48]. Consequently, the development of higher-order corrections with respect to the small parameter Δ can become as (or more) laborious as developing a numerical approximation.

The first theoretical investigation of quasi-spherical vesicles in planar and circular Poiseuille flows is due to [32], who derived an expression for the cross-stream migration velocity and found a strong dependence on the viscosity ratio κ . These authors did not compute the quadratic-flow correction to the intrinsic viscosity, nor did they compute higher-order corrections with respect to Δ . Subsequent studies focused heavily on vesicle migration and the impact of non-spherical shape morphologies (higher values of Δ), both for 2D vesicles [87, 7] and 3D vesicles [50, 52]. Complementary experimental studies were performed by [28, 27] to quantify vesicle migration and the shape diagram.

To date, an analytical Stokes-flow solution for the motion of a quasi-spherical vesicle in an *arbitrary* quadratic flow has not been developed. [114] presented a general methodology for developing such solutions for droplets, but their methodology has not yet been applied to the motion of vesicles. Moreover, only the shear contribution to the extra pressure drop Δp^+ (alternatively, the intrinsic viscosity) has been reported for vesicles. The quadratic contribution to the extra pressure drop represents a higher-order correction (with respect to the small parameter a) except in cases when the local shear rate vanishes (e.g., when the vesicle has migrated to the centerline in a symmetric Poiseuille flow). Detailed knowledge of the local flow field in and around a vesicle for arbitrary radius ratios a requires computation of hydrodynamic interactions induced by the channel walls. For small values of a , a good approximation of the wall interactions can be determined using the *method of reflections* [16, 75]. This method relies on knowledge of the specific geometry of the channel, precluding a general formulation for arbitrary cross sections. Furthermore, computation of reflections is typically a laborious procedure that involves transformation between a spherical coordinate system, which is suitable for describing the geometric properties of quasi-spherical vesicles, and a coordinate system that is more appropriate to describe the channel geometry. Such analyses are typically only feasible for relatively simple cross sections – circular tubes, for instance, naturally call upon the use of a cylindrical coordinate system. Even in such simple cases, satisfaction of the channel boundary conditions involves the solution of complicated integral equations in the Fourier domain.

Brenner circumvented the need for the method of reflections in his study of spherical particles and droplets in channel flows by use of the *reciprocal theorem* [14, 15]. By exploiting the reciprocity of Stokes flow, he derived an expression for the dimensionless extra pressure drop $\Delta p^+ R / (\mu V)$, to leading order in the radius ratio a , that depends only integrals of the velocity and stress fields

produced by a freely suspended particle (of arbitrary shape and type, including rigid particles and droplets) over a fictitious surface in the far field. This formula, which is presented later in this chapter [cf. (6.4.9) in §6.4], does not require specific knowledge of the channel geometry nor evaluation of wall reflections. Only the mean channel velocity V and cross sectional area A_x (both of which are integral quantities), as well as solutions for the velocity and stress fields for the appropriate *unbounded* Stokes-flow problem, are required. The relative velocity U/V , to leading order in a , may be similarly evaluated by means of a force balance on the particle without the need for wall reflections.

The methods outlined by Brenner can be generically applied to any kind of particle in an arbitrary channel flow, but to the best of our knowledge has not yet been applied to the motion of vesicles in channel flows. Thus, a central goal of this chapter is to derive general expressions for the relative velocity U/V and dimensionless extra pressure drop $\Delta p^+ R / (\mu V)$ for an *arbitrary* quadratic flow in the regime where the radius ratio a and excess surface area Δ are both small. As was mentioned in the previous section, this regime has practical value and “completes,” in some sense, our study of the hydrodynamics of vesicles in channel flows in various regimes of confinement. In developing a solution, we follow the general procedure outlined by [53] for the study of droplets and linear flows and later adopted by [31, 30] for vesicles, which makes use of tensorial representations of spherical harmonics. We apply this methodology to a general quadratic flow, based on analogous work by [114] for droplets. Our solutions are more general than those developed by [32], who considered the specific cases of planar and circular Poiseuille flows, and in fact we modernize their results in terms of a tensorial formalism (their work is developed using scalar spherical harmonics). Rather than focus on the vesicle migration behavior, which has been investigated exhaustively by other authors, our primary goal is to compute the hydrodynamical quantities U/V and $\Delta p^+ R / (\mu V)$. Comparison with analogous results for rigid particles is provided.

The remainder of this chapter is organized as follows. In §6.3, the undisturbed velocity, pressure, and stress fields in an arbitrary channel flow are Taylor-expanded near the vesicle’s center of mass up to second order in the position vector \mathbf{x} . The coefficient tensors are then expressed in terms of their irreducible parts. In §6.4, the disturbance fields induced by the vesicle are defined. The Stokes-flow initial-boundary value problem, including integral expressions for the vesicle velocity and extra pressure drop, are also presented in this section. We pursue a solution of this problem by means of tensorial harmonic expansions (presented in §6.5), making use of Lamb’s general solution of Stokes’ equations (§6.6). The vesicle geometry is defined in §6.7. A perturbative solution for small Δ is then developed in §6.8 in successive powers of Δ , including general expressions for the relative velocity and dimensionless extra pressure drop. Concluding remarks are given in §6.9.

6.3 Undisturbed flow

The undisturbed (i.e., vesicle-free) velocity and pressure fields are \mathbf{u}^∞ and p^∞ , respectively. These fields are the solutions to the Stokes equations for a bounded conduit flow in the absence of suspended vesicles. Expanding \mathbf{u}^∞ and p^∞ in Taylor series about $\mathbf{x} = \mathbf{0}$ (\mathbf{x} being the local position vector, with modulus $r = |\mathbf{x}|$, measured from the vesicle's center of mass) yields, up to quadratic order in \mathbf{x} , the following expressions [14]:

$$\mathbf{u}^\infty = \mathbf{u}_0^\infty + \mathbf{x} \cdot (\nabla \mathbf{u}^\infty)_0 + \frac{1}{2} \mathbf{x} \mathbf{x} : (\nabla \nabla \mathbf{u}^\infty)_0, \quad (6.3.1a)$$

$$p^\infty = \mu [\mathbf{x} \cdot (\nabla^2 \mathbf{u}^\infty)_0]. \quad (6.3.1b)$$

Here, \mathbf{u}_0^∞ is the local undisturbed velocity, $(\nabla \mathbf{u}^\infty)_0$ is the velocity-gradient (second-order) tensor, and $(\nabla \nabla \mathbf{u}^\infty)_0$ is the velocity-curvature (third-order) tensor. The subscript “0” ascribed to the tensorial coefficients implies evaluation at $\mathbf{x} = \mathbf{0}$. The undisturbed velocity \mathbf{u}^∞ and pressure p^∞ satisfy the Stokes-flow boundary-value problem,

$$\nabla \cdot \mathbf{u}^\infty = \mathbf{0}, \quad (6.3.2a)$$

$$\nabla \cdot \boldsymbol{\sigma}^\infty = -\nabla p^\infty + \mu \nabla^2 \mathbf{u}^\infty = \mathbf{0}, \quad (6.3.2b)$$

$$\mathbf{u}^\infty = \mathbf{0} \quad \text{on the channel wall,} \quad (6.3.2c)$$

where $\boldsymbol{\sigma}^\infty = -p^\infty \boldsymbol{\delta} + \mu [\nabla \mathbf{u}^\infty + (\nabla \mathbf{u}^\infty)^\dagger]$ is the undisturbed stress tensor. By incompressibility, $(\nabla \cdot \mathbf{u}^\infty)_0 = 0$ and so the velocity-gradient and velocity-curvature tensors satisfy,

$$(\nabla \mathbf{u}^\infty)_0 : \boldsymbol{\delta} = 0, \quad (\nabla \nabla \mathbf{u}^\infty)_0 : \boldsymbol{\delta} = \mathbf{0}. \quad (6.3.3)$$

The commutativity of partial derivatives also confers the following symmetry property to the velocity-curvature tensor:

$$\left(\frac{\partial u_k^\infty}{\partial x_i \partial x_j} \right)_0 = \left(\frac{\partial u_k^\infty}{\partial x_j \partial x_i} \right)_0, \quad (6.3.4)$$

where $i, j, k = 1, 2$, or 3 and $x_1 = x$, $x_2 = y$, $x_3 = z$.

For the special case of Poiseuille flow in a circular tube, the Taylor series truncates at quadratic order in \mathbf{x} . Letting R be the tube radius and $Q = \pi R^2 V$ the flow rate, the undisturbed velocity and pressure fields have the special form (modulo an arbitrary reference pressure),

$$\mathbf{u}^\infty = 2V \left(1 - \frac{\bar{\rho}^2}{R^2} \right) \hat{\mathbf{e}}_x, \quad (6.3.5a)$$

$$p^\infty = -\frac{8\mu V}{R^2} x, \quad (6.3.5b)$$

where $\bar{\rho}$ is the cylindrical radius measured from the tube axis and x is the axial coordinate. Suppose that the position vector \mathbf{x} is measured from an origin separated from the tube axis by $-y_0 \hat{\mathbf{e}}_y$ (Figure 6.1). The conversion between the cylindrical radius $\bar{\rho}$ and the spherical radius r is then given by,

$$\bar{\rho}^2 = (r - x^2) + 2y_0 y + y_0^2 = \mathbf{x} \cdot (\delta - \hat{\mathbf{e}}_x \hat{\mathbf{e}}_x) + 2y_0 (\mathbf{x} \cdot \hat{\mathbf{e}}_y) + y_0^2. \quad (6.3.6)$$

Using this relationship between $\bar{\rho}$ and r , one may straightforwardly derive the tensorial coefficients \mathbf{u}_0^∞ , $(\nabla \mathbf{u}^\infty)_0$, and $(\nabla \nabla \mathbf{u}^\infty)_0$ for circular Poiseuille flow:

$$\mathbf{u}_0^\infty = 2V \left(1 - \frac{y_0^2}{R^2} \right) \hat{\mathbf{e}}_x, \quad (6.3.7a)$$

$$(\nabla \mathbf{u}^\infty)_0 = -\frac{4V y_0}{R^2} \hat{\mathbf{e}}_y \hat{\mathbf{e}}_x, \quad (6.3.7b)$$

$$(\nabla \nabla \mathbf{u}^\infty)_0 = -\frac{4V}{R^2} (\delta - \hat{\mathbf{e}}_x \hat{\mathbf{e}}_x) \hat{\mathbf{e}}_x. \quad (6.3.7c)$$

For the purposes of calculation, the undisturbed fields \mathbf{u}^∞ and p^∞ must be expressed as polyads of \mathbf{x} with *irreducible* tensorial coefficients [101]. The leading coefficient \mathbf{u}_0^∞ is a vector and thus is automatically irreducible. The velocity-gradient tensor $(\nabla \mathbf{u}^\infty)_0$ may be decomposed as follows:

$$(\nabla \mathbf{u}^\infty)_0 = \dot{\gamma} + \boldsymbol{\omega} = \dot{\gamma} - \frac{1}{2} \boldsymbol{\epsilon} \cdot \mathbf{w}, \quad (6.3.8)$$

where $\dot{\gamma}$ is the rate-of-strain (second-order, symmetric and traceless) tensor, $\boldsymbol{\omega}$ is the vorticity (second-order, antisymmetric) tensor, and $\mathbf{w} = \boldsymbol{\epsilon} : \boldsymbol{\omega}$ is the vorticity pseudovector. We may express $\dot{\gamma}$, $\boldsymbol{\omega}$, and \mathbf{w} in terms of $(\nabla \mathbf{u}^\infty)_0$ as follows:

$$\dot{\gamma} = \frac{1}{2} [(\nabla \mathbf{u}^\infty)_0 + (\nabla \mathbf{u}^\infty)_0^\dagger], \quad (6.3.9a)$$

$$\boldsymbol{\omega} = \frac{1}{2} [(\nabla \mathbf{u}^\infty)_0 - (\nabla \mathbf{u}^\infty)_0^\dagger], \quad (6.3.9b)$$

$$\mathbf{w} = (\nabla \times \mathbf{u}^\infty)_0. \quad (6.3.9c)$$

For circular Poiseuille flow,

$$\dot{\gamma} = -\frac{2Vb}{R^2} (\hat{\mathbf{e}}_y \hat{\mathbf{e}}_x + \hat{\mathbf{e}}_x \hat{\mathbf{e}}_y) \quad (6.3.10a)$$

$$\boldsymbol{\omega} = -\frac{2Vb}{R^2} (\hat{\mathbf{e}}_y \hat{\mathbf{e}}_x - \hat{\mathbf{e}}_x \hat{\mathbf{e}}_y), \quad (6.3.10b)$$

$$\mathbf{w} = -\frac{4Vb}{R^2} (\hat{\mathbf{e}}_x \times \hat{\mathbf{e}}_y) = -\frac{4Vb}{R^2} \hat{\mathbf{e}}_z. \quad (6.3.10c)$$

The velocity-curvature tensor $(\nabla \nabla \mathbf{u}^\infty)_0$ may be similarly decomposed as follows (expressed in index

notation) [114]:

$$\left(\frac{\partial^2 v_k}{\partial x_i \partial x_j} \right)^\infty = 2\eta_{ijk} - \frac{1}{3}(\epsilon_{ikl}\delta_{mj} + \epsilon_{jkl}\delta_{mi})\theta_{lm} + \frac{1}{5}(4\delta_{ij}\delta_{kl} - \delta_{ik}\delta_{jl} - \delta_{jk}\delta_{il})d_l, \quad (6.3.11)$$

where $\boldsymbol{\eta}$ is a (third-order, symmetric and traceless in any two indices) tensor, $\boldsymbol{\theta}$ is a (second-order, symmetric and traceless) pseudotensor, and \mathbf{d} is a vector. We may express $\boldsymbol{\eta}$, $\boldsymbol{\theta}$, and \mathbf{d} in terms of $(\nabla \nabla \mathbf{u}^\infty)_0$ as follows:

$$\begin{aligned} \eta_{ijk} &= \frac{1}{6} \left[\left(\frac{\partial^2 v_k}{\partial x_i \partial x_j} \right)^\infty + \left(\frac{\partial^2 v_j}{\partial x_k \partial x_i} \right)^\infty + \left(\frac{\partial^2 v_i}{\partial x_j \partial x_k} \right)^\infty \right] \\ &\quad - \frac{1}{30} \left[\delta_{ij} \left(\frac{\partial^2 v_k}{\partial x_l \partial x_l} \right)^\infty + \delta_{ik} \left(\frac{\partial^2 v_j}{\partial x_l \partial x_l} \right)^\infty + \delta_{jk} \left(\frac{\partial^2 v_i}{\partial x_l \partial x_l} \right)^\infty \right]. \end{aligned} \quad (6.3.12a)$$

$$\theta_{ij} = \frac{1}{2} \left[\left(\frac{\partial^2 v_l}{\partial x_i \partial x_k} \right)^\infty \epsilon_{lkj} + \left(\frac{\partial^2 v_l}{\partial x_j \partial x_k} \right)^\infty \epsilon_{lki} \right] \quad (6.3.12b)$$

$$d_i = \frac{1}{2} \left(\frac{\partial^2 v_i}{\partial x_j \partial x_j} \right)^\infty, \quad (6.3.12c)$$

For circular Poiseuille flow,

$$\boldsymbol{\eta} = \frac{2V}{R^2} \left\{ \hat{\mathbf{e}}_x \hat{\mathbf{e}}_x \hat{\mathbf{e}}_x - \frac{1}{5} [\boldsymbol{\delta} \hat{\mathbf{e}}_x + (\boldsymbol{\delta} \hat{\mathbf{e}}_x)^\dagger + \hat{\mathbf{e}}_x \boldsymbol{\delta}] \right\}, \quad (6.3.13a)$$

$$\boldsymbol{\theta} = \mathbf{0}, \quad (6.3.13b)$$

$$\mathbf{d} = -\frac{4V}{R^2} \hat{\mathbf{e}}_x. \quad (6.3.13c)$$

Using the above definitions, the undisturbed velocity \mathbf{u}^∞ and pressure p^∞ may be expressed in terms of the irreducible tensors:

$$\mathbf{u}^\infty = \mathbf{u}_0^\infty + \frac{1}{2}(\mathbf{w} \times \mathbf{x}) + \dot{\gamma} \cdot \mathbf{x} + \boldsymbol{\eta} : \mathbf{x} \mathbf{x} - \frac{1}{3}[(\mathbf{x} \cdot \boldsymbol{\theta}) \times \mathbf{x}] + \frac{1}{5}[2r^2 \mathbf{d} - (\mathbf{d} \cdot \mathbf{x}) \mathbf{x}], \quad (6.3.14a)$$

$$p^\infty = 2\mu(\mathbf{d} \cdot \mathbf{x}). \quad (6.3.14b)$$

The undisturbed stress tensor $\boldsymbol{\sigma}^\infty$ straightforwardly follows:

$$\begin{aligned} \boldsymbol{\sigma}^\infty &= -p^\infty \boldsymbol{\delta} + \mu[\nabla \mathbf{u}^\infty + (\nabla \mathbf{u}^\infty)^\dagger] \\ &= 2\mu\dot{\gamma} + 4\mu(\boldsymbol{\eta} \cdot \mathbf{x}) - \frac{1}{3}\mu[(\boldsymbol{\theta} \times \mathbf{x}) + (\boldsymbol{\theta} \times \mathbf{x})^\dagger] + \frac{3}{5}\mu[\mathbf{d} \mathbf{x} + \mathbf{x} \mathbf{d} - 4(\mathbf{d} \cdot \mathbf{x}) \boldsymbol{\delta}]. \end{aligned} \quad (6.3.14c)$$

6.4 Disturbance fields

When vesicles are freely suspended in a viscous fluid flowing through a conduit, they induce a hydrodynamic disturbance to the flow field. We define the exterior disturbance fields \mathbf{u}' , p' , and $\boldsymbol{\sigma}'$ by,

$$\mathbf{u}' = \mathbf{u} - \mathbf{u}^\infty, \quad (6.4.1a)$$

$$p' = p - p^\infty, \quad (6.4.1b)$$

$$\boldsymbol{\sigma}' = \boldsymbol{\sigma} - \boldsymbol{\sigma}^\infty. \quad (6.4.1c)$$

The interior disturbance fields $\check{\mathbf{u}}'$, \check{p}' , and $\check{\boldsymbol{\sigma}}'$ are given by,

$$\check{\mathbf{u}}' = \check{\mathbf{u}}, \quad (6.4.2a)$$

$$\check{p}' = \check{p}, \quad (6.4.2b)$$

$$\check{\boldsymbol{\sigma}}' = \check{\boldsymbol{\sigma}}. \quad (6.4.2c)$$

It is our goal to obtain expressions for the disturbance fields corresponding to the flow induced by a small, quasi-spherical vesicle freely suspended in conduit flow. The governing equations presented in §2.3 may be recast in terms of the disturbance fields:

$$\left. \begin{aligned} \nabla \cdot \mathbf{u}' &= 0, \\ \nabla \cdot \boldsymbol{\sigma}' &= -\nabla p' + \mu \nabla^2 \mathbf{u}' = \mathbf{0}, \end{aligned} \right\} \quad \text{in the suspending fluid,} \quad (6.4.3a)$$

$$\left. \begin{aligned} \nabla \cdot \check{\mathbf{u}}' &= 0, \\ \nabla \cdot \check{\boldsymbol{\sigma}}' &= -\nabla \check{p}' + \check{\mu} \nabla^2 \check{\mathbf{u}}' = \mathbf{0}, \end{aligned} \right\} \quad \text{inside the vesicles,} \quad (6.4.3b)$$

$$\mathbf{u}' = \mathbf{0} \quad \text{on the channel wall,} \quad (6.4.4)$$

$$\mathbf{u}' = \mathbf{0} \quad \text{in the far field,} \quad (6.4.5)$$

$$\left. \begin{aligned} \mathbf{u}' - \check{\mathbf{u}}' &= -\mathbf{u}^\infty \\ (\boldsymbol{\sigma}' - \check{\boldsymbol{\sigma}}') \cdot \hat{\mathbf{n}} &= -\boldsymbol{\sigma}^\infty \cdot \hat{\mathbf{n}} + \{-2H\tau + 2E_B [\nabla_s^2 H + 2(H^2 - K)H]\} \hat{\mathbf{n}} \\ &\quad - \nabla_s \tau \\ \nabla_s \cdot \mathbf{u}' &= -\nabla_s \cdot \mathbf{u}^\infty, \quad \nabla_s \cdot \check{\mathbf{u}}' = \mathbf{0} \end{aligned} \right\} \quad \text{on the vesicle membrane.} \quad (6.4.6)$$

The vesicle translational velocity \mathbf{U} and rotational velocity $\boldsymbol{\Omega}$ are given by (2.4.1) and (2.4.2), respectively. In terms of the disturbance fields, we have,

$$\mathbf{U} = \frac{1}{\Omega_0} \int_{\partial\gamma_0} \mathbf{x} [\hat{\mathbf{n}} \cdot (\mathbf{u}' + \mathbf{u}^\infty)] dS = \frac{1}{\Omega_0} \int_{\partial\gamma_0} \mathbf{x} (\hat{\mathbf{n}} \cdot \ddot{\mathbf{u}}') dS, \quad (6.4.7)$$

$$\boldsymbol{\Omega} = \frac{1}{\Omega_0} \int_{\partial\gamma_0} \frac{1}{2} [\hat{\mathbf{n}} \times (\mathbf{u}' + \mathbf{u}^\infty)] dS = \frac{1}{\Omega_0} \int_{\partial\gamma_0} \frac{1}{2} (\hat{\mathbf{n}} \times \check{\mathbf{u}}') dS. \quad (6.4.8)$$

In addition to the motion of the vesicle, we also seek the extra dissipation created by its presence in the conduit. Brenner derived the following reciprocal theorem for the extra pressure drop Δp^+ [14, 15]:

$$-\Delta p^+ V A_x = \int_{\mathcal{S}_\infty} \hat{\mathbf{n}} \cdot (\boldsymbol{\sigma}^\infty \cdot \mathbf{u}' - \boldsymbol{\sigma}' \cdot \mathbf{u}^\infty) dS, \quad (6.4.9)$$

where \mathcal{S}_∞ is a fictitious far-field surface enclosing the channel and the vesicle. The significance of (6.4.9) is that we may obtain an expression for Δp^+ without the need for wall reflections. In the forthcoming development, it will be convenient to define \mathcal{S}_∞ as a sphere of radius r and take the limit as $r \rightarrow \infty$. Thus, only the leading-order terms in the disturbance flow field contribute to the extra pressure drop Δp^+ .

In this chapter, we shall pursue a solution of (6.4.3)-(6.4.9) by means of harmonic expansions. The linearity of the Stokes equations implies that the solutions for the velocity and pressure fields be linear in the forcing functions \mathbf{u}_0^∞ , \mathbf{w} , $\dot{\gamma}$, $\boldsymbol{\omega}$, \mathbf{d} , $\boldsymbol{\theta}$, and $\boldsymbol{\eta}$. Following [76], we shall make use of the invariant form of the fundamental harmonics, introduced in the next section.

6.5 Fundamental harmonics

The tensorial harmonic $\overset{(n)}{\mathbf{H}}(\mathbf{x})$ of order n satisfies Laplace's equation,

$$\nabla^2 \overset{(n)}{\mathbf{H}} = \mathbf{0}, \quad (6.5.1)$$

with $n = 0, 1, 2, \dots$. The solutions of Laplace's equation come in two flavors: those which decay asymptotically with increasing \mathbf{x} but are singular at $\mathbf{x} = \mathbf{0}$ and those which grow without bound with increasing \mathbf{x} but are regular (i.e., bounded) at $\mathbf{x} = \mathbf{0}$. The general formula for the n th order *decaying harmonic* is given by,

$$\overset{(n)}{\mathbf{H}}^- = \underbrace{\nabla \cdots \nabla}_{n \text{ times}} \left(\frac{1}{r} \right). \quad (6.5.2)$$

The decaying harmonics are applicable to *exterior problems*. The first (scalar) decaying harmonic $\overset{(0)}{\Phi}^-$ is the *fundamental solution* of Laplace's equation and is sometimes called a “monopole” in connection with the electrodynamics literature [67]. The ascending harmonics $\overset{(1)}{\mathbf{H}}^-, \overset{(2)}{\mathbf{H}}^-, \overset{(3)}{\mathbf{H}}^-, \dots$ are likewise called the “dipole,” “quadrupole,” “octupole,” and so on. The generic n th order *growing harmonic*

is obtained by simply multiplying the like-ordered decaying harmonic by r^{2n+1} :

$$\overset{(n)}{\mathbf{H}}^+ = r^{2n+1} \underbrace{\nabla \cdots \nabla}_{n \text{ times}} \left(\frac{1}{r} \right). \quad (6.5.3)$$

The growing harmonics are applicable to *interior problems*. Since Laplace's equation is linear, general solutions may be constructed via superposition. The fundamental harmonics $\overset{(n)}{\mathbf{H}}^-$ and $\overset{(n)}{\mathbf{H}}^+$ with $n = 0, 1, 2, \dots$ form a complete basis for constructing any solution of Laplace's equation.

For problems with spherical symmetry, it is convenient to separate the fundamental harmonics $\overset{(n)}{\mathbf{H}}$ into radial and angular parts:

$$\overset{(n)}{\mathbf{H}}^-(\mathbf{x}) = r^{-(n+1)} \overset{(n)}{\mathbf{Y}}(\hat{\mathbf{x}}), \quad (6.5.4a)$$

$$\overset{(n)}{\mathbf{H}}^+(\mathbf{x}) = r^n \overset{(n)}{\mathbf{Y}}(\hat{\mathbf{x}}), \quad (6.5.4b)$$

where $\hat{\mathbf{x}} = \mathbf{x}/r$ is the unit vector in the radial direction. The function $\overset{(n)}{\mathbf{Y}}(\hat{\mathbf{x}})$ is called the *surface spherical harmonic of order n* and is generally given by,

$$\overset{(n)}{\mathbf{Y}} = r^{n+1} \underbrace{\nabla \cdots \nabla}_{n \text{ times}} \left(\frac{1}{r} \right) = \text{polyad of } \hat{\mathbf{x}} \text{ and } \boldsymbol{\delta}. \quad (6.5.5)$$

It is clear by the definition (6.5.5) that tensorial harmonics $\overset{(n)}{\mathbf{Y}}(\hat{\mathbf{x}})$ for which $n \geq 2$ are symmetric and traceless in any two indices.¹ The first few surface spherical harmonics, expressed in index notation, are,

$$\begin{aligned} \overset{(0)}{Y} &= 1, \\ \overset{(1)}{Y}_i &= -\hat{x}_i, \\ \overset{(2)}{Y}_{ij} &= 3\hat{x}_i\hat{x}_j - \delta_{ij}, \\ \overset{(3)}{Y}_{ijk} &= -15\hat{x}_i\hat{x}_j\hat{x}_k + 3(\delta_{ij}\hat{x}_k + \delta_{ik}\hat{x}_j + \delta_{jk}\hat{x}_i), \\ \overset{(4)}{Y}_{ijkl} &= 105\hat{x}_i\hat{x}_j\hat{x}_k\hat{x}_l - 15(\delta_{ij}\hat{x}_k\hat{x}_l + \delta_{ik}\hat{x}_j\hat{x}_l + \delta_{il}\hat{x}_j\hat{x}_k + \delta_{jk}\hat{x}_i\hat{x}_l + \delta_{jl}\hat{x}_i\hat{x}_k + \delta_{kl}\hat{x}_i\hat{x}_j) \\ &\quad + 3(\delta_{ij}\delta_{kl} + \delta_{ik}\delta_{jl} + \delta_{il}\delta_{jk}), \\ \text{etc.}, \end{aligned}$$

It is straightforward to show that $\overset{(n)}{\mathbf{Y}}(\hat{\mathbf{x}})$ satisfies Legendre's equation,

$$\nabla_{\Omega}^2 \overset{(n)}{\mathbf{Y}} = -n(n+1) \overset{(n)}{\mathbf{Y}}, \quad (6.5.6)$$

¹The symmetry statement follows from the commutativity of the gradient operator ∇ . Traclessness is obvious from the fact $1/r$ is the fundamental solution of Laplace's equation, $\nabla^2(1/r) = 0$.

where Ω is the solid angle and

$$\nabla_\Omega = r\nabla - \mathbf{x}\frac{\partial}{\partial r} = \hat{\mathbf{e}}_\theta\frac{\partial}{\partial\theta} + \frac{\hat{\mathbf{e}}_\phi}{\sin\theta}\frac{\partial}{\partial\phi}$$

is the surface gradient operator on the unit sphere. Thus, $\overset{(n)}{\mathbf{Y}}$ is the eigenfunction for the n th deformation mode of the unit sphere, with associated eigenvalue $-n(n+1)$. The surface spherical harmonics are mutually orthogonal, viz.,

$$\int_{\mathcal{S}_\Omega} \overset{(n)}{\mathbf{Y}}(\hat{\mathbf{x}}) \overset{(m)}{\mathbf{Y}}(\hat{\mathbf{x}}) d\Omega = \begin{cases} \text{polyad of } \boldsymbol{\delta} & \text{if } m = n, \\ \mathbf{0} & \text{otherwise,} \end{cases} \quad (6.5.7)$$

where S_Ω is the surface of the unit sphere with surface element $d\Omega = \sin\theta d\theta d\phi$. The first few orthogonality relations, expressed in index notation, are,

$$\begin{aligned} \int_{\mathcal{S}_\Omega} \overset{(0)(0)}{Y} \overset{(0)(0)}{Y} d\Omega &= 4\pi, \\ \int_{\mathcal{S}_\Omega} \overset{(1)(1)}{Y_i} \overset{(1)(1)}{Y_j} d\Omega, &= \frac{4}{3}\pi\delta_{ij} \\ \int_{\mathcal{S}_\Omega} \overset{(2)}{Y_{ij}} \overset{(2)}{Y_{kl}} d\Omega &= \frac{12}{5}\pi(\delta_{il}\delta_{jk} + \delta_{ik}\delta_{jl}) - \frac{8}{5}\pi\delta_{ij}\delta_{kl}, \\ \int_{\mathcal{S}_\Omega} \overset{(3)}{Y_{ijk}} \overset{(3)}{Y_{lpq}} d\Omega &= \frac{60}{7}\pi(\delta_{iq}\delta_{jp}\delta_{kl} + \delta_{ip}\delta_{jq}\delta_{kl} + \delta_{iq}\delta_{jl}\delta_{kp} + \delta_{il}\delta_{jq}\delta_{kp} + \delta_{ip}\delta_{jl}\delta_{kq} + \delta_{il}\delta_{jp}\delta_{kq}) \\ &\quad - \frac{24}{7}\pi(\delta_{iq}\delta_{jk}\delta_{lp} + \delta_{ik}\delta_{jq}\delta_{lp} + \delta_{ij}\delta_{kq}\delta_{lp} + \delta_{ip}\delta_{jk}\delta_{lq} + \delta_{ik}\delta_{jp}\delta_{lq} + \delta_{ij}\delta_{kp}\delta_{lq}) \\ &\quad + \delta_{il}\delta_{jk}\delta_{pq} + \delta_{ik}\delta_{jl}\delta_{pq} + \delta_{ij}\delta_{kl}\delta_{pq}), \\ \int_{\mathcal{S}_\Omega} \overset{(3)}{Y_{ijkl}} \overset{(3)}{Y_{pqrs}} d\Omega &= \frac{140}{3}\pi(\delta_{is}\delta_{jr}\delta_{kq}\delta_{lp} + 23 \text{ other terms}) - \frac{40}{3}\pi(\delta_{is}\delta_{jr}\delta_{kl}\delta_{pq} + 71 \text{ other terms}) \\ &\quad + \frac{32}{3}\pi(\delta_{il}\delta_{jk}\delta_{ps}\delta_{qr} + 8 \text{ other terms}), \end{aligned}$$

etc.

6.6 Lamb's general solution

The utility of the fundamental harmonics is that they form a basis for solutions of Laplace's equation. As such, they also form the natural basis for solutions of Stokes' equations, for upon taking the divergence of the equation of motion and applying the incompressibility condition, one obtains the following governing equations for the disturbance fields \mathbf{u}' and p' :

$$\nabla^2 \mathbf{u}' = -\frac{1}{\mu} \nabla p', \quad (6.6.1a)$$

$$\nabla^2 p' = 0. \quad (6.6.1b)$$

Similar equations may be written for $\check{\mathbf{u}}'$ and \check{p}' . Clearly, the disturbance pressure p' is a harmonic function (i.e., a solution of Laplace's equation). The disturbance velocity \mathbf{u}' comprises a homogeneous solution, which satisfies Laplace's equation, and a particular solution due to the forcing term on the right-hand side of (6.6.1a).

A general solution of (6.6.1) in spherical coordinates was presented by Lamb [98, 72]. An invariant form of Lamb's general solution was later presented by Hinch [76].²

$$\mathbf{u}' = \nabla(\mathbf{x} \cdot \mathbf{A} + \Phi) + \mathbf{x} \times \nabla\Psi - 2\mathbf{A}, \quad (6.6.2a)$$

$$p' = p_{\text{ref}} + 2\mu(\nabla \cdot \mathbf{A}), \quad (6.6.2b)$$

where p_{ref} is a reference pressure and \mathbf{A} , Φ , and Ψ are harmonic functions. Similar expressions may be written for the general solution of $\check{\mathbf{u}}'$ and \check{p}' .

Clearly, \mathbf{A} is a vector, Φ a scalar, and Ψ a pseudoscalar. These functions may be constructed by superposing the fundamental harmonics $\overset{(n)}{\mathbf{H}}(\mathbf{x})$, $n = 0, 1, 2, \dots$ with multiplicative (tensorial) coefficients determined from boundary conditions. Completely general expressions for \mathbf{A} , Φ , and Ψ are given by,

$$\mathbf{A}(\mathbf{x}, t) = \sum_{n=0}^{\infty} \overset{(n+1)}{\mathbf{A}}(t)(\cdot)^n \overset{(n)}{\mathbf{H}}(\mathbf{x}), \quad (6.6.3a)$$

$$\Phi(\mathbf{x}, t) = \sum_{n=0}^{\infty} \overset{(n)}{\Phi}(t)(\cdot)^n \overset{(n)}{\mathbf{H}}(\mathbf{x}), \quad (6.6.3b)$$

$$\Psi(\mathbf{x}, t) = \sum_{n=0}^{\infty} \overset{(n)}{\Psi}(t)(\cdot)^n \overset{(n)}{\mathbf{H}}(\mathbf{x}), \quad (6.6.3c)$$

where $\overset{(n)}{\mathbf{A}}$, $\overset{(n)}{\Phi}$, and $\overset{(n)}{\Psi}$ are the tensorial coefficients of order n and $(\cdot)^n$ denotes an n -fold inner product. Note that the functions depend parametrically on time t through the kinematic condition for the vesicle shape.

Supposing that the origin at $\mathbf{x} = \mathbf{0}$ is located at the vesicle's center of mass, then the exterior disturbance fields \mathbf{u}' and p' must be constructed using only the *decaying harmonics* $\overset{(n)}{\mathbf{H}}^-$. By contrast, the interior disturbance fields $\check{\mathbf{u}}'$ and \check{p}' must be constructed using only the *growing harmonics* $\overset{(n)}{\mathbf{H}}^+$. The membrane tension τ , which must also be determined as part of the solution and cannot depend on r , is similarly expanded in a series of *surface spherical harmonics* in order to fulfill the stress boundary conditions on the membrane.

²Tran-Cong and Blake proposed a similar solution [162], but neglected to include the term containing Ψ in (6.6.2a).

6.7 Vesicle geometry

Recall the definition of the excess surface area Δ in (2.5.12). For quasi-spherical vesicles, $\Delta \ll 1$ and it is convenient to adopt an Eulerian representation for the vesicle shape:

$$\mathbf{x}_s(\hat{\mathbf{x}}, t) = \mathbf{x}_c(t) + r_s(\hat{\mathbf{x}}, t)\hat{\mathbf{x}}, \quad (6.7.1)$$

where

$$r_s(\hat{\mathbf{x}}, t) = r_0 + \Delta^{\frac{1}{2}} f(\hat{\mathbf{x}}, t), \quad (6.7.2)$$

and

$$\frac{D\mathbf{x}_c}{Dt} = \mathbf{U}, \quad r_s \frac{D\hat{\mathbf{x}}}{Dt} = (\boldsymbol{\delta} - \hat{\mathbf{x}}\hat{\mathbf{x}}) \cdot (\mathbf{u} - \mathbf{U}), \quad (6.7.3)$$

by the kinematic condition (2.1.1). The power of $\frac{1}{2}$ ascribed to Δ in the second term on the right-hand side of (6.7.2) is chosen in order to conserve surface area at all orders in Δ . The surface unit normal $\hat{\mathbf{n}}$, surface metric G_s , and surface element dS have the following representation in spherical coordinates (see Appendix A.7.4):

$$\hat{\mathbf{n}} = \frac{r_s \hat{\mathbf{x}} - \nabla_\Omega r_s}{\sqrt{r_s^2 + (\nabla_\Omega r_s) \cdot (\nabla_\Omega r_s)}}, \quad (6.7.4)$$

$$G_s = r_s \sin \theta \sqrt{r_s^2 + (\nabla_\Omega r_s) \cdot (\nabla_\Omega r_s)}, \quad (6.7.5)$$

$$dS = G_s d\theta d\phi = r_s \sqrt{r_s^2 + (\nabla_\Omega r_s) \cdot (\nabla_\Omega r_s)} d\Omega. \quad (6.7.6)$$

By definition, $\partial f / \partial r = 0$ and so

$$\nabla_\Omega f = r \nabla f - \mathbf{x} \frac{\partial f}{\partial r} = r \nabla f. \quad (6.7.7)$$

Since f does not depend on r , its expansion depends only on the surface spherical harmonics $\overset{(n)}{\mathbf{Y}}$, $n = 0, 1, 2, \dots$. The kinematic condition (2.2.1) stipulates that,

$$\Delta^{\frac{1}{2}} \left(\frac{\partial f}{\partial t} + \mathbf{u}_s \cdot \nabla f \right) = \hat{\mathbf{x}} \cdot (\mathbf{u}_s - \mathbf{U}), \quad (6.7.8)$$

where $\mathbf{u}_s = \mathbf{u}' + \mathbf{u}^\infty = \check{\mathbf{u}}'$ at $r = r_s$. The membrane tension $\tau = \tau(\hat{\mathbf{x}}, t)$ is treated as a function of the spherical angular coordinates θ and ϕ (as well as time t), whence $\partial \tau / \partial r = 0$ in the Eulerian representation of the vesicle surface. Thus,

$$\nabla_\Omega \tau = r \nabla \tau - \mathbf{x} \frac{\partial \tau}{\partial r} = r \nabla \tau. \quad (6.7.9)$$

Following [53] and using the relations given in Appendix A.7.4, we may express the geometrical

properties of the vesicle surface (transferred to the spherical surface at $r = r_0$) in perturbation series with respect to $\Delta^{\frac{1}{2}}$:

$$G_s/(r_s^2 \sin \theta) = 1 + \frac{1}{2} \Delta (\nabla f) \cdot (\nabla f) - \Delta^{\frac{3}{2}} (f/r_0) (\nabla f) \cdot (\nabla f) + O(\Delta^2), \quad (6.7.10)$$

$$\hat{\mathbf{n}} = \hat{\mathbf{x}} - \Delta^{\frac{1}{2}} \nabla f + \Delta [(f/r_0) (\nabla f) - \frac{1}{2} (\nabla f) \cdot (\nabla f) \hat{\mathbf{x}}] + O(\Delta^{\frac{3}{2}}), \quad (6.7.11)$$

$$2H = -r_0^{-1} \left\{ 2 - \Delta^{\frac{1}{2}} (2f/r_0 + r_0 \nabla^2 f) + 2\Delta [(f/r_0)^2 + f \nabla^2 f] \right\} + O(\Delta^{\frac{3}{2}}/r_0), \quad (6.7.12)$$

$$\begin{aligned} 2\nabla_s^2 H + 4(H^2 - K)H \\ = \Delta^{\frac{1}{2}} \nabla^4 f - \Delta r_0^{-1} [4f \nabla^4 f + 4(\nabla^2 f)(\nabla f) \cdot (\nabla f) + 2(\nabla \nabla f) : (\nabla \nabla f) + (\nabla^2 f)^2] + O(\Delta^{\frac{3}{2}}/r_0^3). \end{aligned} \quad (6.7.13)$$

We must also expand the surface gradient of τ , which appears in the tangential stress condition on the vesicle membrane:

$$\nabla_s \tau = \nabla \tau + \Delta^{\frac{1}{2}} [\hat{\mathbf{x}} (\nabla f) \cdot \nabla \tau - (f/r_0) \nabla \tau] + O(\Delta \tau / r_0). \quad (6.7.14)$$

Here, we have made use of the identity $\partial \tau / \partial r = 0$.

The vesicle's enclosed volume Ω_0 and surface area A_0 may be expressed as follows:

$$\Omega_0 = \int_{\mathcal{S}_\Omega} \frac{1}{2} r_s^2 d\Omega = \frac{4}{3} \pi r_0^3, \quad (6.7.15a)$$

$$A_0 = \int_{\mathcal{S}_\Omega} \frac{G_s}{\sin \theta} d\Omega = (4\pi + \Delta) r_0^2, \quad (6.7.15b)$$

By (2.3.8), the quantities Ω_0 and A_0 are required to be time invariant in the Lagrangian sense. It was shown by [112] that the surface-area constraint (6.7.15b) renders the initial-boundary-value problem nonlinear even at lowest order in the deformation parameter $\Delta^{\frac{1}{2}}$. This facet of the problem is not present for droplets, for which only the enclosed volume Ω_0 is conserved and the small-deformation analysis results in linear equations at each order. The consequences of this constraint will be made explicit in subsequent sections, wherein we shall develop a formal perturbation theory in terms of $\Delta^{\frac{1}{2}}$.

6.8 Small- Δ expansion

We now develop a formal perturbation theory in a manner similar to Chapter 3. First, we expand all dependent variables in a perturbation series with respect to $\Delta^{\frac{1}{2}}$. For the generic field ψ , we have,

$$\psi(\mathbf{x}, t) = \psi_0(\mathbf{x}, t) + \Delta^{\frac{1}{2}} \psi_1(\mathbf{x}, t) + \Delta \psi_2(\mathbf{x}, t) + \dots \quad (6.8.1)$$

To the perturbation-series expansion for τ we must add an isotropic, singular contribution $\tau_{-1}\Delta^{-\frac{1}{2}}$, which balances the static pressure jump $2\tau_{-1}\Delta^{-\frac{1}{2}}$ across the membrane. This contribution is spatially homogeneous on the membrane, and so its direct contribution to the Stokes-flow solution is only through the normal stress condition on the membrane. However, it also admits an *indirect* contribution to the flow in that the velocity and pressure fields will depend on the value of τ_{-1} . It will be shown that this value is determined from the constraint on the membrane surface area.

By expanding the dependent variables in powers of $\Delta^{\frac{1}{2}}$ and collecting terms of like order in $\Delta^{\frac{1}{2}}$ from the equations presented §6.4, an ordered set of perturbation equations is obtained. The reader is referred to Appendix G for an ordered list of the perturbation equations. These equations are to be solved sequentially, beginning by setting $\Delta = 0$ so as to derive the so-called “leading-order solution.” Corrections to this solution are subsequently obtained by expanding the perturbation equations to higher order in $\Delta^{\frac{1}{2}}$. By making the quasi-spherical assumption, a solution can be efficiently obtained by use of spherical-harmonic expansions. In order to facilitate use of the surface spherical harmonics, we must first transfer boundary conditions on the vesicle membrane to a spherical surface of radius r_0 . This procedure is outlined below.

6.8.1 Transfer of boundary conditions

In §6.7, we transferred the geometrical properties of the vesicle to the spherical surface $r = r_0$. We must now apply the same procedure to the disturbance fields, membrane tension τ , and shape function f . Generally, we transfer the boundary value of some field ψ to the surface $r = r_0$ by expanding ψ in a Taylor series about $r = r_0$ and evaluating the result at $r = r_s$:

$$\begin{aligned} \psi|_{r=r_s} &= \left[\psi + \Delta^{\frac{1}{2}} f \frac{\partial \psi}{\partial r} + \frac{\Delta f^2}{2} \frac{\partial^2 \psi}{\partial r^2} + \dots \right] \Big|_{r=r_0} \\ &= \left\{ \psi_0 + \Delta^{\frac{1}{2}} \left(\psi_1 + f_0 \frac{\partial \psi_0}{\partial r} \right) + \Delta \left[\psi_2 + f_0 \frac{\partial \psi_1}{\partial r} + \left(f_1 + \frac{f_0^2}{2} \frac{\partial}{\partial r} \right) \frac{\partial \psi_0}{\partial r} \right] + O(\Delta^{\frac{3}{2}}) \right\} \Big|_{r=r_0}. \end{aligned} \quad (6.8.2)$$

The upper bound of integration in integrals of ψ over $0 \leq r \leq r_0 + \Delta^{\frac{1}{2}} f$ must also be transferred to the new surface:

$$\begin{aligned} \int_0^{r_0 + \Delta^{\frac{1}{2}} f} \psi dr &= \int_0^{r_0} \psi dr + \int_{r_0}^{r_0 + \Delta^{\frac{1}{2}} f} \psi dr \\ &= \int_0^{r_0} \psi dr + \int_{r_0}^{r_0 + \Delta^{\frac{1}{2}} f} \left[\psi|_{r=r_0} + (r - r_0) \frac{\partial \psi}{\partial r} \Big|_{r=r_0} + \frac{(r - r_0)^2}{2} \frac{\partial^2 \psi}{\partial r^2} \Big|_{r=r_0} + \dots \right] dr \\ &= \left[\int_0^{r_0} \psi dr + \Delta^{\frac{1}{2}} f \psi + \frac{\Delta f^2}{2} \frac{\partial \psi}{\partial r} + \dots \right] \Big|_{r=r_0} \\ &= \left\{ \int_0^{r_0} \psi_0 dr + \Delta^{\frac{1}{2}} \left(\int_0^{r_0} \psi_1 dr + f_0 \psi_0 \right) \right. \end{aligned}$$

$$+ \Delta \left[\int_0^{r_0} \psi_2 dr + f_0 \psi_1 + \left(f_1 + \frac{f_0^2}{2} \frac{\partial}{\partial r} \right) \psi_0 \right] + O(\Delta^{\frac{3}{2}} \Big\} \Big|_{r=r_0}. \quad (6.8.3)$$

The last expression is useful for volume integrals over the vesicle region. Alternatively, it is oftentimes possible to convert volume integrals to surface integrals by use of the divergence theorem. We adopt the latter method throughout this chapter, obviating the need for (6.8.3).

6.8.2 Leading-order solution

We now pursue a solution to zeroth order in Δ . In order to facilitate analysis, we shall assume *a priori* that the characteristic vesicle dimension is small compared to the channel hydraulic radius R . Thus, we pursue a solution first for *unbounded quadratic flow*, following closely the original theory of [32]. Corrections due to wall effects can be incorporated using the method of reflections [16]. Our main objective here is to calculate the relative velocity U/V and dimensionless extra pressure drop $\Delta p^+ R / (\mu V)$, which to the best of our knowledge has not been computed by other authors who have examined this problem. Most of the focus in the literature has been on vesicle migration [28, 32, 52] and shape dynamics [86, 88, 50, 27, 7].

Since we have assumed an unbounded system at leading order, the vesicle radius r_0 supersedes R as the natural choice for a characteristic length scale. The natural time scale is then r_0/V and the stress scale is $\mu V/r_0$. Unless otherwise specified, all variables appearing hereafter will be rendered dimensionless using these characteristic scales. The vesicle boundary (transferred to the surface of a sphere) is thus defined at $r = 1$, the surface of the unit sphere \mathcal{S}_Ω . The radius ratio a and viscosity ratio κ have already been defined as relevant dimensionless parameters. A new bending parameter χ is defined as,

$$\chi = \frac{E_B}{\mu V r_0^2} \quad (\text{the bending parameter}). \quad (2.5.10)$$

Clearly, χ and β are related by $\chi = \beta/a^2$.

At leading order in Δ , the governing equations are,

$$\nabla \cdot \mathbf{u}'_0 = 0, \quad \nabla \cdot \boldsymbol{\sigma}'_0 = -\nabla p'_0 + \nabla^2 \mathbf{u}'_0 = \mathbf{0}, \quad (6.8.4)$$

$$\nabla \cdot \check{\mathbf{u}}'_0 = 0, \quad \nabla \cdot \check{\boldsymbol{\sigma}}'_0 = -\nabla \check{p}'_0 + \kappa \nabla^2 \check{\mathbf{u}}'_0 = \mathbf{0}, \quad (6.8.5)$$

at $r = 1$:

$$\frac{\partial}{\partial r} (\hat{\mathbf{x}} \cdot \mathbf{u}'_0) = -\frac{\partial}{\partial r} (\hat{\mathbf{x}} \cdot \mathbf{u}^\infty) \quad \text{or} \quad \frac{\partial}{\partial r} (\hat{\mathbf{x}} \cdot \check{\mathbf{u}}'_0) = 0, \quad (6.8.6a)$$

$$\mathbf{u}'_0 - \check{\mathbf{u}}'_0 = -\mathbf{u}^\infty, \quad (6.8.6b)$$

$$\hat{\mathbf{x}} \cdot (\boldsymbol{\sigma}'_0 - \check{\boldsymbol{\sigma}}'_0) \cdot \hat{\mathbf{x}} = -\hat{\mathbf{x}} \cdot \boldsymbol{\sigma}^\infty \cdot \hat{\mathbf{x}} + 2\tau_0 - \tau_{-1}(2f_0 + \nabla^2 f_0) + \bar{\chi} \nabla^4 f_0, \quad (6.8.6c)$$

$$(\delta - \hat{x}\hat{x}) \cdot (\sigma'_0 - \check{\sigma}'_0) \cdot \hat{x} = -(\delta - \hat{x}\hat{x}) \cdot \sigma^\infty \cdot \hat{x} - \nabla\tau_0, \quad (6.8.6d)$$

$$\frac{\partial f_0}{\partial \bar{t}} - \hat{x} \cdot (\mathbf{u}'_0 - \mathbf{U}_0) = \hat{x} \cdot \mathbf{u}^\infty \quad \text{or} \quad \frac{\partial f_0}{\partial \bar{t}} - \hat{x} \cdot (\check{\mathbf{u}}'_0 - \mathbf{U}_0) = 0, \quad (6.8.6e)$$

$$\int_{\mathcal{S}_\Omega} [(\nabla f_0) \cdot (\nabla f_0) - 2f_0^2] d\Omega = 2, \quad (6.8.6f)$$

$$\int_{\mathcal{S}_\Omega} f_0 d\Omega = 0, \quad (6.8.6g)$$

$$\frac{4}{3}\pi U_0 = \int_{\mathcal{S}_\Omega} \hat{x}[\hat{x} \cdot (\mathbf{u}'_0 + \mathbf{u}^\infty)] d\Omega = \int_{\mathcal{S}_\Omega} \hat{x}(\hat{x} \cdot \check{\mathbf{u}}'_0) d\Omega, \quad (6.8.6h)$$

$$\frac{4}{3}\pi \Omega_0 = \int_{\mathcal{S}_\Omega} \frac{1}{2}[\hat{x} \times (\mathbf{u}'_0 + \mathbf{u}^\infty)] d\Omega = \int_{\mathcal{S}_\Omega} \frac{1}{2}(\hat{x} \times \check{\mathbf{u}}'_0) d\Omega, \quad (6.8.6i)$$

$$-\Delta p_0^+ A_\times = \lim_{r \rightarrow \infty} r^2 \int_{\mathcal{S}_\Omega} \hat{x} \cdot (\sigma^\infty \cdot \mathbf{u}'_0 - \sigma'_0 \cdot \mathbf{u}^\infty) d\Omega, \quad (6.8.6j)$$

$$\text{as } |x| \rightarrow \infty : \quad \mathbf{u}'_0 = \mathbf{0}. \quad (6.8.7)$$

(See also Appendix G.) Here, we have rescaled the time variable $\bar{t} = \Delta^{-\frac{1}{2}}t$ and bending parameter $\bar{\chi} = \Delta^{\frac{1}{2}}\chi$. The far-field velocity \mathbf{u}^∞ , pressure p^∞ , and stress σ^∞ are given by (6.3.14) (rewritten below in dimensionless form):

$$\mathbf{u}^\infty = \mathbf{u}_0^\infty + \frac{1}{2}(\mathbf{w} \times \mathbf{x}) + \dot{\gamma} \cdot \mathbf{x} + \boldsymbol{\eta} : \mathbf{x}\mathbf{x} - \frac{1}{3}[(\mathbf{x} \cdot \boldsymbol{\theta}) \times \mathbf{x}] + \frac{1}{5}[2r^2 \mathbf{d} - (\mathbf{d} \cdot \mathbf{x})\mathbf{x}], \quad (6.3.14a)$$

$$p^\infty = 2(\mathbf{d} \cdot \mathbf{x}), \quad (6.3.14b)$$

$$\sigma^\infty = 2\dot{\gamma} + 4(\boldsymbol{\eta} \cdot \mathbf{x}) - \frac{1}{3}[(\boldsymbol{\theta} \times \mathbf{x}) + (\boldsymbol{\theta} \times \mathbf{x})^\dagger] + \frac{3}{5}[\mathbf{d}\mathbf{x} + \mathbf{x}\mathbf{d} - 4(\mathbf{d} \cdot \mathbf{x})\boldsymbol{\delta}]. \quad (6.3.14c)$$

It is clear from the surface-area constraint (6.8.6f) that the initial-boundary-value problem is nonlinear at leading order. This issue was originally pointed out by [112], who contrasted the problem of vesicles in shear flow with the analogous problem for droplets. Solutions of nonlinear equations cannot generally be constructed using the superposition principle. However, we may render the problem tractable by considering only a finite subset of shape deformation modes. This strategy was adopted by [30] for shear flow and [32] for planar and circular Poiseuille flows. Specifically, these authors obtained solutions of the small-deformation problem by expanding the shape function $f_0(\hat{x}, t)$ in an infinite series of surface spherical harmonics $\overset{(n)}{\mathbf{Y}}(\hat{x})$ with unknown tensorial coefficients $\overset{(n)}{\mathbf{F}}_0(t)$ and truncating the series after only a couple of terms.³ This procedure of expanding f_0 in terms of tensorial harmonics is inspired in part by the work of [53], who derived a constitutive equation for a dilute emulsion in shear flow based on the evolution of the second-order harmonic. For quadratic flows, it is only necessary to include second- and third-order harmonics in order to

³Farutin and coworkers noted the need for higher harmonics when carrying out the perturbation expansion to $O(\Delta)$ [48], although this will be of little concern for our purposes.

satisfy all of the boundary conditions [32]:

$$\begin{aligned} f_0(\hat{\mathbf{x}}, t) &= \overset{(2)}{\mathbf{F}_0}(t) : \overset{(2)}{\mathbf{Y}}(\hat{\mathbf{x}}) + \overset{(3)}{\mathbf{F}_0}(t)(\cdot)^3 \overset{(3)}{\mathbf{Y}}(\hat{\mathbf{x}}) \\ &= \overset{(2)}{\mathbf{F}_0}(t) : (3\hat{\mathbf{x}}\hat{\mathbf{x}} - \boldsymbol{\delta}) + \overset{(3)}{\mathbf{F}_0}(t)(\cdot)^3 \{ -15\hat{\mathbf{x}}\hat{\mathbf{x}}\hat{\mathbf{x}} + 3[\boldsymbol{\delta}\hat{\mathbf{x}} + (\boldsymbol{\delta}\hat{\mathbf{x}})^\dagger + \hat{\mathbf{x}}\boldsymbol{\delta}] \}. \end{aligned} \quad (6.8.9)$$

The volume constraint (6.8.6g) is automatically satisfied by (6.8.9) via the orthogonality of the surface spherical harmonics. The zeroth and first harmonics are not needed in the expansion. The zeroth harmonic contributes an isotropic shape deformation, which is forbidden by volume incompressibility. The first harmonic contributes an unwanted translation of the vesicle. We are left with the unknown tensorial coefficients $\overset{(2)}{\mathbf{F}_0}$ and $\overset{(3)}{\mathbf{F}_0}$, which are governed by the kinematic condition (6.8.6e). Since the surface spherical harmonics $\overset{(2)}{\mathbf{Y}}$ and $\overset{(3)}{\mathbf{Y}}$ are symmetric and traceless in any two indices, the same must be true for the coefficient tensors $\overset{(2)}{\mathbf{F}_0}$ and $\overset{(3)}{\mathbf{F}_0}$.

Given our shape ansatz (6.8.9), we construct the solution of (6.8.4)-(6.8.7) in the following manner. The disturbance fields \mathbf{u}'_0 , p'_0 , $\check{\mathbf{u}}'_0$, and \check{p}'_0 are constructed using the general solution of Stokes' equations (6.6.2):

$$\mathbf{u}'_0 = \nabla(\mathbf{x} \cdot \mathbf{A}_0 + \Phi_0) + \mathbf{x} \times \nabla\Psi_0 - 2\mathbf{A}_0, \quad (6.8.10a)$$

$$p'_0 = 2(\nabla \cdot \mathbf{A}_0), \quad (6.8.10b)$$

$$\check{\mathbf{u}}'_0 = \nabla(\mathbf{x} \cdot \check{\mathbf{A}}_0 + \check{\Phi}_0) + \mathbf{x} \times \nabla\check{\Psi}_0 - 2\check{\mathbf{A}}_0, \quad (6.8.11a)$$

$$\check{p}'_0 = \check{p}_{\text{ref}} + 2\kappa(\nabla \cdot \check{\mathbf{A}}_0), \quad (6.8.11b)$$

where \mathbf{A}_0 , Φ_0 , Ψ_0 , $\check{\mathbf{A}}_0$, $\check{\Phi}_0$, and $\check{\Psi}_0$ are harmonic functions. They are developed from the fundamental harmonics as in (6.6.3). Without loss of generality, we have set the reference pressure in the exterior fluid equal to zero. The interior reference \check{p}_{ref} is unknown *a priori* and must be determined as part of the solution. The surface tension τ_0 is similarly expanded in a series of surface spherical harmonics in order to satisfy the boundary conditions at $r = 1$:

$$\tau_0 = \tau_0^* + \Gamma_0(\hat{\mathbf{x}}, t), \quad (6.8.12)$$

where τ_0^* is an isotropic contribution and Γ_0 is expanded as,

$$\Gamma_0(\hat{\mathbf{x}}, t) = \sum_{n=1}^{\infty} \overset{(n)}{\Gamma_0}(t)(\cdot)^n \overset{(n)}{\mathbf{Y}}(\hat{\mathbf{x}}). \quad (6.8.13)$$

The singular contribution to the tension τ_{-1} is a scalar to be determined as part of the solution.

The functions \mathbf{A}_0 , Φ_0 , Ψ_0 , $\check{\mathbf{A}}_0$, $\check{\Phi}_0$, $\check{\Psi}_0$, and Γ_0 must be linear in the forcing functions \mathbf{u}_0^∞ , \mathbf{w} , $\dot{\gamma}$, $\boldsymbol{\omega}$, $\boldsymbol{\eta}$, $\boldsymbol{\theta}$, \mathbf{d} , $\overset{(2)}{\mathbf{F}_0}$, and $\overset{(3)}{\mathbf{F}_0}$, with unknown scalar prefactors. The numerical values of these prefactors are to be determined from the boundary conditions (6.8.6) at $r = 1$. Since the nonlinearity is isolated to the surface-area constraint (6.8.6f), we may construct the solutions for \mathbf{u}'_0 , p'_0 , $\check{\mathbf{u}}'_0$, \check{p}'_0 , and τ_0 in a piecewise manner, considering each of the forcing functions \mathbf{u}_0^∞ , \mathbf{w} , etc. separately, and superposing the solutions afterward. One needs only apply four boundary conditions in order to solve for the velocity, pressure, and tension fields (up to an undetermined constant representing an isotropic correction to the membrane tension):

1. the surface-area incompressibility condition (6.8.6a),
2. the kinematic continuity condition (6.8.6b),
3. the normal stress condition (6.8.6c),
4. the tangential stress condition (6.8.6d).

The leading-order shape function f_0 is prescribed by the ansatz (6.8.9). The evolution equations for the shape functions $\overset{(2)}{\mathbf{F}_0}$, and $\overset{(3)}{\mathbf{F}_0}$ are to be determined from the kinematic condition (6.8.6e). The isotropic, static contribution to the membrane tension τ_{-1} is determined by combining the kinematic condition with time derivative of (6.8.6f), which ensures that the total surface area to be time invariant in the Eulerian sense. We shall apply these boundary conditions last.

The tensorial algebra involved in satisfying the boundary conditions at $r = 1$ has been reported by others [112, 30, 32] and is similar to the procedure for droplets [53, 114]. A symbolic algebra software was developed for this problem by Einarsson, based on previous work for rigid particles in elastic fluids [39], in order expedite the algebraic manipulations. The software essentially postulates the general solutions (6.8.10)-(6.8.11) with unknown tensorial coefficients, evaluates these solutions at $r = 1$, and then uses the four boundary conditions listed above in order to specify the tensorial coefficients. We quote the main results below, including the solutions for the exterior disturbance velocity and pressure,

$$\begin{aligned} \mathbf{u}'_0 = & \left[\frac{5}{2} \left(\frac{23\kappa - 16}{23\kappa + 32} \right) \frac{\mathbf{x}\mathbf{x}\mathbf{x}\mathbf{x}}{r^5} + \frac{1}{2} \left(\frac{23\kappa - 8}{23\kappa + 32} \right) \left(-\frac{2\delta\mathbf{x}}{r^5} + \frac{5\mathbf{x}\mathbf{x}\mathbf{x}\mathbf{x}}{r^7} \right) \right] : \dot{\gamma} \\ & + \left[\frac{7}{2} \left(\frac{19\kappa - 10}{76\kappa + 85} \right) \left(\frac{\delta\mathbf{x}\mathbf{x}}{r^5} - \frac{5\mathbf{x}\mathbf{x}\mathbf{x}\mathbf{x}}{r^7} \right) + \frac{5}{2} \left(\frac{19\kappa - 5}{76\kappa + 85} \right) \left(-\frac{3\delta\mathbf{x}\mathbf{x}}{r^7} + \frac{7\mathbf{x}\mathbf{x}\mathbf{x}\mathbf{x}}{r^9} \right) \right] (\cdot)^3 \boldsymbol{\eta} \\ & - \frac{1}{3} \left(\frac{\kappa - 1}{\kappa + 4} \right) \frac{\mathbf{x}}{r^5} \times (\mathbf{x} \cdot \boldsymbol{\theta}) + \frac{1}{15} \left(-\frac{\delta}{r^3} + \frac{3\mathbf{x}\mathbf{x}}{r^5} \right) \cdot \mathbf{d} \\ & - \left[168 \left(\frac{6\bar{\chi} + \tau_{-1}}{23\kappa + 32} \right) \frac{\mathbf{x}\mathbf{x}\mathbf{x}\mathbf{x}}{r^5} + 24 \left(\frac{6\bar{\chi} + \tau_{-1}}{23\kappa + 32} \right) \left(-\frac{2\delta\mathbf{x}}{r^5} + \frac{5\mathbf{x}\mathbf{x}\mathbf{x}\mathbf{x}}{r^7} \right) \right] : \overset{(2)}{\mathbf{F}_0}(t) \\ & + \left[1,125 \left(\frac{12\bar{\chi} + \tau_{-1}}{76\kappa + 85} \right) \left(\frac{\delta\mathbf{x}\mathbf{x}}{r^5} - \frac{5\mathbf{x}\mathbf{x}\mathbf{x}\mathbf{x}}{r^7} \right) + 675 \left(\frac{12\bar{\chi} + \tau_{-1}}{76\kappa + 85} \right) \left(-\frac{3\delta\mathbf{x}\mathbf{x}}{r^7} + \frac{7\mathbf{x}\mathbf{x}\mathbf{x}\mathbf{x}}{r^9} \right) \right] (\cdot)^3 \overset{(3)}{\mathbf{F}_0}(t) \\ & + \text{additional terms with coefficients } \overset{(n)}{\mathbf{F}_0}(t), n = 4, 5, \dots, \end{aligned} \quad (6.8.14a)$$

$$\begin{aligned}
p'_0 = & 5 \left(\frac{23\kappa - 16}{23\kappa + 32} \right) \frac{\mathbf{x}\mathbf{x}}{r^5} : \dot{\gamma} - 35 \left(\frac{19\kappa - 10}{76\kappa + 85} \right) \frac{\mathbf{x}\mathbf{x}\mathbf{x}}{r^7} (\cdot)^3 \boldsymbol{\eta} \\
& - 288 \left(\frac{6\bar{\chi} + \tau_{-1}}{23\kappa + 32} \right) \frac{\mathbf{x}\mathbf{x}}{r^5} : \overset{(2)}{\mathbf{F}_0}(t) - 11,250 \left(\frac{12\bar{\chi} + \tau_{-1}}{76\kappa + 85} \right) \frac{\mathbf{x}\mathbf{x}\mathbf{x}}{r^7} (\cdot)^3 \overset{(3)}{\mathbf{F}_0}(t) \\
& + \text{additional terms with coefficients } \overset{(n)}{\mathbf{F}_0}(t), n = 4, 5, \dots,
\end{aligned} \tag{6.8.14b}$$

the interior disturbance velocity and pressure,

$$\begin{aligned}
\tilde{\mathbf{u}}'_0 = & \mathbf{u}_0^\infty + \frac{1}{2}(\mathbf{w} \times \mathbf{x}) \\
& + \left[\left(\frac{90}{23\kappa + 32} \right) \delta\mathbf{x} + \left(\frac{10}{23\kappa + 32} \right) (-5r^2 \delta\mathbf{x} + 2\mathbf{x}\mathbf{x}\mathbf{x}) \right] : \dot{\gamma} \\
& + \left[\left(\frac{350}{76\kappa + 85} \right) \delta\mathbf{x}\mathbf{x} + \frac{1}{2} \left(\frac{175}{76\kappa + 85} \right) (-3r^2 \delta\mathbf{x}\mathbf{x} + \mathbf{x}\mathbf{x}\mathbf{x}\mathbf{x}) \right] (\cdot)^3 \boldsymbol{\eta} \\
& + \frac{1}{3} \left(\frac{5}{\kappa + 4} \right) \mathbf{x} \times (\mathbf{x} \cdot \boldsymbol{\theta}) + \frac{\mathbf{d}}{3} \\
& - \left[108 \left(\frac{6\bar{\chi} + \tau_{-1}}{23\kappa + 32} \right) \delta\mathbf{x} + 12 \left(\frac{6\bar{\chi} + \tau_{-1}}{23\kappa + 32} \right) (-5r^2 \delta\mathbf{x} + 2\mathbf{x}\mathbf{x}\mathbf{x}) \right] : \overset{(2)}{\mathbf{F}_0}(t) \\
& - \left[3,600 \left(\frac{12\bar{\chi} + \tau_{-1}}{76\kappa + 85} \right) \delta\mathbf{x}\mathbf{x} + 900 \left(\frac{12\bar{\chi} + \tau_{-1}}{76\kappa + 85} \right) (-3r^2 \delta\mathbf{x}\mathbf{x} + \mathbf{x}\mathbf{x}\mathbf{x}\mathbf{x}) \right] (\cdot)^3 \overset{(3)}{\mathbf{F}_0}(t) \\
& + \text{additional terms with coefficients } \overset{(n)}{\mathbf{F}_0}(t), n = 4, 5, \dots,
\end{aligned} \tag{6.8.15a}$$

$$\begin{aligned}
\tilde{p}'_0 = & 2\tau_0^* - \left(\frac{210}{23\kappa + 32} \right) \mathbf{x}\mathbf{x} : \dot{\gamma} - \left(\frac{1,050}{76\kappa + 85} \right) \mathbf{x}\mathbf{x}\mathbf{x} (\cdot)^3 \boldsymbol{\eta} \\
& + 252 \left(\frac{6\bar{\chi} + \tau_{-1}}{23\kappa + 32} \right) \mathbf{x}\mathbf{x} : \overset{(2)}{\mathbf{F}_0}(t) + 10,800 \left(\frac{12\bar{\chi} + \tau_{-1}}{76\kappa + 85} \right) \mathbf{x}\mathbf{x}\mathbf{x} (\cdot)^3 \overset{(3)}{\mathbf{F}_0}(t) \\
& + \text{additional terms with coefficients } \overset{(n)}{\mathbf{F}_0}(t), n = 4, 5, \dots,
\end{aligned} \tag{6.8.15b}$$

and the membrane tension,

$$\begin{aligned}
\tau_0 = & \tau_0^* - \frac{5}{2} \left(\frac{19\kappa + 16}{23\kappa + 32} \right) \frac{\mathbf{x}\mathbf{x}}{r^2} : \dot{\gamma} - \frac{35}{2} \left(\frac{11\kappa + 10}{76\kappa + 85} \right) \frac{\mathbf{x}\mathbf{x}\mathbf{x}}{r^3} (\cdot)^3 \boldsymbol{\eta} - \frac{\mathbf{x}}{r} \cdot \mathbf{d} \\
& - 12 \left(\frac{(\kappa + 4)(6\bar{\chi} + \tau_{-1})}{23\kappa + 32} \right) \frac{\mathbf{x}\mathbf{x}}{r^2} : \overset{(2)}{\mathbf{F}_0}(t) - 150 \left(\frac{(2\kappa + 5)(12\bar{\chi} + \tau_{-1})}{76\kappa + 85} \right) \frac{\mathbf{x}\mathbf{x}\mathbf{x}}{r^3} (\cdot)^3 \overset{(3)}{\mathbf{F}_0}(t) \\
& + \text{additional terms with coefficients } \overset{(n)}{\mathbf{F}_0}(t), n = 4, 5, \dots
\end{aligned} \tag{6.8.16}$$

The isotropic contribution to the membrane tension τ_0^* remains unknown must be determined as part of the solution to the $O(\Delta^{\frac{1}{2}})$ problem. The singular contribution τ_{-1} is to be determined by requiring the total surface area remain constant with time [the final expression for τ_{-1} is given by (6.8.29), below].

In equations (6.8.14)-(6.8.16), we note that additional terms arise if a more general shape ansatz

than the one given in (6.8.9) is assumed. Danker and coworkers originally made the ansatz (6.8.16) and found, as we have verified, that this choice is sufficient to satisfy Stokes' equations and the boundary conditions [32]. However, the solution thus obtained represents only a subset of possible solutions for an arbitrary shape. A trivial generalization of (6.8.9) would be,

$$f_0(\hat{\mathbf{x}}, t) = \sum_{n=2}^{\infty} {}^{(n)}\mathbf{F}_0(t)(\cdot)^n {}^{(n)}\mathbf{Y}(\hat{\mathbf{x}}). \quad (6.8.17)$$

At this point, we cannot guarantee that the more general ansatz (6.8.17) reduces to (6.8.9) at long times. Physical intuition suggests that the reduced ansatz (6.8.9) will yield the important hydrodynamical results, since the second- and third-order shape modes are excited by the far-field flow[see equation (6.8.23), below] [30]. However, inclusion of additional shape modes will have a qualitative effect on the vesicle dynamics, as pointed out by [32, 48] and others.

Inserting the solution for the disturbance velocity into (6.8.6h) and (6.8.6i) yields, respectively, the translational and rotational velocity of the vesicle:

$$\mathbf{U}_0 = \mathbf{u}_0^\infty + \frac{\mathbf{d}}{3}, \quad (6.8.18)$$

$$\boldsymbol{\Omega}_0 = \frac{\mathbf{w}}{2}. \quad (6.8.19)$$

This result is equivalent to equations (3.16) and (3.18) in [14] for rigid, spherical particles. The vesicle moves with translational velocity in excess of the mean flow by $\mathbf{d}/3$. The rotational velocity of the vesicle is given by one-half the vorticity in the far field, $\mathbf{w}/2$. By construction, the vesicle is force- and torque-free. This result follows from the fact that we have assumed no net body forces or body couples in the interior fluid and that the membrane is in mechanical equilibrium (free of inertia or weight). By use of the reciprocal theorem (6.8.6j), we may also compute the extra pressure drop (multiplied by the cross-sectional area of the channel):

$$\begin{aligned} \Delta p_0^+ A_\times &= \frac{20\pi}{3} \left(\frac{23\kappa - 16}{23\kappa + 32} \right) \dot{\gamma} : \dot{\gamma} + \frac{56\pi}{3} \left(\frac{19\kappa - 10}{76\kappa + 85} \right) \boldsymbol{\eta}(\cdot)^3 \boldsymbol{\eta} + \frac{4\pi}{9} \left(\frac{\kappa - 1}{\kappa + 4} \right) \boldsymbol{\theta} : \boldsymbol{\theta} + \frac{8\pi}{15} \mathbf{d} \cdot \mathbf{d} \\ &\quad + 384\pi \left(\frac{6\bar{\chi} + \tau_{-1}}{23\kappa + 32} \right) \dot{\gamma} : {}^{(2)}\mathbf{F}_0 - 6,000\pi \left(\frac{12\bar{\chi} + \tau_{-1}}{76\kappa + 85} \right) \boldsymbol{\eta}(\cdot)^3 {}^{(3)}\mathbf{F}_0. \end{aligned} \quad (6.8.20)$$

This is an important result that, to the best of our knowledge, has never been reported in the literature. Equation (6.8.20) gives the extra pressure drop created by a small, quasi-spherical vesicle in a general, quadratic flow. The first term on the right-hand side is the *shear contribution*, and scales with the square of the rate-of-strain in the far field. The second, third, and fourth terms are the *quadratic contributions*. The last two terms arise from coupling between flow and surface deformation. The expression remains incomplete, however, because τ_{-1} has yet to be determined [see equation (6.8.29), below].

We have yet to determine the evolution of the shape. The coefficient tensors $\overset{(2)}{\mathbf{F}}_0$ and $\overset{(3)}{\mathbf{F}}_0$ are coupled through the kinematic condition (6.8.6e):

$$\frac{d\overset{(2)}{\mathbf{F}}_0}{dt} : \overset{(2)}{\mathbf{Y}} + \frac{d\overset{(3)}{\mathbf{F}}_0}{dt} (\cdot)^3 \overset{(3)}{\mathbf{Y}} = \hat{\mathbf{x}} \cdot (\mathbf{u}'_0 + \mathbf{u}^\infty) = \hat{\mathbf{x}} \cdot \tilde{\mathbf{u}}'_0. \quad (6.8.21)$$

Obviously, including more shape modes in the ansatz (6.8.9) would lead to additional terms appearing on the left-hand side of (6.8.21). Multiplying (6.8.21) by either $\overset{(2)}{\mathbf{Y}} d\Omega$ or $\overset{(3)}{\mathbf{Y}} d\Omega$, integrating over the surface of the unit sphere \mathcal{S}_Ω , and exploiting the orthogonality of the surface spherical harmonics [cf. (6.5.7)] yields a pair of evolution equations for $\overset{(2)}{\mathbf{F}}_0$ and $\overset{(3)}{\mathbf{F}}_0$:

$$\frac{24\pi}{5} \frac{d\overset{(2)}{\mathbf{F}}_0}{dt} = \int_{\mathcal{S}_\Omega} [\hat{\mathbf{x}} \cdot (\mathbf{u}'_0 + \mathbf{u}^\infty)] \overset{(2)}{\mathbf{Y}} d\Omega = \int_{\mathcal{S}_\Omega} (\hat{\mathbf{x}} \cdot \tilde{\mathbf{u}}'_0) \overset{(2)}{\mathbf{Y}} d\Omega, \quad (6.8.22a)$$

$$\frac{360\pi}{7} \frac{d\overset{(3)}{\mathbf{F}}_0}{dt} = \int_{\mathcal{S}_\Omega} [\hat{\mathbf{x}} \cdot (\mathbf{u}'_0 + \mathbf{u}^\infty)] \overset{(3)}{\mathbf{Y}} d\Omega = \int_{\mathcal{S}_\Omega} (\hat{\mathbf{x}} \cdot \tilde{\mathbf{u}}'_0) \overset{(3)}{\mathbf{Y}} d\Omega. \quad (6.8.22b)$$

Inserting our solution for the disturbance fields into (6.8.22) then gives,

$$\frac{d\overset{(2)}{\mathbf{F}}_0}{dt} = \frac{20}{23\kappa + 32} \dot{\gamma} - \frac{24(6\bar{\chi} + \tau_{-1})}{23\kappa + 32} \overset{(2)}{\mathbf{F}}_0, \quad (6.8.23a)$$

$$\frac{d\overset{(3)}{\mathbf{F}}_0}{dt} = -\frac{35}{3(76\kappa + 85)} \boldsymbol{\eta} - \frac{120(12\bar{\chi} + \tau_{-1})}{76\kappa + 85} \overset{(3)}{\mathbf{F}}_0. \quad (6.8.23b)$$

[See also equation (47) in [30] and equations (7)-(8) in [32]]. Equations (6.8.23) are the equations of motion or the deformation coefficients $\overset{(2)}{\mathbf{F}}_0$ and $\overset{(3)}{\mathbf{F}}_0$, which may be advanced from some initial configuration. The flow coefficients $\dot{\gamma}$ and $\boldsymbol{\eta}$ enter as source terms on the right-hand side, which force the evolution of the shape modes. Higher-order modes $\overset{(n)}{\mathbf{F}}_0$, $n = 4, 5, \dots$ are not directly excited by the flow. However, they are *indirectly* influenced by the flow through the nonlinear surface-area constraint (6.8.6f), which couples all shape modes together. We consider this condition below.

Inserting (6.8.9) into (6.8.6f), which conserves membrane surface area globally, leads to the following nonlinear constraint for the coefficient tensors $\overset{(2)}{\mathbf{F}}_0$ and $\overset{(3)}{\mathbf{F}}_0$:

$$\frac{96\pi}{5} \overset{(2)}{\mathbf{F}}_0 : \overset{(2)}{\mathbf{F}}_0 + \frac{3,600\pi}{7} \overset{(3)}{\mathbf{F}}_0 (\cdot)^3 \overset{(3)}{\mathbf{F}}_0 = 2. \quad (6.8.24)$$

Equation (6.8.24) must be satisfied for all t . Taking the time derivative of (6.8.24) and exploiting the symmetries of $\overset{(2)}{\mathbf{F}}_0$ and $\overset{(3)}{\mathbf{F}}_0$ gives,

$$\frac{96\pi}{5} \overset{(2)}{\mathbf{F}}_0 : \frac{d\overset{(2)}{\mathbf{F}}_0}{dt} + \frac{3,600\pi}{7} \overset{(3)}{\mathbf{F}}_0 (\cdot)^3 \frac{d\overset{(3)}{\mathbf{F}}_0}{dt} = 0. \quad (6.8.25)$$

To determine τ_{-1} , we combine (6.8.25) and (6.8.22):

$$4\overset{(2)}{\mathbf{F}}_0 : \int_{\mathcal{S}_\Omega} [\hat{\mathbf{x}} \cdot (\mathbf{u}'_0 + \mathbf{u}^\infty)] \overset{(2)}{\mathbf{Y}} d\Omega + 10\overset{(3)}{\mathbf{F}}_0(\cdot)^3 \int_{\mathcal{S}_\Omega} [\hat{\mathbf{x}} \cdot (\mathbf{u}'_0 + \mathbf{u}^\infty)] \overset{(3)}{\mathbf{Y}} d\Omega = 0, \quad (6.8.26)$$

or, in terms of the interior flow field,

$$4\overset{(2)}{\mathbf{F}}_0 : \int_{\mathcal{S}_\Omega} (\hat{\mathbf{x}} \cdot \check{\mathbf{u}}'_0) \overset{(2)}{\mathbf{Y}} d\Omega + 10\overset{(3)}{\mathbf{F}}_0(\cdot)^3 \int_{\mathcal{S}_\Omega} (\hat{\mathbf{x}} \cdot \check{\mathbf{u}}'_0) \overset{(3)}{\mathbf{Y}} d\Omega = 0. \quad (6.8.27)$$

Using (6.8.26) or (6.8.27) and our solution for the flow field, we obtain the following constraint on the membrane tension τ_{-1} :

$$\begin{aligned} & \frac{384\pi}{23\kappa + 32} \dot{\gamma} : \overset{(2)}{\mathbf{F}}_0 - \frac{6,000\pi}{76\kappa + 85} \boldsymbol{\eta}(\cdot)^3 \overset{(3)}{\mathbf{F}}_0 \\ & - \frac{2304\pi}{5(23\kappa + 32)} (6\bar{\chi} + \tau_{-1}) \overset{(2)}{\mathbf{F}}_0 : \overset{(2)}{\mathbf{F}}_0 - \frac{432,000\pi}{7(76\kappa + 85)} (12\bar{\chi} + \tau_{-1}) \overset{(3)}{\mathbf{F}}_0(\cdot)^3 \overset{(3)}{\mathbf{F}}_0 = 0. \end{aligned} \quad (6.8.28)$$

Solving for τ_{-1} yields the complicated expression,

$$\begin{aligned} \tau_{-1} = & \left(\frac{8}{23\kappa + 32} \dot{\gamma} : \overset{(2)}{\mathbf{F}}_0 - \frac{125}{76\kappa + 85} \boldsymbol{\eta}(\cdot)^3 \overset{(3)}{\mathbf{F}}_0 - \frac{288\bar{\chi}}{5(23\kappa + 32)} \overset{(2)}{\mathbf{F}}_0 : \overset{(2)}{\mathbf{F}}_0 - \frac{108,000\bar{\chi}}{7(76\kappa + 85)} \overset{(3)}{\mathbf{F}}_0(\cdot)^3 \overset{(3)}{\mathbf{F}}_0 \right) \\ & \times \left(\frac{48}{5(23\kappa + 32)} \overset{(2)}{\mathbf{F}}_0 : \overset{(2)}{\mathbf{F}}_0 + \frac{9,000}{7(76\kappa + 85)} \overset{(3)}{\mathbf{F}}_0(\cdot)^3 \overset{(3)}{\mathbf{F}}_0 \right)^{-1}. \end{aligned} \quad (6.8.29)$$

Clearly, τ_{-1} depends on the straining and quadratic parts of the flow as well as the shape deformation function. It is clear that inserting (6.8.29) into (6.8.23) yields nonlinear evolution equations for $\overset{(2)}{\mathbf{F}}_0$ and $\overset{(3)}{\mathbf{F}}_0$. Hence, the disturbance fields and (non-isotropic part of the) membrane tension are also nonlinear in the forcing functions.

To conclude this subsection, we consider the steady-state shape by setting the right-hand side of (6.8.23) equal to zero:

$$\overset{(2)}{\mathbf{F}}_0 = \frac{5}{6(6\bar{\chi} + \tau_{-1})} \dot{\gamma}, \quad \overset{(3)}{\mathbf{F}}_0 = -\frac{7}{72(12\bar{\chi} + \tau_{-1})} \boldsymbol{\eta} \quad \text{at steady state.} \quad (6.8.30)$$

Note that these are implicit equations for $\overset{(2)}{\mathbf{F}}_0$ and $\overset{(3)}{\mathbf{F}}_0$, since τ_{-1} depends on these tensors through (6.8.29). [50] showed that the steady solutions (6.8.30) are parametrized by the viscosity contrast κ and bending parameter $\bar{\chi}$. Inserting (6.8.30) into (6.8.20) yields the steady-state pressure drop,

$$\Delta p_0^+ A_\times = \frac{20\pi}{3} \dot{\gamma} : \dot{\gamma} + \frac{14\pi}{3} \boldsymbol{\eta}(\cdot)^3 \boldsymbol{\eta} + \frac{4\pi}{9} \left(\frac{\kappa - 1}{\kappa + 4} \right) \boldsymbol{\theta} : \boldsymbol{\theta} + \frac{8\pi}{15} \mathbf{d} \cdot \mathbf{d} \quad \text{at steady state.} \quad (6.8.31)$$

Taking the limit as the viscosity ratio $\kappa \rightarrow \infty$ returns the same pressure drop induced by a neutrally buoyant, rigid sphere in a quadratic flow [14]. The first, second, and fourth terms on the right-hand side are independent of κ and are equivalent to the rigid-sphere result forced by $\dot{\gamma}$, $\boldsymbol{\eta}$, and \mathbf{d} ,

respectively. The third-term depends on κ and is equivalent to the result for a liquid droplet forced by $\boldsymbol{\theta}$. This term is induced by a jump in tangential stress across the membrane due to a viscosity contrast between the exterior and interior fluids, and generally is nonzero for quadratic flows with broken symmetry (e.g., Poiseuille flow through a rectangular duct has a non-vanishing $\boldsymbol{\theta}$ -tensor). clearly, this contribution vanishes when the exterior and interior fluids are identical ($\kappa = 1$).

Below, we apply the steady-state results to two special cases: flow in circular tubes and in square ducts.

Flow through circular tubes

For the special case of steady, circular Poiseuille flow, the irreducible flow coefficients are given by (6.3.7a), (6.3.10a), (6.3.10c), and (6.3.13) (reproduced below in dimensionless form):

$$\mathbf{u}_0^\infty = 2(1 - b^2)\hat{\mathbf{e}}_x, \quad (6.3.7a)$$

$$\dot{\gamma} = -2ab(\hat{\mathbf{e}}_y\hat{\mathbf{e}}_x + \hat{\mathbf{e}}_x\hat{\mathbf{e}}_y) \quad (6.3.10a)$$

$$\mathbf{w} = -4ab\hat{\mathbf{e}}_z, \quad (6.3.10c)$$

$$\boldsymbol{\eta} = 2a^2 \left\{ \hat{\mathbf{e}}_x\hat{\mathbf{e}}_x\hat{\mathbf{e}}_x - \frac{1}{5}[\boldsymbol{\delta}\hat{\mathbf{e}}_x + (\boldsymbol{\delta}\hat{\mathbf{e}}_x)^\dagger + \hat{\mathbf{e}}_x\boldsymbol{\delta}] \right\}, \quad (6.3.13a)$$

$$\boldsymbol{\theta} = \mathbf{0}, \quad (6.3.13b)$$

$$\mathbf{d} = -4a^2\hat{\mathbf{e}}_x, \quad (6.3.13c)$$

where $a = r_0/R$ and $b = y_0/R$ (recall that y_0 is the separation distance between the tube centerline and the vesicle center of mass). Taking the square of $\dot{\gamma}$, $\boldsymbol{\eta}$, $\boldsymbol{\theta}$, and \mathbf{d} gives,

$$\dot{\gamma} : \dot{\gamma} = 8(ab)^2, \quad \boldsymbol{\eta}(\cdot)^3\boldsymbol{\eta} = \frac{8a^4}{5}, \quad \boldsymbol{\theta} : \boldsymbol{\theta} = \mathbf{0}, \quad \mathbf{d} \cdot \mathbf{d} = 16a^4.$$

Using these coefficients for circular Poiseuille flow, we determine the translational and rotational velocity of the vesicle,

$$\mathbf{U}_0 = 2 \left(1 - b^2 - \frac{2a^2}{3} \right) \hat{\mathbf{e}}_x, \quad \boldsymbol{\Omega}_0 = -2ab\hat{\mathbf{e}}_z, \quad (6.8.33)$$

as well as the extra pressure drop,

$$\frac{\pi\Delta p_0^+}{a^2} = \frac{160\pi(ab)^2}{3} + 16\pi a^4. \quad (6.8.34)$$

Equation (6.8.34) is equivalent to (4.4) in [14] derived by Brenner for rigid, spherical particles in circular tubes. The result does not depend on the viscosity ratio κ because $\boldsymbol{\theta} = \mathbf{0}$ in circular Poiseuille flow.

Flow through square ducts

Equations (6.8.33)-(6.8.34) are appropriate for the motion of small, quasi-spherical vesicles in circular tubes. Circular-tube flow was considered in Chapters 3 and 4, for generally aspherical vesicles at moderate to high confinement. Flow through square ducts was considered in Chapter 5, and it behooves us to write equivalent expressions for the translational velocity \mathbf{U}_0 , rotational velocity $\boldsymbol{\Omega}_0$, and extra pressure drop Δp_0^+ for small, quasi-spherical vesicles in square ducts. The general off-centerline motion in a square duct is complicated by the solution for the far-field velocity and pressure distribution, which is most easily expressed as an infinite series (presented below in dimensional form):

$$\mathbf{u}^\infty = \frac{16GR^2}{\mu\pi^3} \sum_{n=0}^{\infty} \frac{(-1)^n}{(2n+1)^3} \left[1 - \frac{\cosh[(2n+1)\pi y/(2R)]}{\cosh[(2n+1)\pi/2]} \right] \cos\left[\frac{(2n+1)\pi z}{2R}\right] \hat{\mathbf{e}}_x, \quad (6.8.35a)$$

$$p^\infty = -Gx \quad (6.8.35b)$$

where

$$G = \frac{7.113539\dots\mu V}{R^2}$$

is the mean pressure gradient. The solution (6.8.35) is easily derived by use of eigenfunction expansions. The forcing functions \mathbf{u}_0^∞ , \mathbf{w} , $\dot{\gamma}$, $\boldsymbol{\omega}$, \mathbf{d} , $\boldsymbol{\theta}$, and $\boldsymbol{\eta}$ are then obtained from (6.8.35) by successive differentiation. For the very special case where the vesicle is *on the centerline*, we obtain the following expressions for the flow coefficients (in dimensionless form):

$$\mathbf{u}_0^\infty = 2.096253\dots \hat{\mathbf{e}}_x, \quad (6.8.36a)$$

$$\dot{\gamma} = \mathbf{0} \quad (6.8.36b)$$

$$\mathbf{w} = \mathbf{0}, \quad (6.8.36c)$$

$$\boldsymbol{\eta} = 1.778385\dots a^2 \left\{ \hat{\mathbf{e}}_x \hat{\mathbf{e}}_x \hat{\mathbf{e}}_x - \frac{1}{5} [\boldsymbol{\delta} \hat{\mathbf{e}}_x + (\boldsymbol{\delta} \hat{\mathbf{e}}_x)^\dagger + \hat{\mathbf{e}}_x \boldsymbol{\delta}] \right\}, \quad (6.8.36d)$$

$$\boldsymbol{\theta} = \mathbf{0}, \quad (6.8.36e)$$

$$\mathbf{d} = -3.55677\dots a^2 \hat{\mathbf{e}}_x, \quad (6.8.36f)$$

where $a = r_0/R$, as before. Note the similarity between these expressions and (6.3.7a), (6.3.10a), (6.3.10c), and (6.3.13) above with $b = 0$. Taking the squares, we obtain,

$$\dot{\gamma} : \dot{\gamma} = 0, \quad \boldsymbol{\eta}(\cdot)^3 \boldsymbol{\eta} = 1.265061\dots a^4, \quad \boldsymbol{\theta} : \boldsymbol{\theta} = \mathbf{0}, \quad \mathbf{d} \cdot \mathbf{d} = 12.650613\dots a^4.$$

Using these coefficients for square Poiseuille flow, we determine the translational and rotational velocity of a concentric vesicle,

$$\mathbf{U}_0 = 2.096253 \dots \left(1 - \frac{2a^2}{3}\right) \hat{\mathbf{e}}_x, \quad \boldsymbol{\Omega}_0 = \mathbf{0}, \quad (6.8.37)$$

as well as the extra pressure drop,

$$\frac{4\Delta p_0^+}{a^2} = 39.743071 \dots a^4. \quad (6.8.38)$$

Thus, for the concentric case the solutions for \mathbf{U}_0 , $\boldsymbol{\Omega}_0$, and Δp_0^+ are similar to those derived for circular Poiseuille flow, with different numerical prefactors. For the more general, eccentric case, the solution will also depend on the center-of-mass displacement from the centerline, which is represented by the dimensionless groups $b = y_0/R$ and $c = z_0/R$ (y_0 and z_0 being the y - and z -coordinates of the vesicle center of mass). Similar expressions for other non-circular ducts may be obtained via the general (steady-state) formula (6.8.31).

6.8.3 Higher-order corrections

From the leading-order problem, we derived results for an apparently spherical vesicle in a general, quadratic flow. Higher-order corrections with respect to the excess surface area Δ can be used to elucidate the effects of membrane deformation. At next order in $\Delta^{\frac{1}{2}}$, the $O(\Delta^{\frac{1}{2}})$ fields are forced by the leading-order solution at $r = 1$. The governing equations are,

$$\nabla \cdot \mathbf{u}'_1 = 0, \quad \nabla \cdot \boldsymbol{\sigma}'_1 = -\nabla p'_1 + \nabla^2 \mathbf{u}'_1 = \mathbf{0}, \quad (6.8.39)$$

$$\nabla \cdot \check{\mathbf{u}}'_1 = 0, \quad \nabla \cdot \check{\boldsymbol{\sigma}}'_1 = -\nabla \check{p}'_1 + \kappa \nabla^2 \check{\mathbf{u}}'_1 = \mathbf{0}, \quad (6.8.40)$$

at $r = 1$:

$$\begin{aligned} \frac{\partial}{\partial r} (\hat{\mathbf{x}} \cdot \mathbf{u}'_1) &= -f_0 \frac{\partial^2}{\partial r^2} [\hat{\mathbf{x}} \cdot (\mathbf{u}'_0 + \mathbf{u}^\infty)] + [\hat{\mathbf{x}} (\nabla f_0) + (\nabla f_0) \hat{\mathbf{x}}] : \nabla (\mathbf{u}'_0 + \mathbf{u}^\infty) \\ \text{or } \frac{\partial}{\partial r} (\hat{\mathbf{x}} \cdot \check{\mathbf{u}}'_1) &= -f_0 \frac{\partial^2}{\partial r^2} (\hat{\mathbf{x}} \cdot \check{\mathbf{u}}'_0) + [\hat{\mathbf{x}} (\nabla f_0) + (\nabla f_0) \hat{\mathbf{x}}] : \nabla \check{\mathbf{u}}'_0, \end{aligned} \quad (6.8.41a)$$

$$\mathbf{u}'_1 - \check{\mathbf{u}}'_1 = -f_0 \frac{\partial}{\partial r} (\mathbf{u}'_0 - \check{\mathbf{u}}'_0 + \mathbf{u}^\infty), \quad (6.8.41b)$$

$$\begin{aligned} \hat{\mathbf{x}} \cdot (\boldsymbol{\sigma}'_1 - \check{\boldsymbol{\sigma}}'_1) \cdot \hat{\mathbf{x}} &= -f_0 \frac{\partial}{\partial r} [\hat{\mathbf{x}} \cdot (\boldsymbol{\sigma}'_0 - \check{\boldsymbol{\sigma}}'_0 + \boldsymbol{\sigma}^\infty) \cdot \hat{\mathbf{x}}] + 2\hat{\mathbf{x}} \cdot (\boldsymbol{\sigma}'_0 - \check{\boldsymbol{\sigma}}'_0 + \boldsymbol{\sigma}^\infty) \cdot \nabla f_0 \\ &\quad + 2\tau_1 - \tau_0 (2f_0 + \nabla^2 f_0) - \tau_{-1} (2f_1 + \nabla^2 f_1 - 2f_0^2 - 2f_0 \nabla^2 f_0) \\ &\quad + \bar{\chi} [\nabla^4 f_1 - 4f_0 \nabla^4 f_0 - 4(\nabla f_0) \cdot (\nabla \nabla^2 f_0) - 2(\nabla \nabla f_0) : (\nabla \nabla f_0) - (\nabla^2 f_0)^2], \end{aligned} \quad (6.8.41c)$$

$$\begin{aligned}
(\boldsymbol{\delta} - \hat{\mathbf{x}}\hat{\mathbf{x}}) \cdot (\boldsymbol{\sigma}'_1 - \check{\boldsymbol{\sigma}}'_1) \cdot \hat{\mathbf{x}} &= -f_0 \frac{\partial}{\partial r} [(\boldsymbol{\delta} - \hat{\mathbf{x}}\hat{\mathbf{x}}) \cdot (\boldsymbol{\sigma}'_0 - \check{\boldsymbol{\sigma}}'_0 + \boldsymbol{\sigma}^\infty) \cdot \hat{\mathbf{x}}] + (\boldsymbol{\delta} - 2\hat{\mathbf{x}}\hat{\mathbf{x}}) \cdot (\boldsymbol{\sigma}'_0 - \check{\boldsymbol{\sigma}}'_0 + \boldsymbol{\sigma}^\infty) \cdot \nabla f_0 \\
&\quad - [\hat{\mathbf{x}} \cdot (\boldsymbol{\sigma}'_0 - \check{\boldsymbol{\sigma}}'_0 + \boldsymbol{\sigma}^\infty) \cdot \hat{\mathbf{x}}] \nabla f_0 - \nabla \tau_1 - \hat{\mathbf{x}}(\nabla f) \cdot \nabla \tau_0 - (f_0/r_0) \nabla \tau_0,
\end{aligned} \tag{6.8.41d}$$

$$\begin{aligned}
\frac{\partial f_1}{\partial t} - \hat{\mathbf{x}} \cdot (\mathbf{u}'_1 - \mathbf{U}_1) &= f_0 \frac{\partial}{\partial r} [\hat{\mathbf{x}} \cdot (\mathbf{u}'_0 + \mathbf{u}^\infty)] - (\mathbf{u}'_0 + \mathbf{u}^\infty) \cdot \nabla f_0 \\
\text{or } \frac{\partial f_1}{\partial t} - \hat{\mathbf{x}} \cdot (\check{\mathbf{u}}'_1 - \mathbf{U}_1) &= f_0 \frac{\partial}{\partial r} (\hat{\mathbf{x}} \cdot \check{\mathbf{u}}'_0) - \check{\mathbf{u}}'_0 \cdot \nabla f_0,
\end{aligned} \tag{6.8.41e}$$

$$\int_{\mathcal{S}_\Omega} \{(\nabla f_0) \cdot (\nabla f_1) - 2f_0 f_1 + f_0 [(\nabla f_0) \cdot (\nabla f_0) - \frac{2}{3} f_0^2]\} d\Omega = 0, \tag{6.8.41f}$$

$$\int_{\mathcal{S}_\Omega} (f_1 + f_0^2) d\Omega = 0, \tag{6.8.41g}$$

$$\begin{aligned}
\frac{4}{3}\pi \mathbf{U}_1 &= \int_{\mathcal{S}_\Omega} \hat{\mathbf{x}} \left(\hat{\mathbf{x}} \cdot \mathbf{u}'_1 + f_0 \frac{\partial}{\partial r} [\hat{\mathbf{x}} \cdot (\mathbf{u}'_0 + \mathbf{u}^\infty)] - (\nabla f_0) \cdot (\mathbf{u}'_0 + \mathbf{u}^\infty) \right) d\Omega \\
&= \int_{\mathcal{S}_\Omega} \hat{\mathbf{x}} \left(\hat{\mathbf{x}} \cdot \check{\mathbf{u}}'_1 + f_0 \frac{\partial}{\partial r} (\hat{\mathbf{x}} \cdot \check{\mathbf{u}}'_0) - (\nabla f_0) \cdot \check{\mathbf{u}}'_0 \right) d\Omega,
\end{aligned} \tag{6.8.41h}$$

$$\begin{aligned}
\frac{4}{3}\pi \boldsymbol{\Omega}_1 &= \int_{\mathcal{S}_\Omega} \frac{1}{2} \left(\hat{\mathbf{x}} \times \mathbf{u}'_1 + f_0 \frac{\partial}{\partial r} [\hat{\mathbf{x}} \times (\mathbf{u}'_0 + \mathbf{u}^\infty)] - (\nabla f_0) \times (\mathbf{u}'_0 + \mathbf{u}^\infty) \right) d\Omega \\
&= \int_{\mathcal{S}_\Omega} \frac{1}{2} \left(\hat{\mathbf{x}} \times \check{\mathbf{u}}'_1 + f_0 \frac{\partial}{\partial r} (\hat{\mathbf{x}} \times \check{\mathbf{u}}'_0) - (\nabla f_0) \times \check{\mathbf{u}}'_0 \right) d\Omega,
\end{aligned} \tag{6.8.41i}$$

$$-\Delta p_0^+ A_\times = \lim_{r \rightarrow \infty} r^2 \int_{\mathcal{S}_\Omega} \hat{\mathbf{x}} \cdot (\boldsymbol{\sigma}^\infty \cdot \mathbf{u}'_1 - \boldsymbol{\sigma}'_1 \cdot \mathbf{u}^\infty) d\Omega, \tag{6.8.41j}$$

$$\text{as } |x| \rightarrow \infty : \quad \mathbf{u}'_1 = \mathbf{0}. \tag{6.8.42}$$

(See also Appendix G.) Since the problem is made fully nonlinear through the surface-area constraint, the general solution for the disturbance fields must be constructed from products of the flow coefficients and the shape coefficients. The number of tensorial combinations needed in the general solution is quite large for an arbitrary flow field. Thus, in this section we focus our attention on the subset of solutions forced by the quadratic contribution,

$$\mathbf{u}^\infty = \mathbf{u}_0^\infty + \boldsymbol{\eta} : \mathbf{x}\mathbf{x} + \frac{1}{5}[2r^2 \mathbf{d} - (\mathbf{d} \cdot \mathbf{x})\mathbf{x}], \tag{6.8.43a}$$

$$p^\infty = 2(\mathbf{d} \cdot \mathbf{x}), \tag{6.8.43b}$$

$$\boldsymbol{\sigma}^\infty = 4(\boldsymbol{\eta} \cdot \mathbf{x}) + \frac{3}{5}[\mathbf{d}\mathbf{x} + \mathbf{x}\mathbf{d} - 4(\mathbf{d} \cdot \mathbf{x})\boldsymbol{\delta}], \tag{6.8.43c}$$

which is equivalent to setting $\dot{\gamma} = \mathbf{0}$, $\mathbf{w} = \mathbf{0}$, and $\boldsymbol{\theta} = \mathbf{0}$ in the previous section. Physically, this case corresponds to a concentric vesicle in a symmetric Poiseuille flow (e.g., in a circular tube or square duct). Assuming $\overset{(2)}{\mathbf{F}_0} = \mathbf{0}$, the minimal ansatz for the $O(\Delta^{\frac{1}{2}})$ correction to the shape function

is given by,

$$f_1(\hat{\mathbf{x}}, t) = \overset{(2)}{\mathbf{F}}_1(t) : \overset{(2)}{\mathbf{Y}}(\hat{\mathbf{x}}) + \overset{(4)}{\mathbf{F}}_1(t)(\cdot)^4 \overset{(4)}{\mathbf{Y}}(\hat{\mathbf{x}}) + \overset{(5)}{\mathbf{F}}_1(t)(\cdot)^5 \overset{(5)}{\mathbf{Y}}(\hat{\mathbf{x}}) + \overset{(6)}{\mathbf{F}}_1(t)(\cdot)^6 \overset{(6)}{\mathbf{Y}}(\hat{\mathbf{x}}) - \frac{90}{7} \overset{(3)}{\mathbf{F}}_0(t)(\cdot)^3 \overset{(3)}{\mathbf{F}}_0(t). \quad (6.8.44)$$

The last term in (6.8.44) is needed in order to conserve the vesicle volume. Obviously, the more general ansatz (6.8.17) for f_0 behooves a different ansatz for f_1 , but this is beyond the scope of the present work. The singular contribution to the membrane tension (6.8.29) reduces to the relatively simple form,

$$\tau_{-1} = -\frac{7\eta(\cdot)^3 \overset{(3)}{\mathbf{F}}_0}{72 \overset{(3)}{\mathbf{F}}_0(\cdot)^3 \overset{(3)}{\mathbf{F}}_0} - 12\bar{\chi}, \quad (6.8.45)$$

for a purely quadratic flow. The static tension τ_{-1} , which appears in the normal stress condition (6.8.41c), is a nonlinear function of $\overset{(3)}{\mathbf{F}}_0$. Hence, the $O(\Delta^{\frac{1}{2}})$ fields will also be nonlinear in the forcing functions.

The solution of (6.8.39)-(6.8.44) has been carried out using a symbolic algebra software. We report here only the main results. The $O(\Delta^{\frac{1}{2}})$ problem admits no correction to the vesicle velocity:

$$\mathbf{U}_1 = \mathbf{0}, \quad (6.8.46)$$

$$\boldsymbol{\Omega}_1 = \mathbf{0}. \quad (6.8.47)$$

The correction to the extra pressure drop is,

$$\Delta p_1^+ A_x = -6,000\pi \left(\frac{\tau_0^*}{76\kappa + 85} \right) \eta(\cdot)^3 \overset{(3)}{\mathbf{F}}_0, \quad (6.8.48)$$

where τ_0^* is the isotropic contribution to the $O(1)$ tension field. This contribution has yet to be computed, and is obtained from requiring that the correction to the total surface area [given by (6.8.41f)] remain constant with time. For the purely quadratic flow considered here, it is straightforward to show that,

$$\tau_0^* = 0, \quad (6.8.49)$$

and hence,

$$\Delta p_1^+ = 0. \quad (6.8.50)$$

That is, the $O(\Delta^{\frac{1}{2}})$ problem admits no correction to the extra pressure drop. We reiterate that this result holds only for the particular subset of shape modes considered here. Further corrections to the leading-order solution are not pursued here.

6.9 Concluding remarks

We have determined the velocity and pressure drop for a small, quasi-spherical vesicle in a conduit of arbitrary cross section by means of small-deformation analysis. A formal perturbative solution was constructed in terms of the vesicle excess area Δ , in the spirit of previous works by other authors. We have extended these theories in several respects:

1. We derived general solutions of the Stokes equations for a quasi-spherical vesicle in an arbitrary flow up to quadratic order in \boldsymbol{x} . The solutions are presented here in invariant tensor notation.
2. We derived general expressions for the vesicle translational and rotational velocities (6.8.18)-(6.8.19), as well as the extra pressure drop (6.8.20). The latter is coupled to evolution equations for the \mathbf{F} -tensors (6.8.23), which have been derived elsewhere by other authors [30, 32].
3. We applied our predictions to steady flow through circular tubes and square ducts, in complement to results from previous chapters.
4. We computed the first correction in the quasi-spherical limit, showing no additional pressure drop or modification of the vesicle velocity.

At leading order in Δ , the steady motion of the vesicle resembles a rigid, spherical particle of radius r_0 . We present some of the main results below (using dimensional variables) for the steady, concentric case. For steady Poiseuille flow in a circular tube of radius R , a concentric vesicle has relative velocity,

$$\frac{U}{V} = 2 \left(1 - \frac{2}{3} a^2 \right) + \text{h.o.t.}, \quad (6.9.1)$$

and extra pressure drop,

$$\frac{\Delta p_0^+ R}{\mu V} = 16a^5 + \text{h.o.t.} \quad (6.9.2)$$

where $a = r_0/R = v^{1/3}\lambda$ and “h.o.t.” stands for “higher order terms.” The analogous expressions for a concentric vesicle in a square duct are given by,

$$\frac{U}{V} = 2.096253\dots \left(1 - \frac{2a^2}{3} \right) + \text{h.o.t.}, \quad (6.9.3)$$

$$\frac{\Delta p_0^+ R}{\mu V} = 9.935768\dots a^5 + \text{h.o.t.} \quad (6.9.4)$$

Clearly, equations (6.9.1)-(6.9.2) and (6.9.3)-(6.9.4) differ only by their numerical prefactors. For off-centerline motion, the shear contribution dominates the pressure drop and the vesicle rotates at a finite speed.

The results of this chapter apply to quasi-spherical vesicles. For vesicles of lower reduced volume v (i.e., higher excess surface area Δ), the small-deformation analysis fails to accurately capture the vesicle deformation unless many orders in $\Delta^{\frac{1}{2}}$ are included in the expansion. However, even the leading-order problem is complicated by the necessity of higher-order shape modes than what is included in the simplistic shape ansatz (6.8.9) [the more general ansatz (6.8.17) is required for lower reduced volumes]. A more appropriate approach for highly aspherical vesicles would be to abandon the small-deformation analysis entirely and solve the unbounded Stokes-flow problem numerically (e.g., using the boundary element method), as was done in Chapters 4 and 5 for the bounded case. By applying the reciprocal theorem (6.4.9) to a fictitious surface enclosing the vesicle, one can compute the extra pressure drop numerically. The dependence of the quantities \mathbf{U} , $\boldsymbol{\Omega}$, and Δp^+ on the radius ratio a can be elucidated by examining their dependence on the flow-coefficient tensors $\dot{\gamma}$, $\boldsymbol{\eta}$, etc. Such unbounded-flow calculations have been performed by Farutin and coworkers [52, 49] (for circular Poiseuille flow) in order to determine vesicle shape deformation and migration. However, the influence of large shape deformations on the vesicle velocity and extra pressure drop remains an open question.

Chapter 7

Conclusions and directions for future work

7.1 Conclusions

In this thesis, we analyzed the motion of vesicles in pressure-driven flow through conduits of various cross section. Unlike droplets, which admit volume-preserving deformations under flow, vesicles deform while conserving both their surface area and enclosed volume due to the elasticity of their bounding membrane. The membrane shape is determined through a balance between membrane tension (which acts to preserve surface area locally), membrane bending elasticity (which resists changes in local curvature), and fluid flow (which imposes a traction on the membrane, forcing the vesicle out of equilibrium). Through rigorous hydrodynamical analysis, we computed the vesicle mobility – i.e., the relative velocity U/V – and the wall resistance – i.e., the dimensionless extra pressure drop $\Delta p^+ R / (\mu V)$ – as functions of vesicle sphericity, flow confinement, and membrane bending stiffness. Different regimes of the parameter space were investigated using a variety of theoretical tools. Below, we summarize the main takeaways from each chapter.

In Chapter 1, we introduced the reader to vesicles in both equilibrium and non-equilibrium settings. At rest, the vesicle adopts a shape determined by minimizing its surface curvature energy (weighted by a bending modulus), which leads to a family of shapes parametrized by the vesicle reduced volume v . When subjected to flow, vesicles deform and disturb the surrounding fluid. The flow of particulate matter through conduits was introduced to the reader, using the motion of rigid particles and red blood cells through circular tubes as model systems. Previous studies have shown that red blood cells can squeeze through tubes of smaller dimension than can equally sized, rigid particles. We raised questions about membrane-enclosed fluids of arbitrary shape and size, which cannot be understood based solely on the red-blood-cell literature. We also pointed out the need for

a rigorous, continuum-mechanical theory – one that is applicable to various channel geometries – as well as quantification of the hydrodynamic parameters U/V and $\Delta p^+R/(\mu V)$. Previous studies of the motion of vesicles in channel flow have not fully addressed these questions.

In Chapter 2, we postulated a theoretical geometry consisting of a vesicle suspension flowing through a conduit of some cross section. We formulated an initial-boundary-value problem for the fluid velocity and pressure, membrane tension, and membrane shape. At every point in time, the instantaneous fluid motion (governed by Stokes' equations) is intrinsically coupled to the membrane mechanics through stress balance conditions. The evolution of the membrane is governed by the kinematic condition. Solutions of the problem are parametrized by five dimensionless group: the aforementioned reduced volume v , the radius ratio λ , the bending parameter β , the viscosity ratio κ , and the suspension concentration c .

In Chapter 3, we developed a solution to the initial-boundary-value problem in the regime where the vesicle is highly confined in a steady, circular-tube flow, using the method of matched asymptotic expansions. An “inner region” was defined in the area where the vesicle membrane and the tube wall come into near-contact, while the “outer region” was defined at the front and rear ends of the vesicle. Asymptotic expansions for the dependent variables (the velocity and pressure fields, membrane tension, and membrane shape) were developed in terms of a small parameter $\epsilon \approx 1 - \lambda/\lambda^*$, where λ^* is the critical (or maximum) radius ratio. We showed in this chapter that the vesicle reduced length ℓ needed to be introduced as a parameter (replacing the reduced volume v) in order to analyze different shapes. We considered the dilute limit ($c \ll 1$) for vesicles containing a fluid with similar properties to the suspending medium [$\kappa = O(1)$]. We found that “long vesicles” are spherocylindrical and admit shape deformations resembling those of large bubbles; “short vesicles” are spherical and have very large membrane tensions. Due to the circular symmetry of the geometry, the membrane velocity is uniform on the surface. Consequently, the vesicle can be modeled as a rigid particle with a shape determined by a balance between membrane tension, membrane bending elasticity, and fluid flow. Flow confinement suppresses the effect of membrane bending elasticity, and so the vesicle motion is mainly controlled by the *geometry* of the system. The relative velocity U/V and dimensionless extra pressure drop $\Delta p^+R/(\mu V)$ admit the following expansions as $\lambda \rightarrow \lambda^*$ (neglecting the effect of membrane bending elasticity):

$$\frac{U}{V} = 1 + \frac{4}{3} \left(\frac{3\lambda^{*2} - 2}{4\lambda^{*2} - 3} \right) \left(1 - \frac{\lambda}{\lambda^*} \right) + O \left[\left(1 - \frac{\lambda}{\lambda^*} \right)^2 \right], \quad (3.9.1a)$$

$$\frac{\Delta p^+R}{\mu V} = 4(\lambda^{*2} - 1) \left(1 - \frac{\lambda}{\lambda^*} \right)^{-1} + \left(\frac{4\sqrt{2}\pi}{4\lambda^{*2} - 3} \right) \left(1 - \frac{\lambda}{\lambda^*} \right)^{-\frac{1}{2}} + O(1). \quad (3.9.1b)$$

The critical radius ratio λ^* is uniquely related to v through equations (3.1.10). Equations (3.9.1) reproduce previously derived results for rigid spheres ($v = 1$) and red blood cells ($v \simeq 0.61$), and

supply predictions for intermediate reduced volumes. Membrane bending elasticity – quantified by the bending parameter β – modifies (3.9.1) by forcing the vesicle back into its equilibrium shape, which may be geometrically prohibited by the tube boundary. At lower flow confinement, large values of β can result in an increase in the drag and a reduction in vesicle mobility as the vesicle attempts to access its equilibrium configuration. However, the exact dependence of the vesicle motion on β was shown to be highly complex and dependent on the family of accessible shape configurations (which, in turn, depends on the values of v on λ).

The asymptotic results of Chapter 3 are limited to the high-confinement regime ($\lambda \rightarrow \lambda^*$). In Chapter 4, we extended these results to lower confinement by performing direct numerical calculations of vesicles in circular tubes. Our main workhorse was the boundary element method (BEM), through which we performed large-scale 3D computations of the full Stokes-flow problem. Membrane incompressibility was approximately enforced through a predictor-corrector algorithm, yielding corrections to the membrane surface velocity and tension. The kinematic condition was advected through an Euler timestepping scheme. In all of our numerical computations, the viscosity ratio was set equal to unity ($\kappa = 1$). We showed that the axisymmetric shape solution is indeed the stable shape solution so long as the vesicle is sufficiently confined; when axial symmetry is attained, the membrane velocity is uniform and the vesicle behaves like a rigid particle. At low confinement, an initially axisymmetric vesicle can break symmetry and undergo temporal dynamics, though the effect on the relative velocity and extra pressure drop is small. Several three-dimensional shapes, hitherto not reported, were presented for vesicles in circular tubes, including a “two-lobed shape.” At high confinement, computational limitations preclude the use of the 3D BEM to solve the full Stokes-flow problem. Thus, an axisymmetric lubrication theory was developed in order to develop approximate analytical solutions for the flow field (axial symmetry being retained at high confinement). We showed that this approximate theory unified results from the 3D BEM simulations and the narrow-gap asymptotic theory of Chapter 3. Rational fraction approximants were fit to the numerical results in order to quantify the dependence of U/V and $\Delta p^+ R/(\mu V)$ on λ , for different values of v and small values of β . The effect of membrane bending elasticity was extensively explored at various reduced volumes v and radius ratios λ . Significantly, at low reduced volumes the dependence of U/V and $\Delta p^+ R/(\mu V)$ on β is non-monotonic. The effect of hydrodynamic interactions was briefly explored through a periodic-train model of the suspension configuration. Due to the exponential decay of the velocity disturbance in channel flow, vesicle-vesicle interactions are dominated by pairwise interactions between nearest neighbors. We showed that these interactions play only a small role (as compared to vesicle sphericity and flow confinement) in altering the relative velocity and extra pressure drop. We expect the situation to qualitatively change at lower confinement (i.e., lower values of λ) and higher suspension concentrations c .

Motivated by recent experimental measurements of vesicles flowing through microfluidic channels,

in Chapter 5 we studied the motion of a single vesicle ($c \ll 1$) driven by a pressure gradient through a conduit of square cross section. (In fact, we formulated the theory to be generally applicable to ducts of any polygonal cross section.) Vesicles in square ducts exhibit interesting shapes with four-fold symmetry. In this chapter, we focused our attention onto a particular regime of the parameter space, specifically examining high-reduced-volume vesicles ($0.85 \leq v \leq 1$) with relatively “floppy” membranes ($\beta = 0$) at unit viscosity ratio ($\kappa = 1$). We developed theoretical predictions using a combination of 3D BEM simulations and non-axisymmetric lubrication theory. Our predictions were compared against experimental measurements, conducted by our collaborators at Texas Tech University. Unlike in the circular-tube problem, in the square-duct problem the lubrication solutions incur significant errors at low confinement. By examining ducts of different polygonal cross section (i.e., varying the number of sides), we found that these errors originate from the neglect of velocity gradients along the azimuth in the equations of motion and stress boundary conditions. Nevertheless, we expect the lubrication approximation to be valid at very high confinement, and we used these solutions to predict the critical vesicle geometry (i.e., the critical radius ratio λ^* and apparent contact area for lubrication A^*). Theoretical correlations between the aspect ratio $L/(2R)$ and reduced volume v were used to estimate v in the experiments. Our predictions of the relative velocity U/V , and dimensionless extra pressure drop $\Delta p^+ R/(\mu V)$ were in good agreement with the experimental predictions, once the distribution of reduced volumes is taken into account. Significantly, a new phenomenon was observed wherein the asymmetric geometry permits a non-uniform membrane flow field. In a reference frame moving with the vesicle, the near-wall region of the membrane translates in the direction opposite to the mean flow while the corner region translates with the mean flow. Thus, the vesicle “tank treads” through a square duct. At sufficiently high confinement, subunit relative velocities $U/V < 1$ are predicted and measured experimentally, indicating that the vesicle moves *slower* than the mean flow.

In Chapter 6, we examined the motion of a small, quasi-spherical vesicle subjected to the general, quadratic flow,

$$\mathbf{u}^\infty = \mathbf{u}_0^\infty + \frac{1}{2}(\mathbf{w} \times \mathbf{x}) + \dot{\gamma} \cdot \mathbf{x} + \boldsymbol{\eta} : \mathbf{x} \mathbf{x} - \frac{1}{3}[(\mathbf{x} \cdot \boldsymbol{\theta}) \times \mathbf{x}] + \frac{1}{5}[2r^2 \mathbf{d} - (\mathbf{d} \cdot \mathbf{x}) \mathbf{x}], \quad (6.3.14a)$$

$$p^\infty = 2\mu(\mathbf{d} \cdot \mathbf{x}). \quad (6.3.14b)$$

Here, \mathbf{x} is the position vector measured from the vesicle’s center and \mathbf{u}_0^∞ , \mathbf{w} , $\dot{\gamma}$, $\boldsymbol{\omega}$, \mathbf{d} , $\boldsymbol{\theta}$, and $\boldsymbol{\eta}$ are the flow-coefficient tensors. We analyzed the problem by means of spherical-harmonic expansions, defining the excess surface area Δ (which replaces the reduced volume v) as a small parameter. To leading order in Δ , the relative velocity of a concentrically positioned vesicle is given by,

$$\frac{U}{V} = \frac{1}{V} \left(\mathbf{u}_0^\infty + \frac{\mathbf{d}}{3} \right) \cdot \hat{\mathbf{e}}_x + \text{h.o.t.}, \quad (6.8.18)$$

where ‘‘h.o.t.’’ stands for ‘‘higher order terms.’’ The (steady-state) extra pressure drop is given by,

$$\frac{\Delta p^+ R}{\mu V} = \frac{\pi r_0^3 R}{V^2 A_x} \left\{ \frac{20}{3} \dot{\gamma} : \dot{\gamma} + r_0^2 \left[\frac{14}{3} \boldsymbol{\eta}(\cdot)^3 \boldsymbol{\eta} + \frac{4}{9} \left(\frac{\kappa - 1}{\kappa + 4} \right) \boldsymbol{\theta} : \boldsymbol{\theta} + \frac{8}{15} \mathbf{d} \cdot \mathbf{d} \right] \right\} + \text{h.o.t..} \quad (6.8.31)$$

where $r_0 = v^{\frac{1}{3}} \lambda R$ is the volumetric vesicle radius and A_x is the channel cross sectional area. Significantly, the relative velocity is exactly that which would be predicted for a rigid sphere. The extra pressure drop is exactly the rigid-sphere result except for the term multiplied by $\boldsymbol{\theta} : \boldsymbol{\theta}$, which is non-vanishing for an asymmetric flow and for non-unit viscosity ratios. This latter term is exactly that which would be predicted for a spherical droplet, since the $\boldsymbol{\theta}$ -term in the imposed flow field only probes the tangential part of the kinematic-continuity and stress-balance conditions on the vesicle membrane. We applied equations (6.8.18) and (6.8.31) to the special cases of circular-tube flow and square-duct flow.

7.2 Future prospects

The work conducted in this thesis can be extended in several ways. For one, we have only scratched the surface of examining vesicle motion through complex geometries. However, we have developed theoretical tools that can in principle be applied to a variety of channel-flow geometries beyond the ones considered in this thesis. In particular, the methods developed in Chapters 5 and 6 can be applied to channels of different cross section (e.g., rectangular cross section), converging (or expanding) nozzles, and bifurcations. Moreover, it is worth emphasizing the importance of simulating fully 3D geometries in addition to simplified systems that obey certain symmetry rules. Complex geometries, such as the contraction-expansion geometry considered in Chapter 5, require the use of fully 3D numerical methods.

In Chapter 4, we showed that the shapes of low-reduced-volume vesicles at low confinement can dynamically evolve in time. There is significant literature precedent for the existence of these shape solutions. It is clear from our results that the axisymmetric shape solution is not necessarily a stable one. What is *not* clear whether these vesicles will continue to evolve in time or whether they will eventually reach a steady state. The simulations were run for many – $O(100 tV/R)$ – timesteps, but presumably would have to be continued for longer times in order to fully characterize the dynamics. Such a study would be interesting, but time-consuming. A linear stability analysis of the axisymmetric base-state would elucidate the mechanism by which the vesicle leaves the axisymmetric configuration.

In Chapter 6, we examined the regime of low flow confinement for quasi-spherical vesicles. A more general formulation for an arbitrary vesicle in an unbounded flow can be tackled numerically, by defining suitable far-field boundary conditions. Such a formulation would allow us to investigate

vesicles of various reduced volume at low flow confinement, which in turn could be unified with our numerical and theoretical results at higher confinement. This problem is beyond the scope of the present work, but is left for a future study.

We briefly examined the effect of vesicle-vesicle hydrodynamic interactions in Chapter 4. We showed that the vesicle motion is relatively insensitive to vesicle-vesicle interactions, at least when the flow confinement is high. However, we hypothesized that the situation is qualitatively different at higher suspension concentrations c and at lower radius ratios λ . At low confinement, it would be interesting to examine how hydrodynamic interactions affect the pair migration behavior of vesicles under channel confinement. This is a current topic of active investigation in the scientific community. The dependence of the vesicle velocities and extra pressure drop on the suspension concentration c would be useful for the purposes of flow measurement and control of vesicle suspensions.

When considering multiple vesicles in the domain (Chapter 4), we focused our attention on a periodic arrangement along the channel axis. Periodicity was strictly imposed by the boundary conditions. A more general formulation would leave the vesicle configurations as additional degrees of freedom. It would be interesting to determine how the pair-separation and pair-orientation distributions of a vesicle suspension are affected by channel flow confinement, and how these configurations affect the total stress in the fluid. A linear stability analysis of the periodic base case would indicate whether or not the periodic configuration is stable to concentration fluctuations. The effect of polydispersity, which is known to play a major role in suspension separation processes, could also be explored.

Finally, there is significant interest into the connection between membrane tension induced by flow confinement and transmembrane transport of molecular species. This subject is of great practical value since vesicles are biocompatible drug delivery vehicles. However, the question just raised is fundamentally a biophysics question, requiring detailed information about the molecular structure of biomembranes. Both passive and active mechanisms of transmembrane transport – with and without the assistance of integral membrane proteins, respectively — are feasible. A possible method of probing this connection experimentally is to quantify uptake of a particular molecular species and then draw correlations with measurements of the relative velocity and dimensionless extra pressure drop. Through application of a suitable membrane model (e.g., the Helfrich model used in our work for lipid bilayers), one can deduce the membrane tension and potentially make quantitative predictions of transmembrane permeability.

7.3 Further reading

The content of Chapter 3 is associated with the following article, which is already in print:

J. M. Barakat and E. S. G. Shaqfeh. The steady motion of a closely fitting vesicle in a

tube. *J. Fluid Mech.*, 835:721–761, 2018.

The content of Chapter 4 will appear in the following article, which has been submitted for publication:

J. M. Barakat and E. S. G. Shaqfeh. Stokes flow of vesicles in a circular tube. *submitted*.

The content of Chapter 5 is being prepared in a separate article for publication:

J. M. Barakat, S. M. Ahmmmed, S. A. Vanapalli and E. S. G. Shaqfeh. Pressure-driven flow of a vesicle through a square microchannel. *in prep.*

Appendices

Appendix A

Differential geometry of surfaces in space

By their very nature, free surfaces are not constrained to conform to the level surface of a fixed coordinate system (e.g., planes, cylinders, and spheres). Rather, their position in space is determined such that the governing conservation laws of physics (e.g., that of mass and momentum) are satisfied. It is for this reason that the study of free-surface flow phenomena necessitates a certain level of comfort with the mathematics of differentiable manifolds. Unfortunately, this subject is not commonly taught in modern chemical engineering curricula. Moreover, most of the useful references that exist are written using a notation that, while familiar to mathematical physicists, may appear foreign to engineers and fluid mechanicians. The purpose of this appendix is to present some useful results from differential geometry using a notation that should be familiar to the reader without having to “water down” the content. For a more complete discussion, the reader is referred to [95, 111].

A.1 Review of vector and tensor analysis

A working knowledge of the algebra and calculus of three-dimensional vectors and tensors is assumed here. A comprehensive introduction can be found in Chapters 2, 3, and 7 of [8]. In our convention, *scalars* will be denoted by italicized Latin and Greek letters; *vectors* will be denoted by boldfaced, italicized Latin letters; (second-order) *tensors* will be denoted by boldfaced, italicized Greek letters. For example,

ψ is a scalar,

\mathbf{v} is a vector (or first-order tensor),

$\boldsymbol{\tau}$ is a second-order tensor.

On occasion, we shall also use a boldfaced, calligraphic letter to denote a tensorial quantity, e.g., \mathcal{A} is a second-order tensor.

With any three-dimensional vector space comes a triad of unit basis vectors $\hat{\mathbf{e}}_{(1)}, \hat{\mathbf{e}}_{(2)}, \hat{\mathbf{e}}_{(3)}$ that together define a right-handed, orthonormal coordinate system. Examples of particular relevance to mathematical physics are,

the Cartesian basis $(\hat{\mathbf{e}}_x, \hat{\mathbf{e}}_y, \hat{\mathbf{e}}_z)$,

the cylindrical basis $(\hat{\mathbf{e}}_\rho, \hat{\mathbf{e}}_\phi, \hat{\mathbf{e}}_z)$,

the spherical basis $(\hat{\mathbf{e}}_r, \hat{\mathbf{e}}_\theta, \hat{\mathbf{e}}_\phi)$.

Vectors and tensors may be expressed in any chosen basis and their components converted between bases by the usual conventions of orthogonal transformations [8]. The calculus of vectors and tensors on a differentiable manifold is facilitated by the gradient or “del” operator ∇ , which is defined in the usual fashion. A detailed background on basis systems for orthogonal curvilinear coordinates can be found in the appendix of [12, 72].

The most important example of a second-order tensor is the so-called *unit tensor* δ , whose indexed components are defined by the dot product of any two unit basis vectors,

$$\delta_{ij} = \hat{\mathbf{e}}_{(i)} \cdot \hat{\mathbf{e}}_{(j)} = \begin{cases} 1 & \text{if } i = j, \\ 0 & \text{otherwise,} \end{cases} \quad (\text{A.1.1})$$

with i, j taking values of 1, 2, or 3. The unit tensor is so named because its dot product with any vector \mathbf{v} returns the vector unchanged, e.g., $\delta \cdot \mathbf{v} = \mathbf{v}$. Furthermore, the inverse of a (nonsingular) second-order tensor $\boldsymbol{\tau}$ is defined such that

$$\boldsymbol{\tau}^{-1} \cdot \boldsymbol{\tau} = \boldsymbol{\tau} \cdot \boldsymbol{\tau}^{-1} = \delta. \quad (\text{A.1.2})$$

The transpose of a tensor is denoted by $\boldsymbol{\tau}^\dagger$. A second-order tensor is *symmetric* if $\boldsymbol{\tau}^\dagger = \boldsymbol{\tau}$. Any second-order tensor $\boldsymbol{\tau}$ may be characterized by its three principal scalar invariants, namely,

the trace $\text{tr}(\boldsymbol{\tau}) = \delta_{ij}\tau_{ji} = \tau_{ii}$,

the sum of principal minors $\frac{1}{2} [\text{tr}^2(\boldsymbol{\tau}) - \text{tr}(\boldsymbol{\tau}^\dagger \cdot \boldsymbol{\tau})] = \frac{1}{2}(\tau_{ii}\tau_{jj} - \tau_{ij}\tau_{ji})$,

the determinant $\det(\boldsymbol{\tau}) = \frac{1}{6}\epsilon_{ijk}\epsilon_{lmn}\tau_{il}\tau_{jm}\tau_{kn}$,

where summation is implied over repeated indices. Tensors $\boldsymbol{\tau}$ for which $\det(\boldsymbol{\tau}) = 0$ are called

degenerate, and in such cases the inverse τ^{-1} appearing in (A.1.2) does not formally exist.

Tensors of higher order will occasionally appear in this thesis. Unfortunately, there is no standard convention in Gibbs notation that distinguishes second-order tensors from tensors of higher order. It is usually necessary to switch to Einstein notation, wherein a tensor is represented by its indexed components (making the order of the tensor obvious) and summation is implied over repeated indices. Boldfaced Greek and calligraphic letters will be used to represent higher-order tensors in Gibbs notation, and in such cases direct reference is made to the order of the tensor so as to distinguish it from tensors of lower order. The most prevalent example of a third-order tensor is the so-called *permutation tensor* ϵ . The indexed components of ϵ are defined by the scalar triple product of any three basis vectors,

$$\epsilon_{ijk} = \hat{\mathbf{e}}_{(i)} \cdot (\hat{\mathbf{e}}_{(j)} \times \hat{\mathbf{e}}_{(k)}) = \begin{cases} 1 & \text{if } ijk \text{ is a positive permutation,} \\ -1 & \text{if } ijk \text{ is a negative permutation,} \\ 0 & \text{otherwise,} \end{cases} \quad (\text{A.1.3})$$

with i, j, k taking values of 1, 2, or 3. Clearly, the permutation tensor ϵ is a *pseudotensor* – that is, its components change sign under an orientation-reversing coordinate transformation.

We conclude this section with a presentation of key integral theorems from vector and tensor calculus. Consider first a surface \mathcal{S} with bounding contour $\partial\mathcal{S}$. Suppose that a vector field \mathbf{v} is everywhere regular in \mathcal{S} . *Stokes' curl theorem* states,

$$\int_{\partial\mathcal{S}} \mathbf{v} \cdot d\mathbf{s} = \int_{\mathcal{S}} (\nabla \times \mathbf{v}) \cdot d\mathbf{S}, \quad (\text{A.1.4})$$

which, in physical terms, relates the flux of material through a contour to the circulation in the surface. Now consider a volume \mathcal{V} with bounding surface $\partial\mathcal{V}$ and let \mathbf{v} be regular within the volume. *Gauss' divergence theorem* states,

$$\int_{\partial\mathcal{V}} \mathbf{v} \cdot d\mathbf{S} = \int_{\mathcal{V}} (\nabla \cdot \mathbf{v}) d^3x, \quad (\text{A.1.5})$$

which, in physical terms, relates the flux of material through a surface to the dilatation in the volume. Although (A.1.4) and (A.1.5) are written for a vector \mathbf{v} , in fact these relations may be trivially generalized to tensors of higher order.

A.2 Dual bases for a surface

A *surface* is a two-parameter set of contiguous positions in space $\mathbf{x}_s(\xi, \eta)$, where ξ and η are the local surface coordinates. We demarcate the location of the surface in space by the vector equation,

$$\mathbf{x} = \mathbf{x}_s(\xi, \eta), \quad (\text{A.2.1})$$

where \mathbf{x} is the position vector. Technically, we may allow the locations of the surface points to also vary parametrically with time t , but for the sake of brevity this dependence is suppressed. As an alternative to (A.2.1), we may define the level set function $\varphi(\mathbf{x})$ such that,¹

$$\varphi(\mathbf{x}) = 0 \quad \text{at} \quad \mathbf{x} = \mathbf{x}_s. \quad (\text{A.2.2})$$

As an example, the thickness of a falling film adhered to an inclined slab may be easily represented in Cartesian coordinates by the level set function $\varphi(x, y, z) = z - z_s(x, y)$, with $\xi = x$ and $\eta = y$ (here, z is the coordinate normal to the slab and z_s is the film thickness).

From analyzing how the surface positions \mathbf{x}_s vary with ξ and η , one can derive geometrical properties of the surface. The (generally non-unit) tangential vectors of the surface are obtained by taking partial derivatives of the surface position \mathbf{x}_s with respect to the surface coordinates ξ and η :

$$\mathbf{t}_{(1)} = \frac{\partial \mathbf{x}_s}{\partial \xi}, \quad \mathbf{t}_{(2)} = \frac{\partial \mathbf{x}_s}{\partial \eta}. \quad (\text{A.2.3})$$

Strictly speaking, these are the *covariant* tangential vectors – that is, their magnitude changes in proportion to the change of length scale of the local surface coordinate. As an example, suppose that $\xi = R\theta$ and $\eta = R\phi$ measure the polar and azimuthal arc lengths, respectively, on the surface of a sphere of radius R . The tangential vectors for this surface are $\mathbf{t}_{(1)} = R\hat{\mathbf{e}}_\theta$ and $\mathbf{t}_{(2)} = R\sin\theta\hat{\mathbf{e}}_\phi$. Now if the radius of the sphere is doubled from R to $R' = 2R$ (that is, the length scale of the surface coordinate has increased by a factor of two), then the tangential vectors $\mathbf{t}_{(1)}$ and $\mathbf{t}_{(2)}$ will double in magnitude. This response to “stretching” the surface coordinate axes is “co-varying” and hence the term covariant.

Armed solely with the tangential vectors $\mathbf{t}_{(1)}$ and $\mathbf{t}_{(2)}$, we can already calculate some important geometric properties of the surface. For the purposes of line integration, we define the line elements,

$$ds_1 = |\mathbf{t}_{(1)}| d\xi, \quad ds_2 = |\mathbf{t}_{(2)}| d\eta. \quad (\text{A.2.4})$$

¹ One has to be careful with defining properties of a surface with respect to φ , which is a function of three coordinates! To be clear, the addendum “at $\mathbf{x} = \mathbf{x}_s$ ” is always used to indicate that the property of interest is evaluated on the surface after performing operations in three dimensions (an important example being the gradient $\nabla\varphi$).

For surface integration, we define the surface element,

$$dS = |\mathbf{t}_{(1)} \times \mathbf{t}_{(2)}| d\xi d\eta. \quad (\text{A.2.5})$$

Thus, the covariant tangential vectors provide measures of *distance* on the surface with respect to variations in the surface coordinates.

In order to form a complete basis in three dimensions, one requires a third vector that is orthogonal to both $\mathbf{t}_{(1)}$ and $\mathbf{t}_{(2)}$. Hence, we define the unit normal vector of the surface as,

$$\hat{\mathbf{n}} = \frac{\mathbf{t}_{(1)} \times \mathbf{t}_{(2)}}{|\mathbf{t}_{(1)} \times \mathbf{t}_{(2)}|}. \quad (\text{A.2.6})$$

By construction, $|\hat{\mathbf{n}}| = 1$. Unlike $\mathbf{t}_{(1)}$ and $\mathbf{t}_{(2)}$, the unit normal $\hat{\mathbf{n}}$ is *invariant* (its magnitude does not change) with respect to a stretching of the surface coordinate axes. In the course of solving problems, it may be desirable to reverse the order of $\mathbf{t}_{(1)}$ and $\mathbf{t}_{(2)}$ so that $\hat{\mathbf{n}}$ points outward from the surface. In some textbooks, it is common to see the unit normal defined with respect to the level set function (A.2.2),

$$\hat{\mathbf{n}} = \frac{\nabla \varphi}{|\nabla \varphi|} \quad \text{at } \mathbf{x} = \mathbf{x}_s, \quad (\text{A.2.7})$$

which is a perfectly suitable definition.

The covariant basis $(\mathbf{t}_{(1)}, \mathbf{t}_{(2)}, \hat{\mathbf{n}})$ need not be orthonormal (or even orthogonal). Thus, it is necessary to define a reciprocal or *contravariant* basis $(\mathbf{t}^{(1)}, \mathbf{t}^{(2)}, \hat{\mathbf{n}})$. As the term “contravariant” suggests, the magnitude of $\mathbf{t}^{(1)}$ and $\mathbf{t}^{(2)}$ is reduced by one-half when the scale of the surface coordinate axes is doubled. By construction, the unit normal $\hat{\mathbf{n}}$ is orthogonal to $\mathbf{t}^{(1)}$ and $\mathbf{t}^{(2)}$ and hence is a member of the reciprocal basis. The contravariant tangential vectors are defined by the simultaneous equations,

$$\begin{aligned} \mathbf{t}^{(1)} \cdot \mathbf{t}_{(1)} &= 1, & \mathbf{t}^{(1)} \cdot \mathbf{t}_{(2)} &= 0, \\ \mathbf{t}^{(2)} \cdot \mathbf{t}_{(1)} &= 0, & \mathbf{t}^{(2)} \cdot \mathbf{t}_{(2)} &= 1, \end{aligned} \quad (\text{A.2.8})$$

whose solution is given by,

$$\mathbf{t}^{(1)} = \frac{\mathbf{t}_{(2)} \times \hat{\mathbf{n}}}{G_s}, \quad \mathbf{t}^{(2)} = \frac{\hat{\mathbf{n}} \times \mathbf{t}_{(1)}}{G_s}. \quad (\text{A.2.9})$$

The scalar G_s appearing in (A.2.9) is called the *surface metric* and is defined by the scalar triple product,

$$G_s = (\mathbf{t}_{(1)} \times \mathbf{t}_{(2)}) \cdot \hat{\mathbf{n}} = |\mathbf{t}_{(1)} \times \mathbf{t}_{(2)}|. \quad (\text{A.2.10})$$

From (A.2.5) and (A.2.10), it is clear that G_s provides a measure of the local change in surface area with respect to variation of the surface coordinates. Taking again the example of a sphere of radius R , we find the contravariant tangential vectors to be $\mathbf{t}^{(1)} = \hat{\mathbf{e}}_\theta/R$ and $\mathbf{t}^{(2)} = \hat{\mathbf{e}}_\phi/(R \sin \theta)$. The surface metric for the same surface is $G_s = R^2 \sin \theta$.

Taken together, the dual bases $(\mathbf{t}_{(1)}, \mathbf{t}_{(2)}, \hat{\mathbf{n}})$ and $(\mathbf{t}^{(1)}, \mathbf{t}^{(2)}, \hat{\mathbf{n}})$ supply most of the geometrical information about a surface. Namely, one can define the *surface unit tensor* δ_s by any one of the identities,

$$\delta_s = \mathbf{t}^{(1)}\mathbf{t}_{(1)} + \mathbf{t}^{(2)}\mathbf{t}_{(2)} \quad (\text{A.2.11a})$$

$$= \mathbf{t}_{(1)}\mathbf{t}^{(1)} + \mathbf{t}_{(2)}\mathbf{t}^{(2)} \quad (\text{A.2.11b})$$

$$= \delta - \hat{\mathbf{n}}\hat{\mathbf{n}} \quad \text{at } \mathbf{x} = \mathbf{x}_s. \quad (\text{A.2.11c})$$

Several comments are in order. First, from the last expression (A.2.11c) it is clear that δ_s acts as a surface projection operator – that is, the projection $\delta_s \cdot \mathbf{v}$ removes the components of \mathbf{v} that are normal to the surface. Second, it can be readily verified that δ_s is symmetric and invariant with respect to stretching of the surface coordinate axes. Third, it is clear that δ_s degenerates in three dimensions, which precludes the definition of an inverse according to (A.1.2). We will return to this conundrum in §A.5 during our discussion of surface curvature.

A.3 Surface components of vectors and tensors

Having established the dual bases of the surface, we can express vectorial and tensorial quantities in terms of either of these bases. Contraction of a vector \mathbf{v} with either $\mathbf{t}_{(\alpha)}$ or $\mathbf{t}^{(\alpha)}$ ($\alpha = 1$ or 2) returns, respectively, the covariant and contravariant tangential components of that vector. However, we are most interested in the *invariant components* of \mathbf{v} (also called the *physical components*) with respect to the local surface basis. Since $\hat{\mathbf{n}}$ is an invariant quantity, the invariant component of \mathbf{v} in the normal direction is simply given by $\hat{\mathbf{n}} \cdot \mathbf{v}$. Similar invariant components may be defined in the tangential directions via multiplication by the appropriate Jacobian $\partial s_1 / \partial \xi$ or $\partial s_2 / \partial \eta$ [cf. (A.2.4)]. Thus, we define the surface components of \mathbf{v} by,

$$\text{normal:} \quad v_n = \hat{\mathbf{n}} \cdot \mathbf{v}, \quad (\text{A.3.1a})$$

$$\text{tangent along } s_1: \quad v_{s_1} = |\mathbf{t}_{(1)}|(\mathbf{t}^{(1)} \cdot \mathbf{v}) = |\mathbf{t}_{(1)}|[(\mathbf{t}^{(1)} \cdot \mathbf{t}^{(1)})(\mathbf{t}_{(1)} \cdot \mathbf{v}) + (\mathbf{t}^{(1)} \cdot \mathbf{t}^{(2)})(\mathbf{t}_{(2)} \cdot \mathbf{v})], \quad (\text{A.3.1b})$$

$$\text{tangent along } s_2: \quad v_{s_2} = |\mathbf{t}_{(2)}|(\mathbf{t}^{(2)} \cdot \mathbf{v}) = |\mathbf{t}_{(2)}|[(\mathbf{t}^{(2)} \cdot \mathbf{t}^{(1)})(\mathbf{t}_{(1)} \cdot \mathbf{v}) + (\mathbf{t}^{(2)} \cdot \mathbf{t}^{(2)})(\mathbf{t}_{(2)} \cdot \mathbf{v})], \quad (\text{A.3.1c})$$

where v_n , v_{s_1} , and v_{s_2} are all invariant. The vector \mathbf{v} is then represented in terms of the surface basis by the vector equation,

$$\mathbf{v} = v_n \hat{\mathbf{n}} + v_{s_1} \frac{\mathbf{t}_{(1)}}{|\mathbf{t}_{(1)}|} + v_{s_2} \frac{\mathbf{t}_{(2)}}{|\mathbf{t}_{(2)}|}. \quad (\text{A.3.2})$$

Similar arguments lead to the surface components of a second-order tensor τ . We need not list

all of them; for our purposes, the surface components of the vector $\tau \cdot \hat{\mathbf{n}}$ are of most practical value:

$$\text{normal: } \tau_{nn} = \hat{\mathbf{n}} \cdot \tau \cdot \hat{\mathbf{n}}, \quad (\text{A.3.3})$$

$$\text{tangent along } s_1: \tau_{s_1 n} = |\mathbf{t}_{(1)}|(\mathbf{t}^{(1)} \cdot \tau \cdot \hat{\mathbf{n}}) = |\mathbf{t}_{(1)}|[(\mathbf{t}^{(1)} \cdot \mathbf{t}^{(1)})(\mathbf{t}_{(1)} \cdot \tau \cdot \hat{\mathbf{n}}) + (\mathbf{t}^{(1)} \cdot \mathbf{t}^{(2)})(\mathbf{t}_{(2)} \cdot \tau \cdot \hat{\mathbf{n}})], \quad (\text{A.3.4})$$

$$\text{tangent along } s_2: \tau_{s_2 n} = |\mathbf{t}_{(2)}|(\mathbf{t}^{(2)} \cdot \tau \cdot \hat{\mathbf{n}}) = |\mathbf{t}_{(2)}|[(\mathbf{t}^{(2)} \cdot \mathbf{t}^{(1)})(\mathbf{t}_{(1)} \cdot \tau \cdot \hat{\mathbf{n}}) + (\mathbf{t}^{(2)} \cdot \mathbf{t}^{(2)})(\mathbf{t}_{(2)} \cdot \tau \cdot \hat{\mathbf{n}})]. \quad (\text{A.3.5})$$

We may represent the vector $\tau \cdot \hat{\mathbf{n}}$ as,

$$\tau \cdot \hat{\mathbf{n}} = \tau_{nn} \hat{\mathbf{n}} + \tau_{s_1 n} \frac{\mathbf{t}_{(1)}}{|\mathbf{t}_{(1)}|} + \tau_{s_2 n} \frac{\mathbf{t}_{(2)}}{|\mathbf{t}_{(2)}|}. \quad (\text{A.3.6})$$

A.4 Surface gradient

Variations of a field quantity (say ψ , \mathbf{v} , or τ) with respect to changes in the local surface coordinates ξ and η are measured by the surface gradient operator ∇_s :

$$\nabla_s = \mathbf{t}^{(1)} \frac{\partial}{\partial \xi} + \mathbf{t}^{(2)} \frac{\partial}{\partial \eta}. \quad (\text{A.4.1})$$

This operator is related to the usual gradient operator ∇ by,

$$\nabla_s = \delta_s \cdot \nabla \quad \text{at} \quad \mathbf{x} = \mathbf{x}_s, \quad (\text{A.4.2})$$

where the δ_s -operation has the effect of removing gradients in the direction normal to the surface. An important property of ∇_s is that it is invariant with respect to a stretching of the surface coordinate axes. This can be seen from the fact that $\mathbf{t}^{(1)}$ and $\mathbf{t}^{(2)}$ are both contravariant, whereas the partial derivatives $\partial/\partial\xi$ and $\partial/\partial\eta$ are covariant. The product of a contravariant quantity with a covariant quantity is an invariant quantity; hence, ∇_s is invariant.

We now consider variations of fields over the surface. Clearly, the surface gradient of a scalar field ψ is given by,

$$\nabla_s \psi = \mathbf{t}^{(1)} \frac{\partial \psi}{\partial \xi} + \mathbf{t}^{(2)} \frac{\partial \psi}{\partial \eta}. \quad (\text{A.4.3})$$

Now consider the surface divergence of a vector field $\mathbf{v} = \mathbf{t}_{(1)}(\mathbf{t}^{(1)} \cdot \mathbf{v}) + \mathbf{t}_{(2)}(\mathbf{t}^{(2)} \cdot \mathbf{v}) + \hat{\mathbf{n}}(\hat{\mathbf{n}} \cdot \mathbf{v})$ (p. 187 of [111]):

$$\begin{aligned} \nabla_s \cdot \mathbf{v} &= \nabla_s \cdot [\mathbf{t}_{(1)}(\mathbf{t}^{(1)} \cdot \mathbf{v}) + \mathbf{t}_{(2)}(\mathbf{t}^{(2)} \cdot \mathbf{v}) + \hat{\mathbf{n}}(\hat{\mathbf{n}} \cdot \mathbf{v})] \\ &= \frac{1}{G_s} \frac{\partial}{\partial \xi} (G_s \mathbf{t}^{(1)} \cdot \mathbf{v}) + \frac{1}{G_s} \frac{\partial}{\partial \eta} (G_s \mathbf{t}^{(2)} \cdot \mathbf{v}) + (\nabla_s \cdot \hat{\mathbf{n}})(\hat{\mathbf{n}} \cdot \mathbf{v}). \end{aligned} \quad (\text{A.4.4})$$

where the identity $\hat{\mathbf{n}} \cdot \nabla_s = 0$ has been used. Equation (A.4.4) expresses the divergence of \mathbf{v} in terms of its tangential and normal components and can be trivially extended to tensors of higher order. By combining this expression with (A.4.3), we can easily derive an expression for the surface Laplacian of a scalar field ψ ,

$$\nabla_s^2 \psi = \nabla_s \cdot \nabla_s \psi = \frac{1}{G_s} \frac{\partial}{\partial \xi} \left[G_s \mathbf{t}^{(1)} \cdot \left(\mathbf{t}^{(1)} \frac{\partial \psi}{\partial \xi} + \mathbf{t}^{(2)} \frac{\partial \psi}{\partial \eta} \right) \right] + \frac{1}{G_s} \frac{\partial}{\partial \eta} \left[G_s \mathbf{t}^{(2)} \cdot \left(\mathbf{t}^{(1)} \frac{\partial \psi}{\partial \xi} + \mathbf{t}^{(2)} \frac{\partial \psi}{\partial \eta} \right) \right]. \quad (\text{A.4.5})$$

Before proceeding, it is worth noting that the surface divergence δ_s does not vanish, viz.,

$$\nabla_s \cdot \delta_s = -(\nabla_s \cdot \hat{\mathbf{n}}) \hat{\mathbf{n}}. \quad (\text{A.4.6})$$

Physically, this expression gives a measure of the areal dilatation that results from variations in the unit normal $\hat{\mathbf{n}}$ along the surface. The scalar quantity $-(\nabla_s \cdot \hat{\mathbf{n}})$ is related to the *curvature* of the surface, which is the subject of the next section.

A.5 Surface curvature

At the end of the last section, we noted that the surface divergence of δ_s does not vanish due to the fact that $\hat{\mathbf{n}}$ varies with surface position. As a consequence, the quantity $-(\nabla_s \cdot \hat{\mathbf{n}})$ appears on the right-hand side of (A.4.4) and (A.4.6). In fact, this quantity is one of the principal invariants of the *surface curvature tensor*,

$$\kappa_s = -\nabla_s \hat{\mathbf{n}}, \quad (\text{A.5.1})$$

which, together with the surface unit tensor δ_s , completely specifies all of the geometric information about the surface.

It is instructive to examine the properties of the curvature tensor κ_s . First, it can be shown that the unit normal $\hat{\mathbf{n}}$ is irrotational in the (ξ, η) -plane,

$$\nabla_s \times \hat{\mathbf{n}} = \mathbf{0}, \quad (\text{A.5.2})$$

whence κ_s is symmetric with respect to rotations in the (ξ, η) -plane. It follows that,

$$\hat{\mathbf{n}} \cdot \nabla_s \hat{\mathbf{n}} = \mathbf{0} \quad \text{and} \quad (\nabla_s \hat{\mathbf{n}}) \cdot \hat{\mathbf{n}} = \mathbf{0}, \quad (\text{A.5.3})$$

which implies that κ_s , like δ_s , degenerates in three dimensions. Its two non-vanishing eigenvalues κ_1

and κ_2 are called the *principal curvatures* of the surface. They satisfy the characteristic quadratic,

$$\kappa_\alpha^2 - 2H\kappa_\alpha + K = 0 \quad (\alpha = 1 \text{ or } 2), \quad (\text{A.5.4})$$

where

$$2H = \kappa_1 + \kappa_2 = \text{tr}(\boldsymbol{\kappa}_s) = -\nabla_s \cdot \hat{\mathbf{n}}, \quad (\text{A.5.5a})$$

$$2K = 2\kappa_1\kappa_2 = \text{tr}^2(\boldsymbol{\kappa}_s) - \text{tr}(\boldsymbol{\kappa}_s \cdot \boldsymbol{\kappa}_s) = (\nabla_s \cdot \hat{\mathbf{n}})^2 - \nabla_s \hat{\mathbf{n}} : \nabla_s \hat{\mathbf{n}}. \quad (\text{A.5.5b})$$

The principal scalar invariants H and K are the *mean and Gaussian curvatures* of the surface, respectively. They may be alternatively expressed in terms of the level set function $\varphi(\mathbf{x})$ as follows:

$$2H = -\nabla \cdot \left(\frac{\nabla \varphi}{|\nabla \varphi|} \right), \quad (\text{A.5.6a})$$

$$2K = \left[\nabla \cdot \left(\frac{\nabla \varphi}{|\nabla \varphi|} \right) \right]^2 - \nabla \left(\frac{\nabla \varphi}{|\nabla \varphi|} \right) : \nabla \left(\frac{\nabla \varphi}{|\nabla \varphi|} \right). \quad (\text{A.5.6b})$$

These definitions follow from the fact that $\hat{\mathbf{n}} \cdot \hat{\mathbf{n}} = 1$ and hence $\nabla(\hat{\mathbf{n}} \cdot \hat{\mathbf{n}}) = 2(\nabla \hat{\mathbf{n}}) \cdot \hat{\mathbf{n}} = \mathbf{0}$. Making use of (A.5.3), it follows that

$$\nabla_s \cdot \hat{\mathbf{n}} = \nabla \cdot \hat{\mathbf{n}}, \quad \nabla_s \hat{\mathbf{n}} : \nabla_s \hat{\mathbf{n}} = \nabla \hat{\mathbf{n}} : \nabla \hat{\mathbf{n}} \quad \text{at} \quad \mathbf{x} = \mathbf{x}_s.$$

Inserting these expressions into (A.5.5) and making use of (A.2.7) then leads directly to (A.5.6).

Since H and K are the only non-vanishing principal scalar invariants of $\boldsymbol{\kappa}_s$, then the Cayleigh-Hamilton theorem states,

$$\boldsymbol{\kappa}_s \cdot \boldsymbol{\kappa}_s - 2H\boldsymbol{\kappa}_s + K\boldsymbol{\delta}_s = \mathbf{0}, \quad (\text{A.5.7})$$

which is the tensorial analog of (A.5.4). Taking the trace of (A.5.7) and rearranging the result leads to the following identity:

$$2D^2 = 2(H^2 - K) = \frac{1}{2}(\kappa_1 - \kappa_2)^2 = \nabla_s \hat{\mathbf{n}} : \nabla_s \hat{\mathbf{n}} - \frac{1}{2}(\nabla_s \cdot \hat{\mathbf{n}})^2, \quad (\text{A.5.8})$$

where D is the so-called *deviatoric curvature*. Clearly, D is not independent of H and K and in fact they are related by (A.5.8). The sign of D may be chosen arbitrarily.

Equation (A.5.7) implies that a suitable inverse of $\boldsymbol{\kappa}_s$ exists in two dimensions provided that $K \neq 0$, despite the fact that $\boldsymbol{\kappa}_s$ is degenerate in three dimensions. If we restrict our attention to the (ξ, η) -plane, then the inverse tensor $\boldsymbol{\kappa}_s^{-1}$ may be defined to satisfy the relation,

$$\boldsymbol{\kappa}_s^{-1} \cdot \boldsymbol{\kappa}_s = \boldsymbol{\kappa}_s \cdot \boldsymbol{\kappa}_s^{-1} = \boldsymbol{\delta}_s. \quad (\text{A.5.9})$$

Comparing (A.5.9) to (A.1.2) shows this definition to be something of a bastardization of the tensorial inverse. Nevertheless, the quantity κ_s^{-1} , which had no meaning in three dimensions, is now well defined according to (A.5.9). Thus, we shall restrict our use of this “liberal” definition of the inverse to our discussion of two-dimensional tensors.

We concluded the previous section with an expression for the surface divergence of δ_s , which may now be rewritten in terms of the mean curvature H :

$$\nabla_s \cdot \delta_s = 2H\hat{n}. \quad (\text{A.4.6})$$

We conclude this section with an analogous expression for the surface divergence of κ_s :

$$\nabla_s \cdot \kappa_s = \nabla_s(2H), \quad (\text{A.5.10})$$

which can be readily verified by exploiting the symmetry of κ_s .

A.6 Surface divergence theorem

The last topic in our discussion of surfaces is the analog of the divergence theorem in two dimensions. Consider a vector field v defined (and everywhere regular) on a surface \mathcal{S} with unit normal \hat{n} and bounding contour $\partial\mathcal{S}$. Our starting point is Stokes’ curl theorem (A.1.4) applied to the vector field $v \times \hat{n}$:

$$\int_{\partial\mathcal{S}} (v \times \hat{n}) \cdot (t_{(1)}d\xi + t_{(2)}d\eta) = \int_{\mathcal{S}} [\nabla \times (v \times \hat{n})] \cdot \hat{n} dS,$$

where we have substituted $ds = t_{(1)}d\xi + t_{(2)}d\eta$ and $dS = \hat{n} dS$. Now using elementary vector identities, we may rewrite this expression as,

$$\int_{\partial\mathcal{S}} v \cdot [(\hat{n} \times t_{(1)})d\xi + (\hat{n} \times t_{(2)})d\eta] = \int_{\mathcal{S}} [(\hat{n} \cdot v)(\nabla \cdot \hat{n}) - v \cdot (\nabla \hat{n}) \cdot \hat{n} - (\delta - \hat{n} \hat{n}) : \nabla v] \cdot \hat{n} dS.$$

But $x = x_s$ on \mathcal{S} , so we may use (A.2.9) and (A.2.11c) as well as the identities $\nabla \cdot \hat{n} = \nabla_s \cdot \hat{n}$ and $(\nabla \hat{n}) \cdot \hat{n} = \frac{1}{2}\nabla(\hat{n} \cdot \hat{n}) = \mathbf{0}$. We obtain,

$$-\int_{\partial\mathcal{S}} G_s v \cdot (t^{(2)}d\xi - t^{(1)}d\eta) = \int_{\mathcal{S}} (2H\hat{n} \cdot v + \nabla_s \cdot v) dS. \quad (\text{A.6.1})$$

The last expression is known as the *surface divergence theorem* [8].

A.7 Surface geometry in various coordinate systems

A.7.1 Cartesian coordinates, $z = z_s(x, y)$

Level set function:

$$\varphi(x, y, z) = z - z_s(x, y) = 0 \quad \text{on the surface.} \quad (\text{A.7.1})$$

Surface position vector:

$$\mathbf{x}_s(x, y) = \hat{\mathbf{e}}_x x + \hat{\mathbf{e}}_y y + \hat{\mathbf{e}}_z z_s(x, y). \quad (\text{A.7.2})$$

Surface metric:

$$G_s = \sqrt{1 + \left(\frac{\partial z_s}{\partial x}\right)^2 + \left(\frac{\partial z_s}{\partial y}\right)^2}. \quad (\text{A.7.3})$$

Unit normal vector:

$$\hat{\mathbf{n}} = \frac{1}{G_s} \left(\hat{\mathbf{e}}_z - \hat{\mathbf{e}}_x \frac{\partial z_s}{\partial x} - \hat{\mathbf{e}}_y \frac{\partial z_s}{\partial y} \right). \quad (\text{A.7.4})$$

Covariant tangential vectors:

$$\mathbf{t}_{(1)} = \hat{\mathbf{e}}_x + \hat{\mathbf{e}}_z \frac{\partial z_s}{\partial x}, \quad (\text{A.7.5a})$$

$$\mathbf{t}_{(2)} = \hat{\mathbf{e}}_y + \hat{\mathbf{e}}_z \frac{\partial z_s}{\partial y}. \quad (\text{A.7.5b})$$

Contravariant tangential vectors:

$$\mathbf{t}^{(1)} = \frac{1}{G_s^2} \left\{ \hat{\mathbf{e}}_x \left[1 + \left(\frac{\partial z_s}{\partial y}\right)^2 \right] - \hat{\mathbf{e}}_y \frac{\partial z_s}{\partial x} \frac{\partial z_s}{\partial y} + \hat{\mathbf{e}}_z \frac{\partial z_s}{\partial x} \right\}, \quad (\text{A.7.6a})$$

$$\mathbf{t}^{(2)} = \frac{1}{G_s^2} \left\{ \hat{\mathbf{e}}_y \left[1 + \left(\frac{\partial z_s}{\partial x}\right)^2 \right] - \hat{\mathbf{e}}_x \frac{\partial z_s}{\partial x} \frac{\partial z_s}{\partial y} + \hat{\mathbf{e}}_z \frac{\partial z_s}{\partial y} \right\}. \quad (\text{A.7.6b})$$

Line elements:

$$ds_1 = \sqrt{1 + \left(\frac{\partial z_s}{\partial x}\right)^2} dx, \quad (\text{A.7.7a})$$

$$ds_2 = \sqrt{1 + \left(\frac{\partial z_s}{\partial y}\right)^2} dy. \quad (\text{A.7.7b})$$

Surface element:

$$dS = \sqrt{1 + \left(\frac{\partial z_s}{\partial x}\right)^2 + \left(\frac{\partial z_s}{\partial y}\right)^2} dx dy. \quad (\text{A.7.8})$$

Mean curvature:

$$H = \frac{1}{2G_s^3} \left\{ \frac{\partial^2 z_s}{\partial x^2} \left[1 + \left(\frac{\partial z_s}{\partial y}\right)^2 \right] + \frac{\partial^2 z_s}{\partial y^2} \left[1 + \left(\frac{\partial z_s}{\partial x}\right)^2 \right] - 2 \frac{\partial z_s}{\partial x} \frac{\partial z_s}{\partial y} \frac{\partial^2 z_s}{\partial x \partial y} \right\}. \quad (\text{A.7.9})$$

Gaussian curvature:

$$K = \frac{1}{G_s^4} \left[\frac{\partial^2 z_s}{\partial x^2} \frac{\partial^2 z_s}{\partial y^2} - \left(\frac{\partial^2 z_s}{\partial x \partial y} \right)^2 \right]. \quad (\text{A.7.10})$$

Surface components of \mathbf{v} :

$$v_n = \frac{1}{G_s} \left(v_z - v_x \frac{\partial z_s}{\partial x} - v_y \frac{\partial z_s}{\partial y} \right), \quad (\text{A.7.11a})$$

$$v_{s_1} = \frac{\sqrt{1 + (\partial z_s / \partial x)^2}}{G_s^2} \left\{ v_x \left[1 + \left(\frac{\partial z_s}{\partial y} \right)^2 \right] - v_y \frac{\partial z_s}{\partial x} \frac{\partial z_s}{\partial y} + v_z \frac{\partial z_s}{\partial x} \right\}, \quad (\text{A.7.11b})$$

$$v_{s_2} = \frac{\sqrt{1 + (\partial z_s / \partial y)^2}}{G_s^2} \left\{ v_y \left[1 + \left(\frac{\partial z_s}{\partial x} \right)^2 \right] - v_x \frac{\partial z_s}{\partial x} \frac{\partial z_s}{\partial y} + v_z \frac{\partial z_s}{\partial y} \right\}. \quad (\text{A.7.11c})$$

Surface components of $\boldsymbol{\tau} \cdot \hat{\mathbf{n}}$:

$$\begin{aligned} \tau_{nn} &= \frac{1}{G_s^2} \left[\tau_{zz} - \tau_{zx} \frac{\partial z_s}{\partial x} - \tau_{zy} \frac{\partial z_s}{\partial y} - \left(\tau_{xz} - \tau_{xx} \frac{\partial z_s}{\partial x} - \tau_{xy} \frac{\partial z_s}{\partial y} \right) \frac{\partial z_s}{\partial x} \right. \\ &\quad \left. - \left(\tau_{yz} - \tau_{yx} \frac{\partial z_s}{\partial x} - \tau_{yy} \frac{\partial z_s}{\partial y} \right) \frac{\partial z_s}{\partial y} \right], \end{aligned} \quad (\text{A.7.12a})$$

$$\begin{aligned} \tau_{s_1 n} &= \frac{\sqrt{1 + (\partial z_s / \partial x)^2}}{G_s^3} \left\{ \left(\tau_{xz} - \tau_{xx} \frac{\partial z_s}{\partial x} - \tau_{xy} \frac{\partial z_s}{\partial y} \right) \left[1 + \left(\frac{\partial z_s}{\partial y} \right)^2 \right] \right. \\ &\quad \left. - \left(\tau_{yz} - \tau_{yx} \frac{\partial z_s}{\partial x} - \tau_{yy} \frac{\partial z_s}{\partial y} \right) \frac{\partial z_s}{\partial x} \frac{\partial z_s}{\partial y} + \left(\tau_{zz} - \tau_{zx} \frac{\partial z_s}{\partial x} - \tau_{zy} \frac{\partial z_s}{\partial y} \right) \frac{\partial z_s}{\partial x} \right\}, \end{aligned} \quad (\text{A.7.12b})$$

$$\begin{aligned} \tau_{s_2 n} &= \frac{\sqrt{1 + (\partial z_s / \partial y)^2}}{G_s^3} \left\{ \left(\tau_{yz} - \tau_{yx} \frac{\partial z_s}{\partial x} - \tau_{yy} \frac{\partial z_s}{\partial y} \right) \left[1 + \left(\frac{\partial z_s}{\partial x} \right)^2 \right] \right. \\ &\quad \left. - \left(\tau_{xz} - \tau_{xx} \frac{\partial z_s}{\partial x} - \tau_{xy} \frac{\partial z_s}{\partial y} \right) \frac{\partial z_s}{\partial x} \frac{\partial z_s}{\partial y} + \left(\tau_{zz} - \tau_{zx} \frac{\partial z_s}{\partial x} - \tau_{zy} \frac{\partial z_s}{\partial y} \right) \frac{\partial z_s}{\partial y} \right\}. \end{aligned} \quad (\text{A.7.12c})$$

Surface gradient of ψ :

$$\begin{aligned} \nabla_s \psi &= \frac{1}{G_s^2} \left\{ \hat{\mathbf{e}}_x \left[1 + \left(\frac{\partial z_s}{\partial y} \right)^2 \right] - \hat{\mathbf{e}}_y \frac{\partial z_s}{\partial x} \frac{\partial z_s}{\partial y} + \hat{\mathbf{e}}_z \frac{\partial z_s}{\partial x} \right\} \frac{\partial \psi}{\partial x} \\ &\quad + \frac{1}{G_s^2} \left\{ \hat{\mathbf{e}}_y \left[1 + \left(\frac{\partial z_s}{\partial x} \right)^2 \right] - \hat{\mathbf{e}}_x \frac{\partial z_s}{\partial x} \frac{\partial z_s}{\partial y} + \hat{\mathbf{e}}_z \frac{\partial z_s}{\partial y} \right\} \frac{\partial \psi}{\partial y}. \end{aligned} \quad (\text{A.7.13})$$

Surface divergence of \mathbf{v} :

$$\begin{aligned} \nabla_s \cdot \mathbf{v} &= \frac{1}{G_s} \frac{\partial}{\partial x} \left(\frac{1}{G_s} \left\{ v_x \left[1 + \left(\frac{\partial z_s}{\partial y} \right)^2 \right] - v_y \frac{\partial z_s}{\partial x} \frac{\partial z_s}{\partial y} + v_z \frac{\partial z_s}{\partial x} \right\} \right) \\ &\quad + \frac{1}{G_s} \frac{\partial}{\partial y} \left(\frac{1}{G_s} \left\{ v_y \left[1 + \left(\frac{\partial z_s}{\partial x} \right)^2 \right] - v_x \frac{\partial z_s}{\partial x} \frac{\partial z_s}{\partial y} + v_z \frac{\partial z_s}{\partial y} \right\} \right) \end{aligned}$$

$$-\frac{2H}{G_s} \left(v_z - v_x \frac{\partial z_s}{\partial x} - v_y \frac{\partial z_s}{\partial y} \right), \quad (\text{A.7.14a})$$

$$= \frac{1}{G_s} \frac{\partial}{\partial x} (G_s v_x) + \frac{1}{G_s} \frac{\partial}{\partial y} (G_s v_y) \quad \text{if } v_n = 0. \quad (\text{A.7.14b})$$

Surface Laplacian of ψ :

$$\begin{aligned} \nabla_s^2 \psi &= \frac{1}{G_s} \frac{\partial}{\partial x} \left(\frac{1}{G_s} \left\{ \left[1 + \left(\frac{\partial z_s}{\partial y} \right)^2 \right] \frac{\partial \psi}{\partial x} - \frac{\partial z_s}{\partial x} \frac{\partial z_s}{\partial y} \frac{\partial \psi}{\partial y} \right\} \right) \\ &\quad + \frac{1}{G_s} \frac{\partial}{\partial y} \left(\frac{1}{G_s} \left\{ \left[1 + \left(\frac{\partial z_s}{\partial x} \right)^2 \right] \frac{\partial \psi}{\partial y} - \frac{\partial z_s}{\partial x} \frac{\partial z_s}{\partial y} \frac{\partial \psi}{\partial x} \right\} \right). \end{aligned} \quad (\text{A.7.15})$$

A.7.2 Cylindrical coordinates, $\rho = \rho_s(\phi, z)$

Level set function:

$$\varphi(\rho, \phi, z) = \rho - \rho_s(\phi, z) = 0 \quad \text{on the surface.} \quad (\text{A.7.16})$$

Surface position vector:

$$\mathbf{x}_s(\phi, z) = \hat{\mathbf{e}}_\rho(\phi) \rho_s(\phi, z) + \hat{\mathbf{e}}_z z. \quad (\text{A.7.17})$$

Surface metric:

$$G_s = \sqrt{\left(\frac{\partial \rho_s}{\partial \phi} \right)^2 + \rho_s^2 \left[1 + \left(\frac{\partial \rho_s}{\partial z} \right)^2 \right]}. \quad (\text{A.7.18})$$

Unit normal vector:

$$\hat{\mathbf{n}} = \frac{1}{G_s} \left(\hat{\mathbf{e}}_\rho \rho_s - \hat{\mathbf{e}}_\phi \frac{\partial \rho_s}{\partial \phi} - \hat{\mathbf{e}}_z \rho_s \frac{\partial \rho_s}{\partial z} \right). \quad (\text{A.7.19})$$

Covariant tangential vectors:

$$\mathbf{t}_{(1)} = \hat{\mathbf{e}}_\phi \rho_s + \hat{\mathbf{e}}_\rho \frac{\partial \rho_s}{\partial \phi}, \quad (\text{A.7.20a})$$

$$\mathbf{t}_{(2)} = \hat{\mathbf{e}}_z + \hat{\mathbf{e}}_\rho \frac{\partial \rho_s}{\partial z}. \quad (\text{A.7.20b})$$

Contravariant tangential vectors:

$$\mathbf{t}^{(1)} = \frac{1}{G_s^2} \left\{ \hat{\mathbf{e}}_\phi \rho_s \left[1 + \left(\frac{\partial \rho_s}{\partial z} \right)^2 \right] - \hat{\mathbf{e}}_z \frac{\partial \rho_s}{\partial z} \frac{\partial \rho_s}{\partial \phi} + \hat{\mathbf{e}}_\rho \frac{\partial \rho_s}{\partial \phi} \right\}, \quad (\text{A.7.21a})$$

$$\mathbf{t}^{(2)} = \frac{1}{G_s^2} \left\{ \hat{\mathbf{e}}_z \left[\rho_s^2 + \left(\frac{\partial \rho_s}{\partial \phi} \right)^2 \right] - \hat{\mathbf{e}}_\phi \rho_s \frac{\partial \rho_s}{\partial z} \frac{\partial \rho_s}{\partial \phi} + \hat{\mathbf{e}}_\rho \rho_s^2 \frac{\partial \rho_s}{\partial z} \right\}. \quad (\text{A.7.21b})$$

Line elements:

$$ds_1 = \sqrt{\rho_s^2 + \left(\frac{\partial \rho_s}{\partial \phi} \right)^2} d\phi, \quad (\text{A.7.22a})$$

$$ds_2 = \sqrt{1 + \left(\frac{\partial \rho_s}{\partial z}\right)^2} dz. \quad (\text{A.7.22b})$$

Surface element:

$$dS = \sqrt{\left(\frac{\partial \rho_s}{\partial \phi}\right)^2 + \rho_s^2 \left[1 + \left(\frac{\partial \rho_s}{\partial z}\right)^2\right]} d\phi dz. \quad (\text{A.7.23})$$

Mean curvature:

$$H = \frac{1}{2G_s^3} \left\{ \rho_s \frac{\partial^2 \rho_s}{\partial z^2} \left[\rho_s^2 + \left(\frac{\partial \rho_s}{\partial \phi}\right)^2 \right] + \rho_s \frac{\partial^2 \rho_s}{\partial \phi^2} \left[1 + \left(\frac{\partial \rho_s}{\partial z}\right)^2 \right] - 2\rho_s \frac{\partial \rho_s}{\partial z} \frac{\partial \rho_s}{\partial \phi} \frac{\partial^2 \rho_s}{\partial z \partial \phi} - \left(\frac{\partial \rho_s}{\partial \phi}\right)^2 \right\} - \frac{1}{2G_s}. \quad (\text{A.7.24})$$

Gaussian curvature:

$$K = \frac{1}{G_s^4} \left\{ \rho_s^2 \left[\frac{\partial^2 \rho_s}{\partial \phi^2} \frac{\partial^2 \rho_s}{\partial z^2} - \left(\frac{\partial^2 \rho_s}{\partial z \partial \phi}\right)^2 \right] - \rho_s \frac{\partial^2 \rho_s}{\partial z^2} \left[\rho_s^2 + 2\left(\frac{\partial \rho_s}{\partial \phi}\right)^2 \right] + \frac{\partial \rho_s}{\partial z} \frac{\partial \rho_s}{\partial \phi} \left(2\rho_s \frac{\partial^2 \rho_s}{\partial z \partial \phi} - \frac{\partial \rho_s}{\partial z} \frac{\partial \rho_s}{\partial \phi} \right) \right\}. \quad (\text{A.7.25})$$

Surface components of \mathbf{v} :

$$v_n = \frac{1}{G_s} \left(v_\rho \rho_s - v_\phi \frac{\partial \rho_s}{\partial \phi} - v_z \rho_s \frac{\partial \rho_s}{\partial z} \right), \quad (\text{A.7.26a})$$

$$v_{s_1} = \frac{\sqrt{\rho_s^2 + (\partial \rho_s / \partial \phi)^2}}{G_s^2} \left\{ v_\phi \rho_s \left[1 + \left(\frac{\partial \rho_s}{\partial z}\right)^2 \right] - v_z \frac{\partial \rho_s}{\partial z} \frac{\partial \rho_s}{\partial \phi} + v_\rho \frac{\partial \rho_s}{\partial \phi} \right\}, \quad (\text{A.7.26b})$$

$$v_{s_2} = \frac{\sqrt{1 + (\partial \rho_s / \partial z)^2}}{G_s^2} \left\{ v_z \left[\rho_s^2 + \left(\frac{\partial \rho_s}{\partial \phi}\right)^2 \right] - v_\phi \rho_s \frac{\partial \rho_s}{\partial z} \frac{\partial \rho_s}{\partial \phi} + v_\rho \rho_s^2 \frac{\partial \rho_s}{\partial z} \right\}. \quad (\text{A.7.26c})$$

Surface components of $\boldsymbol{\tau} \cdot \hat{\mathbf{n}}$:

$$\begin{aligned} \tau_{nn} &= \frac{1}{G_s^2} \left[\left(\tau_{\rho\rho} \rho_s - \tau_{\rho\phi} \frac{\partial \rho_s}{\partial \phi} - \tau_{\rho z} \rho_s \frac{\partial \rho_s}{\partial z} \right) \rho_s - \left(\tau_{\phi\rho} \rho_s - \tau_{\phi\phi} \frac{\partial \rho_s}{\partial \phi} - \tau_{\phi z} \rho_s \frac{\partial \rho_s}{\partial z} \right) \frac{\partial \rho_s}{\partial \phi} \right. \\ &\quad \left. - \left(\tau_{z\rho} \rho_s - \tau_{z\phi} \frac{\partial \rho_s}{\partial \phi} - \tau_{zz} \rho_s \frac{\partial \rho_s}{\partial z} \right) \rho_s \frac{\partial \rho_s}{\partial z} \right], \end{aligned} \quad (\text{A.7.27a})$$

$$\begin{aligned} \tau_{s_1 n} &= \frac{\sqrt{\rho_s^2 + (\partial \rho_s / \partial \phi)^2}}{G_s^3} \left\{ \left(\tau_{\phi\rho} \rho_s - \tau_{\phi\phi} \frac{\partial \rho_s}{\partial \phi} - \tau_{\phi z} \rho_s \frac{\partial \rho_s}{\partial z} \right) \rho_s \left[1 + \left(\frac{\partial \rho_s}{\partial z}\right)^2 \right] \right. \\ &\quad \left. - \left(\tau_{z\rho} \rho_s - \tau_{z\phi} \frac{\partial \rho_s}{\partial \phi} - \tau_{zz} \rho_s \frac{\partial \rho_s}{\partial z} \right) \frac{\partial \rho_s}{\partial z} \frac{\partial \rho_s}{\partial \phi} + \left(\tau_{\rho\rho} \rho_s - \tau_{\rho\phi} \frac{\partial \rho_s}{\partial \phi} - \tau_{\rho z} \rho_s \frac{\partial \rho_s}{\partial z} \right) \frac{\partial \rho_s}{\partial \phi} \right\}, \end{aligned} \quad (\text{A.7.27b})$$

$$\begin{aligned} \tau_{s_2 n} &= \frac{\sqrt{1 + (\partial \rho_s / \partial z)^2}}{G_s^3} \left\{ \left(\tau_{z\rho} \rho_s - \tau_{z\phi} \frac{\partial \rho_s}{\partial \phi} - \tau_{zz} \rho_s \frac{\partial \rho_s}{\partial z} \right) \left[\rho_s^2 + \left(\frac{\partial \rho_s}{\partial \phi}\right)^2 \right] \right. \\ &\quad \left. - \left(\tau_{\rho\rho} \rho_s - \tau_{\rho\phi} \frac{\partial \rho_s}{\partial \phi} - \tau_{\rho z} \rho_s \frac{\partial \rho_s}{\partial z} \right) \rho_s^2 \right\} \end{aligned}$$

$$-\left(\tau_{\phi\rho}\rho_s - \tau_{\phi\phi}\frac{\partial\rho_s}{\partial\phi} - \tau_{\phi z}\rho_s\frac{\partial\rho_s}{\partial z}\right)\rho_s\frac{\partial\rho_s}{\partial z}\frac{\partial\rho_s}{\partial\phi} + \left(\tau_{\rho\rho}\rho_s - \tau_{\rho\phi}\frac{\partial\rho_s}{\partial\phi} - \tau_{\rho z}\rho_s\frac{\partial\rho_s}{\partial z}\right)\rho_s^2\frac{\partial\rho_s}{\partial z}\Bigg\}. \quad (\text{A.7.27c})$$

Surface gradient of ψ :

$$\begin{aligned} \nabla_s\psi &= \frac{1}{G_s^2} \left\{ \hat{e}_\phi\rho_s \left[1 + \left(\frac{\partial\rho_s}{\partial z} \right)^2 \right] - \hat{e}_z \frac{\partial\rho_s}{\partial z} \frac{\partial\rho_s}{\partial\phi} + \hat{e}_\rho \frac{\partial\rho_s}{\partial\phi} \right\} \frac{\partial\psi}{\partial\phi} \\ &\quad + \frac{1}{G_s^2} \left\{ \hat{e}_z \left[\rho_s^2 + \left(\frac{\partial\rho_s}{\partial\phi} \right)^2 \right] - \hat{e}_\phi\rho_s \frac{\partial\rho_s}{\partial z} \frac{\partial\rho_s}{\partial\phi} + \hat{e}_\rho\rho_s^2 \frac{\partial\rho_s}{\partial z} \right\} \frac{\partial\psi}{\partial z}. \end{aligned} \quad (\text{A.7.28})$$

Surface divergence of \mathbf{v} :

$$\begin{aligned} \nabla_s \cdot \mathbf{v} &= \frac{1}{G_s} \frac{\partial}{\partial\phi} \left(\frac{1}{G_s} \left\{ v_\phi\rho_s \left[1 + \left(\frac{\partial\rho_s}{\partial z} \right)^2 \right] - v_z \frac{\partial\rho_s}{\partial z} \frac{\partial\rho_s}{\partial\phi} + v_\rho \frac{\partial\rho_s}{\partial\phi} \right\} \right) \\ &\quad + \frac{1}{G_s} \frac{\partial}{\partial z} \left(\frac{1}{G_s} \left\{ v_z \left[\rho_s^2 + \left(\frac{\partial\rho_s}{\partial\phi} \right)^2 \right] - v_\phi\rho_s \frac{\partial\rho_s}{\partial z} \frac{\partial\rho_s}{\partial\phi} + v_\rho\rho_s^2 \frac{\partial\rho_s}{\partial z} \right\} \right) \\ &\quad - \frac{2H}{G_s} \left(v_\rho\rho_s - v_\phi \frac{\partial\rho_s}{\partial\phi} - v_z\rho_s \frac{\partial\rho_s}{\partial z} \right), \end{aligned} \quad (\text{A.7.29a})$$

$$= \frac{1}{G_s} \frac{\partial}{\partial\phi} \left(\frac{G_s v_\phi}{\rho_s} \right) + \frac{1}{G_s} \frac{\partial}{\partial z} (G_s v_z) \quad \text{if } v_n = 0. \quad (\text{A.7.29b})$$

Surface Laplacian of ψ :

$$\begin{aligned} \nabla_s^2\psi &= \frac{1}{G_s} \frac{\partial}{\partial\phi} \left(\frac{1}{G_s} \left\{ \left[1 + \left(\frac{\partial\rho_s}{\partial z} \right)^2 \right] \frac{\partial\psi}{\partial\phi} - \frac{\partial\rho_s}{\partial z} \frac{\partial\rho_s}{\partial\phi} \frac{\partial\psi}{\partial z} \right\} \right) \\ &\quad + \frac{1}{G_s} \frac{\partial}{\partial z} \left(\frac{1}{G_s} \left\{ \left[\rho_s^2 + \left(\frac{\partial\rho_s}{\partial\phi} \right)^2 \right] \frac{\partial\psi}{\partial z} - \frac{\partial\rho_s}{\partial z} \frac{\partial\rho_s}{\partial\phi} \frac{\partial\psi}{\partial\phi} \right\} \right). \end{aligned} \quad (\text{A.7.30})$$

A.7.3 Cylindrical coordinates, $z = z_s(\rho, \phi)$

Level set function:

$$\varphi(\rho, \phi, z) = z - z_s(\rho, \phi) = 0 \quad \text{on the surface.} \quad (\text{A.7.31})$$

Surface position vector:

$$\mathbf{x}_s(\rho, \phi) = \hat{e}_\rho(\phi)\rho + \hat{e}_z z_s(\rho, \phi). \quad (\text{A.7.32})$$

Surface metric:

$$G_s = \sqrt{\rho^2 \left[1 + \left(\frac{\partial z_s}{\partial \rho} \right)^2 \right] + \left(\frac{\partial z_s}{\partial \phi} \right)^2}. \quad (\text{A.7.33})$$

Unit normal vector:

$$\hat{n} = \frac{1}{G_s} \left(\hat{e}_z \rho - \hat{e}_\rho \rho \frac{\partial z_s}{\partial \rho} - \hat{e}_\phi \frac{\partial z_s}{\partial \phi} \right). \quad (\text{A.7.34})$$

Covariant tangential vectors:

$$\mathbf{t}_{(1)} = \hat{\mathbf{e}}_\rho + \hat{\mathbf{e}}_z \frac{\partial z_s}{\partial \rho}, \quad (\text{A.7.35a})$$

$$\mathbf{t}_{(2)} = \hat{\mathbf{e}}_\phi \rho + \hat{\mathbf{e}}_z \frac{\partial z_s}{\partial \phi}. \quad (\text{A.7.35b})$$

Contravariant tangential vectors:

$$\mathbf{t}^{(1)} = \frac{1}{G_s^2} \left\{ \hat{\mathbf{e}}_\rho \left[\rho^2 + \left(\frac{\partial z_s}{\partial \phi} \right)^2 \right] - \hat{\mathbf{e}}_\phi \rho \frac{\partial z_s}{\partial z} \frac{\partial z_s}{\partial \phi} + \hat{\mathbf{e}}_z \rho^2 \frac{\partial z_s}{\partial \rho} \right\}, \quad (\text{A.7.36a})$$

$$\mathbf{t}^{(2)} = \frac{1}{G_s^2} \left\{ \hat{\mathbf{e}}_\phi \rho \left[1 + \left(\frac{\partial z_s}{\partial \rho} \right)^2 \right] - \hat{\mathbf{e}}_\rho \frac{\partial z_s}{\partial \rho} \frac{\partial z_s}{\partial \phi} + \hat{\mathbf{e}}_z \frac{\partial z_s}{\partial \phi} \right\}. \quad (\text{A.7.36b})$$

Line elements:

$$ds_1 = \sqrt{1 + \left(\frac{\partial z_s}{\partial \rho} \right)^2} d\rho, \quad (\text{A.7.37a})$$

$$ds_2 = \sqrt{\rho^2 + \left(\frac{\partial z_s}{\partial \phi} \right)^2} d\phi. \quad (\text{A.7.37b})$$

Surface element:

$$dS = \sqrt{\rho^2 \left[1 + \left(\frac{\partial z_s}{\partial \rho} \right)^2 \right] + \left(\frac{\partial z_s}{\partial \phi} \right)^2} d\rho d\phi. \quad (\text{A.7.38})$$

Mean curvature:

$$H = \frac{1}{2G_s^3} \left\{ \rho \frac{\partial^2 z_s}{\partial \rho^2} \left[\rho^2 + \left(\frac{\partial z_s}{\partial \phi} \right)^2 \right] + \rho \frac{\partial^2 z_s}{\partial \phi^2} \left[1 + \left(\frac{\partial z_s}{\partial \rho} \right)^2 \right] - 2\rho \frac{\partial z_s}{\partial \rho} \frac{\partial z_s}{\partial \phi} \frac{\partial^2 z_s}{\partial \rho \partial \phi} + \frac{\partial z_s}{\partial \rho} \left(\frac{\partial z_s}{\partial \phi} \right)^2 \right\} + \frac{1}{2G_s} \frac{\partial z_s}{\partial \rho}. \quad (\text{A.7.39})$$

Gaussian curvature:

$$K = \frac{1}{G_s^4} \left\{ \rho^2 \left[\frac{\partial^2 z_s}{\partial \phi^2} \frac{\partial^2 z_s}{\partial \rho^2} - \left(\frac{\partial^2 z_s}{\partial \rho \partial \phi} \right)^2 \right] + \rho^3 \frac{\partial z_s}{\partial \rho} \frac{\partial^2 z_s}{\partial \rho^2} + \frac{\partial z_s}{\partial \phi} \left(2\rho \frac{\partial^2 z_s}{\partial \rho \partial \phi} - \frac{\partial z_s}{\partial \phi} \right) \right\}. \quad (\text{A.7.40})$$

Surface components of \mathbf{v} :

$$v_n = \frac{1}{G_s} \left(v_z \rho - v_\rho \rho \frac{\partial z_s}{\partial \rho} - v_\phi \frac{\partial z_s}{\partial \phi} \right), \quad (\text{A.7.41a})$$

$$v_{s_1} = \frac{\sqrt{1 + (\partial z_s / \partial \rho)^2}}{G_s^2} \left\{ v_\rho \left[\rho^2 + \left(\frac{\partial z_s}{\partial \phi} \right)^2 \right] - v_\phi \rho \frac{\partial z_s}{\partial \rho} \frac{\partial z_s}{\partial \phi} + v_z \rho^2 \frac{\partial z_s}{\partial \rho} \right\}, \quad (\text{A.7.41b})$$

$$v_{s_2} = \frac{\sqrt{\rho^2 + (\partial z_s / \partial \phi)^2}}{G_s^2} \left\{ v_\phi \rho \left[1 + \left(\frac{\partial z_s}{\partial \rho} \right)^2 \right] - v_\rho \frac{\partial z_s}{\partial \rho} \frac{\partial z_s}{\partial \phi} + v_z \frac{\partial z_s}{\partial \phi} \right\}. \quad (\text{A.7.41c})$$

Surface components of $\tau \cdot \hat{\mathbf{n}}$:

$$\begin{aligned}\tau_{nn} &= \frac{1}{G_s^2} \left[\left(\tau_{zz}\rho - \tau_{z\rho}\rho \frac{\partial z_s}{\partial \rho} - \tau_{z\phi}\rho \frac{\partial z_s}{\partial \phi} \right) \rho - \left(\tau_{\rho z}\rho - \tau_{\rho\rho}\rho \frac{\partial z_s}{\partial \rho} - \tau_{\rho\phi}\rho \frac{\partial z_s}{\partial \phi} \right) \rho \frac{\partial z_s}{\partial \rho} \right. \\ &\quad \left. - \left(\tau_{\phi z}\rho - \tau_{\phi\rho}\rho \frac{\partial z_s}{\partial \rho} - \tau_{\phi\phi}\rho \frac{\partial z_s}{\partial \phi} \right) \frac{\partial z_s}{\partial \phi} \right],\end{aligned}\quad (\text{A.7.42a})$$

$$\begin{aligned}\tau_{s_1 n} &= \frac{\sqrt{1 + (\partial z_s / \partial \rho)^2}}{G_s^3} \left\{ \left(\tau_{\rho z}\rho - \tau_{\rho\rho}\rho \frac{\partial z_s}{\partial \rho} - \tau_{\rho\phi}\rho \frac{\partial z_s}{\partial \phi} \right) \left[\rho^2 + \left(\frac{\partial z_s}{\partial \phi} \right)^2 \right] \right. \\ &\quad \left. - \left(\tau_{\phi z}\rho - \tau_{\phi\rho}\rho \frac{\partial z_s}{\partial \rho} - \tau_{\phi\phi}\rho \frac{\partial z_s}{\partial \phi} \right) \rho \frac{\partial z_s}{\partial \rho} \frac{\partial z_s}{\partial \phi} + \left(\tau_{zz}\rho - \tau_{z\rho}\rho \frac{\partial z_s}{\partial \rho} - \tau_{z\phi}\rho \frac{\partial z_s}{\partial \phi} \right) \rho^2 \frac{\partial z_s}{\partial \rho} \right\},\end{aligned}\quad (\text{A.7.42b})$$

$$\begin{aligned}\tau_{s_2 n} &= \frac{\sqrt{\rho^2 + (\partial z_s / \partial \phi)^2}}{G_s^3} \left\{ \left(\tau_{\phi z}\rho - \tau_{\phi\rho}\rho \frac{\partial z_s}{\partial \rho} - \tau_{\phi\phi}\rho \frac{\partial z_s}{\partial \phi} \right) \rho \left[1 + \left(\frac{\partial z_s}{\partial \rho} \right)^2 \right] \right. \\ &\quad \left. - \left(\tau_{\rho z}\rho - \tau_{\rho\rho}\rho \frac{\partial z_s}{\partial \rho} - \tau_{\rho\phi}\rho \frac{\partial z_s}{\partial \phi} \right) \frac{\partial z_s}{\partial \rho} \frac{\partial z_s}{\partial \phi} + \left(\tau_{zz}\rho - \tau_{z\rho}\rho \frac{\partial z_s}{\partial \rho} - \tau_{z\phi}\rho \frac{\partial z_s}{\partial \phi} \right) \frac{\partial z_s}{\partial \phi} \right\}.\end{aligned}\quad (\text{A.7.42c})$$

Surface gradient of ψ :

$$\begin{aligned}\nabla_s \psi &= \frac{1}{G_s^2} \left\{ \hat{\mathbf{e}}_\rho \left[\rho^2 + \left(\frac{\partial z_s}{\partial \phi} \right)^2 \right] - \hat{\mathbf{e}}_\phi \rho \frac{\partial z_s}{\partial z} \frac{\partial z_s}{\partial \phi} + \hat{\mathbf{e}}_z \rho^2 \frac{\partial z_s}{\partial \rho} \right\} \frac{\partial \psi}{\partial \rho} \\ &\quad + \frac{1}{G_s^2} \left\{ \hat{\mathbf{e}}_\phi \rho \left[1 + \left(\frac{\partial z_s}{\partial \rho} \right)^2 \right] - \hat{\mathbf{e}}_\rho \frac{\partial z_s}{\partial \rho} \frac{\partial z_s}{\partial \phi} + \hat{\mathbf{e}}_z \frac{\partial z_s}{\partial \phi} \right\} \frac{\partial \psi}{\partial \phi}.\end{aligned}\quad (\text{A.7.43})$$

Surface divergence of \mathbf{v} :

$$\begin{aligned}\nabla_s \cdot \mathbf{v} &= \frac{1}{G_s} \frac{\partial}{\partial \rho} \left(\frac{1}{G_s} \left\{ v_\rho \left[\rho^2 + \left(\frac{\partial z_s}{\partial \phi} \right)^2 \right] - v_\phi \rho \frac{\partial z_s}{\partial z} \frac{\partial z_s}{\partial \phi} + v_z \rho^2 \frac{\partial z_s}{\partial \rho} \right\} \right) \\ &\quad + \frac{1}{G_s} \frac{\partial}{\partial \phi} \left(\frac{1}{G_s} \left\{ v_\phi \rho \left[1 + \left(\frac{\partial z_s}{\partial \rho} \right)^2 \right] - v_\rho \frac{\partial z_s}{\partial \rho} \frac{\partial z_s}{\partial \phi} + v_z \frac{\partial z_s}{\partial \phi} \right\} \right) \\ &\quad - \frac{2H}{G_s} \left(v_z \rho - v_\rho \rho \frac{\partial z_s}{\partial \rho} - v_\phi \frac{\partial z_s}{\partial \phi} \right),\end{aligned}\quad (\text{A.7.44a})$$

$$= \frac{1}{G_s} \frac{\partial}{\partial \rho} (G_s v_\rho) + \frac{1}{\rho G_s} \frac{\partial}{\partial \phi} (G_s v_\phi) \quad \text{if } v_n = 0. \quad (\text{A.7.44b})$$

Surface Laplacian of ψ :

$$\begin{aligned}\nabla_s^2 \psi &= \frac{1}{G_s} \frac{\partial}{\partial \rho} \left(\frac{1}{G_s} \left\{ \left[\rho^2 + \left(\frac{\partial z_s}{\partial \phi} \right)^2 \right] \frac{\partial \psi}{\partial \rho} - \frac{\partial z_s}{\partial \rho} \frac{\partial z_s}{\partial \phi} \frac{\partial \psi}{\partial \phi} \right\} \right) \\ &\quad + \frac{1}{G_s} \frac{\partial}{\partial \phi} \left(\frac{1}{G_s} \left\{ \left[1 + \left(\frac{\partial z_s}{\partial \rho} \right)^2 \right] \frac{\partial \psi}{\partial \phi} - \frac{\partial z_s}{\partial \rho} \frac{\partial z_s}{\partial \phi} \frac{\partial \psi}{\partial \rho} \right\} \right).\end{aligned}\quad (\text{A.7.45})$$

A.7.4 Spherical coordinates, $r = r_s(\theta, \phi)$

Level set function:²

$$\varphi(r, \theta, \phi) = r - r_s(\theta, \phi) = 0 \quad \text{on the surface.} \quad (\text{A.7.46})$$

Surface position vector:

$$\mathbf{x}_s(\theta, \phi) = \hat{\mathbf{x}}(\theta, \phi) r_s(\theta, \phi). \quad (\text{A.7.47})$$

Surface metric:

$$G_s = r_s \sqrt{\sin^2 \theta \left[r_s^2 + \left(\frac{\partial r_s}{\partial \theta} \right)^2 \right] + \left(\frac{\partial r_s}{\partial \phi} \right)^2} = r_s \sin \theta \sqrt{r_s^2 + (\nabla_\Omega r_s) \cdot (\nabla_\Omega r_s)}. \quad (\text{A.7.48})$$

Unit normal vector:

$$\hat{\mathbf{n}} = \frac{r_s}{G_s} \left(\hat{\mathbf{x}} r_s \sin \theta - \hat{\mathbf{e}}_\theta \sin \theta \frac{\partial r_s}{\partial \theta} - \hat{\mathbf{e}}_\phi \frac{\partial r_s}{\partial \phi} \right) = \frac{r_s \sin \theta}{G_s} (r_s \hat{\mathbf{x}} - \nabla_\Omega r_s). \quad (\text{A.7.49})$$

Covariant tangential vectors:

$$\mathbf{t}_{(1)} = \hat{\mathbf{e}}_\theta r_s + \hat{\mathbf{x}} \frac{\partial r_s}{\partial \theta}, \quad (\text{A.7.50a})$$

$$\mathbf{t}_{(2)} = \hat{\mathbf{e}}_\phi r_s \sin \theta + \hat{\mathbf{x}} \frac{\partial r_s}{\partial \phi}. \quad (\text{A.7.50b})$$

Contravariant tangential vectors:

$$\mathbf{t}^{(1)} = \frac{r_s}{G_s^2} \left\{ \hat{\mathbf{e}}_\theta \left[r_s^2 \sin^2 \theta + \left(\frac{\partial r_s}{\partial \phi} \right)^2 \right] - \hat{\mathbf{e}}_\phi \sin \theta \frac{\partial r_s}{\partial \theta} \frac{\partial r_s}{\partial \phi} + \hat{\mathbf{x}} r_s \sin^2 \theta \frac{\partial r_s}{\partial \theta} \right\}, \quad (\text{A.7.51a})$$

$$\mathbf{t}^{(2)} = \frac{r_s}{G_s^2} \left\{ \hat{\mathbf{e}}_\phi \sin \theta \left[r_s^2 + \left(\frac{\partial r_s}{\partial \theta} \right)^2 \right] - \hat{\mathbf{e}}_\theta \frac{\partial r_s}{\partial \theta} \frac{\partial r_s}{\partial \phi} + \hat{\mathbf{x}} r_s \frac{\partial r_s}{\partial \phi} \right\}. \quad (\text{A.7.51b})$$

Line elements:

$$ds_1 = \sqrt{r_s^2 + \left(\frac{\partial r_s}{\partial \theta} \right)^2} d\theta, \quad (\text{A.7.52a})$$

$$ds_2 = \sqrt{r_s^2 \sin^2 \theta + \left(\frac{\partial r_s}{\partial \phi} \right)^2} d\phi. \quad (\text{A.7.52b})$$

²In spherical coordinates, the unit vector in the r direction is simply $\hat{\mathbf{e}}_r = \hat{\mathbf{x}} = \mathbf{x}/r$. The usual gradient operator has the convenient decomposition,

$$\nabla = \hat{\mathbf{x}} \frac{\partial}{\partial r} + \frac{\nabla_\Omega}{r},$$

where Ω is the solid angle and

$$\nabla_\Omega = r(\delta - \hat{\mathbf{x}}\hat{\mathbf{x}}) \cdot \nabla = \hat{\mathbf{e}}_\theta \frac{\partial}{\partial \theta} + \frac{\hat{\mathbf{e}}_\phi}{\sin \theta} \frac{\partial}{\partial \phi}$$

is the surface gradient operator on the unit sphere. The surface element on the unit sphere is $d\Omega = \sin \theta d\theta d\phi$.

Surface element:

$$dS = r_s \sqrt{\sin^2 \theta \left[r_s^2 + \left(\frac{\partial r_s}{\partial \theta} \right)^2 \right] + \left(\frac{\partial r_s}{\partial \phi} \right)^2} d\theta d\phi = r_s \sqrt{r_s^2 + (\nabla_\Omega r_s) \cdot (\nabla_\Omega r_s)} d\Omega. \quad (\text{A.7.53})$$

Mean curvature:

$$\begin{aligned} H = & \frac{r_s^2 \sin \theta}{2G_s^3} \left\{ \frac{\partial^2 r_s}{\partial \theta^2} \left[r_s^2 \sin^2 \theta + \left(\frac{\partial r_s}{\partial \phi} \right)^2 \right] + \frac{\partial^2 r_s}{\partial \phi^2} \left[r_s^2 + \left(\frac{\partial r_s}{\partial \theta} \right)^2 \right] - 2 \frac{\partial r_s}{\partial \theta} \frac{\partial r_s}{\partial \phi} \frac{\partial^2 r_s}{\partial \theta \partial \phi} \right. \\ & \left. + r_s^3 \sin^2 \theta + \cot \theta \frac{\partial r_s}{\partial \theta} \left(\frac{\partial r_s}{\partial \phi} \right)^2 \right\} - \frac{\sin \theta}{2G_s} \left(3r_s - \cot \theta \frac{\partial r_s}{\partial \theta} \right). \end{aligned} \quad (\text{A.7.54})$$

Gaussian curvature:

$$\begin{aligned} K = & \frac{r_s^3 \sin^2 \theta}{G_s^4} \left\{ r_s \left[\frac{\partial^2 r_s}{\partial \theta^2} \frac{\partial^2 r_s}{\partial \phi^2} - \left(\frac{\partial^2 r_s}{\partial \theta \partial \phi} \right)^2 \right] - \left[\frac{\partial^2 r_s}{\partial \phi^2} - \sin^2 \theta \left(r_s - \cot \theta \frac{\partial r_s}{\partial \theta} \right) \right] \left[r_s^2 + 2 \left(\frac{\partial r_s}{\partial \theta} \right)^2 \right] \right. \\ & - \frac{\partial^2 r_s}{\partial \theta^2} \left[r_s \sin^2 \theta \left(r_s - \cot \theta \frac{\partial r_s}{\partial \theta} \right) + 2 \left(\frac{\partial r_s}{\partial \phi} \right)^2 \right] + 2 \frac{\partial r_s}{\partial \phi} \frac{\partial^2 r_s}{\partial \theta \partial \phi} \left(r_s \cot \theta + 2 \frac{\partial r_s}{\partial \theta} \right) \\ & \left. - \left(\frac{\partial r_s}{\partial \phi} \right)^2 \left(r_s (\cot^2 \theta - 2) + 4 \cot \theta \frac{\partial r_s}{\partial \theta} \right) \right\}. \end{aligned} \quad (\text{A.7.55})$$

Surface components of \mathbf{v} :

$$v_n = \frac{r_s}{G_s} \left(v_r r_s \sin \theta - v_\theta \sin \theta \frac{\partial r_s}{\partial \theta} - v_\phi \frac{\partial r_s}{\partial \phi} \right), \quad (\text{A.7.56a})$$

$$v_{s_1} = \frac{r_s \sqrt{r_s^2 + (\partial r_s / \partial \theta)^2}}{G_s^2} \left\{ v_\theta \left[r_s^2 \sin^2 \theta + \left(\frac{\partial r_s}{\partial \phi} \right)^2 \right] - v_\phi \sin \theta \frac{\partial r_s}{\partial \theta} \frac{\partial r_s}{\partial \phi} + v_r r_s \sin^2 \theta \frac{\partial r_s}{\partial \theta} \right\}, \quad (\text{A.7.56b})$$

$$v_{s_2} = \frac{r_s \sqrt{r_s^2 \sin^2 \theta + (\partial r_s / \partial \phi)^2}}{G_s^2} \left\{ v_\phi \sin \theta \left[r_s^2 + \left(\frac{\partial r_s}{\partial \theta} \right)^2 \right] - v_\theta \frac{\partial r_s}{\partial \theta} \frac{\partial r_s}{\partial \phi} + v_r r_s \frac{\partial r_s}{\partial \phi} \right\}. \quad (\text{A.7.56c})$$

Surface components of $\boldsymbol{\tau} \cdot \hat{\mathbf{n}}$:

$$\begin{aligned} \tau_{nn} = & \frac{r_s^2}{G_s^2} \left[\left(\tau_{rr} r_s \sin \theta - \tau_{r\theta} \sin \theta \frac{\partial r_s}{\partial \theta} - \tau_{r\phi} \frac{\partial r_s}{\partial \phi} \right) r_s \sin \theta \right. \\ & - \left(\tau_{\theta r} r_s \sin \theta - \tau_{\theta\theta} \sin \theta \frac{\partial r_s}{\partial \theta} - \tau_{\theta\phi} \frac{\partial r_s}{\partial \phi} \right) \sin \theta \frac{\partial r_s}{\partial \theta} \\ & \left. - \left(\tau_{\phi r} r_s \sin \theta - \tau_{\phi\theta} \sin \theta \frac{\partial r_s}{\partial \theta} - \tau_{\phi\phi} \frac{\partial r_s}{\partial \phi} \right) \frac{\partial r_s}{\partial \phi} \right], \end{aligned} \quad (\text{A.7.57a})$$

$$\begin{aligned} \tau_{s_1 n} = & \frac{r_s^2 \sqrt{r_s^2 + (\partial r_s / \partial \theta)^2}}{G_s^3} \left\{ \left(\tau_{\theta r} r_s \sin \theta - \tau_{\theta\theta} \sin \theta \frac{\partial r_s}{\partial \theta} - \tau_{\theta\phi} \frac{\partial r_s}{\partial \phi} \right) \left[r_s^2 \sin^2 \theta + \left(\frac{\partial r_s}{\partial \phi} \right)^2 \right] \right. \\ & \left. - \left(\tau_{\phi r} r_s \sin \theta - \tau_{\phi\theta} \sin \theta \frac{\partial r_s}{\partial \theta} - \tau_{\phi\phi} \frac{\partial r_s}{\partial \phi} \right) \sin \theta \frac{\partial r_s}{\partial \theta} \frac{\partial r_s}{\partial \phi} \right\} \end{aligned}$$

$$+ \left(\tau_{rr} r_s \sin \theta - \tau_{r\theta} \sin \theta \frac{\partial r_s}{\partial \theta} - \tau_{r\phi} \frac{\partial r_s}{\partial \phi} \right) r_s \sin^2 \theta \frac{\partial r_s}{\partial \theta} \Bigg\}, \quad (\text{A.7.57b})$$

$$\begin{aligned} \tau_{s_2 n} = & \frac{r_s^2 \sqrt{r_s^2 \sin^2 \theta + (\partial r_s / \partial \phi)^2}}{G_s^3} \left\{ \left(\tau_{\phi r} r_s \sin \theta - \tau_{\phi \theta} \sin \theta \frac{\partial r_s}{\partial \theta} - \tau_{\phi \phi} \frac{\partial r_s}{\partial \phi} \right) \sin \theta \left[r_s^2 + \left(\frac{\partial r_s}{\partial \theta} \right)^2 \right] \right. \\ & - \left(\tau_{\theta r} r_s \sin \theta - \tau_{\theta \theta} \sin \theta \frac{\partial r_s}{\partial \theta} - \tau_{\theta \phi} \frac{\partial r_s}{\partial \phi} \right) \frac{\partial r_s}{\partial \theta} \frac{\partial r_s}{\partial \phi} \\ & \left. + \left(\tau_{rr} r_s \sin \theta - \tau_{r\theta} \sin \theta \frac{\partial r_s}{\partial \theta} - \tau_{r\phi} \frac{\partial r_s}{\partial \phi} \right) r_s \frac{\partial r_s}{\partial \phi} \right\}. \end{aligned} \quad (\text{A.7.57c})$$

Surface gradient of ψ :

$$\begin{aligned} \nabla_s \psi = & \frac{r_s}{G_s^2} \left\{ \hat{e}_\theta \left[r_s^2 \sin^2 \theta + \left(\frac{\partial r}{\partial \phi} \right)^2 \right] - \hat{e}_\phi \sin \theta \frac{\partial r_s}{\partial \theta} \frac{\partial r_s}{\partial \phi} + \hat{x} r_s \sin^2 \theta \frac{\partial r_s}{\partial \theta} \right\} \frac{\partial \psi}{\partial \theta} \\ & + \frac{r_s}{G_s^2} \left\{ \hat{e}_\phi \sin \theta \left[r_s^2 + \left(\frac{\partial r_s}{\partial \theta} \right)^2 \right] - \hat{e}_\theta \frac{\partial r_s}{\partial \theta} \frac{\partial r_s}{\partial \phi} + \hat{x} r_s \frac{\partial r_s}{\partial \phi} \right\} \frac{\partial \psi}{\partial \phi}. \end{aligned} \quad (\text{A.7.58})$$

Surface divergence of \mathbf{v} :

$$\begin{aligned} \nabla_s \cdot \mathbf{v} = & \frac{1}{G_s} \frac{\partial}{\partial \theta} \left(\frac{r_s}{G_s} \left\{ v_\theta \left[r_s^2 \sin^2 \theta + \left(\frac{\partial r}{\partial \phi} \right)^2 \right] - v_\phi \sin \theta \frac{\partial r_s}{\partial \theta} \frac{\partial r_s}{\partial \phi} + v_r r_s \sin^2 \theta \frac{\partial r_s}{\partial \theta} \right\} \right) \\ & + \frac{1}{G_s} \frac{\partial}{\partial \phi} \left(\frac{r_s}{G_s} \left\{ v_\phi \sin \theta \left[r_s^2 + \left(\frac{\partial r_s}{\partial \theta} \right)^2 \right] - v_\theta \frac{\partial r_s}{\partial \theta} \frac{\partial r_s}{\partial \phi} + v_r r_s \frac{\partial r_s}{\partial \phi} \right\} \right) \\ & - \frac{2H r_s}{G_s} \left(v_r r_s \sin \theta - v_\theta \sin \theta \frac{\partial r_s}{\partial \theta} - v_\phi \frac{\partial r_s}{\partial \phi} \right), \end{aligned} \quad (\text{A.7.59a})$$

$$= \frac{1}{G_s} \frac{\partial}{\partial \theta} \left(\frac{G_s v_\theta}{r_s} \right) + \frac{1}{G_s \sin \theta} \frac{\partial}{\partial \phi} \left(\frac{G_s v_\phi}{r_s} \right) \quad \text{if } v_n = 0. \quad (\text{A.7.59b})$$

Surface Laplacian of ψ :

$$\begin{aligned} \nabla_s^2 \psi = & \frac{1}{G_s} \frac{\partial}{\partial \theta} \left(\frac{1}{G_s} \left\{ \left[r_s^2 \sin^2 \theta + \left(\frac{\partial r_s}{\partial \phi} \right)^2 \right] \frac{\partial \psi}{\partial \theta} - \frac{\partial r_s}{\partial \theta} \frac{\partial r_s}{\partial \phi} \frac{\partial \psi}{\partial \phi} \right\} \right) \\ & + \frac{1}{G_s} \frac{\partial}{\partial \phi} \left(\frac{1}{G_s} \left\{ \left[r_s^2 + \left(\frac{\partial r_s}{\partial \theta} \right)^2 \right] \frac{\partial \psi}{\partial \phi} - \frac{\partial r_s}{\partial \theta} \frac{\partial r_s}{\partial \phi} \frac{\partial \psi}{\partial \theta} \right\} \right). \end{aligned} \quad (\text{A.7.60})$$

A.7.5 Two-dimensional Cartesian coordinates, $z = z_s(x)$

Level set function:

$$\varphi(x, z) = z - z_s(x) = 0 \quad \text{on the surface.} \quad (\text{A.7.61})$$

Surface position vector:

$$\mathbf{x}_s(x, y) = \hat{e}_x x + \hat{e}_y y + \hat{e}_z z_s(x). \quad (\text{A.7.62})$$

Surface metric:

$$G_s = \sqrt{1 + \left(\frac{dz_s}{dx}\right)^2}. \quad (\text{A.7.63})$$

Unit normal vector:

$$\hat{n} = \frac{1}{G_s} \left(\hat{e}_z - \hat{e}_x \frac{dz_s}{dx} \right). \quad (\text{A.7.64})$$

Covariant tangential vectors:

$$\mathbf{t}_{(1)} = \hat{e}_x + \hat{e}_z \frac{dz_s}{dx}, \quad (\text{A.7.65a})$$

$$\mathbf{t}_{(2)} = \hat{e}_y. \quad (\text{A.7.65b})$$

Contravariant tangential vectors:

$$\mathbf{t}^{(1)} = \frac{1}{G_s^2} \left\{ \hat{e}_x + \hat{e}_z \frac{dz_s}{dx} \right\}, \quad (\text{A.7.66a})$$

$$\mathbf{t}^{(2)} = \hat{e}_y. \quad (\text{A.7.66b})$$

Line elements:

$$ds_1 = \sqrt{1 + \left(\frac{dz_s}{dx}\right)^2} dx, \quad (\text{A.7.67a})$$

$$ds_2 = dy. \quad (\text{A.7.67b})$$

Surface element:

$$dS = \sqrt{1 + \left(\frac{dz_s}{dx}\right)^2} dx dy. \quad (\text{A.7.68})$$

Mean curvature:

$$H = \frac{1}{2G_s^3} \frac{d^2 z_s}{dx^2}. \quad (\text{A.7.69})$$

Gaussian curvature:

$$K = 0. \quad (\text{A.7.70})$$

Surface components of \mathbf{v} :

$$v_n = \frac{1}{G_s} \left(v_z - v_x \frac{dz_s}{dx} \right), \quad (\text{A.7.71a})$$

$$v_{s_1} = \frac{1}{G_s} \left(v_x + v_z \frac{dz_s}{dx} \right), \quad (\text{A.7.71b})$$

$$v_{s_2} = v_y. \quad (\text{A.7.71c})$$

Surface components of $\tau \cdot \hat{\mathbf{n}}$:

$$\tau_{nn} = \frac{1}{G_s^2} \left[\tau_{zz} - (\tau_{zx} + \tau_{xz}) \frac{dz_s}{dx} + \tau_{xx} \left(\frac{dz_s}{dx} \right)^2 \right], \quad (\text{A.7.72a})$$

$$\tau_{s_1 n} = \frac{1}{G_s^2} \left[\tau_{xz} + (\tau_{zz} - \tau_{xx}) \frac{dz_s}{dx} - \tau_{zx} \left(\frac{dz_s}{dx} \right)^2 \right], \quad (\text{A.7.72b})$$

$$\tau_{s_2 n} = \frac{1}{G_s} \left(\tau_{yz} - \tau_{yx} \frac{dz_s}{dx} \right). \quad (\text{A.7.72c})$$

Surface gradient of ψ :

$$\nabla_s \psi = \frac{1}{G_s^2} \left(\hat{\mathbf{e}}_x + \hat{\mathbf{e}}_z \frac{dz_s}{dx} \right) \frac{\partial \psi}{\partial x} + \hat{\mathbf{e}}_y \frac{\partial \psi}{\partial y}. \quad (\text{A.7.73})$$

Surface divergence of \mathbf{v} :

$$\nabla_s \cdot \mathbf{v} = \frac{1}{G_s} \frac{\partial}{\partial x} \left[\frac{1}{G_s} \left(v_x + v_z \frac{dz_s}{dx} \right) \right] + \frac{\partial v_y}{\partial y} - \frac{2H}{G_s} \left(v_z - v_x \frac{dz_s}{dx} \right), \quad (\text{A.7.74a})$$

$$= \frac{1}{G_s} \frac{\partial}{\partial x} (G_s v_x) + \frac{\partial v_y}{\partial y} \quad \text{if } v_n = 0. \quad (\text{A.7.74b})$$

Surface Laplacian of ψ :

$$\nabla_s^2 \psi = \frac{1}{G_s} \frac{\partial}{\partial x} \left(\frac{1}{G_s} \frac{\partial \psi}{\partial x} \right) + \frac{\partial^2 \psi}{\partial y^2}. \quad (\text{A.7.75})$$

A.7.6 Axisymmetric cylindrical coordinates, $\rho = \rho_s(z)$

Level set function:

$$\varphi(\rho, z) = \rho - \rho_s(z) = 0 \quad \text{on the surface.} \quad (\text{A.7.76})$$

Surface position vector:

$$\mathbf{x}_s(z, \phi) = \hat{\mathbf{e}}_\rho(\phi) \rho_s(z) + \hat{\mathbf{e}}_z z. \quad (\text{A.7.77})$$

Surface metric:

$$G_s = \rho_s \sqrt{1 + \left(\frac{d\rho_s}{dz} \right)^2}. \quad (\text{A.7.78})$$

Unit normal vector:

$$\hat{\mathbf{n}} = \frac{\rho_s}{G_s} \left(\hat{\mathbf{e}}_\rho - \hat{\mathbf{e}}_z \frac{d\rho_s}{dz} \right). \quad (\text{A.7.79})$$

Covariant tangential vectors:

$$\mathbf{t}_{(1)} = \hat{\mathbf{e}}_\phi \rho_s, \quad (\text{A.7.80a})$$

$$\mathbf{t}_{(2)} = \hat{\mathbf{e}}_z + \hat{\mathbf{e}}_\rho \frac{d\rho_s}{dz}. \quad (\text{A.7.80b})$$

Contravariant tangential vectors:

$$\mathbf{t}^{(1)} = \frac{\hat{\mathbf{e}}_\phi}{\rho_s}, \quad (\text{A.7.81a})$$

$$\mathbf{t}^{(2)} = \frac{\rho_s^2}{G_s^2} \left(\hat{\mathbf{e}}_z + \hat{\mathbf{e}}_\rho \frac{d\rho_s}{dz} \right). \quad (\text{A.7.81b})$$

Line elements:

$$ds_1 = \rho_s d\phi, \quad (\text{A.7.82a})$$

$$ds_2 = \sqrt{1 + \left(\frac{d\rho_s}{dz} \right)^2} dz. \quad (\text{A.7.82b})$$

Surface element:

$$dS = \rho_s \sqrt{1 + \left(\frac{d\rho_s}{dz} \right)^2} d\phi dz. \quad (\text{A.7.83})$$

Mean curvature:

$$H = \frac{\rho_s^3}{2G_s^3} \frac{d^2\rho_s}{dz^2} - \frac{1}{2G_s}. \quad (\text{A.7.84})$$

Gaussian curvature:

$$K = -\frac{\rho_s^3}{G_s^4} \frac{d^2\rho_s}{dz^2}. \quad (\text{A.7.85})$$

Surface components of \mathbf{v} :

$$v_n = \frac{\rho_s}{G_s} \left(v_\rho - v_z \frac{d\rho_s}{dz} \right), \quad (\text{A.7.86a})$$

$$v_{s_1} = v_\phi, \quad (\text{A.7.86b})$$

$$v_{s_2} = \frac{\rho_s}{G_s} \left(v_z + v_\rho \frac{d\rho_s}{dz} \right). \quad (\text{A.7.86c})$$

Surface components of $\boldsymbol{\tau} \cdot \hat{\mathbf{n}}$:

$$\tau_{nn} = \frac{\rho_s^2}{G_s^2} \left[\tau_{\rho\rho} - (\tau_{z\rho} + \tau_{\rho z}) \frac{d\rho_s}{dz} + \tau_{zz} \left(\frac{d\rho_s}{dz} \right)^2 \right], \quad (\text{A.7.87a})$$

$$\tau_{s_1 n} = \frac{\rho_s}{G_s} \left(\tau_{\phi\rho} - \tau_{\phi z} \frac{d\rho_s}{dz} \right), \quad (\text{A.7.87b})$$

$$\tau_{s_2 n} = \frac{\rho_s^2}{G_s^2} \left[\tau_{z\rho} + (\tau_{\rho\rho} - \tau_{zz}) \frac{d\rho_s}{dz} - \tau_{\rho z} \left(\frac{d\rho_s}{dz} \right)^2 \right]. \quad (\text{A.7.87c})$$

Surface gradient of ψ :

$$\nabla_s \psi = \frac{\hat{e}_\phi}{\rho_s} \frac{\partial \psi}{\partial \phi} + \frac{\rho_s^2}{G_s^2} \left(\hat{e}_z + \hat{e}_\rho \frac{d\rho_s}{dz} \right) \frac{\partial \psi}{\partial z}. \quad (\text{A.7.88})$$

Surface divergence of \mathbf{v} :

$$\nabla_s \cdot \mathbf{v} = \frac{1}{\rho_s} \frac{\partial v_\phi}{\partial \phi} + \frac{1}{G_s} \frac{\partial}{\partial z} \left[\frac{\rho_s^2}{G_s} \left(v_z + v_\rho \frac{d\rho_s}{dz} \right) \right] - \frac{2H\rho_s}{G_s} \left(v_\rho - v_z \frac{d\rho_s}{dz} \right), \quad (\text{A.7.89a})$$

$$= \frac{1}{\rho_s} \frac{\partial v_\phi}{\partial \phi} + \frac{1}{G_s} \frac{\partial}{\partial z} (G_s v_z) \quad \text{if } v_n = 0. \quad (\text{A.7.89b})$$

Surface Laplacian of ψ :

$$\nabla_s^2 \psi = \frac{1}{\rho_s^2} \frac{\partial^2 \psi}{\partial \phi^2} + \frac{1}{G_s} \frac{\partial}{\partial z} \left(\frac{\rho_s^2}{G_s} \frac{\partial \psi}{\partial z} \right). \quad (\text{A.7.90})$$

A.7.7 Axisymmetric cylindrical coordinates, $z = z_s(\rho)$

Level set function:

$$\varphi(\rho, z) = z - z_s(\rho) = 0 \quad \text{on the surface.} \quad (\text{A.7.91})$$

Surface position vector:

$$\mathbf{x}_s(\rho, \phi) = \hat{e}_\rho(\phi) \rho + \hat{e}_z z_s(\rho). \quad (\text{A.7.92})$$

Surface metric:

$$G_s = \rho \sqrt{1 + \left(\frac{dz_s}{d\rho} \right)^2}. \quad (\text{A.7.93})$$

Unit normal vector:

$$\hat{n} = \frac{\rho}{G_s} \left(\hat{e}_z - \hat{e}_\rho \frac{dz_s}{d\rho} \right). \quad (\text{A.7.94})$$

Covariant tangential vectors:

$$\mathbf{t}_{(1)} = \hat{e}_\rho + \hat{e}_z \frac{dz_s}{d\rho}, \quad (\text{A.7.95a})$$

$$\mathbf{t}_{(2)} = \hat{e}_\phi \rho. \quad (\text{A.7.95b})$$

Contravariant tangential vectors:

$$\mathbf{t}^{(1)} = \frac{\rho^2}{G_s^2} \left(\hat{e}_\rho + \hat{e}_z \frac{dz_s}{d\rho} \right), \quad (\text{A.7.96a})$$

$$\mathbf{t}^{(2)} = \frac{\hat{e}_\phi}{\rho}. \quad (\text{A.7.96b})$$

Line elements:

$$ds_1 = \sqrt{1 + \left(\frac{dz_s}{d\rho}\right)^2} d\rho, \quad (\text{A.7.97a})$$

$$ds_2 = \rho d\phi. \quad (\text{A.7.97b})$$

Surface element:

$$dS = \rho \sqrt{1 + \left(\frac{dz_s}{d\rho}\right)^2} d\rho d\phi. \quad (\text{A.7.98})$$

Mean curvature:

$$H = \frac{\rho^3}{2G_s^3} \frac{d^2 z_s}{d\rho^2} + \frac{1}{2G_s} \frac{dz_s}{d\rho} = \frac{1}{2\rho} \frac{d}{d\rho} \left(\frac{\rho^2}{G_s} \frac{dz_s}{d\rho} \right). \quad (\text{A.7.99})$$

Gaussian curvature:

$$K = \frac{\rho^3}{G_s^4} \frac{dz_s}{d\rho} \frac{d^2 z_s}{d\rho^2}. \quad (\text{A.7.100})$$

Surface components of \mathbf{v} :

$$v_n = \frac{\rho}{G_s} \left(v_z - v_\rho \frac{dz_s}{d\rho} \right), \quad (\text{A.7.101a})$$

$$v_{s_1} = \frac{\rho}{G_s} \left(v_\rho + v_z \frac{dz_s}{d\rho} \right), \quad (\text{A.7.101b})$$

$$v_{s_2} = v_\phi. \quad (\text{A.7.101c})$$

Surface components of $\boldsymbol{\tau} \cdot \hat{\mathbf{n}}$:

$$\tau_{nn} = \frac{\rho^2}{G_s^2} \left[\tau_{zz} - (\tau_{z\rho} + \tau_{\rho z}) \frac{dz_s}{d\rho} + \tau_{\rho\rho} \left(\frac{dz_s}{d\rho} \right)^2 \right], \quad (\text{A.7.102a})$$

$$\tau_{s_1 n} = \frac{\rho^2}{G_s^2} \left[\tau_{\rho z} + (\tau_{zz} - \tau_{\rho\rho}) \frac{dz_s}{d\rho} - \tau_{z\rho} \left(\frac{dz_s}{d\rho} \right)^2 \right], \quad (\text{A.7.102b})$$

$$\tau_{s_2 n} = \frac{\rho}{G_s} \left(\tau_{\phi z} - \tau_{\phi\rho} \frac{dz_s}{d\rho} \right). \quad (\text{A.7.102c})$$

Surface gradient of ψ :

$$\nabla_s \psi = \frac{\rho^2}{G_s^2} \left(\hat{\mathbf{e}}_\rho + \hat{\mathbf{e}}_z \frac{dz_s}{d\rho} \right) \frac{\partial \psi}{\partial \rho} + \frac{\hat{\mathbf{e}}_\phi}{\rho} \frac{\partial \psi}{\partial \phi}. \quad (\text{A.7.103})$$

Surface divergence of \mathbf{v} :

$$\nabla_s \cdot \mathbf{v} = \frac{1}{G_s} \frac{\partial}{\partial \rho} \left[\frac{\rho^2}{G_s} \left(v_\rho + v_z \frac{dz_s}{d\rho} \right) \right] + \frac{1}{\rho} \frac{\partial v_\phi}{\partial \phi} - \frac{2H\rho}{G_s} \left(v_z - v_\rho \frac{dz_s}{d\rho} \right), \quad (\text{A.7.104a})$$

$$= \frac{1}{G_s} \frac{\partial}{\partial \rho} (G_s v_\rho) + \frac{1}{\rho} \frac{\partial v_\phi}{\partial \phi} \quad \text{if } v_n = 0. \quad (\text{A.7.104b})$$

Surface Laplacian of ψ :

$$\nabla_s^2 \psi = \frac{1}{G_s} \frac{\partial}{\partial \rho} \left(\frac{\rho^2}{G_s} \frac{\partial \psi}{\partial \rho} \right) + \frac{1}{\rho^2} \frac{\partial^2 \psi}{\partial \phi^2}. \quad (\text{A.7.105})$$

Appendix B

Ordered perturbation equations in the narrow-gap limit

In Chapter 3, we developed an asymptotic solution to the initial-boundary-value problem in the limit as $\epsilon \rightarrow 0$, where ϵ (the clearance parameter) was defined by equation (2.5.7) in the main text. In this appendix, we present the ordered perturbation equations for the outer and inner region, obtained by expanding the dependent variable in perturbation series with respect to $\epsilon^{\frac{1}{2}}$, inserting the expansions into the equations presented in §3.4, and collecting terms of like order in $\epsilon^{\frac{1}{2}}$. All variables in this appendix are rendered dimensionless using the following characteristic scales: R (the tube radius), V (the mean tube velocity), and μ (the suspending fluid viscosity). Variables with an overbar are rescaled as described in §3.4.

B.1 Outer equations

Equations of continuity and motion in the exterior fluid:

$$O(1) : \quad \frac{\partial u_{x0}}{\partial x} + \left(\frac{\partial}{\partial \rho} + \frac{1}{\rho} \right) u_{\rho0} = 0, \quad \frac{\partial \bar{p}_0}{\partial x} = 0, \quad \frac{\partial \bar{p}_0}{\partial \rho} = 0, \quad (\text{B.1.1a})$$

$$O(\epsilon^{\frac{1}{2}}) : \quad \frac{\partial u_{x1}}{\partial x} + \left(\frac{\partial}{\partial \rho} + \frac{1}{\rho} \right) u_{\rho1} = 0, \quad \frac{\partial \bar{p}_1}{\partial x} = 0, \quad \frac{\partial \bar{p}_1}{\partial \rho} = 0, \quad (\text{B.1.1b})$$

$$O(\epsilon) : \quad \frac{\partial u_{x2}}{\partial x} + \left(\frac{\partial}{\partial \rho} + \frac{1}{\rho} \right) u_{\rho2} = 0, \quad \frac{\partial \bar{p}_2}{\partial x} = 0, \quad \frac{\partial \bar{p}_2}{\partial \rho} = 0, \quad (\text{B.1.1c})$$

etc.

Equations of continuity and motion in the interior fluid:

$$O(1) : \quad \frac{\partial \check{u}_{x0}}{\partial x} + \left(\frac{\partial}{\partial \rho} + \frac{1}{\rho} \right) \check{u}_{\rho0} = 0, \quad \frac{\partial \check{p}_0}{\partial x} = 0, \quad \frac{\partial \check{p}_0}{\partial \rho} = 0, \quad (\text{B.1.2a})$$

$$O(\epsilon^{\frac{1}{2}}) : \quad \frac{\partial \check{u}_{x1}}{\partial x} + \left(\frac{\partial}{\partial \rho} + \frac{1}{\rho} \right) \check{u}_{\rho 1} = 0, \quad \frac{\partial \check{p}_1}{\partial x} = 0, \quad \frac{\partial \check{p}_1}{\partial \rho} = 0, \quad (\text{B.1.2b})$$

$$O(\epsilon) : \quad \frac{\partial \check{u}_{x2}}{\partial x} + \left(\frac{\partial}{\partial \rho} + \frac{1}{\rho} \right) \check{u}_{\rho 2} = 0, \quad \frac{\partial \check{p}_2}{\partial x} = 0, \quad \frac{\partial \check{p}_2}{\partial \rho} = 0, \quad (\text{B.1.2c})$$

etc.

Exterior velocity boundary condition on the tube wall:

at $\rho = 1$:

$$O(1) : \quad u_{x0} = -1 - 2q_0, \quad u_{\rho 0} = 0, \quad (\text{B.1.3a})$$

$$O(\epsilon^{\frac{1}{2}}) : \quad u_{x1} = -2q_1, \quad u_{\rho 1} = 0, \quad (\text{B.1.3b})$$

$$O(\epsilon) : \quad u_{x2} = -2q_2, \quad u_{\rho 2} = 0, \quad (\text{B.1.3c})$$

etc.

Exterior velocity boundary condition on the vesicle membrane:

at $\rho = \rho_{s0}$:

$$O(1) : \quad u_{x0} = 0, \quad u_{\rho 0} = 0, \quad (\text{B.1.4a})$$

$$O(\epsilon^{\frac{1}{2}}) : \quad u_{x1} = -\rho_{s1} \frac{\partial u_{x0}}{\partial \rho}, \quad u_{\rho 1} = -\rho_{s1} \frac{\partial u_{\rho 0}}{\partial \rho}, \quad (\text{B.1.4b})$$

$$O(\epsilon) : \quad u_{x2} = -\rho_{s1} \frac{\partial u_{x1}}{\partial \rho} - \left(\rho_{s2} + \frac{\rho_{s1}^2}{2} \frac{\partial}{\partial \rho} \right) \frac{\partial u_{x0}}{\partial \rho}, \quad u_{\rho 2} = -\rho_{s1} \frac{\partial u_{\rho 1}}{\partial \rho} - \left(\rho_{s2} + \frac{\rho_{s1}^2}{2} \frac{\partial}{\partial \rho} \right) \frac{\partial u_{\rho 0}}{\partial \rho}, \quad (\text{B.1.4c})$$

etc.

Exterior velocity boundary condition in the far field:

as $x \rightarrow \pm\infty$:

$$O(1) : \quad u_{x0} = 2(1 - \rho^2) - 1 - 2q_0, \quad u_{\rho 0} = 0, \quad (\text{B.1.5a})$$

$$O(\epsilon^{\frac{1}{2}}) : \quad u_{x1} = -2q_1, \quad u_{\rho 1} = 0, \quad (\text{B.1.5b})$$

$$O(\epsilon) : \quad u_{x2} = -2q_2, \quad u_{\rho 2} = 0, \quad (\text{B.1.5c})$$

etc.

Interior velocity boundary condition on the tube centerline:

at $\rho = 0$:

$$O(1) : \quad \frac{\partial \check{u}_{x0}}{\partial \rho} = 0, \quad \check{u}_{\rho0} = 0, \quad (\text{B.1.6a})$$

$$O(\epsilon^{\frac{1}{2}}) : \quad \frac{\partial \check{u}_{x1}}{\partial \rho} = 0, \quad \check{u}_{\rho1} = 0 \quad (\text{B.1.6b})$$

$$O(\epsilon) : \quad \frac{\partial \check{u}_{x2}}{\partial \rho} = 0, \quad \check{u}_{\rho2} = 0 \quad (\text{B.1.6c})$$

etc.

Interior velocity boundary condition on the vesicle membrane:

at $\rho = \rho_{s0}$:

$$O(1) : \quad \check{u}_{x0} = 0, \quad \check{u}_{\rho0} = 0, \quad (\text{B.1.7a})$$

$$O(\epsilon^{\frac{1}{2}}) : \quad \check{u}_{x1} = -\rho_{s1} \frac{\partial \check{u}_{x0}}{\partial \rho}, \quad \check{u}_{\rho1} = -\rho_{s1} \frac{\partial \check{u}_{\rho0}}{\partial \rho}, \quad (\text{B.1.7b})$$

$$O(\epsilon) : \quad \check{u}_{x2} = -\rho_{s1} \frac{\partial \check{u}_{x1}}{\partial \rho} - \left(\rho_{s2} + \frac{\rho_{s1}^2}{2} \frac{\partial}{\partial \rho} \right) \frac{\partial \check{u}_{x0}}{\partial \rho}, \quad \check{u}_{\rho2} = -\rho_{s1} \frac{\partial \check{u}_{\rho1}}{\partial \rho} - \left(\rho_{s2} + \frac{\rho_{s1}^2}{2} \frac{\partial}{\partial \rho} \right) \frac{\partial \check{u}_{\rho0}}{\partial \rho}, \quad (\text{B.1.7c})$$

etc.

Normal stress boundary condition on the vesicle membrane:

at $\rho = \rho_{s0}$:

$$O(1) : \quad (\bar{p}_0 - \check{p}_0)|_{\rho=\rho_{s0}} = -\bar{\tau}_0 \left(\frac{1}{\rho_{s0} \sqrt{1 + (d\rho_{s0}/dx)^2}} - \frac{d^2 \rho_{s0}/dx^2}{\sqrt{1 + (d\rho_{s0}/dx)^2}^3} \right), \quad (\text{B.1.8a})$$

$$\begin{aligned} O(\epsilon^{\frac{1}{2}}) : \quad & \left(\bar{p}_1 + \rho_{s1} \frac{\partial \bar{p}_0}{\partial \rho} - \check{p}_1 - \rho_{s1} \frac{\partial \check{p}_0}{\partial \rho} \right) \Big|_{\rho=\rho_{s0}} \\ &= -\bar{\tau}_1 \left(\frac{1}{\rho_{s0} \sqrt{1 + (d\rho_{s0}/dx)^2}} - \frac{d^2 \rho_{s0}/dx^2}{\sqrt{1 + (d\rho_{s0}/dx)^2}^3} \right) \\ &+ \bar{\tau}_0 \left[\frac{\rho_{s1}}{\rho_{s0}^2 \sqrt{1 + (d\rho_{s0}/dx)^2}} + \left(\frac{d\rho_{s0}/dx}{\rho_{s0} \sqrt{1 + (d\rho_{s0}/dx)^2}^3} \right. \right. \\ &\quad \left. \left. - \frac{3(d\rho_{s0}/dx)(d^2 \rho_{s0}/dx^2)}{\sqrt{1 + (d\rho_{s0}/dx)^2}^5} \right) \frac{d\rho_{s1}}{dx} + \frac{d^2 \rho_{s1}/dx^2}{\sqrt{1 + (d\rho_{s0}/dx)^2}^3} \right], \end{aligned} \quad (\text{B.1.8b})$$

$$O(\epsilon) : \quad \left[\bar{p}_2 + \rho_{s1} \frac{\partial \bar{p}_1}{\partial \rho} + \left(\rho_{s2} + \frac{\rho_{s1}^2}{2} \frac{\partial}{\partial \rho} \right) \frac{\partial \bar{p}_0}{\partial \rho} - \check{p}_2 - \rho_{s1} \frac{\partial \check{p}_1}{\partial \rho} - \left(\rho_{s2} + \frac{\rho_{s1}^2}{2} \frac{\partial}{\partial \rho} \right) \frac{\partial \check{p}_0}{\partial \rho} \right] \Big|_{\rho=\rho_{s0}}$$

$$\begin{aligned}
&= -\bar{\tau}_2 \left(\frac{1}{\rho_{s0} \sqrt{1 + (\partial \rho_{s0}/\partial x)^2}} - \frac{\partial^2 \rho_{s0}/\partial x^2}{\sqrt{1 + (\partial \rho_{s0}/\partial x)^2}^3} \right) \\
&\quad + \bar{\tau}_1 \left[\frac{\rho_{s1}}{\rho_{s0}^2 \sqrt{1 + (\partial \rho_{s0}/\partial x)^2}} + \left(\frac{\partial \rho_{s0}/\partial x}{\rho_{s0} \sqrt{1 + (\partial \rho_{s0}/\partial x)^2}^3} \right. \right. \\
&\quad \left. \left. - \frac{3(\partial \rho_{s0}/\partial x)(\partial^2 \rho_{s0}/\partial x^2)}{\sqrt{1 + (\partial \rho_{s0}/\partial x)^2}^5} \right) \frac{\partial \rho_{s1}}{\partial x} + \frac{\partial^2 \rho_{s1}/\partial x^2}{\sqrt{1 + (\partial \rho_{s0}/\partial x)^2}^3} \right] \\
&\quad + \bar{\tau}_0 \left[\frac{\rho_{s2}}{\rho_{s0}^2 \sqrt{1 + (\partial \rho_{s0}/\partial x)^2}} - \frac{\rho_{s1}^2}{\rho_{s0}^3 \sqrt{1 + (\partial \rho_{s0}/\partial x)^2}} \right. \\
&\quad \left. + \left(\frac{\partial \rho_{s0}/\partial x}{\rho_{s0} \sqrt{1 + (\partial \rho_{s0}/\partial x)^2}^3} - \frac{3(\partial \rho_{s0}/\partial x)(\partial^2 \rho_{s0}/\partial x^2)}{\sqrt{1 + (\partial \rho_{s0}/\partial x)^2}^5} \right) \frac{\partial \rho_{s2}}{\partial x} \right. \\
&\quad \left. - \left(\frac{\partial \rho_{s0}/\partial x}{\rho_{s0} \sqrt{1 + (\partial \rho_{s0}/\partial x)^2}^3} + \frac{3(\partial \rho_{s0}/\partial x)(\partial^2 \rho_{s0}/\partial x^2)}{\sqrt{1 + (\partial \rho_{s0}/\partial x)^2}^5} \right) \rho_{s1} \frac{\partial \rho_{s1}}{\partial x} \right. \\
&\quad \left. - \left(\frac{2(\partial \rho_{s0}/\partial x)^2 - 1}{2\rho_{s0} \sqrt{1 + (\partial \rho_{s0}/\partial x)^2}^5} + \frac{3[1 - 4(\partial \rho_{s0}/\partial x)^2](\partial^2 \rho_{s0}/\partial x^2)}{2\sqrt{1 + (\partial \rho_{s0}/\partial x)^2}^7} \right) \left(\frac{\partial \rho_{s1}}{\partial x} \right)^2 \right. \\
&\quad \left. + \frac{\partial^2 \rho_{s2}/\partial x^2}{\sqrt{1 + (\partial \rho_{s0}/\partial x)^2}^3} \right] \\
&\quad + \bar{\beta} \left\{ \frac{1}{2} \left(\frac{1}{\rho_{s0} \sqrt{1 + (\partial \rho_{s0}/\partial x)^2}} + \frac{\partial^2 \rho_{s0}/\partial x^2}{\sqrt{1 + (\partial \rho_{s0}/\partial x)^2}^3} \right)^2 + \frac{1}{1 + (\partial \rho_{s0}/\partial x)^2} \frac{\partial^2}{\partial x^2} \right. \\
&\quad \left. - \frac{1}{\sqrt{1 + (\partial \rho_{s0}/\partial x)^2}} \frac{\partial \rho_{s0}}{\partial x} \left(- \frac{1}{\rho_{s0} \sqrt{1 + (\partial \rho_{s0}/\partial x)^2}} + \frac{\partial^2 \rho_{s0}/\partial x^2}{\sqrt{1 + (\partial \rho_{s0}/\partial x)^2}^3} \right) \frac{d}{dx} \right\} \\
&\quad \times \left(- \frac{1}{\rho_{s0} \sqrt{1 + (\partial \rho_{s0}/\partial x)^2}} + \frac{\partial^2 \rho_{s0}/\partial x^2}{\sqrt{1 + (\partial \rho_{s0}/\partial x)^2}^3} \right), \tag{B.1.8c}
\end{aligned}$$

etc.

Tangential stress boundary condition on the vesicle membrane:

at $\rho = \rho_{s0}$:

$$O(1) : \quad \frac{d\bar{\tau}_0}{dx} = 0, \tag{B.1.9a}$$

$$O(\epsilon^{1/2}) : \quad \frac{d\bar{\tau}_1}{dx} = 0, \tag{B.1.9b}$$

$$O(\epsilon) : \quad \frac{d\bar{\tau}_2}{dx} = 0, \tag{B.1.9c}$$

etc.

Shape boundary condition at the front nose:

at $x = 0$:

$$O(1) : \quad \rho_{s0} = 0, \quad \frac{1}{\sqrt{1 + (\mathrm{d}\rho_{s0}/\mathrm{d}x)^2}} \frac{\mathrm{d}\rho_{s0}}{\mathrm{d}x} = -1, \quad (\text{B.1.10a})$$

$$O(\epsilon^{\frac{1}{2}}) : \quad \rho_{s1} = 0, \quad (\text{B.1.10b})$$

$$O(\epsilon) : \quad \rho_{s2} = 0, \quad (\text{B.1.10c})$$

etc.

Shape boundary condition at the rear tail:

at $x = -\ell$:

$$O(1) : \quad \rho_{s0} = 0, \quad \frac{1}{\sqrt{1 + (\mathrm{d}\rho_{s0}/\mathrm{d}x)^2}} \frac{\mathrm{d}\rho_{s0}}{\mathrm{d}x} = +1, \quad (\text{B.1.11a})$$

$$O(\epsilon^{\frac{1}{2}}) : \quad \rho_{s1} = 0, \quad (\text{B.1.11b})$$

$$O(\epsilon) : \quad \rho_{s2} = 0, \quad (\text{B.1.11c})$$

etc.

Kinematic condition:

$$O(1) : \quad \frac{\mathrm{d}q_0}{\mathrm{d}x} = 0, \quad (\text{B.1.12a})$$

$$O(\epsilon^{\frac{1}{2}}) : \quad \frac{\mathrm{d}q_1}{\mathrm{d}x} = 0, \quad (\text{B.1.12b})$$

$$O(\epsilon) : \quad \frac{\mathrm{d}q_2}{\mathrm{d}x} = 0, \quad (\text{B.1.12c})$$

etc.

Mass balance in the exterior fluid:

$$O(1) : \quad q_0 + \int_{\rho_{s0}}^1 \rho u_{x0} \mathrm{d}\rho = 0, \quad (\text{B.1.13a})$$

$$O(\epsilon^{\frac{1}{2}}) : \quad q_1 + \int_{\rho_{s0}}^1 \rho u_{x1} \mathrm{d}\rho = \rho_{s1} \rho_{s0} u_{x0} \Big|_{\rho=\rho_{s0}}, \quad (\text{B.1.13b})$$

$$O(\epsilon) : \quad q_2 + \int_{\rho_{s0}}^1 \rho u_{x2} \mathrm{d}\rho = \left\{ \rho_{s1} \rho_{s0} u_{x1} + \left[\rho_{s2} \rho_{s0} + \frac{\rho_{s1}^2}{2} \left(1 + r_0 \frac{\partial}{\partial \rho} \right) \right] u_{x0} \right\} \Big|_{\rho=\rho_{s0}}, \quad (\text{B.1.13c})$$

etc.

Force balance in the exterior fluid:

$$O(1) : \quad \Delta\bar{p}_0^{+(\text{outer})} = 0, \quad (\text{B.1.14a})$$

$$O(\epsilon^{\frac{1}{2}}) : \quad \Delta\bar{p}_1^{+(\text{outer})} = - \int_{-\infty}^{-\ell+1} \left[2 \left(\frac{\partial u_{x0}}{\partial \rho} + \frac{\partial u_{\rho0}}{\partial x} \right) \Big|_{\rho=1} + 8 \right] dx - \int_{-1}^{\infty} \left[2 \left(\frac{\partial u_{x0}}{\partial \rho} + \frac{\partial u_{\rho0}}{\partial x} \right) \Big|_{\rho=1} + 8 \right] dx, \quad (\text{B.1.14b})$$

$$O(\epsilon) : \quad \Delta\bar{p}_2^{+(\text{outer})} = - \int_{-\infty}^{-\ell+1} 2 \left(\frac{\partial u_{x1}}{\partial \rho} + \frac{\partial u_{\rho1}}{\partial x} \right) \Big|_{\rho=1} dx - \int_{-1}^{\infty} 2 \left(\frac{\partial u_{x1}}{\partial \rho} + \frac{\partial u_{\rho1}}{\partial x} \right) \Big|_{\rho=1} dx, \quad (\text{B.1.14c})$$

etc.

B.2 Inner equations

Equations of continuity and motion in the exterior fluid:

$$O(1) : \quad \frac{\partial \bar{u}_{\bar{x}0}}{\partial \bar{x}} + \frac{\partial \bar{u}_{\bar{y}0}}{\partial \bar{y}} = 0, \quad \frac{\partial \bar{p}_0}{\partial \bar{x}} - \frac{\partial^2 \bar{u}_{\bar{x}0}}{\partial \bar{y}^2} = 0, \quad \frac{\partial \bar{p}_0}{\partial \bar{y}} = 0, \quad (\text{B.2.1a})$$

$$O(\epsilon^{\frac{1}{2}}) : \quad \frac{\partial \bar{u}_{\bar{x}1}}{\partial \bar{x}} + \frac{\partial \bar{u}_{\bar{y}1}}{\partial \bar{y}} = 0, \quad \frac{\partial \bar{p}_1}{\partial \bar{x}} - \frac{\partial^2 \bar{u}_{\bar{x}1}}{\partial \bar{y}^2} = 0, \quad \frac{\partial \bar{p}_1}{\partial \bar{y}} = 0, \quad (\text{B.2.1b})$$

$$O(\epsilon) : \quad \frac{\partial \bar{u}_{\bar{x}2}}{\partial \bar{x}} + \frac{\partial \bar{u}_{\bar{y}2}}{\partial \bar{y}} = 0, \quad \frac{\partial \bar{p}_2}{\partial \bar{x}} - \frac{\partial^2 \bar{u}_{\bar{x}2}}{\partial \bar{y}^2} = \left(\frac{\partial^2}{\partial \bar{x}^2} - \frac{\partial}{\partial \bar{y}} \right) \bar{u}_{\bar{x}0}, \quad \frac{\partial \bar{p}_2}{\partial \bar{y}} = \frac{\partial^2 \bar{u}_{\bar{y}0}}{\partial \bar{y}^2}, \quad (\text{B.2.1c})$$

etc.

Equations of continuity and motion in the interior fluid:

$$O(1) : \quad \frac{\partial \check{u}_{\bar{x}0}}{\partial \bar{x}} + \left(\frac{\partial}{\partial \rho} + \frac{1}{\rho} \right) \check{u}_{\rho0} = 0, \quad \frac{\partial \check{p}_0}{\partial \bar{x}} = 0, \quad \frac{\partial \check{p}_0}{\partial \rho} - \kappa \frac{\partial^2 \check{u}_{\rho0}}{\partial \bar{x}^2} = 0, \quad (\text{B.2.2a})$$

$$O(\epsilon^{\frac{1}{2}}) : \quad \frac{\partial \check{u}_{\bar{x}1}}{\partial \bar{x}} + \left(\frac{\partial}{\partial \rho} + \frac{1}{\rho} \right) \check{u}_{\rho1} = 0, \quad \frac{\partial \check{p}_1}{\partial \bar{x}} = 0, \quad \frac{\partial \check{p}_1}{\partial \rho} - \kappa \frac{\partial^2 \check{u}_{\rho1}}{\partial \bar{x}^2} = 0, \quad (\text{B.2.2b})$$

$$O(\epsilon) : \quad \frac{\partial \check{u}_{\bar{x}2}}{\partial \bar{x}} + \left(\frac{\partial}{\partial \rho} + \frac{1}{\rho} \right) \check{u}_{\rho2} = 0, \quad \frac{\partial \check{p}_2}{\partial \bar{x}} = \kappa \frac{\partial^2 \check{u}_{\bar{x}0}}{\partial \bar{x}^2}, \quad \frac{\partial \check{p}_2}{\partial \rho} - \kappa \frac{\partial^2 \check{u}_{\rho2}}{\partial \bar{x}^2} \\ = \kappa \left(\frac{\partial^2}{\partial \rho^2} + \frac{1}{\rho} \frac{\partial}{\partial \rho} - \frac{1}{\rho^2} \right) \check{u}_{\rho0}, \quad (\text{B.2.2c})$$

etc.

Exterior velocity boundary condition on the tube wall:

at $\bar{y} = 0$:

$$O(1) : \quad \bar{u}_{\bar{x}0} = -1, \quad \bar{u}_{\bar{y}0} = 0, \quad (\text{B.2.3a})$$

$$O(\epsilon^{\frac{1}{2}}) : \quad \bar{u}_{\bar{x}1} = 0, \quad \bar{u}_{\bar{y}1} = 0, \quad (\text{B.2.3b})$$

$$O(\epsilon) : \quad \bar{u}_{\bar{x}2} = -2\bar{q}_0, \quad \bar{u}_{\bar{y}2} = 0, \quad (\text{B.2.3c})$$

etc.

Exterior velocity boundary condition on the vesicle membrane:

at $\bar{y} = \bar{h}_0$:

$$O(1) : \quad \bar{u}_{\bar{x}0} = 0, \quad \bar{u}_{\bar{y}0} = 0, \quad (\text{B.2.4a})$$

$$O(\epsilon^{\frac{1}{2}}) : \quad \bar{u}_{\bar{x}1} = -\bar{h}_1 \frac{\partial \bar{u}_{\bar{x}0}}{\partial \bar{y}}, \quad \bar{u}_{\bar{y}1} = -\bar{h}_1 \frac{\partial \bar{u}_{\bar{y}0}}{\partial \bar{y}}, \quad (\text{B.2.4b})$$

$$O(\epsilon) : \quad \bar{u}_{\bar{x}2} = -\bar{h}_1 \frac{\partial \bar{u}_{\bar{x}1}}{\partial \bar{y}} - \left(\bar{h}_2 + \frac{\bar{h}_1^2}{2} \frac{\partial}{\partial \bar{y}} \right) \frac{\partial \bar{u}_{\bar{x}0}}{\partial \bar{y}}, \quad \bar{u}_{\bar{y}2} = -\bar{h}_1 \frac{\partial \bar{u}_{\bar{y}1}}{\partial \bar{y}} - \left(\bar{h}_2 + \frac{\bar{h}_1^2}{2} \frac{\partial}{\partial \bar{y}} \right) \frac{\partial \bar{u}_{\bar{y}0}}{\partial \bar{y}}, \quad (\text{B.2.4c})$$

etc.

Interior velocity boundary condition on the tube centerline:

at $\rho = 0$:

$$O(1) : \quad \frac{\partial \check{u}_{\bar{x}0}}{\partial \rho} = 0, \quad \check{u}_{\rho 0} = 0, \quad (\text{B.2.5a})$$

$$O(\epsilon^{\frac{1}{2}}) : \quad \frac{\partial \check{u}_{\bar{x}1}}{\partial \rho} = 0, \quad \check{u}_{\rho 1} = 0, \quad (\text{B.2.5b})$$

$$O(\epsilon) : \quad \frac{\partial \check{u}_{\bar{x}2}}{\partial \rho} = 0, \quad \check{u}_{\rho 2} = 0, \quad (\text{B.2.5c})$$

etc.

Interior velocity boundary condition on the vesicle membrane:

at $\rho = 1$:

$$O(1) : \quad \check{u}_{\bar{x}0} = 0, \quad \check{u}_{\rho 0} = 0, \quad (\text{B.2.6a})$$

$$O(\epsilon^{\frac{1}{2}}) : \quad \check{u}_{\bar{x}1} = 0, \quad \check{u}_{\rho 1} = 0, \quad (\text{B.2.6b})$$

$$O(\epsilon) : \quad \check{u}_{\bar{x}2} = \bar{h}_0 \frac{\partial \check{u}_{\bar{x}0}}{\partial \rho}, \quad \check{u}_{\rho 2} = \bar{h}_0 \frac{\partial \check{u}_{\rho 0}}{\partial \rho}, \quad (\text{B.2.6c})$$

etc.

Normal stress boundary condition on the vesicle membrane:

at $\bar{y} = \bar{h}_0$, $\rho = 1$:

$$O(1) : \quad \bar{p}_0|_{\bar{y}=\bar{h}_0} - \check{p}_0|_{\rho=1} = -\bar{\tau}_0 \left(1 + \frac{d^2 \bar{h}_0}{d\bar{x}^2} \right) + \bar{\beta} \frac{d^4 \bar{h}_0}{d\bar{x}^4}, \quad (\text{B.2.7a})$$

$$O(\epsilon^{\frac{1}{2}}) : \quad \left(\bar{p}_1 + \bar{h}_1 \frac{\partial \bar{p}_0}{\partial \bar{y}} \right) \Big|_{\bar{y}=\bar{h}_0} - \check{p}_1|_{\rho=1} = -\bar{\tau}_1 \left(1 + \frac{d^2 \bar{h}_0}{d\bar{x}^2} \right) - \bar{\tau}_0 \frac{d^2 \bar{h}_1}{d\bar{x}^2} + \bar{\beta} \frac{d^4 \bar{h}_1}{d\bar{x}^4}, \quad (\text{B.2.7b})$$

$$\begin{aligned} O(\epsilon) : \quad & \left[\bar{p}_2 + \bar{h}_1 \frac{\partial \bar{p}_1}{\partial \bar{y}} + \left(\bar{h}_2 + \frac{\bar{h}_1^2}{2} \frac{\partial}{\partial \bar{y}} \right) \frac{\partial \bar{p}_0}{\partial \bar{y}} - 2 \left(\frac{\partial \bar{u}_{\bar{y}0}}{\partial \bar{y}} - \frac{d\bar{h}_0}{d\bar{x}} \frac{\partial \bar{u}_{\bar{x}0}}{\partial \bar{y}} \right) \right] \Big|_{\bar{y}=\bar{h}_0} \\ & - \left[\check{p}_2 - \bar{h}_0 \frac{\partial \check{p}_0}{\partial \rho} - 2\kappa \left(\frac{\partial}{\partial \rho} + \frac{d\bar{h}_0}{d\bar{x}} \frac{\partial}{\partial \bar{x}} \right) \check{u}_{\rho 0} \right] \Big|_{\rho=1} \\ & = -\bar{\tau}_2 \left(1 + \frac{d^2 \bar{h}_0}{d\bar{x}^2} \right) - \bar{\tau}_1 \frac{d^2 \bar{h}_1}{d\bar{x}^2} - \bar{\tau}_0 \left[\frac{d^2 \bar{h}_2}{d\bar{x}^2} + \bar{h}_0 - \frac{1}{2} \left(\frac{d\bar{h}_0}{d\bar{x}} \right)^2 \left(1 + 3 \frac{d^2 \bar{h}_0}{d\bar{x}^2} \right) \right] \\ & + \bar{\beta} \left[\frac{d^4 \bar{h}_2}{d\bar{x}^4} + \frac{1}{2} \left(1 + \frac{d^2 \bar{h}_0}{d\bar{x}^2} \right) - \frac{3}{2} \left(\frac{d^2 \bar{h}_0}{d\bar{x}^2} \right)^2 - 2 \frac{d\bar{h}_0}{d\bar{x}} \frac{d^3 \bar{h}_0}{d\bar{x}^3} \right. \\ & \left. - \frac{5}{2} \left(\frac{d^2 \bar{h}_0}{d\bar{x}^2} \right)^3 - 10 \frac{d\bar{h}_0}{d\bar{x}} \frac{d^2 \bar{h}_0}{d\bar{x}^2} \frac{d^3 \bar{h}_0}{d\bar{x}^3} - \frac{5}{2} \left(\frac{d\bar{h}_0}{d\bar{x}} \right)^2 \frac{d^4 \bar{h}_0}{d\bar{x}^4} \right], \quad (\text{B.2.7c}) \end{aligned}$$

etc.

Tangential stress boundary condition on the vesicle membrane:

at $\bar{y} = \bar{h}_0$, $\rho = 1$:

$$O(1) : \quad \frac{d\bar{\tau}_0}{d\bar{x}} = 0, \quad (\text{B.2.8a})$$

$$O(\epsilon^{\frac{1}{2}}) : \quad \frac{d\bar{\tau}_1}{d\bar{x}} = 0, \quad (\text{B.2.8b})$$

$$O(\epsilon) : \quad \frac{d\bar{\tau}_2}{d\bar{x}} = \frac{\partial \bar{u}_{\bar{x}0}}{\partial \bar{y}} \Big|_{\bar{y}=\bar{h}_0} + \kappa \frac{\partial \check{u}_{\rho 0}}{\partial \bar{x}} \Big|_{\rho=1}, \quad (\text{B.2.8c})$$

etc.

Shape boundary condition at the middle axial plane:

at $\bar{x} = -\bar{\ell}$ (or $\bar{x}^* = \bar{\ell}$) :

$$O(1) : \quad \bar{h}_0 = 1, \quad (\text{B.2.9a})$$

$$O(\epsilon^{\frac{1}{2}}) : \quad \bar{h}_1 = 0, \quad (\text{B.2.9b})$$

$$O(\epsilon) : \quad \bar{h}_2 = 0, \quad (\text{B.2.9c})$$

etc.

Kinematic condition:

$$O(1) : \quad \frac{d\bar{q}_0}{d\bar{x}} = 0, \quad (\text{B.2.10a})$$

$$O(\epsilon^{\frac{1}{2}}) : \quad \frac{d\bar{q}_1}{d\bar{x}} = 0, \quad (\text{B.2.10b})$$

$$O(\epsilon) : \quad \frac{d\bar{q}_2}{d\bar{x}} = 0, \quad (\text{B.2.10c})$$

etc.

Mass balance in the exterior fluid:

$$O(1) : \quad \bar{q}_0 + \int_0^{\bar{h}_0} \bar{u}_{\bar{x}0} d\bar{y} = 0, \quad (\text{B.2.11a})$$

$$O(\epsilon^{\frac{1}{2}}) : \quad \bar{q}_1 + \int_0^{\bar{h}_0} \bar{u}_{\bar{x}1} d\bar{y} = -\bar{h}_1 \bar{u}_{\bar{x}0}|_{\bar{y}=\bar{h}_0}, \quad (\text{B.2.11b})$$

$$O(\epsilon) : \quad \bar{q}_2 + \int_0^{\bar{h}_0} \bar{u}_{\bar{x}2} d\bar{y} = \int_0^{\bar{h}_0} \bar{y} \bar{u}_{\bar{x}0} d\bar{y} - \left[\bar{h}_1 \bar{u}_{\bar{x}1} + \left(\bar{h}_2 + \frac{\bar{h}_1^2}{2} \frac{\partial}{\partial \bar{y}} \right) \bar{u}_{\bar{x}0} \right] \Big|_{\bar{y}=\bar{h}_0}, \quad (\text{B.2.11c})$$

etc.

Force balance in the exterior fluid:

$$O(1) : \quad \Delta \bar{p}_0^{+(\text{inner})} = \int_{-\infty}^{\bar{\ell}} 2 \frac{\partial \bar{u}_{\bar{x}0}}{\partial \bar{y}} \Big|_{\bar{y}=0} d\bar{x}^* + \int_{-\bar{\ell}}^{\infty} 2 \frac{\partial \bar{u}_{\bar{x}0}}{\partial \bar{y}} \Big|_{\bar{y}=0} d\bar{x}, \quad (\text{B.2.12a})$$

$$O(\epsilon^{\frac{1}{2}}) : \quad \Delta \bar{p}_1^{+(\text{inner})} = \int_{-\infty}^{\bar{\ell}} 2 \frac{\partial \bar{u}_{\bar{x}1}}{\partial \bar{y}} \Big|_{\bar{y}=0} d\bar{x}^* + \int_{-\bar{\ell}}^{\infty} 2 \frac{\partial \bar{u}_{\bar{x}1}}{\partial \bar{y}} \Big|_{\bar{y}=0} d\bar{x}, \quad (\text{B.2.12b})$$

$$O(\epsilon) : \quad \Delta \bar{p}_2^{+(\text{inner})} = \int_{-\infty}^{\bar{\ell}} \left[2 \left(\frac{\partial \bar{u}_{\bar{x}2}}{\partial \bar{y}} + \frac{\partial \bar{u}_{\bar{y}0}}{\partial \bar{x}} \right) \Big|_{\bar{y}=0} - 8 \right] d\bar{x}^* + \int_{-\bar{\ell}}^{\infty} \left[2 \left(\frac{\partial \bar{u}_{\bar{x}2}}{\partial \bar{y}} + \frac{\partial \bar{u}_{\bar{y}0}}{\partial \bar{x}} \right) \Big|_{\bar{y}=0} - 8 \right] d\bar{x}, \quad (\text{B.2.12c})$$

etc.

B.3 Matching conditions

Shape matching condition at the front end:

at $x = -1$, $\bar{x} \rightarrow \infty$:

$$O(1) : \quad \rho_{s0}(-1) = 1, \quad (\text{B.3.1a})$$

$$O(\epsilon^{\frac{1}{2}}) : \quad \left(\rho_{s1} + \bar{x} \frac{d\rho_{s0}}{dx} \right) \Big|_{x=-1} = 0, \quad (\text{B.3.1b})$$

$$O(\epsilon) : \quad \left(\rho_{s2} + \bar{x} \frac{d\rho_{s1}}{dx} + \frac{\bar{x}^2}{2} \frac{d^2\rho_{s0}}{dx^2} \right) \Big|_{x=-1} = \lim_{\bar{x} \rightarrow \infty} (-\bar{h}_0), \quad (\text{B.3.1c})$$

etc.

Shape matching condition at the rear end:

at $x = -\ell + 1$, $\bar{x}^* \rightarrow -\infty$:

$$O(1) : \quad \rho_{s0}(-\ell + 1) = 1, \quad (\text{B.3.2a})$$

$$O(\epsilon^{\frac{1}{2}}) : \quad \left(\rho_{s1} + \bar{x}^* \frac{d\rho_{s0}}{dx} \right) \Big|_{x=-\ell+1} = 0, \quad (\text{B.3.2b})$$

$$O(\epsilon) : \quad \left(\rho_{s2} + \bar{x}^* \frac{d\rho_{s1}}{dx} + \frac{\bar{x}^{*2}}{2} \frac{d^2\rho_{s0}}{dx^2} \right) \Big|_{x=-\ell+1} = \lim_{\bar{x}^* \rightarrow -\infty} (-\bar{h}_0), \quad (\text{B.3.2c})$$

etc.

Appendix C

Short, spherical vesicles in the narrow-gap limit

In this appendix, an asymptotic solution to (3.5.30) and (3.5.50) is derived for small $\bar{\ell}$ and $\bar{\beta} = 0$ using the method of matched asymptotic expansions. The results are summarized in Table 3.2 and in equations (3.6.18) and (3.6.26) in the main text. All variables are rendered dimensionless using the following characteristic scales: R (the tube radius), V (the mean tube velocity), and μ (the suspending fluid viscosity). Variables with an overbar are rescaled as described in §3.4. Variables with an overtilde are rescaled as described in §3.6.2.

C.1 Zeroth-order solution in $\epsilon^{\frac{1}{2}}$

C.1.1 Outer equations

Recall the boundary-value problem in the infinite domain $\bar{\xi} \in (-\infty, \infty)$:

$$\tilde{\tau}_0 \frac{d^3 \bar{h}_0}{d \bar{\xi}^3} = \frac{6 \bar{\ell}^{\frac{1}{2}}}{\bar{h}_0^2} \left(1 - \frac{2 \bar{q}_0}{\bar{h}_0} \right), \quad (3.6.12)$$

$$\text{at } \bar{\xi} = 0 : \quad \bar{h}_0 = 1. \quad (3.6.13)$$

The outer region for small $\bar{\ell}$ denotes the region where $\bar{\xi} = O(1)$ and $\bar{h}_0 = O(1)$. Since the membrane tension is only constrained by matching conditions, it is stretched in this region. Asymptotic expansions in $\bar{\ell}^{\frac{1}{2}}$ may be constructed for the generic “outer variable,” viz.,

$$\psi_n(\bar{\xi}) = \psi_{n0}(\bar{\xi}) + \bar{\ell}^{\frac{1}{2}} \psi_{n1}(\bar{\xi}) + \bar{\ell} \psi_{n2}(\bar{\xi}) + \dots \quad (C.1.1)$$

In any double subscript “ nm ,” n indicates the order in $\epsilon^{\frac{1}{2}}$ while m indicates the order in $\bar{\ell}^{\frac{1}{2}}$. Expanding the dependent variables in powers of $\bar{\ell}^{\frac{1}{2}}$ and collecting like-ordered terms yields the following, ordered perturbation equations for the outer region:

$$O(1) : \quad \tilde{\tau}_{00} \frac{d^3 \bar{h}_{00}}{d\tilde{\xi}^3} = 0, \quad (\text{C.1.2a})$$

$$O(\bar{\ell}^{\frac{1}{2}}) : \quad \tilde{\tau}_{00} \frac{d^3 \bar{h}_{01}}{d\tilde{\xi}^3} = -\tilde{\tau}_{01} \frac{d^3 \bar{h}_{00}}{d\tilde{\xi}^3} + \frac{6}{\bar{h}_{00}^2} \left(1 - \frac{2\bar{q}_{00}}{\bar{h}_{00}} \right), \quad (\text{C.1.2b})$$

$$O(\bar{\ell}) : \quad \tilde{\tau}_{00} \frac{d^3 \bar{h}_{02}}{d\tilde{\xi}^3} = -\tilde{\tau}_{02} \frac{d^3 \bar{h}_{00}}{d\tilde{\xi}^3} - \tilde{\tau}_{01} \frac{d^3 \bar{h}_{01}}{d\tilde{\xi}^3} - \frac{12}{\bar{h}_{00}^2} \left[\left(1 - \frac{3\bar{q}_{00}}{\bar{h}_{00}} \right) \frac{\bar{h}_{01}}{\bar{h}_{00}} + \frac{\bar{q}_{01}}{\bar{h}_{00}} \right], \quad (\text{C.1.2c})$$

etc.

at $\tilde{\xi} = 0$:

$$O(1) : \quad \bar{h}_{00} = 1, \quad (\text{C.1.3a})$$

$$O(\bar{\ell}^{\frac{1}{2}}) : \quad \bar{h}_{01} = 0, \quad (\text{C.1.3b})$$

$$O(\bar{\ell}) : \quad \bar{h}_{02} = 0, \quad (\text{C.1.3c})$$

etc.

C.1.2 Inner equations

Recall the boundary value problem defined within two semi-infinite domains $\tilde{\xi} \in (-\infty, 0^-) \cup (0^+, \infty)$:

$$\tilde{\tau}_0 \frac{d^3 \tilde{h}_0}{d\tilde{\xi}^3} = \frac{6\bar{\ell}^2}{\tilde{h}_0^2} - \frac{12\bar{\ell}^3 \tilde{q}_0}{\tilde{h}_0^3}, \quad (3.6.14)$$

$$\text{as } \tilde{\xi} \rightarrow \infty : \quad \tilde{h}_0 \rightarrow \frac{1}{2}\tilde{\xi}^2 + \bar{\ell}\tilde{b}_0 - \bar{\ell}^{\frac{3}{2}}\tilde{\xi} + \frac{1}{2}\bar{\ell}^3, \quad (3.6.15)$$

$$\text{as } \tilde{\xi} \rightarrow -\infty : \quad \tilde{h}_0 \rightarrow \frac{1}{2}\tilde{\xi}^2 + \bar{\ell}\tilde{b}_0^* + \bar{\ell}^{\frac{3}{2}}\tilde{\xi} + \frac{1}{2}\bar{\ell}^3. \quad (3.6.16)$$

Asymptotic expansions in $\bar{\ell}^{\frac{1}{2}}$ may be constructed for the generic “inner variable,” viz.,

$$\tilde{\psi}_n(\tilde{\xi}) = \tilde{\psi}_{n0}(\tilde{\xi}) + \bar{\ell}^{\frac{1}{2}} \tilde{\psi}_{n1}(\tilde{\xi}) + \bar{\ell} \tilde{\psi}_{n2}(\tilde{\xi}) + \dots \quad (\text{C.1.4})$$

Expanding the dependent variables in powers of $\bar{\ell}^{\frac{1}{2}}$ and collecting like-ordered terms yields the following, ordered perturbation equations for the inner region:

$$O(1) : \quad \tilde{\tau}_{00} \frac{d^3 \tilde{h}_{00}}{d\tilde{\xi}^3} = 0, \quad (\text{C.1.5a})$$

$$O(\bar{\ell}^{\frac{1}{2}}) : \quad \tilde{\tau}_{00} \frac{d^3 \tilde{h}_{01}}{d\tilde{\xi}^3} = -\tilde{\tau}_{01} \frac{d^3 \tilde{h}_{00}}{d\tilde{\xi}^3}, \quad (\text{C.1.5b})$$

$$O(\bar{\ell}) : \quad \tilde{\tau}_{00} \frac{d^3 \tilde{h}_{02}}{d\tilde{\xi}^3} = -\tilde{\tau}_{02} \frac{d^3 \tilde{h}_{00}}{d\tilde{\xi}^3} - \tilde{\tau}_{01} \frac{d^3 \tilde{h}_{01}}{d\tilde{\xi}^3}, \quad (\text{C.1.5c})$$

etc.

as $\tilde{\xi} \rightarrow \infty$:

$$O(1) : \quad \tilde{h}_{00} \rightarrow \frac{1}{2} \tilde{\xi}^2, \quad (\text{C.1.6a})$$

$$O(\bar{\ell}^{\frac{1}{2}}) : \quad \tilde{h}_{01} \rightarrow 0, \quad (\text{C.1.6b})$$

$$O(\bar{\ell}) : \quad \tilde{h}_{02} \rightarrow \tilde{b}_{00}, \quad (\text{C.1.6c})$$

etc.

as $\tilde{\xi} \rightarrow -\infty$:

$$O(1) : \quad \tilde{h}_{00} \rightarrow \frac{1}{2} \tilde{\xi}^2, \quad (\text{C.1.7a})$$

$$O(\bar{\ell}^{\frac{1}{2}}) : \quad \tilde{h}_{01} \rightarrow 0, \quad (\text{C.1.7b})$$

$$O(\bar{\ell}) : \quad \tilde{h}_{02} \rightarrow \tilde{b}_{00}^*, \quad (\text{C.1.7c})$$

etc.

C.1.3 Matching conditions

Recall the matching conditions,

$$\lim_{\tilde{\xi} \rightarrow 0^+} \tilde{h}_0 = \lim_{\tilde{\xi} \rightarrow \infty} \bar{\ell} \bar{h}_0, \quad (3.6.17a)$$

$$\lim_{\tilde{\xi} \rightarrow 0^-} \tilde{h}_0 = \lim_{\tilde{\xi}^* \rightarrow -\infty} \bar{\ell} \bar{h}_0. \quad (3.6.17b)$$

The limits are interpreted in the spirit of the matching principle of van Dyke [166]. The matching conditions must be expanded in powers of $\bar{\ell}^{\frac{1}{2}}$. Expanding $\tilde{h}_0(\tilde{\xi})$ in a Taylor series about $\tilde{\xi} = 0$ and rewriting the series in terms of the outer coordinate yields,

$$\begin{aligned}\tilde{h}_0(\tilde{\xi}) &= \tilde{h}_0(0) + \frac{d\tilde{h}_0}{d\tilde{\xi}}\Big|_{\tilde{\xi}=0} \tilde{\xi} + \frac{1}{2} \frac{d^2\tilde{h}_0}{d\tilde{\xi}^2}\Big|_{\tilde{\xi}=0} \tilde{\xi}^2 + \dots \\ &= \left[\tilde{h}_{00} + \bar{\ell}^{\frac{1}{2}} \left(\tilde{h}_{01} + \bar{\xi} \frac{d\tilde{h}_{00}}{d\tilde{\xi}} \right) + \bar{\ell} \left(\tilde{h}_{02} + \bar{\xi} \frac{d\tilde{h}_{01}}{d\tilde{\xi}} + \frac{\bar{\xi}^2}{2} \frac{d^2\tilde{h}_{00}}{d\tilde{\xi}^2} \right) + O(\bar{\ell}^{\frac{3}{2}}) \right] \Big|_{\tilde{\xi}=0}.\end{aligned}$$

The ordered matching conditions may then be written as,

at $\tilde{\xi} = 0^+$, $\bar{\xi} \rightarrow \infty$:

$$O(1): \quad \tilde{h}_{00}(0^+) = 0, \quad (\text{C.1.9a})$$

$$O(\bar{\ell}^{\frac{1}{2}}): \quad \left(\tilde{h}_{01} + \bar{\xi} \frac{d\tilde{h}_{00}}{d\tilde{\xi}} \right) \Big|_{\tilde{\xi}=0^+} = 0, \quad (\text{C.1.9b})$$

$$O(\bar{\ell}): \quad \left(\tilde{h}_{02} + \bar{\xi} \frac{d\tilde{h}_{01}}{d\tilde{\xi}} + \frac{\bar{\xi}^2}{2} \frac{d^2\tilde{h}_{00}}{d\tilde{\xi}^2} \right) \Big|_{\tilde{\xi}=0^+} = \lim_{\tilde{\xi} \rightarrow \infty} \bar{h}_{00}, \quad (\text{C.1.9c})$$

etc.

at $\tilde{\xi} = 0^-$, $\bar{\xi} \rightarrow -\infty$:

$$O(1): \quad \tilde{h}_{00}(0^-) = 0, \quad (\text{C.1.10a})$$

$$O(\bar{\ell}^{\frac{1}{2}}): \quad \left(\tilde{h}_{01} + \bar{\xi} \frac{d\tilde{h}_{00}}{d\tilde{\xi}} \right) \Big|_{\tilde{\xi}=0^-} = 0, \quad (\text{C.1.10b})$$

$$O(\bar{\ell}): \quad \left(\tilde{h}_{02} + \bar{\xi} \frac{d\tilde{h}_{01}}{d\tilde{\xi}} + \frac{\bar{\xi}^2}{2} \frac{d^2\tilde{h}_{00}}{d\tilde{\xi}^2} \right) \Big|_{\tilde{\xi}=0^-} = \lim_{\tilde{\xi} \rightarrow -\infty} \bar{h}_{00}, \quad (\text{C.1.10c})$$

etc.

C.1.4 Solution

It is now possible to solve the ordered perturbation equations sequentially. It turns out that the complete, leading-order solution for all of the dependent variables actually requires several orders of accuracy in both the outer and inner regions, with successive matching between the two regions

where appropriate. Fortunately, since bending elasticity has been neglected, analytical solutions in both regions may be derived.

Beginning with the $O(1)$ inner problem, (C.1.5a) – together with the boundary conditions (C.1.6a), (C.1.7a), (C.1.9a), and (C.1.10a) – is satisfied by the parabolic solution,

$$\tilde{\bar{h}}_{00} = \frac{1}{2}\tilde{\xi}^2. \quad (\text{C.1.11})$$

Hence, the $O(\bar{\ell}^{\frac{1}{2}})$ inner problem – equations (C.1.5b), (C.1.6b), (C.1.7b), (C.1.9b), and (C.1.10b) – becomes homogeneous, resulting in no correction at that order:

$$\tilde{\bar{h}}_{01} = 0. \quad (\text{C.1.12})$$

Further corrections in the inner region require the solution of the $O(1)$ outer problem, which is given by (C.1.2a), (C.1.3a), (C.1.9c), and (C.1.10c). The solution of these equations is a shifted parabola:

$$\bar{h}_{00} = 1 + \frac{1}{2}\bar{\xi}^2. \quad (\text{C.1.13})$$

This “outer” result forces the $O(\bar{\ell})$ inner problem, which is given by (C.1.5c), (C.1.6c), (C.1.7c), (C.1.9c), and (C.1.10c). In particular, the only solution which satisfies these equations is

$$\tilde{\bar{h}}_{02} = 1, \quad (\text{C.1.14})$$

$$\text{with } \tilde{b}_{00} = \tilde{b}_{00}^* = 1. \quad (\text{C.1.15})$$

Returning once again to the outer region, the $O(\bar{\ell}^{\frac{1}{2}})$ outer equation (C.1.2b) reduces to

$$\tilde{\tau}_{00} \frac{d^3\bar{h}_{01}}{d\bar{\xi}^3} = \frac{6}{(1 + \frac{1}{2}\bar{\xi}^2)^2} \left(1 - \frac{2\bar{q}_{00}}{1 + \frac{1}{2}\bar{\xi}^2} \right), \quad (\text{C.1.16})$$

where \bar{q}_{00} is to be determined as part of the solution. The boundary conditions for \bar{h}_{01} include the gap condition (C.1.3b) as well as matching conditions:

$$\text{at } \bar{\xi} = 0 : \quad \bar{h}_{01} = 0, \quad (\text{C.1.17})$$

$$\text{as } \bar{\xi} \rightarrow \infty : \quad \bar{h}_{01} \rightarrow e_{01}, \quad (\text{C.1.18})$$

$$\text{as } \bar{\xi} \rightarrow -\infty : \quad \bar{h}_{01} \rightarrow e_{01}^*, \quad (\text{C.1.19})$$

where

$$e_{01} = \tilde{h}_{03}(0^+), \quad e_{01}^* = \tilde{h}_{03}(0^-) \quad (\text{C.1.20})$$

are constants of integration. Solvability requires

$$\bar{q}_{00} = \frac{2}{3}, \quad (\text{C.1.21})$$

whence the particular solution to (C.1.16)-(C.1.19) is

$$\bar{h}_{01} = \frac{2\sqrt{2}}{\tilde{\tau}_{00}} \arctan\left(\frac{\bar{\xi}}{\sqrt{2}}\right), \quad (\text{C.1.22})$$

with

$$e_{01} = -e_{01}^* = \frac{\sqrt{2}\pi}{\tilde{\tau}_{00}}. \quad (\text{C.1.23})$$

The membrane tension $\tilde{\tau}_{00}$ is as of yet undetermined. Its solution requires higher-order corrections in both regions. The governing equation for \tilde{h}_{03} is the same as in previous orders in the inner region,

$$\tilde{\tau}_{00} \frac{d^3 \tilde{h}_{03}}{d\tilde{\xi}^3} = 0, \quad (\text{C.1.24})$$

with the boundary conditions,

$$\text{as } \tilde{\xi} \rightarrow 0^+ : \quad \bar{h}_{03} \rightarrow e_{01} = \frac{\sqrt{2}\pi}{\tilde{\tau}_{00}}, \quad (\text{C.1.25})$$

$$\text{as } \tilde{\xi} \rightarrow 0^- : \quad \bar{h}_{03} \rightarrow e_{01}^* = -\frac{\sqrt{2}\pi}{\tilde{\tau}_{00}}, \quad (\text{C.1.26})$$

$$\text{as } \tilde{\xi} \rightarrow \infty : \quad \bar{h}_{01} \rightarrow \tilde{b}_{01} - \tilde{\xi}, \quad (\text{C.1.27})$$

$$\text{as } \tilde{\xi} \rightarrow -\infty : \quad \bar{h}_{01} \rightarrow \tilde{b}_{01}^* + \tilde{\xi}. \quad (\text{C.1.28})$$

The particular solution to (C.1.24)-(C.1.28) is

$$\tilde{h}_{03} = \begin{cases} \frac{\sqrt{2}\pi}{\tilde{\tau}_{00}} - \tilde{\xi} & \text{for } \tilde{\xi} \in (0^+, \infty), \\ -\frac{\sqrt{2}\pi}{\tilde{\tau}_{00}} + \tilde{\xi} & \text{for } \tilde{\xi} \in (-\infty, 0^-), \end{cases} \quad (\text{C.1.29})$$

$$\text{with } \tilde{b}_{01} = -\tilde{b}_{01}^* = \frac{\sqrt{2}\pi}{\tilde{\tau}_{00}}. \quad (\text{C.1.30})$$

The final step is to calculate the $O(\bar{\ell})$ correction in the outer region, which is necessary in order to produce the leading-order solution for the membrane tension. Equation (C.1.2c) reduces to

$$\begin{aligned} \tilde{\tau}_{00} \frac{d^3 \bar{h}_{02}}{d\tilde{\xi}^3} = -\frac{2}{(1 + \frac{1}{2}\tilde{\xi}^2)^2} & \left\{ \frac{\tilde{\tau}_{01}}{\tilde{\tau}_{00}} \left(3 - \frac{4}{1 + \frac{1}{2}\tilde{\xi}^2} \right) \right. \\ & \left. + \frac{6}{1 + \frac{1}{2}\tilde{\xi}^2} \left[\left(1 - \frac{2}{1 + \frac{1}{2}\tilde{\xi}^2} \right) \frac{2\sqrt{2}}{\tilde{\tau}_{00}} \arctan\left(\frac{\bar{\xi}}{\sqrt{2}}\right) + \bar{q}_{01} \right] \right\}, \end{aligned} \quad (\text{C.1.31})$$

where \bar{q}_{01} is to be determined as part of the solution. The boundary conditions for \bar{h}_{02} include the

gap condition (C.1.3c) as well as matching conditions:

$$\text{at } \bar{\xi} = 0 : \quad \bar{h}_{02} = 0, \quad (\text{C.1.32})$$

$$\text{as } \bar{\xi} \rightarrow \infty : \quad \bar{h}_{02} \rightarrow e_{02} - \bar{\xi}, \quad (\text{C.1.33})$$

$$\text{as } \bar{\xi} \rightarrow -\infty : \quad \bar{h}_{02} \rightarrow e_{02}^* + \bar{\xi}, \quad (\text{C.1.34})$$

where

$$e_{02} = \tilde{h}_{04}(0^+), \quad e_{02}^* = \tilde{h}_{04}(0^-) \quad (\text{C.1.35})$$

are constants of integration. Solvability requires

$$\bar{q}_{01} = 0, \quad \tilde{\tau}_{00} = \sqrt{\frac{\pi}{2\sqrt{2}}}, \quad (\text{C.1.36})$$

whence a particular solution to (C.1.31)-(C.1.34) may be determined. Without much additional effort, it can be shown that

$$\tilde{\tau}_{01} = 0. \quad (\text{C.1.37})$$

Thus, the particular solution for \bar{h}_{02} is

$$\begin{aligned} \bar{h}_{02} = & -\frac{3\sqrt{2}\pi}{2}\bar{\xi}^2 + \frac{11\sqrt{2}}{3\pi}\left(\frac{\bar{\xi}^2}{1+\frac{1}{2}\bar{\xi}^2}\right) + \left(22 - \frac{8}{1+\frac{1}{2}\bar{\xi}^2}\right)\frac{\bar{\xi}}{\pi}\arctan\left(\frac{\bar{\xi}}{\sqrt{2}}\right) \\ & + \frac{6\sqrt{2}\bar{\xi}^2}{\pi}\arctan^2\left(\frac{\bar{\xi}}{\sqrt{2}}\right). \end{aligned} \quad (\text{C.1.38})$$

By forming an additive composite of the outer and inner expansions [166], we obtain a uniformly valid solution for \bar{h}_0 up to $O(\bar{\ell})$ (presented in the main text):

$$\begin{aligned} \bar{h}_0 = & 1 + \frac{1}{2}\bar{\xi}^2 + \left(\frac{\sqrt{2}\bar{\ell}}{\pi}\right)^{\frac{1}{2}}4\arctan\left(\frac{\bar{\xi}}{\sqrt{2}}\right) + \left(\frac{\sqrt{2}\bar{\ell}}{\pi}\right)\left[-\frac{3\pi^2\bar{\xi}^2}{2} + \frac{11}{3}\left(\frac{\bar{\xi}^2}{1+\frac{1}{2}\bar{\xi}^2}\right)\right. \\ & \left. + \left(22 - \frac{8}{1+\frac{1}{2}\bar{\xi}^2}\right)\frac{\bar{\xi}}{\sqrt{2}}\arctan\left(\frac{\bar{\xi}}{\sqrt{2}}\right) + 6\bar{\xi}^2\arctan^2\left(\frac{\bar{\xi}}{\sqrt{2}}\right)\right] + O\left[\left(\frac{\sqrt{2}\bar{\ell}}{\pi}\right)^{\frac{3}{2}}\right]. \end{aligned} \quad (3.6.18)$$

The solutions for the other variables are summarized in Table 3.2.

C.2 First-order solution in $\epsilon^{\frac{1}{2}}$

C.2.1 Outer equations

Recall the boundary-value problem,

$$\tilde{\tau}_0 \frac{d^3\tilde{h}_1}{d\bar{\xi}^3} = -\frac{6\tilde{\tau}_1}{\bar{h}_0^2\tilde{\tau}_0}\left(1 - \frac{2\bar{q}_0}{\bar{h}_0}\right) - \frac{12\bar{\ell}^{\frac{1}{2}}\tilde{h}_1}{\bar{h}_0^3}\left(1 - \frac{3\bar{q}_0}{\bar{h}_0}\right) - \frac{12\bar{\ell}\bar{q}_1}{\bar{h}_0^3}, \quad (3.6.20)$$

$$\text{at } \bar{\xi} = 0 : \quad \tilde{\bar{h}}_1 = 0, \quad (3.6.21)$$

Following the same procedure as in §C.1, we expand all dependent variables to give the following, ordered perturbation equations:

$$O(1) : \quad \tilde{\tau}_{00} \frac{d^3 \tilde{\bar{h}}_{10}}{d\bar{\xi}^3} = -\frac{6\tilde{\tau}_{10}}{\tilde{\tau}_{00}\bar{h}_{00}^2} \left(1 - \frac{2\bar{q}_{00}}{\bar{h}_{00}} \right), \quad (\text{C.2.1a})$$

$$\begin{aligned} O(\bar{\ell}^{\frac{1}{2}}) : \quad \tilde{\tau}_{00} \frac{d^3 \tilde{\bar{h}}_{11}}{d\bar{\xi}^3} &= \frac{12\tilde{\tau}_{10}}{\tilde{\tau}_{00}\bar{h}_{00}^2} \left[\frac{\bar{h}_{01}}{\bar{h}_{00}} \left(1 - \frac{3\bar{q}_{00}}{\bar{h}_{00}} \right) + \frac{\bar{q}_{01}}{\bar{h}_{00}} \right] \\ &\quad - \frac{6}{\bar{h}_{00}^2} \left(\frac{\tilde{\tau}_{11}}{\tilde{\tau}_{00}} - \frac{\tilde{\tau}_{10}\tilde{\tau}_{01}}{\tilde{\tau}_{00}^2} \right) \left(1 - \frac{2\bar{q}_{00}}{\bar{h}_{00}} \right) - \frac{12\tilde{\bar{h}}_{10}}{\bar{h}_{00}^3} \left(1 - \frac{3\bar{q}_{00}}{\bar{h}_{00}} \right), \end{aligned} \quad (\text{C.2.1b})$$

$$\begin{aligned} O(\bar{\ell}) : \quad \tilde{\tau}_{00} \frac{d^3 \tilde{\bar{h}}_{12}}{d\bar{\xi}^3} &= \frac{6\tilde{\tau}_{10}}{\tilde{\tau}_{00}\bar{h}_{00}^2} \left(\frac{2\bar{h}_{02}}{\bar{h}_{00}} - \frac{3\bar{h}_{01}^2}{\bar{h}_{00}^2} \right) \left(1 - \frac{2\bar{q}_{00}}{\bar{h}_{00}} \right) \\ &\quad + \frac{12\tilde{\tau}_{10}}{\tilde{\tau}_{00}\bar{h}_{00}^2} \left[\left(\frac{\bar{h}_{02}}{\bar{h}_{00}} - \frac{\bar{h}_{01}^2}{\bar{h}_{00}^2} \right) \frac{\bar{q}_{00}}{\bar{h}_{00}} + \frac{\bar{h}_{01}\bar{q}_{01}}{\bar{h}_{00}^2} - \frac{\bar{q}_{02}}{\bar{h}_{00}} \right] \\ &\quad - \frac{6}{\bar{h}_{00}^2} \left(\frac{\tilde{\tau}_{12}}{\tilde{\tau}_{00}} - \frac{\tilde{\tau}_{11}\tilde{\tau}_{01} + \tilde{\tau}_{10}\tilde{\tau}_{02}}{\tilde{\tau}_{00}^2} + \frac{\tilde{\tau}_{01}^2}{\tilde{\tau}_{00}^3} \right) \left(1 - \frac{2\bar{q}_{00}}{\bar{h}_{00}} \right) \\ &\quad - \frac{12\tilde{\bar{h}}_{11}}{\bar{h}_{00}^3} \left(1 - \frac{3\bar{q}_{00}}{\bar{h}_{00}} \right) + \frac{36\tilde{\bar{h}}_{10}}{\bar{h}_{00}^3} \left[\frac{\bar{h}_{01}}{\bar{h}_{00}} \left(1 - \frac{3\bar{q}_{00}}{\bar{h}_{00}} \right) + \frac{\bar{q}_{01}}{\bar{h}_{00}} \right] - \frac{12\bar{q}_{10}}{\bar{h}_{00}^3}, \end{aligned} \quad (\text{C.2.1c})$$

etc.

$$\text{at } \bar{\xi} = 0 :$$

$$O(1) : \quad \tilde{\bar{h}}_{10} = 0, \quad (\text{C.2.2a})$$

$$O(\bar{\ell}^{\frac{1}{2}}) : \quad \tilde{\bar{h}}_{11} = 0, \quad (\text{C.2.2b})$$

$$O(\bar{\ell}) : \quad \tilde{\bar{h}}_{12} = 0, \quad (\text{C.2.2c})$$

etc.

C.2.2 Inner equations

Recall the boundary-value problem,

$$\tilde{\tau}_0 \frac{d^3 \tilde{\bar{h}}_1}{d\tilde{\xi}^3} = -\frac{6\bar{\ell}^{\frac{1}{2}}\tilde{\tau}_1}{\tilde{\bar{h}}_0^2\tilde{\tau}_0} + \frac{12\bar{\ell}^{\frac{3}{2}}\tilde{q}_0\tilde{\tau}_1}{\tilde{\bar{h}}_0^3\tilde{\tau}_0} - \frac{12\bar{\ell}^{\frac{5}{2}}\tilde{q}_1}{\tilde{\bar{h}}_0^3} + \frac{36\bar{\ell}^3\tilde{\bar{h}}_1\tilde{q}_0}{\tilde{\bar{h}}_0^4}, \quad (3.6.22)$$

$$\text{as } \tilde{\xi} \rightarrow \infty : \quad \tilde{h}_1 \rightarrow \tilde{b}_1 - \tilde{b}_0 \tilde{\xi} + \bar{\ell}^{\frac{3}{2}} \tilde{b}_0, \quad (3.6.23)$$

$$\text{as } \tilde{\xi} \rightarrow -\infty : \quad \tilde{h}_1 \rightarrow \tilde{b}_1^* + \tilde{b}_0^* \tilde{\xi} + \bar{\ell}^{\frac{3}{2}} \tilde{b}_0^*, \quad (3.6.24)$$

Expanding gives,

$$O(1) : \quad \tilde{\tau}_{00} \frac{d^3 \tilde{h}_{10}}{d \tilde{\xi}^3} = 0, \quad (\text{C.2.3a})$$

$$O(\bar{\ell}^{\frac{1}{2}}) : \quad \tilde{\tau}_{00} \frac{d^3 \tilde{h}_{11}}{d \tilde{\xi}^3} = -\tilde{\tau}_{01} \frac{d^3 \tilde{h}_{10}}{d \tilde{\xi}^3} - \frac{6 \tilde{\tau}_{10}}{\tilde{\tau}_{00} \tilde{h}_{00}^2}, \quad (\text{C.2.3b})$$

$$O(\bar{\ell}) : \quad \tilde{\tau}_{00} \frac{d^3 \tilde{h}_{12}}{d \tilde{\xi}^3} = -\tilde{\tau}_{02} \frac{d^3 \tilde{h}_{10}}{d \tilde{\xi}^3} - \tilde{\tau}_{01} \frac{d^3 \tilde{h}_{11}}{d \tilde{\xi}^3} - \frac{6}{\tilde{h}_{00}^2} \left(\frac{\tilde{\tau}_{11}}{\tilde{\tau}_{00}} - \frac{\tilde{\tau}_{10} \tilde{\tau}_{01}}{\tilde{\tau}_{00}^2} \right) + \frac{12 \tilde{\tau}_{10} \tilde{h}_{01}}{\tilde{\tau}_{00} \tilde{h}_{00}^3}, \quad (\text{C.2.3c})$$

etc.

as $\tilde{\xi} \rightarrow \infty :$

$$O(1) : \quad \tilde{h}_{10} \rightarrow \tilde{b}_{10} - \tilde{b}_{00} \tilde{\xi}, \quad (\text{C.2.4a})$$

$$O(\bar{\ell}^{\frac{1}{2}}) : \quad \tilde{h}_{11} \rightarrow \tilde{b}_{11} - \tilde{b}_{01} \tilde{\xi}, \quad (\text{C.2.4b})$$

$$O(\bar{\ell}) : \quad \tilde{h}_{12} \rightarrow \tilde{b}_{12} - \tilde{b}_{02} \tilde{\xi}, \quad (\text{C.2.4c})$$

etc.

as $\tilde{\xi} \rightarrow -\infty :$

$$O(1) : \quad \tilde{h}_{10} \rightarrow \tilde{b}_{10}^* + \tilde{b}_{00}^* \tilde{\xi}, \quad (\text{C.2.5a})$$

$$O(\bar{\ell}^{\frac{1}{2}}) : \quad \tilde{h}_{11} \rightarrow \tilde{b}_{11}^* + \tilde{b}_{01}^* \tilde{\xi}, \quad (\text{C.2.5b})$$

$$O(\bar{\ell}) : \quad \tilde{h}_{12} \rightarrow \tilde{b}_{12}^* + \tilde{b}_{02}^* \tilde{\xi}, \quad (\text{C.2.5c})$$

etc.

C.2.3 Matching conditions

Recall the matching conditions,

$$\lim_{\tilde{\xi} \rightarrow 0^+} \tilde{h}_1 = \lim_{\tilde{\xi} \rightarrow \infty} \tilde{h}_1, \quad (3.6.25a)$$

$$\lim_{\tilde{\xi} \rightarrow 0^-} \tilde{h}_1 = \lim_{\tilde{\xi}^* \rightarrow -\infty} \tilde{h}_1. \quad (3.6.25b)$$

Expanding gives,

at $\tilde{\xi} = 0^+, \tilde{\xi} \rightarrow \infty$:

$$O(1) : \quad \tilde{h}_{10}(0^+) = \lim_{\tilde{\xi} \rightarrow \infty} \tilde{h}_{10}, \quad (C.2.7a)$$

$$O(\bar{\ell}^{\frac{1}{2}}) : \quad \left(\tilde{h}_{11} + \bar{\xi} \frac{d\tilde{h}_{10}}{d\tilde{\xi}} \right) \Big|_{\tilde{\xi}=0^+} = \lim_{\tilde{\xi} \rightarrow \infty} \tilde{h}_{11}, \quad (C.2.7b)$$

$$O(\bar{\ell}) : \quad \left(\tilde{h}_{12} + \bar{\xi} \frac{d\tilde{h}_{11}}{d\tilde{\xi}} + \frac{\bar{\xi}^2}{2} \frac{d^2\tilde{h}_{10}}{d\tilde{\xi}^2} \right) \Big|_{\tilde{\xi}=0^+} = \lim_{\tilde{\xi} \rightarrow \infty} \tilde{h}_{12}, \quad (C.2.7c)$$

etc.

at $\tilde{\xi} = 0^-, \tilde{\xi} \rightarrow -\infty$:

$$O(1) : \quad \tilde{h}_{10}(0^-) = \lim_{\tilde{\xi} \rightarrow -\infty} \tilde{h}_{10}, \quad (C.2.8a)$$

$$O(\bar{\ell}^{\frac{1}{2}}) : \quad \left(\tilde{h}_{11} + \bar{\xi} \frac{d\tilde{h}_{10}}{d\tilde{\xi}} \right) \Big|_{\tilde{\xi}=0^-} = \lim_{\tilde{\xi} \rightarrow -\infty} \tilde{h}_{11}, \quad (C.2.8b)$$

$$O(\bar{\ell}) : \quad \left(\tilde{h}_{12} + \bar{\xi} \frac{d\tilde{h}_{11}}{d\tilde{\xi}} + \frac{\bar{\xi}^2}{2} \frac{d^2\tilde{h}_{10}}{d\tilde{\xi}^2} \right) \Big|_{\tilde{\xi}=0^-} = \lim_{\tilde{\xi} \rightarrow -\infty} \tilde{h}_{12}, \quad (C.2.8c)$$

etc.

C.2.4 Solution

The starting point of the solution procedure is the $O(1)$ inner problem. The particular solution to (C.2.3a), (C.2.4a), and (C.2.5a) with (C.1.15) is

$$\tilde{h}_{10} = \begin{cases} \tilde{b}_{10} - \tilde{\xi} & \text{for } \tilde{\xi} \in (0^+, \infty), \\ \tilde{b}_{10}^* + \tilde{\xi} & \text{for } \tilde{\xi} \in (-\infty, 0^-). \end{cases} \quad (C.2.9)$$

The integration constants \tilde{b}_{10} and \tilde{b}_{10}^* are to be determined from matching conditions. The $O(1)$ outer problem is governed by (C.2.1a), which upon substituting (C.1.13), (C.1.21), and (C.1.36)

reduces to

$$\frac{d^3 \tilde{\tilde{h}}_{10}}{d\tilde{\xi}^3} = -\frac{4\sqrt{2}\tilde{\tau}_{10}}{\pi(1+\frac{1}{2}\tilde{\xi}^2)^2} \left(3 - \frac{4}{1+\frac{1}{2}\tilde{\xi}^2}\right), \quad (\text{C.2.10})$$

The boundary conditions for $\tilde{\tilde{h}}_{10}$ are given by (C.2.2a), (C.2.7a), and (C.2.8a):

$$\text{at } \tilde{\xi} = 0 : \quad \tilde{\tilde{h}}_{10} = 0, \quad (\text{C.2.11})$$

$$\text{as } \tilde{\xi} \rightarrow \infty : \quad \tilde{\tilde{h}}_{10} \rightarrow \tilde{b}_{10}, \quad (\text{C.2.12})$$

$$\text{as } \tilde{\xi} \rightarrow -\infty : \quad \tilde{\tilde{h}}_{10} \rightarrow \tilde{b}_{10}^*. \quad (\text{C.2.13})$$

The particular solution is

$$\tilde{\tilde{h}}_{10} = -\frac{8\tilde{\tau}_{10}}{\pi} \arctan\left(\frac{\tilde{\xi}}{\sqrt{2}}\right), \quad (\text{C.2.14})$$

with

$$\tilde{b}_{10} = -\tilde{b}_{10}^* = -4\tilde{\tau}_{10}. \quad (\text{C.2.15})$$

Returning to the inner region, the $O(\bar{\ell}^{\frac{1}{2}})$ inner problem is governed by

$$\frac{d^3 \tilde{\tilde{h}}_{11}}{d\tilde{\xi}^3} = -\frac{48\sqrt{2}\tilde{\tau}_{10}}{\pi\tilde{\xi}^4}, \quad (\text{C.2.16})$$

with the boundary conditions,

$$\text{as } \tilde{\xi} \rightarrow \infty : \quad \tilde{\tilde{h}}_{11} \rightarrow \tilde{b}_{11} - 2 \times 2^{\frac{1}{4}}\sqrt{\pi}\tilde{\xi}, \quad (\text{C.2.17})$$

$$\text{as } \tilde{\xi} \rightarrow -\infty : \quad \tilde{\tilde{h}}_{11} \rightarrow \tilde{b}_{11}^* - 2 \times 2^{\frac{1}{4}}\sqrt{\pi}\tilde{\xi}. \quad (\text{C.2.18})$$

The particular solution is

$$\tilde{\tilde{h}}_{11} = \begin{cases} \tilde{b}_{11} - 2 \times 2^{\frac{1}{4}}\sqrt{\pi}\tilde{\xi} + \frac{8\sqrt{2}\tilde{\tau}_{10}}{\pi\tilde{\xi}} & \text{for } \tilde{\xi} \in (0^+, \infty), \\ \tilde{b}_{11}^* - 2 \times 2^{\frac{1}{4}}\sqrt{\pi}\tilde{\xi} + \frac{8\sqrt{2}\tilde{\tau}_{10}}{\pi\tilde{\xi}} & \text{for } \tilde{\xi} \in (-\infty, 0^-). \end{cases} \quad (\text{C.2.19})$$

The $O(\bar{\ell}^{\frac{1}{2}})$ outer problem is governed by

$$\frac{d^3 \tilde{\tilde{h}}_{11}}{d\tilde{\xi}^3} = \frac{48\sqrt{2}\tilde{\tau}_{10}}{\tilde{\tau}_{00}^3(1+\frac{1}{2}\tilde{\xi}^2)^3} \left(1 - \frac{2}{1+\frac{1}{2}\tilde{\xi}^2}\right) \arctan\left(\frac{\tilde{\xi}}{\sqrt{2}}\right) - \frac{2\tilde{\tau}_{11}}{\tilde{\tau}_{00}^2(1+\frac{1}{2}\tilde{\xi}^2)^2} \left(3 - \frac{4}{1+\frac{1}{2}\tilde{\xi}^2}\right), \quad (\text{C.2.20})$$

with the boundary condition,

$$\text{at } \tilde{\xi} = 0 : \quad \tilde{\tilde{h}}_{11} = 0. \quad (\text{C.2.21})$$

The inner solution (C.2.19) induces a $1/\tilde{\xi}$ term, which cannot be matched to the solution of (C.2.20) using van Dyke's matching rule. Therefore, matching to the outer solution must be done by intermediate variable [77]. Without going into the details, matching the outer solution to the inner solution yields the following solvability conditions for (C.2.20):

$$\tilde{\tau}_{10} = -\sqrt{\frac{\pi}{8\sqrt{2}}}, \quad (\text{C.2.22})$$

$$\tilde{b}_{11} = -\frac{8\sqrt{2}}{3\pi} - 4\tilde{\tau}_{11}, \quad (\text{C.2.23})$$

$$\tilde{b}_{11}^* = -\frac{8\sqrt{2}}{3\pi} + 4\tilde{\tau}_{11}. \quad (\text{C.2.24})$$

With little additional effort, it may be shown that

$$\tilde{\tau}_{11} = 0. \quad (\text{C.2.25})$$

Thus, the particular solution for \tilde{h}_{11} is

$$\begin{aligned} \tilde{h}_{11} = & -\frac{3}{2}\sqrt{2}\pi\bar{\xi}^2 + \frac{11}{3}(\sqrt{2}/\pi)\left(\frac{\bar{\xi}^2}{1+\frac{1}{2}\bar{\xi}^2}\right) + \left(22 - \frac{8}{1+\frac{1}{2}\bar{\xi}^2}\right)\frac{\bar{\xi}}{\pi}\arctan\left(\frac{\bar{\xi}}{\sqrt{2}}\right) \\ & + \frac{6\sqrt{2}\bar{\xi}^2}{\pi}\arctan^2\left(\frac{\bar{\xi}}{\sqrt{2}}\right), \end{aligned} \quad (\text{C.2.26})$$

It is noteworthy that $\tilde{h}_{10} = \frac{1}{2}\bar{h}_{01}$ and $\tilde{h}_{11} = \bar{h}_{02}$ [cf. (C.1.22) and (C.1.38)]. The solution for \bar{q}_{10} , which requires higher-order corrections in both regions, will not be pursued here.

The solution for \bar{h}_1 up to $O(\bar{\ell}^{\frac{1}{2}})$ is given in the main text and is obtained from composing the outer and inner solutions:

$$\begin{aligned} \bar{h}_1 = & \left(\frac{\sqrt{2}}{\pi\bar{\ell}}\right)^{\frac{1}{2}} \left\{ 2\arctan\left(\frac{\bar{\xi}}{\sqrt{2}}\right) + \left(\frac{\sqrt{2}\bar{\ell}}{\pi}\right)^{\frac{1}{2}} \left[-\frac{3\pi^2\bar{\xi}^2}{2} + \frac{11}{3}\left(\frac{\bar{\xi}^2}{1+\frac{1}{2}\bar{\xi}^2}\right) \right. \right. \\ & \left. \left. + \left(22 - \frac{8}{1+\frac{1}{2}\bar{\xi}^2}\right)\frac{\bar{\xi}}{\sqrt{2}}\arctan\left(\frac{\bar{\xi}}{\sqrt{2}}\right) + 6\bar{\xi}^2\arctan^2\left(\frac{\bar{\xi}}{\sqrt{2}}\right) \right] + O\left(\frac{\sqrt{2}\bar{\ell}}{\pi}\right) \right\}. \end{aligned} \quad (\text{3.6.26})$$

Higher-order corrections are not pursued here. It is worth reiterating that the results just derived are strictly valid for $\bar{\beta} = 0$ and $\epsilon^{\frac{1}{2}}$, $\bar{\ell}^{\frac{1}{2}}$ both small. For $\bar{\beta} \neq 0$, analytical solutions are not possible and one has to resort to numerical methods in order to compute each term in the double-series expansion with respect to $\epsilon^{\frac{1}{2}}$ and $\bar{\ell}^{\frac{1}{2}}$. However, for quasi-spherical vesicles at high confinement, the solution is relatively insensitive to the value of β (see Figure 3.8c). Hence, bending elasticity can typically be neglected if $\epsilon^{\frac{1}{2}}$ and $\bar{\ell}^{\frac{1}{2}}$ are both small.

Appendix D

Periodic fundamental solutions of creeping flow

In Chapters 4 and 5, we employed the boundary integral equations using Green's functions \mathcal{G} (for the velocity) and \mathcal{T} (for the stress) based on the periodic fundamental solution of the Stokes equations. In this appendix, we derive the fundamental tensors from the periodic boundary-value problem of Stokes flow, following closely the original derivation by Hasimoto [73]. As the derivation requires a great deal of tensorial algebra, we shall adopt Einstein notation for representing vectors and tensors. Thus, all tensors will be represented by their indexed components with indices i, j, k, l, \dots and summation is implied over repeated indices. In this notation, the Cartesian coordinates are denoted by $x_1 = x$, $x_2 = y$, and $x_3 = z$.

D.1 Periodic boundary-value problem for the Green's functions

Consider the rectangular cuboid illustrated in Figure 4.2 with dimensions $L_1 \times L_2 \times L_3$. The cuboid is periodically replicated in the x_1 , x_2 , and x_3 directions.¹ The region bounded by a periodic cell is denoted by \mathcal{V} , where

$$\mathcal{V} = [0, L_1] \times [0, L_2] \times [0, L_3]. \quad (\text{D.1.1})$$

The volume of the cell is $\Omega = L_1 L_2 L_3$. In the boundary integral formulation, point singularities (e.g., forces, couples, stresslets, sources, and so on) are embedded in the surfaces contained within the periodic cell, forming surface density fields of unknown strengths. These surface density fields are weighted by *Green's functions* (or fundamental solutions), which satisfy the periodic boundary

¹In general, we may choose a periodic lattice cell that is not rectangular, e.g., a parallelepiped. Rectangularity affords a Cartesian basis in both the physical and reciprocal lattices, which simplifies the analysis.

conditions. The objective of this section is to derive these Green's functions.

The appropriate Green's functions for the velocity \mathbf{u} and stress $\boldsymbol{\sigma} = -p\delta + \mu[\nabla\mathbf{u} + (\nabla\mathbf{u})^\dagger]$ satisfy the creeping flow equations with a point-force inhomogeneity distributed periodically at lattice sites $\mathbf{x}_0 + \mathbf{x}^{(\mathbf{n})}$, where

$$x_i^{(\mathbf{n})} = n_1 L_1 \delta_{i1} + n_2 L_2 \delta_{i2} + n_3 L_3 \delta_{i3} \quad (\text{D.1.2})$$

and $n_j = 0, \pm 1, \pm 2, \dots$. The boundary-value problem with periodic boundary conditions reads

$$\frac{\partial u_j}{\partial x_j} = 0, \quad (\text{D.1.3a})$$

$$\frac{\partial \sigma_{ji}}{\partial x_j} = -\frac{\partial p}{\partial x_i} + \mu \frac{\partial^2 u_i}{\partial x_j \partial x_j} = -F_i \delta(\mathbf{x} - \mathbf{x}_0), \quad (\text{D.1.3b})$$

$$u_i(\mathbf{x}) = u_i(\mathbf{x} + \mathbf{x}^{(\mathbf{n})}), \quad (\text{D.1.3c})$$

$$\frac{\partial p}{\partial x_i}(\mathbf{x}) = \frac{\partial p}{\partial x_i}(\mathbf{x} + \mathbf{x}^{(\mathbf{n})}), \quad (\text{D.1.3d})$$

where \mathbf{F} is the strength of the point force and $\delta(\mathbf{x})$ is the Dirac delta function. The Dirac delta function has the following properties:

$$\delta(\mathbf{x} - \mathbf{x}_0) = 0 \quad \text{for } \mathbf{x} \neq \mathbf{x}_0, \quad (\text{D.1.4a})$$

$$\int_{\mathcal{V}} \psi(\mathbf{x}) \delta(\mathbf{x} - \mathbf{x}_0) d^3x = \begin{cases} \psi(\mathbf{x}_0) & \text{for } \mathbf{x}_0 \in \mathcal{V}, \\ 0 & \text{for } \mathbf{x}_0 \notin \mathcal{V}, \end{cases} \quad (\text{D.1.4b})$$

where $\psi(\mathbf{x})$ is an analytic function (regular everywhere in \mathcal{V} , the region of one periodic cell). Note that we may alternatively formulate the boundary-value problem by removing the source term on the right-hand side of (D.1.3b) and instead enforcing the integral condition,

$$\int_{\partial\mathcal{V}_\epsilon} \sigma_{ij}(\mathbf{x}) \hat{n}_j(\mathbf{x}) dS(\mathbf{x}) = F_i, \quad (\text{D.1.5})$$

where integration is carried out over an arbitrary surface (with unit normal $\hat{\mathbf{n}}$) bounding a region \mathcal{V}_ϵ that contains the source point \mathbf{x}_0 .

D.1.1 Fourier transform of the creeping flow equations

Hasimoto derived the solution of the periodic point-force boundary-value problem by means of the Fourier transform [73]. We reproduce his derivation below. Let

$$r_i = x_i - x_{i0} \quad (\text{D.1.6})$$

denote the vector pointing from the source point to the field point and

$$k_i = (n_1/L_1)\delta_{i1} + (n_2/L_2)\delta_{i2} + (n_3/L_3)\delta_{i3} \quad (\text{D.1.7})$$

denote the wavevector of the reciprocal space. In this appendix and in Appendix E, we shall denote the modulus of \mathbf{r} by r (though usually this variable is reserved for the modulus of \mathbf{x}). Since the periodic cell is rectangular, the basis vectors for the physical and reciprocal lattices are the Cartesian basis vectors.

For some arbitrary field $\psi(\mathbf{x})$ whose Fourier transform is $\tilde{\psi}(\mathbf{k})$, we define the Fourier transform pair as follows:

$$\tilde{\psi}(\mathbf{k}) = \int_{\mathcal{V}} \psi(\mathbf{x}) \exp(2\pi i \mathbf{k} \cdot \mathbf{r}) d^3x, \quad (\text{D.1.8a})$$

$$\psi(\mathbf{x}) = \frac{1}{(2\pi)^3} \int_{\tilde{\mathcal{V}}} \tilde{\psi}(\mathbf{k}) \exp(-2\pi i \mathbf{k} \cdot \mathbf{r}) d^3k, \quad (\text{D.1.8b})$$

where $\tilde{\mathcal{V}}$ denotes the reciprocal volume. Here, we use an “overtilde” to denote a Fourier transformed variable. The Fourier waves are of orthogonality,

$$\frac{1}{\Omega} \int_{\mathcal{V}} \exp(2\pi i \mathbf{k} \cdot \mathbf{r}) \exp(-2\pi i \mathbf{k}' \cdot \mathbf{r}) d^3x = \begin{cases} 1 & \text{for } \mathbf{k} = \mathbf{k}', \\ 0 & \text{for } \mathbf{k} \neq \mathbf{k}'. \end{cases} \quad (\text{D.1.9})$$

Since the flow field is periodic, \mathbf{u} and $-\nabla p$ may expanded in Fourier series:

$$u_i(\mathbf{x}) = \sum_{\mathbf{k}} \tilde{u}_i^{(\mathbf{k})} \exp(-2\pi i \mathbf{k} \cdot \mathbf{r}), \quad (\text{D.1.10})$$

$$-\frac{\partial p}{\partial x_i}(\mathbf{x}) = \sum_{\mathbf{k}} \tilde{g}_i^{(\mathbf{k})} \exp(-2\pi i \mathbf{k} \cdot \mathbf{r}), \quad (\text{D.1.11})$$

where $\tilde{\mathbf{u}}^{(\mathbf{k})}$ and $\tilde{\mathbf{g}}^{(\mathbf{k})}$ are the Fourier coefficients.

Multiplying each term in (D.1.3a)-(D.1.3b) by $(1/\Omega) \exp(2\pi i \mathbf{k} \cdot \mathbf{r}) d^3x$ and integrating over \mathcal{V} yields the following transforms:

$$\begin{aligned} \int_{\mathcal{V}} \frac{1}{\Omega} \exp(2\pi i \mathbf{k} \cdot \mathbf{r}) \frac{\partial u_i}{\partial x_i} d^3x &= \frac{1}{\Omega} \int_{\mathcal{V}} \exp(2\pi i \mathbf{k} \cdot \mathbf{r}) \frac{\partial}{\partial x_i} \sum_{\mathbf{k}'} \tilde{u}_i^{(\mathbf{k}')} \exp(-2\pi i \mathbf{k}' \cdot \mathbf{r}) d^3x \\ &= \frac{1}{\Omega} \sum_{\mathbf{k}'} \tilde{u}_i^{(\mathbf{k}')} \int_{\mathcal{V}} \exp(2\pi i \mathbf{k} \cdot \mathbf{r}) \frac{\partial}{\partial x_i} \exp(-2\pi i \mathbf{k}' \cdot \mathbf{r}) d^3x \\ &= -\frac{2\pi i}{\Omega} \sum_{\mathbf{k}'} k'_i \tilde{u}_i^{(\mathbf{k}')} \int_{\mathcal{V}} \exp(2\pi i \mathbf{k} \cdot \mathbf{r}) \exp(-2\pi i \mathbf{k}' \cdot \mathbf{r}) d^3x \\ &= -2\pi i k_i \tilde{u}_i^{(\mathbf{k})} \quad \text{by (D.1.9),} \end{aligned} \quad (\text{D.1.12})$$

$$\begin{aligned}
\int_{\gamma} \frac{\mu}{\Omega} \exp(2\pi i \mathbf{k} \cdot \mathbf{r}) \frac{\partial^2 u_i}{\partial x_j \partial x_j} d^3x &= \frac{1}{\Omega} \int_{\gamma} \exp(2\pi i \mathbf{k} \cdot \mathbf{r}) \frac{\partial^2}{\partial x_j \partial x_j} \sum_{\mathbf{k}'} \tilde{u}_i^{(\mathbf{k}')} \exp(-2\pi i \mathbf{k}' \cdot \mathbf{r}) d^3x \\
&= \frac{\mu}{\Omega} \sum_{\mathbf{k}'} \tilde{u}_i^{(\mathbf{k}')} \int_{\gamma} \exp(2\pi i \mathbf{k} \cdot \mathbf{r}) \frac{\partial^2}{\partial x_j \partial x_j} \exp(-2\pi i \mathbf{k}' \cdot \mathbf{r}) d^3x \\
&= -\frac{4\pi^2 \mu}{\Omega} \sum_{\mathbf{k}'} k'^2 \tilde{u}_i^{(\mathbf{k}')} \int_{\gamma} \exp(2\pi i \mathbf{k} \cdot \mathbf{r}) \exp(-2\pi i \mathbf{k}' \cdot \mathbf{r}) d^3x \\
&= -4\pi^2 \mu k^2 \tilde{u}_i^{(\mathbf{k})} \quad \text{by (D.1.9),}
\end{aligned} \tag{D.1.13}$$

$$\begin{aligned}
-\int_{\gamma} \frac{1}{\Omega} \exp(2\pi i \mathbf{k} \cdot \mathbf{r}) \frac{\partial p}{\partial x_i} d^3x &= \frac{1}{\Omega} \int_{\gamma} \exp(2\pi i \mathbf{k} \cdot \mathbf{r}) \sum_{\mathbf{k}'} \tilde{g}_i^{(\mathbf{k}')} \exp(-2\pi i \mathbf{k}' \cdot \mathbf{r}) d^3x \\
&= \frac{1}{\Omega} \sum_{\mathbf{k}'} \tilde{g}_i^{(\mathbf{k}')} \int_{\gamma} \exp(2\pi i \mathbf{k} \cdot \mathbf{r}) \exp(-2\pi i \mathbf{k}' \cdot \mathbf{r}) d^3x \\
&= \tilde{g}_i^{(\mathbf{k})} \quad \text{by (D.1.9),}
\end{aligned} \tag{D.1.14}$$

$$\begin{aligned}
-\int_{\gamma} \frac{1}{\Omega} \exp(2\pi i \mathbf{k} \cdot \mathbf{r}) F_i \delta(\mathbf{r}) d^3x &= -\frac{F_i}{\Omega} \int_{\gamma} \exp(2\pi i \mathbf{k} \cdot \mathbf{r}) \delta(\mathbf{r}) d^3x \\
&= -\frac{F_i}{\Omega} \quad \text{by (D.1.4),}
\end{aligned} \tag{D.1.15}$$

Thus, the Fourier-transformed boundary-value problem reads,

$$k_j \tilde{u}_j^{(\mathbf{k})} = 0, \tag{D.1.16a}$$

$$\tilde{g}_i^{(\mathbf{k})} - 4\pi^2 \mu k^2 \tilde{u}_i^{(\mathbf{k})} = -\frac{F_i}{\Omega}. \tag{D.1.16b}$$

By Fourier transforming the creeping flow equations, differential operations in physical space have been converted to algebraic operations in the reciprocal space. This transformation facilitates the solution for the velocity and pressure gradient. Note that the periodic boundary conditions are automatically satisfied through the Fourier representation.

D.1.2 Solution for the velocity and pressure gradient in the reciprocal space

We begin by solving for the pressure gradient. First, we consider the degenerate wavevector,

$$k_i = 0,$$

whence the equation of motion reduces to

$$\tilde{g}_i^{(0)} = -\frac{F_i}{\Omega}, \quad (\text{D.1.17})$$

which implies that there is a mean pressure gradient in the flow. Note that this is why it was important to Fourier transform the pressure *gradient* rather than the pressure, for the presence of the mean pressure gradient is easily deduced. Disregard of this term would lead to divergence of the velocity field.

Now consider all other wavevectors,

$$k_i \neq 0.$$

First, we express $\tilde{\mathbf{g}}^{(\mathbf{k})}$ in terms of its projections parallel and perpendicular to \mathbf{k}/k ,

$$\tilde{g}_i^{(\mathbf{k})} = \frac{k_i k_j}{k^2} \tilde{g}_j^{(\mathbf{k})} + \left(\delta_{ij} - \frac{k_i k_j}{k^2} \right) \tilde{g}_j^{(\mathbf{k})}, \quad k_i \neq 0. \quad (\text{D.1.18})$$

The second term may be shown to vanish by recalling that, since

$$\epsilon_{ijk} \frac{\partial^2 p}{\partial x_j \partial x_k} = 0,$$

(that is, the curl of the gradient vanishes) then

$$\epsilon_{ijk} k_j \tilde{g}_k^{(\mathbf{k})} = 0. \quad (\text{D.1.19})$$

Multiplying the last equation by $(k_p/k^2)\epsilon_{pqi}$ then gives

$$\begin{aligned} \epsilon_{pqi} \epsilon_{ijk} \frac{k_j k_p}{k^2} \tilde{g}_k^{(\mathbf{k})} &= (\delta_{pj} \delta_{qk} - \delta_{pk} \delta_{qj}) \frac{k_j k_p}{k^2} \tilde{g}_k^{(\mathbf{k})} \\ &= \left(\delta_{qk} - \frac{k_q k_k}{k^2} \right) \tilde{g}_k^{(\mathbf{k})} = 0, \end{aligned}$$

which implies that the tangential projection of $\tilde{\mathbf{g}}^{(\mathbf{k})}$ vanishes and, as previously indicated, is simply a restatement that the pressure gradient is irrotational. Thus,

$$\tilde{g}_i^{(\mathbf{k})} = \frac{k_i k_j}{k^2} \tilde{g}_j^{(\mathbf{k})}, \quad k_i \neq 0. \quad (\text{D.1.20})$$

Multiplying the Fourier transformed equation of motion by k_i and using the equation of continuity gives

$$k_i \tilde{g}_i^{(\mathbf{k})} = -\frac{k_i F_i}{\Omega}, \quad (\text{D.1.21})$$

which, from the previous result, implies that

$$\tilde{g}_i^{(\mathbf{k})} = -\frac{F_j}{\Omega} \frac{k_j k_i}{k^2}, \quad k_i \neq 0. \quad (\text{D.1.22})$$

Inserting this result into the equation of motion and rearranging then gives the solution for the velocity coefficients associated with non-degenerate wavevectors,

$$\tilde{u}_i^{(\mathbf{k})} = \frac{F_j}{4\pi^2 \mu \Omega} \left(\frac{\delta_{ji}}{k^2} - \frac{k_j k_i}{k^4} \right), \quad k_i \neq 0. \quad (\text{D.1.23})$$

D.1.3 Inverting the Fourier transforms

It remains to invert the Fourier transforms, thus expressing the physical components of \mathbf{u} and $-\nabla p$ in terms of their Fourier coefficients. Again, we start with the pressure gradient. Multiplying $\tilde{\mathbf{g}}^{(\mathbf{k})}$ by $\exp(-2\pi i \mathbf{k} \cdot \mathbf{r})$ and summing over \mathbf{k} gives

$$\begin{aligned} -\frac{\partial p}{\partial x_i}(\mathbf{x}) &= \sum_{\mathbf{k}} \tilde{g}_i^{(\mathbf{k})} \exp(-2\pi i \mathbf{k} \cdot \mathbf{r}) \\ &= -\frac{F_i}{\Omega} - \frac{F_j}{\Omega} \sum_{\mathbf{k} \neq \mathbf{0}} \frac{k_j k_i}{k^2} \exp(-2\pi i \mathbf{k} \cdot \mathbf{r}) \\ &= -\frac{F_i}{\Omega} + \frac{F_j}{4\pi^2 \Omega} \frac{\partial^2}{\partial x_j \partial x_i} \sum_{\mathbf{k} \neq \mathbf{0}} \frac{\exp(-2\pi i \mathbf{k} \cdot \mathbf{r})}{k^2}. \end{aligned} \quad (\text{D.1.24})$$

Now we invert the transform for the velocity field. Multiplying $\tilde{\mathbf{u}}^{(\mathbf{k})}$ by $\exp(-2\pi i \mathbf{k} \cdot \mathbf{r})$ and summing over \mathbf{k} gives

$$\begin{aligned} u_i(\mathbf{x}) &= \sum_{\mathbf{k}} \tilde{u}_i^{(\mathbf{k})} \exp(-2\pi i \mathbf{k} \cdot \mathbf{r}) \\ &= \langle u_i \rangle + \frac{F_j}{4\pi^2 \mu \Omega} \sum_{\mathbf{k} \neq \mathbf{0}} \left(\frac{\delta_{ji}}{k^2} - \frac{k_j k_i}{k^4} \right) \exp(-2\pi i \mathbf{k} \cdot \mathbf{r}) \\ &= \langle u_i \rangle + \frac{F_i}{4\pi^2 \mu \Omega} \sum_{\mathbf{k} \neq \mathbf{0}} \frac{\exp(-2\pi i \mathbf{k} \cdot \mathbf{r})}{k^2} + \frac{F_j}{16\pi^4 \mu \Omega} \frac{\partial^2}{\partial x_j \partial x_i} \sum_{\mathbf{k} \neq \mathbf{0}} \frac{\exp(-2\pi i \mathbf{k} \cdot \mathbf{r})}{k^4}, \end{aligned} \quad (\text{D.1.25})$$

where the first term is the mean velocity (associated with $\mathbf{k} = \mathbf{0}$) due to the mean pressure gradient,

$$\langle u_i \rangle = \frac{1}{\Omega} \int_{\mathcal{V}} u_i(\mathbf{x}) d^3 \mathbf{x}. \quad (\text{D.1.26})$$

We now define the sums,

$$\Sigma_1 = \frac{1}{\pi \Omega} \sum_{\mathbf{k} \neq \mathbf{0}} \frac{\exp(-2\pi i \mathbf{k} \cdot \mathbf{r})}{k^2}, \quad \Sigma_2 = -\frac{1}{4\pi^3 \Omega} \sum_{\mathbf{k} \neq \mathbf{0}} \frac{\exp(-2\pi i \mathbf{k} \cdot \mathbf{r})}{k^4}, \quad (\text{D.1.27})$$

The sums Σ_1 and Σ_2 are given by [73] and satisfy the boundary-value problem,

$$\frac{\partial^2 \Sigma_2}{\partial x_j \partial x_j} = \Sigma_1, \quad (\text{D.1.28a})$$

$$\frac{\partial^2 \Sigma_1}{\partial x_j \partial x_j} = -4\pi \left(\delta(\mathbf{x} - \mathbf{x}_0) - \frac{1}{\Omega} \right), \quad (\text{D.1.28b})$$

$$\Sigma_2(\mathbf{x}) = \Sigma_2(\mathbf{x} + \mathbf{x}^{(n)}), \quad (\text{D.1.28c})$$

$$\Sigma_1(\mathbf{x}) = \Sigma_1(\mathbf{x} + \mathbf{x}^{(n)}). \quad (\text{D.1.28d})$$

The solutions for \mathbf{u} and $-\nabla p$ may now be expressed in the form,

$$u_i(\mathbf{x}) = \langle u_i \rangle + \frac{F_j}{4\pi\mu} \left(\delta_{ji} \Sigma_1 - \frac{\partial^2 \Sigma_2}{\partial x_j \partial x_i} \right), \quad (\text{D.1.29})$$

$$-\frac{\partial p}{\partial x_i}(\mathbf{x}) = -\frac{F_i}{\Omega} + \frac{F_j}{4\pi} \frac{\partial^2 \Sigma_1}{\partial x_j \partial x_i}. \quad (\text{D.1.30})$$

Note that the second equation may be integrated to give the pressure,

$$p(\mathbf{x}) = \frac{F_j x_j}{\Omega} - \frac{F_j}{4\pi} \frac{\partial \Sigma_1}{\partial x_j}. \quad (\text{D.1.31})$$

modulo an arbitrary constant (a reference pressure).

It is important to realize that, although the point forces are periodically distributed in the physical lattice, the fact that all of the point forces are *directed* (breaking symmetry) induces a mean pressure gradient,

$$\left\langle \frac{\partial p}{\partial x_i} \right\rangle = \frac{1}{\Omega} \int_{\gamma} \frac{\partial p}{\partial x_i}(\mathbf{x}) d^3x = \frac{F_i}{\Omega}. \quad (\text{D.1.32})$$

D.1.4 Green's functions for the velocity, pressure, and stress

The above solutions for the velocity \mathbf{u} and pressure p may be recast in the form

$$u_i(\mathbf{x}) = \langle u_i \rangle + \frac{F_j \mathcal{G}_{ji}(\mathbf{x}, \mathbf{x}_0)}{8\pi\mu}, \quad (\text{D.1.33a})$$

$$p(\mathbf{x}) = \frac{F_j \mathcal{P}_j(\mathbf{x}, \mathbf{x}_0)}{8\pi}, \quad (\text{D.1.33b})$$

where

$$\mathcal{G}_{ij}(\mathbf{x}, \mathbf{x}_0) = 2 \left(\delta_{ij} \Sigma_1 - \frac{\partial^2 \Sigma_2}{\partial x_i \partial x_j} \right) \quad (\text{D.1.34a})$$

is the Green's function for the velocity and

$$\mathcal{P}_i(\mathbf{x}, \mathbf{x}_0) = 2 \left(\frac{4\pi x_i}{\Omega} - \frac{\partial \Sigma_1}{\partial x_i} \right) \quad (\text{D.1.34b})$$

is the Green's functions for the pressure. The Green's function for the stress is denoted by \mathcal{T} and is related to \mathcal{G} and \mathcal{P} by,

$$\begin{aligned}\mathcal{T}_{ijk}(\mathbf{x}, \mathbf{x}_0) &= -\mathcal{P}_j \delta_{ik} + \frac{\partial \mathcal{G}_{ij}}{\partial x_k} + \frac{\partial \mathcal{G}_{kj}}{\partial x_i}, \\ &= 2 \left[-\frac{4\pi x_j \delta_{ik}}{\Omega} + \left(\delta_{ik} \frac{\partial}{\partial x_j} + \delta_{ij} \frac{\partial}{\partial x_k} + \delta_{kj} \frac{\partial}{\partial x_i} \right) \Sigma_1 - 2 \frac{\partial^3 \Sigma_2}{\partial x_i \partial x_j \partial x_k} \right],\end{aligned}\quad (\text{D.1.34c})$$

whence,

$$\sigma_{ik}(\mathbf{x}) = \frac{F_j \mathcal{T}_{ijk}(\mathbf{x})}{8\pi}. \quad (\text{D.1.35})$$

Although the solution for the velocity is periodic in x_1 , x_2 , and x_3 , the pressure and stress contain both a linear part and a periodic part. The periodic part of \mathcal{P} and \mathcal{T} is denoted by \mathcal{P}^p and \mathcal{T}^p , respectively. These Green's functions are defined by

$$\mathcal{P}_i(\mathbf{x}, \mathbf{x}_0) = \frac{8\pi x_i}{\Omega} + \mathcal{P}_i^p(\mathbf{x}, \mathbf{x}_0), \quad (\text{D.1.36})$$

$$\mathcal{T}_{ijk}(\mathbf{x}, \mathbf{x}_0) = -\frac{8\pi x_j \delta_{ik}}{\Omega} + \mathcal{T}_{ijk}^p(\mathbf{x}, \mathbf{x}_0). \quad (\text{D.1.37})$$

The Green's functions \mathcal{G} , \mathcal{P}^p , and \mathcal{T}^p are periodic and have zero mean, viz.,

$$\mathcal{G}_{ij}(\mathbf{x}, \mathbf{x}_0) = \mathcal{G}_{ij}(\mathbf{x} + \mathbf{x}^{(n)}, \mathbf{x}_0), \quad \int_{\gamma} \mathcal{G}_{ij}(\mathbf{x}, \mathbf{x}_0) d^3x = 0, \quad (\text{D.1.38a})$$

$$\mathcal{P}_i^p(\mathbf{x}, \mathbf{x}_0) = \mathcal{P}_i^p(\mathbf{x} + \mathbf{x}^{(n)}, \mathbf{x}_0), \quad \int_{\gamma} \mathcal{P}_i^p(\mathbf{x}, \mathbf{x}_0) d^3x = 0, \quad (\text{D.1.38b})$$

$$\mathcal{T}_{ijk}^p(\mathbf{x}, \mathbf{x}_0) = \mathcal{T}_{ijk}^p(\mathbf{x} + \mathbf{x}^{(n)}, \mathbf{x}_0), \quad \int_{\gamma} \mathcal{T}_{ijk}^p(\mathbf{x}, \mathbf{x}_0) d^3x = 0. \quad (\text{D.1.38c})$$

The Green's functions \mathcal{G} and \mathcal{T} , defined by (D.1.34a) and (D.1.34c) above, appear in the representation theorem (4.2.1) in the main text. The periodic contributions \mathcal{G} and \mathcal{T}^p are symmetric in any two indices.

D.2 Ewald summation formula for the Green's functions

As written above, the Green's functions (or fundamental tensors) are expressed as gradients of the infinite series Σ_1 and Σ_2 . Direct calculation by “brute force” is infeasible due to the slow convergence of these series. Fortunately, there is a method of splitting the series into two contributions, each of which may be evaluated rapidly and thus reducing the computational cost. This splitting method, which is the subject of the present section, was originally presented by Ewald for the calculation of electrostatic energies in ionic crystals [47]. It was later adopted by Hasimoto for periodically distributed bodies in Stokes flows [73], and has since become the cornerstone of modern numerical methods for computation of many-body hydrodynamic interactions in infinite suspensions [146, 134].

Firstly, the sums Σ_1 and Σ_2 may be expressed in the form,

$$\Sigma_1 = \frac{s_1}{\pi\Omega}, \quad \Sigma_2 = -\frac{s_2}{4\pi^3\Omega}, \quad (\text{D.2.1})$$

where

$$s_m = \sum_{\mathbf{k} \neq \mathbf{0}} \frac{\exp(-2\pi i \mathbf{k} \cdot \mathbf{r})}{k^{2m}}, \quad m = 1 \text{ or } 2. \quad (\text{D.2.2})$$

The decomposition of s_m is due to [73], who utilized the integral representation for k^{-2m} ,

$$\frac{1}{k^{2m}} = \frac{(\pi\alpha)^m}{\Gamma(m)} \int_0^\infty \exp(-\bar{k}^2\xi) \xi^{m-1} d\xi, \quad (\text{D.2.3})$$

and made use of Ewald's theta transformation rule [47],

$$\sum_{\mathbf{k} \neq \mathbf{0}} \exp(-\bar{k}^2\xi) \exp(-2\pi i \mathbf{k} \cdot \mathbf{r}) = -1 + \frac{\Omega}{(\alpha\xi)^{\frac{3}{2}}} \sum_{\mathbf{n}} \exp(-\bar{r}^2), \quad (\text{D.2.4})$$

where $\bar{r} = \sqrt{\pi/\alpha}(\mathbf{r} - \mathbf{x}^{(\mathbf{n})}) = \sqrt{\pi/\alpha}(\mathbf{x} - \mathbf{x}_0 - \mathbf{x}^{(\mathbf{n})})$ is a dimensionless separation vector, $\bar{\mathbf{k}} = \sqrt{\pi\alpha}\mathbf{k}$ is a dimensionless wavevector, and $\sqrt{\alpha}$ is a length scale that determines the balance of the decomposition. Using this transformation rule, s_m may be written as [equation (3.5) in [73]],

$$s_m = \frac{(\pi\alpha)^m}{\Gamma(m)} \left[-\frac{1}{m} + \Omega\alpha^{-\frac{3}{2}} \sum_{\mathbf{n}} \Gamma_{-m+\frac{1}{2}}(\bar{r}^2) + \sum_{\mathbf{k} \neq \mathbf{0}} \Gamma_{m-1}(\bar{k}^2) \exp(-2\pi i \mathbf{k} \cdot \mathbf{r}) \right], \quad (\text{D.2.5})$$

where

$$\Gamma_\nu(\xi) = \int_1^\infty \xi^\nu e^{-\nu\xi} d\xi \quad (\text{D.2.6})$$

is the incomplete gamma function. The $\Gamma_\nu(\xi)$ satisfy the recurrence relations,

$$\Gamma'_\nu(\xi) = -\Gamma_{\nu+1}(\xi), \quad \xi\Gamma_\nu(\xi) = e^{-\xi} + \nu\Gamma_{\nu-1}(\xi). \quad (\text{D.2.7})$$

The Ewald decomposition separates the sum s_m into two parts: a short-range, singular component that is evaluated in the physical space and a long-range, smooth component in the reciprocal space (an illustration is given in Figure 3.3.1 of [54]). Inserting this formula into the expressions for Σ_1 and Σ_2 gives

$$\Sigma_1 = \frac{s_1}{\pi\Omega} = -\frac{\alpha}{\Omega} + \frac{1}{\sqrt{\alpha}} \sum_{\mathbf{n}} \Gamma_{-\frac{1}{2}}(\bar{r}^2) + \frac{\alpha}{\Omega} \sum_{\mathbf{k} \neq \mathbf{0}} \Gamma_0(\bar{k}^2) \exp(-2\pi i \mathbf{k} \cdot \mathbf{r}), \quad (\text{D.2.8a})$$

$$\Sigma_2 = -\frac{s_2}{4\pi^3\Omega} = \frac{\alpha^2}{8\pi\Omega} - \frac{\sqrt{\alpha}}{4\pi} \sum_{\mathbf{n}} \Gamma_{-\frac{3}{2}}(\bar{r}^2) - \frac{\alpha^2}{4\pi\Omega} \sum_{\mathbf{k} \neq \mathbf{0}} \Gamma_1(\bar{k}^2) \exp(-2\pi i \mathbf{k} \cdot \mathbf{r}), \quad (\text{D.2.8b})$$

It is necessary to evaluate gradients of Σ_1 and Σ_2 , as these appear in the expressions for the Green's

functions:

$$\frac{\partial \Sigma_1}{\partial x_i} = -\frac{2\sqrt{\pi}}{\alpha} \sum_{\mathbf{n}} \bar{r}_i \Gamma_{\frac{1}{2}}(\bar{r}^2) - \frac{2\sqrt{\pi\alpha} i}{\Omega} \sum_{\mathbf{k} \neq \mathbf{0}} \bar{k}_i \Gamma_0(\bar{k}^2) \exp(-2\pi i \mathbf{k} \cdot \mathbf{r}), \quad (\text{D.2.9a})$$

$$\frac{\partial^2 \Sigma_2}{\partial x_i \partial x_j} = \frac{1}{2\sqrt{\alpha}} \sum_{\mathbf{n}} [\delta_{ij} \Gamma_{-\frac{1}{2}}(\bar{r}^2) - 2\bar{r}_i \bar{r}_j \Gamma_{\frac{1}{2}}(\bar{r}^2)] + \frac{\alpha}{\Omega} \sum_{\mathbf{k} \neq \mathbf{0}} \bar{k}_i \bar{k}_j \Gamma_1(\bar{k}^2) \exp(-2\pi i \mathbf{k} \cdot \mathbf{r}), \quad (\text{D.2.9b})$$

$$\begin{aligned} \frac{\partial^3 \Sigma_2}{\partial x_i \partial x_j \partial x_k} &= \frac{\sqrt{\pi}}{\alpha} \sum_{\mathbf{n}} [\delta_{ij} \bar{r}_k \Gamma_{-\frac{1}{2}}(\bar{r}^2) - \delta_{ik} \bar{r}_j \Gamma_{\frac{1}{2}}(\bar{r}^2) - \delta_{jk} \bar{r}_i \Gamma_{\frac{1}{2}}(\bar{r}^2) + 2\bar{r}_i \bar{r}_j \bar{r}_k \Gamma_{\frac{3}{2}}(\bar{r}^2)] \\ &\quad - \frac{2\sqrt{\pi\alpha} i}{\Omega} \sum_{\mathbf{k} \neq \mathbf{0}} \bar{k}_i \bar{k}_j \bar{k}_k \Gamma_1(\bar{k}^2) \exp(-2\pi i \mathbf{k} \cdot \mathbf{r}), \end{aligned} \quad (\text{D.2.9c})$$

where we have used the aforementioned recurrence relations for the incomplete gamma functions. Note that it may be proven that $\nabla^2 \Sigma_2 = \Sigma_1$ by means of Ewald's theta transformation rule and recurrence relations for the incomplete gamma functions. The incomplete gamma functions that appear in the above expressions are

$$\Gamma_{-\frac{1}{2}}(\xi) = \frac{\sqrt{\pi} \operatorname{erfc} \sqrt{\xi}}{\sqrt{\xi}}, \quad \Gamma_0(\xi) = \frac{e^{-\xi}}{\xi}, \quad \Gamma_{\frac{1}{2}}(\xi) = \Gamma_0(\xi) + \frac{\Gamma_{-\frac{1}{2}}(\xi)}{2\xi},$$

$$\Gamma_{-\frac{3}{2}}(\xi) = 2 \exp(-\xi) - 2\sqrt{\pi} \sqrt{\xi} \operatorname{erfc} \sqrt{\xi}, \quad \Gamma_1(\xi) = \frac{1+\xi}{\xi} \Gamma_0(\xi).$$

With the above definitions, the (periodic part of the) Green's functions for the velocity, pressure, and stress may be easily calculated:

$$\begin{aligned} \mathcal{G}_{ij}(\mathbf{x}, \mathbf{x}_0) &= 2 \left(\delta_{ij} \Sigma_1 - \frac{\partial^2 \Sigma_2}{\partial x_i \partial x_j} \right) \\ &= \frac{1}{\sqrt{\alpha}} \sum_{\mathbf{n}} \left[\left(\delta_{ij} + \frac{\bar{r}_i \bar{r}_j}{\bar{r}^2} \right) \Gamma_{-\frac{1}{2}}(\bar{r}^2) - 2(\bar{r}^2 \delta_{ij} - \bar{r}_i \bar{r}_j) \Gamma_0(\bar{r}^2) \right] \\ &\quad + \frac{2\alpha}{\Omega} \sum_{\mathbf{k} \neq \mathbf{0}} (\bar{k}^2 \delta_{ij} - \bar{k}_i \bar{k}_j) \Gamma_1(\bar{k}^2) \exp(-2\pi i \mathbf{k} \cdot \mathbf{r}), \end{aligned} \quad (\text{D.2.10a})$$

$$\begin{aligned} \mathcal{P}_i^p(\mathbf{x}, \mathbf{x}_0) &= -2 \frac{\partial \Sigma_1}{\partial x_i} \\ &= \frac{4\sqrt{\pi}}{\alpha} \sum_{\mathbf{n}} \bar{r}_i \Gamma_{\frac{1}{2}}(\bar{r}^2) + \frac{4\sqrt{\pi\alpha} i}{\Omega} \sum_{\mathbf{k} \neq \mathbf{0}} \bar{k}_i \Gamma_0(\bar{k}^2) \exp(-2\pi i \mathbf{k} \cdot \mathbf{r}), \end{aligned} \quad (\text{D.2.10b})$$

$$\begin{aligned} \mathcal{T}_{ijk}^p(\mathbf{x}, \mathbf{x}_0) &= 2 \left(\delta_{ik} \frac{\partial}{\partial x_j} + \delta_{ij} \frac{\partial}{\partial x_k} + \delta_{kj} \frac{\partial}{\partial x_i} \right) \Sigma_1 - 4 \frac{\partial^3 \Sigma_2}{\partial x_i \partial x_j \partial x_k} \\ &= -\frac{8\sqrt{\pi}}{\alpha} \sum_{\mathbf{n}} \bar{r}_i \bar{r}_j \bar{r}_k \Gamma_{\frac{3}{2}}(\bar{r}^2) \\ &\quad + \frac{4\sqrt{\pi\alpha} i}{\Omega} \sum_{\mathbf{k} \neq \mathbf{0}} [(\bar{k}_j \delta_{ik} + \bar{k}_k \delta_{ij} + \bar{k}_i \delta_{kj}) \Gamma_0(\bar{k}^2) - 2\bar{k}_i \bar{k}_j \bar{k}_k \Gamma_1(\bar{k}^2)] \exp(-2\pi i \mathbf{k} \cdot \mathbf{r}), \end{aligned} \quad (\text{D.2.10c})$$

where we have exploited Ewald's theta transformation rule and recurrence relations for the incomplete gamma functions.

Though it may not be immediately obvious, this method of “Ewald splitting” introduced in (D.2.10a)-(D.2.10c) greatly accelerates the evaluation of the sums Σ_1 and Σ_2 . The short-range contribution (evaluated in the physical space over all separation vectors \bar{r}) decays exponentially with increasing separation distance when $\bar{r} \gg 1$, while the long-range contribution (evaluated in the reciprocal space over all wavevectors \bar{k}) decays exponentially with increasing wavenumber when $\bar{k} \gg 1$ [180].

D.3 Numerical evaluation of the Green's functions

In the boundary collocation method, the boundaries contained within the periodic volume \mathcal{V} are discretized into N collocation points, over which the surface density fields are approximated by piecewise continuous shape functions (either linear or quadratic in polynomial order). The Green's functions are evaluated on these boundaries, and serve as weighting functions (or kernels) that are convolved with the surface density distributions in the boundary integral equations [cf. (4.2.2)].

The Green's functions given by (D.2.10) depend on the length scale $\sqrt{\alpha}$, which controls the partitioning of the Ewald sum. The value of α is typically chosen to minimize computational cost. That is to say, we would like to split the sum (one part containing the long-range hydrodynamic interaction, the other part containing the short-range interaction) in such a way that optimizes the speed of evaluation of its constituent parts. The physical part of the sum is evaluated directly to within some prescribed tolerance $\varepsilon_{\text{phys}}$. Given this tolerance $\varepsilon_{\text{phys}}$ and some cutoff radius r_{cutoff} , the parameter α may be chosen to make the functions of \bar{r} appearing in (D.2.10) smaller than $\varepsilon_{\text{phys}}$ whenever $r \geq r_{\text{cutoff}}$ [134]. This judicious choice of α essentially restricts the short-range part of the hydrodynamic interaction to within a sphere of radius r_{cutoff} , independent of the size of the domain [134, 160]. Since the terms in the physical sum decay exponentially with increasing \bar{r} , the number of collocation points contained within this fictitious sphere is generally small and requires only $O(N)$ floating-point operations [134, 54].

With the advent of the fast Fourier transform (FFT), the long-range contribution can be evaluated quite rapidly in the reciprocal space using the so-called Smooth Particle Mesh Ewald (SPME) method [40, 134, 180]. This is done by first discretizing the reciprocal space into a rectangular grid with $M_1 \times M_2 \times M_3$ points. (The M are chosen to scale proportionally to the system size N). The functions of \bar{k} appearing in (D.2.10) are interpolated onto this grid using cardinal B-splines (of order N_B) and evaluated by FFT. The total cost of the evaluation is $O(N \log N)$, a significant improvement over the naïve $O(N^2)$ implementation by “brute-force calculation.”

Several parameters just introduced affect the accuracy and efficiency of the numerical evaluation

of the Green's functions:

1. the tolerance of the physical sum $\varepsilon_{\text{phys}}$,
2. the cutoff radius r_{cutoff} ,
3. the number of grid points in the reciprocal space M ,
4. the order of the cardinal B-splines N_B .

For a given choice of $\varepsilon_{\text{phys}}$ and r_{cutoff} , the partitioning coefficient α is uniquely specified. This choice has the greatest impact on the computational *efficiency*. The other parameters are generally chosen to improve computational *accuracy*. It is important to keep in mind the order of accuracy of the numerical method when choosing these parameters, as typically the truncation error in approximating integrals and derivatives by discrete analogs exceeds the error incurred by either (i) truncating the series in (D.2.10), or (ii) using lower-order interpolants (cardinal B-splines). For more details on parameter selection and a thorough discussion of practical issues with Ewald summation methods, the reader is referred to [160].

Appendix E

Boundary integral equations for vesicles in channel flow

The boundary element method (BEM) implemented in Chapters 4 and 5 is based the one originally devised by Zhao and coworkers for studying red blood cells in the microcirculation [180, 54, 184]. In this appendix, we derive the boundary integral equations (4.2.2), which are solved using the BEM. A good discussion of boundary integral equation methods (including the BEM and singularity methods) can be found in [125].

Starting from the reciprocal identity of Stokes flow, the representation theorem (4.2.1) for the velocity field \mathbf{u} is derived as convolutions of density fields (surface velocities and surface tractions) weighted by the Green's functions \mathcal{G} and \mathcal{T} . From there, the boundary integral equations straightforwardly follow. We follow the same convention used in Appendix D by representing vectors and tensors by their indexed components with implied summation over repeated indices (Einstein notation).

E.1 Reciprocal identity

The starting point for any representation theory of creeping flow is a *reciprocal identity* between two flow fields. Let \mathbf{u} , $\boldsymbol{\sigma}$ be the desired solution of the creeping flow problem under consideration and \mathbf{u}' , $\boldsymbol{\sigma}'$ be associated with the flow due to a periodic array of point forces of strength \mathbf{F} placed at a positions $\mathbf{x}_0 + \mathbf{x}^{(n)}$ (using the same nomenclature as in Appendix D). Thus,

$$\frac{\partial u_i}{\partial x_i} = 0, \quad (\text{E.1.1a})$$

$$\frac{\partial \sigma_{ji}}{\partial x_j} = -\frac{\partial p}{\partial x_i} + \mu \frac{\partial^2 u_i}{\partial x_j \partial x_j} = 0, \quad (\text{E.1.1b})$$

$$+ \text{ boundary conditions,} \quad (\text{E.1.1c})$$

and

$$\frac{\partial u'_i}{\partial x_i} = 0, \quad (\text{E.1.2a})$$

$$\frac{\partial \sigma'_{ji}}{\partial x_j} = -\frac{\partial p'}{\partial x_i} + \mu \frac{\partial^2 u'_i}{\partial x_j \partial x_j} = -F_i \delta(\mathbf{x} - \mathbf{x}_0), \quad (\text{E.1.2b})$$

$$u'_i(\mathbf{x}) = u'_i(\mathbf{x} + \mathbf{x}^{(n)}), \quad (\text{E.1.2c})$$

$$\frac{\partial p'}{\partial x_i}(\mathbf{x}) = \frac{\partial p'}{\partial x_i}(\mathbf{x} + \mathbf{x}^{(n)}). \quad (\text{E.1.2d})$$

The solution of the last set of equations, modulo a reference pressure, is the fundamental solution (see Appendix D),

$$u'_i(\mathbf{x}) = \langle u'_i \rangle + \frac{F_j \mathcal{G}_{ji}(\mathbf{x}, \mathbf{x}_0)}{8\pi\mu}, \quad (\text{E.1.3a})$$

$$p'(\mathbf{x}) = \frac{F_j \mathcal{P}_j(\mathbf{x}, \mathbf{x}_0)}{8\pi}, \quad (\text{E.1.3b})$$

$$\sigma'_{ik}(\mathbf{x}) = \frac{F_j \mathcal{T}_{ijk}(\mathbf{x}, \mathbf{x}_0)}{8\pi}, \quad (\text{E.1.3c})$$

where the Green's functions \mathcal{G} , \mathcal{P} , and \mathcal{T} satisfy the boundary-value problem,

$$\frac{\partial \mathcal{G}_{ij}}{\partial x_j} = 0, \quad (\text{E.1.4a})$$

$$\frac{\partial \mathcal{T}_{kji}}{\partial x_k} = -\frac{\partial \mathcal{P}_j}{\partial x_i} + \frac{\partial^2 \mathcal{G}_{ij}}{\partial x_k \partial x_k} = -8\pi \delta_{ij} \delta(\mathbf{x} - \mathbf{x}_0), \quad (\text{E.1.4b})$$

$$\mathcal{G}_{ij}(\mathbf{x}, \mathbf{x}_0) = \mathcal{G}_{ij}(\mathbf{x} + \mathbf{x}^{(n)}, \mathbf{x}_0), \quad (\text{E.1.4c})$$

$$\frac{\partial \mathcal{P}_j}{\partial x_i}(\mathbf{x}, \mathbf{x}_0) = \frac{\partial \mathcal{P}_j}{\partial x_i}(\mathbf{x} + \mathbf{x}^{(n)}, \mathbf{x}_0). \quad (\text{E.1.4d})$$

We now consider an *arbitrary* control volume \mathcal{V} within a periodic cell and exclude a volume \mathcal{V}_e from this region that contains the source point \mathbf{x}_0 . In order to derive the reciprocal identity, we first multiply (E.1.1b) by \mathcal{G} , (E.1.4b) by $\mu \mathbf{u}$, and subtract the results to get

$$\frac{\partial \sigma_{ki}(\mathbf{x})}{\partial x_k} \mathcal{G}_{ij}(\mathbf{x}, \mathbf{x}_0) - \mu \frac{\partial \mathcal{T}_{kji}(\mathbf{x}, \mathbf{x}_0)}{\partial x_k} u_i(\mathbf{x}) = 0. \quad (\text{E.1.5})$$

The right-hand side is zero because we have excluded \mathbf{x}_0 from the domain. Since \mathcal{G} and \mathbf{u} are divergence-free (by incompressibility) and

$$\sigma_{ik} = \sigma_{ki} = -p \delta_{ik} + \mu \left(\frac{\partial u_k}{\partial x_i} + \frac{\partial u_i}{\partial x_k} \right), \quad (\text{E.1.6})$$

$$\mathcal{T}_{ijk} = \mathcal{T}_{kji} = -\mathcal{P}_j \delta_{ik} + \frac{\partial \mathcal{G}_{kj}}{\partial x_i} + \frac{\partial \mathcal{G}_{ij}}{\partial x_k}, \quad (\text{E.1.7})$$

then it may be shown that

$$\frac{\partial}{\partial x_k} [\sigma_{ik}(\mathbf{x}) \mathcal{G}_{ij}(\mathbf{x}, \mathbf{x}_0) - \mu u_i(\mathbf{x}) \mathcal{T}_{ijk}(\mathbf{x}, \mathbf{x}_0)] = 0, \quad (\text{E.1.8})$$

which is the desired reciprocal identity.

E.2 Volume integral of the reciprocal identity

The Green's functions \mathcal{G} and \mathcal{T} are to be convolved with surface density fields in order to solve for the velocity, pressure, and stress distributions in a flow system. This forms the basis for the *representation theorem* – a general solution to the creeping flow equations in terms of an integral representation with built-in boundary conditions. To obtain this theorem, we first integrate the reciprocal identity (E.1.8) over the volume $\mathcal{V} \setminus \mathcal{V}_\epsilon$,

$$\int_{\mathcal{V} \setminus \mathcal{V}_\epsilon} \frac{\partial}{\partial x_k} [\sigma_{ik}(\mathbf{x}) \mathcal{G}_{ij}(\mathbf{x}, \mathbf{x}_0) - \mu u_i(\mathbf{x}) \mathcal{T}_{ijk}(\mathbf{x}, \mathbf{x}_0)] d^3x = 0, \quad (\text{E.2.1})$$

or, upon application of the divergence theorem,¹

$$\begin{aligned} & - \int_{\partial \mathcal{V}} [\sigma_{ik}(\mathbf{x}) \hat{n}_k(\mathbf{x}) \mathcal{G}_{ij}(\mathbf{x}, \mathbf{x}_0) - \mu u_i(\mathbf{x}) \mathcal{T}_{ijk}(\mathbf{x}, \mathbf{x}_0) \hat{n}_k(\mathbf{x})] dS(\mathbf{x}) \\ & - \int_{\partial \mathcal{V}_\epsilon} [\sigma_{ik}(\mathbf{x}) \hat{n}'_k(\mathbf{x}) \mathcal{G}_{ij}(\mathbf{x}, \mathbf{x}_0) - \mu u_i(\mathbf{x}) \mathcal{T}_{ijk}(\mathbf{x}, \mathbf{x}_0) \hat{n}'_k(\mathbf{x})] dS(\mathbf{x}) = 0, \end{aligned} \quad (\text{E.2.2})$$

where \hat{n} and \hat{n}' are unit normals that point *into* $\mathcal{V} \setminus \mathcal{V}_\epsilon$ (the region inside \mathcal{V} that excludes \mathcal{V}_ϵ).

It now remains to evaluate the second integral on the left-hand side of (E.2.2) and subsequently take the limit as \mathcal{V}_ϵ shrinks to a point. We consider three special cases:

1. The source point lies outside \mathcal{V} , $\mathbf{x}_0 \notin \mathcal{V}$.
2. The source point lies inside \mathcal{V} , $\mathbf{x}_0 \in \mathcal{V} \setminus \partial \mathcal{V}$.
3. The source point lies on the boundary, $\mathbf{x}_0 \in \partial \mathcal{V}$.

¹Note that it is straightforward to apply the divergence theorem here, since we have excluded \mathbf{x}_0 from the domain of integration and thus the kernels are analytic everywhere in the domain of integration (assuming \mathbf{u} and $\boldsymbol{\sigma}$ are also analytic).

E.2.1 Case 1: the source point lies outside the volume

The case where \mathbf{x}_0 lies somewhere outside \mathcal{V} (and thus, outside \mathcal{V}_ϵ) is trivial, since it is not necessary to exclude a region \mathcal{V}_ϵ from the region of interest. Thus, we may set

$$\int_{\partial\mathcal{V}_\epsilon} [\sigma_{ik}(\mathbf{x})\hat{n}_k(\mathbf{x})\mathcal{G}_{ij}(\mathbf{x}, \mathbf{x}_0) - \mu u_i(\mathbf{x})\mathcal{T}_{ijk}(\mathbf{x}, \mathbf{x}_0)\hat{n}_k(\mathbf{x})] dS(\mathbf{x}) = 0 \quad \text{for } \mathbf{x}_0 \notin \mathcal{V}. \quad (\text{E.2.3})$$

Equivalently, we need not have defined \mathcal{V}_ϵ to begin with and instead could have applied the divergence theorem directly to the volume integral over \mathcal{V} .

E.2.2 Case 2: the source point lies inside the volume

For the case where \mathbf{x}_0 lies somewhere inside \mathcal{V} , we choose the excluded region \mathcal{V}_ϵ to be a sphere of radius ϵ centered about \mathbf{x}_0 and let ϵ tend to zero (i.e., let \mathbf{x} approach the singular point \mathbf{x}_0). The unit normal of the bounding surface is $\hat{\mathbf{n}}' = \mathbf{r}/r$, where $\mathbf{r} = \mathbf{x} - \mathbf{x}_0$ and $r = |\mathbf{r}|$ [cf. (D.1.6)]. As $r \rightarrow 0$, \mathbf{u} and $\boldsymbol{\sigma}$ (assumed to be regular functions) tend to their values at \mathbf{x}_0 . In addition, the sums Σ_1 and Σ_2 [cf. (D.1.27)] tend to their asymptotic values as $r \rightarrow 0$:

$$\begin{aligned} \Sigma_1 &\sim \frac{1}{r}, \quad \frac{\partial^2 \Sigma_1}{\partial x_i} \sim -\frac{r_i}{r}, \\ \Sigma_2 &\sim \frac{r}{2}, \quad \frac{\partial^2 \Sigma_2}{\partial x_i \partial x_j} \sim \frac{1}{2} \left(\frac{\delta_{ij}}{r} - \frac{r_i r_j}{r^3} \right), \\ \frac{\partial^3 \Sigma_2}{\partial x_i \partial x_j \partial x_k} &\sim \frac{1}{2} \left(\frac{3r_i r_j r_k}{r^5} - \frac{r_i \delta_{jk} + r_j \delta_{ik} + r_k \delta_{ij}}{r^3} \right). \end{aligned}$$

These expressions may be derived directly from (D.2.8)-(D.2.9) in Appendix D. The Green's functions \mathcal{G} , \mathcal{P} , and \mathcal{T} [cf. (D.1.34)] also tend to their asymptotic values as $r \rightarrow 0$:

$$\begin{aligned} \mathcal{G}_{ij}(\mathbf{x}, \mathbf{x}_0) &\sim \frac{\delta_{ij}}{r} + \frac{r_i r_j}{r^3}, \\ \mathcal{P}_i(\mathbf{x}, \mathbf{x}_0) &\sim \frac{8\pi x_i}{\Omega} + 2\frac{r_i}{r}, \\ \mathcal{T}_{ijk}(\mathbf{x}, \mathbf{x}_0) &\sim -\frac{8\pi x_j \delta_{ik}}{\Omega} - 6\frac{r_i r_j r_k}{r^5}, \end{aligned}$$

which may be obtained directly from (D.2.10). Thus, the Green's functions in the vicinity of the source point appear to contain two parts: one part due to a point force in an unbounded flow, the other due to a mean flow driven by a pressure gradient. The latter part is most easily evaluated as a volume integral, rather than a surface integral.

Taking only the leading-order terms with respect to ϵ (noting that $r \sim \epsilon$, $dS \sim \epsilon^2$, with \mathbf{u} and $\boldsymbol{\sigma}$ bounded) and letting $\epsilon \rightarrow 0$, the integral over $\partial\mathcal{V}_\epsilon$ in (E.2.2) may be recast as,

$$\int_{\partial\mathcal{V}_\epsilon} [\sigma_{ik}(\mathbf{x})\hat{n}'_k(\mathbf{x})\mathcal{G}_{ij}(\mathbf{x}, \mathbf{x}_0) - \mu u_i(\mathbf{x})\mathcal{T}_{ijk}(\mathbf{x}, \mathbf{x}_0)\hat{n}'_k(\mathbf{x})] dS(\mathbf{x})$$

$$\begin{aligned}
&= \sigma_{ik}(\mathbf{x}_0) \int_{\partial\mathcal{V}_\epsilon} \left(\frac{\delta_{ij}r_k}{r^2} + \frac{r_i r_j r_k}{r^4} \right) dS(\mathbf{x}) + 6\mu u_i(\mathbf{x}_0) \int_{\partial\mathcal{V}_\epsilon} \frac{r_i r_j}{r^4} dS(\mathbf{x}) \\
&\quad + \frac{8\pi\mu}{\Omega} \int_{\mathcal{V}_\epsilon} \frac{\partial}{\partial x_k} [x_j u_k(\mathbf{x})] d^3\mathbf{x} \\
&= \epsilon \sigma_{ik}(\mathbf{x}_0) \int_{\mathcal{S}_\Omega} (\delta_{ij}\hat{r}_k + \hat{r}_i \hat{r}_j \hat{r}_k) d\Omega + 6\mu u_i(\mathbf{x}_0) \int_{\mathcal{S}_\Omega} \hat{r}_i \hat{r}_j d\Omega \\
&\quad + \frac{8\pi\mu}{\Omega} \int_{\mathcal{V}_\epsilon} \frac{\partial}{\partial x_k} [x_j u_k(\mathbf{x})] d^3\mathbf{x}, \tag{E.2.4}
\end{aligned}$$

where an “overhat” on a vector quantity indicates normalization, Ω is the solid angle, and \mathcal{S}_Ω is the surface of the unit sphere. Clearly, the resulting integrals are regular in ϵ . The surface integrals over \mathcal{S}_Ω may be evaluated using well known orthogonality relations for the surface spherical harmonics:

$$\int_{\mathcal{S}_\Omega} (\delta_{ij}\hat{r}_k + \hat{r}_i \hat{r}_j \hat{r}_k) d\Omega = 0, \quad \int_{\mathcal{S}_\Omega} \hat{r}_i \hat{r}_j d\Omega = \frac{4}{3}\pi\delta_{ij}.$$

The volume integral over \mathcal{V}_ϵ may be evaluated directly by first applying the product rule to the integrand and then using the incompressibility condition,

$$\int_{\mathcal{V}_\epsilon} \frac{\partial}{\partial x_k} [x_j u_k(\mathbf{x})] d^3\mathbf{x} = \int_{\mathcal{V}_\epsilon} \left(u_j(\mathbf{x}) + x_j \frac{\partial u_k}{\partial x_k}(\mathbf{x}) \right) d^3\mathbf{x} = \int_{\mathcal{V}_\epsilon} u_j(\mathbf{x}) d^3\mathbf{x} \sim O(\epsilon^3).$$

The term on the right-hand side of the last expression vanishes as \mathcal{V}_ϵ shrinks to a point, since \mathbf{u} is analytic everywhere in \mathcal{V} . The final result is,

$$\begin{aligned}
&\int_{\partial\mathcal{V}_\epsilon} [\sigma_{ik}(\mathbf{x}) \hat{n}'_k(\mathbf{x}) \mathcal{G}_{ij}(\mathbf{x}, \mathbf{x}_0) - \mu u_i(\mathbf{x}) \mathcal{T}_{ijk}(\mathbf{x}, \mathbf{x}_0) \hat{n}'_k(\mathbf{x})] dS(\mathbf{x}) \\
&= 8\pi\mu u_i(\mathbf{x}_0) \quad \text{for } \mathbf{x}_0 \in \mathcal{V} \setminus \partial\mathcal{V}. \tag{E.2.5}
\end{aligned}$$

E.2.3 Case 3: the source point lies on the boundary

For the case where \mathbf{x}_0 lies on the boundary of \mathcal{V} , we define the excluded region \mathcal{V}_ϵ enclosing \mathbf{x}_0 to be a hemisphere of radius ϵ (where ϵ tends to zero) and whose circular base lies on the bounding surface of \mathcal{V} . The center of the base is coincident with \mathbf{x}_0 . The bounding surface of \mathcal{V}_ϵ is defined in a piecewise manner: there is a “cup” surface $\partial\mathcal{V}_\epsilon^{\text{cup}}$ whose unit normal is $\hat{\mathbf{n}}' = \mathbf{r}/r$ and a “base” surface $\partial\mathcal{V}_\epsilon^{\text{base}}$ whose unit normal is $\hat{\mathbf{n}}' = \hat{\mathbf{n}}$.

Before proceeding, we should note an important assumption made in the forthcoming derivation: we are implicitly assuming that the surface $\partial\mathcal{V}$ is *locally smooth everywhere* (*a Lyapunov surface*). This is not the case, for instance, when the boundary of \mathcal{V} contains corners! A more general approach (though not the one taken here) would choose \mathcal{V}_ϵ to enclose a region other than a hemisphere, e.g., a torus, and take the limit as a length scale $\epsilon \rightarrow 0$. The main difference in the final result [equation (E.2.7), below] is the coefficient multiplying the velocity $\mathbf{u}(\mathbf{x}_0)$ on the right-hand side will be a

“principal value tensor” \mathcal{C} that depends on the local geometry of the boundary. As will be shown momentarily, $\mathcal{C} = \delta$ for a Lyapunov surface.

Following the same procedure as in Case 2, the integral over $\partial\mathcal{V}_\epsilon$ becomes

$$\begin{aligned} & \int_{\partial\mathcal{V}_\epsilon} [\sigma_{ik}(\mathbf{x})\hat{n}'_k(\mathbf{x})\mathcal{G}_{ij}(\mathbf{x}, \mathbf{x}_0) - \mu u_i(\mathbf{x})\mathcal{T}_{ijk}(\mathbf{x}, \mathbf{x}_0)\hat{n}'_k(\mathbf{x})] dS(\mathbf{x}) \\ &= \sigma_{ik}(\mathbf{x}_0) \int_{\partial\mathcal{V}_\epsilon^{\text{cup}}} \left(\frac{\delta_{ij}r_k}{r^2} + \frac{r_i r_j r_k}{r^4} \right) dS(\mathbf{x}) + \sigma_{ik}(\mathbf{x}_0) \int_{\partial\mathcal{V}_\epsilon^{\text{base}}} \left(\frac{\delta_{ij}}{r} + \frac{r_i r_j}{r^3} \right) \hat{n}_k dS(\mathbf{x}) \\ &+ 6\mu u_i(\mathbf{x}_0) \int_{\partial\mathcal{V}_\epsilon^{\text{cup}}} \frac{r_i r_j}{r^4} dS(\mathbf{x}) + 6\mu u_i(\mathbf{x}_0) \int_{\partial\mathcal{V}_\epsilon^{\text{base}}} \frac{r_i r_j r_k}{r^5} \hat{n}_k dS(\mathbf{x}) \\ &+ \frac{8\pi\mu}{\Omega} \int_{\mathcal{V}_\epsilon} \frac{\partial}{\partial x_k} [x_j u_k(\mathbf{x})] d^3\mathbf{x}. \end{aligned} \quad (\text{E.2.6})$$

The surface $\partial\mathcal{V}_\epsilon^{\text{cup}}$ and volume \mathcal{V}_ϵ are half that of a complete sphere, so we can apply the results of Case 2 to some of these integrals:

$$\begin{aligned} & \sigma_{ik}(\mathbf{x}_0) \int_{\partial\mathcal{V}_\epsilon^{\text{cup}}} \left(\frac{\delta_{ij}r_k}{r^2} + \frac{r_i r_j r_k}{r^4} \right) dS(\mathbf{x}) = 0, \\ & 6\mu u_i(\mathbf{x}_0) \int_{\partial\mathcal{V}_\epsilon^{\text{cup}}} \frac{r_i r_j}{r^4} dS(\mathbf{x}) = 4\pi\mu u_j(\mathbf{x}_0), \\ & \frac{8\pi\mu}{\Omega} \int_{\mathcal{V}_\epsilon} \frac{\partial}{\partial x_k} [x_j u_k(\mathbf{x})] d^3\mathbf{x} = \frac{8\pi\mu}{\Omega} \int_{\mathcal{V}_\epsilon} u_j(\mathbf{x}) d^3\mathbf{x} \sim O(\epsilon^3). \end{aligned}$$

The last result vanishes after taking the limit as $\epsilon \rightarrow 0$. Next, we have to evaluate the integrals over $\partial\mathcal{V}_\epsilon^{\text{base}}$. The stress kernel vanishes, since $\mathbf{r} \cdot \hat{\mathbf{n}} = 0$ as $\epsilon \rightarrow 0$. This leaves the convolution with the velocity kernel, which also vanishes in the limit $\epsilon \rightarrow 0$ since $dS \sim \epsilon^2$ and $r \sim \epsilon$ on the base. Thus, the only contribution is due to the convolution of the stress kernel over the cup surface:

$$\begin{aligned} & \int_{\partial\mathcal{V}_\epsilon} [\sigma_{ik}(\mathbf{x})\hat{n}'_k(\mathbf{x})\mathcal{G}_{ij}(\mathbf{x}, \mathbf{x}_0) - \mu u_i(\mathbf{x})\mathcal{T}_{ijk}(\mathbf{x}, \mathbf{x}_0)\hat{n}'_k(\mathbf{x})] dS(\mathbf{x}) \\ &= 4\pi\mu u_j(\mathbf{x}_0) \quad \text{for } \mathbf{x}_0 \in \partial\mathcal{V}. \end{aligned} \quad (\text{E.2.7})$$

The integral evaluated by this limiting procedure is called the *Cauchy principal value*.

The important distinction from Case 2 is that the convolution of the stress kernel returns $4\pi\mu\mathbf{u}(\mathbf{x}_0)$ rather than $8\pi\mu\mathbf{u}(\mathbf{x}_0)$. If one were to perform the same procedure, but approach the boundary from the *exterior* of \mathcal{V} rather than from the interior, then one would obtain $-4\pi\mu\mathbf{u}(\mathbf{x}_0)$ (since the unit normal $\hat{\mathbf{n}}$ changes direction). Thus, the stress kernel undergoes a jump across $\partial\mathcal{V}$. By contrast, the velocity kernel is continuous across $\partial\mathcal{V}$.

E.3 Representation theorem

Combining (E.2.2), (E.2.3), (E.2.5), and (E.2.7) leads to the *representation theorem of creeping flow*:

$$\begin{aligned} -\frac{1}{8\pi\mu} \int_{\partial\mathcal{V}} \sigma_{ik}(\mathbf{x}) \hat{\mathbf{n}}_k(\mathbf{x}) \mathcal{G}_{ij}(\mathbf{x}, \mathbf{x}_0) dS(\mathbf{x}) + \frac{1}{8\pi} \int_{\partial\mathcal{V}} u_i(\mathbf{x}) \mathcal{T}_{ijk}(\mathbf{x}, \mathbf{x}_0) \hat{\mathbf{n}}_k(\mathbf{x}) dS(\mathbf{x}) \\ = \begin{cases} 0 & \text{for } \mathbf{x}_0 \notin \mathcal{V}, \\ u_j(\mathbf{x}_0) & \text{for } \mathbf{x}_0 \in \mathcal{V} \setminus \partial\mathcal{V}, \\ \frac{1}{2}u_j(\mathbf{x}_0) & \text{for } \mathbf{x}_0 \in \partial\mathcal{V}, \end{cases} \end{aligned} \quad (\text{E.3.1})$$

where it is assumed that $\hat{\mathbf{n}}$ points *into* \mathcal{V} . The names of the integrals appearing on the left-hand side of (E.3.1) are inspired by the electrostatics literature. The first integral is called the *single-layer potential* and represents a convolution of point forces distributed over the surface $\partial\mathcal{V}$. The second is called the *double-layer potential* and represents a convolution of a distribution of point-force dipoles on $\partial\mathcal{V}$. In the last case where the source point lies on the particle surface, the double layer potential is evaluated in the principal value sense.

We conclude this section with two remarks. First, we note that if the surface $\partial\mathcal{V}$ is not locally smooth everywhere, then the right-hand side of the last case would read,

$$\frac{1}{2}\mathcal{C}_{jk}u_k(\mathbf{x}_0) \quad \text{for } \mathbf{x}_0 \in \partial\mathcal{V}, \quad (\text{E.3.2})$$

where \mathcal{C} is the *principal value tensor*. Second, we could alternatively have written the single layer potential using the surface traction $\mathbf{f}(\mathbf{x})$ as the density field, with

$$f_i = \sigma_{ik}\hat{\mathbf{n}}_k. \quad (\text{E.3.3})$$

By applying equations (E.3.2) and (E.3.3) to (E.3.1), one obtains equation (4.2.1) in the main text.

E.4 Boundary integral equations

We are now going to derive the boundary integral equations used in Chapters 4 and 5. In the forthcoming derivation, we will make use of the periodic Green's functions \mathcal{G} and \mathcal{T} [defined by (E.1.4)] as well as the representation theorem (E.3.1).

When applying the representation theorem to unbounded flows [replacing the Green's functions \mathcal{G} and \mathcal{T} in (E.3.1) by their appropriate “free-space” analogs], one typically defines a fictitious surface \mathcal{S}_∞ in the far field that encloses the domain. Then, by exploiting the fact that \mathbf{u} , $\boldsymbol{\sigma}$, \mathcal{G} , and \mathcal{T} decay asymptotically as $|\mathbf{x}| \rightarrow \infty$, one can eliminate surface integrals over \mathcal{S}_∞ . Obviously, the same procedure cannot be applied to the periodic flows considered here. In lieu of defining a

far-field surface \mathcal{S}_∞ , it is necessary to explicitly evaluate surface integrals over the boundary of a periodic cell. One consequence of this procedure, as will be shown shortly, is the appearance of the volume-averaged velocity $\langle \mathbf{u} \rangle$ in the boundary integral equations.

We consider the periodic volume \mathcal{V} depicted in Figure 4.2 containing a vesicle suspension flowing through a conduit. Let \mathcal{V}_0 denote the union of all regions inside the vesicles, \mathcal{V}_1 the region inside the conduit but outside the vesicles, and \mathcal{V}_2 the region outside the conduit. The vesicles and conduit wall are embedded in a rectangular cuboid of dimensions $L_1 \times L_2 \times L_3$ that is periodically replicated in the x_1 , x_2 , and x_3 directions. Thus,

$$\mathcal{V} = \mathcal{V}_0 \cup \mathcal{V}_1 \cup \mathcal{V}_2 = [0, L_1] \times [0, L_2] \times [0, L_3]. \quad (\text{E.4.1})$$

We denote the union of all vesicle surfaces by $\mathcal{S}_s = \partial \mathcal{V}_0$ and the wall surface by \mathcal{S}_w . On the vesicle surface, the surface tractions undergo a finite jump $\mathbf{f}_s = [\![\mathbf{f}(\mathbf{x} \in \mathcal{S}_s)]\!]$. On the wall surface, the no-slip condition stipulates that $\mathbf{u} = \mathbf{0}$. The suspending (exterior) fluid viscosity is μ and the dispersed (interior) fluid viscosity is $\kappa\mu$.

We would like to apply the representation theorem (E.3.1) at a point $\mathbf{x}_0 \in \mathcal{V}$, i.e., a point inside the periodic cell. Furthermore, we would like to express the boundary integrals in terms of density fields evaluated on the vesicle surfaces \mathcal{S}_s and wall surface \mathcal{S}_w . Then, we will take the limit as the field point approaches these surfaces, leading to a system of boundary integral equations to be solved numerically using methods from linear algebra.

E.4.1 Interior points

First, we consider the case where \mathbf{x}_0 lies somewhere within \mathcal{V}_1 and is not coincident with any boundaries, $\mathbf{x}_0 \in \mathcal{V}_1 \setminus (\mathcal{S}_s \cup \mathcal{S}_w)$. Applying the representation theorem (E.3.1) to the regions \mathcal{V}_1 , \mathcal{V}_2 , and \mathcal{V}_0 , noting that $\partial \mathcal{V}_1 = \mathcal{S}_s \cup \mathcal{S}_w$, $\partial \mathcal{V}_+ = \partial \mathcal{V} \cup \mathcal{S}_w$, and $\partial \mathcal{V}_0 = \mathcal{S}_s$, yields the following relations:

for $\mathbf{x} \in \mathcal{V}_1$:

$$\begin{aligned} & -\frac{1}{8\pi\mu} \int_{\mathcal{S}_s} \sigma_{ik}^+(\mathbf{x}) \hat{n}_k(\mathbf{x}) \mathcal{G}_{ij}(\mathbf{x}, \mathbf{x}_0) dS(\mathbf{x}) + \frac{1}{8\pi} \int_{\mathcal{S}_s} u_i(\mathbf{x}) \mathcal{T}_{ijk}(\mathbf{x}, \mathbf{x}_0) \hat{n}_k(\mathbf{x}) dS(\mathbf{x}) \\ & -\frac{1}{8\pi\mu} \int_{\mathcal{S}_w} \sigma_{ik}^+(\mathbf{x}) \hat{n}_k(\mathbf{x}) \mathcal{G}_{ij}(\mathbf{x}, \mathbf{x}_0) dS(\mathbf{x}) + \frac{1}{8\pi} \int_{\mathcal{S}_w} u_i(\mathbf{x}) \mathcal{T}_{ijk}(\mathbf{x}, \mathbf{x}_0) \hat{n}_k(\mathbf{x}) dS(\mathbf{x}) = u_j(\mathbf{x}_0), \end{aligned} \quad (\text{E.4.2})$$

for $\mathbf{x} \in \mathcal{V}_2$:

$$-\frac{1}{8\pi\mu} \int_{\partial \mathcal{V}} \sigma_{ik}(\mathbf{x}) \hat{n}_k(\mathbf{x}) \mathcal{G}_{ij}(\mathbf{x}, \mathbf{x}_0) dS(\mathbf{x}) + \frac{1}{8\pi} \int_{\partial \mathcal{V}} u_i(\mathbf{x}) \mathcal{T}_{ijk}(\mathbf{x}, \mathbf{x}_0) \hat{n}_k(\mathbf{x}) dS(\mathbf{x})$$

$$+ \frac{1}{8\pi\mu} \int_{\mathcal{S}_w} \sigma_{ik}^-(\mathbf{x}) \hat{n}_k(\mathbf{x}) \mathcal{G}_{ij}(\mathbf{x}, \mathbf{x}_0) dS(\mathbf{x}) - \frac{1}{8\pi} \int_{\mathcal{S}_w} u_i(\mathbf{x}) \mathcal{T}_{ijk}(\mathbf{x}, \mathbf{x}_0) \hat{n}_k(\mathbf{x}) dS(\mathbf{x}) = 0, \quad (\text{E.4.3})$$

for $\mathbf{x} \in \mathcal{V}_0$:

$$\frac{1}{8\pi\kappa\mu} \int_{\mathcal{S}_s} \sigma_{ik}^-(\mathbf{x}) \hat{n}_k(\mathbf{x}) \mathcal{G}_{ij}(\mathbf{x}, \mathbf{x}_0) dS(\mathbf{x}) - \frac{1}{8\pi} \int_{\mathcal{S}_s} u_i(\mathbf{x}) \mathcal{T}_{ijk}(\mathbf{x}, \mathbf{x}_0) \hat{n}_k(\mathbf{x}) dS(\mathbf{x}) = 0, \quad (\text{E.4.4})$$

where we have defined the wall and particle normal vectors pointing into \mathcal{V}_1 . A superscripted “+” on $\boldsymbol{\sigma}$ indicates that the stress is evaluated in the region into which $\hat{\mathbf{n}}$ points, whereas a superscripted “-” indicates that the stress is evaluated on the opposite side. This is an important distinction because the stress can undergo a jump across boundaries. This distinction is not important on the surface bounding \mathcal{V} , which is a continuous fluid region; thus, no superscript is assigned to $\boldsymbol{\sigma}$ in the integral over $\partial\mathcal{V}$.

Multiplying (E.4.4) by κ , applying $\mathbf{u}(\mathbf{x}) = \mathbf{0}$ for $\mathbf{x} \in \mathcal{S}_w$ (no slip), and adding up the three equations gives

$$\begin{aligned} & -\frac{1}{8\pi\mu} \int_{\mathcal{S}_s} [\![\sigma_{ik}(\mathbf{x})]\!] \hat{n}_k(\mathbf{x}) \mathcal{G}_{ij}(\mathbf{x}, \mathbf{x}_0) dS(\mathbf{x}) + \frac{1-\kappa}{8\pi} \int_{\mathcal{S}_s} u_i(\mathbf{x}) \mathcal{T}_{ijk}(\mathbf{x}, \mathbf{x}_0) \hat{n}_k(\mathbf{x}) dS(\mathbf{x}) \\ & - \frac{1}{8\pi\mu} \int_{\mathcal{S}_w} [\![\sigma_{ik}(\mathbf{x})]\!] \hat{n}_k(\mathbf{x}) \mathcal{G}_{ij}(\mathbf{x}, \mathbf{x}_0) dS(\mathbf{x}) - \frac{1}{8\pi\mu} \int_{\partial\mathcal{V}} \sigma_{ik}(\mathbf{x}) \hat{n}_k(\mathbf{x}) \mathcal{G}_{ij}(\mathbf{x}, \mathbf{x}_0) dS(\mathbf{x}) \\ & + \frac{1}{8\pi} \int_{\partial\mathcal{V}} u_i(\mathbf{x}) \mathcal{T}_{ijk}(\mathbf{x}, \mathbf{x}_0) \hat{n}_k(\mathbf{x}) dS(\mathbf{x}) = u_j(\mathbf{x}_0), \end{aligned} \quad (\text{E.4.5})$$

where $[\![\cdot]\!] = (\cdot)^+ - (\cdot)^-$ denotes a jump. As previously indicated, the integrals over $\partial\mathcal{V}$ must be evaluated directly. This can be done by converting them back into volume integrals. First, we note that \mathbf{u} and $\boldsymbol{\sigma}$ have the decomposition,

$$u_i = \langle u_i \rangle + u_i^P(\mathbf{x}), \quad (\text{E.4.6})$$

$$\sigma_{ik} = - \left\langle \frac{\partial p}{\partial x_j} \right\rangle x_j \delta_{ik} + \sigma_{ik}^P(\mathbf{x}), \quad (\text{E.4.7})$$

where \mathbf{u}^P and $\boldsymbol{\sigma}^P$ are periodic and have zero mean, viz.,

$$u_i^P(\mathbf{x}) = u_i^P(\mathbf{x} + \mathbf{x}^{(n)}), \quad \int_{\mathcal{V}} u_i^P(\mathbf{x}) d^3x = 0, \quad (\text{E.4.8})$$

$$\sigma_{ik}^P(\mathbf{x}) = \sigma_{ik}^P(\mathbf{x} + \mathbf{x}^{(n)}), \quad \int_{\mathcal{V}} \sigma_{ik}^P(\mathbf{x}) d^3x = 0. \quad (\text{E.4.9})$$

(Note that the periodic boundary conditions forbid a term linear in \mathbf{x} in the velocity expression!) This decomposition satisfies the periodic boundary conditions and mean-velocity integral condition. The no-slip boundary condition and particle stress condition specify the particular form for \mathbf{u}^P and $\boldsymbol{\sigma}^P$. With this decomposition, we may evaluate the integrals over $\partial\mathcal{V}$. Let's start with the

single-layer potential:

$$\begin{aligned}
& -\frac{1}{8\pi\mu} \int_{\partial\mathcal{V}} \sigma_{ik}(\mathbf{x}) \hat{n}_k(\mathbf{x}) \mathcal{G}_{ij}(\mathbf{x}, \mathbf{x}_0) dS(\mathbf{x}) \\
& = -\frac{1}{8\pi\mu} \int_{\partial\mathcal{V}} \left[-\left\langle \frac{\partial p}{\partial x_m} \right\rangle x_m \delta_{ik} + \sigma_{ik}^P(\mathbf{x}) \right] \hat{n}_k(\mathbf{x}) \mathcal{G}_{ij}(\mathbf{x}, \mathbf{x}_0) dS(\mathbf{x}) \\
& = \frac{1}{8\pi\mu} \left\langle \frac{\partial p}{\partial x_m} \right\rangle \int_{\partial\mathcal{V}} x_m \hat{n}_i(\mathbf{x}) \mathcal{G}_{ij}(\mathbf{x}, \mathbf{x}_0) dS(\mathbf{x}) \\
& = -\frac{1}{8\pi\mu} \left\langle \frac{\partial p}{\partial x_m} \right\rangle \int_{\mathcal{V}} \frac{\partial}{\partial x_i} [x_m \mathcal{G}_{ij}(\mathbf{x}, \mathbf{x}_0)] d^3\mathbf{x} \quad (\hat{\mathbf{n}} \text{ points into } \mathcal{V}) \\
& = -\frac{1}{8\pi\mu} \left\langle \frac{\partial p}{\partial x_j} \right\rangle \int_{\mathcal{V}} \left[\mathcal{G}_{mj}(\mathbf{x}, \mathbf{x}_0) + x_j \frac{\partial \mathcal{G}_{ij}(\mathbf{x}, \mathbf{x}_0)}{\partial x_i} \right] d^3\mathbf{x} \\
& = 0,
\end{aligned} \tag{E.4.10}$$

where in the third and last lines we have used the fact that (i) σ^P is periodic with zero mean and (ii) \mathcal{G} is periodic, has zero mean, and is divergence-free. Now we examine the double-layer potential:

$$\begin{aligned}
& \frac{1}{8\pi} \int_{\partial\mathcal{V}} u_i(\mathbf{x}) \mathcal{T}_{ijk}(\mathbf{x}, \mathbf{x}_0) \hat{n}_k(\mathbf{x}) dS(\mathbf{x}) \\
& = \frac{1}{8\pi} \int_{\partial\mathcal{V}} [\langle u_i \rangle + u_i^P(\mathbf{x})] \left[-\frac{8\pi x_j \delta_{ik}}{\Omega} + \mathcal{T}_{ijk}^P(\mathbf{x}, \mathbf{x}_0) \right] \hat{n}_k(\mathbf{x}) dS(\mathbf{x}) \\
& = -\frac{\langle u_i \rangle}{\Omega} \int_{\partial\mathcal{V}} x_j \hat{n}_i(\mathbf{x}) dS(\mathbf{x}) - \frac{1}{\Omega} \int_{\partial\mathcal{V}} x_j u_i^P(\mathbf{x}) \hat{n}_i(\mathbf{x}) dS(\mathbf{x}) \\
& = \frac{\langle u_i \rangle}{\Omega} \int_{\mathcal{V}} \delta_{ij} d^3\mathbf{x} + \frac{1}{\Omega} \int_{\mathcal{V}} \frac{\partial}{\partial x_i} [x_j u_i^P(\mathbf{x})] d^3\mathbf{x} \quad (\hat{\mathbf{n}} \text{ points into } \mathcal{V}) \\
& = \langle u_j \rangle + \frac{1}{\Omega} \int_{\mathcal{V}} \left[u_j^P(\mathbf{x}) + x_j \frac{\partial u_i^P(\mathbf{x})}{\partial x_i} \right] d^3\mathbf{x} \\
& = \langle u_j \rangle,
\end{aligned} \tag{E.4.11}$$

where in the third and last lines we have used the fact that (i) \mathcal{T}^P is periodic with zero mean and (ii) \mathbf{u}^P is periodic, has zero mean, and is divergence-free. With the above results, we may eliminate the integral over the boundary of \mathcal{V} and the representation theorem becomes,

$$\begin{aligned}
u_j(\mathbf{x}_0) & = -\frac{1}{8\pi\mu} \int_{\mathcal{S}_s} [\sigma_{ik}(\mathbf{x})] \hat{n}_k(\mathbf{x}) \mathcal{G}_{ij}(\mathbf{x}, \mathbf{x}_0) dS(\mathbf{x}) + \frac{1-\kappa}{8\pi} \int_{\mathcal{S}_s} u_i(\mathbf{x}) \mathcal{T}_{ijk}(\mathbf{x}, \mathbf{x}_0) \hat{n}_k(\mathbf{x}) dS(\mathbf{x}) \\
& \quad - \frac{1}{8\pi\mu} \int_{\mathcal{S}_w} [\sigma_{ik}(\mathbf{x})] \hat{n}_k(\mathbf{x}) \mathcal{G}_{ij}(\mathbf{x}, \mathbf{x}_0) dS(\mathbf{x}) + \langle u_j \rangle.
\end{aligned} \tag{E.4.12}$$

E.4.2 Points on the wall boundary

Now let's consider the situation where $\mathbf{x}_0 \in \mathcal{S}_w$. Again, we apply the representation theorem to the regions \mathcal{V}_1 , \mathcal{V}_2 , and \mathcal{V}_0 :

for $\mathbf{x} \in \mathcal{V}_1$:

$$\begin{aligned} & -\frac{1}{8\pi\mu} \int_{\mathcal{S}_s} \sigma_{ik}^+(\mathbf{x}) \hat{n}_k(\mathbf{x}) \mathcal{G}_{ij}(\mathbf{x}, \mathbf{x}_0) dS(\mathbf{x}) + \frac{1}{8\pi} \int_{\mathcal{S}_s} u_i(\mathbf{x}) \mathcal{T}_{ijk}(\mathbf{x}, \mathbf{x}_0) \hat{n}_k(\mathbf{x}) dS(\mathbf{x}) \\ & - \frac{1}{8\pi\mu} \int_{\mathcal{S}_w} \sigma_{ik}^+(\mathbf{x}) \hat{n}_k(\mathbf{x}) \mathcal{G}_{ij}(\mathbf{x}, \mathbf{x}_0) dS(\mathbf{x}) + \frac{1}{8\pi} \int_{\mathcal{S}_w} u_i(\mathbf{x}) \mathcal{T}_{ijk}(\mathbf{x}, \mathbf{x}_0) \hat{n}_k(\mathbf{x}) dS(\mathbf{x}) = \frac{1}{2} u_j(\mathbf{x}_0), \end{aligned} \quad (\text{E.4.13})$$

for $\mathbf{x} \in \mathcal{V}_2$:

$$\begin{aligned} & -\frac{1}{8\pi\mu} \int_{\partial\mathcal{V}} \sigma_{ik}(\mathbf{x}) \hat{n}_k(\mathbf{x}) \mathcal{G}_{ij}(\mathbf{x}, \mathbf{x}_0) dS(\mathbf{x}) + \frac{1}{8\pi} \int_{\partial\mathcal{V}} u_i(\mathbf{x}) \mathcal{T}_{ijk}(\mathbf{x}, \mathbf{x}_0) \hat{n}_k(\mathbf{x}) dS(\mathbf{x}) \\ & + \frac{1}{8\pi\mu} \int_{\mathcal{S}_w} \sigma_{ik}^-(\mathbf{x}) \hat{n}_k(\mathbf{x}) \mathcal{G}_{ij}(\mathbf{x}, \mathbf{x}_0) dS(\mathbf{x}) - \frac{1}{8\pi} \int_{\mathcal{S}_w} u_i(\mathbf{x}) \mathcal{T}_{ijk}(\mathbf{x}, \mathbf{x}_0) \hat{n}_k(\mathbf{x}) dS(\mathbf{x}) = \frac{1}{2} u_j(\mathbf{x}_0), \end{aligned} \quad (\text{E.4.14})$$

for $\mathbf{x} \in \mathcal{V}_0$:

$$\begin{aligned} & \frac{1}{8\pi\kappa\mu} \int_{\mathcal{S}_s} \sigma_{ik}^-(\mathbf{x}) \hat{n}_k(\mathbf{x}) \mathcal{G}_{ij}(\mathbf{x}, \mathbf{x}_0) dS(\mathbf{x}) - \frac{1}{8\pi} \int_{\mathcal{S}_s} u_i(\mathbf{x}) \mathcal{T}_{ijk}(\mathbf{x}, \mathbf{x}_0) \hat{n}_k(\mathbf{x}) dS(\mathbf{x}) \\ & = 0, \end{aligned} \quad (\text{E.4.15})$$

where again, we have defined the wall and particle normal vectors pointing into \mathcal{V}_1 . Multiplying the third equation by κ , applying the no-slip conditions $\mathbf{u}(\mathbf{x} \in \mathcal{S}_w) = \mathbf{0}$ and $\mathbf{u}(\mathbf{x}_0) = \mathbf{0}$, integrating the contribution from $\partial\mathcal{V}$ directly, and summing the three equations gives the boundary integral equation for the wall surface:

$$\begin{aligned} 0 = & -\frac{1}{8\pi\mu} \int_{\mathcal{S}_s} [\![\sigma_{ik}(\mathbf{x})]\!] \hat{n}_k(\mathbf{x}) \mathcal{G}_{ij}(\mathbf{x}, \mathbf{x}_0) dS(\mathbf{x}) + \frac{1-\kappa}{8\pi} \int_{\mathcal{S}_s} u_i(\mathbf{x}) \mathcal{T}_{ijk}(\mathbf{x}, \mathbf{x}_0) \hat{n}_k(\mathbf{x}) dS(\mathbf{x}) \\ & - \frac{1}{8\pi\mu} \int_{\mathcal{S}_w} [\![\sigma_{ik}(\mathbf{x})]\!] \hat{n}_k(\mathbf{x}) \mathcal{G}_{ij}(\mathbf{x}, \mathbf{x}_0) dS(\mathbf{x}) + \langle u_j \rangle. \end{aligned} \quad (\text{E.4.16})$$

E.4.3 Points on the vesicle boundary

Now let's consider the situation where $\mathbf{x}_0 \in \mathcal{S}_s$. Again, we apply the representation theorem to the regions \mathcal{V}_1 , \mathcal{V}_2 , and \mathcal{V}_0 :

for $\mathbf{x} \in \mathcal{V}_1$:

$$\begin{aligned} & -\frac{1}{8\pi\mu} \int_{\mathcal{S}_s} \sigma_{ik}^+(\mathbf{x}) \hat{n}_k(\mathbf{x}) \mathcal{G}_{ij}(\mathbf{x}, \mathbf{x}_0) dS(\mathbf{x}) + \frac{1}{8\pi} \int_{\mathcal{S}_s} u_i(\mathbf{x}) \mathcal{T}_{ijk}(\mathbf{x}, \mathbf{x}_0) \hat{n}_k(\mathbf{x}) dS(\mathbf{x}) \\ & - \frac{1}{8\pi\mu} \int_{\mathcal{S}_w} \sigma_{ik}^+(\mathbf{x}) \hat{n}_k(\mathbf{x}) \mathcal{G}_{ij}(\mathbf{x}, \mathbf{x}_0) dS(\mathbf{x}) + \frac{1}{8\pi} \int_{\mathcal{S}_w} u_i(\mathbf{x}) \mathcal{T}_{ijk}(\mathbf{x}, \mathbf{x}_0) \hat{n}_k(\mathbf{x}) dS(\mathbf{x}) = \frac{1}{2} u_j(\mathbf{x}_0), \end{aligned} \quad (\text{E.4.17})$$

for $\mathbf{x} \in \mathcal{V}_2$:

$$\begin{aligned} & -\frac{1}{8\pi\mu} \int_{\partial\mathcal{V}} \sigma_{ik}(\mathbf{x}) \hat{n}_k(\mathbf{x}) \mathcal{G}_{ij}(\mathbf{x}, \mathbf{x}_0) dS(\mathbf{x}) + \frac{1}{8\pi} \int_{\partial\mathcal{V}} u_i(\mathbf{x}) \mathcal{T}_{ijk}(\mathbf{x}, \mathbf{x}_0) \hat{n}_k(\mathbf{x}) dS(\mathbf{x}) \\ & + \frac{1}{8\pi\mu} \int_{\mathcal{S}_w} \sigma_{ik}^-(\mathbf{x}) \hat{n}_k(\mathbf{x}) \mathcal{G}_{ij}(\mathbf{x}, \mathbf{x}_0) dS(\mathbf{x}) - \frac{1}{8\pi} \int_{\mathcal{S}_w} u_i(\mathbf{x}) \mathcal{T}_{ijk}(\mathbf{x}, \mathbf{x}_0) \hat{n}_k(\mathbf{x}) dS(\mathbf{x}) \\ & = 0, \end{aligned} \quad (\text{E.4.18})$$

for $\mathbf{x} \in \mathcal{V}_0$:

$$\frac{1}{8\pi\kappa\mu} \int_{\mathcal{S}_s} \sigma_{ik}^-(\mathbf{x}) \hat{n}_k(\mathbf{x}) \mathcal{G}_{ij}(\mathbf{x}, \mathbf{x}_0) dS(\mathbf{x}) - \frac{1}{8\pi} \int_{\mathcal{S}_s} u_i(\mathbf{x}) \mathcal{T}_{ijk}(\mathbf{x}, \mathbf{x}_0) \hat{n}_k(\mathbf{x}) dS(\mathbf{x}) = \frac{1}{2} u_j(\mathbf{x}_0), \quad (\text{E.4.19})$$

where again, we have defined the wall and particle normal vectors pointing into \mathcal{V}_1 . Multiplying the third equation by κ , applying “no slip” on the wall, evaluating the integrals over $\partial\mathcal{V}$ directly, and summing the three equations yields the boundary integral equation for the particle surface:

$$\begin{aligned} \frac{1+\kappa}{2} u_j(\mathbf{x}_0) &= -\frac{1}{8\pi\mu} \int_{\mathcal{S}_s} [\![\sigma_{ik}(\mathbf{x})]\!] \hat{n}_k(\mathbf{x}) \mathcal{G}_{ij}(\mathbf{x}, \mathbf{x}_0) dS(\mathbf{x}) + \frac{1-\kappa}{8\pi} \int_{\mathcal{S}_s} u_i(\mathbf{x}) \mathcal{T}_{ijk}(\mathbf{x}, \mathbf{x}_0) \hat{n}_k(\mathbf{x}) dS(\mathbf{x}) \\ & - \frac{1}{8\pi\mu} \int_{\mathcal{S}_w} [\![\sigma_{ik}(\mathbf{x})]\!] \hat{n}_k(\mathbf{x}) \mathcal{G}_{ij}(\mathbf{x}, \mathbf{x}_0) dS(\mathbf{x}) + \langle u_j \rangle. \end{aligned} \quad (\text{E.4.20})$$

E.4.4 Summary of the boundary integral equations

The traction jump $\mathbf{f}_s = [\![\mathbf{f}(\mathbf{x} \in \mathcal{S}_s)]\!] = [\![\boldsymbol{\sigma}(\mathbf{x} \in \mathcal{S}_s)]\!] \cdot \hat{\mathbf{n}}(\mathbf{x} \in \mathcal{S}_s)$ across the vesicle surfaces is treated as a known quantity from application of the membrane stress condition (thus, the stress jump across the vesicle surface is determined so long as the vesicle shape and surface kinematics are correctly determined at a particular instant in time). Then, the only unknowns are the membrane surface velocity (or single layer density) $\mathbf{u}_s = \mathbf{u}(\mathbf{x} \in \mathcal{S}_s)$ and wall traction (or double layer density) $\mathbf{f}_w = [\![\mathbf{f}(\mathbf{x} \in \mathcal{S}_w)]\!] = [\![\boldsymbol{\sigma}(\mathbf{x} \in \mathcal{S}_w)]\!] \cdot \hat{\mathbf{n}}(\mathbf{x} \in \mathcal{S}_w)$.

The boundary integral equations (E.4.16) and (E.4.20) may be written as a linear system (originally presented in the main text):

$$\begin{bmatrix} \int_{\mathcal{S}_s} \mathcal{K}_{ssij}(\mathbf{x}, \mathbf{x}_s) & \int_{\mathcal{S}_w} \mathcal{K}_{swij}(\mathbf{x}, \mathbf{x}_s) \\ \int_{\mathcal{S}_s} \mathcal{K}_{wsij}(\mathbf{x}, \mathbf{x}_w) & \int_{\mathcal{S}_w} \mathcal{K}_{wwij}(\mathbf{x}, \mathbf{x}_w) \end{bmatrix} \begin{bmatrix} u_{sj}(\mathbf{x}) \\ f_{wj}(\mathbf{x}) \end{bmatrix} dS(\mathbf{x}) = \begin{bmatrix} s_i(\mathbf{x}_s) \\ s_i(\mathbf{x}_w) \end{bmatrix}, \quad (4.2.2)$$

where

$$\begin{aligned} \mathcal{K}_{ssij}(\mathbf{x}, \mathbf{x}_0) &= \frac{1+\kappa}{2} \delta(\mathbf{x} - \mathbf{x}_0) \delta_{ij} - \frac{1-\kappa}{8\pi} \mathcal{T}_{jik}(\mathbf{x}, \mathbf{x}_0) \hat{n}_k(\mathbf{x}), \\ \mathcal{K}_{wsij}(\mathbf{x}, \mathbf{x}_0) &= \frac{1}{8\pi\mu} \mathcal{G}_{ij}(\mathbf{x}, \mathbf{x}_0), \end{aligned}$$

$$\begin{aligned}\mathcal{K}_{\text{sw}ij}(\mathbf{x}, \mathbf{x}_0) &= -\frac{1-\kappa}{8\pi} \mathcal{T}_{jik}(\mathbf{x}, \mathbf{x}_0) \hat{n}_k(\mathbf{x}), \\ \mathcal{K}_{\text{ww}ij}(\mathbf{x}, \mathbf{x}_0) &= \frac{1}{8\pi\mu} \mathcal{G}_{ij}(\mathbf{x}, \mathbf{x}_0)\end{aligned}$$

are the kernels and

$$s_i(\mathbf{x}_0) = -\frac{1}{8\pi\mu} \int_{\mathcal{S}_s} f_{sj}(\mathbf{x}) \mathcal{G}_{ji}(\mathbf{x}, \mathbf{x}_0) dS(\mathbf{x}) + \langle u_i \rangle$$

is the source. For non-smooth boundaries, the unit tensor δ appearing in the expression for \mathcal{K}_{ss} is replaced by the principal value tensor \mathcal{C} .

E.5 Numerical solution of the linear system

Equation (4.2.2) is a linear system of boundary integral equations for the unknown membrane surface velocities \mathbf{u}_s and wall surface tractions \mathbf{f}_w . We may recast this system in the compact form,

$$\mathbf{K} \cdot \mathbf{y} = \mathbf{s}, \quad (\text{E.5.1})$$

where $\mathbf{y} = [\mathbf{u}_s, \mathbf{f}_w]^\dagger$ is the vector of unknowns. In our implementation of the BEM, the boundary integral equations (E.5.1) are collocated onto unstructured, triangulated meshes approximating the surfaces \mathcal{S}_s and \mathcal{S}_w . The resulting system of algebraic equations [the discrete analog of (E.5.1)] is dense, in contrast to the finite element method (FEM). The advantage of the BEM over the FEM is that the dimensionality of the problem has been reduced by one: the originally 3D problem has been converted to a 2D problem [125]. This reduction in dimensionality was made possible by the fact that the governing Stokes' equations are *linear* in the unknowns, permitting the definition a reciprocal identity and subsequent application of the divergence theorem to volume integrals.

A Fast Fourier Transform (FFT) library was used to numerically evaluate the Green's functions \mathcal{G} and \mathcal{T} (for more details, refer to the last section in Appendix D). Numerical integration was carried out using a standard three-point quadrature on triangles (for regular kernels) or Duffy quadrature (for singular kernels) [37]. The discrete form of (E.5.1) is solved numerically using the (matrix-free) Generalized Minimum Residual (GMRES) method. Our implementation makes use of Krylov subroutines from the Portable, Extensible Toolkit for Scientific Computation (PETSc) and is parallelized using Message Passing Interface (MPI) directives. However, the density of the BEM system (E.5.1) precludes scalability to large numbers (hundreds) of processors on distributed memory parallel computer architectures. The main limitation to scalability arises in the domain decomposition and speed of communication. For more details on the numerical implementation, the reader is referred to [184].

Appendix F

Numerical methods for lubrication calculations

In Chapters 4 and 5, we invoked the lubrication approximation in order to derive approximate solutions of Stokes' equations of motion for a vesicle in channel flow. This approximation yields analytical solutions for the velocity and pressure fields in the suspending fluid phase. However, these fields depend on the vesicle shape, which is governed by nonlinear equations (the normal stress condition coupled to the kinematic condition) that must be solved numerically. In this appendix, we outline the numerical methods appropriate for solution of the shape equations in axisymmetric and non-axisymmetric domains at steady state. The former case results in a system of ordinary differential equations with respect to the axial distance x , which can be reformulated as a dynamical system and integrated using the multiple shooting method (§F.1). The latter case results in a system of (elliptic) partial differential equations in x and ϕ (ϕ being the azimuthal angle), to which we apply the nonlinear finite difference method (§F.2).

F.1 Multiple shooting method

In §4.3, we derived a one-dimensional boundary-value problem [cf. equations (4.3.6)-(4.3.10)] for the pressure $p(x)$, membrane tension $\tau(x)$, and membrane radius $\rho_s(x)$ in the domain $-L \leq x \leq 0$ (L being the vesicle length). This problem governs the motion of an axisymmetric vesicle through a circular tube in the lubrication limit. In order to avoid multivalued solutions, we avail ourselves of the transformation,

$$\rho_s ds = G_s dx, \quad (4.3.11)$$

where s is the meridional arc length. Equation (4.3.11) exchanges s for x as the independent variable. Differential increments in the axial distance x and membrane radius ρ_s can be related to increments

in s via the so-called “tilt angle” ϑ :

$$dx = \cos \vartheta \, ds, \quad d\rho_s = -\sin \vartheta \, ds. \quad (4.3.12)$$

This is a standard transformation for the solution of axisymmetric free-surface problems [100]. The surface metric G_s and curvature invariants H and K attain the forms,

$$G_s = -\frac{1}{\kappa_\phi}, \quad 2H = \kappa_\phi + \kappa_s, \quad K = \kappa_\phi \kappa_s, \quad (F.1.1)$$

where

$$\kappa_\phi = -\frac{\cos \vartheta}{\rho_s}, \quad \kappa_s = -\frac{d\vartheta}{ds} \quad (F.1.2)$$

are the principal curvatures of the surface.

Using the above relations, equations (4.3.6)-(4.3.10) may be recast as a system of first-order, nonlinear, ordinary differential equations with respect to s ,

$$\frac{dx}{ds} = \cos \vartheta, \quad (F.1.3a)$$

$$\frac{d\rho_s}{ds} = -\sin \vartheta, \quad (F.1.3b)$$

$$\frac{d\vartheta}{ds} = -\kappa_s, \quad (F.1.3c)$$

$$\frac{d\kappa_s}{ds} = \frac{\sin \vartheta \cos \vartheta}{\rho_s^2} + \frac{\kappa_s \sin \vartheta}{\rho_s} - \frac{\nu_s}{E_B}, \quad (F.1.3d)$$

$$\frac{d\nu_s}{ds} = \frac{p}{E_B} - \frac{\tau}{E_B} \left(\kappa_s - \frac{\cos \vartheta}{\rho_s} \right) + \frac{1}{2} \left(\kappa_s + \frac{\cos \vartheta}{\rho_s} \right) \left(\kappa_s^2 - \frac{\cos^2 \vartheta}{\rho_s^2} \right) + \frac{\nu_s \sin \vartheta}{\rho_s}, \quad (F.1.3e)$$

$$\frac{dp}{ds} = k^{(p)} \cos \vartheta, \quad (F.1.3f)$$

$$\frac{d\tau}{ds} = k^{(\tau)}, \quad (F.1.3g)$$

$$\frac{dA}{ds} = 2\pi\rho_s, \quad (F.1.3h)$$

$$\frac{d\Omega}{ds} = \pi\rho_s^2 \cos \vartheta, \quad (F.1.3i)$$

$$\frac{dq}{ds} = 0, \quad (F.1.3j)$$

$$\frac{dL}{ds} = 0, \quad (F.1.3k)$$

$$\frac{ds_1}{ds} = 0, \quad (F.1.3l)$$

with linear boundary conditions at the poles,

$$\text{at } s = 0 : \quad x = 0, \quad \rho_s = 0, \quad \vartheta = -\frac{1}{2}\pi, \quad \nu_s = 0, \quad A = 0, \quad \Omega = 0, \quad (F.1.4a)$$

$$\text{at } s = s_1 : \quad x = -L, \quad \rho_s = 0, \quad \vartheta = +\frac{1}{2}\pi, \quad \nu_s = 0, \quad A = A_0, \quad \Omega = \Omega_0. \quad (F.1.4b)$$

Here, $\nu_s = -E_B(dH/ds)$ is the transverse shear tension and

$$\begin{aligned} k^{(p)} &= \frac{8\mu}{R^2 - \rho_s^2} \left[2q - \left(R^2 + \frac{R^2 - \rho_s^2}{2 \log(\rho_s/R)} \right) U \right] \left[R^2 + \rho_s^2 + \frac{R^2 - \rho_s^2}{\log(\rho_s/R)} \right]^{-1}, \\ k^{(\tau)} &= \frac{m^{(p)}}{4} \left(2\rho_s + \frac{R^2 - \rho_s^2}{\rho_s \log(\rho_s/R)} \right) - \frac{\mu U}{\rho_s \log(\rho_s/R)} \end{aligned}$$

are the resistivity functions. The mean fluid velocity V has been exchanged for the leakback flux per unit circumference q by means of the identity,

$$2\pi q = \pi R^2(U - V). \quad (\text{F.1.5})$$

Note that the leakback flux q and vesicle length L are unknown *a priori* and must be determined as part of the solution; thus, they are included as dependent variables in (F.1.3). If bending elasticity is neglected [i.e., the bending parameter $\beta = E_B/(\mu VR^2)$ is vanishingly small], then the meridional curvature κ_s and transverse shear tension ν_s may be eliminated as dependent variables. The order of the dynamical system (F.1.3) reduces by two in this case. This limiting system is called the “isotropic-tension model” by [139].

The free boundary s_1 can be introduced into (F.1.3) as a dependent variable by mapping s onto the unit domain $0 \leq \xi \leq 1$, viz.,

$$s = s_1\xi. \quad (\text{F.1.6})$$

The poles $\xi = 0$ and 1 are singular points of the domain. These points must be excluded during the numerical integration procedure. We perform the numerical integration over a truncated domain, $\epsilon \leq \xi \leq 1 - \epsilon$, where $\epsilon \ll 1$, and assume that the vesicle surface approaching the poles is a spherical section with constant curvature,

$$\kappa_s = \kappa_\phi = -\frac{\cos \vartheta}{\rho_s} = \frac{p}{2\tau}, \quad \nu_s = 0, \quad \text{for } \xi \in [0, \epsilon] \cup [1 - \epsilon, 1]. \quad (\text{F.1.7})$$

Substitution into (F.1.3) and integration with the boundary conditions at $\xi = 0$ and 1 yields the local behavior of x , ρ_s , ϑ , A , and Ω near the poles:

$$x = 0, \quad \rho_s = s_1\xi, \quad \vartheta = -s_1\kappa_s\xi - \frac{\pi}{2}, \quad A = 0, \quad \Omega = 0, \quad \text{for } \xi \in [0, \epsilon], \quad (\text{F.1.8a})$$

$$x = -L, \quad \rho_s = -s_1(\xi - 1), \quad \vartheta = -s_1\kappa_s(\xi - 1) + \frac{\pi}{2}, \quad A = A_0, \quad \Omega = \Omega_0, \quad \text{for } \xi \in [1 - \epsilon, 1]. \quad (\text{F.1.8b})$$

Here, we have expanded the expressions up to linear order in ξ , neglecting errors of $O(\epsilon^2)$.

The system of equations (F.1.3)-(F.1.4) can be written in the compact form,

$$\frac{dy}{d\xi} = \mathbf{g}(\mathbf{y}), \quad \epsilon \leq \xi \leq 1 - \epsilon, \quad (\text{F.1.9})$$

$$\mathbf{r}[\mathbf{y}(\epsilon), \mathbf{y}(1 - \epsilon)] = \mathbf{0}, \quad (\text{F.1.10})$$

where

$$\begin{aligned} y_1 &= x, & y_2 &= \rho_s, & y_3 &= \vartheta, & y_4 &= \kappa_s, & y_5 &= \nu_s, & y_6 &= p, \\ y_7 &= \tau, & y_8 &= A, & y_9 &= \Omega, & y_{10} &= q, & y_{11} &= L, & y_{12} &= s_1 \end{aligned}$$

are the unknowns,

$$g_1 = s_1 \cos \vartheta,$$

$$g_2 = -s_1 \sin \vartheta,$$

$$g_3 = -s_1 \kappa_s,$$

$$g_4 = s_1 \left(\frac{\sin \vartheta \cos \vartheta}{\rho_s^2} + \frac{\kappa_s \sin \vartheta}{\rho_s} - \frac{\nu_s}{E_B} \right),$$

$$g_5 = s_1 \left[\frac{p}{E_B} - \frac{\tau}{E_B} \left(\kappa_s - \frac{\cos \vartheta}{\rho_s} \right) + \frac{1}{2} \left(\kappa_s + \frac{\cos \vartheta}{\rho_s} \right) \left(\kappa_s^2 - \frac{\cos^2 \vartheta}{\rho_s^2} \right) + \frac{\nu_s \sin \vartheta}{\rho_s} \right],$$

$$g_6 = s_1 k^{(p)} \cos \vartheta,$$

$$g_7 = s_1 k^{(\tau)},$$

$$g_8 = 2\pi s_1 \rho_s,$$

$$g_9 = \pi s_1 \rho_s^2 \cos \vartheta,$$

$$g_{10} = g_{11} = g_{12} = 0$$

are the sources, and

$$r_1 = x(\epsilon),$$

$$r_2 = \rho_s(\epsilon) - \epsilon s_1(\epsilon),$$

$$r_3 = \vartheta(\epsilon) + \epsilon s_1(\epsilon) \kappa_s(\epsilon) + \frac{\pi}{2},$$

$$r_4 = \nu_s(\epsilon),$$

$$r_5 = A(\epsilon),$$

$$r_6 = \Omega(\epsilon),$$

$$r_7 = x(1 - \epsilon) + L(1 - \epsilon),$$

$$r_8 = \rho_s(1 - \epsilon) - \epsilon s_1(1 - \epsilon),$$

$$\begin{aligned} r_9 &= \vartheta(1 - \epsilon) - \epsilon s_1(1 - \epsilon)\kappa_s(1 - \epsilon) - \frac{\pi}{2}, \\ r_{10} &= \nu_s(1 - \epsilon), \\ r_{11} &= A(1 - \epsilon), \\ r_{12} &= \Omega(1 - \epsilon) \end{aligned}$$

are the boundary conditions. Equations (F.1.9)-(F.1.10) may be integrated using numerical methods for ordinary differential equations. Shooting methods are particularly useful for ordinary differential equations, since they make use of highly accurate timestepping schemes (e.g., Runge-Kutta methods, which are most commonly used for initial-value problems) in conjunction with an iterative solution procedure for enforcing the boundary conditions. Secomb and coworkers noted that the inclusion of bending elasticity in the membrane shape equation results in very stiff system, which cannot be straightforwardly integrated using the simple shooting method [139]. They suggested the use of the *multiple shooting method*, which is among the most powerful methods for solving stiff, nonlinear boundary-value problems in one dimension [154, 96]. An excellent description of the method, including hints for practical implementation, can be found in §7.3.5 of [154]. Below, we describe in detail our implementation of the multiple shooting method towards the numerical solution of (F.1.9)-(F.1.10). In §F.1.1, we describe a version of the method where integration always proceeds from left to right (through increasing values of ξ). In §F.1.2, we describe an alternative method where integration proceeds from the boundaries towards a “fitting point” within the domain. The latter method is most suitable for solving (F.1.9)-(F.1.10), since the boundaries are singular points.

F.1.1 Shooting from one end

In this section, we follow closely the procedure outlined in §7.3.5 of [154]. The domain of (F.1.9) is subdivided into $N - 1$ intervals separated by “shooting points,”

$$\epsilon = \xi_1 < \xi_2 < \dots < \xi_N = 1 - \epsilon. \quad (\text{F.1.11})$$

Let $\mathbf{n}_n = \mathbf{y}(\xi_n)$, $n = 1, 2, \dots, N$ denote the unknown function sampled at the n th shooting point. Then, let $\mathbf{y}(\xi; \xi_n, \mathbf{n}_n)$ denote the solution of the n th initial-value problem,

$$\frac{d\mathbf{y}}{d\xi} = \mathbf{g}(\mathbf{y}), \quad \xi_n \leq \xi \leq \xi_{n+1}, \quad n = 1, 2, \dots, N - 1, \quad (\text{F.1.12})$$

$$\mathbf{y}(\xi_n) = \mathbf{n}_n. \quad (\text{F.1.13})$$

The sample values η_n of the exact solution $\mathbf{y}(\xi)$ are computed by iteratively enforcing the continuity and boundary conditions,

$$\mathbf{y}(\xi_{n+1}; \xi_n, \eta_n) = \eta_{n+1}, \quad n = 1, 2, \dots, N-1, \quad (\text{F.1.14a})$$

$$\mathbf{r}(\eta_1, \eta_N) = \mathbf{0}. \quad (\text{F.1.14b})$$

For a system of rank M [clearly, $M = 12$ for (F.1.3)-(F.1.4)], equation (F.1.14) comprises a system of NM equations in the NM unknown components η_{nm} , $m = 1, 2, \dots, M$ of the η_n -vectors,

$$\eta_n = \begin{bmatrix} \eta_{n1} & \eta_{n2} & \cdots & \eta_{nM} \end{bmatrix}^\dagger, \quad n = 1, 2, \dots, N. \quad (\text{F.1.15})$$

The nonlinear system (F.1.14) can be expressed as a rank- N system of M -vector equations,

$$\mathbf{f}_1(\eta_1, \eta_2) = \mathbf{y}(\xi_2; \xi_1, \eta_1) - \eta_2 = \mathbf{0},$$

$$\mathbf{f}_2(\eta_2, \eta_3) = \mathbf{y}(\xi_3; \xi_2, \eta_2) - \eta_3 = \mathbf{0},$$

$$\vdots$$

$$\mathbf{f}_{N-1}(\eta_{N-1}, \eta_N) = \mathbf{y}(\xi_N; \xi_{N-1}, \eta_{N-1}) - \eta_N = \mathbf{0},$$

$$\mathbf{f}_N(\eta_1, \eta_N) = \mathbf{r}(\eta_1, \eta_N) = \mathbf{0},$$

or as a single NM -vector equation,

$$\mathbf{f}(\eta) = \mathbf{0}, \quad (\text{F.1.16})$$

where

$$\mathbf{f} = \begin{bmatrix} \mathbf{f}_1 & \mathbf{f}_2 & \cdots & \mathbf{f}_{N-1} & \mathbf{f}_N \end{bmatrix}^\dagger \quad (\text{F.1.17})$$

is the vector function to be zeroed and

$$\eta = \begin{bmatrix} \eta_1 & \eta_2 & \cdots & \eta_{N-1} & \eta_N \end{bmatrix}^\dagger \quad (\text{F.1.18})$$

is the vector of unknowns. Equation (F.1.16) can be solved iteratively using Newton's method. Starting from an initial guess η^* for the unknown sample values η , Newton's method proceeds as follows:

$$\eta^{(k+1)} = \eta^{(k)} - [\mathbf{J}(\eta^{(k)})]^{-1} \cdot \mathbf{f}(\eta^{(k)}), \quad k = 0, 1, 2, \dots, \quad (\text{F.1.19})$$

$$\eta^{(0)} = \eta^*, \quad (\text{F.1.20})$$

where

$$\mathbf{J}(\boldsymbol{\eta}) = [\nabla_{\delta\boldsymbol{\eta}} \mathbf{f}(\boldsymbol{\eta} + \delta\boldsymbol{\eta})]^\dagger \Big|_{\delta\boldsymbol{\eta}=\mathbf{0}} = \left\{ \left[\frac{\partial f_{nm}(\boldsymbol{\eta} + \delta\boldsymbol{\eta})}{\partial \delta\eta_{n'm'}} \right]_{m,m'=1,2,\dots,M} \right\}_{n,n'=1,2,\dots,N} \Big|_{\delta\boldsymbol{\eta}=\mathbf{0}} \quad (\text{F.1.21})$$

is the $NM \times NM$ Jacobian matrix. The k th Newton step $\Delta\boldsymbol{\eta}^{(k)} = \boldsymbol{\eta}^{(k+1)} - \boldsymbol{\eta}^{(k)}$ is obtained from the solution of the linear system,

$$\mathbf{J}^{(k)} \cdot \Delta\boldsymbol{\eta}^{(k)} = -\mathbf{f}^{(k)}, \quad k = 0, 1, 2, \dots, \quad (\text{F.1.22})$$

where $\mathbf{J}^{(k)} = \mathbf{J}(\boldsymbol{\eta}^{(k)})$ and $\mathbf{f}^{(k)} = \mathbf{f}(\boldsymbol{\eta}^{(k)})$. Iteration proceeds until either one of the vector norms $\|\Delta\boldsymbol{\eta}^{(k)}\|$ or $\|\mathbf{f}^{(k)}\|$ falls below a predetermined tolerance ε (e.g., $\varepsilon = 10^{-6}$ is a typical value).

We now address computation of the Jacobian matrix \mathbf{J} . If we define the block matrices,

$$\mathbf{G}_n = [\nabla_{\delta\boldsymbol{\eta}_n} \mathbf{y}(\xi_{n+1}; \xi_n, \boldsymbol{\eta}_n + \delta\boldsymbol{\eta}_n)]^\dagger \Big|_{\delta\boldsymbol{\eta}_n=\mathbf{0}}, \quad n = 1, 2, \dots, N-1, \quad (\text{F.1.23})$$

$$\mathbf{A} = [\nabla_{\delta\boldsymbol{\eta}_1} \mathbf{r}(\boldsymbol{\eta}_1 + \delta\boldsymbol{\eta}_1, \boldsymbol{\eta}_N)]^\dagger \Big|_{\delta\boldsymbol{\eta}_1=\mathbf{0}}, \quad (\text{F.1.24})$$

$$\mathbf{B} = [\nabla_{\delta\boldsymbol{\eta}_N} \mathbf{r}(\boldsymbol{\eta}_1, \boldsymbol{\eta}_N + \delta\boldsymbol{\eta}_N)]^\dagger \Big|_{\delta\boldsymbol{\eta}_N=\mathbf{0}}, \quad (\text{F.1.25})$$

then the explicit structure of \mathbf{J} can be written as,

$$\mathbf{J} = \begin{bmatrix} \mathbf{G}_1 & -\mathbf{I} & & & \\ & \mathbf{G}_2 & -\mathbf{I} & & \\ & & \ddots & \ddots & \\ & & & \mathbf{G}_{N-1} & -\mathbf{I} \\ \mathbf{A} & & & & \mathbf{B} \end{bmatrix}. \quad (\text{F.1.26})$$

The matrices \mathbf{A} and \mathbf{B} can be computed after linearizing the boundary conditions (F.1.10). We approximate the \mathbf{G}_n -matrices by finite differences as follows. Equations (F.1.12)-(F.1.13) are integrated numerically (e.g., using a Runge-Kutta integrator) for two parameters $\boldsymbol{\eta}_n$ and $\boldsymbol{\eta}_n + \delta\boldsymbol{\eta}_n$, where $\|\delta\boldsymbol{\eta}_n\| \ll 1$. Then, the \mathbf{G}_n -matrices are approximated by the finite difference analog,

$$\mathbf{G}_n \approx \left[\frac{y_m(\xi_{n+1}; \xi_n, \boldsymbol{\eta}_n + \delta\boldsymbol{\eta}_n) - y_m(\xi_{n+1}; \xi_n, \boldsymbol{\eta}_n)}{\delta s_{nm'}} \right]_{m,m'=1,2,\dots,M}, \quad n = 1, 2, \dots, N-1. \quad (\text{F.1.27})$$

Numerically approximating the \mathbf{G}_n -matrices is not prohibitively expensive, since the boundary-value problem is one-dimensional. Given the explicit structure of the Jacobian matrix (F.1.26), the linear system (F.1.22) can be solved by direct elimination as follows. First, we note that the NM -vector

equation (F.1.22) is equivalent to the rank- N system of M -vector equations,

$$\begin{aligned}\mathbf{G}_1 \cdot \Delta\boldsymbol{\eta}_1 - \Delta\boldsymbol{\eta}_2 &= -\mathbf{f}_1, \\ \mathbf{G}_2 \cdot \Delta\boldsymbol{\eta}_2 - \Delta\boldsymbol{\eta}_3 &= -\mathbf{f}_2, \\ &\vdots \\ \mathbf{G}_{N-1} \cdot \Delta\boldsymbol{\eta}_{N-1} - \Delta\boldsymbol{\eta}_N &= -\mathbf{f}_{N-1}, \\ \mathbf{A} \cdot \Delta\boldsymbol{\eta}_1 + \mathbf{B} \cdot \Delta\boldsymbol{\eta}_N &= -\mathbf{f}_N.\end{aligned}$$

Here, the superscript “(k)” has been suppressed for the sake of convenience. Starting with the first equation, the $\Delta\boldsymbol{\eta}_n$ can be expressed in terms of $\Delta\boldsymbol{\eta}_1$ by successive substitution,

$$\begin{aligned}\Delta\boldsymbol{\eta}_2 &= \mathbf{G}_1 \cdot \Delta\boldsymbol{\eta}_1 + \mathbf{f}_1, \\ \Delta\boldsymbol{\eta}_3 &= \mathbf{G}_2 \cdot \Delta\boldsymbol{\eta}_2 + \mathbf{f}_2 \\ &= \mathbf{G}_2 \cdot \mathbf{G}_1 \cdot \Delta\boldsymbol{\eta}_1 + \mathbf{G}_2 \cdot \mathbf{f}_1 + \mathbf{f}_2, \\ &\vdots \\ \Delta\boldsymbol{\eta}_N &= \left(\prod_{n=1}^{N-1} \mathbf{G}_{N-n} \right) \cdot \Delta\boldsymbol{\eta}_1 + \sum_{n=1}^{N-1} \left(\prod_{n'=1}^{n-1} \mathbf{G}_{N-n'} \right) \cdot \mathbf{F}_{N-n}.\end{aligned}$$

Combining the last expression with the boundary conditions yields a single $M \times M$ matrix-vector equation for $\Delta\boldsymbol{\eta}_1$:

$$\mathbf{K} \cdot \Delta\boldsymbol{\eta}_1 = \mathbf{w}, \quad (\text{F.1.28})$$

where

$$\mathbf{K} = \mathbf{A} + \mathbf{B} \cdot \left(\prod_{n=1}^{N-1} \mathbf{G}_{N-n} \right), \quad (\text{F.1.29})$$

$$\mathbf{w} = -\mathbf{f}_N - \mathbf{B} \cdot \sum_{n=1}^{N-1} \left(\prod_{n'=1}^{n-1} \mathbf{G}_{N-n'} \right) \cdot \mathbf{F}_{N-n}. \quad (\text{F.1.30})$$

The reduced system (F.1.28) can be solved by Gaussian elimination, and the remaining $\Delta\boldsymbol{\eta}_n$ are obtained by back-substitution.

The global convergence properties of Newton’s method can be accelerated by a line-search and backtracking procedure [154, 127]. Once a solution for $\Delta\boldsymbol{\eta}^{(k)}$ is obtained at the k th iteration, the next iterate $\boldsymbol{\eta}^{(k+1)}$ is updated using a modified form of (F.1.19):

$$\boldsymbol{\eta}^{(k+1)} = \boldsymbol{\eta}^{(k)} - \sigma \Delta\boldsymbol{\eta}^{(k)}, \quad (\text{F.1.31})$$

where σ is a weighting function that lies in the range $0 < \sigma \leq 1$. The idea behind the modified form of Newton's method (F.1.31) is to take fractional steps such that the norm of $\mathbf{f}(\boldsymbol{\eta}^{(k)} + \sigma\Delta\boldsymbol{\eta}^{(k)})$ has decreased sufficiently. However, we must bound σ from below so that the method progresses at a sufficient rate even if $\|\mathbf{f}\|$ does not decrease. For further details on the selection of the weighting function σ , the reader is referred to [127]. Here, we employ a finite search process to select σ [equation (5.4.3.5) on p. 315 of [154]],

$$\sigma = 2^{-j}, \quad j = \min \left\{ i \geq 0 \mid \|\mathbf{f}(\boldsymbol{\eta}^{(k)} + 2^{-i}\Delta\boldsymbol{\eta}^{(k)})\| < \|\mathbf{f}(\boldsymbol{\eta}^{(k)})\| \right\}, \quad (\text{F.1.32})$$

and truncate the search at some upper bound for j , which ensures that the method progresses at a sufficient rate.

In summary, the original boundary-value problem (F.1.9)-(F.1.10) amounts to solving $N - 1$ initial-value problems (F.1.12)-(F.1.13). In the procedure just described, integration always proceeds from left to right through increasing values of ξ . This can pose problems when the right boundary $\xi = 1$ is a singular point. In the next section, we illustrate a modification to the above procedure in which integration always proceeds in the direction *away* from the boundaries towards a fitting point somewhere within the domain.

F.1.2 Shooting from both ends to a fitting point

When the boundary points are singular points, it is good practice to integrate away from the boundaries towards the interior of the domain [127]. In this version of the multiple shooting method, the domain $0 \leq \xi \leq 1$ is subdivided into $2N$ segments:

$$\epsilon = \xi_1 < \xi_2 < \cdots < \xi_{2N+1} = 1 - \epsilon. \quad (\text{F.1.33})$$

The middle point ξ_{N+1} is called the “fitting point.” Integration proceeds from left to right over the interval $\xi_1 \leq \xi \leq \xi_{N+1}$ and from right to left in $\xi_{N+1} \leq \xi \leq \xi_{2N+1}$. The system of nonlinear equations to be solved is given by,

$$\begin{aligned} \mathbf{f}_1(\boldsymbol{\eta}_1, \boldsymbol{\eta}_2) &= \mathbf{y}(\xi_2; \xi_1, \boldsymbol{\eta}_1) - \boldsymbol{\eta}_2 = \mathbf{0}, \\ \mathbf{f}_2(\boldsymbol{\eta}_2, \boldsymbol{\eta}_3) &= \mathbf{y}(\xi_3; \xi_2, \boldsymbol{\eta}_2) - \boldsymbol{\eta}_3 = \mathbf{0}, \\ &\vdots \\ \mathbf{f}_N(\boldsymbol{\eta}_N, \boldsymbol{\eta}_{N+1}) &= \mathbf{y}(\xi_{N+1}; \xi_N, \boldsymbol{\eta}_N) - \boldsymbol{\eta}_{N+1} = \mathbf{0}, \\ \mathbf{f}_{N+1}(\boldsymbol{\eta}_{N+1}, \boldsymbol{\eta}_{N+2}) &= \mathbf{y}(\xi_{N+1}; \xi_{N+2}, \boldsymbol{\eta}_{N+2}) - \boldsymbol{\eta}_{N+1} = \mathbf{0}, \\ &\vdots \end{aligned}$$

$$\begin{aligned}\mathbf{f}_{2N-1}(\boldsymbol{\eta}_{2N-1}, \boldsymbol{\eta}_{2N}) &= \mathbf{y}(\xi_{2N-1}; \xi_{2N}, \boldsymbol{\eta}_{2N}) - \boldsymbol{\eta}_{2N-1} = \mathbf{0}, \\ \mathbf{f}_{2N}(\boldsymbol{\eta}_{2N}, \boldsymbol{\eta}_{2N+1}) &= \mathbf{y}(\xi_{2N}; \xi_{2N+1}, \boldsymbol{\eta}_{2N+1}) - \boldsymbol{\eta}_{2N} = \mathbf{0}, \\ \mathbf{f}_{2N+1}(\boldsymbol{\eta}_1, \boldsymbol{\eta}_{2N+1}) &= \mathbf{r}(\boldsymbol{\eta}_1, \boldsymbol{\eta}_{2N+1}) = \mathbf{0},\end{aligned}$$

The k th Newton step $\Delta\boldsymbol{\eta}^{(k)} = \boldsymbol{\eta}^{(k+1)} - \boldsymbol{\eta}^{(k)}$ is the solution of the following linear system,

$$\mathbf{J}^{(k)} \cdot \Delta\boldsymbol{\eta}^{(k)} = -\mathbf{f}^{(k)}, \quad (\text{F.1.34})$$

where

$$\mathbf{f} = \begin{bmatrix} \mathbf{f}_1 & \mathbf{f}_2 & \cdots & \mathbf{f}_{2N+1} \end{bmatrix}^\dagger, \quad (\text{F.1.35})$$

$$\boldsymbol{\eta} = \begin{bmatrix} \boldsymbol{\eta}_1 & \boldsymbol{\eta}_2 & \cdots & \boldsymbol{\eta}_{2N+1} \end{bmatrix}^\dagger, \quad (\text{F.1.36})$$

$$\Delta\boldsymbol{\eta} = \begin{bmatrix} \Delta\boldsymbol{\eta}_1 & \Delta\boldsymbol{\eta}_2 & \cdots & \Delta\boldsymbol{\eta}_{2N+1} \end{bmatrix}^\dagger, \quad (\text{F.1.37})$$

and

$$\mathbf{J} = \begin{bmatrix} \mathbf{G}_1 & -\mathbf{I} & & & & & \\ & \mathbf{G}_2 & -\mathbf{I} & & & & \\ & & \ddots & \ddots & & & \\ & & & \mathbf{G}_N & -\mathbf{I} & & \\ & & & & -\mathbf{I} & \mathbf{G}_{N+1} & \\ & & & & & \ddots & \ddots \\ & & & & & & -\mathbf{I} & \mathbf{G}_{2N-1} \\ & & & & & & & -\mathbf{I} & \mathbf{G}_{2N} \\ \mathbf{A} & & & & & & & & \mathbf{B} \end{bmatrix}. \quad (\text{F.1.38})$$

The block matrices \mathbf{G}_n , \mathbf{A} , and \mathbf{B} are defined as,

$$\mathbf{G}_n = \begin{cases} [\nabla_{\delta\boldsymbol{\eta}_n} \mathbf{y}(\xi_{n+1}; \xi_n, \boldsymbol{\eta}_n + \delta\boldsymbol{\eta}_n)]^\dagger \Big|_{\delta\boldsymbol{\eta}_n=\mathbf{0}}, & n = 1, 2, \dots, N, \\ [\nabla_{\delta\boldsymbol{\eta}_n} \mathbf{y}(\xi_n; \xi_{n+1}, \boldsymbol{\eta}_{n+1} + \delta\boldsymbol{\eta}_{n+1})]^\dagger \Big|_{\delta\boldsymbol{\eta}_n=\mathbf{0}}, & n = N+1, N+2, \dots, 2N, \end{cases} \quad (\text{F.1.39})$$

$$\mathbf{A} = [\nabla_{\delta\boldsymbol{\eta}_1} \mathbf{r}(\boldsymbol{\eta}_1 + \delta\boldsymbol{\eta}_1, \boldsymbol{\eta}_{2N+1})]^\dagger \Big|_{\delta\boldsymbol{\eta}_1=\mathbf{0}}, \quad (\text{F.1.40})$$

$$\mathbf{B} = [\nabla_{\delta\boldsymbol{\eta}_{2N+1}} \mathbf{r}(\boldsymbol{\eta}_1, \boldsymbol{\eta}_{2N+1} + \delta\boldsymbol{\eta}_{2N+1})]^\dagger \Big|_{\delta\boldsymbol{\eta}_{2N+1}=\mathbf{0}}. \quad (\text{F.1.41})$$

As in §F.1.1, we can reduce the linear system (F.1.34) to a smaller system by exploiting the structure of the Jacobian matrix (F.1.38). Writing out the system explicitly gives,

$$\mathbf{G}_1 \cdot \Delta\boldsymbol{\eta}_1 - \Delta\boldsymbol{\eta}_2 = -\mathbf{f}_1,$$

$$\mathbf{G}_2 \cdot \Delta\boldsymbol{\eta}_2 - \Delta\boldsymbol{\eta}_3 = -\mathbf{f}_2,$$

$$\begin{aligned}
& \vdots \\
& \mathbf{G}_N \cdot \Delta \boldsymbol{\eta}_N - \Delta \boldsymbol{\eta}_{N+1} = -\mathbf{f}_N, \\
& \mathbf{G}_{N+1} \cdot \Delta \boldsymbol{\eta}_{N+2} - \Delta \boldsymbol{\eta}_{N+1} = -\mathbf{f}_{N+1}, \\
& \vdots \\
& \mathbf{G}_{2N-1} \cdot \Delta \boldsymbol{\eta}_{2N} - \Delta \boldsymbol{\eta}_{2N-1} = -\mathbf{f}_{2N-1}, \\
& \mathbf{G}_{2N} \cdot \Delta \boldsymbol{\eta}_{2N+1} - \Delta \boldsymbol{\eta}_{2N} = -\mathbf{f}_{2N}, \\
& \mathbf{A} \cdot \Delta \boldsymbol{\eta}_1 + \mathbf{B} \cdot \Delta \boldsymbol{\eta}_{2N+1} = -\mathbf{f}_{2N+1}.
\end{aligned}$$

Here, the superscript “(k)” has been suppressed for the sake of convenience. We solve for the midpoint element by successive substitution over the lower grid points:

$$\begin{aligned}
\Delta \boldsymbol{\eta}_2 &= \mathbf{G}_1 \cdot \Delta \boldsymbol{\eta}_1 + \mathbf{f}_1, \\
\Delta \boldsymbol{\eta}_3 &= \mathbf{G}_2 \cdot \Delta \boldsymbol{\eta}_2 + \mathbf{f}_2, \\
&= \mathbf{G}_2 \cdot \mathbf{G}_1 \cdot \Delta \boldsymbol{\eta}_1 + \mathbf{G}_2 \cdot \mathbf{f}_1 + \mathbf{f}_2, \\
&\vdots \\
\Delta \boldsymbol{\eta}_{N+1} &= \mathbf{G}_N \cdot \mathbf{G}_{N-1} \cdots \mathbf{G}_1 \cdot \Delta \boldsymbol{\eta}_1 + \mathbf{G}_N \cdot \mathbf{G}_{N-1} \cdots \mathbf{G}_2 \cdot \mathbf{f}_1 + \cdots + \mathbf{G}_N \cdot \mathbf{f}_{N-1} + \mathbf{f}_N, \\
&= \left(\prod_{n=1}^N \mathbf{G}_{N+1-n} \right) \cdot \Delta \boldsymbol{\eta}_1 + \sum_{n=1}^N \left(\prod_{n'=1}^{n-1} \mathbf{G}_{N+1-n'} \right) \cdot \mathbf{f}_{N+1-n}.
\end{aligned}$$

A similar procedure may be applied to the upper grid points:

$$\begin{aligned}
\Delta \boldsymbol{\eta}_{2N} &= \mathbf{G}_{2N} \cdot \Delta \boldsymbol{\eta}_{2N+1} + \mathbf{f}_{2N} \\
\Delta \boldsymbol{\eta}_{2N-1} &= \mathbf{G}_{2N-1} \cdot \Delta \boldsymbol{\eta}_{2N} + \mathbf{f}_{2N-1} \\
&= \mathbf{G}_{2N-1} \cdot \mathbf{G}_{2N} \cdot \Delta \boldsymbol{\eta}_{2N+1} + \mathbf{G}_{2N-1} \cdot \mathbf{f}_{2N} + \mathbf{f}_{2N-1} \\
&\vdots \\
\Delta \boldsymbol{\eta}_{N+1} &= \mathbf{G}_{N+1} \cdot \mathbf{G}_{N+2} \cdots \mathbf{G}_{2N} \cdot \Delta \boldsymbol{\eta}_{2N+1} + \mathbf{G}_{N+1} \cdot \mathbf{G}_{N+2} \cdots \mathbf{G}_{2N-1} \cdot \mathbf{f}_{2N} + \cdots + \mathbf{f}_{N+1} \\
&= \left(\prod_{n=1}^N \mathbf{G}_{N+n} \right) \cdot \Delta \boldsymbol{\eta}_{2N+1} + \sum_{n=1}^N \left(\prod_{n'=1}^{n-1} \mathbf{G}_{N+n'} \right) \cdot \mathbf{f}_{N+n}.
\end{aligned}$$

Subtracting the last two equations gives,

$$\begin{aligned}
& \left(\prod_{n=1}^N \mathbf{G}_{N+1-n} \right) \cdot \Delta \boldsymbol{\eta}_1 - \left(\prod_{n=1}^N \mathbf{G}_{N+n} \right) \cdot \Delta \boldsymbol{\eta}_{2N+1} \\
&= - \sum_{n=1}^N \left[\left(\prod_{n'=1}^{n-1} \mathbf{G}_{N+1-n'} \right) \cdot \mathbf{f}_{N+1-n} - \left(\prod_{n'=1}^{n-1} \mathbf{G}_{N+n'} \right) \cdot \mathbf{f}_{N+n} \right]. \quad (\text{F.1.42})
\end{aligned}$$

Combining this equation with the boundary conditions yields the linear system,

$$\begin{bmatrix} \mathbf{A} & \mathbf{B} \\ \mathbf{C} & \mathbf{D} \end{bmatrix} \cdot \begin{bmatrix} \Delta\eta_1 \\ \Delta\eta_{2N+1} \end{bmatrix} = \begin{bmatrix} -\mathbf{f}_{2N+1} \\ -\mathbf{e} \end{bmatrix} \quad (\text{F.1.43})$$

where

$$\begin{aligned} \mathbf{C} &= \mathbf{C}_{N+1}, & \mathbf{C}_n &= \prod_{n'=1}^{n-1} \mathbf{G}_{N+1-n'}, \\ \mathbf{D} &= \mathbf{D}_{N+1}, & \mathbf{D}_n &= -\prod_{n'=1}^{n-1} \mathbf{G}_{N+n}, \\ \mathbf{e} &= \sum_{n=1}^N (\mathbf{C}_n \cdot \mathbf{f}_{N+1-n} + \mathbf{D}_n \cdot \mathbf{f}_{N+n}). \end{aligned}$$

This is a smaller system of equations for the unknowns $\Delta\eta_1$ and $\Delta\eta_{2N+1}$, which can be solved via Gaussian elimination. The remaining $\Delta\eta_n$ are then computed by back-substitution. Iteration by the modified form of Newton's method proceeds as described in §F.1.1.

Other generalizations of the multiple shooting method are possible. For instance, for domains containing singular points in the interior of the domain, one may construct a system of equations such that integration always proceeds away from the singular point towards the boundaries. A further generalization involves shooting away from the boundaries *and* an interior point towards two fitting points. Higher-order schemes involving multiple fitting points are straightforwardly deduced.

F.2 Nonlinear finite difference method

In §5.3, we derived a two-dimensional boundary-value problem (5.3.14)-(5.3.19) for the pressure $p(\phi, x)$, membrane tension $\tau(\phi, x)$, and membrane radius $\rho_s(\phi, x)$ in the domain $0 \leq \phi \leq \pi/N$, $-L \leq x \leq 0$ (L being the vesicle length and N being the number of sides in the cross section of a polygonal duct). This problem governs the motion of a vesicle through a polygonal duct in the lubrication limit. Unlike in the axisymmetric problem, here the vesicle surface is rotationally asymmetric about the x -axis (although it does possess N -fold reflectional symmetry at the planes $\phi = j\pi/N$, $j = 0, 1, \dots, 2N$). Consequently, the surface curvature tensor $\kappa_s = -\nabla_s \hat{\mathbf{n}}$ (defined in Appendix A.5) does not always have an eigenvector parallel to $\hat{\mathbf{e}}_\phi$, and transformation from the space coordinates (ϕ, x) to surface-conformal coordinates (s_ϕ, s_x) is not as simple as in the axisymmetric problem. The arc lengths s_ϕ and s_x are related to ϕ and x by the differential identities,

$$ds_\phi = \sqrt{\rho_s^2 + (\partial\rho_s/\partial\phi)^2} d\phi, \quad ds_x = \sqrt{1 + (\partial\rho_s/\partial x)^2} dx. \quad (\text{F.2.1})$$

(See Appendix A.7.2.) The surface metric G_s and mean curvature H are related to $\rho_s(\phi, x)$ as follows:

$$G_s = \sqrt{\left(\frac{\partial \rho_s}{\partial \phi}\right)^2 + \rho_s^2 \left[1 + \left(\frac{\partial \rho_s}{\partial x}\right)^2\right]}, \quad (\text{F.2.2})$$

$$H = \frac{1}{2G_s^3} \left\{ \rho_s \frac{\partial^2 \rho_s}{\partial x^2} \left[\rho_s^2 + \left(\frac{\partial \rho_s}{\partial \phi}\right)^2 \right] + \rho_s \frac{\partial^2 \rho_s}{\partial \phi^2} \left[1 + \left(\frac{\partial \rho_s}{\partial x}\right)^2 \right] - 2\rho_s \frac{\partial \rho_s}{\partial x} \frac{\partial \rho_s}{\partial \phi} \frac{\partial^2 \rho_s}{\partial x \partial \phi} - \left(\frac{\partial \rho_s}{\partial \phi}\right)^2 \right\} - \frac{1}{2G_s}. \quad (\text{F.2.3})$$

The Gaussian curvature K is not required because, unlike in the axisymmetric problem, in the forthcoming equations we neglect the effect of bending elasticity. The reasoning behind this choice is that we focus in Chapter 5 on vesicles that are nearly spherical (reduced volumes v close to unity), and so bending stresses are expected to play a minor role. For the non-axisymmetric problem, we adopt the fixed space coordinates ϕ and x as independent variables, obviating the need for a complicated transformation to surface-conformal coordinates. This choice of independent variables would pose problems in cases where the vesicle surface develops concave curvature, since the radius ρ_s would then become a multivalued function of x . However, this issue rarely arises for vesicles that are “sphere-like.”

The vesicle length L can be introduced as a dependent variable by use of the following nonlinear map (introduced in the main text):

$$x = -\frac{L}{2} (1 - \cos \xi), \quad \xi = \arccos \left(1 + \frac{2x}{L}\right), \quad (5.3.21)$$

where $0 \leq \xi \leq \pi$. This coordinate map has the additional benefit of clustering grid points near the boundaries. Derivatives and integrals transform as follows:

$$\frac{\partial \psi}{\partial x} = -\frac{2 \csc \xi}{L} \frac{\partial \psi}{\partial \xi}, \quad (\text{F.2.4a})$$

$$\frac{\partial^2 \psi}{\partial x^2} = \frac{4 \csc^2 \xi}{L^2} \left(\frac{\partial^2 \psi}{\partial \xi^2} - \cot \xi \frac{\partial \psi}{\partial \xi} \right), \quad (\text{F.2.4b})$$

$$\int_{-L}^0 \psi \, dx = \frac{L}{2} \int_0^\pi \psi \sin \xi \, d\xi. \quad (\text{F.2.4c})$$

As in the previous section, the poles $\xi = 0, \pi$ are singular points of the domain. Thus, we numerically integrate over the reduced domain $\epsilon \leq \xi \leq \pi - \epsilon$, where $\epsilon/\pi \ll 1$. In the end regions, we assume that the vesicle adopts a locally parabolic shape:

$$\rho_s \cos \xi - \sin \xi \frac{\partial \rho_s}{\partial \xi} = 0, \quad \frac{\partial}{\partial \phi} \left(\frac{p}{\tau} \right) = 0, \quad \xi \in [0, \epsilon] \cup [\pi - \epsilon, \pi]. \quad (\text{F.2.5})$$

Note that the excluded region contributes a small correction to the total surface area A_0 and enclosed volume Ω_0 ; this correction can usually be neglected, since the value of ϵ is chosen to be less than the grid spacing in the discretized domain. The surface metric G_s and mean curvature H may be evaluated at the poles $\xi = 0$ and π using L'Hôpital's rule:

$$\lim_{\xi \rightarrow 0, \pi} G_s = \frac{2}{L} \left(\frac{\partial \rho_s}{\partial \xi} \right)^2, \quad (\text{F.2.6})$$

$$\begin{aligned} \lim_{\xi \rightarrow 0, \pi} 2H &= \frac{L}{2} \left[2 \left(\frac{\partial \rho_s}{\partial \xi} \right)^{-2} - \left(\frac{\partial \rho_s}{\partial \xi} \right)^{-3} \frac{\partial^3 \rho_s}{\partial \phi^2 \partial \xi} + 3 \left(\frac{\partial \rho_s}{\partial \xi} \right)^{-4} \left(\frac{\partial^2 \rho_s}{\partial \phi \partial \xi} \right)^2 \right] \\ &= \frac{L}{2} \left[2 \left(\frac{\partial \rho_s}{\partial \xi} \right)^{-2} - \left(\frac{\partial \rho_s}{\partial \xi} \right)^{-3} \frac{\partial^3 \rho_s}{\partial \phi^2 \partial \xi} \right] \quad \text{since } \frac{\partial \rho_s}{\partial \phi} = 0 \text{ at } \xi = 0, \pi. \end{aligned} \quad (\text{F.2.7})$$

These results may be easily obtained by noting that ρ_s is an odd function of ξ near $\xi = 0$ and π .

The elliptic boundary-value problem (5.3.14)-(5.3.19) can be written in the compact form,

$$\mathbf{f}[\mathbf{y}(\phi, \xi)] = \mathbf{0}, \quad 0 \leq \phi \leq \frac{\pi}{N}, \quad \epsilon \leq \xi \leq \pi - \epsilon, \quad (\text{F.2.8})$$

where

$$y_1 = p, \quad y_2 = \tau, \quad y_3 = \rho_s, \quad y_4 = L,$$

and¹

$$\begin{aligned} f_1 &= \frac{\partial}{\partial \phi} \left(\frac{m_\phi^{(qp)}}{\rho_s} \frac{\partial p}{\partial \phi} \right) + \frac{\partial}{\partial x} \left(m_x^{(qp)} \frac{\partial p}{\partial x} \right) \\ &\quad + \frac{\partial}{\partial \phi} \left(m_\phi^{(q\tau)} \frac{\partial \tau}{\partial s_\phi} \right) + \frac{\partial}{\partial x} \left(m_x^{(q\tau)} \frac{\partial \tau}{\partial s_x} \right) - \frac{U}{2} \frac{\partial}{\partial x} (R_\phi^2 - \rho_s^2), \\ f_2 &= \frac{\partial}{\partial \phi} \left(\frac{G_s m_\phi^{(up)}}{\rho_s} \frac{\partial p}{\partial \phi} \right) + \frac{\partial}{\partial x} \left(G_s m_x^{(up)} \frac{\partial p}{\partial x} \right) \\ &\quad + \frac{\partial}{\partial \phi} \left(G_s m_\phi^{(u\tau)} \frac{\partial \tau}{\partial s_\phi} \right) + \frac{\partial}{\partial x} \left(G_s m_x^{(u\tau)} \frac{\partial \tau}{\partial s_x} \right) - \frac{\partial}{\partial x} (G_s U), \\ f_3 &= \frac{1}{G_s^3} \left\{ \rho_s \frac{\partial^2 \rho_s}{\partial x^2} \left[\rho_s^2 + \left(\frac{\partial \rho_s}{\partial \phi} \right)^2 \right] + \rho_s \frac{\partial^2 \rho_s}{\partial \phi^2} \left[1 + \left(\frac{\partial \rho_s}{\partial x} \right)^2 \right] - 2 \rho_s \frac{\partial \rho_s}{\partial x} \frac{\partial \rho_s}{\partial \phi} \frac{\partial^2 \rho_s}{\partial x \partial \phi} - \left(\frac{\partial \rho_s}{\partial \phi} \right)^2 \right\} - \frac{1}{G_s} - \frac{p}{\tau}, \\ f_4 &= \frac{\partial}{\partial \phi} \left(\frac{p}{\tau} \right) \Big|_{\xi=\epsilon}, \\ f_5 &= \left[\rho_s \left(1 + \frac{2x}{L} \right) - 2x \left(1 + \frac{x}{L} \right) \frac{\partial \rho_s}{\partial x} \right] \Big|_{\xi=\epsilon}, \\ f_6 &= \frac{\partial}{\partial \phi} \left(\frac{p}{\tau} \right) \Big|_{\xi=\pi-\epsilon}, \end{aligned}$$

¹In the definition of f_8 , we evaluate the integral equation at some arbitrary axial position $\xi = \xi^*$ (e.g., the middle plane $\xi^* = \pi/2$ is usually a good choice).

$$\begin{aligned}
f_7 &= \left[\rho_s \left(1 + \frac{2x}{L} \right) - 2x \left(1 + \frac{x}{L} \right) \frac{\partial \rho_s}{\partial x} \right] \Big|_{\xi=\pi-\epsilon}, \\
f_8 &= \int_0^{\pi/N} 2NG_s \left(m_x^{(up)} \frac{\partial p}{\partial x} + m_x^{(u\tau)} \frac{\partial \tau}{\partial s_x} - U \right) d\phi \Big|_{\xi=\xi^*}, \\
f_9 &= \int_0^{\pi/N} \int_{\xi=\epsilon}^{\xi=\pi-\epsilon} 2NG_s dx d\phi - A_0, \\
f_{10} &= \int_0^{\pi/N} \int_{\xi=\epsilon}^{\xi=\pi-\epsilon} N\rho_s^2 dx d\phi - \Omega_0.
\end{aligned}$$

[The m -functions are defined in Chapter 5, equation (5.3.13).] Here, we have chosen to write the components of \mathbf{f} in terms of operations in the x -domain rather than in the ξ -domain, for the sake of simplicity in notation. It is implied that $x = x(\xi)$ according to (5.3.21) and that derivatives and integrals transform according to (F.2.4). The unknown fields $p(\phi, \xi)$, $\tau(\phi, \xi)$, and $\rho_s(\phi, \xi)$ are governed by a coupled system of elliptic partial differential equations (f_1-f_3), which requires six boundary conditions plus an additional condition in order to determine the free boundary L (f_4-f_{10}). Unlike in the axisymmetric problem, here we have formulated the problem without including the effect of bending elasticity. Inclusion of bending stresses would increase the order of the system by two.

In the remainder of this section, we describe a solution procedure for (F.2.8) by means of the *nonlinear finite difference method*. At this point, we have neither linearized nor discretized the nonlinear system of equations (F.2.8), which applies the spatial operator $\mathbf{f}(\cdot)$ to the continuous fields $\mathbf{y}(\phi, x)$. From here, we can take one of two approaches. In the first approach, we write a discrete analog of (F.2.8) by employing a finite difference analogy for the derivatives and integrals, then linearize the resulting nonlinear algebraic equations for implementation in Newton's method. This is the so-called “discretization-linearization” method. In the second approach, we first linearize the *continuous* equation (F.2.8) and discretize the equations thereafter (the “linearization-discretization” method). We shall adopt the second approach below: linearization first, discretization second.

F.2.1 Linearization

In order to linearize (F.2.8), we perturb the dependent variables $\mathbf{y}' = \mathbf{y} + \delta\mathbf{y}$ and expand $\mathbf{f}(\mathbf{y}')$ in a Taylor series about $\mathbf{y}' = \mathbf{y}$:

$$\mathbf{f}(\mathbf{y} + \delta\mathbf{y}) = \mathbf{f}(\mathbf{y}) + \delta\mathbf{y} \cdot [\nabla_{\delta\mathbf{y}} \mathbf{f}(\mathbf{y} + \delta\mathbf{y})] \Big|_{\delta\mathbf{y}=\mathbf{0}} + O(|\delta\mathbf{y}|^2). \quad (\text{F.2.9})$$

Neglecting the error term and setting the left-hand side equal to zero yields the linearized equation,

$$\mathbf{J}(\mathbf{y}) \cdot \delta\mathbf{y} = -\mathbf{f}(\mathbf{y}), \quad (\text{F.2.10})$$

where

$$\mathbf{J}(\mathbf{y}) = [\nabla_{\delta\mathbf{y}} \mathbf{f}(\mathbf{y} + \delta\mathbf{y})]^\dagger \Big|_{\delta\mathbf{y}=\mathbf{0}} \quad (\text{F.2.11})$$

is the Jacobian matrix. For some initial guess \mathbf{y}^* , Newton's method reads,

$$\mathbf{y}^{(k+1)} = \mathbf{y}^{(k)} - [\mathbf{J}(\mathbf{y}^{(k)})]^{-1} \cdot \mathbf{f}(\mathbf{y}^{(k)}), \quad k = 0, 1, 2, \dots, \quad (\text{F.2.12})$$

$$\mathbf{y}^{(0)} = \mathbf{y}^*. \quad (\text{F.2.13})$$

Iteration proceeds until convergence.

We now address the evaluation of the Jacobian matrix. For the purposes of computation, it is efficient to evaluate the elements of \mathbf{J} analytically and subsequently apply the finite difference analogy to them. Formally, we compute the elements of the vector $\mathbf{J} \cdot \delta\mathbf{y}$ using the directional derivative,

$$(\mathbf{J} \cdot \delta\mathbf{y})_m = \sum_{m'=1}^M J_{mm'} \delta y_{m'} = \frac{d}{d\chi} f_m(\mathbf{y} + \chi \delta\mathbf{y}) \Big|_{\chi=0}, \quad (\text{F.2.14})$$

where χ is some arbitrary constant [clearly, $M = 10$ for (F.2.8)]. Written explicitly,

$$\mathbf{J} \cdot \delta\mathbf{y} = \begin{bmatrix} J_{11} & J_{12} & J_{13} & J_{14} \\ J_{21} & J_{22} & J_{23} & J_{24} \\ J_{31} & J_{32} & J_{33} & J_{34} \\ J_{41} & J_{42} & J_{43} & J_{44} \\ J_{51} & J_{52} & J_{53} & J_{54} \\ J_{61} & J_{62} & J_{63} & J_{64} \\ J_{71} & J_{72} & J_{73} & J_{74} \\ J_{81} & J_{82} & J_{83} & J_{84} \\ J_{91} & J_{92} & J_{93} & J_{94} \\ J_{10,1} & J_{10,2} & J_{10,3} & J_{10,4} \end{bmatrix} \begin{bmatrix} \delta p \\ \delta \tau \\ \delta \rho_s \\ \delta L \end{bmatrix}. \quad (\text{F.2.15})$$

Derivatives and integrals with respect to x are perturbed by variations in the vesicle length L . This can be most easily seen by transforming from x - to ξ -coordinates. The relevant directional derivatives are:

$$\frac{d}{d\chi} \left(\frac{\partial \psi}{\partial x} \Big|_{L \rightarrow L+\chi \delta L} \right) \Big|_{\chi=0} = -\frac{\partial \psi}{\partial x} \frac{\delta L}{L}, \quad (\text{F.2.16})$$

$$\frac{d}{d\chi} \left(\frac{\partial^2 \psi}{\partial x^2} \Big|_{L \rightarrow L+\chi \delta L} \right) \Big|_{\chi=0} = -2 \frac{\partial^2 \psi}{\partial x^2} \frac{\delta L}{L}, \quad (\text{F.2.17})$$

$$\frac{d}{d\chi} \left(\int_{-(L+\chi \delta L)}^0 \psi dx \right) \Big|_{\chi=0} = \int_{-L}^0 \psi dx \frac{\delta L}{L}. \quad (\text{F.2.18})$$

Using the directional derivative (F.2.14), we compute the 40 elements of the Jacobian matrix \mathbf{J} :

$$\begin{aligned}
J_{11}\delta p &= \frac{\partial}{\partial\phi} \left(\frac{m_\phi^{(qp)}}{\rho_s} \frac{\partial\delta p}{\partial\phi} \right) + \frac{\partial}{\partial x} \left(m_\phi^{(qp)} \frac{\partial\delta p}{\partial x} \right), \\
J_{12}\delta\tau &= \frac{\partial}{\partial\phi} \left(\frac{m_\phi^{(q\tau)}}{\rho_s} \frac{\partial\delta\tau}{\partial s_\phi} \right) + \frac{\partial}{\partial x} \left(m_\phi^{(q\tau)} \frac{\partial\delta\tau}{\partial s_x} \right), \\
J_{13}\delta\rho_s &= \frac{\partial}{\partial\phi} \left[\frac{\partial p}{\partial\phi} \left(\frac{\dot{m}_\phi^{(qp)}}{\rho_s} - \frac{m_\phi^{(qp)}}{\rho_s^2} \right) \delta\rho_s \right] + \frac{\partial}{\partial x} \left(\frac{\partial p}{\partial x} \dot{m}_x^{(qp)} \delta\rho_s \right) \\
&\quad + \frac{\partial}{\partial\phi} \left\{ \frac{\partial\tau}{\partial s_\phi} \left[\dot{m}_\phi^{(q\tau)} - \frac{m_\phi^{(q\tau)}}{\rho_s^2 + (\partial\rho_s/\partial\phi)^2} \left(\rho_s + \frac{\partial\rho_s}{\partial\phi} \frac{\partial}{\partial\phi} \right) \right] \delta\rho_s \right\} \\
&\quad + \frac{\partial}{\partial x} \left[\frac{\partial\tau}{\partial s_x} \left(\dot{m}_x^{(q\tau)} - \frac{m_x^{(q\tau)}}{1 + (\partial\rho_s/\partial x)^2} \frac{\partial\rho_s}{\partial x} \frac{\partial}{\partial x} \right) \delta\rho_s \right] \\
&\quad + U \left(\frac{\partial\rho_s}{\partial x} + \rho_s \frac{\partial}{\partial x} \right) \delta\rho_s, \\
J_{14}\delta L &= \left\{ -2 \left[\frac{\partial}{\partial x} \left(m_x^{(qp)} \frac{\partial p}{\partial x} \right) + \frac{\partial}{\partial x} \left(m_x^{(q\tau)} \frac{\partial\tau}{\partial s_x} \right) \right] \right. \\
&\quad \left. + \frac{\partial}{\partial x} \left[\frac{m_x^{(q\tau)}}{1 + (\partial\rho_s/\partial x)^2} \left(\frac{\partial\rho_s}{\partial x} \right)^2 \frac{\partial\tau}{\partial s_x} \right] - U \rho_s \frac{\partial\rho_s}{\partial x} \right\} \frac{\delta L}{L}, \\
J_{21}\delta p &= \frac{\partial}{\partial\phi} \left(\frac{G_s m_\phi^{(up)}}{\rho_s} \frac{\partial\delta p}{\partial\phi} \right) + \frac{\partial}{\partial x} \left(G_s m_x^{(up)} \frac{\partial\delta p}{\partial x} \right), \\
J_{22}\delta\tau &= \frac{\partial}{\partial\phi} \left(G_s m_\phi^{(u\tau)} \frac{\partial\delta\tau}{\partial s_\phi} \right) + \frac{\partial}{\partial x} \left(G_s m_x^{(u\tau)} \frac{\partial\delta\tau}{\partial s_x} \right), \\
J_{23}\delta\rho_s &= \frac{\partial}{\partial\phi} \left[\frac{\partial p}{\partial\phi} \left(\frac{m_\phi^{(up)} \dot{G}_s + G_s \dot{m}_\phi^{(up)}}{\rho_s} - \frac{G_s m_\phi^{(up)}}{\rho_s^2} \right) \delta\rho_s \right] \\
&\quad + \frac{\partial}{\partial x} \left[\frac{\partial p}{\partial x} \left(m_x^{(up)} \dot{G}_s + G_s \dot{m}_x^{(up)} \right) \delta\rho_s \right] \\
&\quad + \frac{\partial}{\partial\phi} \left\{ \frac{\partial\tau}{\partial s_\phi} \left[m_\phi^{(u\tau)} \dot{G}_s + G_s \dot{m}_\phi^{(u\tau)} - \frac{G_s m_\phi^{(u\tau)}}{\rho_s^2 + (\partial\rho_s/\partial\phi)^2} \left(\rho_s + \frac{\partial\rho_s}{\partial\phi} \frac{\partial}{\partial\phi} \right) \right] \delta\rho_s \right\} \\
&\quad + \frac{\partial}{\partial x} \left[\frac{\partial\tau}{\partial s_x} \left(m_x^{(u\tau)} \dot{G}_s + G_s \dot{m}_x^{(u\tau)} - \frac{G_s m_x^{(u\tau)}}{1 + (\partial\rho_s/\partial x)^2} \frac{\partial\rho_s}{\partial x} \frac{\partial}{\partial x} \right) \delta\rho_s \right] \\
&\quad - U \frac{\partial}{\partial x} (\dot{G}_s \delta\rho_s), \\
J_{24}\delta L &= \left\{ -2 \left[\frac{\partial}{\partial x} \left(G_s m_x^{(up)} \frac{\partial p}{\partial x} \right) + \frac{\partial}{\partial x} \left(G_s m_x^{(u\tau)} \frac{\partial\tau}{\partial s_x} \right) \right] \right. \\
&\quad - \frac{\partial}{\partial\phi} \left[\frac{\rho_s m_\phi^{(up)}}{G_s} \left(\frac{\partial\rho_s}{\partial x} \right)^2 \frac{\partial p}{\partial\phi} \right] - \frac{\partial}{\partial x} \left[\frac{\rho_s^2 m_x^{(up)}}{G_s} \left(\frac{\partial\rho_s}{\partial x} \right)^2 \frac{\partial p}{\partial x} \right] \\
&\quad - \frac{\partial}{\partial\phi} \left[\frac{\rho_s^2 m_\phi^{(u\tau)}}{G_s} \left(\frac{\partial\rho_s}{\partial x} \right)^2 \frac{\partial\tau}{\partial s_\phi} \right] - \frac{\partial}{\partial x} \left[\frac{\rho_s^2 m_x^{(u\tau)}}{G_s} \left(\frac{\partial\rho_s}{\partial x} \right)^2 \frac{\partial\tau}{\partial s_x} \right] \\
&\quad \left. + \frac{\partial}{\partial x} \left[\frac{G_s m_x^{(u\tau)}}{1 + (\partial\rho_s/\partial x)^2} \left(\frac{\partial\rho_s}{\partial x} \right)^2 \frac{\partial\tau}{\partial s_x} \right] \right\}
\end{aligned}$$

$$\begin{aligned}
& + U \frac{\partial}{\partial x} \left[G_s + \frac{\rho_s^2}{G_s} \left(\frac{\partial \rho_s}{\partial x} \right)^2 \right] \right\} \frac{\delta L}{L}, \\
J_{31} \delta p &= \frac{\delta p}{\tau}, \\
J_{32} \delta \tau &= -\frac{p \delta \tau}{\tau^2}, \\
J_{33} \delta \rho_s &= -\frac{\dot{G}_s \delta \rho_s}{G_s^2} \\
& - \frac{3}{G_s^4} \left\{ \left(\frac{\partial \rho_s}{\partial \phi} \right)^2 + 2\rho_s \frac{\partial \rho_s}{\partial \phi} \frac{\partial \rho_s}{\partial x} \frac{\partial^2 \rho_s}{\partial x \partial \phi} - \rho_s \frac{\partial^2 \rho_s}{\partial x^2} \left[\rho_s^2 + \left(\frac{\partial \rho_s}{\partial \phi} \right)^2 \right] - \rho_s \frac{\partial^2 \rho_s}{\partial \phi^2} \left[1 + \left(\frac{\partial \rho_s}{\partial x} \right)^2 \right] \right\} \dot{G}_s \delta \rho_s \\
& + \frac{1}{G_s^3} \left\{ 2 \frac{\partial \rho_s}{\partial \phi} \frac{\partial \rho_s}{\partial x} \frac{\partial^2 \rho_s}{\partial x \partial \phi} - \frac{\partial^2 \rho_s}{\partial x^2} \left[3\rho_s^2 + \left(\frac{\partial \rho_s}{\partial \phi} \right)^2 \right] - \frac{\partial^2 \rho_s}{\partial \phi^2} \left[1 + \left(\frac{\partial \rho_s}{\partial x} \right)^2 \right] \right. \\
& + \left(2\rho_s \frac{\partial \rho_s}{\partial \phi} \frac{\partial^2 \rho_s}{\partial x \partial \phi} - \rho_s \frac{\partial^2 \rho_s}{\partial \phi^2} \frac{\partial \rho_s}{\partial x} \right) \frac{\partial}{\partial x} + \left(2 \frac{\partial \rho_s}{\partial \phi} + 2\rho_s \frac{\partial \rho_s}{\partial x} \frac{\partial^2 \rho_s}{\partial x \partial \phi} - \rho_s \frac{\partial^2 \rho_s}{\partial x^2} \frac{\partial \rho_s}{\partial \phi} \right) \frac{\partial}{\partial \phi} \\
& \left. + 2\rho_s \frac{\partial \rho_s}{\partial \phi} \frac{\partial \rho_s}{\partial x} \frac{\partial^2}{\partial x \partial \phi} - \rho_s \left[\rho_s^2 + \left(\frac{\partial \rho_s}{\partial \phi} \right)^2 \right] \frac{\partial^2}{\partial x^2} - \rho_s \left[1 + \left(\frac{\partial \rho_s}{\partial x} \right)^2 \right] \frac{\partial^2}{\partial \phi^2} \right\} \delta \rho_s, \\
J_{34} \delta L &= \left(\frac{1}{G_s^3} \left(\frac{\partial \rho_s}{\partial x} \right)^2 \right. \\
& + \frac{3}{G_s^5} \left(\frac{\partial \rho_s}{\partial x} \right)^2 \\
& \times \left\{ \left(\frac{\partial \rho_s}{\partial \phi} \right)^2 + 2\rho_s \frac{\partial \rho_s}{\partial \phi} \frac{\partial \rho_s}{\partial x} \frac{\partial^2 \rho_s}{\partial x \partial \phi} - \rho_s \frac{\partial^2 \rho_s}{\partial x^2} \left[\rho_s^2 + \left(\frac{\partial \rho_s}{\partial \phi} \right)^2 \right] - \rho_s \frac{\partial^2 \rho_s}{\partial \phi^2} \left[1 + \left(\frac{\partial \rho_s}{\partial x} \right)^2 \right] \right\} \\
& \left. + \frac{2\rho_s}{G_s^3} \left\{ -2 \frac{\partial \rho_s}{\partial \phi} \frac{\partial \rho_s}{\partial x} \frac{\partial^2 \rho_s}{\partial x \partial \phi} + \frac{\partial^2 \rho_s}{\partial x^2} \left[\rho_s^2 + \left(\frac{\partial \rho_s}{\partial \phi} \right)^2 \right] + \frac{\partial^2 \rho_s}{\partial \phi^2} \left(\frac{\partial \rho_s}{\partial x} \right)^2 \right\} \right) \delta L, \\
J_{41} \delta p &= \frac{1}{\tau} \frac{\partial \delta p}{\partial \phi} \Big|_{\xi=\epsilon}, \\
J_{42} \delta \tau &= -\frac{p}{\tau^2} \frac{\partial \delta \tau}{\partial \phi} \Big|_{\xi=\epsilon}, \\
J_{43} \delta \rho_s &= 0, \\
J_{44} \delta L &= 0, \\
J_{51} \delta p &= 0, \\
J_{52} \delta \tau &= 0, \\
J_{53} \delta \rho_s &= \left[\left(1 + \frac{2x}{L} \right) - 2x \left(1 + \frac{x}{L} \right) \frac{\partial}{\partial x} \right] \delta \rho_s \Big|_{\xi=\epsilon}, \\
J_{54} \delta L &= 0, \\
J_{61} \delta p &= \frac{1}{\tau} \frac{\partial \delta p}{\partial \phi} \Big|_{\xi=\pi-\epsilon}, \\
J_{62} \delta \tau &= -\frac{p}{\tau^2} \frac{\partial \delta \tau}{\partial \phi} \Big|_{\xi=\pi-\epsilon}, \\
J_{63} \delta \rho_s &= 0,
\end{aligned}$$

$$J_{64}\delta L = 0,$$

$$J_{71}\delta p = 0,$$

$$J_{72}\delta\tau = 0,$$

$$J_{73}\delta\rho_s = \left[\left(1 + \frac{2x}{L} \right) - 2x \left(1 + \frac{x}{L} \right) \frac{\partial}{\partial x} \right] \delta\rho_s \Big|_{\xi=\pi-\epsilon},$$

$$J_{74}\delta L = 0,$$

$$J_{81}\delta p = \left(\int_0^{\pi/N} 2NG_s m_x^{(up)} \frac{\partial \delta p}{\partial x} d\phi \right) \Big|_{\xi=\xi^*},$$

$$J_{82}\delta\tau = \left(\int_0^{\pi/N} 2NG_s m_x^{(u\tau)} \frac{\partial \delta\tau}{\partial s_x} d\phi \right) \Big|_{\xi=\xi^*},$$

$$J_{83}\delta\rho_s = \left[\int_0^{\pi/N} 2N \left(-U + m_x^{(up)} \frac{\partial p}{\partial x} + m_x^{(u\tau)} \frac{\partial \tau}{\partial s_x} \right) \dot{G}_s \delta\rho_s d\phi \right] \Big|_{\xi=\xi^*} + \left\{ \int_0^{\pi/N} 2NG_s \left[\frac{\partial p}{\partial x} \dot{m}_x^{(up)} + \frac{\partial \tau}{\partial s_x} \left(\dot{m}_x^{(u\tau)} - \frac{m_x^{(u\tau)}}{1 + (\partial\rho_s/\partial x)^2} \frac{\partial\rho_s}{\partial x} \frac{\partial}{\partial x} \right) \right] \delta\rho_s d\phi \right\} \Big|_{\xi=\xi^*},$$

$$J_{84}\delta L = - \left[\int_0^{\pi/N} \frac{2N\rho_s^2}{G_s} \left(\frac{\partial\rho_s}{\partial x} \right)^2 \left(-U + m_x^{(up)} \frac{\partial p}{\partial x} + m_x^{(u\tau)} \frac{\partial \tau}{\partial s_x} \right) d\phi \right] \Big|_{\xi=\xi^*} \frac{\delta L}{L} - \left[\int_0^{\pi/N} 2NG_s \left(m_x^{(up)} \frac{\partial p}{\partial x} + \left[m_x^{(u\tau)} - \frac{m_x^{(u\tau)}}{1 + (\partial\rho_s/\partial x)^2} \left(\frac{\partial\rho_s}{\partial x} \right)^2 \right] \frac{\partial \tau}{\partial s_x} \right) d\phi \right] \Big|_{\xi=\xi^*} \frac{\delta L}{L},$$

$$J_{91}\delta p = 0,$$

$$J_{92}\delta\tau = 0,$$

$$J_{93}\delta\rho_s = \int_0^{\pi/N} \int_{-L}^0 2N\dot{G}_s \delta\rho_s dx d\phi,$$

$$J_{94}\delta L = \left\{ \int_0^{\pi/N} \int_{\xi=\epsilon}^{\xi=\pi-\epsilon} 2NG_s \left[1 - \frac{\rho_s^2}{G_s^2} \left(\frac{\partial\rho_s}{\partial x} \right)^2 \right] dx d\phi \right\} \frac{\delta L}{L},$$

$$J_{10,1}\delta p = 0,$$

$$J_{10,2}\delta\tau = 0,$$

$$J_{10,3}\delta\rho_s = \int_0^{\pi/N} \int_{\xi=\epsilon}^{\xi=\pi-\epsilon} 2N\rho_s \delta\rho_s dx d\phi,$$

$$J_{10,4}\delta L = \left(\int_0^{\pi/N} \int_{\xi=\epsilon}^{\xi=\pi-\epsilon} N\rho_s^2 dx d\phi \right) \frac{\delta L}{L},$$

where

$$\dot{G}_s \delta\rho_s = \frac{1}{G_s} \left\{ \frac{\partial\rho_s}{\partial\phi} \frac{\partial}{\partial\phi} + \rho_s \left[1 + \left(\frac{\partial\rho_s}{\partial x} \right)^2 \right] + \rho_s^2 \frac{\partial\rho_s}{\partial x} \frac{\partial}{\partial x} \right\} \delta\rho_s,$$

and

$$\begin{aligned}
\dot{m}_x^{(qp)} &= \frac{R_\phi^3}{2\mu} \left[\frac{\rho_s}{R_\phi} - \frac{\rho_s^3}{R_\phi^3} + \frac{2\rho_s^3}{R_\phi^3} \log \left(\frac{\rho_s}{R_\phi} \right) \right], \\
\dot{m}_x^{(q\tau)} &= \frac{R_\phi^2}{4\mu} \left[1 - \frac{\rho_s^2}{R_\phi^2} + \frac{6\rho_s^2}{R_\phi^2} \log \left(\frac{\rho_s}{R_\phi} \right) \right], \\
\dot{m}_\phi^{(qp)} &= -\frac{R_\phi^2}{8\mu} \left[1 - \frac{5\rho_s^4}{R_\phi^4} + \frac{4\rho_s^2}{R_\phi^2} + \frac{12\rho_s^2}{R_\phi^2} \log \left(\frac{\rho_s}{R_\phi} \right) \right], \\
\dot{m}_\phi^{(q\tau)} &= \frac{R_\phi}{\mu} \left[\frac{\rho_s^3}{R_\phi^3} - \frac{\rho_s}{R_\phi} - \frac{\rho_s}{R_\phi} \log \left(\frac{\rho_s}{R_\phi} \right) \right], \\
\dot{m}_x^{(up)} &= -\frac{R_\phi}{\mu} \left[\frac{\rho_s}{R_\phi} \log \left(\frac{\rho_s}{R_\phi} \right) \right], \\
\dot{m}_x^{(u\tau)} &= -\frac{1}{\mu} \left[1 + \log \left(\frac{\rho_s}{R_\phi} \right) \right], \\
\dot{m}_\phi^{(up)} &= \frac{1}{4\mu} \left[3 - \frac{3\rho_s^2}{R_\phi^2} + 2 \log \left(\frac{\rho_s}{R_\phi} \right) \right], \\
\dot{m}_\phi^{(u\tau)} &= -\frac{1}{\mu R_\phi} \left(\frac{\rho_s}{R_\phi} \right).
\end{aligned}$$

Special care has to be taken in approaching the boundary value $\rho_s = 0$ at the poles. In particular, application of L'Hôpital's rule to \dot{G}_s (assuming $\delta\rho_s = 0$ at $\xi = 0, \pi$) gives

$$\lim_{\xi \rightarrow 0} \dot{G}_s \delta\rho_s = \frac{4}{L} \left(\frac{\partial \rho_s}{\partial \xi} \right) \frac{\partial \delta\rho_s}{\partial \xi}, \quad \lim_{\xi \rightarrow \pi} \dot{G}_s \delta\rho_s = -\frac{4}{L} \left(\frac{\partial \rho_s}{\partial \xi} \right) \frac{\partial \delta\rho_s}{\partial \xi}.$$

This limit properly accounts for the fact that $\delta\rho_s$ must vanish at $\xi = 0, \pi$.

Now that we have linearized the equations (F.2.8) and have analytically computed the elements of the Jacobian matrix, we proceed to discretize the equations by means of the finite difference analogy.

F.2.2 Discretization

In the previous section, we derived analytical expressions for the Jacobian elements. The Jacobian matrix \mathbf{J} is required in Newton's method (F.2.12)-(F.2.13). In order to implement this method numerically, we must discretize the linearized equations. We approximate the $\phi\xi$ -plane by a discrete set of $(M_\phi + 1)(M_\xi + 1)$ grid points:

$$\phi_j = jd_\phi, \quad j = 0, 1, \dots, M_\phi, \tag{F.2.19a}$$

$$\xi_0 = \epsilon, \quad \xi_{M_\xi} = \pi - \epsilon, \quad \xi_i = id_\xi, \quad i = 1, 2, \dots, M_\xi - 1, \tag{F.2.19b}$$

where $d_\phi = \pi/(NM_\phi)$ and $d_\xi = \pi/M_\xi$. In practice, a uniform grid can be achieved by setting $M_\xi = NM_\phi$, whence $d_\phi = d_\xi = d$. The unknowns p , τ , and ρ_s are sampled at the grid points and sorted into $(M_\phi + 1)(M_\xi + 1)$ -vectors as follows:

$$\mathbf{p} = \begin{bmatrix} p(\phi_0, \xi_0) \\ p(\phi_0, \xi_1) \\ \vdots \\ p(\phi_0, \xi_{M_\xi}) \\ p(\phi_1, \xi_0) \\ \vdots \\ p(\phi_j, \xi_i) \\ \vdots \\ p(\phi_{M_\phi}, \xi_{M_\xi}) \end{bmatrix}, \quad \boldsymbol{\tau} = \begin{bmatrix} \tau(\phi_0, \xi_0) \\ \tau(\phi_0, \xi_1) \\ \vdots \\ \tau(\phi_0, \xi_{M_\xi}) \\ \tau(\phi_1, \xi_0) \\ \vdots \\ \tau(\phi_j, \xi_i) \\ \vdots \\ \tau(\phi_{M_\phi}, \xi_{M_\xi}) \end{bmatrix}, \quad \boldsymbol{\rho}_s = \begin{bmatrix} \rho_s(\phi_0, \xi_0) \\ \rho_s(\phi_0, \xi_1) \\ \vdots \\ \rho_s(\phi_0, \xi_{M_\xi}) \\ \rho_s(\phi_1, \xi_0) \\ \vdots \\ \rho_s(\phi_j, \xi_i) \\ \vdots \\ \rho_s(\phi_{M_\phi}, \xi_{M_\xi}) \end{bmatrix}. \quad (\text{F.2.20})$$

Discrete operations on \mathbf{p} , $\boldsymbol{\tau}$, and $\boldsymbol{\rho}_s$ are given below.

Finite difference operations

Interpolation and differentiation in the $\phi\xi$ -plane are approximated by matrix-vector multiplications. Interpolation matrices are generically denoted by \mathbf{I} and differentiation matrices by \mathbf{D} . The finite difference operations along the ϕ -axis (with ξ held constant) have the following matrix representation in the discrete domain:

$$\mathbf{I}_\phi^0 = \begin{bmatrix} 1 & & & \\ & 1 & & \\ & & \ddots & \\ & & & 1 \end{bmatrix} \quad [(M_\phi + 1) \times (M_\phi + 1) \text{ matrix}], \quad (\text{F.2.21a})$$

$$\mathbf{I}_\phi^+ = \begin{bmatrix} \frac{1}{2} & \frac{1}{2} & & & \\ & \frac{1}{2} & \frac{1}{2} & & \\ & & \ddots & \ddots & \\ & & & \frac{1}{2} & \frac{1}{2} \end{bmatrix} \quad [M_\phi \times (M_\phi + 1) \text{ matrix}], \quad (\text{F.2.21b})$$

$$\mathbf{I}_\phi^- = \begin{bmatrix} 0 & & & & \\ \frac{1}{2} & \frac{1}{2} & & & \\ & \frac{1}{2} & \frac{1}{2} & & \\ & & \ddots & \ddots & \\ & & & \frac{1}{2} & \frac{1}{2} \\ & & & & 0 \end{bmatrix} \quad [(M_\phi + 1) \times M_\phi \text{ matrix}], \quad (\text{F.2.21c})$$

$$\mathbf{D}_\phi^0 = \frac{1}{d} \begin{bmatrix} 0 & 0 \\ -\frac{1}{2} & 0 & \frac{1}{2} \\ & -\frac{1}{2} & 0 & \frac{1}{2} \\ & & \ddots & \ddots & \ddots \\ & & & -\frac{1}{2} & 0 & \frac{1}{2} \\ & & & & 0 & 0 \end{bmatrix} \quad [(M_\phi + 1) \times (M_\phi + 1) \text{ matrix}], \quad (\text{F.2.21d})$$

$$\mathbf{D}_\phi^+ = \frac{1}{d} \begin{bmatrix} -1 & 1 \\ -1 & 1 \\ & \ddots & \ddots \\ & & -1 & 1 \end{bmatrix} \quad [M_\phi \times (M_\phi + 1) \text{ matrix}], \quad (\text{F.2.21e})$$

$$\mathbf{D}_\phi^- = \frac{1}{d} \begin{bmatrix} 2 \\ -1 & 1 \\ -1 & 1 \\ & \ddots & \ddots \\ & & -1 & 1 \\ & & & 2 \end{bmatrix} \quad [(M_\phi + 1) \times M_\phi \text{ matrix}], \quad (\text{F.2.21f})$$

$$\mathbf{D}_{\phi\phi}^0 = \frac{1}{d^2} \begin{bmatrix} -2 & 2 \\ 1 & -2 & 1 \\ & 1 & -2 & 1 \\ & & \ddots & \ddots & \ddots \\ & & & 1 & -2 & 1 \\ & & & & -2 & 2 \end{bmatrix} \quad [(M_\phi + 1) \times (M_\phi + 1) \text{ matrix}], \quad (\text{F.2.21g})$$

Here, a superscripted “0” denotes a centered difference operator, “+” a forward difference operator, and “−” a backward difference operator. The boundary conditions at $\phi = 0$ and π/N have been incorporated into the operators. The analogous operations along the ξ -axis (ϕ held constant) have the matrix form,

$$\mathbf{I}_\xi^0 = \begin{bmatrix} 1 \\ & 1 \\ & & \ddots \\ & & & 1 \end{bmatrix} \quad [(M_\xi + 1) \times (M_\xi + 1) \text{ matrix}], \quad (\text{F.2.22a})$$

$$\mathbf{I}_\xi^{0*} = \begin{bmatrix} 0 & 1 & & \\ & 1 & & \\ & & \ddots & \\ & & & 1 & 0 \end{bmatrix} \quad [(M_\xi - 1) \times (M_\xi + 1) \text{ matrix}], \quad (\text{F.2.22b})$$

$$\mathbf{I}_\xi^+ = \begin{bmatrix} \frac{1}{2} & \frac{1}{2} & & \\ & \frac{1}{2} & \frac{1}{2} & & \\ & & \ddots & \ddots & \\ & & & \frac{1}{2} & \frac{1}{2} \end{bmatrix} \quad [M_\xi \times (M_\xi + 1) \text{ matrix}], \quad (\text{F.2.22c})$$

$$\mathbf{I}_\xi^- = \begin{bmatrix} \frac{1}{2} & \frac{1}{2} & & \\ & \frac{1}{2} & \frac{1}{2} & & \\ & & \ddots & \ddots & \\ & & & \frac{1}{2} & \frac{1}{2} \end{bmatrix} \quad [(M_\xi - 1) \times M_\xi \text{ matrix}], \quad (\text{F.2.22d})$$

$$\mathbf{D}_\xi^0 = \frac{1}{d} \begin{bmatrix} -1 & 1 & & & \\ -\frac{1}{2} & 0 & \frac{1}{2} & & \\ -\frac{1}{2} & 0 & \frac{1}{2} & & \\ & \ddots & \ddots & \ddots & \\ & & -\frac{1}{2} & 0 & \frac{1}{2} \\ & & & -1 & 1 \end{bmatrix} \quad [(M_\xi + 1) \times (M_\xi + 1) \text{ matrix}], \quad (\text{F.2.22e})$$

$$\mathbf{D}_\xi^+ = \frac{1}{d} \begin{bmatrix} -1 & 1 & & & \\ -1 & 1 & & & \\ & \ddots & \ddots & & \\ & & -1 & 1 & \end{bmatrix} \quad [M_\xi \times (M_\xi + 1) \text{ matrix}], \quad (\text{F.2.22f})$$

$$\mathbf{D}_\xi^- = \frac{1}{d} \begin{bmatrix} -1 & 1 & & & \\ -1 & 1 & & & \\ & \ddots & \ddots & & \\ & & -1 & 1 & \end{bmatrix} \quad [(M_\xi - 1) \times M_\xi \text{ matrix}], \quad (\text{F.2.22g})$$

$$\mathbf{D}_{\xi\xi}^0 = \frac{1}{d^2} \begin{bmatrix} 0 & 0 & & & \\ 1 & -2 & 1 & & \\ 1 & -2 & 1 & & \\ & \ddots & \ddots & \ddots & \\ & & 1 & -2 & 1 \\ & & & 0 & 0 \end{bmatrix} \quad [(M_\xi + 1) \times (M_\xi + 1) \text{ matrix}]. \quad (\text{F.2.22h})$$

Again, the boundary conditions at $\xi = \epsilon$ and $\pi - \epsilon$ have been incorporated into the operators. The above finite difference analogs are second-order accurate in the grid spacing d . We note that the ξ -operations can be converted to x -operations via a linear transformation:

$$\mathbf{I}_x^0 = \mathbf{I}_\xi^0 \quad [(M_\xi + 1) \times (M_\xi + 1) \text{ matrix}], \quad (\text{F.2.23a})$$

$$\mathbf{I}_x^{0*} = \mathbf{I}_\xi^{0*} \quad [(M_\xi - 1) \times (M_\xi + 1) \text{ matrix}], \quad (\text{F.2.23b})$$

$$\mathbf{I}_x^+ = \mathbf{I}_\xi^+ \quad [M_\xi \times (M_\xi + 1) \text{ matrix}], \quad (\text{F.2.23c})$$

$$\mathbf{I}_x^- = \mathbf{I}_\xi^- \quad [(M_\xi - 1) \times M_\xi \text{ matrix}], \quad (\text{F.2.23d})$$

$$\mathbf{D}_x^0 = -\frac{2}{L} \begin{bmatrix} \csc \xi_0 & & & \\ & \csc \xi_1 & & \\ & & \ddots & \\ & & & \csc \xi_{M_\xi} \end{bmatrix} \cdot \mathbf{D}_\xi^0 \quad [(M_\xi + 1) \times (M_\xi + 1) \text{ matrix}], \quad (\text{F.2.23e})$$

$$\mathbf{D}_x^+ = -\frac{2}{L} \begin{bmatrix} \csc [\frac{1}{2}(\xi_0 + \xi_1)] & & & \\ & \csc [\frac{1}{2}(\xi_1 + \xi_2)] & & \\ & & \ddots & \\ & & & \csc [\frac{1}{2}(\xi_{M_\xi-1} + \xi_{M_\xi})] \end{bmatrix} \cdot \mathbf{D}_\xi^+ \quad [M_\xi \times (M_\xi + 1) \text{ matrix}], \quad (\text{F.2.23f})$$

$$\mathbf{D}_x^- = -\frac{2}{L} \begin{bmatrix} \csc \xi_1 & & & \\ & \csc \xi_2 & & \\ & & \ddots & \\ & & & \csc \xi_{M_\xi-1} \end{bmatrix} \cdot \mathbf{D}_\xi^- \quad [(M_\xi - 1) \times M_\xi \text{ matrix}], \quad (\text{F.2.23g})$$

$$\mathbf{D}_{xx}^0 = \frac{4}{L^2} \begin{bmatrix} \csc^2 \xi_0 & & & \\ & \csc^2 \xi_1 & & \\ & & \ddots & \\ & & & \csc^2 \xi_{M_\xi} \end{bmatrix} \cdot \left(\mathbf{D}_{\xi\xi}^0 - \begin{bmatrix} \cot \xi_0 & & & \\ & \cot \xi_1 & & \\ & & \ddots & \\ & & & \cot \xi_{M_\xi} \end{bmatrix} \cdot \mathbf{D}_\xi^0 \right) \quad [(M_\xi + 1) \times (M_\xi + 1) \text{ matrix}]. \quad (\text{F.2.23h})$$

The matrices \mathbf{I} and \mathbf{D} are applied to functions of one independent variable, with the other variable held constant. In order to construct operations on functions of two variables, we make use of the *Kronecker product* $\mathbf{A} \otimes \mathbf{B}$. We denote an interpolation matrix multiplying a vector-function of two variables by \mathbb{I} ; similarly, \mathbb{D} denotes a differentiation matrix. Using the Kronecker product, we may define the following matrix operators:

$$\mathbb{I} = \mathbf{I}_\phi^0 \otimes \mathbf{I}_x^0 \quad [(M_\phi + 1)(M_\xi + 1) \times (M_\phi + 1)(M_\xi + 1) \text{ matrix}], \quad (\text{F.2.24a})$$

$$\begin{aligned}
\mathbb{I}_\phi^+ &= \mathbf{I}_\phi^+ \otimes \mathbf{I}_x^0 & [(M_\phi(M_\xi + 1) \times (M_\phi + 1)(M_\xi + 1) \text{ matrix}), & (F.2.24b) \\
\mathbb{I}_\phi^- &= \mathbf{I}_\phi^- \otimes \mathbf{I}_x^{0*} & [(M_\phi + 1)(M_\xi - 1) \times M_\phi(M_\xi + 1) \text{ matrix}], & (F.2.24c) \\
\mathbb{D}_\phi^0 &= \mathbf{D}_\phi^0 \otimes \mathbf{I}_x^0 & [(M_\phi + 1)(M_\xi + 1) \times (M_\phi + 1)(M_\xi + 1) \text{ matrix}], & (F.2.24d) \\
\mathbb{D}_\phi^+ &= \mathbf{D}_\phi^+ \otimes \mathbf{I}_x^0 & [M_\phi(M_\xi + 1) \times (M_\phi + 1)(M_\xi + 1) \text{ matrix}], & (F.2.24e) \\
\mathbb{D}_\phi^- &= \mathbf{D}_\phi^- \otimes \mathbf{I}_x^{0*} & [(M_\phi + 1)(M_\xi - 1) \times M_\phi(M_\xi + 1) \text{ matrix}], & (F.2.24f) \\
\mathbb{D}_{\phi\phi}^0 &= \mathbf{D}_{\phi\phi}^0 \otimes \mathbf{I}_x^0 & [(M_\phi + 1)(M_\xi - 1) \times M_\phi(M_\xi + 1) \text{ matrix}], & (F.2.24g) \\
\mathbb{I}_x^+ &= \mathbf{I}_\phi^0 \otimes \mathbf{I}_x^+ & [(M_\phi + 1)M_\xi \times (M_\phi + 1)(M_\xi + 1) \text{ matrix}], & (F.2.24h) \\
\mathbb{I}_x^- &= \mathbf{I}_\phi^0 \otimes \mathbf{I}_x^- & [(M_\phi + 1)(M_\xi - 1) \times (M_\phi + 1)M_\xi \text{ matrix}], & (F.2.24i) \\
\mathbb{D}_x^0 &= \mathbf{I}_\phi^0 \otimes \mathbf{D}_x^0 & [(M_\phi + 1)(M_\xi + 1) \times (M_\phi + 1)(M_\xi + 1) \text{ matrix}], & (F.2.24j) \\
\mathbb{D}_x^+ &= \mathbf{I}_\phi^0 \otimes \mathbf{D}_x^+ & [(M_\phi + 1)M_\xi \times (M_\phi + 1)(M_\xi + 1) \text{ matrix}], & (F.2.24k) \\
\mathbb{D}_x^- &= \mathbf{I}_\phi^0 \otimes \mathbf{D}_x^- & [(M_\phi + 1)(M_\xi - 1) \times (M_\phi + 1)M_\xi \text{ matrix}], & (F.2.24l) \\
\mathbb{D}_{xx}^0 &= \mathbf{I}_\phi^0 \otimes \mathbf{D}_{\xi\xi}^0 & [(M_\phi + 1)(M_\xi + 1) \times (M_\phi + 1)(M_\xi + 1) \text{ matrix}], & (F.2.24m) \\
\mathbb{D}_{\phi x}^0 &= \mathbf{D}_\phi^0 \otimes \mathbf{D}_x^0 & [(M_\phi + 1)(M_\xi + 1) \times (M_\phi + 1)(M_\xi + 1) \text{ matrix}], & (F.2.24n)
\end{aligned}$$

As an example, the $(M_\phi + 1)(M_\xi + 1)$ -vector whose elements are $\partial\rho_s/\partial x$ evaluated at the grid points is given by $\mathbb{D}_x^0 \cdot \rho_s$.

In addition to interpolation and differentiation, we must also define a numerical approximation for integration (i.e., a quadrature). An integration matrix multiplying a vector-function of two variables is generically denoted by \mathbb{Q} . Integration over the ϕ -axis is approximated by the trapezoidal rule, whose matrix operator is given by,

$$\mathbb{Q}_\phi = 2NLd \left[\begin{array}{cccccc} \frac{1}{2} & & 1 & & 1 & & \cdots & 1 & & \frac{1}{2} \\ & \frac{1}{2} & & 1 & & 1 & & \cdots & 1 & & \frac{1}{2} \\ & & \ddots \\ & & & \frac{1}{2} & & 1 & & 1 & \cdots & & \frac{1}{2} \end{array} \right] \quad [(M_\xi - 1) \times (M_\phi + 1)(M_\xi - 1) \text{ matrix}]. \quad (F.2.25)$$

Double integration over the whole domain is represented by the following matrix (actually, a row vector):

$$\mathbb{Q}_{\phi x} = NLd^2 \left[\begin{array}{cccccccccc} \frac{1}{2} \sin \xi_0 & \sin \xi_1 & \sin \xi_2 & \cdots & \sin \xi_{M_\xi-1} & \frac{1}{2} \sin \xi_{M_\xi} & \frac{1}{2} \sin \xi_0 & \sin \xi_1 & \cdots & \cdots & \frac{1}{2} \sin \xi_{M_\xi} \end{array} \right] \quad [1 \times (M_\phi + 1)(M_\xi + 1) \text{ matrix}]. \quad (F.2.26)$$

This completes the set of finite difference operations that are required for implementation of Newton's

method.

Discrete form of Newton's method

Now that we have defined the finite difference operations, we proceed to write the discrete analogs of \mathbf{y} , \mathbf{f} , and \mathbf{J} , which appear in (F.2.12)-(F.2.13). The elements of \mathbf{y} have the discrete analogs,

$$[y_1] = \mathbf{p}, \quad [y_2] = \boldsymbol{\tau}, \quad [y_3] = \boldsymbol{\rho}_s, \quad [y_4] = L,$$

where \mathbf{p} , $\boldsymbol{\tau}$, and $\boldsymbol{\rho}_s$ are given by (F.2.20).

The elements of \mathbf{f} are discretely evaluated as,

$$\begin{aligned} [f_1] &= \left\{ \mathbb{D}_\phi^- \cdot \text{diag} \left[\mathbb{I}_\phi^+ \cdot \left(\frac{\mathbf{m}_\phi^{(qp)}}{\boldsymbol{\rho}_s} \right) \right] \cdot \mathbb{D}_\phi^+ + \mathbb{D}_x^- \cdot \text{diag} \left(\mathbb{I}_x^+ \cdot \mathbf{m}_x^{(qp)} \right) \cdot \mathbb{D}_x^+ \right\} \cdot \mathbf{p} \\ &\quad + \left\{ \mathbb{D}_\phi^- \cdot \text{diag} \left[\mathbb{I}_\phi^+ \cdot \left(\frac{\mathbf{m}_\phi^{(q\tau)}}{\sqrt{\boldsymbol{\rho}_s^2 + (\mathbb{D}_\phi^0 \cdot \boldsymbol{\rho}_s)^2}} \right) \right] \cdot \mathbb{D}_\phi^+ + \mathbb{D}_x^- \cdot \text{diag} \left[\mathbb{I}_x^+ \cdot \left(\frac{\mathbf{m}_x^{(q\tau)}}{\sqrt{1 + (\mathbb{D}_x^0 \cdot \boldsymbol{\rho}_s)^2}} \right) \right] \cdot \mathbb{D}_x^+ \right\} \cdot \boldsymbol{\tau} \\ &\quad + \frac{1}{2} U \mathbb{D}_x^- \cdot (\mathbb{I}_x^+ \cdot \boldsymbol{\rho}_s^2), \\ [f_2] &= \left\{ \mathbb{D}_\phi^- \cdot \text{diag} \left[\mathbb{I}_\phi^+ \cdot \left(\frac{\mathbf{G}_s \mathbf{m}_\phi^{(up)}}{\boldsymbol{\rho}_s} \right) \right] \cdot \mathbb{D}_\phi^+ + \mathbb{D}_x^- \cdot \text{diag} \left[\mathbb{I}_x^+ \cdot \left(\mathbf{G}_s \mathbf{m}_x^{(up)} \right) \right] \cdot \mathbb{D}_x^+ \right\} \cdot \mathbf{p} \\ &\quad + \left\{ \mathbb{D}_\phi^- \cdot \text{diag} \left[\mathbb{I}_\phi^+ \cdot \left(\frac{\mathbf{G}_s \mathbf{m}_\phi^{(u\tau)}}{\sqrt{\boldsymbol{\rho}_s^2 + (\mathbb{D}_\phi^0 \cdot \boldsymbol{\rho}_s)^2}} \right) \right] \cdot \mathbb{D}_\phi^+ + \mathbb{D}_x^- \cdot \text{diag} \left[\mathbb{I}_x^+ \cdot \left(\frac{\mathbf{G}_s \mathbf{m}_x^{(u\tau)}}{\sqrt{1 + (\mathbb{D}_x^0 \cdot \boldsymbol{\rho}_s)^2}} \right) \right] \cdot \mathbb{D}_x^+ \right\} \cdot \boldsymbol{\tau} \\ &\quad - U \mathbb{D}_x^- \cdot (\mathbb{I}_x^+ \cdot \mathbf{G}_s) \\ [f_3] &= \frac{1}{\mathbf{G}_s^3} \left\{ \boldsymbol{\rho}_s (\mathbb{D}_{xx}^0 \cdot \boldsymbol{\rho}_s) [\boldsymbol{\rho}_s^2 + (\mathbb{D}_\phi^0 \cdot \boldsymbol{\rho}_s)^2] + \boldsymbol{\rho}_s (\mathbb{D}_{\phi\phi}^0 \cdot \boldsymbol{\rho}_s) [1 + (\mathbb{D}_x^0 \cdot \boldsymbol{\rho}_s)^2] - 2\boldsymbol{\rho}_s (\mathbb{D}_x^0 \cdot \boldsymbol{\rho}_s) (\mathbb{D}_\phi^0 \cdot \boldsymbol{\rho}_s) (\mathbb{D}_{\phi x}^0 \cdot \boldsymbol{\rho}_s) \right. \\ &\quad \left. - (\mathbb{D}_\phi^0 \cdot \boldsymbol{\rho}_s)^2 \right\} - \frac{1}{\mathbf{G}_s} - \frac{\mathbf{p}}{\boldsymbol{\tau}}, \\ [f_4] &= \mathbb{D}_\phi^+ \cdot \left(\frac{\mathbf{p}}{\boldsymbol{\tau}} \right) \Big|_{\xi=\xi_0}, \\ [f_5] &= \left[\boldsymbol{\rho}_s \left(1 + \frac{2\mathbf{x}}{L} \right) - 2\mathbf{x} \left(1 + \frac{\mathbf{x}}{L} \right) (\mathbb{D}_x^0 \cdot \boldsymbol{\rho}_s) \right] \Big|_{\xi=\xi_0}, \\ [f_6] &= \mathbb{D}_\phi^+ \cdot \left(\frac{\mathbf{p}}{\boldsymbol{\tau}} \right) \Big|_{\xi=\xi_{M_\xi}}, \\ [f_7] &= \left[\boldsymbol{\rho}_s \left(1 + \frac{2\mathbf{x}}{L} \right) - 2\mathbf{x} \left(1 + \frac{\mathbf{x}}{L} \right) (\mathbb{D}_x^0 \cdot \boldsymbol{\rho}_s) \right] \Big|_{\xi=\xi_{M_\xi}}, \\ [f_8] &= \mathbb{Q}_\phi \cdot \left[\mathbb{I}_x^+ \cdot \left(\mathbf{G}_s \mathbf{m}_x^{(up)} \right) (\mathbb{D}_x^+ \cdot \mathbf{p}) + \mathbb{I}_x^+ \cdot \left(\frac{\mathbf{G}_s \mathbf{m}_x^{(u\tau)}}{\sqrt{1 + (\mathbb{D}_x^0 \cdot \boldsymbol{\rho}_s)^2}} \right) (\mathbb{D}_x^+ \cdot \boldsymbol{\tau}) - U \mathbb{I}_x^+ \cdot \mathbf{G}_s \right], \\ [f_9] &= \mathbb{Q}_{\phi x} \cdot \mathbf{G}_s - A_0, \\ [f_{10}] &= \frac{1}{2} \mathbb{Q}_{\phi x} \cdot \boldsymbol{\rho}_s^2 - \Omega_0. \end{aligned}$$

Here, \mathbf{x} , \mathbf{m} , and \mathbf{G}_s are simply the vectors whose elements are x , m , and G_s sampled at the grid points [sorted in a manner similar to \mathbf{p} , $\boldsymbol{\tau}$, and $\boldsymbol{\rho}_s$ via (F.2.20)]. In the above expressions, a product \mathbf{ab} between two vectors \mathbf{a} and \mathbf{b} denotes a Hadamard product (i.e., element-wise multiplication). The quotient \mathbf{a}/\mathbf{b} similarly denotes element-wise division.

The elements of \mathbf{J} are discretely evaluated as,

$$\begin{aligned}
 [J_{11}] &= \mathbb{D}_\phi^- \cdot \text{diag} \left[\mathbb{I}_\phi^+ \cdot \left(\frac{\mathbf{m}_\phi^{(qp)}}{\boldsymbol{\rho}_s} \right) \right] \cdot \mathbb{D}_\phi^+ + \mathbb{D}_x^- \cdot \text{diag} \left(\mathbb{I}_x^+ \cdot \mathbf{m}_x^{(qp)} \right) \cdot \mathbb{D}_x^+, \\
 [J_{12}] &= \mathbb{D}_\phi^- \cdot \text{diag} \left[\mathbb{I}_\phi^+ \cdot \left(\frac{\mathbf{m}_\phi^{(q\tau)}}{\sqrt{\boldsymbol{\rho}_s^2 + (\mathbb{D}_\phi^0 \cdot \boldsymbol{\rho}_s)^2}} \right) \right] \cdot \mathbb{D}_\phi^+ + \mathbb{D}_x^- \cdot \text{diag} \left[\mathbb{I}_x^+ \cdot \left(\frac{\mathbf{m}_x^{(q\tau)}}{\sqrt{1 + (\mathbb{D}_x^0 \cdot \boldsymbol{\rho}_s)^2}} \right) \right] \cdot \mathbb{D}_x^+, \\
 [J_{13}] &= \mathbb{D}_\phi^- \cdot \text{diag} \left(\mathbb{D}_\phi^+ \cdot \mathbf{p} \right) \cdot \text{diag} \left[\mathbb{I}_\phi^+ \cdot \left(\frac{\dot{\mathbf{m}}_\phi^{(qp)}}{\boldsymbol{\rho}_s} - \frac{\mathbf{m}_\phi^{(qp)}}{\boldsymbol{\rho}_s^2} \right) \right] \cdot \mathbb{I}_\phi^+ \\
 &\quad + \mathbb{D}_x^- \cdot \text{diag} \left(\mathbb{D}_x^+ \cdot \mathbf{p} \right) \cdot \text{diag} \left(\mathbb{I}_x^+ \cdot \dot{\mathbf{m}}_x^{(qp)} \right) \cdot \mathbb{I}_x^+ \\
 &\quad + \mathbb{D}_\phi^- \cdot \text{diag} \left(\mathbb{D}_\phi^+ \cdot \boldsymbol{\tau} \right) \cdot \left\{ \text{diag} \left[\mathbb{I}_\phi^+ \cdot \left(\frac{\dot{\mathbf{m}}_\phi^{(q\tau)}}{\sqrt{\boldsymbol{\rho}_s^2 + (\mathbb{D}_\phi^0 \cdot \boldsymbol{\rho}_s)^2}} \right) \right] \cdot \mathbb{I}_\phi^+ \right. \\
 &\quad \left. - \text{diag} \left[\mathbb{I}_\phi^+ \cdot \left(\frac{\mathbf{m}_\phi^{(q\tau)}}{[\boldsymbol{\rho}_s^2 + (\mathbb{D}_\phi^0 \cdot \boldsymbol{\rho}_s)^2]^{\frac{3}{2}}} \right) \right] \cdot \left[\text{diag} \left(\mathbb{I}_\phi^+ \cdot \boldsymbol{\rho}_s \right) \cdot \mathbb{I}_\phi^+ + \text{diag} \left(\mathbb{D}_\phi^+ \cdot \boldsymbol{\rho}_s \right) \cdot \mathbb{D}_\phi^+ \right] \right\} \\
 &\quad + \mathbb{D}_x^- \cdot \text{diag} \left(\mathbb{D}_x^+ \cdot \boldsymbol{\tau} \right) \cdot \left\{ \text{diag} \left[\mathbb{I}_x^+ \cdot \left(\frac{\dot{\mathbf{m}}_x^{(q\tau)}}{\sqrt{1 + (\mathbb{D}_x^0 \cdot \boldsymbol{\rho}_s)^2}} \right) \right] \cdot \mathbb{I}_x^+ \right. \\
 &\quad \left. - \text{diag} \left[\mathbb{I}_x^+ \cdot \left(\frac{\mathbf{m}_x^{(q\tau)}}{[1 + (\mathbb{D}_x^0 \cdot \boldsymbol{\rho}_s)^2]^{\frac{3}{2}}} \right) \right] \cdot \text{diag} \left(\mathbb{D}_x^+ \cdot \boldsymbol{\rho}_s \right) \cdot \mathbb{D}_x^+ \right\} \\
 &\quad + U \mathbb{I}_x^- \cdot [\text{diag} \left(\mathbb{D}_x^+ \cdot \boldsymbol{\rho}_s \right) \cdot \mathbb{I}_x^+ + \text{diag} \left(\mathbb{I}_x^+ \cdot \boldsymbol{\rho}_s \right) \cdot \mathbb{D}_x^+], \\
 [J_{14}] &= \frac{1}{L} \left\{ -2 \left[\mathbb{D}_x^- \cdot \text{diag} \left(\mathbb{I}_x^+ \cdot \mathbf{m}_x^{(qp)} \right) \cdot (\mathbb{D}_x^+ \cdot \mathbf{p}) + \mathbb{D}_x^- \cdot \text{diag} \left(\mathbb{I}_x^+ \cdot \frac{\mathbf{m}_x^{(q\tau)}}{\sqrt{1 + (\mathbb{D}_x^0 \cdot \boldsymbol{\rho}_s)^2}} \right) \cdot (\mathbb{D}_x^+ \cdot \boldsymbol{\tau}) \right] \right. \\
 &\quad \left. + \mathbb{D}_x^- \cdot \text{diag} \left[\mathbb{I}_x^+ \cdot \left(\frac{\mathbf{m}_x^{(q\tau)} (\mathbb{D}_x^0 \cdot \boldsymbol{\rho}_s)^2}{[1 + (\mathbb{D}_x^0 \cdot \boldsymbol{\rho}_s)^2]^{\frac{3}{2}}} \right) \right] \cdot (\mathbb{D}_x^+ \cdot \boldsymbol{\tau}) - U \mathbb{I}_x^- \cdot \text{diag} \left(\mathbb{I}_x^+ \cdot \boldsymbol{\rho}_s \right) \cdot (\mathbb{D}_x^+ \cdot \boldsymbol{\rho}_s) \right\}, \\
 [J_{21}] &= \mathbb{D}_\phi^- \cdot \text{diag} \left[\mathbb{I}_\phi^+ \cdot \left(\frac{\mathbf{G}_s \mathbf{m}_\phi^{(up)}}{\boldsymbol{\rho}_s} \right) \right] \cdot \mathbb{D}_\phi^+ + \mathbb{D}_x^- \cdot \text{diag} \left[\mathbb{I}_x^+ \cdot \left(\mathbf{G}_s \mathbf{m}_x^{(up)} \right) \right] \cdot \mathbb{D}_x^+, \\
 [J_{22}] &= \mathbb{D}_\phi^- \cdot \text{diag} \left[\mathbb{I}_\phi^+ \cdot \left(\frac{\mathbf{G}_s \mathbf{m}_\phi^{(u\tau)}}{\sqrt{\boldsymbol{\rho}_s^2 + (\mathbb{D}_\phi^0 \cdot \boldsymbol{\rho}_s)^2}} \right) \right] \cdot \mathbb{D}_\phi^+ + \mathbb{D}_x^- \cdot \text{diag} \left[\mathbb{I}_x^+ \cdot \left(\frac{\mathbf{G}_s \mathbf{m}_x^{(u\tau)}}{\sqrt{1 + (\mathbb{D}_x^0 \cdot \boldsymbol{\rho}_s)^2}} \right) \right] \cdot \mathbb{D}_x^+, \\
 [J_{23}] &= \mathbb{D}_\phi^- \cdot \text{diag} \left(\mathbb{D}_\phi^+ \cdot \mathbf{p} \right) \cdot \text{diag} \left[\mathbb{I}_\phi^+ \cdot \left(\frac{\mathbf{m}_\phi^{(up)} \dot{\mathbf{G}}_s + \mathbf{G}_s \dot{\mathbf{m}}_\phi^{(up)}}{\boldsymbol{\rho}_s} - \frac{\mathbf{G}_s \mathbf{m}_\phi^{(up)}}{\boldsymbol{\rho}_s^2} \right) \right] \cdot \mathbb{I}_\phi^+ \\
 &\quad + \mathbb{D}_x^- \cdot \text{diag} \left(\mathbb{D}_x^+ \cdot \mathbf{p} \right) \cdot \text{diag} \left[\mathbb{I}_x^+ \cdot \left(\mathbf{m}_x^{(up)} \dot{\mathbf{G}}_s + \mathbf{G}_s \dot{\mathbf{m}}_x^{(up)} \right) \right] \cdot \mathbb{I}_x^+ \\
 &\quad + \mathbb{D}_\phi^- \cdot \text{diag} \left(\mathbb{D}_\phi^+ \cdot \boldsymbol{\tau} \right) \cdot \left\{ \text{diag} \left[\mathbb{I}_\phi^+ \cdot \left(\frac{\mathbf{m}_\phi^{(u\tau)} \dot{\mathbf{G}}_s + \mathbf{G}_s \dot{\mathbf{m}}_\phi^{(u\tau)}}{\sqrt{\boldsymbol{\rho}_s^2 + (\mathbb{D}_\phi^0 \cdot \boldsymbol{\rho}_s)^2}} \right) \right] \cdot \mathbb{I}_\phi^+ \right\}
 \end{aligned}$$

$$\begin{aligned}
& - \operatorname{diag} \left[\mathbb{I}_\phi^+ \cdot \left(\frac{\mathbf{G}_s \mathbf{m}_\phi^{(u\tau)}}{[\rho_s^2 + (\mathbb{D}_\phi^0 \cdot \boldsymbol{\rho}_s)^2]^{\frac{3}{2}}} \right) \right] \cdot \left[\operatorname{diag} \left(\mathbb{I}_\phi^+ \cdot \boldsymbol{\rho}_s \right) \cdot \mathbb{I}_\phi^+ + \operatorname{diag} \left(\mathbb{D}_\phi^+ \cdot \boldsymbol{\rho}_s \right) \cdot \mathbb{D}_\phi^+ \right] \Bigg\} \\
& + \mathbb{D}_x^- \cdot \operatorname{diag} \left(\mathbb{D}_x^+ \cdot \boldsymbol{\tau} \right) \cdot \left\{ \operatorname{diag} \left[\mathbb{I}_x^+ \cdot \left(\frac{\mathbf{m}_x^{(u\tau)} \dot{\mathbf{G}}_s + \mathbf{G}_s \dot{\mathbf{m}}_x^{(u\tau)}}{\sqrt{1 + (\mathbb{D}_x^0 \cdot \boldsymbol{\rho}_s)^2}} \right) \right] \cdot \mathbb{I}_x^+ \right. \\
& - \operatorname{diag} \left[\mathbb{I}_x^+ \cdot \left(\frac{\mathbf{G}_s \mathbf{m}_x^{(u\tau)}}{[1 + (\mathbb{D}_x^0 \cdot \boldsymbol{\rho}_s)^2]^{\frac{3}{2}}} \right) \right] \cdot \operatorname{diag} \left(\mathbb{D}_x^+ \cdot \boldsymbol{\rho}_s \right) \cdot \mathbb{D}_x^+ \Big\} \\
& - U \mathbb{D}_x^- \cdot \operatorname{diag} \left(\mathbb{I}_x^+ \cdot \dot{\mathbf{G}}_s \right) \cdot \mathbb{I}_x^+, \\
[J_{24}] &= \frac{1}{L} \left\{ -2 \left[\mathbb{D}_x^- \cdot \operatorname{diag} \left[\mathbb{I}_x^+ \cdot \left(\mathbf{G}_s \mathbf{m}_x^{(up)} \right) \right] \cdot (\mathbb{D}_x^+ \cdot \mathbf{p}) + \mathbb{D}_x^- \cdot \operatorname{diag} \left[\mathbb{I}_x^+ \cdot \left(\frac{\mathbf{G}_s \mathbf{m}_x^{(u\tau)}}{\sqrt{1 + (\mathbb{D}_x^0 \cdot \boldsymbol{\rho}_s)^2}} \right) \right] \cdot (\mathbb{D}_x^+ \cdot \boldsymbol{\tau}) \right] \right. \\
& - \mathbb{D}_\phi^- \cdot \operatorname{diag} \left[\mathbb{I}_\phi^+ \cdot \left(\frac{\rho_s \mathbf{m}_\phi^{(up)} (\mathbb{D}_x^0 \cdot \boldsymbol{\rho}_s)^2}{\mathbf{G}_s} \right) \right] \cdot (\mathbb{D}_\phi^+ \cdot \mathbf{p}) \\
& - \mathbb{D}_x^- \cdot \operatorname{diag} \left[\mathbb{I}_x^+ \cdot \left(\frac{\rho_s \mathbf{m}_x^{(up)} (\mathbb{D}_x^0 \cdot \boldsymbol{\rho}_s)^2}{\mathbf{G}_s} \right) \right] \cdot (\mathbb{D}_x^+ \cdot \mathbf{p}) \\
& - \mathbb{D}_\phi^- \cdot \operatorname{diag} \left[\mathbb{I}_\phi^+ \cdot \left(\frac{\rho_s^2 \mathbf{m}_\phi^{(u\tau)} (\mathbb{D}_x^0 \cdot \boldsymbol{\rho}_s)^2}{\mathbf{G}_s \sqrt{\rho_s^2 + (\mathbb{D}_\phi^0 \cdot \boldsymbol{\rho}_s)^2}} \right) \right] \cdot (\mathbb{D}_\phi^+ \cdot \boldsymbol{\tau}) \\
& - \mathbb{D}_x^- \cdot \operatorname{diag} \left[\mathbb{I}_x^+ \cdot \left(\frac{\rho_s^2 \mathbf{m}_x^{(u\tau)} (\mathbb{D}_x^0 \cdot \boldsymbol{\rho}_s)^2}{\mathbf{G}_s \sqrt{1 + (\mathbb{D}_x^0 \cdot \boldsymbol{\rho}_s)^2}} \right) \right] \cdot (\mathbb{D}_x^+ \cdot \boldsymbol{\tau}) \\
& + \mathbb{D}_x^- \cdot \operatorname{diag} \left[\mathbb{I}_x^+ \cdot \left(\frac{\mathbf{G}_s \mathbf{m}_x^{(u\tau)} (\mathbb{D}_x^0 \cdot \boldsymbol{\rho}_s)^2}{[1 + (\mathbb{D}_x^0 \cdot \boldsymbol{\rho}_s)^2]^{\frac{3}{2}}} \right) \right] \cdot (\mathbb{D}_x^+ \cdot \boldsymbol{\tau}) \\
& \left. + U \mathbb{D}_x^- \cdot \mathbb{I}_x^+ \cdot \left[\mathbf{G}_s + \frac{\rho_s^2 (\mathbb{D}_x^0 \cdot \boldsymbol{\rho}_s)^2}{\mathbf{G}_s} \right] \right\}, \\
[J_{31}] &= \operatorname{diag} \left(\frac{1}{\boldsymbol{\tau}} \right), \\
[J_{32}] &= -\operatorname{diag} \left(\frac{\mathbf{p}}{\boldsymbol{\tau}^2} \right), \\
[J_{33}] &= -\operatorname{diag} \left(\frac{\dot{\mathbf{G}}_s}{\mathbf{G}_s^2} \right) \\
& - \operatorname{diag} \left(\frac{3 \dot{\mathbf{G}}_s}{\mathbf{G}_s^4} \left\{ (\mathbb{D}_\phi^0 \cdot \boldsymbol{\rho}_s)^2 + 2 \rho_s (\mathbb{D}_\phi^0 \cdot \boldsymbol{\rho}_s) (\mathbb{D}_x^0 \cdot \boldsymbol{\rho}_s) (\mathbb{D}_{\phi x}^0 \cdot \boldsymbol{\rho}_s) - \boldsymbol{\rho}_s (\mathbb{D}_{xx}^0 \cdot \boldsymbol{\rho}_s) [\rho_s^2 + (\mathbb{D}_\phi^0 \cdot \boldsymbol{\rho}_s)^2] \right. \right. \\
& \left. \left. - \boldsymbol{\rho}_s (\mathbb{D}_{\phi\phi}^0 \cdot \boldsymbol{\rho}_s) [1 + (\mathbb{D}_x^0 \cdot \boldsymbol{\rho}_s)^2] \right\} \right) \\
& + \operatorname{diag} \left(\frac{1}{\mathbf{G}_s^3} \left\{ 2 (\mathbb{D}_\phi^0 \cdot \boldsymbol{\rho}_s) (\mathbb{D}_x^0 \cdot \boldsymbol{\rho}_s) (\mathbb{D}_{\phi x}^0 \cdot \boldsymbol{\rho}_s) - (\mathbb{D}_{xx}^0 \cdot \boldsymbol{\rho}_s) [3 \rho_s^2 + (\mathbb{D}_\phi^0 \cdot \boldsymbol{\rho}_s)^2] \right. \right. \\
& \left. \left. - (\mathbb{D}_{\phi\phi}^0 \cdot \boldsymbol{\rho}_s) [1 + (\mathbb{D}_x^0 \cdot \boldsymbol{\rho}_s)^2] \right\} \right) \\
& + \operatorname{diag} \left\{ \frac{\rho_s}{\mathbf{G}_s^3} [2 (\mathbb{D}_\phi^0 \cdot \boldsymbol{\rho}_s) (\mathbb{D}_{\phi x}^0 \cdot \boldsymbol{\rho}_s) - (\mathbb{D}_{\phi\phi}^0 \cdot \boldsymbol{\rho}_s) (\mathbb{D}_x^0 \cdot \boldsymbol{\rho}_s)] \right\} \cdot \mathbb{D}_x^0
\end{aligned}$$

$$\begin{aligned}
& + \text{diag} \left\{ \frac{1}{\mathbf{G}_s^3} [2(\mathbb{D}_\phi^0 \cdot \boldsymbol{\rho}_s) + 2\boldsymbol{\rho}_s(\mathbb{D}_x^0 \cdot \boldsymbol{\rho}_s)(\mathbb{D}_{\phi x}^0 \cdot \boldsymbol{\rho}_s) - \boldsymbol{\rho}_s(\mathbb{D}_{xx}^0 \cdot \boldsymbol{\rho}_s)(\mathbb{D}_\phi^0 \cdot \boldsymbol{\rho}_s)] \right\} \cdot \mathbb{D}_\phi^0 \\
& + \text{diag} \left\{ \frac{2\boldsymbol{\rho}_s}{\mathbf{G}_s^3} [(\mathbb{D}_\phi^0 \cdot \boldsymbol{\rho}_s)(\mathbb{D}_x^0 \cdot \boldsymbol{\rho}_s)] \right\} \cdot \mathbb{D}_{\phi x}^0 - \text{diag} \left\{ \frac{\boldsymbol{\rho}_s}{\mathbf{G}_s^3} [\boldsymbol{\rho}_s^2 + (\mathbb{D}_\phi^0 \cdot \boldsymbol{\rho}_s)^2] \right\} \cdot \mathbb{D}_{xx}^0 \\
& - \text{diag} \left\{ \frac{\boldsymbol{\rho}_s}{\mathbf{G}_s^3} [1 + (\mathbb{D}_x^0 \cdot \boldsymbol{\rho}_s)^2] \right\} \cdot \mathbb{D}_{\phi\phi}^0, \\
[J_{34}] &= \frac{1}{L} \left(\frac{1}{\mathbf{G}_s^3} (\mathbb{D}_x^0 \cdot \boldsymbol{\rho}_s)^2 \right. \\
&\quad + \frac{3(\mathbb{D}_x^0 \cdot \boldsymbol{\rho}_s)^2}{\mathbf{G}_s^5} \left\{ (\mathbb{D}_\phi^0 \cdot \boldsymbol{\rho}_s)^2 + 2\boldsymbol{\rho}_s(\mathbb{D}_\phi^0 \cdot \boldsymbol{\rho}_s)(\mathbb{D}_x^0 \cdot \boldsymbol{\rho}_s)(\mathbb{D}_{\phi x}^0 \cdot \boldsymbol{\rho}_s) - \boldsymbol{\rho}_s(\mathbb{D}_{xx}^0 \cdot \boldsymbol{\rho}_s) [\boldsymbol{\rho}_s^2 + (\mathbb{D}_\phi^0 \cdot \boldsymbol{\rho}_s)^2] \right. \\
&\quad \left. - \boldsymbol{\rho}_s(\mathbb{D}_\phi^0 \cdot \boldsymbol{\rho}_s)^2 [1 + (\mathbb{D}_x^0 \cdot \boldsymbol{\rho}_s)^2] \right\} \\
&\quad \left. + \frac{2\boldsymbol{\rho}_s}{\mathbf{G}_s^3} \left\{ -2(\mathbb{D}_\phi^0 \cdot \boldsymbol{\rho}_s)(\mathbb{D}_x^0 \cdot \boldsymbol{\rho}_s)(\mathbb{D}_{\phi x}^0 \cdot \boldsymbol{\rho}_s) + (\mathbb{D}_{xx}^0 \cdot \boldsymbol{\rho}_s) [\boldsymbol{\rho}_s^2 + (\mathbb{D}_\phi^0 \cdot \boldsymbol{\rho}_s)^2] + (\mathbb{D}_{\phi\phi}^0 \cdot \boldsymbol{\rho}_s)(\mathbb{D}_x^0 \cdot \boldsymbol{\rho}_s)^2 \right\} \right), \\
[J_{41}] &= \text{diag} \left[\mathbb{I}_\phi^+ \cdot \left(\frac{1}{\boldsymbol{\tau}} \right) \right] \cdot \mathbb{D}_\phi^+ \Big|_{\xi=\xi_0}, \\
[J_{42}] &= -\text{diag} \left[\mathbb{I}_\phi^+ \cdot \left(\frac{\mathbf{P}}{\boldsymbol{\tau}^2} \right) \right] \cdot \mathbb{D}_\phi^+ \Big|_{\xi=\xi_0}, \\
[J_{43}] &= \mathbf{0}, \\
[J_{44}] &= \mathbf{0}, \\
[J_{51}] &= \mathbf{0}, \\
[J_{52}] &= \mathbf{0}, \\
[J_{53}] &= \left\{ \text{diag} \left(1 + \frac{2\mathbf{x}}{L} \right) \cdot \mathbb{I} - \text{diag} \left[2\mathbf{x} \left(1 + \frac{\mathbf{x}}{L} \right) \right] \cdot \mathbb{D}_x^0 \right\} \Big|_{\xi=\xi_0}, \\
[J_{54}] &= \mathbf{0}, \\
[J_{61}] &= \text{diag} \left[\mathbb{I}_\phi^+ \cdot \left(\frac{1}{\boldsymbol{\tau}} \right) \right] \cdot \mathbb{D}_\phi^+ \Big|_{\xi=\xi_{M_\xi}}, \\
[J_{62}] &= -\text{diag} \left[\mathbb{I}_\phi^+ \cdot \left(\frac{\mathbf{P}}{\boldsymbol{\tau}^2} \right) \right] \cdot \mathbb{D}_\phi^+ \Big|_{\xi=\xi_{M_\xi}}, \\
[J_{63}] &= \mathbf{0}, \\
[J_{64}] &= \mathbf{0}, \\
[J_{71}] &= \mathbf{0}, \\
[J_{72}] &= \mathbf{0}, \\
[J_{73}] &= \left\{ \text{diag} \left(1 + \frac{2\mathbf{x}}{L} \right) \cdot \mathbb{I} - \text{diag} \left[2\mathbf{x} \left(1 + \frac{\mathbf{x}}{L} \right) \right] \cdot \mathbb{D}_x^0 \right\} \Big|_{\xi=\xi_{M_\xi}}, \\
[J_{74}] &= \mathbf{0}, \\
[J_{81}] &= \mathbb{Q}_\phi \cdot \text{diag} \left[\mathbb{I}_x^+ \cdot \left(\mathbf{G}_s \mathbf{m}_x^{(up)} \right) \right] \cdot \mathbb{D}_x^+ \Big|_{\xi=\xi^*},
\end{aligned}$$

$$\begin{aligned}
[J_{82}] &= \mathbb{Q}_\phi \cdot \text{diag} \left[\mathbb{I}_x^+ \cdot \left(\frac{\mathbf{G}_s \mathbf{m}_x^{(u\tau)}}{\sqrt{1 + (\mathbb{D}_x^0 \cdot \boldsymbol{\rho}_s)^2}} \right) \right] \cdot \mathbb{D}_x^+ \Big|_{\xi=\xi^*}, \\
[J_{83}] &= \mathbb{Q}_\phi \cdot \left(\text{diag} \left\{ \text{diag} \left[\mathbb{I}_x^+ \cdot \left(\mathbf{m}_x^{(up)} \dot{\mathbf{G}}_s + \mathbf{G}_s \dot{\mathbf{m}}_x^{(up)} \right) \right] \cdot (\mathbb{D}_x^+ \cdot \mathbf{p}) \right. \right. \\
&\quad + \text{diag} \left[\mathbb{I}_x^+ \cdot \left(\frac{\mathbf{m}_x^{(u\tau)} \dot{\mathbf{G}}_s + \mathbf{G}_s \dot{\mathbf{m}}_x^{(u\tau)}}{\sqrt{1 + (\mathbb{D}_x^0 \cdot \boldsymbol{\rho}_s)^2}} \right) \right] \cdot (\mathbb{D}_x^+ \cdot \boldsymbol{\tau}) - U \mathbb{I}_x \cdot \dot{\mathbf{G}}_s \Big\} \cdot \mathbb{I}_x^+ \\
&\quad \left. \left. - \text{diag} \left[\mathbb{I}_x^+ \cdot \left(\frac{\mathbf{G}_s \mathbf{m}_x^{(u\tau)}}{[1 + (\mathbb{D}_x^0 \cdot \boldsymbol{\rho}_s)^2]^{\frac{3}{2}}} \right) (\mathbb{D}_x^+ \cdot \boldsymbol{\rho}_s) (\mathbb{D}_x^+ \cdot \boldsymbol{\tau}) \right] \cdot \mathbb{D}_x^+ \right) \right|_{\xi=\xi^*}, \\
[J_{84}] &= -\frac{1}{L} \mathbb{Q}_\phi \cdot \left(\text{diag} \left[\mathbb{I}_x^+ \cdot \left(\frac{\boldsymbol{\rho}_s^2 (\mathbb{D}_x^0 \cdot \boldsymbol{\rho}_s)^2}{\mathbf{G}_s} \right) \right] \cdot \left\{ \text{diag} \left(\mathbb{I}_x^+ \cdot \mathbf{m}_x^{(up)} \right) \cdot (\mathbb{D}_x^+ \cdot \mathbf{p}) \right. \right. \\
&\quad + \text{diag} \left[\mathbb{I}_x^+ \cdot \left(\frac{\mathbf{m}_x^{(u\tau)}}{\sqrt{1 + (\mathbb{D}_x^0 \cdot \boldsymbol{\rho}_s)^2}} \right) \right] \cdot (\mathbb{D}_x^+ \cdot \boldsymbol{\tau}) - U \mathbf{1} \Big\} \\
&\quad + \text{diag} \left[\mathbb{I}_x^+ \cdot \left(\mathbf{G}_s \mathbf{m}_x^{(up)} \right) \right] \cdot (\mathbb{D}_x^+ \cdot \mathbf{p}) \\
&\quad \left. \left. + \text{diag} \left[\mathbb{I}_x^+ \cdot \left(\frac{\mathbf{G}_s \mathbf{m}_x^{(u\tau)}}{\sqrt{1 + (\mathbb{D}_x^0 \cdot \boldsymbol{\rho}_s)^2}} - \frac{\mathbf{G}_s \mathbf{m}_x^{(u\tau)} (\mathbb{D}_x^0 \cdot \boldsymbol{\rho}_s)^2}{[1 + (\mathbb{D}_x^0 \cdot \boldsymbol{\rho}_s)^2]^{\frac{3}{2}}} \right) \right] \cdot (\mathbb{D}_x^+ \cdot \boldsymbol{\tau}) \right) \right|_{\xi=\xi^*},
\end{aligned}$$

$$[J_{91}] = \mathbf{0},$$

$$[J_{92}] = \mathbf{0},$$

$$[J_{93}] = \mathbb{Q}_{\phi x} \cdot \dot{\mathbf{G}}_s,$$

$$[J_{94}] = \frac{1}{L} \mathbb{Q}_{\phi x} \cdot \left[\mathbf{G}_s - \frac{\boldsymbol{\rho}_s^2 (\mathbb{D}_x^0 \cdot \boldsymbol{\rho}_s)^2}{\mathbf{G}_s} \right],$$

$$[J_{10,1}] = \mathbf{0},$$

$$[J_{10,2}] = \mathbf{0},$$

$$[J_{10,3}] = \mathbb{Q}_{\phi x} \cdot \text{diag} (\boldsymbol{\rho}_s),$$

$$[J_{10,4}] = \frac{1}{2L} \mathbb{Q}_{\phi x} \cdot \boldsymbol{\rho}_s^2.$$

Here, $\dot{\mathbf{m}}$ and $\dot{\mathbf{G}}_s$ are vectors whose elements are \dot{m} and \dot{G}_s sampled at the grid points. This completes the discretization step.

The discrete form of Newton's method,

$$\mathbf{y}^{(k+1)} = \mathbf{y}^{(k)} - \left[\mathbf{J} \left(\mathbf{y}^{(k)} \right) \right]^{-1} \cdot \mathbf{f} \left(\mathbf{y}^{(k)} \right), \quad k = 0, 1, 2, \dots, \quad (\text{F.2.12})$$

$$\mathbf{y}^{(0)} = \mathbf{y}^*, \quad (\text{F.2.13})$$

involves the solution of a $[3(M_\phi + 1)(M_\xi + 1) + 1] \times [3(M_\phi + 1)(M_\xi + 1) + 1]$ linear system at each (k th) iteration. Inserting the discrete analogs of \mathbf{y} , \mathbf{f} , and \mathbf{J} into (F.2.12)-(F.2.13) enables an efficient solution of the linear system by use of a sparse linear solver. Since the boundary-value problem is two-dimensional, an iterative solution procedure is preferred over direct elimination methods (due

to the large system size). Iteration proceeds until either one of the vector norms $\|\mathbf{y}^{(k+1)} - \mathbf{y}^{(k)}\|$ or $\|\mathbf{f}(\mathbf{y}^{(k)})\|$ falls below a predetermined tolerance ε (e.g., $\varepsilon = 10^{-6}$ is a typical value).

Appendix G

Ordered perturbation equations in the quasi-spherical limit

In Chapter 6, we developed an asymptotic solution to the initial-boundary-value problem in the double limit as $a \rightarrow 0$ and $\Delta \rightarrow 0$, where a (the radius ratio) and Δ (the excess surface area) were defined by equations (2.5.11) and (2.5.12) in the main text. In this appendix, we present the ordered perturbation equations for this asymptotic problem, obtained by expanding the dependent variable in perturbation series with respect to $\Delta^{\frac{1}{2}}$, inserting the expansions into the equations presented in §6.4, and collecting terms of like order in $\Delta^{\frac{1}{2}}$. All variables in this appendix are rendered dimensionless using the following characteristic scales: r_0 (the vesicle volumetric radius), V (the mean channel velocity), and μ (the suspending fluid viscosity).

Equations of continuity and motion in the exterior fluid:

$$O(1) : \quad \nabla \cdot \mathbf{u}'_0 = 0, \quad \nabla \cdot \boldsymbol{\sigma}'_0 = -\nabla p'_0 + \nabla^2 \mathbf{u}'_0 = \mathbf{0}, \quad (\text{G.0.1a})$$

$$O(\Delta^{\frac{1}{2}}) : \quad \nabla \cdot \mathbf{u}'_1 = 0, \quad \nabla \cdot \boldsymbol{\sigma}'_1 = -\nabla p'_1 + \nabla^2 \mathbf{u}'_1 = \mathbf{0}, \quad (\text{G.0.1b})$$

etc.

Equations of continuity and motion in the interior fluid:

$$O(1) : \quad \nabla \cdot \check{\mathbf{u}}'_0 = 0, \quad \nabla \cdot \check{\boldsymbol{\sigma}}'_0 = -\nabla \check{p}'_0 + \kappa \nabla^2 \check{\mathbf{u}}'_0 = \mathbf{0}, \quad (\text{G.0.2a})$$

$$O(\Delta^{\frac{1}{2}}) : \quad \nabla \cdot \check{\mathbf{u}}'_1 = 0, \quad \nabla \cdot \check{\boldsymbol{\sigma}}'_1 = -\nabla \check{p}'_1 + \kappa \nabla^2 \check{\mathbf{u}}'_1 = \mathbf{0}, \quad (\text{G.0.2b})$$

etc.

Surface incompressibility condition on the vesicle membrane:¹

at $r = 1$:

$$\begin{aligned} O(1) : \quad & \frac{\partial}{\partial r}(\hat{\mathbf{x}} \cdot \mathbf{u}'_0) = -\frac{\partial}{\partial r}(\hat{\mathbf{x}} \cdot \mathbf{u}^\infty) \\ \text{or} \quad & \frac{\partial}{\partial r}(\hat{\mathbf{x}} \cdot \check{\mathbf{u}}'_0) = 0, \end{aligned} \quad (\text{G.0.3a})$$

$$\begin{aligned} O(\Delta^{\frac{1}{2}}) : \quad & \frac{\partial}{\partial r}(\hat{\mathbf{x}} \cdot \mathbf{u}'_1) = -f_0 \frac{\partial^2}{\partial r^2}[\hat{\mathbf{x}} \cdot (\mathbf{u}'_0 + \mathbf{u}^\infty)] + [\hat{\mathbf{x}}(\nabla f_0) + (\nabla f_0)\hat{\mathbf{x}}] : \nabla(\mathbf{u}'_0 + \mathbf{u}^\infty) \\ \text{or} \quad & \frac{\partial}{\partial r}(\hat{\mathbf{x}} \cdot \check{\mathbf{u}}'_1) = -f_0 \frac{\partial^2}{\partial r^2}(\hat{\mathbf{x}} \cdot \check{\mathbf{u}}'_0) + [\hat{\mathbf{x}}(\nabla f_0) + (\nabla f_0)\hat{\mathbf{x}}] : \nabla \check{\mathbf{u}}'_0, \end{aligned} \quad (\text{G.0.3b})$$

etc.

Exterior velocity boundary condition on the channel wall:

at $\bar{\rho} = R_{\bar{\phi}}$:

$$O(1) : \quad \mathbf{u}'_0 = \mathbf{0}, \quad (\text{G.0.4a})$$

$$O(\Delta^{\frac{1}{2}}) : \quad \mathbf{u}'_1 = \mathbf{0}, \quad (\text{G.0.4b})$$

etc.

Exterior velocity boundary condition in the far field:

as $x \rightarrow \pm\infty$:

$$O(1) : \quad \mathbf{u}'_0 = \mathbf{0}, \quad (\text{G.0.5a})$$

$$O(\Delta^{\frac{1}{2}}) : \quad \mathbf{u}'_1 = \mathbf{0}, \quad (\text{G.0.5b})$$

etc.

Kinematic continuity condition on the vesicle membrane:

at $r = 1$:

$$O(1) : \quad \mathbf{u}'_0 - \check{\mathbf{u}}'_0 = -\mathbf{u}^\infty, \quad (\text{G.0.6a})$$

$$O(\Delta^{\frac{1}{2}}) : \quad \mathbf{u}'_1 - \check{\mathbf{u}}'_1 = -f_0 \frac{\partial}{\partial r}(\mathbf{u}'_0 - \check{\mathbf{u}}'_0 + \mathbf{u}^\infty), \quad (\text{G.0.6b})$$

¹This boundary condition has been simplified by use of the bulk incompressibility condition.

etc.

Normal stress boundary condition on the vesicle membrane (with $\bar{\chi} = \Delta^{\frac{1}{2}}\chi$):

at $r = 1$:

$$O(1): \quad \hat{x} \cdot (\sigma'_0 - \check{\sigma}'_0) \cdot \hat{x} = -\hat{x} \cdot \sigma^\infty \cdot \hat{x} + 2\tau_0 - \tau_{-1}(2f_0 + \nabla^2 f_0) + \bar{\chi} \nabla^4 f_0, \quad (\text{G.0.7a})$$

$$\begin{aligned} O(\Delta^{\frac{1}{2}}): \quad & \hat{x} \cdot (\sigma'_1 - \check{\sigma}'_1) \cdot \hat{x} = -f_0 \frac{\partial}{\partial r} [\hat{x} \cdot (\sigma'_0 - \check{\sigma}'_0 + \sigma^\infty) \cdot \hat{x}] + 2\hat{x} \cdot (\sigma'_0 - \check{\sigma}'_0 + \sigma^\infty) \cdot \nabla f_0 \\ & + 2\tau_1 - \tau_0(2f_0 + \nabla^2 f_0) - \tau_{-1}(2f_1 + \nabla^2 f_1 - 2f_0^2 - 2f_0 \nabla^2 f_0) \\ & + \bar{\chi} [\nabla^4 f_1 - 4f_0 \nabla^4 f_0 - 4(\nabla f_0) \cdot (\nabla \nabla^2 f_0) - 2(\nabla \nabla f_0) : (\nabla \nabla f_0) - (\nabla^2 f_0)^2], \end{aligned} \quad (\text{G.0.7b})$$

etc.

Tangential stress boundary condition on the vesicle membrane:²

at $r = 1$:

$$O(1): \quad (\delta - \hat{x}\hat{x}) \cdot (\sigma'_0 - \check{\sigma}'_0) \cdot \hat{x} = -(\delta - \hat{x}\hat{x}) \cdot \sigma^\infty \cdot \hat{x} - \nabla \tau_0 \quad (\text{G.0.8a})$$

$$\begin{aligned} O(\Delta^{\frac{1}{2}}): \quad & (\delta - \hat{x}\hat{x}) \cdot (\sigma'_1 - \check{\sigma}'_1) \cdot \hat{x} = -f_0 \frac{\partial}{\partial r} [(\delta - \hat{x}\hat{x}) \cdot (\sigma'_0 - \check{\sigma}'_0 + \sigma^\infty) \cdot \hat{x}] \\ & + (\delta - 2\hat{x}\hat{x}) \cdot (\sigma'_0 - \check{\sigma}'_0 + \sigma^\infty) \cdot \nabla f_0 - [\hat{x} \cdot (\sigma'_0 - \check{\sigma}'_0 + \sigma^\infty) \cdot \hat{x}] \nabla f_0 \\ & - \nabla \tau_1 - \hat{x}(\nabla f) \cdot \nabla \tau_0 - (f_0/r_0)\nabla \tau_0, \end{aligned} \quad (\text{G.0.8b})$$

etc.

Kinematic condition on the vesicle membrane (with $\bar{t} = \Delta^{-\frac{1}{2}}t$):

at $r = 1$:

$$\begin{aligned} O(1): \quad & \frac{\partial f_0}{\partial \bar{t}} - \hat{x} \cdot (\mathbf{u}'_0 - \mathbf{U}_0) = \hat{x} \cdot \mathbf{u}^\infty \\ \text{or} \quad & \frac{\partial f_0}{\partial \bar{t}} - \hat{x} \cdot (\check{\mathbf{u}}'_0 - \mathbf{U}_0) = 0, \end{aligned} \quad (\text{G.0.9a})$$

$$\begin{aligned} O(\Delta^{\frac{1}{2}}): \quad & \frac{\partial f_1}{\partial \bar{t}} - \hat{x} \cdot (\mathbf{u}'_1 - \mathbf{U}_1) = f_0 \frac{\partial}{\partial r} [\hat{x} \cdot (\mathbf{u}'_0 + \mathbf{u}^\infty)] - (\mathbf{u}'_0 + \mathbf{u}^\infty) \cdot \nabla f_0 \\ \text{or} \quad & \frac{\partial f_1}{\partial \bar{t}} - \hat{x} \cdot (\check{\mathbf{u}}'_1 - \mathbf{U}_1) = f_0 \frac{\partial}{\partial r} (\hat{x} \cdot \check{\mathbf{u}}'_0) - \check{\mathbf{u}}'_0 \cdot \nabla f_0, \end{aligned} \quad (\text{G.0.9b})$$

²This boundary condition has been simplified by use of $\partial \tau_n / \partial r = 0$ for $n = 0, 1, \dots$ and $\nabla \tau_{-1} = \mathbf{0}$.

etc.

Surface area constraint:³

at $r = 1$:

$$O(1) : \int_{\mathcal{S}_\Omega} [(\nabla f_0) \cdot (\nabla f_0) - 2f_0^2] d\Omega = 2, \quad (\text{G.0.10a})$$

$$O(\Delta^{\frac{1}{2}}) : \int_{\mathcal{S}_\Omega} \{(\nabla f_0) \cdot (\nabla f_1) - 2f_0 f_1 + f_0 [(\nabla f_0) \cdot (\nabla f_0) - \frac{2}{3}f_0^2]\} d\Omega = 0, \quad (\text{G.0.10b})$$

etc.

Volume constraint:

at $r = 1$:

$$O(1) : \int_{\mathcal{S}_\Omega} f_0 d\Omega = 0, \quad (\text{G.0.11a})$$

$$O(\Delta^{\frac{1}{2}}) : \int_{\mathcal{S}_\Omega} (f_1 + f_0^2) d\Omega = 0, \quad (\text{G.0.11b})$$

etc.

Vesicle translational velocity:

at $r = 1$:

$$O(1) : \frac{4}{3}\pi \mathbf{U}_0 = \int_{\mathcal{S}_\Omega} \hat{\mathbf{x}} [\hat{\mathbf{x}} \cdot (\mathbf{u}'_0 + \mathbf{u}^\infty)] d\Omega = \int_{\mathcal{S}_\Omega} \hat{\mathbf{x}} (\hat{\mathbf{x}} \cdot \check{\mathbf{u}}'_0) d\Omega, \quad (\text{G.0.12a})$$

$$\begin{aligned} O(\Delta^{\frac{1}{2}}) : & \frac{4}{3}\pi \mathbf{U}_1 = \int_{\mathcal{S}_\Omega} \hat{\mathbf{x}} \left(\hat{\mathbf{x}} \cdot \mathbf{u}'_1 + f_0 \frac{\partial}{\partial r} [\hat{\mathbf{x}} \cdot (\mathbf{u}'_0 + \mathbf{u}^\infty)] - (\nabla f_0) \cdot (\mathbf{u}'_0 + \mathbf{u}^\infty) \right) d\Omega \\ & = \int_{\mathcal{S}_\Omega} \hat{\mathbf{x}} \left(\hat{\mathbf{x}} \cdot \check{\mathbf{u}}'_1 + f_0 \frac{\partial}{\partial r} (\hat{\mathbf{x}} \cdot \check{\mathbf{u}}'_0) - (\nabla f_0) \cdot \check{\mathbf{u}}'_0 \right) d\Omega, \end{aligned} \quad (\text{G.0.12b})$$

etc.

Vesicle rotational velocity:

³This condition has been simplified by use of the volume constraint (G.0.11).

at $r = 1$:

$$O(1) : \quad \frac{4}{3}\pi\Omega_0 = \int_{\mathcal{S}_\Omega} \frac{1}{2}[\hat{\mathbf{x}} \times (\mathbf{u}'_0 + \mathbf{u}^\infty)] d\Omega = \int_{\mathcal{S}_\Omega} \frac{1}{2}(\hat{\mathbf{x}} \times \check{\mathbf{u}}'_0) d\Omega, \quad (G.0.13a)$$

$$\begin{aligned} O(\Delta^{\frac{1}{2}}) : \quad \frac{4}{3}\pi\Omega_1 &= \int_{\mathcal{S}_\Omega} \frac{1}{2} \left(\hat{\mathbf{x}} \times \mathbf{u}'_1 + f_0 \frac{\partial}{\partial r} [\hat{\mathbf{x}} \times (\mathbf{u}'_0 + \mathbf{u}^\infty)] - (\nabla f_0) \times (\mathbf{u}'_0 + \mathbf{u}^\infty) \right) d\Omega \\ &= \int_{\mathcal{S}_\Omega} \frac{1}{2} \left(\hat{\mathbf{x}} \times \check{\mathbf{u}}'_1 + f_0 \frac{\partial}{\partial r} (\hat{\mathbf{x}} \times \check{\mathbf{u}}'_0) - (\nabla f_0) \times \check{\mathbf{u}}'_0 \right) d\Omega, \end{aligned} \quad (G.0.13b)$$

etc.

Extra pressure drop:

$$O(1) : \quad -\Delta p_0^+ A_\times = \lim_{r \rightarrow \infty} r^2 \int_{\mathcal{S}_\Omega} \hat{\mathbf{x}} \cdot (\boldsymbol{\sigma}^\infty \cdot \mathbf{u}'_0 - \boldsymbol{\sigma}'_0 \cdot \mathbf{u}^\infty) d\Omega, \quad (G.0.14a)$$

$$O(\Delta^{\frac{1}{2}}) : \quad -\Delta p_1^+ A_\times = \lim_{r \rightarrow \infty} r^2 \int_{\mathcal{S}_\Omega} \hat{\mathbf{x}} \cdot (\boldsymbol{\sigma}^\infty \cdot \mathbf{u}'_1 - \boldsymbol{\sigma}'_1 \cdot \mathbf{u}^\infty) d\Omega, \quad (G.0.14b)$$

etc.

Bibliography

- [1] M. Abkarian, M. Faivre, R. Horton, K. Smistrup, C. A. Best-Popescu, and H. A. Stone. Cellular-scale hydrodynamics. *Biomed. Mater.*, 3(3):034011, 2008.
- [2] M. Abkarian, M. Faivre, and H. A. Stone. High-speed microfluidic differential manometer for cellular-scale hydrodynamics. *Proc. Natl. Acad. Sci. U.S.A.*, 103(3):538–542, 2006.
- [3] S. Ahmmmed, N. S. Suteria, V. Garbin, and S. A. Vanapalli. Hydrodynamic mobility of confined polymeric particles, vesicles and cancer cells in a square microchannel. *Biomicrofluidics*, 12(1):014114, 2018.
- [4] K. H. Albrecht, P. Gaehtgens, A. Pries, and M. Heuser. The Fahraeus effect in narrow capillaries (i.d. 3.3 to 11.0 μm). *Microvascular Research*, 18(1):33–47, 1979.
- [5] M. I. Angelova, S. Soléau, P. Méléard, and F. Faucon. Preparation of giant vesicles by external AC electric fields. Kinetics and applications. *Progr. Colloid. Polym. Sci.*, 89:127–131, 1992.
- [6] O. Aouane, A. Farutin, M. Thiébaud, A. Benyoussef, C. Wagner, and C. Misbah. Hydrodynamic pairing of soft particles in a confined flow. *Phys. Rev. Fluids*, 2(6):063102, 2017.
- [7] O. Aouane, M. Thiebaud, A. Benyoussef, C. Wagner, and C. Misbah. Vesicle dynamics in a confined Poiseuille Flow: from steady-state to chaos. *Phys. Rev. E*, 90(3):033011, 2014.
- [8] R. Aris. *Vectors, tensors and the basic equations of fluid mechanics*. Prentice-Hall, 1962.
- [9] G. K. Batchelor. *An Introduction to Fluid Dynamics*. Cambridge University Press, 1967.
- [10] K. Berndl, J. Käs, R. Lipowsky, E. Sackmann, and U. Seifert. Shape transformations of giant vesicles: extreme sensitivity to bilayer asymmetry. *Europhys. Lett.*, 13(7):659–664, 1990.
- [11] A. A. S. Bhagat, H. Bow, H. W. Hou, S. J. Tan, J. Han, and C. T. Lim. Microfluidics for cell separation. *Med. Biol. Eng. Comput.*, 48:999–1014, 2010.
- [12] R. B. Bird, W. E. Stewart, and E. N. Lightfoot. *Transport Phenomena*. John Wiley & Sons, second edition, 2002.

- [13] H. Brenner. Dynamics of a particle in a viscous fluid. *Chem. Eng. Sci.*, 17:435–446, 1962.
- [14] H. Brenner. Pressure drop due to the motion of neutrally buoyant particles in duct flows. *J. Fluid Mech.*, 10(4):641–660, 1970.
- [15] H. Brenner. Pressure drop due to the motion of neutrally buoyant particles in duct flows II. Spherical droplets and bubbles. *Ind. Eng. Chem. Fund.*, 10(4):537–543, 1971.
- [16] H. Brenner and J. Happel. Slow viscous flow past a sphere in a cylindrical tube. *J. Fluid Mech.*, 4(2):195–213, 1958.
- [17] F. P. Bretherton. The motion of long bubbles in tubes. *J. Fluid Mech.*, 10:166–188, 1961.
- [18] R. Bruinsma. Rheology and shape transitions of vesicles under capillary flow. *Physica A*, 234(1–2):249–270, 1996.
- [19] E. Buckingham. On physically similar systems; illustrations of the use of dimensional equations. *Phys. Rev.*, 4(4):345–376, 1914.
- [20] P. M. Bungay and H. Brenner. The motion of a closely-fitting sphere in a fluid-filled tube. *Int. J. Multiphase Flow*, 1(1):25–56, 1973.
- [21] T. J. Byers and D. Branton. Visualization of the protein associations in the erythrocyte membrane skeleton. *Proc. Natl. Acad. Sci. U.S.A.*, 82(18):6153–6157, 1985.
- [22] P. B. Canham and A. C. Burton. Distribution of size and shape in populations of normal human red cells. *Circulation Research*, 22(3):405–422, 1968.
- [23] I. Cantat. Liquid meniscus friction on a wet plate: bubbles, lamellae, and foams. *Phys. Fluids*, 25(3):031303, 2013.
- [24] E. Cerda, K. Ravi-Chandar, and L. Mahadevan. Thin films: wrinkling of an elastic sheet under tension. *Nature*, 419(6907):579–580, 2002.
- [25] T. C. Chen and R. Skalak. Stokes flow in a cylindrical tube containing a line of spheroidal particles. *Appl. Sci. Res.*, 22(1):403–441, 1970.
- [26] Z. Chen and R. P. Rand. The influence of cholesterol on phospholipid membrane curvature and bending elasticity. *Biophys. J.*, 73(1):267–276, 1997.
- [27] G. Coupier, A. Farutin, C. Minetti, T. Podgorski, and C. Misbah. Shape diagram of vesicles in Poiseuille flow. *Phys. Rev. Lett.*, 108(1):178106, 2012.
- [28] G. Coupier, B. Kaoui, T. Podgorski, and C. Misbah. Noninertial lateral migration of vesicles in bounded Poiseuille flow. *Phys. Fluids*, 20(1):1702, 2008.

- [29] J. B. Dahl, V. Narsimhan, B. Gouveia, S. Kumar, E. S. G. Shaqfeh, and S. Muller. Experimental observation of the asymmetric instability of intermediate-reduced-volume vesicles in extensional flow. *Soft Matter*, 12:3787–3796, 2016.
- [30] G. Danker, T. Biben, T. Podgorski, C. Verdier, and C. Misbah. Dynamics and rheology of a dilute suspension of vesicles: higher-order theory. *Phys. Rev. E*, 76(4):041905, 2007.
- [31] G. Danker and C. Misbah. Rheology of a dilute suspension of vesicles. *Phys. Rev. Lett.*, 98(8):088104, 2007.
- [32] G. Danker, P. M. Vlahovska, and C. Misbah. Vesicles in Poiseuille flow. *Phys. Rev. Lett.*, 102(14):148102, 2009.
- [33] Z. Derzko and K. Jacobson. Comparative lateral diffusion of fluorescent lipid analogs in phospholipid multibilayers. *Biochemistry*, 19(26):6050–6057, 1980.
- [34] J. Deschamps, V. Kantsler, and V. Steinberg. Phase diagram of single vesicle dynamical states in shear flow. *Phys. Rev. Lett.*, 102(11):118105, 2009.
- [35] H. N. Dixit and G. M. Homsy. The elastocapillary Landau-Levich problem. *J. Fluid Mech.*, 735:1–28, 2013.
- [36] Harish N. Dixit and G. M. Homsy. The elastic Landau-Levich problem. *J. Fluid Mech.*, 732:5–28, October 2013.
- [37] M. G. Duffy. Quadrature over a pyramid or cube of integrands with a singularity at a vertex. *SIAM J. Num. Anal.*, 19(6):1260–1262, 1982.
- [38] H. P. Duwe, H. Engelhardt, A. Zilker, and E. Sackmann. Curvature elasticity of smectic A lipid bilayers and cell plasma membranes. *Mol. Cryst. Liq. Cryst.*, 152(1):1–7, 1987.
- [39] J. Einarsson, M. Yang, and E. S. G. Shaqfeh. Einstein viscosity with fluid elasticity. *J. Chem. Phys.*, 3(1):013301, 2018.
- [40] U. Essmann, L. Perera, M. L. Berkowitz, T. Darden, H. Lee, and L. G. Pedersen. A smooth particle mesh Ewald method. *J. Chem. Phys.*, 103(1):8577–8593, 1995.
- [41] E. Evans and D. Needham. Giant vesicle bilayers composed of mixtures of lipids, cholesterol and polypeptides. Thermomechanical and (mutual) adherence properties. *Faraday Disc. Chem. Soc.*, 81:267, 1986.
- [42] E. Evans and D. Needham. Physical properties of surfactant bilayer membranes: thermal transitions, elasticity, rigidity, cohesion and colloidal interactions. *J. Phys. Chem.*, 91(16):4219–4228, 1987.

- [43] E. Evans and W. Rawicz. Entropy-driven tension and bending elasticity in condensed-fluid membranes. *Phys. Rev. Lett.*, 64(17):2094–2097, 1990.
- [44] E. Evans and A. Yeung. Hidden dynamics in rapid changes of bilayer shape. *Chem. Phys. Lipids.*, 73:39–56, 1994.
- [45] E. A. Evans and R. Waugh. Osmotic correction to elastic area compressibility measurements on red cell membrane. *Biophys. J.*, 20(3):307–313, 1977.
- [46] E. A. Evans, R. Waugh, and L. Melnik. Elastic area compressibility modulus of red cell membrane. *Biophys. J.*, 16(6):585–595, 1976.
- [47] P. P. Ewald. Die Berechnung optischer und elektrostatischer Gitterpotentiale. *Annalen der Physik*, 369(3):253–287, 1921.
- [48] A. Farutin, T. Biben, and C. Misbah. Analytical progress in the theory of vesicles under linear flow. *Phys. Rev. E*, 81(6):061904, 2010.
- [49] A. Farutin, T. Biben, and C. Misbah. 3D numerical simulations of vesicle and inextensible capsule dynamics. *J. Comp. Phys.*, 275:539–568, 2014.
- [50] A. Farutin and C. Misbah. Symmetry breaking of vesicle shapes in Poiseuille flow. *Phys. Rev. E*, 84(1):011902, 2011.
- [51] A. Farutin and C. Misbah. Squaring, parity breaking, and S tumbling of vesicles under shear flow. *Phys. Rev. Lett.*, 109(24):248106, 2012.
- [52] A. Farutin and C. Misbah. Symmetry breaking and cross-streamline migration of three-dimensional vesicles in an axial Poiseuille flow. *Phys. Rev. E*, 89(4):042709, 2014.
- [53] N. A. Frankel and A. Acrivos. The constitutive equation for a dilute emulsion. *J. Fluid Mech.*, 44(1):65–78, 1970.
- [54] J. Freund and H. Zhao. A high-resolution fast boundary-integral method for multiple interacting blood cells. In *Computational Hydrodynamics of Capsules and Biological Cells*, chapter 3, pages 71–111. CRC Press, 2010.
- [55] P. A. Frost and E. Y. Harper. An extended Padé procedure for constructing global approximations from asymptotic expansions: an explication with examples. *SIAM Review*, 18(1):62–91, 1976.
- [56] L. D. Frye and M. Edidin. The rapid intermixing of cell surface antigens after formation of mouse-human heterokaryons. *J. Cell Sci.*, 7(2):319–335, 1970.

- [57] M. B. Furman and W. L. Olbricht. Unsteady cell distributions in capillary networks. *Biotech. Prog.*, 1(1):26–32, 1985.
- [58] P. Gaehtgens, A. Pries, and K. H. Albrecht. Model experiments on the effect of bifurcations on capillary blood flow and oxygen transport. *Pflugers Arch.*, 380(2):115–120, 1979.
- [59] P. Gaehtgens, G. Will, and F. Schmidt. Comparative rheology of nucleated and non-nucleated red blood cells II. Rheological properties of avian red cells suspensions in narrow capillaries. *Pflugers Arch.*, 390(3):283–287, 1981.
- [60] H. J. Galla, W. Hartmann, U. Theilen, and E. Sackmann. On two-dimensional passive random walk in lipid bilayers and fluid pathways in biomembranes. *J. Membr. Biol.*, 48(3):215–236, 1979.
- [61] V. Giridharan, Y. Yun, P. Hajdu, L. Conforti, B. Collins, Y. Jang, and J. Sankar. Microfluidic platforms for evaluation of nanobiomaterials: a review. *J. Nanomater.*, 2012:1–14, 2012.
- [62] H. L. Goldsmith and S. G. Mason. The flow of suspensions through tubes. I. Single spheres, rods, and discs. *J. Coll. Sci.*, 17(5):448–476, 1962.
- [63] H. L. Goldsmith and R. Skalak. Hemodynamics. *Ann. Rev. Fluid Mech.*, 7(1):213–247, 1975.
- [64] G. Gregoriadis. Drug entrapment in liposomes. *F.E.B.S. Lett.*, 36(3):292–296, 1973.
- [65] G. Gregoriadis. The carrier potential of liposomes in biology and medicine (first of two parts). *N. Engl. J. Med.*, 295(13):704–710, 1976.
- [66] G. Gregoriadis and B. E. Ryman. Liposomes as carriers of enzymes or drugs: a new approach to the treatment of storage diseases. *Biochem. J.*, 124(5):58P, 1971.
- [67] D. J. Griffiths. *Introduction to Electrodynamics*. Prentice Hall, 1962.
- [68] A. Groisman, M. Enzelberger, and S. R. Quake. Microfluidic memory and control devices. *Science*, 300(5621):955–958, 2003.
- [69] A. Guckenberger, M. P. Schraml, P. G. Chen, M. Leonetti, and S. Gekle. On the bending algorithms for soft objects in flows. *Comp. Phys. Comm.*, 207:1–23, 2016.
- [70] W. L. Haberman and R. M. Sayre. Motion of rigid and fluid spheres in stationary and moving liquids inside cylindrical tubes. *David Taylor Model Basin Washington D.C.*, (DTMB-1143):381–400, 1958.
- [71] D. Halpern and T. W. Secomb. The squeezing of red blood cells through capillaries with near-minimal diameters. *J. Fluid Mech.*, 203:381–400, 1989.

- [72] J. Happel and H. Brenner. *Low Reynolds number hydrodynamics: with special applications to particulate media*. Springer, third edition, 1983.
- [73] H. Hasimoto. On the periodic fundamental solutions of the Stokes equations and their application to viscous flow past a cubic array of spheres. *J. Fluid Mech.*, 5(2):317, 1959.
- [74] W. Helfrich. Elastic properties of lipid bilayers: theory and possible experiments. *Z. Naturforsch.*, 28c(11):693–703, 1973.
- [75] G. Hetsroni, S. Haber, and E. Wacholder. The flow fields in and around a droplet moving axially within a tube. *J. Fluid Mech.*, 41:689–705, 1970.
- [76] E. J. Hinch. Hydrodynamics at low Reynolds numbers: a brief and elementary introduction. In *Disorder and Mixing*, chapter 3, pages 43–56. Springer, 1988.
- [77] E. J. Hinch. *Perturbation Methods*. Cambridge University Press, 1991.
- [78] B. P. Ho and L. G. Leal. Inertial migration of rigid spheres in two-dimensional unidirectional flows. *J. Fluid Mech.*, 65(02):365–400, 1974.
- [79] R. M. Hochmuth and S. P. Sutera. Spherical caps in low Reynolds-number tube flow. *Chem. Eng. Sci.*, 25(4):593–604, 1970.
- [80] J. N. Israelachvili. *Intermolecular and Surface Forces*. Elsevier, 3 edition, 2011.
- [81] P. J. A. Janssen, M. D. Baron, P. D. Anderson, J. Blawzdziewicz, M. Loewenberg, and E. Wanryb. Collective dynamics of confined rigid spheres and deformable drops. *Soft Matter*, 8(28):7495–7506, 2012.
- [82] J. T. Jenkins. Static equilibrium configurations of a model red blood cell. *J. Math. Biol.*, 4(2):149–169, 1977.
- [83] V. Kantsler, E. Segre, and V. Steinberg. Critical dynamics of vesicle stretching transition in elongational flow. *Phys. Rev. Lett.*, 101(4):048101, 2008.
- [84] V. Kantsler and V. Steinberg. Orientation and dynamics of a vesicle in tank-treading motion in shear flow. *Phys. Rev. Lett.*, 95(25):258101, 2005.
- [85] V. Kantsler and V. Steinberg. Transition to tumbling and two regimes of tumbling motion of a vesicle in shear flow. *Phys. Rev. Lett.*, 96(3):036001, 2006.
- [86] B. Kaoui, G. Biros, and C. Misbah. Why do red blood cells have asymmetric shapes even in a symmetric flow? *Phys. Rev. Lett.*, 103(18):188101, 2009.

- [87] B. Kaoui, G. H. Ristow, I. Cantat, C. Misbah, and W. Zimmermann. Lateral migration of a two-dimensional vesicle in unbounded Poiseuille flow. *Phys. Rev. E*, 77(2):021903, 2008.
- [88] B. Kaoui, N. Tahiri, T. Biben, H. Ez-Zahraouy, A. Benyoussef, G. Biros, and C. Misbah. Complexity of vesicle microcirculation. *Phys. Rev. E*, 84(4):277, 2011.
- [89] A. Karimi, S. Yazdi, and A. M. Ardekani. Hydrodynamic mechanisms of cell and particle trapping in microfluidics. *Biomicrofluidics*, 7(2):021501, 2013.
- [90] Z. S. Khan, N. Kamyabi, F. Hussain, and S. A. Vanapalli. Passage times and friction due to flow of confined cancer cells, drops, and deformable particles in a microfluidic channel. *Conv. Sci. Phys. Onc.*, 3(2):024001, 2017.
- [91] Z. S. Khan and S. A. Vanapalli. Probing the mechanical properties of brain cancer cells using a microfluidic cell squeezer device. *Biomicrofluidics*, 7(1):011806, 2013.
- [92] S. Kim and S. J. Karrila. *Microhydrodynamics*. Butterworth–Heinemann, 1991.
- [93] D. A. Knoll and D. E. Keys. Jacobian-free Newton-Krylov methods: a survey of approaches and applications. *J. Comp. Phys.*, 193(2):357–397, 2004.
- [94] M. Kraus, W. Wintz, U. Seifert, and R. Lipowsky. Fluid vesicles in shear flow. *Phys. Rev. Lett.*, 77(17):3685–3688, 1996.
- [95] E. Kreyszig. *Differential Geometry*. Dover, 1997.
- [96] M. Kubíček and V. Hlaváček. *Numerical Solution of Nonlinear Boundary Value Problems with Applications*. Dover, 2008.
- [97] R. Kwok and E. Evans. Thermoelasticity of large lecithin bilayer vesicles. *Biophys. J.*, 35(3):637–652, 1981.
- [98] H. Lamb. *Hydrodynamics*. Cambridge University Press, 1932.
- [99] L. Landau and B. Levich. Dragging of a liquid by a moving plate. *Acta Physicochim. (U.R.S.S.)*, 17(1–2):42–54, 1942.
- [100] D. Langbein. *Capillary Surfaces: Shape, Stability, Dynamics, in Particular Under Weightlessness*. Springer, 2002.
- [101] L. G. Leal. *Advanced Transport Phenomena: Fluid Mechanics and Convective Transport Processes*. Cambridge University Press, 2007.
- [102] V. V. Lebedev, K. S. Turitsyn, and S. S. Vergeles. Dynamics of nearly spherical vesicles in an external flow. *Phys. Rev. Lett.*, 99(21):218101, 2007.

- [103] M. J. Lighthill. Pressure-forcing of tightly fitting pellets along fluid-filled elastic tubes. *J. Fluid Mech.*, 34(1):113, 1968.
- [104] N. Liron and S. Mochon. Stokes flow for a Stokeslet between two parallel flat plates. *J. Eng. Math.*, 10:287–303, 1976.
- [105] J. R. Lister, G. G. Peng, and J. A. Neufeld. Viscous control of peeling an elastic sheet by bending and pulling. *Phys. Rev. Lett.*, 111(15):154501, 2013.
- [106] M. Loewenberg and E. J. Hinch. Numerical simulation of a concentrated emulsion in shear flow. *J. Fluid Mech.*, 321:395–419, 1996.
- [107] C. T. Loop. *Smooth Subdivision Surfaces Based on Triangles*. PhD thesis, University of Utah, 1987.
- [108] E. Lorenceau, A. S. Utada, D. R. Link, G. Cristobal, M. Joanicot, and D. A. Weitz. Generation of polymericosomes from double-emulsions. *Langmuir*, 21(20):9183–9186, 2005.
- [109] V. Luzzati and F. Husson. The structure of the liquid-crystalline phases of lipid-water systems. *J. Cell Biol.*, 12:207–219, 1962.
- [110] L. Mazutis, J. Gilbert, W. L. Ung, D. A. Weitz, A. D. Griffiths, and J. A. Heyman. Single-cell analysis and sorting using droplet-based microfluidics. *Nat. Protocols*, 8:870–891, 2013.
- [111] A. J. McConnell. *Applications of Tensor Analysis*. Dover, 1957.
- [112] C. Misbah. Vacillating breathing and tumbling of vesicles under shear flow. *Phys. Rev. Lett.*, 96(2):028104, 2006.
- [113] D. D. Morrison, J. D. Riley, and J. F. Zancanaro. Multiple shooting method for two-point boundary value problems. *Comm. ACM*, 5(12), 1962.
- [114] A. Nadim and H. A. Stone. The motion of small particles and droplets in quadratic flows. *Stud. Appl. Math.*, 85(1):53–73, 1991.
- [115] V. Narsimhan, A. P. Spann, and E. S. G. Shaqfeh. The mechanism of shape instability for a vesicle in extensional flow. *J. Fluid Mech.*, 750:144–190, 2014.
- [116] V. Narsimhan, A. P. Spann, and E. S. G. Shaqfeh. Pearling, wrinkling, and buckling of vesicles in elongational flows. *J. Fluid Mech.*, 777:1–26, 2015.
- [117] D. Needham and E. Evans. Structure and mechanical properties of giant lipid (DMPC) vesicle bilayers from 20 degrees C below to 10 degrees C above the liquid crystal-crystalline phase transition at 24 degrees C. *Biochemistry*, 27(21):8261–8269, 1988.

- [118] D. Needham and R. M. Hochmuth. Electro-mechanical permeabilization of lipid vesicles. Role of membrane tension and compressibility. *Biophys. J.*, 55(5):1001–1009, 1989.
- [119] D. Needham and R. S. Nunn. Elastic deformation and failure of lipid bilayer membranes containing cholesterol. *Biophys. J.*, 58(4):997–1009, 1990.
- [120] J. A. Nichol and O. F. Hutter. Tensile strength and dilatational elasticity of giant sarcolemmal vesicles shed from rabbit muscle. *J. Physiol.*, 493(1):187–198, 1996.
- [121] H. Noguchi and G. Gompper. Shape transitions of fluid vesicles and red blood cells in capillary flows. *Proc. Natl. Acad. Sci. U.S.A.*, 102(40):14159–14164, 2005.
- [122] M. E. O’Neill and K. Stewartson. On the slow motion of a sphere parallel to a nearby plane wall. *J. Fluid Mech.*, 27:705–724, 1967.
- [123] C. W. Park and G. M. Homsy. Two-phase displacement in Hele Shaw cells: theory. *J. Fluid Mech.*, 139:291–308, 1984.
- [124] A. Pommella, N. J. Brooks, J. M. Seddon, and V. Garbin. Selective flow-induced vesicle rupture to sort by membrane mechanical properties. *Sci. Rep.*, 5(1):13163, 2015.
- [125] C. Pozrikidis. *Boundary integral and singularity methods for linearized viscous flow*. Cambridge University Press, 1992.
- [126] C. Pozrikidis. Axisymmetric motion of a file of red blood cells through capillaries. *Phys. Fluids*, 17(3):1503, 2005.
- [127] W. H. Press. *Numerical recipes: the art of scientific computing*. Cambridge University Press, third edition, 2007.
- [128] A. R. Pries, D. Neuhaus, and P. Gaehtgens. Blood viscosity in tube flow: dependence on diameter and hematocrit. *Am. J. Physiol.*, 263(6):H1770–H1778, 1992.
- [129] C. Quéguiner and D. Barthès-Biesel. Axisymmetric motion of capsules through cylindrical channels. *J. Fluid Mech.*, 348(0):349–376, 1997.
- [130] J. Ratulowski and H. C. Chang. Transport of gas bubbles in capillaries. *Phys. Fluids A*, 1(1):1642–1655, 1989.
- [131] W. Rawicz, K. C. Olbrich, T. McIntosh, D. Needham, and E. Evans. Effect of chain length and unsaturation on elasticity of lipid bilayers. *Biophys. J.*, 79(1):328–339, 2000.
- [132] G. Ryskin and L. G. Leal. Numerical solution of free-boundary problems in fluid mechanics. Part 1. The finite-difference technique. *J. Fluid Mech.*, 148:1–17, 1984.

- [133] P G Saffman and M Delbrück. Brownian motion in biological membranes. *Proc. Natl. Acad. Sci. U.S.A.*, 72(8):3111–3113, 1975.
- [134] D. Saintillan, E. Darve, and E. S. G. Shaqfeh. A smooth particle-mesh Ewald algorithm for Stokes suspension simulations: the sedimentation of fibers. *Phys. Fluids*, 17(3):3301, 2005.
- [135] T. Savin, M. M. Bandi, and L. Mahadevan. Pressure-driven occlusive flow of a confined red blood cell. *Soft Matter*, 12(2):562–573, 2016.
- [136] M. B. Schneider, J. T. Jenkins, and W. W. Webb. Thermal fluctuations of large cylindrical phospholipid vesicles. *Biophys. J.*, 45(5):891–899, 1984.
- [137] L. W. Schwartz, H. M. Princen, and A. D. Kiss. On the motion of bubbles in capillary tubes. *J. Fluid Mech.*, 172:259–275, 1986.
- [138] T. W. Secomb. Interaction between bending and tension forces in bilayer membranes. *Biophys. J.*, 54(4):743–746, 1988.
- [139] T. W. Secomb, R. Skalak, N. Oozkaya, and J. F. Gross. Flow of axisymmetric red blood cells in narrow capillaries. *J. Fluid Mech.*, 163:405–423, 1986.
- [140] U. Seifert. Configurations of fluid membranes and vesicles. *Advances in Physics*, 46(1):13–137, 1997.
- [141] U. Seifert, K. Berndl, and R. Lipowsky. Shape transformations of vesicles: phase diagram for spontaneous- curvature and bilayer-coupling models. *Phys. Rev. A*, 44(2):1182–1202, 1991.
- [142] M. Seth, A. Ramachandran, and L. G. Leal. Direct measurements of effect of counterion concentration on mechanical properties of cationic vesicles. *Langmuir*, 29(46):14057–14065, 2013.
- [143] A. Sharei, J. Zoldan, A. Adamo, W. Y. Sim, N. Cho, E. Jackson, S. Mao, S. Schneider, M. J. Han, A. Lytton-Jean, P. A. Basto, S. Jhunjhunwala, J. Lee, D. A. Heller, J. W. Kang, G. C. Hartouarios, K. S. Kim, D. G. Anderson, R. Langer, and K. F. Jensen. A vector-free microfluidic platform for intracellular delivery. *Proc. Natl. Acad. Sci. U.S.A.*, 110(6):2082–2087, 2013.
- [144] S. D. Shoemaker and T. K. Vanderlick. Intramembrane electrostatic interactions destabilize lipid vesicles. *Biophys. J.*, 83(4):2007–2014, 2002.
- [145] H. C. Shum, D. Lee, I. Yoon, T. Kodger, and D. A. Weitz. Double emulsion templated monodisperse phospholipid vesicles. *Langmuir*, 24(15):7651–7653, 2008.

- [146] A. Sierou and J. F. Brady. Accelerated Stokesian dynamics simulations. *J. Fluid Mech.*, 448(0):115–146, 2001.
- [147] S. J. Singer and G. L. Nicolson. The fluid mosaic model of the structure of cell membranes. *Science*, 175(4023):720–731, 1972.
- [148] R. Skalak, A. Tozeren, R. P. Zarda, and S. Chien. Strain energy function of red blood cell membranes. *Biophys. J.*, 13(3):245–264, 1973.
- [149] J. M. Skotheim and L. Mahadevan. Soft lubrication: the elastohydrodynamics of nonconforming and conforming contacts. *Phys. Fluids*, 17(9):092101, 2005.
- [150] J. Song and R. E. Waugh. Bilayer membrane bending stiffness by tether formation from mixed PC-PS lipid vesicles. *J. Biomech. Eng.*, 112(3):235–240, 1990.
- [151] A. P. Spann, H. Zhao, and E. S. G. Shaqfeh. Loop subdivision surface boundary integral method simulations of vesicles at low reduced volume ratio in shear and extensional flow. *Phys. Fluids*, 26:031902, 2014.
- [152] J. E. Spjut. *Trapping, Deformation, and Dynamics of Phospholipid Vesicles*. PhD thesis, University of California, Berkeley, 2010.
- [153] T. M. Squires and S. R. Quake. Microfluidics: Fluid physics at the nanoliter scale. *Rev. Mod. Phys.*, 77(3):977–1026, 2005.
- [154] J. Stoer and R. Bulirsch. *Introduction to Numerical Analysis*, volume 12 of *Texts in Applied Mathematics*. Springer, third edition, 2002.
- [155] S. P. Sutera, V. Sephardi, P. A. Croce, and R. M. Hochmuth. Capillary blood flow II. Deformable model cells in tube flow. *Microvasc. Res.*, 2:420–433, 1970.
- [156] S. P. Sutera and R. Skalak. The history of Poiseuille’s law. *Ann. Rev. Fluid Mech.*, 25(1):1–20, 1993.
- [157] M. Thiebaud and C. Misbah. Rheology of a vesicle suspension with finite concentration: a numerical study. *Phys. Rev. E*, 88(6):062707, 2013.
- [158] G. Tomaiuolo, L. Lanotte, G. Ghigliotti, C. Misbah, and S. Guido. Red blood cell clustering in Poiseuille microcapillary flow. *Phys. Fluids*, 24(5):051903, 2012.
- [159] G. Tomaiuolo, M. Simeone, V. Martinelli, B. Rotoli, and S. Guido. Red blood cell deformation in microconfined flow. *Soft Matter*, 5(19):3736, 2009.
- [160] A. Y. Toukmaji and J. A. Jr. Board. Ewald summation techniques in perspective: a survey. *Comp. Phys. Comm.*, 95(2):73–92, 1996.

- [161] H. Tözeren. Boundary integral equation method for some Stokes problems. *Int. J. Num. Meth. Fluids*, 4(2):159–170, 1984.
- [162] T. Tran-Cong and J. R. Blake. General solutions of the Stokes' flow equations. *J. Math. Anal. Appl.*, 90(1):72–84, 1982.
- [163] R. Trozzo, G. Boedec, M. Leonetti, and M. Jaeger. Axisymmetric boundary element method for vesicles in a capillary. *J. Comp. Phys.*, 289:62–82, 2015.
- [164] D. L. Tullock, N. Phan Thien, and A. L. Graham. Boundary element simulations of spheres settling in circular, square and triangular conduits. *Rheol. Acta*, 31(2):139–150, 1992.
- [165] A. S. Utada, E. Lorenceau, D. R. Link, P. D. Kaplan, H. A. Stone, and D. A. Weitz. Monodisperse double emulsions generated from a microcapillary device. *Science*, 308:537–541, 2005.
- [166] M. van Dyke. *Perturbation Methods in Fluid Mechanics*. Parabolic Press, 1975.
- [167] S. A. Vanapalli, A. G. Banpurkar, D. van den Ende, M. H. G. Duits, and F. Mugele. Hydrodynamic resistance of single confined moving drops in rectangular microchannels. *Lab on a Chip*, 9(7):982–990, 2009.
- [168] S. A. Vanapalli, D. Van den Ende, M. H. G. Duits, and F. Mugele. Scaling of interface displacement in a microfluidic comparator. *Appl. Phys. Lett.*, 90(1):114109, 2007.
- [169] V. Vitkova, M. Mader, and T. Podgorski. Deformation of vesicles flowing through capillaries. *Europhys. Lett.*, 68(3):398–404, 2004.
- [170] P. M. Vlahovska and Ruben S. Gracia. Dynamics of a viscous vesicle in linear flows. *Phys. Rev. E*, 75(1):016313, 2007.
- [171] S. M. Vuong and S. L. Anna. Tuning bubbly structures in microchannels. *Biomicrofluidics*, 6(2):022004, 2012.
- [172] S. Wakiya. Viscous Flows past a spheroid. *J. Phys. Soc. Jpn.*, 12(10):1130–1141, 1957.
- [173] H. Wang and R. Skalak. Viscous flow in a cylindrical tube containing a line of spherical particles. *J. Fluid Mech.*, 38:75–96, 1969.
- [174] F. M. White. *Viscous Fluid Flow*. McGraw-Hill, second edition, 1991.
- [175] H. Wong, S. Morris, and C. J. Radke. Three-dimensional menisci in polygonal capillaries. *J. Coll. Int. Sci.*, 148(2):317–336, 1992.
- [176] H. Wong, C. J. Radke, and S. Morris. The motion of long bubbles in polygonal capillaries. Part 1. Thin films. *Journal of Fluid Mechanics*, 292:71–94, 1995.

- [177] H. Wong, C. J. Radke, and S. Morris. The motion of long bubbles in polygonal capillaries. Part 2. Drag, fluid pressure and fluid flow. *J. Fluid Mech.*, 292:95–110, 1995.
- [178] Y. Xia and G. M. Whitesides. Soft lithography. *Ann. Rev. Mat. Sci.*, 28:153–184, 1998.
- [179] G. K. Youngren and A. Acrivos. Stokes flow past a particle of arbitrary shape: a numerical method of solution. *J. Fluid Mech.*, 69(2):377–403, 1975.
- [180] H. Zhao, A. H. G. Isfahani, L. N. Olson, and J. B. Freund. A spectral boundary integral method for flowing blood cells. *J. Comp. Phys.*, 229(1):3726–3744, 2010.
- [181] H. Zhao and E. S. G. Shaqfeh. The dynamics of a vesicle in simple shear flow. *J. Fluid Mech.*, 674:578–604, 2011.
- [182] H. Zhao and E. S. G. Shaqfeh. The dynamics of a non-dilute vesicle suspension in a simple shear flow. *J. Fluid Mech.*, 725:709–731, 2013.
- [183] H. Zhao and E. S. G. Shaqfeh. The shape stability of a lipid vesicle in a uniaxial extensional flow. *J. Fluid Mech.*, 719:345–361, 2013.
- [184] H. Zhao, E. S. G. Shaqfeh, and V. Narsimhan. Shear-induced particle migration and marginalization in a cellular suspension. *Phys. Fluids*, 24(1):1902, 2012.
- [185] H. Zhao, A. P. Spann, and E. S. G. Shaqfeh. The dynamics of a vesicle in a wall-bound shear flow. *Phys. Fluids*, 23:121901, 2011.
- [186] D. V. Zhelev, D. Needham, and R. M. Hochmuth. A novel micropipet method for measuring the bending modulus of vesicle membranes. *Biophys. J.*, 67(2):720–727, 1994.
- [187] O. Y. Zhong-can and W. Helfrich. Bending energy of vesicle membranes: General expressions for the first, second, and third variation of the shape energy and applications to spheres and cylinders. *Phys. Rev. A*, 39(10):5280–5288, 1989.
- [188] R. Zilionis, J. Nainys, A. Veres, V. Savova, D. Zemmour, A. M. Klein, and L. Mazutis. Single-cell barcoding and sequencing using droplet microfluidics. *Nat. Protoc.*, 12(1):44, 2017.